1997

Technical

Digest Series

Volume 17

Bragg Gratin Photosensitivity, and Poling in Glass Fibers and Waveguides: Applications and Fundamentals

October 26–28, 1997

Williamsburg Marriott
Williamsburg, Virginia

Postconference Edition

Sponsored by
Optical Society of America
in cooperation with
American Ceramic Society

OSA®
Optical Society of America

REPORT DOCUMENTATION PA

AFRL-SR-BL-TR-98-

0494

98

data sources, aspect of this 1215 Jefferson

1. AGENCY USE ONLY (Leave blank)	2. REPORT DATE	Final	03/01/97 - 02/28/98
	May 26, 1998		

4. TITLE AND SUBTITLE
Organization of the 1997 Photonic Science Topical Meetings

5. FUNDING NUMBERS
F49620-97-1-0166
Tops Volume XIV
Source VII
Tops volume XIII
Volume 9

6. AUTHOR(S)
Stephen D. Fantone

7. PERFORMING ORGANIZATION NAME(S) AND ADDRESS(ES)
Optical Society of America
2010 Massachusetts Ave. NW
Washington, DC 20036

8. PERFORMING ORGANIZATION REPORT NUMBER
Volume 17

9. SPONSORING/MONITORING AGENCY NAME(S) AND ADDRESS(ES)
AFOSR/NE
110 Duncan Ave. Room B115
Bolling AFB, DC 20332-8080

10. SPONSORING/MONITORING AGENCY REPORT NUMBER

11. SUPPLEMENTARY NOTES

12a. DISTRIBUTION/AVAILABILITY STATEMENT
Approved for public release
Distribution unlimited

12b. DISTRIBUTION CODE

13. ABSTRACT *(Maximum 200 words)*

The OSA topical meetings that received support under this grant provided a forum for reseracners in various specialty areas to meet and share ideas and technology in their fields.

Follcwing are the meetings that were supported by this grant:

--Optics in Computing-- topics for discussion included optical interconnections within electronic computers, system demonstrations of digital optical computing optical neural networks, optical signal processing and novel optical processing architectures, etc.
--Spatial Light Modulators -- this meeting concentrated on material and device research and development, novel system applications and their requirements on SLMs, and on future directions.
--Ultrafast Electronics and Optoelectronics -- this meeting explored the advances in high speed phenomean in the areas of optics, optoelectronics, and electronics.
Other meetings were in the areas of glass fibers and biomedical optics

14. SUBJECT TERMS

15. NUMBER OF PAGES

16. PRICE CODE

17. SECURITY CLASSIFICATION OF REPORT	18. SECURITY CLASSIFICATION OF THIS PAGE	19. SECURITY CLASSIFICATION OF ABSTRACT	20. LIMITATION OF ABSTRACT
Unclassified	Unclassified	Unclassified	UL

Bragg Gratings, Photosensitivity, and Poling in Glass Fibers and Waveguides: Applications and Fundamentals

Technical Digest

October 26–28, 1997

Williamsburg Marriott
Williamsburg, Virginia

Collocated with
12th International Conference on Optical Fiber Sensors
Glass and Optical Materials Division (GOMD) Meeting

Postconference Edition

Sponsored by
Optical Society of America
in cooperation with
American Ceramic Society

Optical Society of America
2010 Massachusetts Avenue, NW
Washington, DC 20036-1023

OSA.

Articles in this publication may be cited in other publications. To facilitate access to the original publication source, the following form for the citation is suggested:

Name of Author(s), "Title of Paper," in Bragg Gratings, Photosensitivity, and Poling in Glass Fibers and Waveguides: Applications and Fundamentals, Vol. 17, OSA Technical Digest Series (Optical Society of America, Washington DC, 1997), pp. xx-xx.

Optical Society of America

ISBN

Conference Edition	1-55752-516-1
Postconference Edition	1-55752-517-X
1997 Technical Digest Series	1-55752-485-8

Library of Congress Catalogue Card Number

Conference Edition	97-68775
Postconference Edition	97-68776

Printed in the U.S.A.

Contents

Technical Program Committee

Joe Friebele, *U.S. Naval Research Laboratory, General Chair*
Philip Russell, *University of Bath, U.K., General Chair*
Paul Lemaire, *Lucent Technologies, Specialty Fiber Devices, Program Chair*

Applications

Chair: Gary Ball, *Uniphase Telecom Products*
Jean Luc Archambault, *Ciena Corporation*
Vincent Handerek, *King's College, U.K.*
Ken Hill, *Communications Research Center, Canada*
Alan Kersey, *CiDRA Corporation, LIAISON to OFS*
Robert Lieberman, *Physical Optics Corporation*
Graeme Maxwell, *BT Labs, U.K.*
Lawrence Reekie, *University of Southampton, U.K.*
Rene Paul Salathe, *Swiss Federal Institute of Technology, Switzerland*
Ashish Vengsarkar, *Bell Labs, Lucent Technologies*

Gratings

Chair: François Ouellette, *Kromafibre Corporation, Canada*
Charles Askins, *U.S. Naval Research Laboratory*
Ian Bennion, *Aston University, U.K.*
Kevin Byron, *Bell-Northern Research, U.K.*
Marc Douay, *University Science and Technology Lille, France*
Turan Erdogan, *University of Rochester*
Gerry Meltz, *OFT Associates*
Pierre Sansonetti, *Alcatel, France*

Fundamentals

Co-chair: David Griscom, *U.S. Naval Research Laboratory*
Co-chair: Susan Houde-Walter, *University of Rochester*
Jacques Albert, *Communications Research Center, Canada*
Hideo Hosono, *Tokyo Institute of Technology, Japan*
Hiroaki Imai, *Keio University, Japan*
Ulf Osterberg, *Dartmouth University*
Bertrand Poumellec, *U. de Paris-Sud, France*
Krishnan Raghavachari, *Bell Labs, Lucent Technologies*
Alexey Rybaltovsky, *Moscow State University, Russia*
Anatoly Trukhin, *University of Latvia, Latvia*

Poling/SHG

Chair: R. Stolen, *AT&T Laboratories*
Steven Brueck, *University of New Mexico*
Simon Fleming, *University of Sydney, Australia*
Raman Kashyap, *BT Labs, U.K.*
Denise Krol, *Stanford University*
Walter Margulis, *PCU-Rio, Brazil*
Jean Michel Nunzi, *Centre d'etudes Nucleaires de Saclay, France*
Hiromichi Takebe, *Kyushu University, Japan*

Agenda

Sunday
October 26, 1997

Auditorium

8:20am–10:30am
JSuA ■ Joint Plenary Session
Paul Lemaire, *Bell Labs/Lucent Technologies, Presider*
Susan Houde-Walter, *University of Rochester, Presider*

8:20am–8:30am
Opening Remarks

8:30am (Plenary)
JSuA1 ■ The nature of optically active defect centeres in vitreous silicon dioxide, Linards Skuja, *Univ. Latvia, Latvia.* The optical absorption and luminescence bands of defects in glassy silicon dioxide and the presently advanced structural models for the respective point defects are reviewed. **(p. 2)**

9:10am (Plenary)
JSuA2 ■ What can topological models tell us about glass structure and properties?, Linn W. Hobbs, *Massachusetts Institute of Technology.* Topological rules based on crystalline assemblies can be used to assemble models for non-crystalline network structures, such as silicas, using only local information. **(p. 5)**

9:50am (Plenary)
JSuA3 ■ Fiber grating devices for telecommunications applications, P. Sansonetti, *Alcatel Telecom Research, France.* This paper presents the main application of fiber grating devices in photonics networks. **(p. 8)**

Lobby

10:30am–11:00am
Coffee Break

Auditorium

11:00am–12:30pm
BSuB ■ Grating Devices I
Francois Ouellette, *Kromafibre Corporation, Canada, Presider*

11:00am (Invited)
BSuB1 ■ Long-period fiber gratings, Ashish M. Vengsarkar, *Bell Laboratories, Lucent Technologies.* We will highlight key spectral and thermal properties of long-period gratings and present some of the latest device and system results accomplished in the area of broadband amplifiers and high-power fiber lasers. **(p. 12)**

11:30am
BSuB2 ■ Long-period fiber-grating devices based on leaky cladding mode coupling, D.B. Stegall, T. Erdogan, *Univ. Rochester.* The propagation and grating coupling of leaky cladding modes in a fiber surrounded by a high refractive index are investigated for all-fiber device applications. **(p. 16)**

11:45am
BSuB3 ■ Polarization dependence of photoinduced birefringence and its application to fabrication of tailored polarization filters, R. Feced, S.E. Kanellopoulos, R. Griffin, V.A. Handerek, *King's College London, U.K.* The polarization dependence of photoinduced birefringence in elliptical-core fibers is studied and a technique for fabrication of polarization rocking filters with tailored response is demonstrated. **(p. 19)**

12:00m
BSuB4 ■ Polarization-independent strong Bragg gratings in planar lightwave circuits from ArF laser irradiation, J. Albert, F. Bilodeau, D.C. Johnson, K.O. Hill, S.J. Mihailov, D. Stryckman, *Communications Research Centre, Canada;* T. Kitagawa, *NTT Optoelectronics Laboratories, Japan;* Y. Hibino, *Photonic Integration Research Inc.* Bragg gratings with 10^{-3} index modulation and identical spectral responses in TE and TM polarization are reported in standard germanium-doped silica waveguides without hydrogen loading. Polarization independence is achieved through a UV-induced birefringence of 2×10^{-4}. **(p. 22)**

12:15pm
BSuB5 ■ Novel liquid and liquid-crystal cored fiber Bragg gratings, Raman Kashyap, Doug L. Williams, Ray P. Smith, *BT Laboratories, U.K.* Fiber Bragg gratings at 1550 nm are demonstrated in liquid- and liquid-crystal cored, boron-germanium co-doped inner-cladding silica capillary single-mode fiber. **(p. 25)**

12:30pm–2:00pm
Lunch Break

Auditorium

2:00pm–3:30pm

BSuC ■ Grating Devices II

Gerry Meltz, *OFT Associates, Presider*

2:00pm (Invited)

BSuC1 ■ Bragg gratings in telecommunications networks, E. Delevaque, B. Loisel, J.F. Bayon, N. Devoldere, H. Poignant, D. Bosc, *France Telecom, France.* Photoinscription of Bragg gratings within optical waveguides has been shown as a promising technology in the optical telecommunications field. Many applications have already been demonstrated in transport, local or access networks. The robustness, stability and flexibility that photoimprinted components offer, insure a fast widespread of their use in near close future telecommunications networks. **(p. 30)**

2:30pm

BSuC2 ■ Optical space domain reflectometry for determination of strength and chirp distribution along optical fiber gratings, Ernst Brinkmeyer, Gunnar Stolze, Dietmar Johlen, *TU Hamburg-Harburg, Germany.* A method is proposed and tested for direct local readout of the complex coupling coefficient kappa(z) along grating structures of arbitrary strength and chirp. **(p. 33)**

2:45pm

BSuC3 ■ New interferometer for complete design of UV-written fiber Bragg gratings, P.-Y. Fonjallaz, B. Sahlgren, B. Grennberg, R. Stubbe, *Institute of Optical Research, Sweden.* A new interferometer has been developed to easily modify the period of UV laser interference fringes used to fabricate in-fiber Bragg gratings. **(p. 36)**

3:00pm

BSuC4 ■ Short-wavelength, transmission-loss suppression in fiber Bragg gratings, Mikhail N. Zervas, Morten Ibsen, Richard I. Laming, *Univ. Southampton, U.K.* Short-wavelength transmission losses in Bragg gratings practically can be eliminated by damping the resonant excitation of the cladding modes. By applying a thin lossy layer on the fiber cladding surface, a reduction of transmission losses of about 12 dB was achieved. **(p. 39)**

3:15pm

BSuC5 ■ Nonreflecting narrow-band fiber optical Fabry–Perot transmission filter, Dietmar Johlen, Peter Klose, Andreas Ewald, Ernst Brinkmeyer, *Technische Univ. Hamburg-Harburg, Germany.* A pair of tilted fiber Bragg gratings in a two-mode section of an elsewhere single-mode fiber forms a nonreflecting narrowband Fabry–Perot transmission filter. **(p. 42)**

Lobby

3:30pm–4:00pm

Refreshment Break

Auditorium

4:00pm–5:30pm

BSuD ■ Grating Stability and Reliability

Turan Erdogan, *University of Rochester, Presider*

4:00pm (Invited)

BSuD1 ■ Mechanical reliability of UV irradiated fibers: application to Bragg grating fabrication, H.G. Limberger, D. Varelas, R.P. Salathé, *Swiss Federal Institute of Technology, Switzerland.* Fiber gratings irradiated by CW-laser show a breaking strength and a lifetime performance similar to that of pristine fiber, in contrast to pulsed KrF-laser irradiation. **(p. 46)**

4:30pm

BSuD2 ■ Annealing of long period gratings in standard hydrogen-loaded fiber, F. Bakhti, J. Larrey, P. Sansonetti, *Alcatel Alsthom Recherche, France.* We have conducted a study on annealing of long period gratings UV-written in hydrogen-loaded standard fiber at different temperatures during hundreds of hours. **(p. 49)**

4:45pm

BSuD3 ■ Reliability predictions on fiber gratings through alternate methods, Sriraman Kannan, Paul J. Lemaire, Jerry Guo, Michael J. LuValle, *Lucent Technologies, Bell Labs Innovations.* Principles behind the methods to predict fiber grating reliability are discussed and alternate techniques are compared. Considerations in the decay analysis of gratings with simple and complex refractive index profiles are presented. **(p. 52)**

5:00pm

BSuD4 ■ Impact of hydrogen in-fiber and out-fiber diffusion on central wavelength of UV-written long period grating, F. Bakhti, J. Larrey, P. Sansonetti, *Alcatel Alsthom Recherche, France;* B. Poumellec, *CNRS, France.* We present both theoretical and experimental studies on the impact of hydrogen in-fiber and out-fiber diffusion on long period gratings written in standard hydrogen loaded fibers. **(p. 55)**

5:15pm

BSuD5 ■ A novel approach to fabricate high-temperature resistant fiber Bragg gratings, Michael A. Fokine, Bengt E. Sahlgren, Raoul Stubbe, *Institute of Optical Research, Sweden.* A method to fabricate high-temperature resistant Bragg gratings is presented in which the refractive index change is believed to be caused by redistribution of dopants. **(p. 58)**

Adams Room

5:30pm–7:00pm

JSuE ■ Linear and Nonlinear Optical Phenomena in Glass GOMD/BGPP Joint Poster Session

(NOTE: Abstracts for Joint Poster Session are available in the GOMD abstract book and the BGPP Technical Digest.)

JSuE1 ■ 270 nm absorption and 432 nm luminescence bands in doped silica glasses, B. Poumellec, *Univ. Paris Sud, France;* V.M. Mashinsky, *General Physics Institut, Russia.* **(p. 62)**

JSuE2 ■ UV-induced reaction of H_2 with the core of germanosilicate and aluminosilicate fiber preforms, Caroline Dalle, Patrick Cordier, Christophe Depecker, Pascal Bernage, Marc Douay, Pierre Niay, *Univ. Sciences et Technologies de Lille, France;* Jean-François Bayon, *France Telecom, France;* Liang Dong, *Univ. Southampton, U.K.* **(p. 65)**

JSuE3 ■ Effects of molecular hydrogen on low-intensity UV photochemistry of germanosilicate glasses, V.N. Bagratashvili, S.I. Tsypina, *Russian Academy of Sciences, russia;* P.V. Chernov, A.O. Rybaltovskii, Yu.V. Zavorotny, *Moscow State Univ., Russia;* L. Dong, *Univ. Southampton, U.K.* **(p. 68)**

JSuE4 ■ The potential of plasmachemical technology for fabrication of silica-based photosensitive optical fibers, Konstantin Golant, E.M. Dianov, *Fiber Optics Research Center, Russia.* **(p. 71)**

JSuE5 ■ Direct characterization of ultraviolet-light-induced refractive index structures by scanning near-field optical microscopy, M. Svalgaard, S. Madsen, J.M. Hvam, M. Kristensen, *Technical Univ. Denmark, Denmark.* **(p. 74)**

JSuE6 ■ Permanent refractive-index changes in pure GeO_2 glass slabs induced by irradiation with below-gap light, Yuichi Watanabe, Hiroyuki Moriwaki, Genjiro Furuhashi, *Science Univ. Tokyo, Japan;* Junji Nishii, *Osaka National Research Institute, Japan;* Hideo Hosono, Hiroshi Kawazoe, *Tokyo Institute of Technology, Japan.* **(p. 77)**

JSuE7 ■ Defect population in Ge doped silica studied by fluorescence spectroscopy, B. Poumellec, H. Cens, *Thermodynamique et Physico-Chimie des Matériaux, France;* A. Trukhin, *Univ. Latvia, Latvia;* J.C. Krupa, *Institut de Physique Nucléaire, France;* B. Leconte, *Univ. des Sciences et Techniques de Lille, France;* M. Bubnov, *Fiber Optics Research Center at General Physics Inst., Russia.* **(p. 80)**

JSuE8 ■ The role of extrinsic species on the nonlinear absorption of bulk and thin film sulfide glasses, T. Cardinal, K. Richardson, H. Shin, G. Stegeman, L. Glebov, *CREOL, Univ. Central Florida;* J. Viens, A. Villeneuve, *Univ. Laval, Canada* **(p. 83)**

JSuE9 ■ Formation and photosensitivity of defects in Se implanted silica, R. Magruder, III, *Belmont Univ.;* R. Weeks, *Vanderbilt Univ.;* R. Zuhr, *Oak Ridge National Laboratory.* **(p. 83)**

JSuE10 ■ Refractive index dispersion of gallium lanthanum sulfide and oxysulfide glasses, H. Takebe, H. Yayama, S. Fujino, K. Morinaga, *Kyushu Univ., Japan;* D. Hewak, *Univ. Southampton, U.K.* **(p. 83)**

JSuE11 ■ Volume grating recording in fluorinated silicate glasses, L. Glebov, L. Glebova, M. Moharam, K. Richardson, V. Smirnov, *Univ. Central Florida.* **(p. 83)**

JSuE12 ■ Bragg gratings inscription in rare earth doped fluoride glasses, F. Smektala, R. Sramek, J. Lucas, *Univ. de Rennes, France;* W. Xie, P. Bernage, P. Niay, *Univ. de Lille, France.* **(p. 83)**

JSuE13 ■ Comparing the effect for second harmonic generation by electron beam scanning and α-beam irradiating on glass, M. Qiu, *Kyushu Univ., Japan;* F. Pi, G. Orriols, *Univ. Autonoma de Barcelona, Spain.* **(p. 83)**

JSuE14 ■ Photosensitivity as it relates with glass macroproperties, A. Cardoso, *CETEC, Brazil.* **(p. 84)**

JSuE15 ■ Periodic structures in photo-thermo-refractive glasses induced by homogeneous UV irradiation, V. Smirnov, L. Glebov, *Univ. Central Florida.* **(p. 84)**

JSuE16 (Invited) ■ Photosensitive thin film materials and devices, K. Simmons-Potter, B. Potter, M. Sinclair, D. Meister, *Sandia National Laboratories.* **(p. 84)**

JSuE17(Invited) ■ Processing-induced defects in optical waveguide materials, G. Sigel, Jr., J. Lee, *Rutgers Univ.* **(p. 84)**

JSuE18 ■ Photosensitivity in multi-valent rare earth ion doped alumino silicate glass optical fiber, K. Oh, U. Paek, *Kwangju Inst. of Science and Technology, Korea;* T. Morse, *Brown Univ.* **(p. 84)**

JSuE19 (Invited) ■ Material and fiber device aspects of poled fused silica, S. Brueck, T. Alley, X.-C. Long, *Univ. New Mexico;* R. Myers, *Univ. Auckland, New Zealand.* **(p. 84)**

JSuE20 ■ Report on second harmonic generation in soda-lime glass and relative new phenomena, M. Qiu, *Kyushu Univ., Japan;* F. Pi, G. Orriols, M. Bibiche, *Univ. Autonoma de Barcelona, Spain.* **(p. 85)**

JSuE21 ■ Refractive index changes in Ge-doped silica glass induced by a KrF excimer laser irradiation, H. Nishikawa, Y. Miyake, E. Watanabe, D. Ito, *Tokyo Metropolitan Univ., Japan.* **(p. 85)**

JSuE22 ■ Yellow/blue luminescences of Dy^{3+} doped borate glasses and their anomalous temperature variations, S. Tanabe, J. Kang, T. Hanada, N. Soga, *Kyoto Univ., Japan.* **(p. 85)**

JSuE23 (Invited) ■ Er^{3+} doped phosphate glasses and lasers, S. Jiang, N. Peyghambarian, *Univ. Arizona;* M. Myers, *Kigre Inc.* **(p. 85)**

JSuE24 ■ Photochromic/photoconductive effects in cadmium-alumino fluorosilicates, L. Cornelius, P. A. Tick, N.F. Borrelli, *Corning Inc.* **(p. 85)**

JSuE25 ■ Pr^{3+} and Dy^{3+}-doped Ge-S-I glasses suitable for active fiber optic devices, V. Krasteva, G. Sigel, *Rutgers Univ.;* S. Semjonov, M. Bubnov, *Fiber Optic Research Center, Russia.* **(p. 85)**

JSuE26 ■ Spectroscopy and quantum efficiency of halide-modified gallium-lanthanum sulfide glasses doped with praseodymium, W. Brocklesby, J. Hector, J. Wang, D. Brady, M. Kluth, D. Hewak, D. Payne, *Univ. Southampton, U.K.* **(p. 86)**

JSuE27 ■ Optical absorption and magnetic circular dichroism of $ER^{(3+)}$-doped aluminosilicate glasses, D. Johnson, D. Poulios, N. Bigelow, *Univ. Rochester;* J. Spoonhower, *Eastman Kodak Company.* **(p. 86)**

JSuE28 ■ Rare earth doped PZG fluoride glass channel waveguides: spectroscopy and signal amplification, E.C. Lebrasseur, Bernard Jacquier, *UCBL-UMR CNRS, France;* Brigitte Boulard, *Univ. du Maine, France;* Roger Rimet, *LEMO/INPG UMR CNRS, France.* **(p. 86)**

JSuE29 ■ Rare-earth-doped glass thin films for integrated photonics, A.J. Bruce, *Lucent Technologies.* **(p. 86)**

JSuE30 ■ Preparation and nonlinear optical properties of Au/glass composite thin films, I. Tanahashi, T. Tohda, *CRL Matsushita Electric Ind. Co. Ltd., Japan;* H. Inouye, *ERATO, Japan;* A. Mito, *NRL of Meterology, Japan.* **(p. 86)**

JSuE31 ■ Nonlinear response of gold nanoparticles embedded in glass matrix, H. Inouye, *ERATO, Japan;* K. Tanaka, K. Hirao, *Kyoto Univ., Japan;* I. Tanahashi, *CRL Matsushita Electric Ind. Co. Ltd., Japan.* **(p. 86)**

JSuE32 ■ Nonlinear index of refraction of germanium selenide glass at 10.6 μm, C. Schardt, J. Simmons, *Univ. Florida;* L. LeNeindre, P. Lucas, J. Lucas, *Univ. Rennes, France.* **(p. 87)**

JSuE33 ■ Chalcogenide glasses with high nonlinear refractive index, F. Smektala, C. Quemard, L. LeNeindre, J. Lucas, *Univ. de Rennes, France;* A. Barthelemy, *Univ. de Limoges, France.* **(p. 87)**

JSuE34 ■ Solarization of soda-lime-silicate glass containing manganese, B. Long, L. Peters, H. Schreiber, *Virginia Military Inst.* **(p. 87)**

JSuE35 (Invited) ■ Mid-IR high power transmission through chalcogenide glass fibers, L. Busse, J. Sanghera, I. Aggarwal, *U.S. Naval Research Laboratory.* **(p. 87)**

JSuE36 ■ Optical properties of gold (and other precious metals) in acetate glasses, N. Wilk, Jr., H. Schreiber, *Virginia Military Inst.* **(p. 87)**

JSuE37 ■ Fluorescent cooling of ytterbium-doped heavy metal fluoride hosts, M. Mortagh, G. Sigel, Jr., *Rutgers Univ.;* J. Fajardo, *Corning Inc.;* B. Edwards, R. Epstein, *Los Alamos National Laboratory.* **(p. 87)**

JSuE38 ■ NMR and IR study of the functionality of electrode glasses, C. Jäger, *Friedrich Schiller Univ., Germany;* K. Glock, B. Thomas, *Univ. Mining and Technology, Germany.* **(p. 88)**

JSuE39 ■ Possibilities of 119-Tin NMR for the characterization of glasses, C. Jäger, M. Braun, *Friedrich Schiller Univ., Germany;* D. Ehrt, A. Daniel, *Otto-Schott Inst. fur Glaschemie, Germany.* **(p. 88)**

JSuE40 ■ Ion-exchange processes in silicate glasses: the role of oxygen, V. Belostotsky. **(p. 88)**

JSuE41 ■ Residual stresses due to refractory inclusions in silica glass, D. Wissuchek, *Corning Inc.* **(p. 88)**

JSuE42 ■ Investigation of optical and radiation properties of oxygen deficient silica glasses, A.N. Trukhin, *Univ. Latvia;* H.-J. Fitting, *Rostock Univ., Germany.* **(p. 89)**

Adams Room

6:30pm–8:00pm
Conference Reception

■ Monday
■ October 27, 1997

JOINT SYMPOSIUM ON VITREOUS SILICA AND RELATED MATERIALS (Sessions JMA, JMD, JMF, JMH)

Auditorium

8:00am–10:30am

JMA ■ Joint Session on Hydrogen in Glass and Fibers

David Griscom, *U.S. Naval Research Laboratory, Presider*

8:00am (Invited)

JMA1 ■ Radiation-induced density and absorption changes in fused silica, T.P. Seward III, C. Smith, N.F. Borrelli, D.C. Allan, R.J. Araujo, *Corning Inc.* We report effects of 193 and 248 nm excimer laser irradiation on fused silica used for microlithography lenses. Color center formation and densification are described. **(p. 94)**

8:30am

JMA2 ■ Hydrogen, defects, and compaction of pure and doped vitreous silica, James Shelby, Marie Bergomi, *Alfred Univ.* Abstract available in GOMD Abstract Book and BGPP Technical Digest. **(p. 97)**

8:45am

JMA3 ■ Mechanisms of index change induced by near-UV light in hydrogen-loaded fibers, V. Grubsky, D.S. Starodubov, J. Feinberg, *Univ. Southern California.* The photosensitivity in H_2-free fibers follows the excitation spectrum of GODC triplet state, while in H_2-loaded fibers it is different. In loaded fibers the effect of near-UV light is similar to 240 nm excitation. **(p. 98)**

9:00am

JMA4 ■ Kinetics of defect center formation and photosensitivity in Ge-SiO_2 of various compositions, Tsung-Ein Tsai, E. Joseph Friebele, *U.S. Naval Research Laboratory.* Generation kinetics of defect centers in Ge-SiO_2 core fibers of various compositions are studied and discussed along with their photosensitive phenomena. **(p. 101)**

9:15am

JMA5 ■ Photosensitivity of oxygen deficient type bulk silica and fibers, J. Lee, G. Sigel, Jr., *Rutgers Univ.;* Jie Li, *SpecTran Specialty Optics Co.* Abstract available in GOMD Abstract Book and BGPP Technical Digest. **(p. 104)**

9:30am

JMA6 ■ Mode profile modification of H^+ beam-implanted waveguides with use of UV processing, J. Canning, *Univ. Sydney, Australia;* M. von Bibra, A. Roberts, *Univ. Melbourne, Australia.* Large negative index changes are observed in buried H^+ beam-implanted waveguides with 193 nm irradiation by measuring increases in the mode profile dimensions. These changes are up to 10% of the core-cladding index difference and are more pronounced in the vertical axis. This allows the possibility of tailoring the mode profile shape. **(p. 105)**

9:45am

JMA7 ■ Large refractive index changes observed in silicon-implanted silica exposed to high cumulative doses of ArF laser light, M. Verhaegen, J.L. Brebner, *Univ. Montréal, Canada;* J. Albert, *Communications Research Centre, Canada.* Kramers–Kronig analysis explains UV light-induced index change in implanted silica in the low cumulative dose regime but fails in high dose regime. **(p. 108)**

10:00am

JMA8 ■ Vacancies in as-grown and electron irradiated α-SiO_2, S. Dannefaer, D. Craigen, D. Kerr, *Univ. Winnipeg, Canada.* Abstract available in GOMD Abstract Book and BGPP Technical Digest. **(p. 111)**

10:15am

JMA9 ■ Molecular dynamics simulations of defects and excitons in glasses, L. Rene Corrales, *Pacific Northwest National Laboratory.* Abstract available in GOMD Abstract Book and BGPP Technical Digest. **(p. 112)**

Washington/Wilson Room

8:00am–9:15am

BMB ■ Pulse Propagation in Gratings

Ian Bennion, *Aston University, U.K., Presider*

8:00am (Invited)

BMB1 ■ High intensity pulse propagation in fiber Bragg gratings, B.J. Eggleton, R.E. Slusher, T.A. Strasser, *Bell Laboratories, Lucent Technologies;* C.M. de Sterke, *Univ. Sydney, Australia.* We review our recent nonlinear propagation experiments in fiber Bragg gratings. These experiments demonstrate nonlinear pulse compression, grating soliton generation and pulse shaping, and also show how a train of soliton-like pulses may be generated from a single input pulse. **(p. 114)**

8:30am

BMB2 ■ Ultrashort pulse propagation through fiber gratings: theory and experiment, L.R. Chen, S.D. Benjamin, P.W.E. Smith, J.E. Sipe, *Univ. Toronto, Canada.* We theoretically and experimentally investigate the temporal response of transform-limited picosecond Gaussian pulses reflected and transmitted from fiber gratings. Experimental measurements are in excellent agreement with theoretical calculations. **(p. 117)**

8:45am
BMB3 ■ Nonlinear self-switching and multiple gap soliton formation in a fiber Bragg grating, D. Taverner, N.G.R. Broderick, D.J. Richardson, R.I. Laming, M. Ibsen, *Southampton Univ., U.K.* We report for the first time, we believe, the experimental observation of quasi-cw nonlinear switching and multiple gap soliton formation within the bandgap of a fiber Bragg grating. **(p. 120)**

9:00am
BMB4 ■ The optical pushbroom in action, N.G.R. Broderick, D. Taverner, D.J. Richardson, M. Ibsen, R.I. Laming, *Univ. Southampton, U.K.* We report the first demonstration of the optical pushbroom—a novel form of all-optical switching involving a nonlinear Bragg grating, a strong pump pulse and a weak CW probe beam. **(p. 123)**

Washington/Wilson Room

9:15am–10:15am
BMC ■ Fiber Lasers
Jean-Luc Archambault, *Ciena Corporation, Presider*

9:15am (Invited)
BMC1 ■ Cascaded Raman fiber lasers and amplifiers, Stephen G. Grubb, *SDL Inc.* The recent availability of high power cladding pumped fiber lasers and low loss fiber resonators enabled with fiber Bragg grating technology, have made efficient CW Raman frequency conversion extremely efficient. The technology of cascaded Raman lasers and amplifiers will be reviewed. **(p. 128)**

9:45am
BMC2 ■ Novel high power 1.24 μm and 1.48 μm Raman lasers based on phosphosilicate fiber, E.M. Dianov, M.V. Grekov, I.A. Bufetov, S.A. Vasiliev, O.I. Medvedkov, G.A. Ivanov, A.V. Belov, V.G. Plotnichenko, V.V. Koltashev, A.M. Prokhorov, *Russian Academy of Sciences, Russia.* We report the first efficient resonant conversion of cw 1.06 μm radiation to the first (1.24 μm) and second (1.48 μm) Raman Stokes in a phosphosilicate fiber. **(p. 129)**

10:00am
BMC3 ■ Performance characteristics of single frequency Er^{3+}:Yb^{3+} co-doped fiber lasers, W.H. Loh, B.N. Samson, L. Dong, G.J. Cowle, *Univ. Southampton, U.K.;* K. Hsu, *Micron Optics Inc.* The performance of Er^{3+}:Yb^{3+} single frequency fiber lasers are reported. With lasing powers up to 60 mW, they are shown to have excellent specifications in terms of optical linewidth, signal-to-noise ratio, RIN, SMSR, and polarization purity. **(p. 132)**

The Harrison/Jefferson/Madison/ Monroe Rooms
10:30am–11:00am
Coffee Break/Exhibits

Auditorium

11:00am–12:30pm
JMD ■ Joint Session on Fundamental Mechanisms
Tsung Tsai, *U.S. Naval Research Laboratory, Presider*

11:00am (Invited)
JMD1 ■ Dielectric characteristics of silica and inference of related defects, Minoru Tomozawa, *Rensselaer Polytechnic Institute;* Dong-Wook Shin, *Samsung Electronics Co., Korea.* Dielectric properties of silica glasses were measured and their relationship with the reported second harmonic generation in silica glasses by poling is discussed. **(p. 136)**

11:30am
JMD2 ■ Determination of the visible-range optical absorption spectrum of peroxy radicals in gamma-irradiated fused silica, David L. Griscom, *U.S. Naval Research Laboratory;* Masafumi Mizuguchi, *Tokyo Institute of Technology, Japan.* High-purity fused silicas in fiber and bulk forms γ-irradiated to doses of ~12 MGy were studied by electron spin resonance and optical methods and isochronal annealing. **(p. 139)**

11:45am (Invited)
JMD3 ■ The point defects with low-coordinated Si or Ge atoms on silica surface: Surface and bulk centers comparison, Victor A. Radzig, *Russian Academy of Sciences, Russia.* The spectra, structure, and reactivity of paramagnetic and diamagnetic point defects containing low-coordinated Si or Ge atoms in vitreous silica are discussed. **(p. 142)**

12:15pm
JMD4 ■ Relationship between Ge lone pair center and Ge electron center, Koichi Awazu, *Univ. Montréal, Canada;* Yuichi Morishita, Ken-ichi Muta, *Showa Electric Wire and Cable Co. Ltd., Japan.* Relationship between Ge lone pair center and Ge electron center in Ge doped silicas was examined with changing the excitation energy and the generation mechanism was proposed. **(p. 145)**

Washington/Wilson Room

11:00am–12:30pm
BME ■ Novel Grating Materials and Fabrication Methods
Charles Askins, *U.S. Naval Research Laboratory, Presider*

11:00am (Invited)
BME1 ■ Bragg grating fabrication in fibers by near-UV light, D.S. Starodubov, *General Physics Institute of the Russian Academy of Sciences, Russia;* V. Grubsky, J. Feinberg, *Univ. Southern California.* Near-UV light produces fiber Bragg gratings even through the polymer jacket, and reveals the underlying microscopic mechanisms of grating formation. **(p. 150)**

11:30am
BME2 ■ Highly photosensitive germanosilicate fiber co-doped with nitrogen, E.M. Dianov, K.M. Golant, V.M. Mashinsky, O.I. Medvedkov, I.V. Nikolin, O.D. Sazhin, S.A. Vasiliev, *Russian Academy of Sciences, Russia.* A germanosilicate fiber co-doped with nitrogen has been fabricated by the surface plasma CVD process. The induced indices amounted to 2.8×10^{-3} and 1×10^{-2} for unloaded and hydrogen loaded fibers, respectively. **(p. 153)**

11:45am
BME3 ■ Wide-range and linearity of near-UV induced index change in hydrogen-loaded fibers: applications for Bragg grating fabrication, V. Grubsky, D.S. Starodubov, J. Feinberg, *Univ. Southern California.* Near-UV induced index change in hydrogen-loaded fibers increases linearly with fluence, saturating at $\Delta n \sim 10^{-2}$. We fabricated two Bragg gratings in the same location. **(p. 156)**

12:00m
BME4 ■ 157-nm photosensitivity in germanosilicate waveguides, Peter R. Herman, Keith Beckley, Sola Ness, *Univ. Toronto, Canada.* The photosensitivity response of germanium-doped silica fibers and planar waveguides was characterized by near bandgap, 157-nm radiation for the first time, we believe. **(p. 159)**

12:15pm
BME5 ■ Strong higher-order fiber Bragg gratings written with an amplitude mask, J.L. Wagener, R.P. Espindola, A.M. Vengsarkar, *Bell Laboratories, Lucent Technologies.* We have written 4th and 5th order Bragg gratings in deuterium loaded optical fiber using a standard chrome-on-silica amplitude mask. Grating reflectivities up to 99.9% are reported. **(p. 162)**

12:30pm–1:30pm
Lunch Break

Auditorium

1:30pm–3:30pm
JMF ■ Joint Session on Germanium-Doped Silica
E.J. Friebele, *U.S. Naval Research Laboratory, Presider*

1:30pm (Invited)
JMF1 ■ Defects associated with photosensitivity in GeO_2-SiO_2 glasses, Hideo Hosono, *Tokyo Inst. of Technology, Japan.* Defects associated with photosensitivity, nanometer-scale heterogeneity and photoreactions in Ge-doped SiO_2 glasses are described along with structural changes in UV-induced defects. **(p. 166)**

2:00pm
JMF2 ■ Local Kramers–Kronig analysis of UV-induced absorption changes: dynamics of excess loss induced by exposure to light at 248 nm or 193 nm in Ge:SiO_2 preforms, B. Leconte, W.X. Xie, M. Douay, P. Bernage, P. Niay, *Univ. Lille I, France;* J.F. Bayon, E. Delevaque, H. Poignant, *France Telecom CNET.* Dynamics of 248 nm or 193 nm light-induced excess loss in Ge:SiO_2 glass have been recorded. Index changes have been studied through a local Kramers–Kronig analysis. **(p. 169)**

2:15pm
JMF3 ■ Rise and decay of 3.15 eV luminescence in germanosilicate glass: influence of glass densification, E.M. Dianov, V.M. Mashinsky, V.B. Neustruev, O.D. Sazhin, V.A. Sidorov, *Russian Academy of Sciences, Russia.* Initial rise of 3.15 eV luminescence band at 3.68 eV excitation is found in germanosilicate glass. Densification of glass reduces the rise of the luminescence. **(p. 172)**

2:30pm
JMF4 ■ Germanosilicate glass refractive index change under singlet and triplet excitation of germanium oxygen deficient centers, E.M. Dianov, S.A. Vasiliev, A.A. Frolov, O.I. Medvedkov, *Russian Academy of Sciences, Russia.* Refractive index changes induced in a Ge-doped silica core fiber by photoexcitation of the singlet and triplet bands of the germanium oxygen deficient centers have been investigated and compared. **(p. 175)**

2:45pm
JMF5 ■ Links between writing and erasing (or stability) of Bragg gratings in disordered media, B. Poumellec, *Univ. de Paris Sud, France.* Stating that index change can be accounted for by a reversible physico-chemical equation dependent on an energetic disorder, I suggest a link between stability and elaboration. **(p. 178)**

3:00pm
JMF6 ■ Growth kinetics of photoinduced gratings and paramagnetic centers in high NA, heavily Ge-doped silica optical fibers, T. Taunay, T.E. Tsai, E.J. Friebele, *U.S. Naval Research Laboratory;* P. Niay, *Univ. Sciences et Technologies de Lille, France;* J.F. Bayon, *France Télécom, France.* Stretching the fiber during UV exposure modified not only the kinetics of Type IIa grating formation but the magnitude and growth behavior of the paramagnetic defect centers. **(p. 181)**

3:15pm
JMF7 ■ Two types of photosensitivity observed in hollow cathode PECVD germanosilica planar waveguides, M.V. Bazylenko, D. Moss, *Optical Fibre Technology Centre, Australia.* Photosensitive effects known in fibers as photosensitivity type I and type IIA have been observed in HCPECVD germanosilica waveguides, but in a much more pronounced form. **(p. 184)**

The Harrison/Jefferson/Madison/ Monroe Rooms

3:30pm–4:30pm
Refreshment Break/Exhibits

The Promenade

3:30pm–4:30pm
BMG ■ Poster Session II

BMG1 ■ Widely wavelength tunable external cavity laser by use of fiber Bragg grating embedded optical switch, Masakazu Shigehara, Hiroshi Kohda, Kazuhito Saito, Hiroo Kanamori, *Sumitomo Electric Industries Ltd., Japan.* A wavelength tunable laser that uses a fiber Bragg grating embedded in an optical switch as an external cavity mirror has been proposed, and oscillation at four wavelengths was successfully demonstrated by operating the switch to select the fiber Bragg gratings. **(p. 188)**

BMG2 ■ Narrow transmission bandpass filters with use of Bragg grating-assisted mode conversion, John Canning, David Moss, *Australian Photonics Cooperative Research Centre, Australia.* A narrow transmission bandpass filter with 15 dB signal-to-noise levels is demonstrated with use of Bragg grating-assisted mode conversion in transmission. **(p. 191)**

BMG3 ■ Rapid thermal annealing of chalcogenide glasses for photodarkened waveguide and grating applications, Siddharth Ramachandran, S.G. Bishop, *Univ. Illinois.* Rapid thermal annealing of sputtered chalcogenide glass films is demonstrated to increase surface quality and the largest photoinduced index change possible (5%). Holographic gratings and channel waveguides are directly patterned on this glass and their characteristics are compared with devices on conventionally annealed chalcogenide films. **(p. 194)**

BMG4 ■ Z-scan study of thin chalcogenide As_2S_3 glass films and holographic fabrication of microlens networks, A. Saliminia, T.V. Galstyan, A. Villeneuve, *Univ. Laval, Canada;* K. Richardson, *Univ. Central Florida.* The photoresponse of chalcogenide glasses is studied using the time-resolved Z-scan technique. The observed complex refractive index and surface profile change allow the holographic fabrication of 1D (cylindrical) and 2D microlens structures. **(p. 197)**

BMG5 ■ Analysis of an optical frequency-hop encoder using strain-tuned Bragg gratings, H. Fathallah, S. LaRochelle, L.A. Rusch, *Univ. Laval, Canada.* We propose fast optical frequency-hop code division multiple access (FH-CDMA) for high capacity local area networks. Encoding and decoding are achieved by tunable fiber gratings. **(p. 200)**

BMG6 ■ Effects of doping of H_2O and Na on second-order nonlinearity in poled silica glass, Hiroaki Imai, Suguru Horinouchi, Naoko Asakuma, Kazuhiro Fukao, Daizaburo Matsuki, Hiroshi Hirashima, Keisuke Sasaki, *Keio Univ., Japan.* Doping of H_2O increased a second-order nonlinearity in the whole region of poled type III silica glass, whereas Na increased that in the near-surface region. **(p. 203)**

BMG7 ■ A thermally poled electro-optic fiber, X.-C. Long, S.R.J. Brueck, *Univ. New Mexico.* A planarized fiber poling structure compatible with high-speed microstrip electrodes defined by standard lithography is presented. Present results include a $V_\pi L$ product of 900 V-cm. **(p. 204)**

BMG8 ■ UV and thermal poling of germanosilicate fiber, Y. Quiquempois, G. Martinelli, P. Bernage, M. Douay, P. Niay, *Univ. Lille, France;* E. Delevaque, H. Poignant, B. Loisel, J.F. Bayon, *CNET Lannion, France.* Polings have been achieved in a specially designed germanosilicate fiber by use of two methods. Both the poling techniques and the results concerning the linear electro-optic coefficient are presented. **(p. 207)**

BMG9 ■ The influence of phase mask stitch errors on the performance of UV-written Bragg gratings, X. Liu, R.M. De La Rue, P.V.S. Marques, S. Thoms, J.S. Aitchison, *Univ. Glasgow, U.K.;* L.A. Everall, J.A.R. Williams, I. Bennion, *Aston Univ., U.K.* We quantify the effect of stitching errors in binary phase masks on the reflection spectra of UV-written Bragg gratings and assess the maximum acceptable error. **(p. 210)**

BMG10 ■ Dynamics of coupling peaks by H_2 diffusion in long-period grating filter, Joo-Nyung Jang, Kyung-Ho Kwack, *Samsung Electronics Co. Ltd., Korea;* Sang-Bae Lee, Sang-Sam Choi, *Korea Institute of Science and Technology, Korea.* Behavior of loss peaks by H_2 diffusion after exposure of UV-source and the spectral change even with same Δn during the annealing process is presented. **(p. 213)**

BMG11 ■ Analysis of narrow depressed-cladding fibers for minimization of cladding and radiation mode losses in fiber Bragg gratings, C.W. Haggans, W.F. Varner, *3M Fiber Optics Laboratory;* H. Singh, *3M Bragg Grating Technologies;* J.-S. Wang, *3M Specialty Optical Fibers.* The cladding and radiation mode loss characteristics of photoinduced gratings written in fibers with a narrow depressed inner cladding are compared with the properties of gratings written in matched-clad, photosensitive clad, and wide depressed-cladding fibers. **(p. 216)**

BMG12 ■ Strong LP_{11}-mode splitting in UV side-written tilted fiber gratings, Hagen Renner, Dietmar Johlen, Peter Klose, Ernst Brinkmeyer, *TU Hamburg-Harburg, Germany.* The LP_{11}-mode degeneracy can be broken strongly by UV side-writing for widely separating the resonance peaks in tilted fiber gratings. **(p. 219)**

BMG13 ■ The effect of profile noise on the spectral response of fiber gratings, François Ouellette, *Kromafibre Inc., Canada.* When the spatial profile of a fiber grating coupling coefficient or period is noisy, the spectral response can be dramatically degraded. The cases of short apodized gratings and long chirped gratings are investigated. **(p. 222)**

BMG14 ■ Thermal stabilities of strong UV written gratings in sol-gel germanosilicate planar waveguides, A.D. Razafimahatratra, M. Benatsou, M. Bouazaoui, W.X. Xie, M. Douay, *Univ. Lille I, France;* C. Mathieu, A. Dacosta, *Univ. Artois à Lens, France.* Planar waveguides are elaborated by the sol-gel process at 700 °C. Pulsed or cw irradiation at 244 nm lead to photorefraction, photoexpansion, or densification and photoablation in the waveguides. Thermal stabilities of the photoinduced refractive index of 5×10^{-3} are presented. **(p. 225)**

BMG15 ■ Fabrication of in-fiber Moiré filters using a 5 cm nondedicated chirped phase mask, L.A. Everall, K. Sugden, J.A.R. Williams, I. Bennion, *Aston Univ., U.K.;* X. Liu, J.S. Aitchison, R.M. De La Rue, *Univ. Glasgow, U.K.* Fabrication of Moiré filters with very narrow stopbands and high rejection levels >35 dB using a 5-cm nondedicated chirped phase mask is presented. **(p. 228)**

BMG16 ■ Equalization of spectral nonuniformities in broadband chirped fiber gratings, Michael K. Durkin, Morten Ibsen, Richard I. Laming, *Univ. Southampton, U.K.;* Valeria Gusmeroli, *Pirelli Cavi SpA, Italy.* We present a novel application of apodization to equalize the spectral nonuniformities caused by cladding-mode losses in broadband chirped fiber Bragg gratings. **(p. 231)**

BMG17 ■ Long period gratings formed in depressed cladding fibers, Liang Dong, Laurence Reekie, Jose L. Cruz, *Univ. Southampton, U.K.* In a single-mode fiber of a depressed cladding design, the LP_{11} mode is leaky but can propagate over a short length of fiber. This leaky LP_{11} mode instead of the conventional cladding modes can be used in long period gratings, with two extra benefits: I) a larger overlap gives stronger coupling, and II) coupling is insensitive to the glass-air interface; therefore packaging is easier. **(p. 234)**

Auditorium

4:30pm–5:30pm

JMH ■ Joint Session on Photoinduced Effects in Novel Materials

Koichi Awazu, *Electrotechnical Laboratory, Presider*

4:30pm

JMH1 ■ Photosensitivity of tin doped phosphosilicate glasses, P.V.S. Marques, J.R. Bonar, A. Glidle, A. McLaughlin, J.S. Aitchison, *Univ. Glasgow, U.K.;* A.M.P. Leite, *Centro de Física do Porto, Portugal.* The UV absorption of tin doped phosphosilicate glasses produced by flame hydrolysis deposition is reported. Two different methods of doping (aerosol and solution doping) are compared. **(p. 240)**

4:45pm

JMH2 ■ Photoinduced integrated optical devices in sulfide chalcogenide glasses, J.-F. Viens, A. Villeneuve, T. Galstian, M.A. Duguay, *Univ. Laval, Canada;* K.A. Cerqua-Richardson, S. Schwartz, *Univ. Central Florida.* We demonstrate the fabrication of integrated optical devices in arsenic (S,Se)-based chalcogenide glasses using laser writing. Results on photoinduced gratings, waveguides, and couplers are presented. **(p. 243)**

5:00pm

JMH3 ■ Temperature dependence of UV-induced defects in thulium-doped ZBLAN fibers, Pierre Laperle, Réal Vallée, Sophie LaRochelle, *Univ. Laval, Canada;* Alain Chandonnet, *Institut National d'Optique, Canada.* Photoinduced absorption in ZBLAN fibers was produced by direct UV exposure. Thermal annealing is described by stretched-exponential functions in darkened and photobleached samples. **(p. 246)**

5:15pm

JMH4 ■ The origin of photoinduced anisotropy in germanium sulfide-based glasses, Victor Tikhomirov, P. Hertogen, G. Adriaenssens, *Katholieke Univ. Leuven, Belgium;* V. Krasteva, G. Sigel, *Rutgers Univ.* Metastable photoinduced anisotropy generated by linearly polarized sub-bandgap light in Pr-doped Ge-S-I glasses is reported. The microscopic model for this effect is proposed. **(p. 249)**

Auditorium

5:30pm

Postdeadline Paper Session

Jacques Albert, *Communication Research Center, Canada, Presider*

Tuesday
October 28, 1997

Room 18

8:00am–10:15am
BTuA ■ WDM Applications
Gary Ball, *Uniphase Telecom Products, Presider*

8:00am (Invited)
BTuA1 ■ Fiber grating devices for WDM communication systems, Thomas A. Strasser, *Bell Laboratories, Lucent Technologies.* This talk will discuss the properties of UV-induced fiber gratings, and how these properties are critical to enable numerous devices required for future Wavelength Division Multiplexing (WDM) communication systems. **(p. 254)**

8:30am
BTuA2 ■ An all-fiber, zero insertion loss, add/drop filter for wavelength division multiplexing, Anthony S. Kewitsch, George A. Rakuljic, Phil A. Willems, Amnon Yariv, *Arroyo Optics Inc.* An all-fiber add/drop filter with an insertion loss of ~0.1 dB was fabricated by recording a Bragg grating in the waist of an asymmetric mode converter/coupler. **(p. 256)**

8:45am
BTuA3 ■ Low crosstalk optical add-drop multiplexer based on a planar silica-on-silicon Mach–Zehnder interferometer with UV-induced Bragg gratings and UV trimming, J.-M. Jouanno, D. Zauner, M. Svalgaard, M. Kristensen, *Technical Univ. Denmark, Denmark.* We present a low crosstalk optical add-drop multiplexer made in silica-on-silicon waveguides by writing Bragg gratings in a Mach–Zehnder interferometer and subsequently tuned by UV trimming. **(p. 259)**

9:00am
BTuA4 ■ Apodized UV-induced gratings in planar waveguides for compact add-drop filters, C.K. Madsen, J.J. DeMarco, C.H. Henry, E.J. Laskowski, R.E. Scotti, T.A. Strasser, *Lucent Technologies, Bell Laboratories.* Results are presented for 1-cm-long apodized gratings in planar waveguide Mach–Zehnder interferometers that are suitable for 100 GHz channel spacing add-drop filters. **(p. 262)**

9:15am
BTuA5 ■ Efficient active Bragg grating tunable filters, H.G. Limberger, Nguyen Hong Ky, D.M. Costantini, R.P. Salathé, C.A.P. Müller, G.R. Fox, *Swiss Federal Institute of Technology, Switzerland.* New active Bragg grating devices based on thin metallic and piezoelectric coatings have been demonstrated showing efficiencies of 4 nm/W and 12 pm/V, respectively. **(p. 265)**

9:30am
BTuA6 ■ Chirped Moiré fiber gratings operating on two wavelength-channels for use as dual channel dispersion compensators, Morten Ibsen, Michael K. Durkin, Richard I. Laming, *Univ. Southampton, U.K.* Long continuously chirped Moiré fiber gratings are demonstrated. Clean, dual-channel operation with dispersion equivalent to 100 km and 200 km of standard fiber is shown. **(p. 268)**

9:45am (Invited)
BTuA7 ■ Dispersion compensation gratings, Richard T. Laming, M. Ibsen, M. Durkin, M.J. Cole, M.N. Zervas, K.E. Ennser, *Univ. Southampton, U.K.*; V. Gusmeroli, *Pirelli Cavi SpA, Italy.* Broadband chirped fiber gratings allow the upgrade of the existing nondispersion shifted fiber network to high data rate operation within the 1.55 μm low-loss window. The design, fabrication, performance and application of these devices is covered. **(p. 271)**

The Harrison/Jefferson/Madison/ Monore Rooms
10:15am–10:45am
Coffee Break/Exhibits

Room 18

10:45am–12:15pm
BTuB ■ Planar Waveguide Devices
Graeme Maxwell, *BT Labs, U.K., Presider*

10:45am (Invited)
BTuB1 ■ Application of photosensitivity in planar silica-on-silicon optical waveguides, Y. Hibino, *Photonic Integration Research, Inc.* This paper reviews recent progress on photosensitivity in silica-based planar waveguides. The main focus is on the photosensitivity due to 193 nm irradiation, which can induce large refractive index changes in the waveguide without special treatment. Discussed are the basics of these phenomena and device applications. **(p. 276)**

11:15am
BTuB2 ■ Direct writing of planar waveguide devices with use of ultraviolet light, M. Svalgaard, M. Kristensen, *Technical Univ. Denmark, Denmark.* Planar waveguide power splitters and directional couplers exhibiting low loss have been fabricated in silica-on-silicon by use of a continuous wave UV laser beam. **(p. 279)**

11:30am
BTuB3 ■ Self-writing in photosensitive materials: theory and experiment, Tanya Monro, D. Moss, C.M. de Sterke, L. Poladian, *Australian Photonics CRC, Australia.* Simulations indicate that waveguides can be self-written in photosensitive materials. We analyze the effect of loss, and present the first experimental confirmation of this process. **(p. 282)**

11:45am (Invited)
BTuB4 ■ Writing waveguides and gratings in silica and related materials by femtosecond laser, K. Hirao, *Kyoto Univ., Japan.* Creating waveguides and optical devices in bulk glasses with an ultrafast femtosecond laser were successfully carried out. **(p. 285)**

12:15pm–1:15pm
Lunch Break

Room 18

1:15pm–3:15pm
BTuC ■ Poling I
Roger Stolen, *AT&T Labs-Research, Presider*

1:15pm (Invited)
BTuC1 ■ Large SHG in UV-poled silica glass, Takumi Fujiwara, Akira J. Ikushima, *Toyota Technological Institute, Japan;* Masahide Takahashi, *Kobe Univ., Japan.* Large SHG in a germanosilicate glass, induced by UV-poling at 193 nm, is reported. Measured SHG coefficient in a UV-poled glass was found to exceed d_{22} of $LiNbO_3$. **(p. 290)**

1:45pm
BTuC2 ■ An ion exchange model for extended-duration thermal poling of bulk fused silica, Thomas G. Alley, S.R.J. Brueck, *Univ. New Mexico;* Richard A. Myers, *Univ. Auckland, New Zealand.* We present experiments and a model demonstrating the importance of hydrogen ion exchange for the $\chi^{(2)}$ formation in bulk SiO_2. **(p. 293)**

2:00pm
BTuC3 ■ Effect of minority species on thermal poling of fused silica glasses, Noriyuki Wada, Kenji Morinaga, *Kyushu Univ., Japan;* Hiromichi Takebe, Valerio Pruneri, Peter G. Kazansky, *Univ. Southampton, U.K.* We carried out a systematic analysis of oxygen-related defects and impurities in commercial fused silica glasses and discuss their effects on poling. **(p. 296)**

2:15pm
BTuC4 ■ Absolute prism-assisted Maker fringe measurements of the nonlinear profile in thermally poled silica, Alice Liu, M.J.F. Digonnet, G.S. Kino, *Stanford Univ.;* D. Pureur, *Univ. des Sciences et Technologies de Lille, France.* The nonlinear profile of thermally poled silica is characterized by use of a prism-assisted absolute Maker fringe measurement. A buried Gaussian profile is inferred from the measurement. **(p. 299)**

2:30pm
BTuC5 ■ Improving the nonlinearity of silica by poling at higher temperature and voltage, Alice Liu, M.J.F. Digonnet, G.S. Kino, *Stanford Univ.;* D. Pureur, *Univ. des Sciences et Technologies de Lille, France.* Stronger and deeper nonlinear regions are demonstrated by poling at both higher temperature (400 °C) and higher voltage (>10 kV). **(p. 302)**

2:45pm (Invited)
BTuC6 ■ Fundamentals of glass poling: from self-organization to electric-field poling, Peter G. Kazansky, Valerio Pruneri, *Univ. Southampton, U.K.* What is the limit of a second-order nonlinearity in glass? Mechanisms of glass poling answering this question are reviewed. **(p. 305)**

The Harrison/Jefferson/Madison/ Monroe Rooms
3:15pm–3:45pm
Refreshment Break/Exhibits

Room 18

3:45pm–5:15pm
BTuD ■ Poling II
Raman Kashyap, *BT Laboratories, U.K., Presider*

3:45pm
BTuD1 ■ Creating a second order nonlinearity and a waveguide in soft glasses by poling, W. Margulis, F.C. Garcia, E.N. Hering, I.C.S. Carvalho, *Pontificia Univ. Católica do Rio de Janeiro, Brazil;* B. Lesche, *Univ. Federal do Rio de Janeiro, Brazil;* F. Laurell, *Royal Institute of Technology, Sweden.* Poling is used to induce a second-order nonlinearity in bulk soda lime and make single mode waveguides in a depressed cladding configuration. **(p. 310)**

4:00pm
BTuD2 ■ Electro-thermal poling of microfibers, Isabel Carvalho, C.M.B. Cordeiro, L.C. Guedes Valente, E.N. Hering, W. Margulis, *Pontificia Univ. Catolica do Rio de Janeiro, Brazil;* F. Laurell, R. Stubbe, *Royal Institute of Technology, Sweden.* Standard telecom fibers were etched to the core and the microfibers that formed were poled at several kilovolts at 250 °C. **(p. 313)**

4:15pm (Invited)
BTuD3 ■ Electric-field poling of polymers, Reimund Gerhard-Multhaupt, *Univ. Potsdam, Germany.* Chromophore dipoles in amorphous nonlinear optical polymers are oriented with electric fields from electrodes or charge layers. Recently developed poling techniques permit three-dimensional orientation structures. **(p. 316)**

4:45pm (Invited)
BTuD4 ■ Seeding and all-optical patterning of polymers, J.-M. Nunzi, C. Fiorini, A.-C. Etilé, P. Raimond, *LETI, France;* F. Charra, *DRECAM, France.* All-optical poling is based on the excitation of nonlinear molecules using dual-frequency beams. In polymers, the process permits the optical patterning of 3-dimensional spatio-tensorial micro-structures. **(p. 319)**

Bragg Gratings, Photosensitivity, and Poling in Glass Fibers and Waveguides: Applications and Fundamentals

Joint Plenary Session

Sunday, October 26, 1997

Paul Lemaire, Bell Labs/Lucent Technologies
Susan Houde-Walter, University of Rochester
Presiders

JSuA
8:20am–10:30am
Auditorium

The nature of optically active defect centers in vitreous silicon dioxide.

Linards Skuja
Institute of Solid State Physics, University of Latvia,
8 Kengaraga Str.LV 1063 Riga, Latvia, E-mail: skuja@acad.latnet.lv

Point defects are detrimental to the most applications which make use of the otherwise excellent optical and dielectric properties of vitreous SiO_2. One notable exception to this rule is the writing of photoinduced gratings in SiO_2:GeO_2 glass fibers. There is ample evidence that the photosensitivity is connected to the presence of point defects in the glass, particularly, to the presence of the so called "oxygen deficiency centers" (ODC's). While significant advances in optimizing the photoinduced grating writing have been made in recent years, the basic understanding of the underlying microscopic defect processes is still insufficient. The nature of a number of defect-related optical bands is still a matter of discussions. Most unsatisfactorily, the structure of the "key defect" to the fiber writing, the ODC, remains controversial.

The optical and electron paramagnetic resonance (EPR) properties of point defects in vitreous SiO_2 have been last reviewed by Griscom 6 years ago [1]. The present paper reviews the more recent advances in this field, with a particular emphasis on the optical spectroscopy. This review will concentrate on the basic intrinsic defects and on the most common impurity-related defects occurring in synthetic vitreous SiO_2. The properties of some of these defects are summarized in Table 1. Germanium ODC is included due to its key role in photoinduced grating writing and because of it's close relationship to the intrinsic Si-related ODC. A comprehensive review on defects occurring in germanosilicate glasses has been published recently by Neustruev [2].

One of the prime objectives of the present paper is to reassess the often conflicting experimental and theoretical evidence concerning the structural origin of ODC's.

In the past, the major steps in elucidating the structure of defects in vitreous SiO_2 have been made almost exclusively using the techniques of EPR. The three milestones achieved this way are the characterization of the E'-center, nonbridging-oxygen hole center (NBOHC) and peroxy radical (POR). Unlike defect studies in other materials, the optical methods have played here often a secondary role. In the case of diamagnetic defects, like ODC's which are invisible by EPR, the experimental evidence which could be related to their structure is much more scarce. However, new developments based on the optical methods have emerged in the last years. Several of them are listed below and will be discussed in the present paper:

- Application of the site selective luminescence excitation techniques. This techniques has significantly improved the understanding of the optical properties of NBOHC's.

Table I
Color centers in glassy SiO_2 caused by intrinsic defects and by the most common impurities

Commonly used defect name(s) or acronym(s)	Suggested structural model(s)	Peak positions of the optical absorption/ excitation bands (eV)	Halfwidth (eV)	Oscillator strength f or abs. cross section σ (cm2)	Peaks of excited photolumi-nescence bands (eV)	Electron paramag-netic resonance signal
Oxygen deficiency- related centers						
E'-centers: E'_α,E'_β,E'_γ; E'_δ	≡Si•...(Si≡) SiO_4 vacancy	5.7-5.8	0.8	f=0.14	Not observed	g_{iso}=2.0010 g_{iso}=2.0020
Si Oxygen Deficiency Center, Si (ODC), B_2-center, B_2(Si), Si_2^0, oxygen vacancy, oxygen divacancy	oxygen vacancy; oxygen divacancy; 2-fold coordinated silicon	6.8-7.0 4.95-5.05 3.15	0.4 0.3 0.3	f=0.1-0.4(?) f=0.2 f≈10^{-6}	4.3-4.4; 2.7-2.8	None (diamag-netic center)
Ge Oxygen Deficiency Center(s), Ge (ODC), B_2(Ge), Ge_2^0, oxygen vacancy, Ge^{2+}	oxygen vacancy, oxygen divacancy, 2-fold coordinated Ge	6.8 5.1-5.4 3.7	0.4 0.42 0.4	f=0.1-0.4(?) f=0.14 f=1.5*10^{-4}	4.2-4.3; 3.0-3.2	None (diamag-netic center)
Si-Si bond, oxygen vacancy	≡Si-Si≡ ≡Si...Si≡	7.6	0.5	σ= 7.5*10^{-17} cm^{-2}.	Si ODC emission bands	None (diamag-netic center)
H(I) center, "7.4 mT doublet"	≡Si-H• ≡Si-H •Si≡	4.8	0.6		Not observed	g_{iso}=2.001 A_{iso}(H)= 7.4 mT
H(II) center, 11.9 mT doublet	≡Ge-H• ≡Ge-H •Si≡	?	?		Not observed	g_{iso}=1.997 A_{iso}(H)= 11.9 mT
Oxygen excess- related centers						
Non-Bridging Oxygen Hole Center (NBOHC)	≡Si-O•	4.8 2.0	1.05 0.18	f=0.2 f=4*10^{-4}	1.85-1.95	g_1=2.0010 g_2=2.0095 g_3≈2.08
Peroxide Radical (POR)	≡Si-O-O•	4.8-6.0 (?) 7.6	1.1-1.4	σ≈5*10^{-18} cm^2 (?)	Not observed	g_1=2.0018 g_2=2.0078 g_3≈2.067
Interstitial O_2	O=O	edge≈7eV 1.62 0.975	continuum 0.012 0.011	σ=10^{-19} cm^2 f=10^{-8} -10^{-9} f=10^{-8} -10^{-10}	0.975	Triplet ground state
Interstitial O_3, ozone	O / \ O O	4.8	1.0	σ=5*10^{-18} cm^2	O_2 band at 0.97 eV (expected)	None (diamag-netic center)
"3.8 eV band"	≡Si-OO-Si≡ Interstitial Cl_2	3.8	0.7	σ=10^{-19} cm^2	Not observed	None (diamag-netic center)

- Realization that inhomogeneous broadening effects due to the glassy disorder are important in the optical spectra of vitreous SiO_2 and in a number of cases can cause "anomalous" behavior of the optical bands. Any defect scheme assuming existence of several closely spaced discrete optical bands should be first weighed against the possibility of disorder-induced inhomogeneous broadening effects.
- Studying glass-specific defects embedded in α-quartz lattice environment. The attractive possibility, to study the defects embedded in the orderly, crystalline environment of α-quartz instead of the glass matrix have been hampered for a long time by the fact that most defects (except for the E' center) are inherent specifically to the glassy state of SiO_2 and do not occur in quartz. However, it was found that such defects exist on the boundaries of the amorphous microregions created in α-quartz lattice by particle irradiation.
- Utilizing analogies between the bulk and surface defects. Almost all of the defects listed in Table 1 can be created on the surface of mechanically ground SiO_2 particles. This provides an excellent opportunity to study the (photo)chemical transformations of the defects without the diffusion-imposed limitations complicating similar studies of the bulk defects.
- Realization that dissolved gases are important to defect (radio/photo) chemistry coupled with the ability to detect them with direct spectroscopic methods. The long-standing ideas that interstitial gas molecules of O_2 and Cl_2 are an important participant in defect processes in glassy SiO_2 are now supported by a direct spectral evidence.
- Scrutiny of the vacuum ultraviolet region. Although the optical absorption band at 7.6 eV is the only direct spectroscopic signature of the most abundant oxygen deficiency-related defect in SiO_2, this technically difficult spectral region up until recently has remained relatively little explored. The recent experimental evidence and the suggested connection between the 7.6 eV center ("Si-Si bond") and Si ODC will be discussed.

References

1. D.L.Griscom, Optical Properties and Structure of Defects in Silica Glass. J.Cer. Soc.Jap., **99**, 923-942 (1991).
2.V.B.Neustruev Colour centres in gemanosilicate glass and optical fibers. J.Phys:Condens.Matter, **6**, 6901-6936 (1994)

WHAT CAN TOPOLOGICAL MODELS TELL US ABOUT GLASS STRUCTURE AND PROPERTIES?

Linn W. Hobbs
Department of Material Science and Engineering
Massachusetts Institute of Technology
Room 13-4062, 77 Massachusetts Avenue, Cambridge, MA 02139
Tel: (617) 253-6835 *Fax:* (617) 252-1020 *e-mail:* hobbs@mit.edu

Space Filling and Topology

Atomic arrangements in condensed matter partition three-dimensional space into polyhedra whose edges are interatomic vectors. These polyhedra, formally known as void polytopes, fill (tesselate) space, and their identity and arrangement can provide one description of a given atomic arrangement (Figure 1a) [1]. Other tessellations associated with space-filling of random structures are Voronoi polyhedral cells [2] and their dual the Delauney network [3]. These tessellations are relatively intuitive in two dimensions, but considerably more complex in three-dimensions—for example in tetrahedral networks like SiO_2—where a set of as many as 126 void polyhedra may be required to model interstitial space [1]. Because many arrangements favor particular coordination of one atom by others, owing to bond orbital, radius ratio, or local electrostatic neutrality considerations, discrete coordination polyhedra comprise a subset of the possible void polytopes, and the structure may be described by the way in which coordination polyhedra are connected together and fill space by defining the remaining void polytopes. Space filling by connected structural units was a favorite description tool of early crystal chemists [4], and in fact the connectivity of such structural polytopes (number of polytopes sharing vertices, edges and faces) has been shown to correlate with glass-forming ability and extendability of aperiodic networks [5] and to govern the amorphizability of crystalline solids [6].

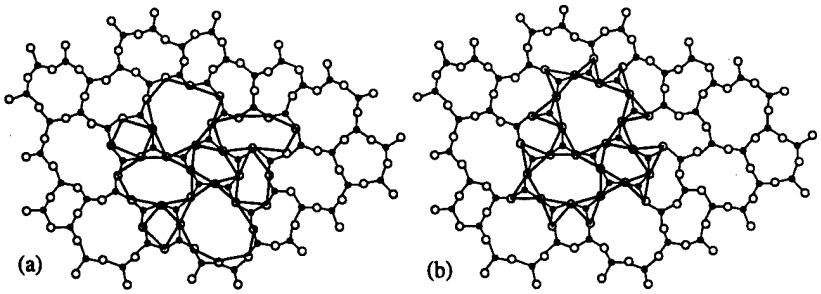

Figure 1: Alternative representations of the Zachariasen two-dimensional continuous random network [7] by (a) interstitial voids, (b) local cluster of primitive rings.

Rings and Clusters

A simpler one-dimensional characterization of three-dimensional tetrahedral networks (e.g. SiO_2, SiC, Si_3N_4) can however be effected which, though an incomplete tessellation of Euclidean space, nevertheless retains uniqueness at least for the set of crystalline polymorphs [8]. The description is based on rings (Figure 1b), which are closed circuits along nodal connections, for example through

tetrahedra (e.g $[SiO_4]$) in the tetrahedral network. The existence of rings is a steric necessity: a network without rings is an ever-branching tree, whose density increases exponentially; paths which close back on themselves to form rings keep the density in check. The important rings are those minimal circuits which are not the sum of two smaller circuits; these have been termed *primitive rings* [9] and their number and size are characteristic of the tetrahedral arrangements [10], for example the crystalline silica polymorphs [11,12]. There is a correlation between density and ring size, because larger rings can fold back on themselves and establish denser structures (the interstitial voids are smaller).

The set of all tetrahedra which are part of the primitive rings associated with a tetrahedron is called the *local cluster* of that tetrahedron. The local cluster is a characteristic structural unit, much like a unit cell for a crystal, which represents all *local* topological properties (rather than embodying the local symmetries) and is equally applicable to crystalline and non-crystalline arrangements alike. For example, the local clusters of cristobalite and quartz are compared in Figure 2. The first contains 29 tetrahedra and only 6-rings; the second contains 63 tetrahedra and is dominated by 8-rings.

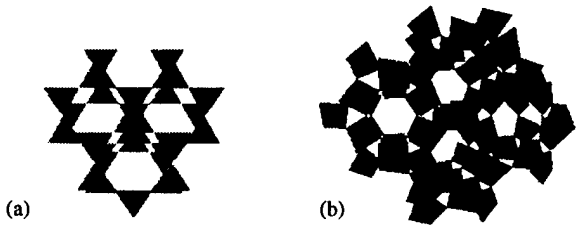

Figure 2: Local clusters of a) cristobalite (29 tetrahedra, 6 12 -rings), and b) quartz (63 tetrahedra, 40 8-rings, 6 6-rings).

Local Rules and Self-Assembly

Investigation of the local topological properties of network structures requires a means for rapid assembly of large models. Structures, such as viruses, have been shown to self-assemble according to sets of local rules [13], and the approach can be applied to computer-based self-assembly of tetrahedra in tetrahedral networks which mimics crystal growth or glass formation from a liquid [12]. The local rules for crystalline assembly are surprisingly simple (Figure 3a), even for polymorphs of low symmetry and high complexity. A tetrahedron is established in some initial orientation (offset), then copied, rotated according to the rules for each of the four vertices in turn, and connected to the initial tetrahedron. Assembly is rapid ($>$ 1000 tetrahedra/minute), with the full adjacency matrix and all atom coordinates available; models of 2,000-10,000 tetrahedra are routinely constructed to minimize influence of surfaces.

It is reasonable to assume that in glass formation similar but slightly deviant rules are obeyed, involving small changes in initial offset or rotation rules. Figure 3b illustrates a set of deviant rules based on β-cristobalite. 200-tetrahedra assemblies of both crystalline and glass structures are shown in Figure 4. Two optimization routines are required in such non-crystalline assemblies. An intersection check continually monitors steric compatibility, and all vertices are connected by Hookeian springs which are minimized globally in total stored elastic energy after every addition to preclude

(a)
```
Beta-Cristobalite
1
4 1
REGULAR
y 23 ;
0 1  z 90 ;
0 0  z -90 ;
0 3  z 90 ;
0 2  z -90 ;
```

(b)
```
a-Cristobalite
1
4 1
REGULAR
y 23 ;
0 1  z 85 ;
0 0  z -85 ;
0 3  z 85 ;
0 2  z -85 ;
```

Figure 3: Local rules for a) β-cristobalite, b) a cristobalite-like glass based on a 5° rotation error. The fifth line represents initial tetrahedron offset, the next four lines the assembly rotations of 4 added tetrahedra.

underconnection. The topologies of such rapidly-erected glass models can be quickly explored. Two local clusters in Figure 5 show that the topology is similar but distinguishable from that of the crystalline analogue.

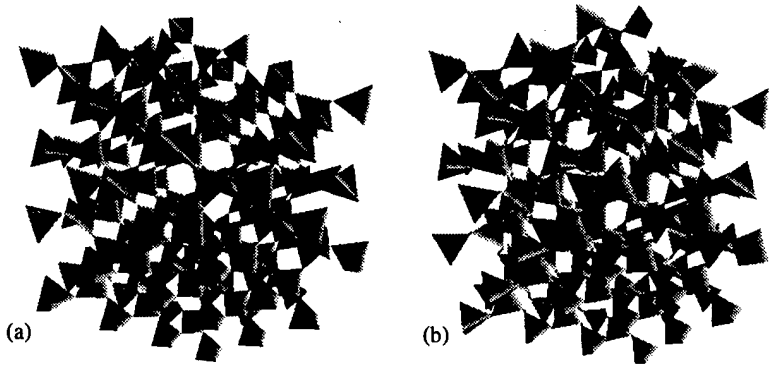

Figure 4: 200-tetrahedra models of a) β-cristobalite and b) cristobalite-like glass, assembled according to the rules in Figure 3.

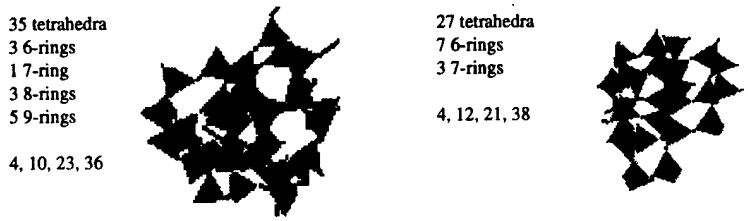

Figure 5: Two local clusters of cristobalite-like silica assembled with the rules in Figure 3b with number of tetrahedra in the cluster, ring counts, and first-fourth neighbor counts indicated.

[1] J.F. Shackleford, J. Non-Cryst. Solids **204** (1996) 205.[2] G.F. Voronoi, J. Reine Angew. Math. **134** (1908) 198. [3] B. N. Delauney, Sov. Math. **2** (1961) 812. [4] E. von Federov, Z. Kristallogr. **38** (1904) 321. [5] P.K. Gupta, J. Amer. Ceram. Soc. **76** (1993) 1088. [6] L. W. Hobbs, A. N. Sreeram, C. E. Jesurum & B. A. Berger, Nucl. Instrum. Meth. **B 116** (1996) 18. [7] W. H. Zachariasen, J. Amer. Chem. Soc. **54** (1932) 3841. [8] L. W. Hobbs, J. Non-Cryst. Solids **192&193** (1995) 79. [9] C. S. Marians & L. W. Hobbs, Diff. & Defect Data **53&54** (1987) 31. [10] C. S. Marians & L. W. Hobbs, J. Non-Cryst. Solids **119** (1987) 269. [11] C. S. Marians & L. W. Hobbs, J. Non-Cryst. Solids **124** (1990) 242. [12] L. W. Hobbs, C. E. Jesurum, V. Pulim & B. Berger, "Local topology of silica networks," Phil. Mag. B (in press, 1997). [13] B. Berger, A. P. Shor, L. Tucker-Kellogg & J. King, Natl. Acad. Sci. **91** (1994) 7732.

FIBRE GRATING DEVICES FOR TELECOMMUNICATIONS APPLICATIONS

P. SANSONETTI
ALCATEL TELECOM RESEARCH DIVISION
c/o ALCATEL ALSTHOM RECHERCHE
Route de Nozay
91460 MARCOUSSIS FRANCE
email: Pierre.Sansonetti@aar.alcatel-alsthom.fr

INTRODUCTION

Photosentivity occuring in germanium-doped silica [1] allows, through UV side holography [2], the simple and straightforward realization of permanent refractive index gratings in optical fibres. Low cost, low loss and very efficient all fibre filtering or multiplexing devices can therefore be realized, with extreme interest for future Transparent Optical Networks based on Wavelength Division Multiplexing (WDM), including chirped grating Chromatic Dispersion Compensator allowing to cope with bit rate increase per channel.

APPLICATIONS OF FIBRE GRATING DEVICES

The main applications of Fibre Grating Devices for photonics networks are now presented.

Optical Amplifier

Fibre grating can strongly improve the Erbium Doped Fibre Amplifier (EDFA) characteristics. The first application is gain equalization for WDM systems, which is necessary to transmit all wavelengths with the same quality, with equalization window being possibly as large as 30 nm. Slanted Bragg Grating [3] and Long Period Grating (LPG) [4] offer wideband-non reflective solutions, although LPG, based on the forward coupling between the fundamental mode and a cladding mode, is more sensitive than Bragg grating to fibre and manufacturing parameters, as well as presently temperature. Classical reflective Bragg grating can also be used [5], offering more mature technology, although an isolator is required to prevent feedback in the amplifier. It is foreseen that cross optimization of EDFA and filters will facilitate ultimate wideband operation.
Bragg gratings also allow the implementation of other functions like gain clamping through oscillation at a side wavelength [6], pump recycling in the amplifier [7], 980 nm pump spectral stabilization [8], high power 1480 nm pumping through either oscillation in Tm^{3+} doped fluoride fibres [9] or cascaded Raman lasers [10].

Optical Add Drop Multiplexers

The OADM is a key device for routing wavelengths in WDM transparent optical networks, since it can locally add and drop wavelength. Presently used solution is based on a grating located between two circulators. Although it works well and can offer some reconfigurability in term of wavelength, it is relatively expensive and has insertion loss of about 2 dB. Work is therefore being carried out on the association of fused coupler and fibre grating technologies to reach low cost-low loss devices. Devices are based on gratings in Mach-Zehnder [11] and more recently grating in 100% coupler [12] with potential for high stability.

Chromatic Dispersion Compensators

Chromatic Dispersion Compensation is very important since chromatic dispersion will become the limiting factor when bit rate increases in future networks. Linearly chirped grating offers very efficient solution to this [13], with high compensation and high Figure of Merit (ratio of chromatic dispersion to insertion loss). Although initial limitation on the length of the device restricted such compensation to a single channel, solutions for multi-wavelength operation [14] or wideband operation [15,16] have now been demonstrated, whilst remaining issues concern linearity of group delay and packaging. Third order dispersion compensation is also possible [17]. All these realizations show the strong potential of this technology, which will have to be compared to Dispersion Compensating Fibre (DCF), which lends itself naturally to WDM operation, but offers lower Figure of Merit and lower potential to tailor compensation characteristics than grating devices.

Band Pass filters

Although fibre Bragg grating is intrinsically reflective, several configurations have been studied to realize band-pass filtering, like those used for dropping in OADM with effort on apodized grating for dense WDM, as well as solutions based on single fibre, like Moiré grating [18], chirped grating [19], or phase shifted structures [20,21].

Sources

DFB fibre laser was recently reported [22], showing high efficiency, single frequency operation and linear polarisation state, which represents an important step for this technology. Fibre grating/semiconductor laser diode DBR configuration has also been reported [23] to exhibit low chirp and excellent direct modulation characteristics.

An important issue is the temperature sensitivity of Fibre Grating Devices, with drift of 0.01 nm/°C and 0.05 nm/°C for Bragg Grating and LPG respectively. Passive compensation of Bragg gratings has been demonstrated with specific packaging [24,25] or coating [26], whilst specific fibre was shown to be able to decrease the LPG figure [27]. Depending on the device requirements, passive compensation or active temperature stabilization could have to be used, for instance when dealing with dense WDM frequency grid.

CONCLUSIONS

UV-written Fibre grating devices have already entered the field of sub-systems or systems, usually as classical Bragg grating, like pump stabilizers, gratings with circulators for band-pass filter or OADM and medium-band gain equalizers. Further developments will involve devices like non reflecting wideband gain equalizers, Chromatic Dispersion Compensators, and grating/coupler OADM. The continuous evolution of fibre grating technology in terms of fibre and writing process should allow the development of extremely efficient devices, allowing to reach ultimate number of WDM channels and bit rate, with extensive use in photonics networks.

REFERENCES

[1] K.O. Hill et al, Appl. Phys. Lett., Vol 32, No 10, 647, 1978
[2] G. Meltz et al , Opt. Lett., 14 (15), 823, 1989
[3] R. Kashyap et al , Elect. Lett., 29(11), 1025, 1993
[4] P.F. Wysocki et al , Post Deadline Paper PD2, OFC Conference, 1997
[5] O. Gautheron et al, to be published at ECOC Conference, 1997
[6] E. Delevaque et al , Elect. Lett., Vol. 29, No. 12, 1993, p 1112
[7] I. Riant et al, Elect. Lett., Vol. 30, No. 3, 1994, p 221
[8] B.F. Ventrudo et al, Elect. Lett., 30, 2147, 1994
[9] P. Bousselet et al, Topical Meeting on Optical Amplifier, 1995
[10] S.G. Grubb et al, Topical Meeting on Optical Amplifier, 1995
[11] F. Bilodeau et al , OFC Conference, 1995, p 130
[12] F. Bakhti et al, Elect. Lett., Vol. 33, No. 9, p 803, 1997
[13] F. Ouellette, Opt. Lett., 12, p 847, 1987
[14] R. Kashyap et al, Paper MoB.4.3, ECOC Conference, 1996
[15] R. Kashyap et al, Post Deadline paper ThB3.2, ECOC Conference, 1996
[16] M.J. Cole et al, Post Deadline paper ThB3.5, ECOC Conference, 1996
[17] J.A.R. Williams et al, IEEE Phot. Tech. Lett., Vol. 8, No. 9, p 1187, 1996
[18] S. Legoubin et al, , Elect. Lett., Vol 27, No 21, 1945, 1991
[19] L. Zhang et al, Photosensitivity and Quadratic Non Linearity in Glass Waveguides, paper SuB11, 1995
[20] R. Kashyap et al, Elect. Lett., Vol. 30, No. 23, p 1977, 1994
[21] F. Bakhti et al, Elect. Lett., Vol. 32, No. 6, p 581, 1996
[22] L. Dong et al, Opt. Lett., Vol. 22, p 694, 1997
[23] F.N. Timofeev et al, Paper ThM1, OFC Conference, 1997
[24] Hamon et al, 1st OECC Conference, paper 18C1-2, 1996
[25] D.L. Weidman et al, Paper MoB.3.5, ECOC Conference, 1996
[26] T. Iwashima et al, Elect. Lett., Vol. 33, No. 5, p 417, 1997
[27] J.B. Judkins et al, Post Deadline Paper PD1, OFC Conference, 1996

Bragg Gratings, Photosensitivity, and Poling in Glass Fibers and Waveguides: Applications and Fundamentals

Grating Devices I

Sunday, October 26, 1997

Francois Ouellette, Kromafibre Corporation, Canada
Presider

BSuB
11:00am–12:30pm
Auditorium

Long-period fiber gratings

Ashish M. Vengsarkar
Bell Laboratories, Lucent Technologies
600 Mountain Avenue, Murray Hill, NJ 07974
email: ashish@lucent.com

Introduction

Long period fiber gratings that couple light from guided core modes to non-guided cladding modes provide a means of introducing wavelength dependent losses in optical fiber systems.[1] As a result, these in-fiber devices have found use as gain-equalizers in broadband optical fiber amplifiers,[2] as band-rejection filters in high-power cascaded Raman fiber lasers and amplifiers,[3] and as stabilizers in 980 nm pump diodes.[4] In addition, the ability to access the cladding mode has rendered them sensitive to external perturbations such as temperature, pressure and refractive-index with obvious applications as sensors.[5, 6] In this review, we highlight recent results and describe some of the key spectral and thermal properties of long-period fiber gratings.

Long-period gratings operate on the principle of phase-matching between two modes in a fiber, with the peak wavelength of coupling being given by

$$\lambda_p = (n_{01} - n_{lm})\,\Lambda\,, \qquad (1)$$

where Λ is the period of the grating, and n_{lm} are the effective indices of the LP_{lm} modes. In Eq. (1), we have specifically considered the coupling between the fundamental LP_{01} mode and an LP_{lm} mode, which is usually a cladding mode. Using Eq. (1), one can obtain a set of λ vs. Λ calibration curves for different cladding modes. Since we consider coupling between two co-propagating modes, the periodicity is in the hundreds of microns and the backreflection from such a grating is negligible. The transmission spectrum of a long-period grating is shown in Fig. 1.

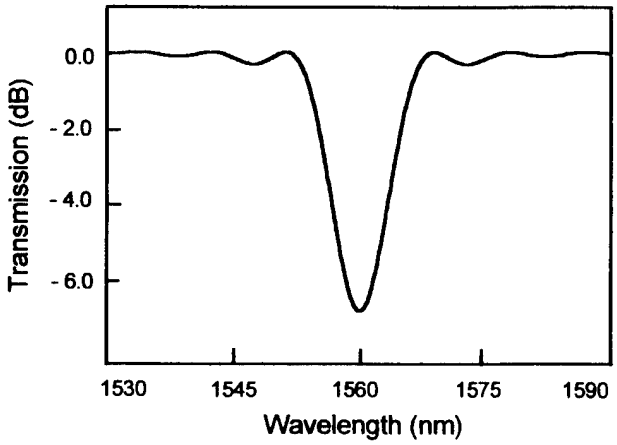

Figure 1. Transmission spectrum of a long-period grating. Peak losses can be as high as 30dB.

While the ability to attain a spectrally dependent loss is useful, it is more important to be able to tailor the spectrum to a pre-specified shape. This property is most useful in the design of gain equalizers for erbium doped fiber amplifiers. There are several techniques to modify the symmetric transmission spectrum shown in Fig. 1. Varying the uv-induced index along the length of the

grating, chirping the periodicity of the grating and adding dc-components to the ac-variations are obvious extensions of well-known techniques in the Bragg grating domain. Another simple manner of accomplishing complex shapes is to decompose a multi-peaked spectrum into its basic components, fabricate the individual gratings and concatenate the gratings.

Gain-equalization

A recent example of a gain-flattened erbium amplifier[7] used the long-period grating filter shown in Figure 2. The solid line is the theoretical inverse of the erbium gain spectrum and the dotted line is a composite spectrum of the long-period gratings fabricated for equalization. The two-stage amplifier with a 16 dB deep mid-stage grating yielded a gain of 22 dB over a 40 nm bandwidth with < 1 dB ripple and an internal optical noise figure of 4 dB.

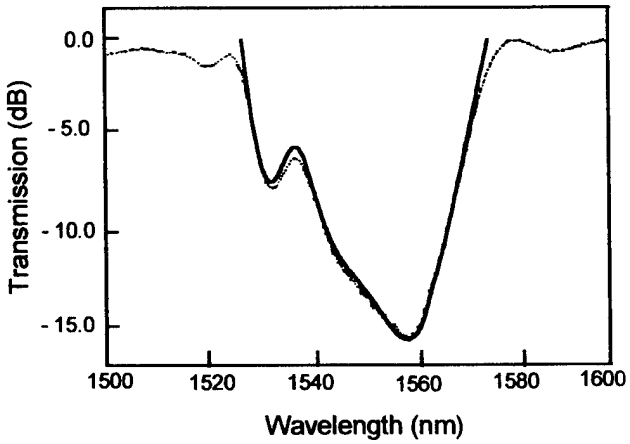

Figure 2. Long-period grating spectrum for 40 nm gain-flattened fiber amplifier.

Long-period grating-based equalizers have also been successfully used in system experiments where error-free 32 × 10 Gb/s transmission over 640 km was achieved through a chain of eight amplifiers, each gain flattened over a 35 nm bandwidth.[8]

Temperature-sensitivity

The exact shaping of grating spectra is extremely critical in efficiently using the entire bandwidth of erbium-doped amplifiers. For example, small deviations from the pre-specified shape can lead to large ripples in the flattened gain spectrum (Figure 3). Matters are further complicated when the grating spectrum changes due to temperature variations. We analyze the dependence of the peak wavelength on temperature by differentiating Eq. (1), viz.,

$$\frac{d\lambda_p}{dT} = \Lambda \cdot \frac{(\Delta n)^2}{\Delta n_g} \cdot \left(\frac{1}{(\Delta n)} \cdot \frac{d(\Delta n)}{dT} + \alpha \right), \qquad (2)$$

where α is the thermal expansion coefficient of the glass, Δn is the difference in effective indices ($\Delta n = n_{01} - n_{lm}$), and Δn_g is the difference in the group indices of the modes ($\Delta n_g = \Delta n -$

$\lambda\, d(\Delta n)/d\lambda)$. Since the core and the cladding modes occupy different regions of the composite fiber structure and are governed by dissimilar wave-guiding conditions, the effective indices of the two modes change differently with temperature; in communication-grade fiber, peak wavelength shifts range between 5 and 10 nm for a 100 °C change in temperature. From Fig. 3, we see that a 10°C change in temperature will lead to a peak shift of 0.5 to 1 nm, resulting in unacceptable gain ripples. From Eq. (2), the condition for temperature insensitivity in any long-period fiber grating can be written simply as $d(\Delta n)/dT = -(\Delta n)\alpha$. This condition shows that a suitable fiber design or choice of fiber materials can lead to reduced temperature sensitivity.

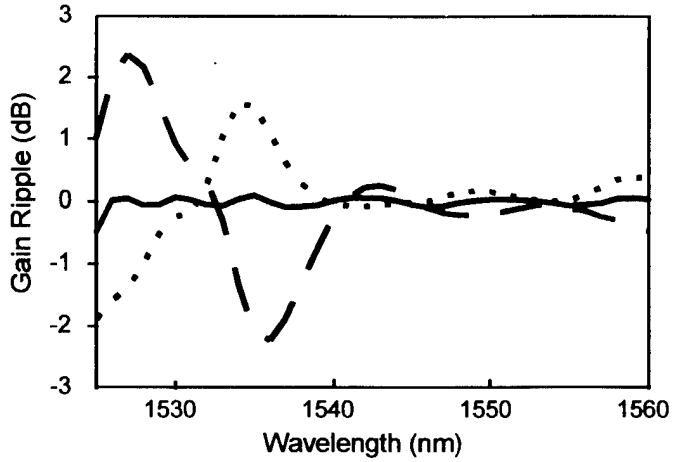

Figure 3. Gain flattened amplifier (solid line) and the impact of – 0.5 nm deviation (dotted line) and + 1.5 nm deviation (dashed line) from peak wavelength of gratings.

Temperature insensitive gratings have been demonstrated using two techniques. First, novel refractive index profiles[9] have been designed to make the entire right hand side of Eq. (2) equal zero.[10] Such long-period gratings in multi-layer fibers have led to a complete elimination of temperature dependence. Temperature-insensitive gratings with $d\lambda/dT$ between -0.4 and 0.1 nm/100°C have been demonstrated. One such example is shown in Figure 4.

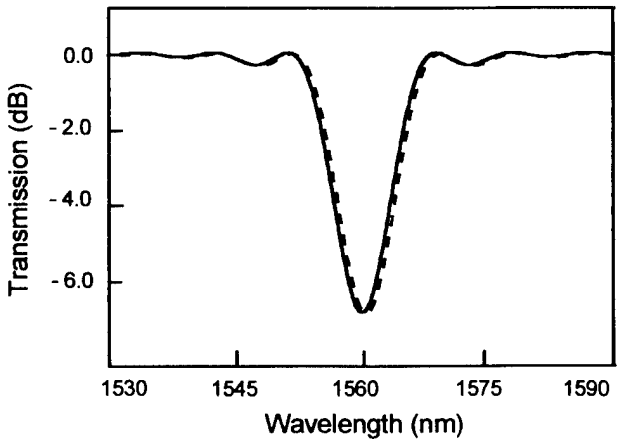

Figure 4. Spectra from a temperature-insensitive long-period grating. The curves are barely differentiable for a 100 °C change in temperature.

Another technique involves modifying the composition of the core by doping only the central section of the core with a negative thermal coefficient material such as B_2O_3.[11] This technique ignores the thermal expansion coefficient and reduces the temperature dependence by effectively reducing the value of $d(\Delta n)/dT$. Experimentally, we have observed that a desirable condition for temperature insensitivity is that the slope of the λ vs. Λ calibration curve be negative ($d\lambda/d\Lambda < 0$).

Current Status

Long-period gratings have become increasingly popular in a multitude of applications owing to their ease of fabrication, low insertion losses (outside the band of interest), low back-reflections, low polarization sensitivities, and compact sizes (typically a few centimeters in length). Further, basic issues regarding manufacturing, reliability, and packaging are well understood and long-period grating-based gain-equalizers and band-rejection filters are commercially available.

The dependence of their spectral properties on strain, bending, and pressure has been studied empirically but not completely and carefully characterized. As sensing applications proliferate, a theoretical understanding of this behavior can lead to a design of measurand-specific gratings. Another important property of these gratings that has not been fully exploited pertains to the ease of access to the out-coupled cladding mode. The cladding modes straddle the cladding-air boundary and the index layer at this interface can be externally modulated via the application of nonlinear materials. While optically induced nonlinear properties of such gratings have been recently investigated,[12] work in this domain has been sparse. Actively modulating long-period gratings either by deposition of nonlinear materials or by high-energy optical pulses can lead to a treasure trove of practical fiber devices.

Acknowledgments

I would like to thank R. P. Espindola, J. B. Judkins, J. L. Wagener, and P. F. Wysocki, all of Lucent Technologies. The material presented here is generously borrowed from their work.

References

1. A. M. Vengsarkar, *et al.*, J. Lightwave Technol. 58 (1996).
2. A. M. Vengsarkar, *et al.*, Opt. Lett., 336 (1996).
3. D. Inniss, *et al.*, CLEO '97, Paper PD10, Baltimore, Maryland, May 1997.
4. G. Jacobovitz-Veselka, *et al.*, Opt. Amp. Mtg., Paper FC4, Davos, Switzerland, June 1995.
5. V. Bhatia and A. M. Vengsarkar, Opt. Lett., 692 (1996).
6. H. J. Patrick, *et al.*, IEEE Photon. Technol. Lett., 1223 (1996).
7. P. Wysocki *et al.*, OFC '97, Paper PD2, Dallas, Texas, February 1997.
8. A. K. Srivastava *et al.*, OFC '97, Paper PD18, Dallas, Texas, February 1997.
9. J. B. Judkins, *et al.*, OFC '96, Paper PD1, San Jose, California, February 1996.
10. Note that Eq. (2) in this paper differs from Eq. (3) of Ref. 9 by a multiplication factor. We believe Eq. (2) in this paper is in the correct format.
11. K. Shima, *et al.*, Proc. OFC '97, Paper FB2, p. 347, Dallas, Texas, February 1997.
12. B. J. Eggleton, *et al.*, Opt. Lett., 884 (1997).

Long-period fiber-grating devices based on leaky cladding mode coupling

D. B. Stegall and T. Erdogan
The Institute of Optics, University of Rochester, Rochester, NY 14627

Fiber gratings allow great flexibility in the design of all-fiber devices by enabling control over the wavelength, direction, polarization, and mode characteristics of light. In particular, long-period, or transmission, fiber gratings produce devices based on co-directional mode coupling which naturally result in a desirable transmissive rather than reflective output. In a single-mode fiber, coupling to cladding modes can be utilized for various functions, especially wavelength-dependent loss filtering [1]. In this paper we describe alternative applications of transmission fiber grating devices based on coupling to *leaky* cladding modes.

In conventional cladding-mode coupling fiber gratings the single core mode is converted to guided cladding modes which are totally internally reflected by the cladding-surround interface. Typically the region surrounding the cladding is air, but because the cladding mode effective indexes are sensitive to the refractive index n_s of the surround, and the wavelength of maximum coupling to a cladding mode by a grating of period Λ is given by

$$\lambda_{max} = \left(n_{eff,co} - n_{eff,cl}\right)\Lambda, \tag{1}$$

where $n_{eff,co}$ and $n_{eff,cl}$ are the effective indexes of the core and cladding modes, respectively, these gratings make effective sensors of the index surrounding a conventional single-mode fiber [2,3]. The sensitivity can be increased by increasing the length traveled by the cladding mode, either by making the grating longer, or by combining gratings interferometrically, such as in the Mach-Zehnder configuration shown in Figure 1. Here two 3-dB fiber gratings function like 50% beam splitters, and the two "arms" of the interferometer are the paths traveled by the core mode and the cladding mode.

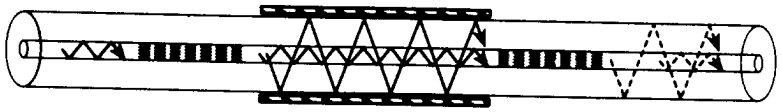

Figure 1: a Mach-Zehnder mode interferometer.

Sensing is an important application for cladding-mode coupling fiber gratings. But the flexibility for making *devices* afforded by the ability to temporarily and non-destructively extract light from the core of a single-mode fiber and propagate it in an "accessible" cladding mode should not be overlooked. For example, if the surround region in the device shown in Figure 1 contains a material with gain, loss, or a refractive index that can be controlled externally by either light or an electrical signal, the optical signal output in the single-mode core can be externally switched or spectrally controlled.

While such devices might appear simple to implement, unfortunately few materials with desirable, adjustable optical properties have an index of refraction less than that of glass ($n \approx 1.45$), and thus cladding modes may not be supported by total internal reflection. The ability to easily apply materials such as polymers, liquid crystals, or certain semiconductors to a fiber places further constraints on material choice. As a result, it is apparently useful to investigate how well cladding modes may be guided in the leaky, "hollow-waveguide" geometry, in which the surround index is substantially *greater* than that of the glass cladding.

A simple and reasonably accurate estimate of the propagation of circularly symmetric leaky modes in a "hollow" dielectric cylinder can be obtained by analyzing the corresponding planar waveguide geometry. (Note that a transversely uniform, non-tilted fiber grating efficiently couples light only to the circularly symmetric cladding modes [4].) Marcuse treats this case using a power flow approach [5]. For a simpler, more intuitive picture, consider a ray of light bouncing in the hollow

waveguide (of index n_{cl}) with an angle of incidence θ at the two cladding-surround interfaces, as depicted in Figure 2. Constructive interference and hence mode-like propagation of the plane waves associated with the ray occurs only at angles θ_m such that

$$\cos\theta_m = m\lambda/2Dn_{cl}\ ;\ m = 1,2,3\ldots, \qquad (2)$$

where D is the waveguide width (corresponding to the fiber diameter). Eq. (2) thus determines the mode bounce angles. Leakage occurs because in the absence of total internal reflection not all of the light is reflected at each bounce. If we define the loss length L to be the distance traveled before the power drops by a factor of $1/e^2$, then we find

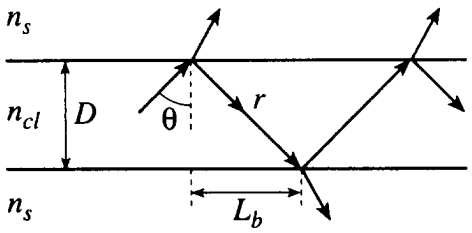

Figure 2: Ray picture of leaky modes in a "hollow" dielectric waveguide.

$$L \approx -(1 + 1/\ln|r|)\,L_b, \qquad (3)$$

where r is the familiar Fresnel reflection (amplitude) coefficient and $L_b = D\tan\theta$ is the distance between successive ray bounces. Figure 3 shows the power loss (in dB/cm) corresponding to the loss length in Eq. (3) for the first 10 modes of a 125 μm diameter waveguide with an index of n_{cl} = 1.45. Clearly the lowest order modes can sustain losses smaller than a few tenths of a dB/cm, which are reasonable values for devices.

Patrick, et al, reported experimental evidence of coupling to leaky modes in transmission fiber gratings in Ref. [3]. Here, to further test the leaky-mode losses and quantify the ability to efficiently couple light from the core of a single-mode fiber to these leaky modes, we wrote a number of transmission fiber gratings and examined the propagation of light through these for various surround indexes. For example, Figure 4 shows the measured transmission of the LP_{01} core mode through one such grating as a function of wavelength. The grating is slightly apodized (hence the asymmetric spectrum), about 20 mm long, and written in Corning Flexcore 1060 fiber. The resonance shown corresponds to the 6th strongly coupled cladding mode (mode 11 using the notation of [4], and mode 6 in Figure 3). The surround index was varied by immersing the bare fiber in commercial index-matching fluids of known refractive index. When the surround index (listed on the plot) is smaller than the fiber cladding index, a strong cladding mode resonance occurs. Here most efficient coupling occurs for $n_s \sim 1.4$, for which the minimum transmission is less than –30 dB (measurement noise limited), implying greater than 99.9% coupling to the

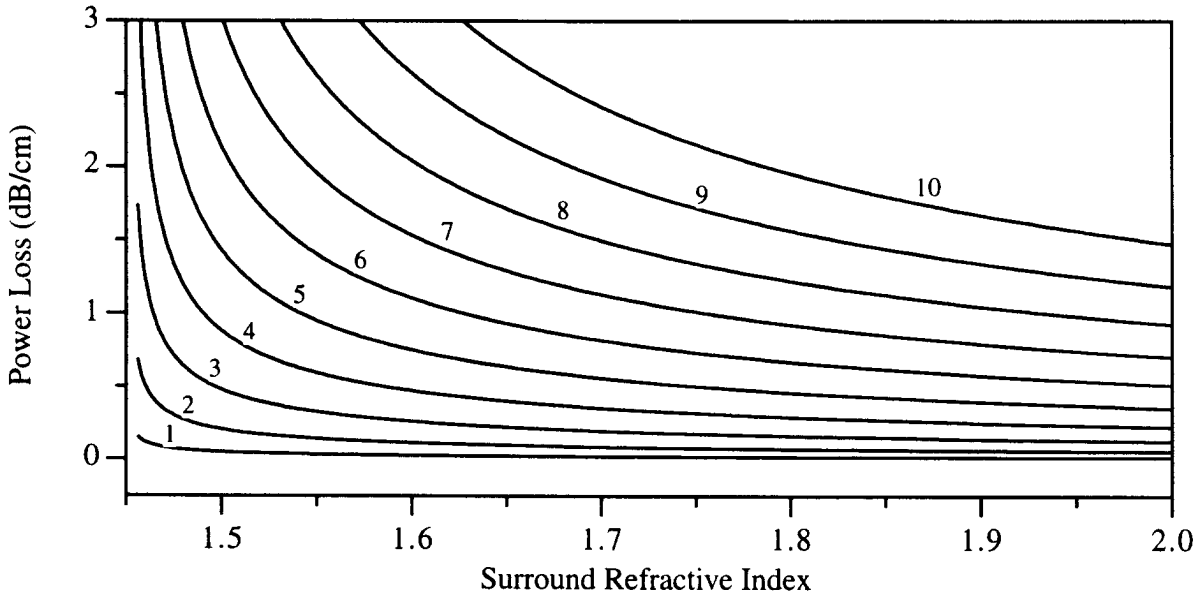

Figure 3: Power loss vs. the index surrounding a hollow dielectric waveguide of core index 1.45 for the first 10 modes from a simple ray analysis.

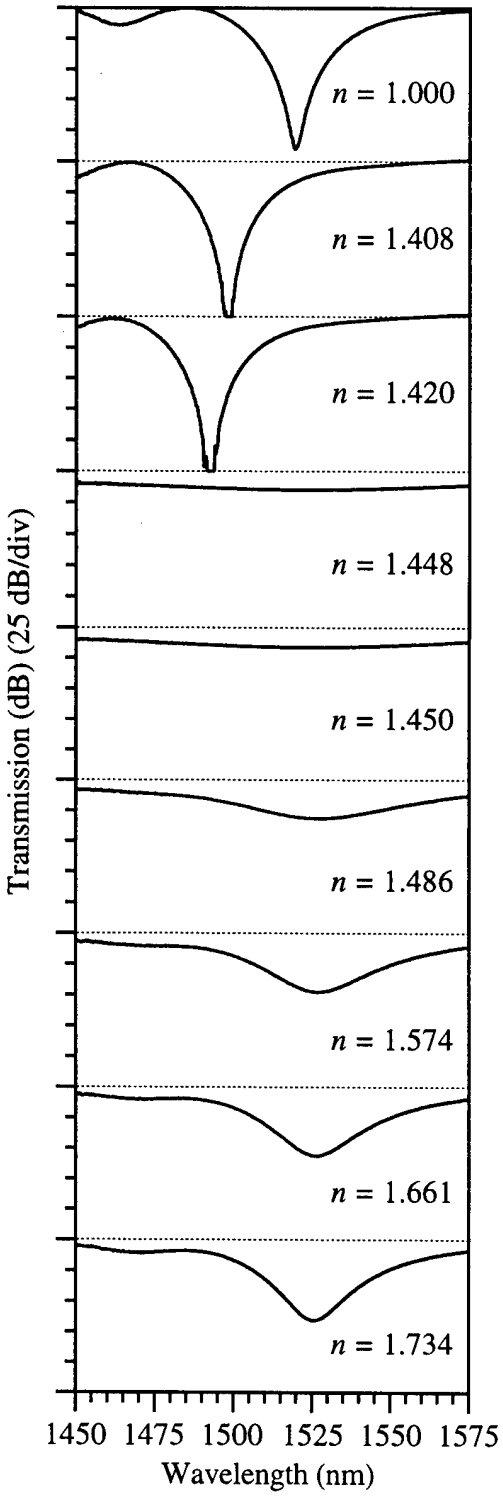

Figure 4: Measured transmission spectra through a long-period fiber grating as the refractive index of the region surrounding the fiber is varied.

cladding mode. When the surround index is approximately equal to the cladding index, there is a few dB of broadband radiation-mode coupling loss, but no distinct resonances. As the surround index is further increased, resonances begin to develop associated with coupling to the leaky modes of the hollow waveguide geometry. For this grating, when n_s exceeds about 1.7 the resonance dip falls to –13 dB, implying about 95% coupling to the leaky mode. According to Figure 3, this leaky mode should propagate with just under 1 dB/cm of loss. The measured spectra can be shown to agree with theoretical calculations of mode coupling in a transmission fiber grating in which the cladding modes have losses given by the estimated leaky-mode losses.

In summary, this paper describes an investigation of the utility of leaky cladding modes for transmission fiber-grating devices. It is shown that efficient coupling to leaky modes with reasonably low losses can be obtained. Currently a number of device concepts are under investigation.

References:

[1] A.M. Vengsarkar, P.J. Lemaire, J.B. Judkins, V. Bhatia, T. Erdogan, and J.E. Sipe, "Long-period fiber gratings as band-rejection filters," *J. Lightwave Tech.*, vol. 14, pp. 58-65, 1996.

[2] V. Bhatia and A.M. Vengsarkar, "Optical fiber long-period grating sensors," *Opt. Lett.*, vol. 21, pp. 692-694, 1996.

[3] H. Patrick, A.D. Kersey, F. Bucholtz, K.J. Ewing, J.B. Judkins, and A. M. Vengsarkar, "Chemical sensor based on long-period fiber grating response to index of refraction," Paper CThQ5, Conf. on Lasers and Electro-Optics, Baltimore, MD, May 18-23, 1997.

[4] T. Erdogan, "Cladding-mode resonances in short- and long-period fiber grating filters," *J. Opt. Soc. Am. A*, vol. 14, no. 8, 1997.

[5] D. Marcuse, *Theory of Dielectric Optical Waveguides*, (Boston, Academic, 1991), 1.5-1.6.

Polarization dependence of photo-induced birefringence and its application to fabrication of tailored polarization filters

R. Feced, S. E. Kanellopoulos, R. A. Griffin*, V. A. Handerek.

Department of Electronic and Electrical Engineering
King's College London, Strand, London WC2R 2LS, U. K.
Phone : 44 171 836 5454 ext. 1259; Fax: 44 171 873 2844

1. Introduction

Photo-induced anisotropy has been observed in optical fibers exposed to polarized blue-green[1-4] and U.V. light[6-10]. The control of the fiber birefringence has permitted the fabrication of polarization rocking filters, which have found use in both sensing and communication applications. The physical mechanism underlying this effect is thought to be the preferential excitation and depletion of those anisotropic defects whose polarizability is aligned with the incident field polarization, causing a reduction of polarizability along that direction[3,4,11]. In this paper, we study the polarization dependence of photo-induced birefringence in elliptical core fibers and, as a consequence, propose a technique for fabrication of polarization rocking filters with tailored coupling spectrum.

2. Characterization of polarization rocking filters

A polarization rocking filter with an average rocking period Λ is characterized through its coupling function $\kappa(z)$:

$$\kappa(z) = c(z)\Lambda\, e^{j2\pi\frac{z}{\Lambda}} + \text{c.c.} \qquad (1)$$

where $c(z)$ is a complex slowly varying function and c.c. stands for complex conjugated. $c(z)\Lambda$ is the coupling strength per period Λ of the filter. If $E_x(z)$ and $E_y(z)$ are the electric field amplitudes ($e_{x,y}(z,t) = E_{x,y}(z)e^{-jkn_{x,y}z}e^{j\omega t}$), then the field evolution along the filter is described through the coupled equations:

$$\frac{dE_x}{dz} = -jc(z)\; e^{j2\pi\frac{z}{\Lambda}}\, e^{-j\int_0^z \frac{2\pi}{L_B(\lambda,z')}dz'}\, E_y$$
$$\frac{dE_y}{dz} = -jc^*(z)\, e^{-j2\pi\frac{z}{\Lambda}}\, e^{+j\int_0^z \frac{2\pi}{L_B(\lambda,z')}dz'}\, E_x \qquad (2)$$

where $L_B(\lambda,z')$ is the local beatlength at position z' and wavelength λ.

3. Polarization dependence of photo-induced birefringence: experiments with green light

We wrote rocking filters by the internal method[1,2] launching linearly polarized CW green light from an Ar-ion laser at different angles ϕ with respect to the slow axis of an elliptical core fiber (Fig.1). The fiber, manufactured by Andrew Corporation, had core dimensions of 1x2 μm, a core-cladding index difference of 0.03 and was single mode at 514 nm. The total length of the filters was 132 beatlengths, each beatlength being 4.5 mm at 514 nm. The fibers were exposed to 140 mW for 15 minutes. After the exposure, we monitored the coupling spectrum of each filter, observing that their resonance wavelengths depended on the angle ϕ. These wavelength shifts are due to a change in the background fiber birefringence (or beatlength) produced by the asymmetry of the writing process:

$$\Delta L_B(\phi) \approx -2\frac{\partial L_B}{\partial \lambda}\Delta\lambda(\phi) \qquad (3)$$

where $\Delta\lambda(\phi)$ are the resonance wavelength shifts and $\Delta L_B(\phi)$ the corresponding beatlength changes at 514 nm (Fig.1).

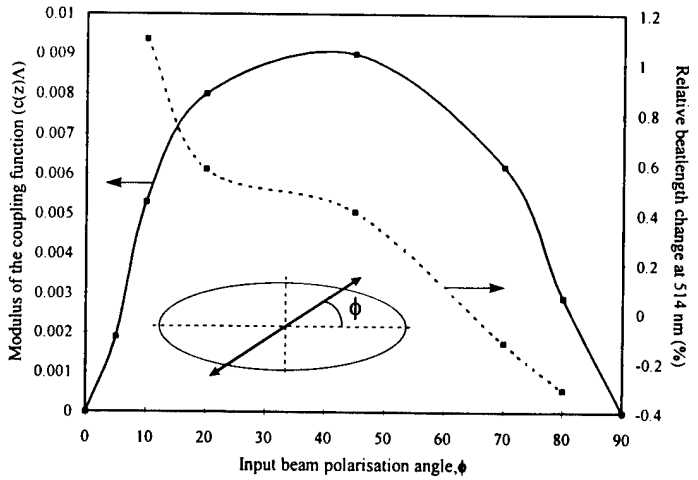

Figure 1. Angular dependence of photoinduced birefringence

We also monitored the dependence of the coupling function c(z)Λ on the angle ϕ (Fig.1). The following conclusions can be drawn from this experiment:

- When green light is polarized mainly along the slow axis, there is a reduction in the fiber birefringence. Conversely, when the green light is polarized along the fast axis, there is an increase in birefringence. These results are in agreement with the depletion model[11].
- The coupling function (c(z)Λ) is asymmetric with respect to ϕ=45°. This is consistent with the filter growth dynamics previously reported[4]. An important consequence of this experiment is that the coupling function c(z)Λ decreases near the polarization axes, showing that the angle ϕ could be used to control the strength of the coupler.

4. Fabrication of tailored polarization rocking filters with U.V. light

The usual procedure to write rocking filters that operate at long wavelengths is to externally expose the fiber point by point to U.V. polarized light[6,7]. Devices with tailored coupling spectrum will be necessary for practical applications, e.g. apodised filters. The fabrication of these tailored polarization rocking filters requires an accurate control of the phase and modulus of c(z).

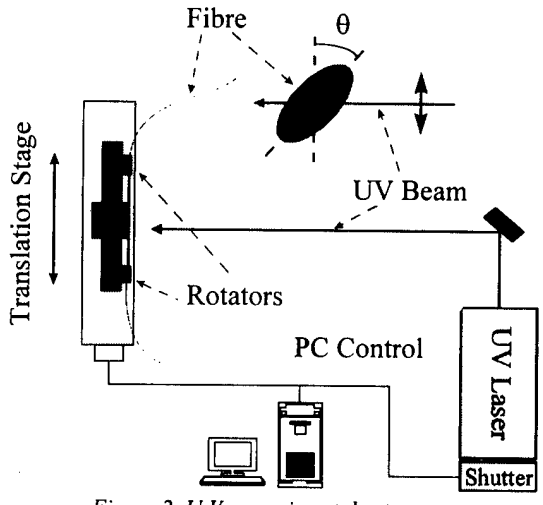

Figure 2. U.V. experimental set-up

In our set-up, the U.V. beam is polarized perpendicularly to the plane defined by the fiber and the incident beam, and the slow axis of the elliptical core fiber forms an angle θ (usually 45°) with respect to this U.V. polarization (Fig.2). The phase of c(z) can be controlled by changing the distance between adjacent points of exposure. The modulus of c(z), on the other hand, could be in principle tailored by monitoring the total fluence delivered to each exposed point. However, this method is not reliable because of the nonlinear fiber response due to saturation of the photo-induced birefringence. Besides, it has also been shown that for high fluences the fiber response could be non-monotonic[10].

From the previous experiments with green light, it is clear that an alternative procedure could be to control accurately the angle θ between the fiber's slow axis and the polarization of the U.V. beam. c(z) would then

be proportional to $F \cdot \sin(2\theta)$, where F is the total fluence of the exposure. It can be appreciated that the sign of $\kappa(z)$ in (1) will depend both on the angle θ ($\sin 2\theta \gtrless 0$) and on the position of exposure (phase of $c(z)$)[8].

A polarization Moiré grating is an example of a device that needs control of the coupling function. We have carried out several experiments during this work which show that, contrary to the case of Moiré Bragg gratings, double exposure techniques[12] fail in the fabrication of polarization Moiré gratings. The reason is that, due to the reversibility of the photo-induced birefringence[3,9], the final change of birefringence is not the linear sum of the changes induced in each individual exposure. The coupling function $\kappa(z)$ of a Moiré grating is proportional to $\cos(\pi z/L)\cdot\sin(2\pi z/\Lambda)$, where L is the total length of the filter. To achieve this perturbation of birefringence with the present technique, the axes of the fiber were uniformly twisted from an angle θ equal to 45° at the beginning of the filter ($z=0$) to an angle of -45° at the filter's end ($z=L$) during the U.V. exposure. The elliptical core fiber used, made by Andrew Corporation, had a beatlength of 4.4 mm at 658 nm. It was exposed to 240 nm U.V. light in 40 equidistant points with one beatlength separation between adjacent points. Each point had a longitudinal exposed length of 2 mm and received a total fluence of 11 J/cm^2. The coupling spectrum of the Moiré grating is shown in Fig.3. From the phase and modulus of the filter response, we calculated, in first order Born approximation, the phase and modulus of the coupling function $c(z)\Lambda$ along the filter (Fig.4). It can be observed that the modulus is maximum near to the beginning and end of the filter where the angle θ was 45° and -45° respectively. There is also an abrupt change of π in the phase of the coupling function as the angle θ passes through 0°.

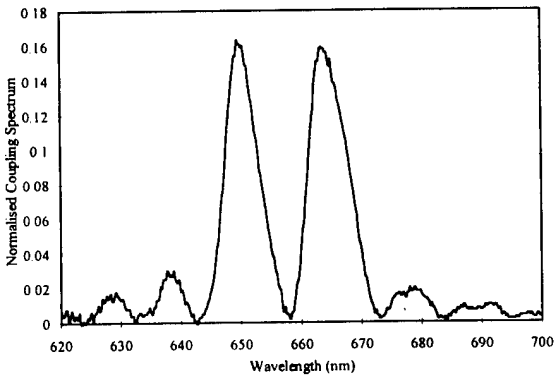

Figure 3. Moiré coupling spectrum

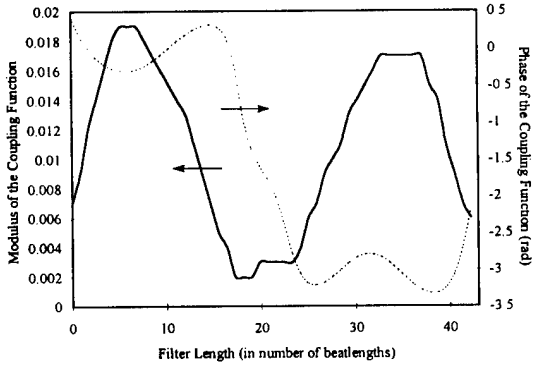

Figure 4. Modulus and phase of the coupling function $c(z)\Lambda$

5. Conclusion

In this paper we have studied the polarization dependence of photo-induced birefringence in elliptical core fibers. The angular dependence of the coupling strength of these filters was characterized, showing that it could be used to fabricate polarization rocking filters with tailored coupling spectrum.

R. Feced thanks L. Gómez-Rojas for his help, and BICC Cables Limited for financial support.

1. P. St. J. Russell, D. P. Hand, Electron. Lett. 26, 1846 (1990).
2. S.E. Kanellopoulos, L.G. Valente, V.A. Handerek, A.J. Rogers, IEEE Phot. Tech. Lett. 3, 806 (1991).
3. S. Bardal, A. Kamal, P. St. J. Russell, Opt. Lett. 17, 411 (1992).
4. J. Lauzon, D. Gagnon, S. LaRochelle, A. Blouin, F. Ouellette , Opt. Lett. 17, 1664 (1992).
6. K. O. Hill, F. Bilodeau, B. Malo, D. C.Johnson, Electron. Lett. 27, 1548 (1991).
7. S. E. Kanellopoulos, V. A. Handerek and A. J. Rogers, Electron. Lett. 28, 1558 (1992).
8. D.C. Psaila, C. Martijn de Sterke, F. Ouellette, Electron. Lett. 31, 1093 (1995).
9. T. Meyer, P.A.Nicati, P.A.Robert, D.Varelas, H.G.Limberger, R.P. Salathé, Opt. Lett. 21, 1661 (1996).
10. D.C. Psaila, F. Ouellette, C. Martijn de Sterke, Appl. Phys. Lett. 68, 900 (1996).
11. A. Kamal and P. St. J. Russell, J. Opt. Soc. Am. B 11, 1577 (1994).
12. S. Legoubin,E.Fertein,M.Douay,P.Bernage, P.Niay, F.Bayon,T.Georges, Electron.Lett.27,1945(1991).

*Current address: Dept. Electronic & Electrical Eng. University College London. Torrington Place. London WC1E 7JE

Polarization-independent strong Bragg gratings in Planar Lightwave Circuits from ArF laser irradiation through a phase mask.

J. Albert, F. Bilodeau, D. C. Johnson, K. O. Hill, S. J. Mihailov and D. Stryckman
Communications Research Centre, P.O. Box 11490 Station H, Ottawa (ONT)
CANADA K2H 8S2
T. Kitagawa
NTT Optoelectronics Laboratories, Tokai, Ibaraki 319-11, JAPAN
Y. Hibino
Photonic Integration Research, Inc. (PIRI), 2727 Scioto Parkway, Columbus, OH 43221-4658

Highly functional Planar Lightwave Circuits (PLC) can be designed using silica-on-silicon waveguide technology,[1] and the possibility of writing Bragg gratings in such waveguides further enhances their potential uses.[2] Strong Bragg gratings photoinduced in planar silica-on-silicon waveguides with a germanium-doped core are usually obtained by high pressure hydrogen loading of the glass prior to exposure.[2,3] In the work presented here we demonstrate that hydrogen loading is not necessary when high intensity light at 193 nm from an ArF laser is used to produce the index change, an effect originally observed in germanium-doped optical fibers.[4,5] The waveguides used are standard PLCs with a core index difference (Δ) of 0.75% (commercially available) and 1%.[1] One drawback of silica-on-silicon waveguides is their small strain birefringence.[6,7] We show here that there is a sizeable birefringence in the ArF laser-induced average index change that is large enough and of the proper sign to compensate for the initial waveguide birefringence. For demonstration, 4 mm-long Bragg grating filters with more than 30 dB of transmission loss at the Bragg wavelength are presented.

The Bragg gratings are fabricated using a 5 mm-long phase mask with a grating period of 1.050 μm and groove depth of 220 nm which was carefully positioned in front of the waveguide. This mask was not designed specifically for this work and has imperfect zero order nulling (10% transmission) at 193 nm, thereby reducing the modulation contrast of the grating.[8] The exposure of the guide through the phase mask is carried out with a Lumonics EX-500 excimer laser filled with an argon fluoride mixture to produce ~10 ns pulses of 193 nm light. A combination of slits, lenses, and mirrors is used to control the light spot intensity and size at the waveguide. The exposure conditions for most of the work reported here are a pulse repetition rate of 100 pulses per second with an average fluence between 200 and 300 mJ/cm^2 at the waveguide. For measurements of the spectral response, broadband light from the spontaneous emission of a 980 nm pumped erbium doped fiber is transmitted through a polarization control device and butt-coupled to a waveguide through polarization maintaining fiber. The output of the waveguide is butt-coupled to standard single mode telecommunications fiber and detected by an optical spectrum analyzer. The index modulation amplitudes are calculated from the grating extinction ratio, and the average index by the shift of the Bragg wavelength.

As shown in Figure 1, UV-induced refractive index modulations approaching 2 X 10^{-3} are obtained in PLCs with Δ of 1% without the need for hydrogen loading (for commercially available PLCs (Δ=0.75%), the largest index modulation achieved so far is 1.2X10^{-3}). The fluence per pulse was 250 mJ/cm^2 and the total exposure time less than 14 minutes at 100 pps. In

addition, the average UV-induced index growth is anomalous in the sense that it is much smaller than the index modulation, opposite to what is observed in fibers (especially with non ideal zero order nulling in the phase mask). The irradiation was interrupted several times to allow detailed measurements without noticeable effect on the growth of the grating. When the irradiation suddenly stops, the Bragg wavelength of the grating rapidly shifts towards the blue by less than 0.2 nm, indicating that the temperature rise during the exposure is less than about 20 degrees C.

In addition to being smaller than the index modulation, the UV-induced average index is birefringent.[5] The results of Figure 2 (PLCs with $\Delta = 0.75\%$) show that the Bragg wavelength (or average induced index) grows at a different rate for the two polarizations and crosses over when the growth in the index modulation amplitude reaches roughly 3×10^{-4}. The crossover point depends on the details of the exposure and must be monitored in real time to achieve identical Bragg spectra for the two polarizations. By exposing further it can be seen that the birefringence between the TM and TE modes can be reversed, i.e. going from -2×10^{-4} to $+2 \times 10^{-4}$. The final result (Figure 3) shows that devices of high spectral quality and polarization independent operation can be fabricated in the commercially available PLCs. In this case a Mach-Zehnder interferometer circuit was defined on the planar waveguide with Δ of 0.75% and 3.8 mm-long Bragg gratings written separately in the two arms of the interferometer. The details and performance of this device will be presented elsewhere but the output spectra of the through port indicate a transmission dip of -35 dB, and a Bragg wavelength difference of less than 0.03 nm between the TE and TM modes. It is noteworthy that while the growth of the average index is different for TE and TM modes, the index modulation amplitude grows at the same rate. It is this peculiarity which allows polarization independent devices (same Bragg wavelength and reflectivity) to be fabricated.

The UV induced birefringence and anomalous ratio of index modulation to average induced index are thought to arise from bulk dilatation of the glass, possibly due to laser induced strutural damage at the silica-silicon interface. Such dilatation would induce a *negative* average index change which would cause the apparent net average index change to be smaller than expected. This would also explain the growth of the birefringence in the average index since the planar geometry of the waveguide structure restricts the expansion differently in the parallel (TE modes) and perpendicular (TM modes) directions relative to the waveguide surface. The index modulation is not affected by this phenomenon.

REFERENCES

[1] M. Kawachi, IEE Proc.-Optoelectron. **143**, 257 (1996)
[2] Y. Hibino *et al.*, Photon. Technol. Lett. **8**, 84 (1996)
[3] P. J. Lemaire *et al.*, Electron. Lett. **29**, 1191 (1993)
[4] J. Albert *et al.*, Opt. Lett. **19**, 387 (1994)
[5] B. Malo *et al.* Electron. Lett. **31**, 879 (1995)
[6] M. Abe *et al.*, Proc. MOC/GRIN'93, paper D4, p.66 (1993)
[7] J. Canning *et al.*, Electron. Lett. **32**, 1479 (1996)
[8] K. O. Hill *et al.*, Appl. Phys. Lett. **62**, 1035 (1993)

Fig. 1 UV-induced index changes

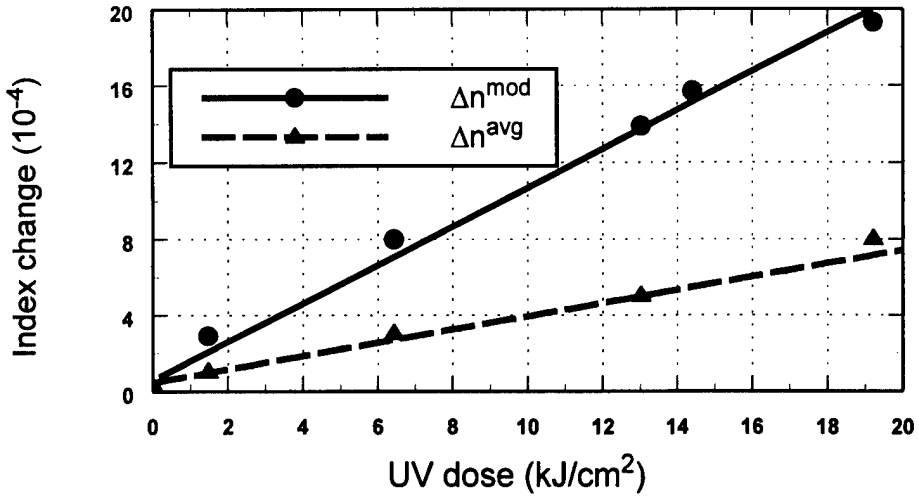

Fig. 2 Bragg wavelength shift vs growth of index modulation

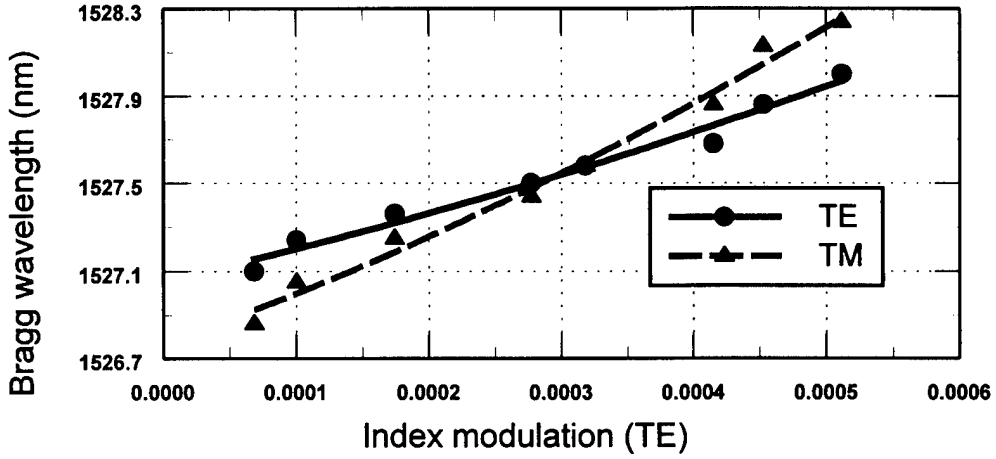

Fig. 3 Final transmission spectra for strong Bragg gratings

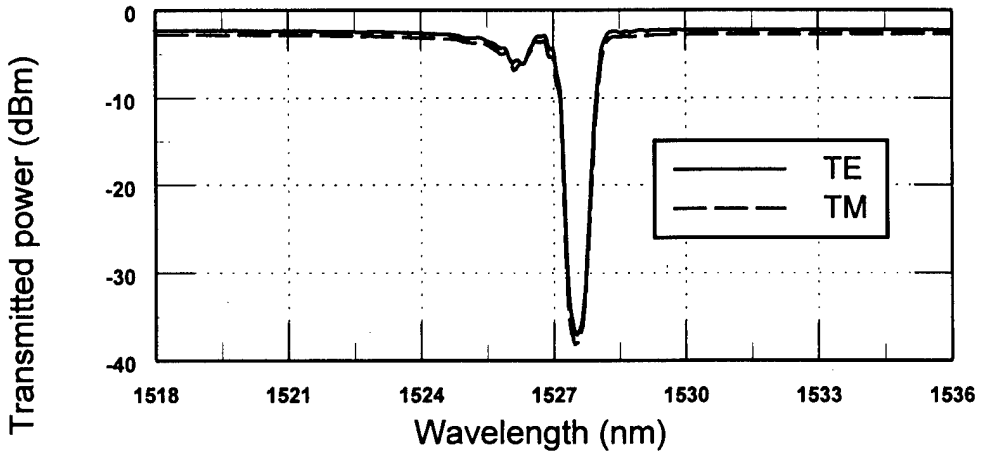

Novel Liquid and Liquid Crystal Cored Fibre Bragg Gratings

Raman Kashyap, Doug L Williams & Ray P Smith
BT Laboratories, Martlesham Heath, Ipswich IP5 3RE, United Kingdom
Tel: +44 1473 645363; Fax: +44 1473 646885
email: raman.kashyap@bt-sys.bt.co.uk

Tunable filters are useful for a number of applications. Recently, fibre Bragg gratings were written in poled silica fibres[1]. The reflectivity of the grating and partial tuning was subsequently achieved by the application of an electric field. An alternative scheme for a tunable filter is proposed in this paper using liquid-crystal or liquid cores.

This paper demonstrates oil and liquid-crystal-cored fibre Bragg gratings using a special fibre-capillary with an inner photosensitive cladding. This fibre waveguide has special properties, for example, a negative temperature coefficient of Bragg wavelength shift, counter to normal fibres, and is potentially tunable by the application of an electric field.

The capillary fibre with an inner photo-sensitive cladding is shown in Figure 1. By co-doping germania with boron[2] the inner cladding is matched to the silica tube. In the capillary tubes reported in this paper, the refractive index of the deposited cladding was slightly lower than silica (~0.001). The fibre was drawn from the preform in a standard fibre-drawing tower. The fibre had an outside diameter of 125 μm with a hole of ~6 μm diameter. The matched cladding thickness was also ~ 6 microns. A 6mm long Bragg grating was written in the empty capillary using a frequency doubled Argon laser operating at 244nm and a phase-mask[3], after being soaked in deuterium for 14 days under high pressure. The piece of the capillary fibre was 83mm long and had the Bragg grating was situated ~54 mm from the end. This was butt coupled to a connectorised fibred circulator with a de-mountable standard single-mode fibre pigtail. The liquid-crystal was filled by capillary action. The average refractive index of the liquid crystal is ~1.461[4] at around room temperature.

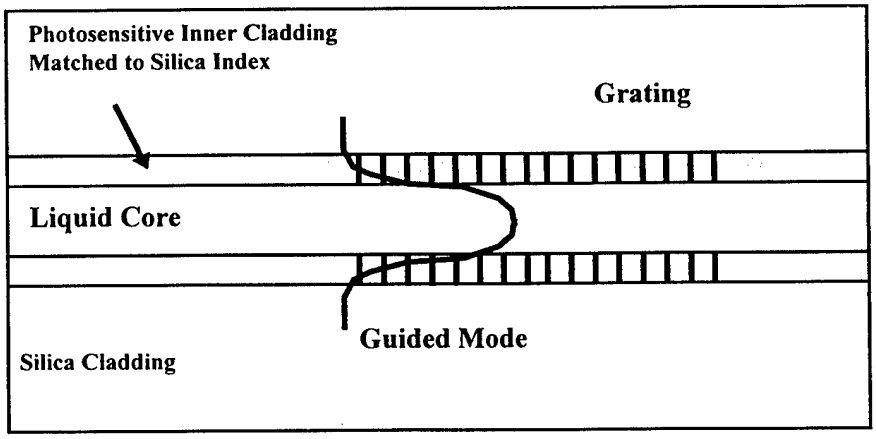

Figure 1. The liquid-cored Bragg grating fibre with an inner photosensitive matched cladding[5].

Using an ELED source, the reflected signal was monitored on a spectrum analyser while the guide was filling. When the reflected signal was observed, the output was also butt coupled to another single-mode fibre and the transmission displayed on the spectrum analyser. Figure 2 shows the measured launched, reflected and transmitted spectra. The insertion loss of the whole was measured to be ~ 2dB, while the loss in reflection was ~3dB. An insertion loss of ~0.75dB was due to the circulator; the actual loss in reflection is therefore only 2.25dB. The grating reflectivity was measured to be ~21dB.

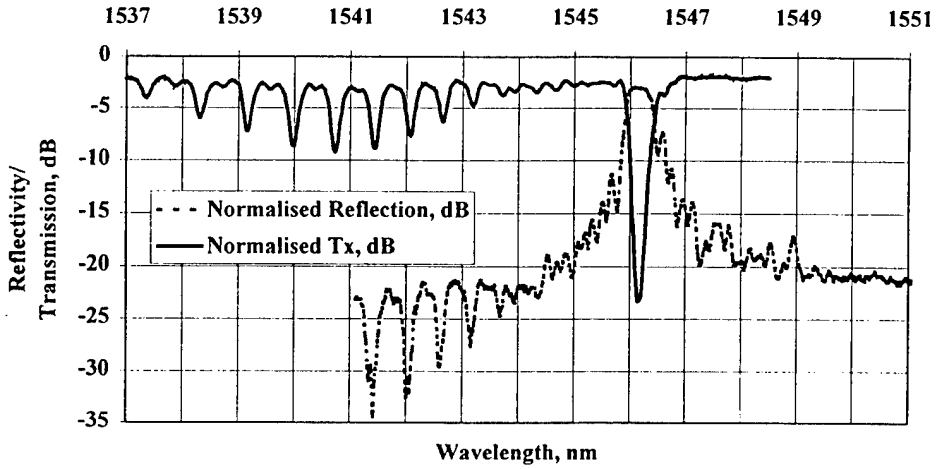

Figure 2. The transmission and reflection spectrum of a liquid-crystal cored optical fibre Bragg grating. The zero level is the transmitted signal from the circulator at the input to the butt-coupling fibre. The reflection spectrum includes a 0.75dB insertion loss of the circulator.

A second 50mm long fibre was filled with a standard refractive index matching oil (n =1.460) after a grating was written into it following the procedure already described. The reflection spectrum was measured as heat was applied to the grating with a soldering iron. The Bragg wavelength moved to *shorter* wavelengths with increasing temperature, quite the opposite to Bragg gratings in normal fibre, which has a positive wavelength dependence with temperature. The wavelength change with temperature is shown in Figure 3, and shows a slope of ~ -0.17nm $°C^{-1}$. However , when the liquid crystal cored fibre was heated, the wavelength drifted to longer wavelengths as in normal fibre.

To our knowledge, this is the first demonstration of fibre Bragg gratings which may be used with a liquid core. There are several interesting features of this fibre. Firstly, the negative temperature coefficient of the oil filled fibre is due to the dominant negative refractive index change of the liquid; the small positive refractive change in the cladding glass increases the net temperature coefficient of the wavelength shift. Secondly, there are no differential strain effects between the core and cladding, so that the fibre should demonstrate a smaller change in the birefringence with temperature. Note that straining the fibre changes the refractive index *only* of the cladding which acts in the opposite sense to temperature. Consequently, temperature and strain may be easily discriminated when used in conjunction with a conventional fibre Bragg grating. Gratings may be easily tuned or chirped by temperature or by the application of electric fields in the case of the liquid-crystal cored fibre[6]. Uniform electric fields may be used to tune gratings with planar external electrodes[7].

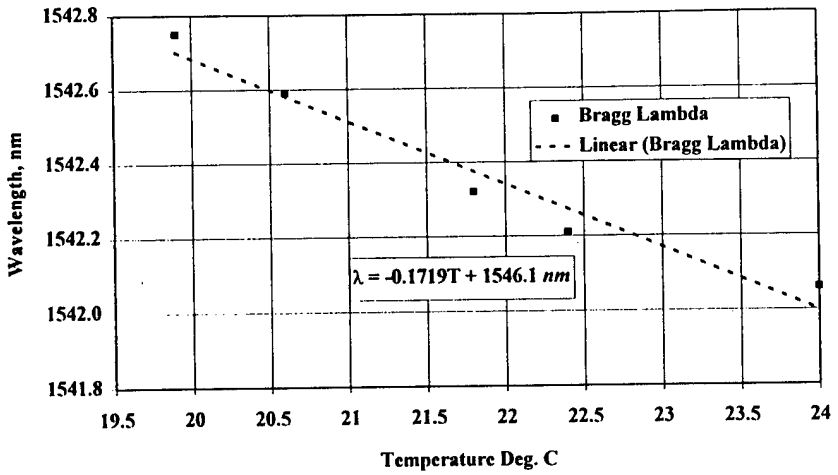

Figure 3. Bragg wavelength shift as a function of temperature of the fibre.

The liquid crystal cored fibre was removed from the butt-coupling fibres and re-placed into the same set-up several days later. Measurement showed *identical* results in reflection and transmission, indicating that such waveguides can be handled with reasonable ease after filling. The guiding properties of the fibre may be easily altered by inserting a different refractive index core liquid, allowing tuning of the Bragg wavelength. Nonlinear switching becomes feasible using a highly nonlinear liquid core in conjunction with a Bragg grating in the cladding. Long period gratings written into this type of fibre will also demonstrate a negative temperature coefficient of wavelength shift. Finally, the low insertion loss makes these devices attractive for device applications, such as tunable Fabry-Perot etalons, soliton sliding-guiding filters, band-pass filters, radiation mode couplers, external fibre Bragg grating cavity lasers, as well as electrically tunable chirped fibre Bragg gratings with liquid crystalline cores.

This device opens new opportunities in telecommunications and sensing applications.

References:

1 Fujiwara T, Wong D, Zhao Y, Fleming S, Poole S & Sceats M, *Electron. Lett. 31*(7), 573, 1995.
2 Williams D L, Ainslie B J, Armitage J R , Kashyap R & Campbell R J, *Electron. Lett. 29* (1), 45-46, January 1993.
3 Kashyap R, Wyatt R & Campbell R J, *Electron. Lett. 29* (2), 154-155, 21 January 1993.
4 Kashyap R, Winter C S & Nayar B K, *Opt. Lett. 13* (5), 401-403, May 1988.
5 'Optical fibre cladding grating' *BT Patent Applied For.*
6 Wong C S I, Liu Jian-Yu & Johnson K M, 'Liquid crystal fiber phase modulator', *In Technical Digest of OFC '97*, paper WL12, pp173-174, 1997.
7 Kashyap R, "Nonlinear interactions in devices with cylindrical geometry", SPIE: Molecular and Polymeric Optoelectronic Materials: Fundamantals and Applications, Proc #682, San Diego, USA, August 1986.

Bragg Gratings, Photosensitivity, and Poling in Glass Fibers and Waveguides: Applications and Fundamentals

Grating Devices II

Sunday, October 26, 1997

Gerry Meltz, OFT Associates
Presider

BSuC
2:00pm–3:30pm
Auditorium

BRAGG GRATINGS IN TELECOMMUNICATIONS NETWORKS

E. Delevaque, B. Loisel, J.F. Bayon, N. Devoldere, H. Poignant and D. Bosc

FRANCE TELECOM, Branche Développement, DTD/TSO/PIH
CNET LANNION - 22307 Lannion Cedex FRANCE

Abstract :

Photoinscription of Bragg gratings within optical waveguides has been shown as a promising technology in the optical telecommunications field. Many applications have already been demonstrated in transport, local or access networks. The robustness, stability and flexibility that photoimprinted components offer insure a fast widespread of their use in near close future telecommunications networks.

Introduction

Since the discovery by K.O. Hill et al. of the silica photosensitivity, and the demonstration by G. Morey et al. of the transverse holographic method, the photoinscription technology has been found as a promising issue in several fields as optical telecommunications, sensoring, medical and instrumentation applications. The aim of this paper is to survey the photoinscription technology applications in the optical telecommunication networks. For sake of simplicity we will distinguish three main types of networks having their specificities (figure 1). Transport networks are supposed to be high bit rate meshed networks. Local networks connected to the transport network at high bit rate node, will be seen as multiwavelength loops shared by secondary nodes. Access networks are thought to be arborescent networks with a main station and optical network units (ONU).

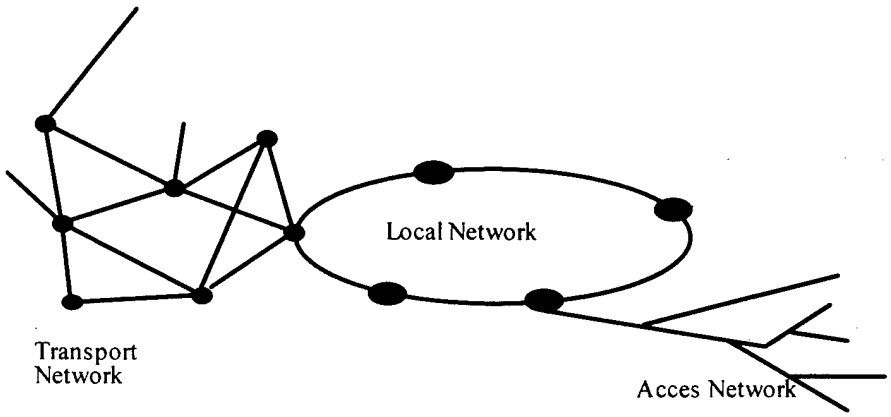

Figure 1 : Schematic diagram of telecommunication networks

Transport and local Networks

A transport network can be seen as point to point long distance systems connected together to form a meshed network. The emergence of Wavelength Division Multiplexing for high bit rate systems is felt as a chance for the photoinscription technology.

WDM systems require frequency stable sources. The first photoinduced Bragg grating source in the 1.5 μm band was realized in a doped planar waveguide (R. Kasyap et al.). Following this first demonstration many single frequency fibre lasers have been reported in DBR and DFB configurations. Fiber Bragg grating based single frequency lasers can be tunable over more than 30 nm. Their Relative Intensity Noise performances and thermal stability make these sources an interesting alternative to the semiconductor sources. Fiber Bragg gratings have been incorporated to stabilized semiconductor amplifier pump power sources and signal sources.

In WDM applications, the filtering is an important key point. The flexibility of the Bragg grating technology has already given numerous solutions. However, intrinsic characteristics of in-fiber Bragg gratings need to be improved in terms of spectral shape (apodisation) and losses (coupling to the radiation modes). The fiber Bragg gratings and optical circulators association allows the achievement of optical functions : Optical Add/Drop Multiplexers, bi-directionnal amplifiers, Step delay lines. All of these can be electrically tunable or programmable by gluing the fibre gratings on piezo-ceramic elements. Transmissions at bit rates greater than 10 Gbit/s are limited in distance to a few tens of km (typically 60 km) on standard fibers due to the group delay dispersion in the 1.5 μm band. Realisations of chirped gratings, designed to compensate for the chromatic dispersion are of particular interest since Fiber Bragg Grating Chromatic Dispersion Compensators (FBGCDC) are compact, low-lossy, polarisation insensitive and do not generate non-linear perturbations.

Optical amplification in the local and transport networks using the WDM technique should present some specific charateristics. The spectral gain of WDM amplifiers requires flatness to insure a correct transmission for all the optical carriers. Blazed or long period dissipative gratings have been included in Erbium doped fiber amplifiers to flatten the spectral gain.

Access Networks

The main feature of the access networks is the cost of the front end components since they are installed close to the customers, and thus at a large scale. The planar waveguide technology could potentially answer this low cost requirement. Gratings photoinscription in planar Si/SiO2 waveguides have been investigated in the last few years. As an example, this technique allows the realisation of Bragg gratings with different wavelengths in planar waveguides with a 250 μm pitch. Futhermore this technology, being compatible with the hybridation of array lasers could provide an alternative solution for the low cost multiwavelength sources at the central office for WDM access networks. On the other hand, combination of various materials (ie : polymer or silica can lead to temperature insensitive integrated Bragg gratings. As result, this method could provide suitable filters for access networks.

As far as the fiber technology is concerned, the photoinscription technique allows the realisation of bidirectional amplifications in different configurations. The filtering is also a major issue in this type of networks. The fiber Bragg gratings have been used for the supervision of a passive access network in the real time of traffic exploitation.

Optical space domain reflectometry (OSDR) for determination of strength and chirp distribution along optical fiber gratings

Ernst Brinkmeyer, Gunnar Stolze, and Dietmar Johlen
Technische Universität Hamburg-Harburg, Eissendorfer Str. 40, 21073 Hamburg, Germany
Tel.: + 40 7718 3114 Fax: + 40 7718 2860 email: brinkmeyer@tu-harburg.d400.de

Fiber gratings are primarily characterized by the distribution of grating strength and chirp along the structure. These properties are comprised in the complex coupling coefficient $\kappa(z)$. Whilst for simple fiber gratings used in simple applications the ability to determine the complete, complex distribution of the coupling coefficient $\kappa(z)$ may be of secondary importance, it is useful and sometimes mandatory for evaluating more complicated designs, e.g. those based on localized phase shifts to create transmission windows in the stop band, Fabry-Perot structures, dispersion compensating gratings etc.

For a partial grating characterization the so-called side-scatter technique [1] may be used which yields the modulus of $\kappa(z)$, i.e. the local grating strength. Its phase $\phi_\kappa(z)$, however, associated with varying grating periods $\Lambda(z)$ cannot be revealed. A complete $\kappa(z)$ determination is possible by means of measuring the wavelength dependence of the complex amplitude reflection factor or by means of reflection measurements with a phase sensitive coherence domain reflectometer [see e.g. 2-4]. The information on $\kappa(z)$ is generally deeply buried in these data and has to be dug out using inverse scattering procedures. These procedures are cumbersome in most cases, vulnerable by errors in experimental data and therefore often yield spurious grating structures at locations where they definitely do not exist.

In the OSDR-method proposed here we aim at a relation between experimental data and $\kappa(z)$-data which is local rather than integral and as direct as possible. The scheme under consideration is based on a reflection measurement performed at one particular optical wavelength, suitably chosen as discussed below. For a grating of length L and in the regime where the standard coupled mode equations are valid, the complex amplitude reflection factor r at any wavelength is given by [3]

$$r(\nu) = -\int_0^L \kappa(z)\cdot\exp(-j2\pi\nu\, z)\,dz - p(\nu) \quad \text{where} \quad \nu = \frac{k\cdot n_{eff}}{\pi} - \frac{1}{\overline{\Lambda}} = 2n_{eff}\cdot\left[\frac{1}{\lambda} - \frac{1}{\overline{\lambda}_B}\right] \quad (1)$$

The spectral variable ν measures the deviation of the operation wavelength λ from some reasonably (but basically arbitrarily) chosen mean Bragg wavelength $\overline{\lambda}_B$. $\overline{\Lambda}$ is the mean grating constant corresponding to $\overline{\lambda}_B$. The term abbreviated by p(ν) in eq.(1) consists of a double integral over κ-values at different locations z', z" and an exponential with an argument proportional to ν (cp.[3]). Intuitively it acounts for multiple reflections within the grating structure. Qualitative reasoning suggests that the term p(ν) can be omitted if the grating is sufficiently weak, i.e. $|\kappa(z)|$ sufficiently small, or the operating wavelenght $\lambda = \lambda_{meas}$ is sufficiently apart from $\overline{\lambda}_B$, i.e. $|\nu|$ sufficiently large. The latter condition is tried to be met in this paper.

Obviously, the measurement of just one reflection factor $r(\nu_{meas})$ is not sufficient to determine $\kappa(z)$ along the grating. In our approach a slight, localized, and transient disturbance is introduced in addition and has to be moved along the grating. The particular reversible disturbance we use in this paper is a phase shift which can be implemented by local heating with a focussed laser beam (Fig.1).

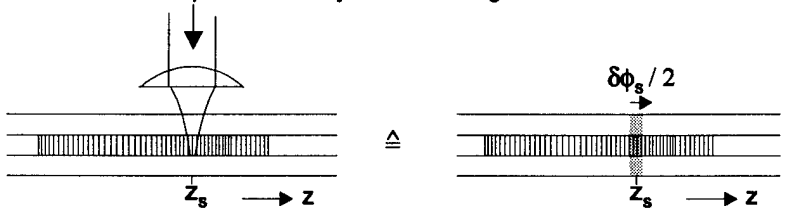

Fig.1: *Local heating causes a localized phase shift. For a 1 °C temperature change in a range* δz_s = 100 µm *the round-trip phase shift* $\delta\Phi_s$ *is of the order of* 10^{-2}.

In that situation the coupling coefficient changes from κ(z) to :

$$\tilde{\kappa}(z)=\begin{cases}\kappa(z) & \text{für } z<z_S\\ \kappa(z)\cdot\exp(j\,\delta\Phi_S) & \text{für } z>z_S\end{cases} \qquad (2)$$

Thus, with an operating wavelength well outside the stop band where the reflection factor is low and p(ν) can be neglected, and assuming $\delta\Phi_S << 1$, the modified complex reflection factor is

$$\tilde{r}(z_s;\nu_{meas})=-\int_0^L\tilde{\kappa}(z)\cdot\exp\left(-j2\pi\nu_{meas}z\right)dz=r(\nu_{meas})-j\,\delta\Phi_S\cdot\int_{z_S}^L\kappa(z)\cdot\exp\left(-j2\pi\nu_{meas}z\right)dz \qquad (3)$$

The derivative of $\tilde{r}(z_s;\nu_{meas})$ with respect to the location z_S of the disturbance (and the derivative of the reflection factor change $\Delta r(z_s;\nu_{meas})=\tilde{r}(z_s;\nu_{meas})-r(\nu_{meas})$, respectively) directly yields

$$\frac{\partial\,\tilde{r}(z_S;\nu_{meas})}{\partial z_S}=\frac{\partial\,\Delta r(z_S;\nu_{meas})}{\partial z_S}=j\,\delta\Phi_S\cdot\kappa(z_S)\cdot\exp\left(-j2\pi\nu_{meas}z_S\right) \qquad (4)$$

This equation is the desired simple and local relation between the experimental data and the coupling coefficient to be determined (note that $\delta\Phi_S$ and ν_{meas} are fixed constants). Moreover, it is worth while stating that appreciable values of $\Delta r(z_s;\nu_{meas})$ will arise (see eq.(3), assume typical grating data, and use a $\delta\Phi_S$-estimate as given in Fig.1), even at a λ_{meas} (or ν_{meas}, equivalently) where the reflection of the undisturbed grating is zero.

The derivation of eq.(4) is based on neglecting the multireflection term p(ν) in eq.(1). As discussed above, this assumption is "approximately" true no matter how strong the grating might be if the operating wavelength is "sufficiently" apart from the high reflection range. For a quantitative check we followed the procedure shown in the diagram

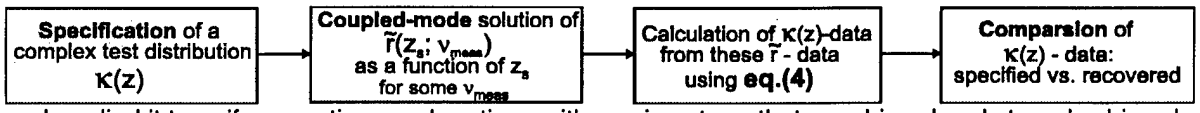

and applied it to uniform gratings and gratings with varying strength, to unchirped and strongly chirped, symmetrical and unsymmetrical ones, Fabry-Perot structures and gratings with phase shifts. The results promise that deviations between specified and recovered κ-data below 1% in the modulus of κ and less than 0.1 radians in κ's phase can be achieved throughout the gratings. An example is shown in Fig.2:

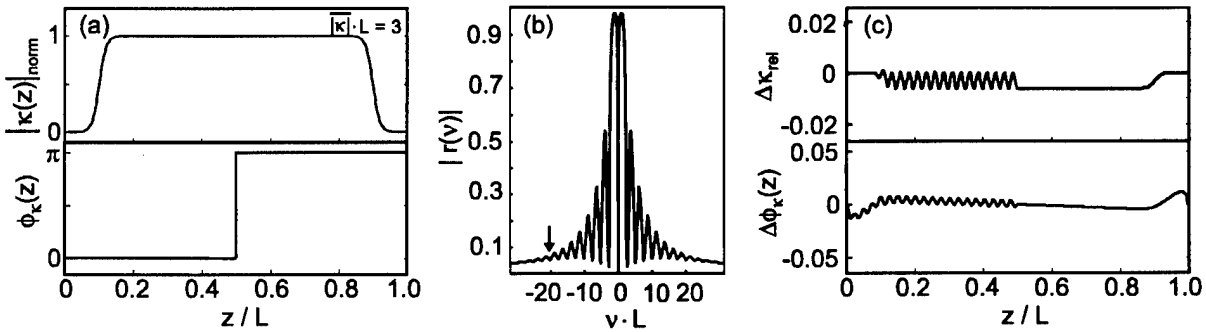

Fig.2: *Example of numerical simulation of complex* κ(z) *determination by OSDR.* (a) *specification of an apodized grating with* π*-phase shift in its center* (b) *resulting amplitude reflection spectrum* |r(ν)|; *the arrow marks the* ν_{meas} *-value chosen in this OSDR simulation* (c) *deviations of recovered* κ*-values from specified ones; the maximum error in* |κ| and arg(κ) *is about 0.5% and 0.01 radians, respectively.*

The complex reflection factor and in particular its derivative with respect to z_S, which is the basis of the evaluation according to eq.(4), can be determined by usual interferometric means, e.g. by superimposing a reference wave the phase of which can be adjusted to yield two quadrature signals for determining κ(z).

A special and favorable feature in this application is the fact that the interferometer can be easily stabilized by making use of the interference signal obtained if the disturbance of the grating is switched off.

So far we did not yet try an interferometric setup as mentioned above. Instead, we started with a simpler setup which is sufficient in many cases. A sketch of it is shown in Fig.3, where light from a tunable laser diode is launched into the grating under test. To introduce the localized phase shift, a focussed He-Ne laser beam with a waist diameter of about 10 μm is moved along the grating which is coated by a thin absorbing layer. The He-Ne light is chopped at a frequency of 330 Hz and the AC optical output power from the grating is synchronously detected.

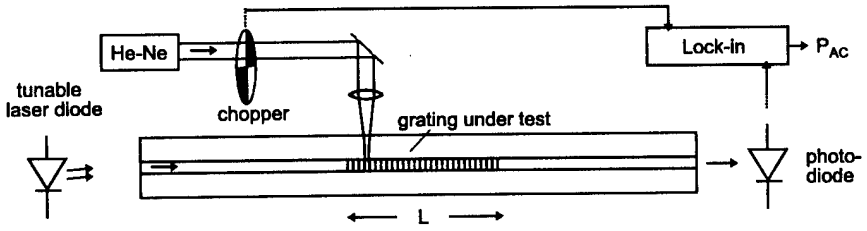

Fig.3: *Schematic view of the present non-interferometric OSDR-setup*

The reason why the power transmission factor T contains the desired information is given by the following sequence of simple equations:

$$\frac{\partial\, T(z_s;\nu_{meas})}{\partial\, z_s} = \frac{\partial\left[1-R(z_s;\nu_{meas})\right]}{\partial\, z_s} = -r^*(\nu_{meas})\cdot\frac{\partial\,\Delta r(z_s;\nu_{meas})}{\partial\, z_s} - \text{c.c.}$$

$$= 2\left|r(\nu_{meas})\right|\cdot\delta\Phi_s\cdot\left|\kappa(z_s)\right|\cdot\cos\left[2\pi\nu_{meas}z_s - \phi_\kappa(z_s) + \phi_{0\nu}\right] \qquad (5)$$

This spatial derivative of T is a cosine function where the varying amplitude is a measure of the modulus of $\kappa(z)$ while the argument of the cosine - apart from a carrier at a spatial frequency ν_{meas} - yields the phase $\phi_\kappa(z)$. If ν_{meas} which is a measure of the difference between operating and mean Bragg wavelength is large enough, the analytic signal belonging to these data can be calculated numerically and yields both $|\kappa(z)|$ and $\phi_\kappa(z)$. A first example of such a measurement and its evaluation is given in Fig. 4 [5].

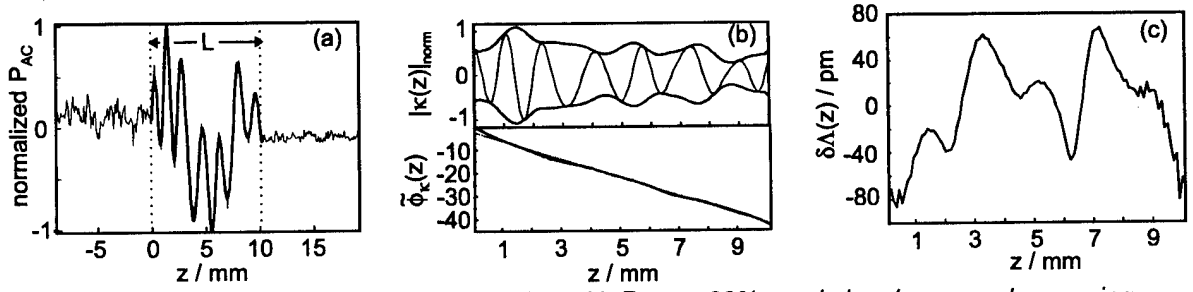

Fig.4: *Experimental result and evaluation (grating with R_{max} > 99%, made by phase-mask-scanning technique,* L_{mask}=10.0 mm, Λ_{mask}=1069nm, 244nm- *Ar-Laser Coherent FRED)* (a) *raw data of AC output power ;slightly smoothed fit superimposed in the grating range* (b) *result of evaluation: variation of grating strength; nonlinearly varying phase* $\tilde{\phi}_\kappa(z) = \phi_\kappa(z) - 2\pi\nu_{meas}z$ (c) *deviation of local (average over resolution length* $\delta z_s \approx 100\mu m$*) from mean grating constant, calculated from* $\tilde{\phi}_\kappa(z)$.

In conclusion, the OSDR-technique proposed here is able to yield a complete $\kappa(z)$-characterization of waveguide gratings of arbitrary strength and chirp. Its most important feature is the direct and local readout making it appreciably less prone to errors than methods relying on inverse scattering.

References: [1] P.A. Krug, R. Stolte, and R. Ulrich, Opt. Lett. 20, p.1767-1769 (1995)
[2] S. Barcelos et. al., Electr. Lett. 31, p. 1280-1282 (1995)
[3] E. Brinkmeyer, Opt. Lett. 20, p. 810-812 (1995)
[4] D. Sandel and R. Noe, Proc. 22nd ECOC, Oslo, 1996
[5] The photosensitive fiber used was supplied by the OFTC, Sydney/Australia

New Interferometer for Complete Design of UV-written Fibre Bragg Gratings

P.-Y. Fonjallaz, B. Sahlgren, B. Grennberg, and R. Stubbe
Institute of Optical research, Lindstedtsvägen 24, S-100 44 Stockholm
phone: + 46 8 791 13 22 fax: + 46 8 789 66 72
E-mail: pyf@optics.kth.se

Bragg gratings in optical fibres have been the subject of a very intense activity of research since the first demonstration of the side-writing technique with a UV laser by Meltz et al. in 1989[1]. Since then, many improvements have been realised and other techniques have been developed. We present here a novel interferometer which allows a modification of the fringes period by changing only one parameter, the position of two mutually attached mirrors. This new system, in combination with the technique of writing long gratings by the superposition of subgratings while the fibre has an interferometrically controlled motion[2], gives complete freedom for the design of gratings.

To change the period of the fringes with a Mach-Zehnder interferometer, three parameters have to be modified: the orientation of the two last deviating mirrors and the distance of the fibre relative to them (or the distance between them). Another writing scheme, which contrary to that requires a good spatial coherence, is the so-called Lloyd interferometer[3]. It consists of placing a mirror at right angles to the fibre to be irradiated and almost in contact with it. The laser beam is then centred at the mirror-fibre intersection point. The period of the fringes can be easily changed by rotating the mirror-fibre assembly. For both the Lloyd and the Mach-Zehnder interferometers, another way to change the period of the fringes is to tune the wavelength of the UV laser, but it is difficult to keep the position of the output beam constant.

The idea behind our new interferometer of Mach-Zehnder type is to use cylindrical lenses to collimate the two interfering beams (Figure 1). By displacing laterally the two beams impinging on the lenses in a symmetric way, the periodicity of the fringes can be changed without changing the position at which the two beams intersect. This symmetric displacement can be realised by changing only one parameter, the position of two mutually attached mirrors. The laser beam is first deviated at right angles by a simple mirror (A in Figure 1) onto a beam-splitter (B) which is at the right angle of a triangular loop. The two mirrors (C and D) deviating the beam at 45 degrees in this loop are fixed on a motorised translation stage. They can be translated along the basis of this triangle. The result is that the beams rotating in the clockwise and anticlockwise directions are displaced laterally at the output, symmetrical to the incoming beam. The two beams are then deviated by two prisms (E) and two mirrors (F) to make them intersect like in a usual Mach-Zehnder interferometer. When cylindrical lenses are placed in front of the fibre at a distance equal to their focal distance, the two beams will always cross at the same location (intersection of the lenses focal planes) independently of the lateral position at which the beams are impinging on the lenses. In order to achieve collimated beams intersecting at the fibre location, the beams are focused in front of the lenses at their focal distance. This new interferometer allows variation of the Bragg gratings resonance wavelengths between 900 nm and 1600 nm. In addition to its versatility in changing the gratings period, it has several important advantages. The first one is that the two interfering beams experience exactly the same number of reflections so that they perfectly overlap at the fibre location. Even if the

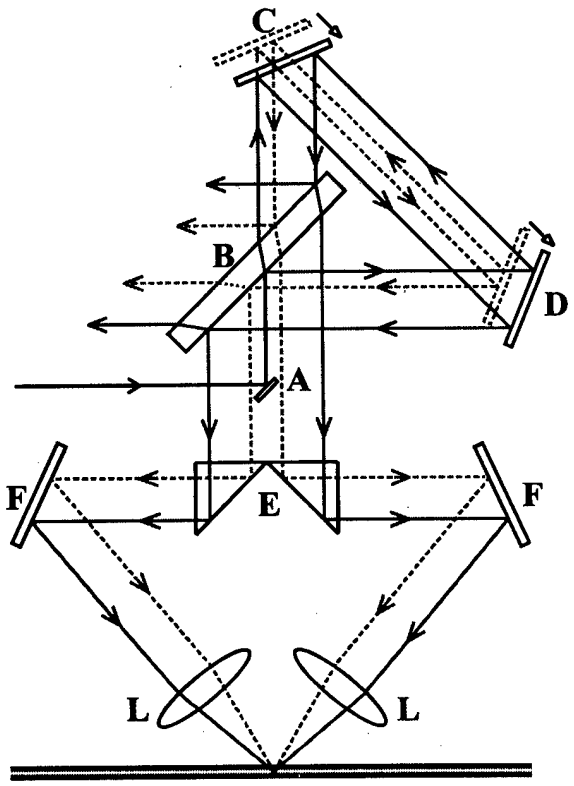

Figure 1: Loop beam-splitter Mach-Zehnder interferometer. Solid and broken lines: two different positions of mirrors C and D.

beam-splitter does not have a perfect 50:50 splitting ratio, the two beams coming out of the triangular loop will have exactly the same intensity, since they will both be transmitted through and reflected by the beam-splitter. The second advantage is that the two beams are really separated only at the latest stage of the interferometer (from the prisms, E).This means that the sensitivity to refractive index fluctuations is strongly reduced in the upper part of the interferometer where the two beams are relatively close. The period of the interference fringes can be chosen with a precision of 40 pm at 1.55 μm, and 20 pm at 1.0 μm, with a very good reproducibility. Naturally this interferometer has also some drawbacks. Firstly, half of the light is actually lost from the triangular loop beam-splitter. The energy per pulse from our laser (a frequency-doubled dye laser), is however usually sufficient to destroy the fibre if the beams are strongly focused perpendicularly to the fibre axis. Another problem could be that the size of the interference pattern is rather small with this configuration, since the incoming beam is focused with a long focal length lens before the two beams are generated. The numerical aperture of the beams impinging on the cylindrical lenses is then very small. This is not a problem in our case since we can write long gratings by superposing subgratings while the fibre has an interferometrically controlled motion. Our subgratings have lengths in the order of 200 to 400 microns. Finally, the spherical aberration of the cylindrical lenses is not negligible for large period variations.

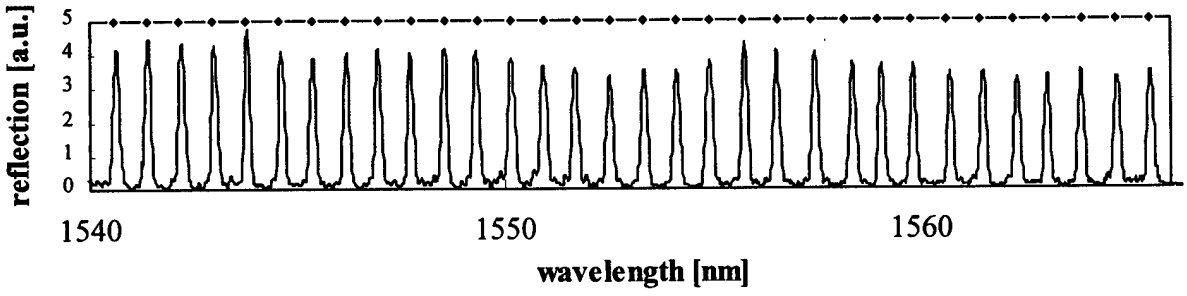

Figure 2: 32 Bragg gratings with 100 GHz separation according to the WDM specifications. The dots represent the positions at which the peaks should be.

To demonstrate the versatility of this new interferometer, a series of 32 gratings with a separation of 100 GHz according to the WDM standards has been fabricated (central frequency: 193.1 THz). Each grating has a length of 5 mm and the separation between two gratings is not more than a few millimetres. The total length of fibre containing the gratings is thus not more than about 20 cm. The time required for the fabrication of this series of gratings was not more than about three hours. By writing all the gratings at once, without interrupting the phase, the minimum would be twenty minutes. Figure 2 shows the result obtained. The intensity of the 14 last reflection peaks has been multiplied by a factor of 5 in order to compensate for the much lower intensities of the light source at those wavelengths.

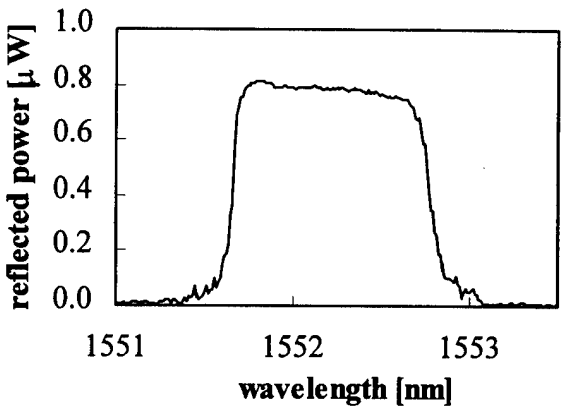

Figure 3: 1-nm step-chirped grating.

Another demonstration of this interferometer is the fabrication of a 1 nm step-chirped grating (see Figure 3). The grating is formed of 26 sections with constant periods. The total length is 52 mm. The increase of the resonance wavelength between successive sections is 40 pm. The reflection spectrum measured with a tuneable diode laser (from the shortest wavelength side) shows the excellent quality of this grating. The maximal reflectivity, deduced from a transmission measurement is larger than 99,7%. Even if the transmission is constantly lower than 0.3% over about 0.8 nm, the reflectivity decreases with a constant rate of about 7% per nanometer.

A new interferometer has been developed to easily change the period of UV laser interference fringes. The resonance wavelength of fibre Bragg gratings can presently be chosen between 900 nm and 1600 nm. In combination with the writing technique consisting of superposing subgratings while the fibre has an interferometrically controlled motion, this interferometer gives complete freedom for the design of in-fibre Bragg gratings.

References

1. G. Meltz, W.W. Morey and W.H. Glenn, "Formation of Bragg gratings in optical fibres by a transverse holographic method.", Opt. Lett. 14 (15), pp. 823-825, 1989.
2. A. Asseh et al., "A writing technique for long fibre Bragg gratings with complex reflectivity profiles.", accepted for publication in Journal of Lightwave Technology, July 1997.
3. P.-Y. Fonjallaz, H.G. Limberger and R.P. Salathé, "Direct determination of main fibre Bragg grating parameters using OLCR.", IEE Proc.-Optoelectron., Vol. 141, No. 2, pp. 141-143, 1994.

Short-wavelength, transmission-loss suppression in Fibre Bragg Gratings

Mikhail N. Zervas, Morten Ibsen and Richard I. Laming

Optoelectronics Research Centre, University of Southampton, Southampton SO17 1BJ, U.K.
Tel: +44 1703 593147, Fax: +44 1703 593149, email: mnz@orc.soton.ac.uk

Introduction

Fibre Bragg Gratings (FBG's) are known to suffer from short-wavelength, transmission losses due to resonant coupling into backward-propagating cladding modes [1,2]. Figure 1 shows a typical transmission spectrum of a 10cm standard FBG. The cladding mode losses increase with grating reflectivity and could eventually impose severe limitations in the use of FBG's. The problem can be quite acute in the case that FBG wavelength-multiplexing is required. So far, several attempts have been made to eliminate the short-wavelength, transmission losses and improve grating performance [2-5]. In all cases, the resonant coupling of the forward-propagating core mode to the backward-propagating cladding modes is minimised by reducing the coupling strength.

In this paper, we report on a novel method for reducing cladding-mode transmission losses in standard FBG's. We show that short wavelength, transmission losses can be practically eliminated by *damping* the resonant excitation of the cladding modes. The damping is achieved by properly introducing a substantial propagation loss into the cladding modes. For maximum effect, the core mode should experience no extra propagation losses. By applying a thin lossy layer on the fibre cladding surface, a reduction of cladding-mode-losses of about 12dB was achieved.

Transmission-loss suppression

The cladding mode attenuation can be easily achieved by depositing a thin lossy layer on the cladding surface. Alternatively, the same effect can be accomplished by introducing one or more lossy layers into the fibre cladding during the fabrication process. The latter will result in a stronger cladding-mode/lossy-material overlap and, therefore, produce higher propagation losses.

A. Theory

The presence of losses in the cladding modes renders their propagation constants complex, i.e. $\beta'_n = \beta^{cl}_n + i\alpha^{cl}_n$ ($\alpha^{cl}_n < 0$). The core mode is supposed to remain lossless ($\alpha^{c}_0 = 0$). The transmission coefficient of a grating which couples the forward-propagating core mode into the nth-order backward-propagating cladding mode is given by:

$$t_{0n} = \frac{s_{0n}}{s_{0n}\cosh(s_{0n}L) + i\frac{\delta_{0n}}{2}\sinh(s_{0n}L)} e^{-i(\beta_0^c - \frac{\delta_{0n}}{2})L}$$

where κ_{0n} is the coupling coefficient and δ_{0n} is the complex momentum mismatch, given by:

$$\delta_{0n} = \beta_0^c + (\beta_n^{cl} + i\alpha_n^{cl}) - K_0 \qquad \text{and} \qquad s_{0n} = \sqrt{\kappa_{0n}^2 - \left(\frac{\delta}{2}\right)^2}$$

Figure 2 shows the transmission spectra of the grating-assisted coupling between the forward-propagating core mode and the backward-propagating n^{th}-order cladding mode, for various propagation losses. The grating length (L) is 10cm and the normalised refractive index perturbation ($\Delta n/n_0$) is 2×10^{-6}. The n^{th}-

cladding-mode loss (α^{cl}_n) varies between -1.0 and -20dB/cm. The lossless case ($\alpha^{cl}_n = 0$) is also shown for comparison. It is observed that as the cladding mode loss is gradually increased, the resonant coupling between the forward-propagating core mode and backward-propagating cladding mode is severely damped, resulting in a dramatic reduction of the grating transmissivity. However, as expected, the reduction of the peak transmission loss is attained at the expense of an increased transmission-loss bandwidth. Figure 2 shows the transmission loss corresponding to only one of the cladding modes. It is obvious that the rest of the cladding modes will show similar transmission-loss reductions, provided they experience comparable propagation losses.

The amount of transmission-loss reduction, achieved by a certain lossy material, depends on the initial maximum transmission loss of the grating. Figure 3 shows the required cladding-mode loss that should be applied in order to achieve a certain level of final (residual) transmission loss, as a function of the initial maximum transmission loss. The grating length is 10cm.

B. Experimental Results

Several strong Bragg gratings where written in different fibres exhibiting a number of short-wavelength sharp notches due to coupling into different backward-propagating cladding modes. Figure 4 shows part of a typical transmission-loss spectrum (dashed line) of a 10cm grating. The grating reflectivity was about 30dB. The solid line shows the transmission-loss spectrum after the grating was coated with a thin ink layer. A dramatic reduction in the short-wavelength transmission loss from about -14dB to about -2dB was observed. According to Figure 3, such a reduction implies that the thin ink layer introduces a cladding-mode propagation loss of about 1dB/cm. The broadening of the damped transmission resonance is also apparent (cf. Figure 2). Similar thin ink layers were applied to weaker gratings, with maximum short-wavelength transmission losses of about 1dB, resulting in a complete restoration of the transmission spectrum.

Figure 5 shows the variation of the transmission loss as a function of the grating length over which the lossy ink layer has been applied. The grating length was 10cm. It was shown that the transmission loss was decreased quasi-linearly with the coated length (or equivalently, with the total applied cladding-mode propagation loss). The maximum transmission-loss reduction was achieved when the entire grating was coated with the lossy layer. According to Figure 3, a reduction of transmission losses from about -4.5dB to about -0.5dB implies again that the thin ink layer introduces a cladding-mode propagation loss of about 1dB/cm. Figure 5 also suggests that control of the cladding-mode propagation losses can be used as a means of achieving a variable strength and bandwidth grating notch filter.

Discussion - Conclusions

In this paper, we have shown that short-wavelength transmission losses in standard FBG's can be practically eliminated by *damping* the resonant excitation of the cladding modes. By applying a thin lossy layer on the fibre-cladding surface, a reduction in cladding-mode-losses of about 12dB was achieved. Such a film induces a moderate cladding-mode propagation loss (about 1dB/cm). Using different lossy materials and/or including them into the cladding can provide higher cladding-mode propagation losses and result in stronger reduction of grating transmission losses. The initial narrow-band transmission notches are significantly reduced and spread evenly over a much wider bandwidth. When such a grating is used in WDM applications will provide an insignificant wide bandwidth loss. The proposed method can be used in conjunction with any of the other proposed methods [2-5] for the total elimination of cladding mode losses.

The Optoelectronics Research Centre is an EPSRC-funded Interdisciplinary Research Centre.

References

[1] S. J. Hewlett, et al., *Electron. Lett.*, vol. **31**(10), pp. 820-821 (1995).
[2] V. Mizrahi and J. E. Sipe, *Journal of Lightwave Technology*, vol. **11**, no. 10, pp. 1513-1517 (1993).
[3] E. Delevaque, et al., *Optical Fiber Communications '95*, Postdeadline paper PD5 (1995).

[4] T. Komukai et al., *ECOC '95*, paper Mo.A.3.3, pp. 31-34 (1995).
[5] L. Dong, et al., *IEEE Photon. Technol. Lett.*, vol. **9** (1), pp. 64-66 (1997).

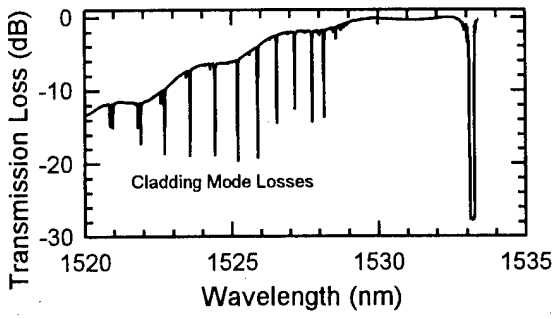

Figure 1: Typical transmission sprectrum of a 10cm Fiber Bragg Grating.

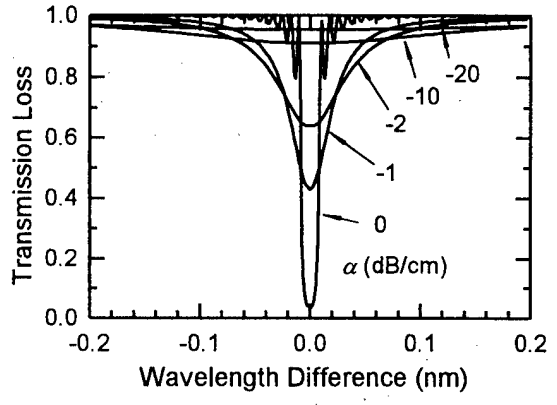

Figure 2: Transmission spectra of the coupling to the backward-propagating n^{th}-order cladding mode, for various propagation losses.

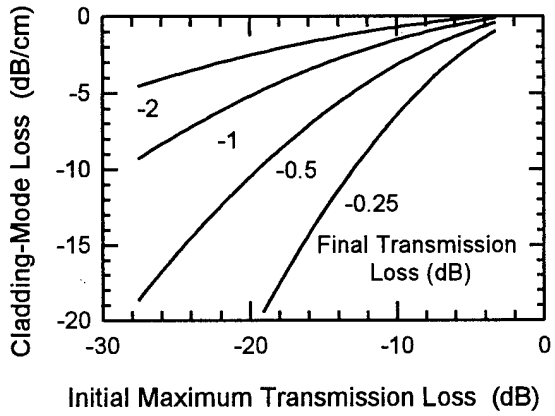

Figure 3: Required cladding-mode-loss in order to achieve a certain level of final transmission loss, as a function of the initial maximum transmission loss.

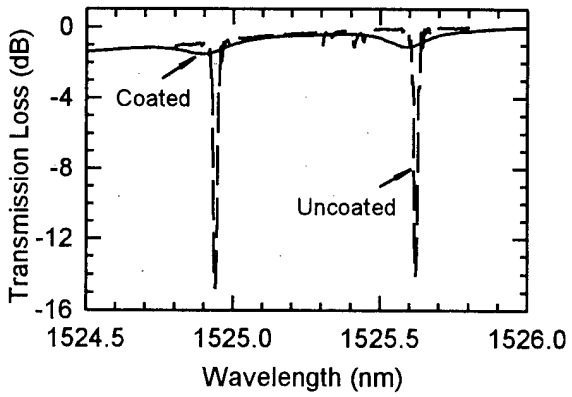

Figure 4: Part of a typical transmission-loss spectrum of a 10cm uncoated and coated FBG.

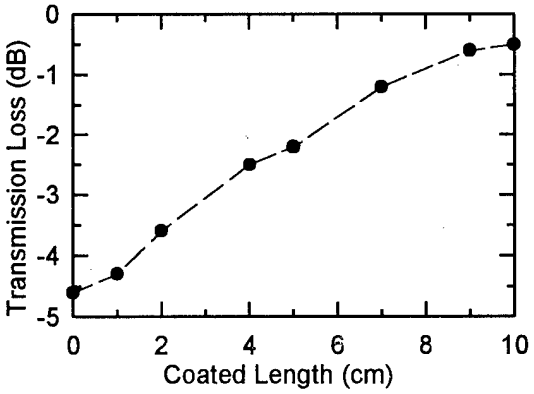

Figure 5: Variation of the transmission loss as a function of the coated grating length.

Non-reflecting narrow-band fiber optical Fabry-Perot transmission filter

Dietmar Johlen, Peter Klose, Andreas Ewald, and Ernst Brinkmeyer
Technische Universität Hamburg-Harburg, Eißendorfer Str. 40, D-21073 Hamburg, Germany
Tel.: ++49-40-7718/3437, Fax.: ++49-40-7718/2860, email: johlen@tu-harburg.d400.de

Tilted Bragg gratings have been used for intermodal conversion in dual-mode fibers [1]. In this paper we demonstrate that such gratings in combined single-mode/dual mode structures are attractive for optical filter design. In particular, this concept is used here to realize narrow-band Fabry-Perot transmission filters which - unlike ordinary FP-resonators - do not reflect the incident light at either side of the transmission peak.

For preparing a structure like that we start with a truly single-mode, photosensitive fiber[2]. In a predetermined section, typically 10 mm long, this fiber is irradiated homogeneously with a specified fluence by UV-light. In this way, the refractive index of the fiber core is increased up to a level where this fiber section becomes two-moded while all the rest of the fiber remaines single-mode. After that, two tilted Bragg gratings are written at either end of the two-mode section as schematically shown in Fig.1.

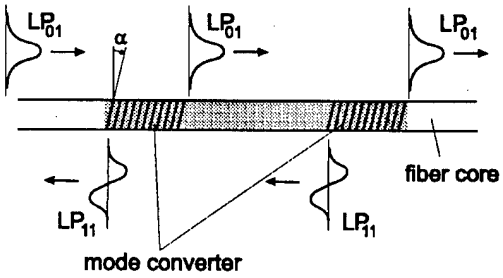

Figure 1: The two tilted fiber Bragg gratings form a Fabry-Perot transmission filter. A two-mode section in the elsewhere single-mode fiber is prepared by UV-irradiation marked by the gray shaded core area.

In a particular wavelength range given by the effective indices of the two modes in the intermediate section a mode coupling between the fundamental LP_{01} and the higher order LP_{11} mode occurs. If the tilt angle is properly chosen the conversion is highly efficient. In this wavelength range an incident fundamental mode travelling in +z- direction will be nearly completely converted by the gratings to the LP_{11}-mode. Vice versa, a LP_{11}-mode travelling in (-z)-direction is reconverted to the LP_{01}-mode. Therefore, starting with an input wave in +z-direction, all forward modes tend to be LP_{01} while all backward modes are essentially LP_{11}. In this way, a resonator is formed which behaves like a 2-mirror Fabry-

Perot. In particular, at resonance all the reflected LP_{11}-modes interfere destructively so that the transmission factor (consisting of fundamental mode power) tends to unity. At either side from the transmission peak the reflected waves do not eliminate each other but interfere constructively in part. Nevertheless, no reflection occurs at the input port of this device because the backward waves are LP_{11} which do not propagate in the leading single-mode section.

Since the conversion factors can be close to unity, the structure presented in Fig.1 is able to work as a Fabry-Perot with high finesse and negligible reflection. It is limited, however, to a certain wavelength range where the mode conversion takes place.

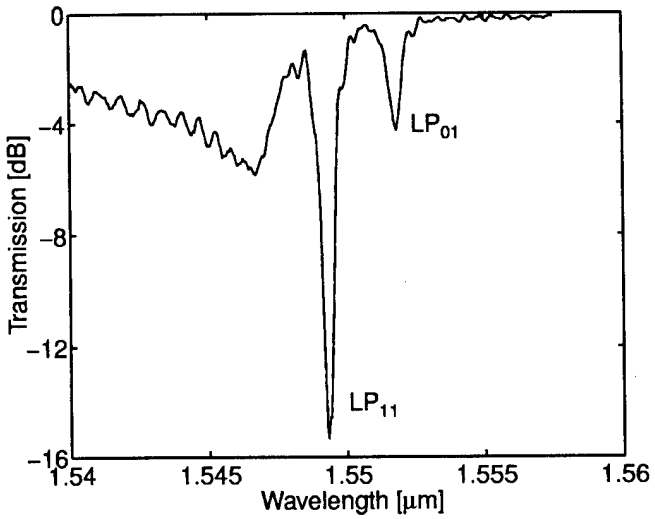

Figure 2: The transmission spectrum of a non-reflecting Fabry-Perot transmission filter for $\alpha = 3^0$ tilted gratings. The two minima are caused by phase matching between the LP_{01} mode and the reflected LP_{01} and LP_{11} modes. The resolution of 0.2nm of the spectrum analyser is not sufficient to resolve the Fabry-Perot resonances.

The non-reflecting Fabry-Perot transmission filters outlined above are fabricated in hydrogen sensitized (3 mol%) single-mode germanosilicate fibers [2] by means of a frequency doubled Argon-Ion Laser (Innova Fred 300, Coherent) at $\lambda = 244$nm. The pre-irradiation for creating the two-mode section is carried out by scanning the focussed UV-beam along the fiber at a specified power and writing speed. Next, a phase mask (Λ=1069 nm) is placed on top of the fiber at an angle α' as to yield a blaze angle of $\alpha = 3^0$ for the grating inside the fiber core. The two gratings which are to serve as mode converters are written one after the other in a scanning mode. The normalized transmission spectrum of the Fabry-Perot filter made in this way and measured with a grating spectrometer is shown in Fig.2. The two prominent transmission minima at different wavelengths correspond to $LP_{01} - LP_{01}$ and $LP_{01} - LP_{11}$ conversion. Note, that the Fabry-perot resonances are far to narrow to be resolved in this way. Therefore, the spectrum in Fig.2 is similar to that one of a corresponding one-grating structure.

The wavelength range of interest here is the $LP_{01} - LP_{11}$ conversion-peak (transmission

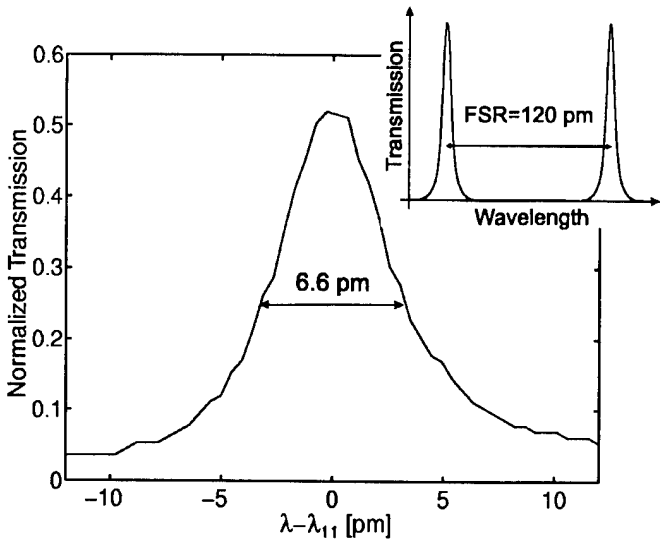

Figure 3: Scan of the Fabry-Perot resonance around λ_{11} =1549nm. Within the stop-band of the fiber Bragg grating the resonances have a FWHM width of 6.6pm and a free spectral range of 120pm.

minimum) located around λ_{11} = 1549nm. Using a tunable laser diode in a piezo controlled continuous scanning mode the Fabry-Perot resonances can be detected. The transmission near a resonance is shown in Fig.3. Its FWHM width is 6.6pm. Since the continuous scanning range is limited to about 25 pm the neighbour resonances cannot be measured in a single scan but can be determined by using the coarse scanning mode. The result is a free spectral range FSR= 120 pm and thus a finesse of $\mathcal{F}$=18. Due to resonator losses which are not yet fully understood the maximum transmittance is T_{max} = 52% at present. The minimum transmission is more than 12dB below its maximum and, most important, the return loss is higher than 20dB.

The non-reflecting Fabry-Perot transmission filter presented above may be useful in filter applications where reflections must be avoided. It could be used, e.g., as an intracavity filter in narrow-band lasers. In the field of instrumentation, the splitting of the narrow transmission peak could be applied to precisely measure index differences due to birefringence and, in particular, to investigate UV-induced birefringence effects.

References

[1] T.A. Strasser, J.R. Pedrazzani, M.j. Andrejco, Optical Fiber Communication Conference, Vol.6 of 1997 OSA Technical Digest Series (Optical Society of America, Washington, D.C., 1997), paper FB3.

[2] Ge-doped single-mode fiber, OFTC, Sydney, Australia.

Bragg Gratings, Photosensitivity, and Poling in Glass Fibers and Waveguides: Applications and Fundamentals

Grating Stability and Reliability

Sunday, October 26, 1997

Turan Erdogan, University of Rochester
Presider

BSuD
4:00pm–5:30pm
Auditorium

Mechanical Reliability of UV Irradiated Fibers: Application to Bragg Grating Fabrication

H.G. Limberger, D. Varelas, R.P. Salathé
Institute of Applied Optics
Swiss Federal Institute of Technology, CH-1015 Lausanne, Switzerland.
Tel. +41 21 693 5183
Fax. +41 21 693 6108

Intra core fiber grating components [1] like reflection-, transmission-, and loss filters play a major role in telecommunication [2] and sensor networks [3]. The reliability of such components is crucial since survival times of up to 50 years are needed. The fiber strength that characterizes the mechanical reliability is determined by the distribution of intrinsic and extrinsic defects, called flaws. Intrinsic and extrinsic flaws are related to defects in the silica bond structure and surface microcracks due to fiber manufacturing, respectively. UV absorption in the fiber core creates new intrinsic defects leading to a core tension increase due to compaction of the glass structure [4]. In this paper we report on the mechanical reliability of fibers irradiated by UV light using the side exposure technique [5]. Homogeneous excimer laser irradiation reduces the mechanical resistance considerably depending on the fluence per pulse [6, 7] and the laser wavelength [8]. With increasing pulse energy density the mechanical resistance is lowered. In contrary, homogeneous CW irradiated fibers show almost the same fiber strength as compared with pristine fiber [9].

The mechanical reliability of optical fibers can be expressed by their long term behavior under applied service tension. Based on dynamic fatigue test data, the fiber lifetime, t_f, under applied service stress, σ_α, can be estimated using a lifetime model based on crack growth theory [10, 11] by

$$t_f(L,F,\sigma_\alpha) = \frac{\sigma_f^{n+1}(1)}{n+1}\left(\frac{L_0}{L}F\right)^{\frac{(n+1)}{m}}\sigma_\alpha^{-n} \qquad (1)$$

where L is the service length, L_0 is the fiber gauge length, and m is the Weibull shape constant for inert strength distribution. The corrosion susceptibility n as well as $\sigma_f(1)$ are determined experimentally from Weibull plots for different stress rates [10] and F is the cumulative failure probability which is given by

$$F = 1 - \exp\left[-L \cdot N(\sigma_f)\right] \qquad (2)$$

where $N(\sigma_f) = (1/L_0)(\sigma_f/\sigma_0)^m$ is the distribution of flaws per unit length (Weibull distribution), σ_f is the failure stress, and σ_0 is a scaling parameter. To compare different Weibull distributions, the median breaking stress, σ_{med}, which corresponds to a 50 % failure probability is often used.

A hydrogen loaded standard telecommunication fiber (fiber 1) and a 22 mol% GeO_2 doped fiber (fiber 2) with and without hydrogen loading were investigated. H_2 loading was typically performed at ≈150 bar for 2 weeks. Prior to irradiation, the acrylate coating has to be removed. Mechanical stripping reduces the breaking strength dramatically while H_2SO_4 chemical stripping preserves the mechanical reliability [6]. The influence of Hydrogen loading is shown in Fig. 1. To investigate the worst case, a sample of fiber 2 was chosen that was loaded for 16 months at ≈150 bar. The pristine fiber showed a median breaking stress of 4.74 GPa. The hydrogen loading reduced the median breaking stress by 0.1 GPa and enlarged the Weibull distribution indicated by a lower m-value of 70 compared to 150 for the pristine fiber.

90 fiber Bragg gratings (FBG) were fabricated in the H_2 loaded fiber 1 by a pulsed KrF-excimer laser and 60 FBG's in fiber 2 using a CW- frequency doubled Ar^+ laser. In both cases, the laser beam dimensions exceeded the fiber diameter. Three different sets of FBG's with 2 (FBG 1), 4 (FBG 2) and 10 mm length (FBG 3) were made by pulsed laser irradiation. Fluences of about 150 mJ/cm^2 corresponding to an intensity of 75 MW/cm^2 per pulse and a total dose of ≈1 kJ/cm^2 were used. FBG's of 8 mm length were formed in the hydrogen loaded (FBG 5) and unloaded fiber 2 (FBG 4) by the CW-laser, with an intensity of 1.25 W/cm^2 and a total dose of 75 J/cm^2. To obtain the stress corrosion coefficients n in both cases, pulsed and CW, Weibull distributions of FBG's 1 and 4 were determined for different stress rates. Table I shows mechanical reliability parameters and irradiation conditions for the irradiated gratings.

The Weibull distributions of pristine fiber 1, FBG 2 and 3 formed by pulsed UV laser are shown in figure 2. The FBG's have reflectivities of 51 and 92 %, respectively. The median breaking strength and the m-value are strongly reduced for both series in comparison with pristine fiber. In addition, the median breaking stress decreases with increasing length.

Figure 3 shows the Weibull distribution of gratings with high (FBG 5) and low reflectivity (FBG 4) fabricated using the CW-laser. No changes in the median breaking stresses were observed as compared to pristine fiber. No influence of H_2 loading is observed in this case. The m-values are reduced from 152 for the pristine fiber to 57 and 71 for FBG 4 and 5, respectively. This increase in the width of the distribution influences the long term failure behavior.

Figure 4 shows the stress rate dependence of the median breaking stresses σ_{med} for FBG 1 and 4. The n value is given by $n = (1/s) - 1$, where s is the slope of the line. n-values of 13 and 14 were obtained for pristine fiber 1 and 2, respectively. For FBG 1 and FBG 4 the obtained n-values were 12 and 14, respectively. We observe that for KrF-irradiation the stress corrosion coefficient is reduced by 8 %, while no such reduction is observed for CW irradiation.

Applying the model of Refs. [10, 11] developed for fiber lifetime predictions, the failure time of KrF-excimer and CW-laser irradiated fibers was calculated after Eq. (1) as a function of service stress for FBG 1 and 4, as well as the lifetime of pristine fibers as a reference (Fig. 5). The service length was 10 cm and the calculations were made for a 50 year lifetime and a failure probability of 0.001. For pristine fiber 2 a 50 year survival time is expected for an applied service stress of 1.0 GPa. The m value change from 112 to 57 for CW-laser formed FBG 4 reduces the possible applied service stress by 6 % to 0.96 GPa. This value has to be compared with a maximum service stress of 0.06 GPa for KrF-excimer laser irradiated FBG 1.

In conclusion, the mechanical reliability of UV irradiated optical fibers is evaluated using a lifetime model based on crack growth theory and Weibull statistics. The number of flaws is amplified by UV side irradiation as shown in the case of Bragg gratings. Pulsed irradiation leads to a dramatic decrease of the fiber breaking stress and thus to lifetime reduction. In contrary, CW irradiation preserves the breaking strength and results in a small reduction of the applied service tension for a lifetime of 50 years as compared to that of pristine fiber.

References:

1. K.O. Hill, Y. Fujii, D.C. Johnson, B.S. Kawasaki, Appl. Phys. Lett. **32,** 647 (1978).
2. R. Kashyap, Optical Fiber Technol. **1** (1), 17 (1994).
3. W. W. Morey, G. Meltz, W. H. Glenn, *Proc. of SPIE* **1169**, 98 (1989).
4. P.Y. Fonjallaz, H.G. Limberger, R.P. Salathé, F. Cochet, B. Leuenberger, Opt. Lett. **20** (11), 1346 (1995).
5. G. Meltz, W.W. Morey, W.H. Glenn, Opt. Lett. **14** (15), 823 (1989).
6. H.G. Limberger, D. Varelas, R.P. Salathé, G. Kotrotsios, *Proc. of SPIE* **2841** 84 (1996).
7. D. Varelas, H.G. Limberger, R.P. Salathé, G. Kotrotsios, Electron. Lett. **33** (9), 804 (1997).
8. R. Feced, M.P. Roe-Edwards, S.E. Kanellopoulos, N.H. Taylor, V.A. Handerek, Electron. Lett. **33** (2), 157 (1997).
9. D. Varelas, H.G. Limberger, R.P. Salathé, Electron. Lett. **33** (8), 704 (1997).
10. F.P. Kapron, H.H. Yuce, Opt. Eng. **30** (6), 700 (1991).
11. W. Griffioen, Opt. Eng. **33** (2), 488 (1994).

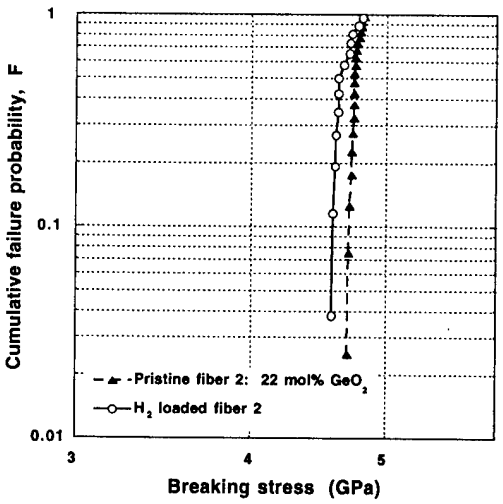

Fig. 1: Weibull distribution of H_2 loaded and pristine fiber 2.

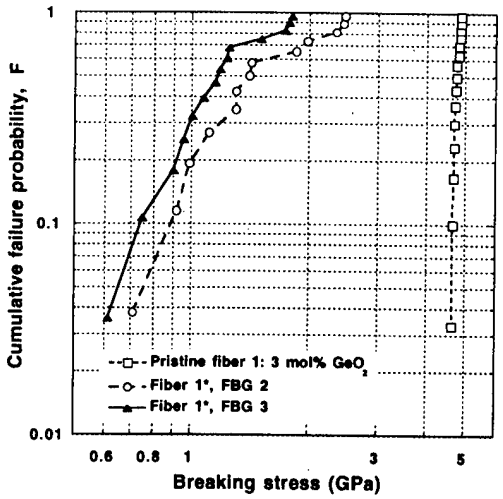

Fig. 2: Weibull distribution of FBG 's fabricated using pulsed excimer laser in H_2 loaded fiber 1.

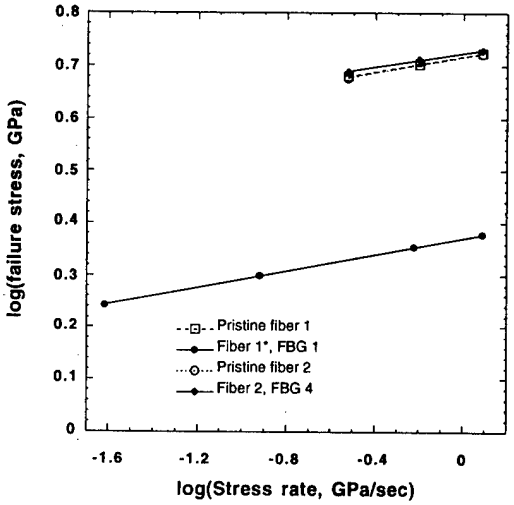

Fig. 4: Stress rate dependence FBG 1 & 4.

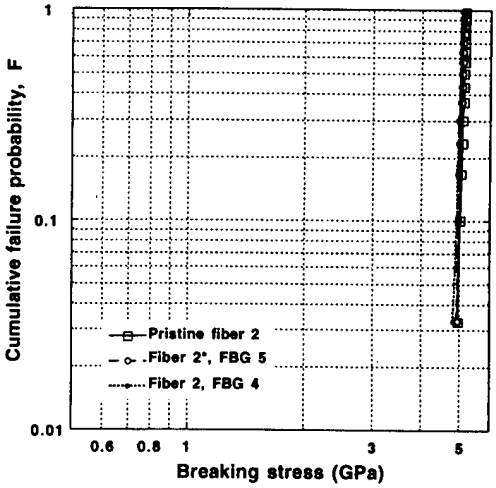

Fig. 3: Weibull distribution of FBG's fabricated using CW laser.

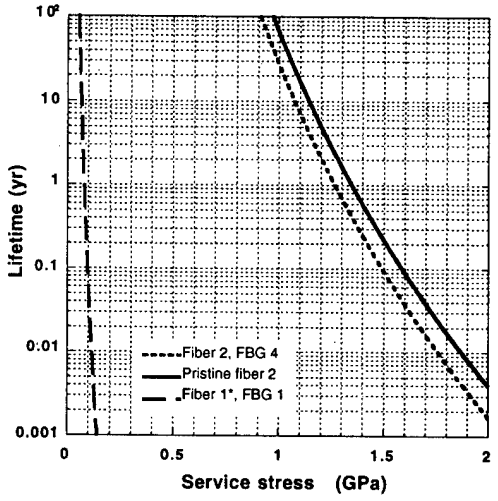

Fig. 5: Calculated lifetime of FBG 1 & 4.

Table I: Irradiation conditions and mechanical reliability data

set	Fiber No.	Irrad. cond	L_B (mm)	R (%)	σ_{med} (GPa)	m	n
pristine	1				4.9	184	13
FBG 1	1*	pulsed	2	50	2.3	3.7	12
FBG 2	1*	pulsed	4	51	1.4	3.7	/
FBG 3	1*	pulsed	10	92	1.2	3	/
pristine	2				5.1	112	14
FBG 4	2	CW	8	21	5.1	57	14
FBG 5	2*	CW	8	99.9	5.1	71	/

* H_2 loaded

Annealing of Long Period Gratings in Standard Hydrogen-Loaded Fiber

F. Bakhti, J. Larrey, P. Sansonetti
Alcatel Telecom Research Division c/o Alcatel Alsthom Recherche
route de Nozay, 91460 Marcoussis, France
Tel: (33)-(0)1-69-63-12-67, e-mail: bakhti@aar.alcatel-alsthom.fr

Introduction: Long period gratings (LPG) are commonly fabricated in hydrogen-loaded fibers [1]. As classical Fiber Bragg Gratings (FBGs), LPGs have to be annealed at elevated temperature to stabilize their spectral response. Since a LPG of period Λ is coupling the propagating mode with cladding modes (in this paper we focuse on LP01-LP05 coupling), the grating central wavelength λ_c is varying with the difference of effective indices between the two coupled modes, Δneff, by $\lambda_c=\Delta neff\ \Lambda$. As a consequence, a variation of $2\ 10^{-6}$ on Δneff will induce a variation of about 1nm on λ_c whereas for FBG, this kind of index variation has negligible effect. Taking into account the specification of the coupling induced by the LPG, we studied its thermal annealing during a long period of time (more than 100 hours) to observe index modulation change in the order of 10^{-6}. In this paper, we present investigations on thermal annealing of LPG at temperature ranging from 110°C to 250°C, and with duration greater than 200h.

Experimental setup: LPGs of length 4cm and 6cm were realized using a 242nm excimer pumped dye laser (fluence per pulse 80mJ/cm^2) irradiating a standard hydrogen loaded fiber (SMF28 from Corning) through an amplitude mask. The photoinduced index differences reached are ranging from $4\ 10^{-5}$ to $10\ 10^{-5}$. The fiber used was directly taken from hydrogenation set-up or stored during few hours at -13°C. After realization, gratings were installed in ovens. The minimum transmission of the LPG at λ_c, T_m, expressed by the relation $T_m=\cos^2[\Delta n\ K_o\ L]$, (L=length, Ko=coupling coefficient), was then measured during few weeks.

Annealing at 110°C during 2100 hours: Two gratings written on the same portion of fiber were annealed at 110°C during 2100 hours. The evolution of Δneff versus the time of annealing is represented in Figure 1. It is shown that at 110°C, the stabilization takes more than 1000h and Δneff is varying by less than 10^{-7} after 2000h . During the annealing, two behaviours are observed: below 1000h, a slow decrease occurs whereas almost no change happened after and the stabilization is reached. As described by Patrick *et al.*[2] for FBGs, these behaviours suggest a distribution of activation energies extended to very low energies. Whereas for FBG ($10^{-4}<\Delta n\_mean<10^{-3}$) sufficient spectral stabilization is obtained at 110°C after few tens hours of annealing, for LPG ($10^{-5}<\Delta n\_mean<10^{-4}$), evolutions of 10^{-6} are easily detectable and occur during 1000h.

Annealing at 160°C, 200°C and 250°C during more than 200h: We have conducted a study of annealing of LPGs at higher annealing temperatures. In figure 2, we report the decay of the normalised amplitude of index modulation $\Delta n/\Delta no$ for each temperature. It is

shown that the saturation occurs after more than 80h at high temperature (250°C). Using the Erdogan model [3], with the power law $(\Delta n/\Delta no)=1/1+A(t/t_1)^{\alpha}$, we fitted for each temperature of annealing the experimental values. We found two differents behaviours: one represents a fast decrease during 100h (250°C) to 1000h (110°C) (fit in dotted line) and the other a saturation type decrease (fit in full line). For each temperature, the time decay is not well described by the Erdogan law and parameters A and α were not conclusive at all. In figure 3, for each grating at given temperature, we plotted the normalised ratio of central wavelength $NCW=(\lambda c-\lambda c_o)/(\lambda co-\lambda c_{initial})$, λc_o being the central wavelength at the end of the writing and $\lambda c_{initial}$ the estimated central wavelength at the begining of the writing. The main remark is that the fast decrease of this ratio depends on temperature and on hydrogen out-fiber diffusion level at the time of writing [4]. Reported by Riant *et al.* [5], for FBGs written in standard hydrogen loaded fiber and annealed at low temperature (T<250°C), the distribution of activation energy is centred at 1.67eV with To=4000K. From our fits, taking a mean value of the coefficients α and A obtained, giving a range of temperature To around To=4300K, and considering a defect distribution centred at 1.67eV, we found (figure 4) that the evolution of $\Delta n/\Delta no$ in function of the demarcation energy Ed is more consistent with this distribution at low energy than at higher energy centred at 2.6eV.

Conclusion: We have shown that annealing of Long Period Gratings, (studied coupling between LP01 and LP05) with low index modulation varying from 10^{-5} to 10^{-4}, presents a longer time of stabilization than classical Bragg gratings due to LPG's higher sensitivity to low index variations in the order of 10^{-6}. At 110°C, evolution of Δneff reaches value less than 10^{-7} after 2100h of annealing. This study, envolving low index of modulation, also confirmed low energy defect distribution for standard hydrogen loaded fiber already observed with high index modulation in classical FBG.

References:

[1] A. M. Vengsarkar *et al.*, J. Light. Tech., 14, 1996, pp. 58-65.
[2] H. Patrick *et al.*, J. Appl. Phys., 78, 1995, pp. 2940-2945.
[3] T. Erdogan *et al.*, J. Appl. Phys., 76, 1994, pp. 73-80.
[4] F. Bakhti *et al.*, submitted to BGPP meeting, OSA, 1997.
[5] I. Riant *et al.*, OFC, 1997 OSA Technical Digest Series, paper WL18.

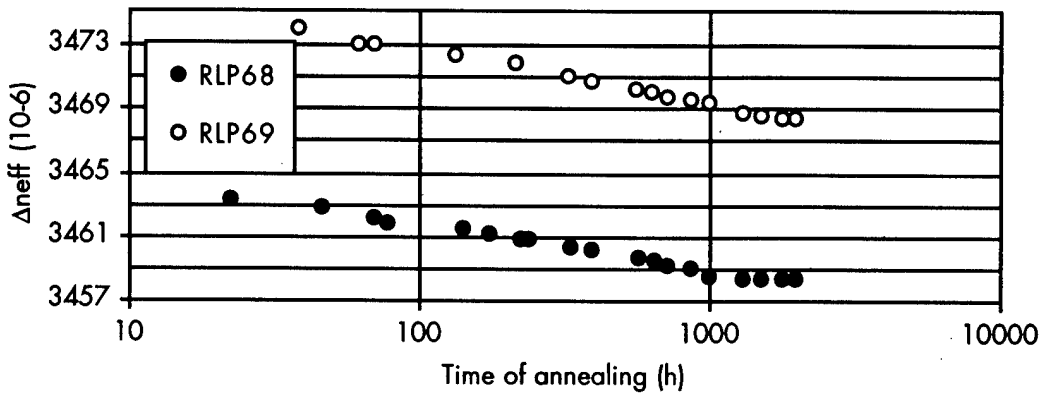

Figure 1: Evolution of Δneff during annealing at T=110°C.

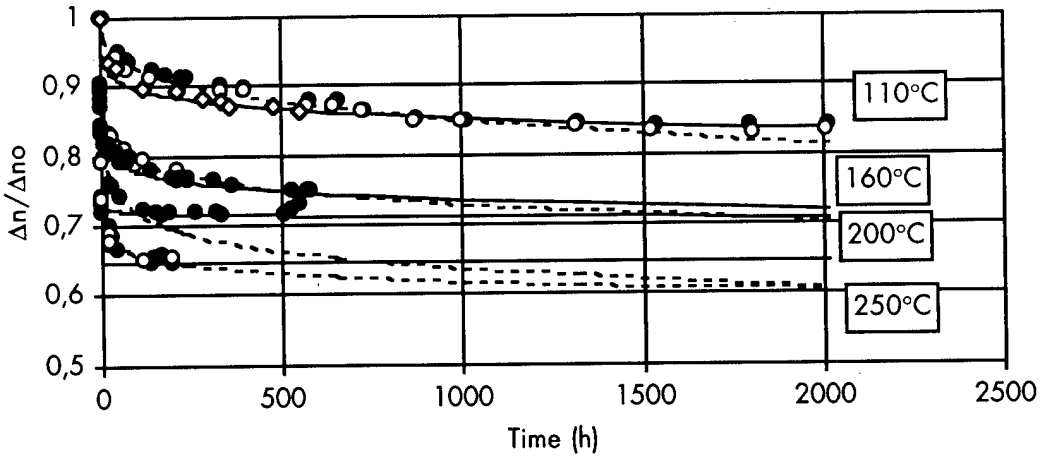

Figure 2: Evolution of Δn/Δno during annealing for different temperatures

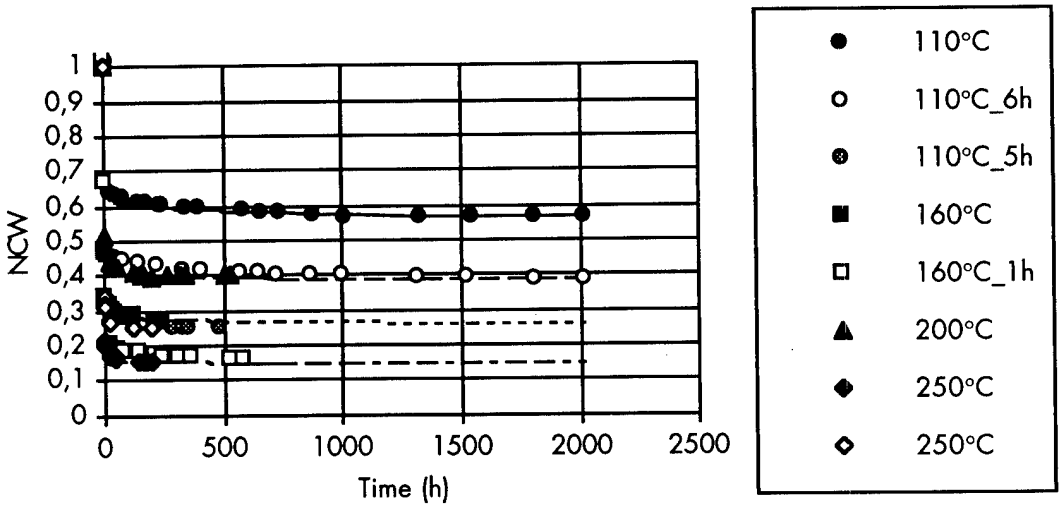

Figure 3: Evolution of NCW=($\lambda c-\lambda c_o$)/($\lambda co-\lambda c_{initial}$) during annealing for different temperatures

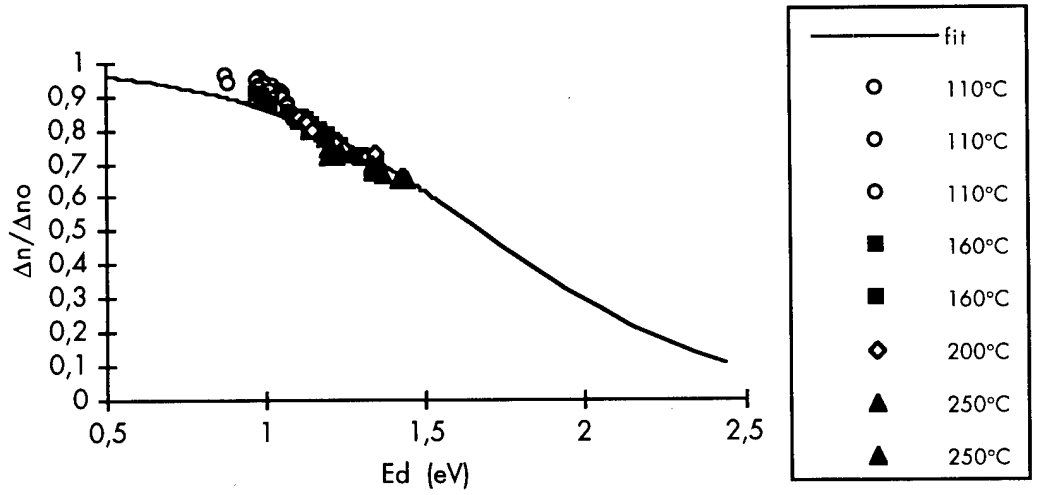

Figure 4: Evolution Δn/Δno in function of energy of demarcation, for To=4300 K and a distribution E=1,67eV.

Reliability predictions on fiber gratings through alternate methods

Sriraman Kannan, Paul J. Lemaire, Jerry Guo and Michael J. LuValle

Specialty Fiber Devices
Lucent Technologies, Bell Labs Innovations
600 Mountain Avenue 4-209A
Murray Hill, NJ 07974

Phone : 908-582-7369 Fax : 908-582-2422
E-mail : sri@lucent.com

Numerous advances have been made since the discovery of photosensitivity in optical fibers [1], but none perhaps more significant than fiber based gratings. Gratings are modulated refractive index patterns inscribed in the core of photosensitive optical fibers. In Bragg gratings, light propagating down the fiber length is selectively reflected at the wavelength which satisfies the Bragg condition. Long period gratings which involve coupling into forward propagating cladding modes are a second type of fiber based gratings. Gratings are most commonly written in fibers with germanium doped silica core. Photosensitivity has been also been demonstrated in germanosilicate fibers with codopants such as boron [2] and tin [3]. It has also been shown [4] that "loading" fibers with hydrogen or deuterium, greatly enhances their photosensitivity. This facilitates easy writing of gratings even in compositions that are otherwise minimally photosensitive, for instance, in phosphorus doped silica fiber [5].

Gratings are written by side exposure of fibers to an interfering pattern of light - either by an interferometric technique [6] or by using a phase mask [7-9]. Regardless of the type of the writing method, gratings are typically inscribed in germanosilicate fibers using UV light. Grating formation involves UV-induced defects. When the gratings are subjected to elevated temperatures, decay is observed suggesting that these defects are not thermodynamically stable but are rather sites that can be reversed resulting in a change in index. Gratings are usually subjected to a *stabilization* treatment, which is a controlled high temperature anneal carried out to remove the most unstable defect sites. Properly chosen stabilization treatment can deliver gratings with stability that are well within the system tolerances over the lifetime of deployment. In order to ensure that this is indeed the case, it is essential to analyze and predict the almost imperceptible decay of such gratings over their lifetime of use. To this end, two methods have emerged based on the work of Erdogan *et al.* [10] in this area - (1) the aging curve / master curve approach and (2) the power law approach.

Both the techniques mentioned above are based on the same physical principles [10-12]. These may be summarized as follows :

- the index raising UV-induced defects may be visualized as sites with trapped species
- associated with such sites is an activation energy barrier which the trapped species attempts to overcome with thermal assistance
- when the trapped species overcomes the activation energy barrier the contribution of that site to the overall index change is lost, leading to grating decay
- due to the inherent disorder of the glass the activation energy assumes not a unique, but rather a range of values
- sites with low activation energy decay fast as compared to sites that have a higher activation energy, which decay more gradually
- the net decay is then a summation of all the individual decay components, manifesting an initial rapid decrease followed by a progressively diminishing but non-zero rate.

In the *aging curve* approach to decay analysis, carefully constructed experiments are carried out at elevated temperatures (typically 100°C - 250°C). A quantity proportional to the refractive index modulation is measured as a function of time. This is the spectral width in the case of the strongly reflecting gratings and the integrated coupling coefficient (given by $\tanh^{-1}\sqrt{R}$), in the case of the weak (R<99%) gratings. In an accelerated aging experiment, the extent of aging on grating at any temperature (T) and time (t) is described by an aging parameter,

$$\chi = kT\ln(vt) \qquad \text{(eq. 1)}$$

where k is the Boltzman's constant and ν is an attempt frequency term, which is obtained by acquiring sets of data at different temperatures and fitting them together. The plot of χ vs. $(\Delta n/\Delta n_o)$ is the *aging curve* (or *master curve*) for that particular type of grating.

Figure 1 shows a sample aging curve obtained through a set of accelerated aging experiments on strongly reflecting gratings written in deuterium loaded AT&T/Lucent 5D fibers. These unchirped gratings were written using an excimer pumped dye laser operating at 242 nm and had a starting spectral width of about 2.5 nm at 5 dB below the maximum. In this case, the optimal value of ν for which the different sets of data combined together was 2×10^{10} /s. Once the aging curve is derived for a particular type of grating, the behavior of the grating at any given operating temperature can be predicted.

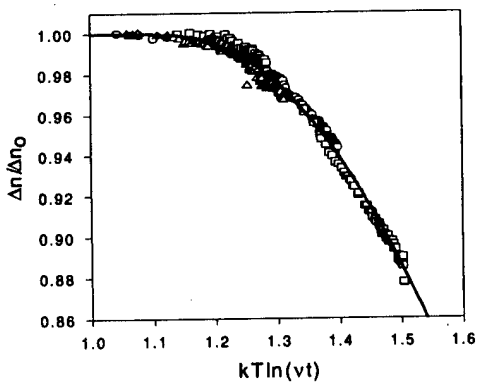

Figure 1: A sample aging curve obtained from curve fit to experimental data

Figure 2 shows the predicted behavior of the grating for which the aging curve is given by Figure 1. The expected decay at an operating temperature of 40°C is 0.5% at the end of a period as long as 25 years. Even at 70°C, the predicted decay is only 2.8%. It should be noted that it was possible to achieve such superior stability through prior stabilization of these gratings. The appropriate stabilization conditions are determined by factors such as system tolerances, fiber and grating types and operating conditions. The aging curve approach can itself be used to arrive at the *appropriate* stabilization conditions for any grating. This topic and further discussion on the aging curve technique will be presented.

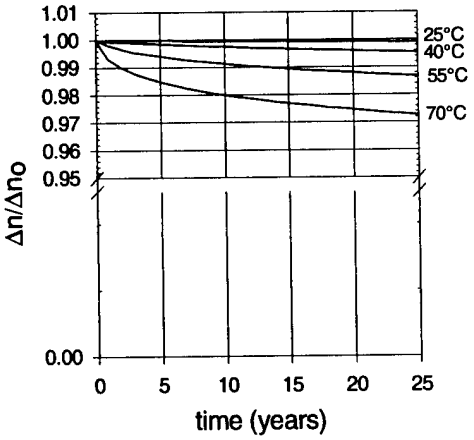

Figure 2 : Predicted thermal stability of the grating in Figure 1 at various temperatures

The second approach to analyzing accelerated aging data of grating is what has come to be known as the *power law* method [10]. Here, the decay in the UV-induced refractive index change is expressed as:

$$\eta = 1/(1+A(t/t_1)^{\alpha}) \qquad \text{(eq. 2)}$$

where t is the time, t_1 is a time unit dimension factor. Ideally, according to this model, the factor A and exponent α should be related to temperature in the following manner :

$$A \propto \exp(T) \qquad \text{(eq. 3)}$$

$$\alpha \propto T \qquad \text{(eq. 4)}$$

However, the present work shows that the latter relationship (eq. 4) does not hold for all gratings.

The power law technique also involves carrying out accelerated aging experiments at several elevated temperatures similar to the aging curve approach. The data at each temperature is then fit to equation 2 to obtain A and α for that temperature. By repeating this at several temperatures, the exact A vs. T and α vs. T relationships are established for that grating. It is then possible to predict the stability of that grating type at any given operating temperature.

In previous work [10], the power law has been applied to as-written, unstabilized gratings. However, when this approach was applied to stabilized gratings of various types in the present work, it was observed that the α vs. T relationship was not in accordance with equation 4. Forcing a fit yields α values, which lead to deviant reliability predictions. For example, Figure 3 shows the reliability predictions on weak (starting R = 20%) stabilized gratings written in hydrogen loaded fibers. The continuous and the broken lines represent

decay predicted by the aging curve and the power law methods respectively at 200°C. The symbols represent data obtained from an actual experiment on the grating carried out at 200°C. It can be noted that the aging curve predictions show excellent agreement to the experimental data, while the power law prediction overestimates the expected decay.

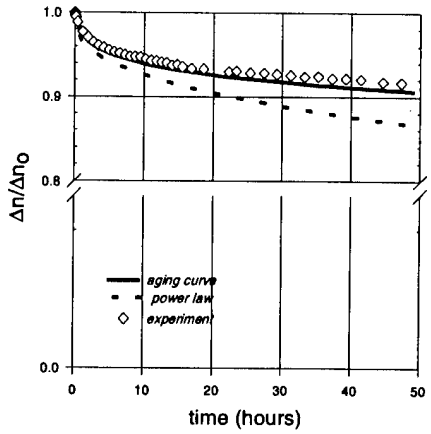

Figure 3: Comparison of reliability predictions by different methods of analysis.

The reason for the discrepancy in power law predictions arises from the fact that this approach assumes specific initial distributions of activation energies for the defect population [10]. Even in those cases where such an assumption is valid for as-written gratings, the act of stabilization will alter the situation, leading to a distribution other than that assumed by the power law. The aging curve approach on the other hand does not assume any specific initial distribution and hence can be applied more generally without any regard to the actual distribution. The presentation will address specific details of this comparison.

The above discussion does not imply that the power law is invalid for all types of gratings. It could be used for gratings with a certain type of activation energy distribution (for which, $\alpha \propto T$), whereas the aging curve can be applied more generally. In this sense, the power law model can be viewed as a special case of the more general model. All things considered however, the aging curve analysis is preferable since it is certain to work and involves just as much or less experimentation than the other method.

Although it is clear that the aging curve approach is a powerful and general method to grating decay analysis, it should be noted that there is no single *universal* aging curve for all types of gratings. Grating stability is dependent on fiber parameters, material composition and writing technique. It is essential to derive the aging curve for any particular type of grating to predict the stability for *that* type of grating.

The aging curve method described in previous pages are appropriate for gratings with simple refractive index profiles. We have developed variations of the method for other types of gratings such as those with complex UV-induced index profiles as well as for other types of gratings such as the long period gratings. An interesting example is the analysis of apodised add/drop gratings for deployment in WDM systems. In this case, the grating is characterized with two aging curves - signifying defect populations with two different activation energy distributions corresponding to sections of the grating with large and small UV-induced defect levels. Reliability predictions are then made with these aging curves. This procedure will be described further in the presentation.

References :

[1] K.O. Hill, Y. Fujii, D.C. Johnson, and B.S. Kawasaki, *Appl. Phys. Lett.*, vol. 32, no. 10, 647 (1978).

[2] D.L. Williams, B.J. Ainslie, J.R. Armitage, R. Kashyap, and R.J. Campbell, *Electron. Lett.*, vol. 29, no. 1, 45 (1993).

[3] L. Dong, J.L. Cruz, L. Reekie, M.G. Xu and D.N. Payne, *Tech. Dig. Conf. Photosensitivity and Quadratic Nonlinearity in Glass Waveguides*, SuA2, 70 (1995).

[4] P.J. Lemaire, R.M. Atkins, V. Mizrahi, and W.A. Reed, *Electron. Lett.*, vol. 29, no. 13, 1191 (1993).

[5] T.A. Strasser, A.E. White, M.F. Yan, P.J. Lemaire and T. Erdogan, *Tech. Dig. OFC'95*, WN2, 159 (1995).

[6] G. Meltz, W.W. Morey, and W.H. Glenn, *Opt. Lett.*, vol. 14, no. 15, 823 (1989).

[7] D.Z. Anderson, V. Mizrahi, T. Erdogan, and A.E. White, *Tech. Dig. OFC'93*, PD 16, 68 (1993).

[8] K.O. Hill, B. Malo, F. Bilodeau, D.C. Johnson, and J. Albert, *Appl. Phys. Lett.*, vol. 62, no. 10, 1035 (1993).

[9] R. Kashyap, J.R. Armitage, R.J. Campbell, D.L. Williams, G.D. Maxwell, B.J. Ainslie, and C.A. Millar, *BT Technol. J.*, vol. 11, no. 2, (1993).

[10] T. Erdogan, V. Mizrahi, P.J. Lemaire, and D. Monroe, *J. Appl. Phys.*, vol. 76, no. 1, 73 (1994)

[11] P.J. Lemaire and T. Erdogan, *Tech. Dig. Conf. Photosensitivity and Quadratic Nonlinearity in Glass Waveguides*, SuA4, 78, (1995).

[12] S. Kannan and P.J. Lemaire, *Tech. Dig. OFC'96*, TuO4, 84 (1996).

Impact of Hydrogen in-fiber and out-fiber Diffusion on central wavelength of UV-written Long Period Grating

F. Bakhti, J. Larrey, P. Sansonetti, B. Poumellec*
Alcatel Telecom Research Division c/o Alcatel Alsthom Recherche
Route de Nozay, 91460 Marcoussis, France, e-mail: bakhti@aar.Alcatel-alsthom.fr
*CNRS URA 446 Bât. 415, UPS Orsay, 91405 Orsay, France

Introduction: Hydrogen loaded standard fibers are routinely used for writing fiber gratings as the diffusion of molecular hydrogen strongly enhances the fiber photosensitivity [1]. Out-fiber diffusion of molecular hydrogen occurs when fiber is removed from hydrogen pressure. If the out-fiber diffusion after few hours at room temperature has negligible effect on the value of the initial Bragg wavelength for classical Bragg gratings (FBG), for long-period gratings (LPG) we show that this out-diffusion considerably changes the value of the initial central wavelength. Furthermore, in a reciprocal way, the in-fiber diffusion of hydrogen in LPG can induce strong shift of the central wavelength. In this paper, we present for the first time to our knowledge, both theoretical and experimental studies on the impact of hydrogen in-fiber or out-fiber diffusion on Long-Period Gratings.

Modelling of hydrogen diffusion in standard fiber: Considering the fiber as a perfect cylinder of radius R, with the core and the cladding assumed to have uniform hydrogen diffusion coefficient D taken from [3] as: $D = 2.83\,10^{-4} \exp\left(\frac{-40.19\,kJ/mol}{RT}\right) cm^2/s$, we solved for the hydrogen concentration C(r,t), the Fick's diffusion equation in polar coordinates [2]: $\frac{\partial C}{\partial t} = D^2\left(\frac{\partial^2 C}{\partial r^2} + \frac{1}{r}\frac{\partial C}{\partial r}\right)$ (r=radial coordinate, t=time). With initial condition: $C(r,0) = \varphi(r)$, $C(r,t) = \frac{2}{R^2}\sum_1^\infty \frac{J_0\left(\mu n \frac{r}{R}\right)}{J_1^2\left(\mu n \frac{r}{R}\right)} \exp\left(-D\left(\frac{\mu n}{R}\right)^2 t\right) \int_0^R \rho\,\varphi(\rho)\, J_0\left(\mu n \frac{\rho}{R}\right) d\rho$,

J_0 and J_1 are the Bessel functions, μn the n^{th} root of J_0, and n to have value from 1 to 3200.

We present in figure 1 the diffusion profile for different time for in-fiber hydrogen diffusion at room temperature (RT) and high pressure (figure 1b), and of out-fiber hydrogen diffusion at RT (figure 1a).

UV-writing: impact of hydrogen out-fiber diffusion on LPG initial central wavelength

Standard fiber (SMF28 from Corning) was hydrogen loaded during few weeks at 140 bars and room temperature until saturation, and then, stored at -13°C. In these conditions, the diffusion coefficient is nearly ten times less than at 23°C and for FBGs, this way of storing the fiber allows reproducible writing during several days. We successively UV-wrote 23 LPGs (length=6cm, period Λ=440μm) corresponding to a storing time from 0 to 180h, using an excimer pumped dye laser (242nm, fluence per pulse of 80mJ/cm2) through an amplitude mask. Our study was focused on the peak provided by the coupling of LP01 and LP05 modes. The LPG central initial wavelength λ_c is related to the difference of effective

indices of the two modes by: $\lambda_C = (neff_1 - neff_5)\Lambda$. In figure 2, we report the measured initial central wavelength of each grating versus the storing time at -13°C: it is seen that after 170 hours (≈20 hours at 23°C), the initial central wavelength dramatically shifts by 85nm. During this period of time, as the hydrogen out-diffuses from the fiber, according to figure 1, we can see that the effective index neff1 is not very affected whereas the cladding effective index neff5 is more perturbed and decreases, inducing an increase of λ_C. Using a perturbation model [4] and diffusion profiles for given r and t, assuming that at saturation the effect of hydrogen in FBG is about 7pm/atm [5], we calculated the impact of hydrogen diffusion on $neff_1$ and $neff_5$. As hydrogen increases the refractive index by $n^2 = n_0^2 + \partial n^2$, the perturbation on the effective index can be written as: $\partial neff^2 = A\frac{\iint \partial n^2 \Psi^2 dS}{\iint \Psi^2 dS}$ (A=scale factor, Ψ= electric field distribution of considered mode, dS=r dr dθ). In figure 2, we compare the calculated values with measured ones and show that our model fits the experiment. It is shown that in order to get LPGs writing reproducibility of the initial λ_C, the hydrogen loaded fiber has to be stored at much lower temperature.

At the annealing: impact of hydrogen out-diffusion on LPG central wavelength

After the writing of LPG in H_2-loaded fiber, due to hydrogen out diffusion, λ_C first increases by tens of nanometers before decreasing when hydrogen totally disappears. For an annealing temperature of 110°C, we measured during 6hours the evolution of λc and compare with calculated values (figure 3). Our model fits the behaviour of λc by increasing before decreasing to reach saturation. The observed difference is attributed to the begining of ageing of the mean UV-written index change.

Impact of hydrogen in-diffusion on central wavelength of thermally stabilized LPG

A LPG (fiber SMF28, length= 6cm, period= 420μm, λ_C=1530nm), previously stabilized at 110°C during 500h, was hydrogen loaded at 165 bars during two weeks. After removing from hydrogen chamber, the grating was set at room temperature and λc measured during 200h: its evolution is reported in figure 4. It is shown that our model simulates quite well the observation and we can extend these results to the effect of H2 in-fiber diffusion on λc when a pressure of 1bar is applied (figure5). It is shown that λc shifts by about -1nm before the recovery of its initial value when H2 reaches saturation in the fiber. For a pressure of 0.01bar, this shift is -0.01nm. An interesting point concerns the use of such filter in submarine repeater. Hydrogen pressure could then progressively increase during several months: the grating will not see an abrupt hydrogen in-fiber diffusion but rather a progressive one, the evolution of λc being then negligible.

Conclusion: We have presented both theoretical and experimental studies on the impact of hydrogen in-fiber and out-fiber diffusion on LPGs. We have calculated the hydrogen concentration profile in the fiber for given times and positions. A model of perturbation was used to explain the effect of out-fiber diffusion and found that reproducibility of λc at the writing of LPG in H_2-loaded fiber requires the fiber to be stored at low temperature (<-20°C) before the writing, to avoid the shift of tens of nanometres for initial λc. We also found that H_2 in-fiber diffusion generates negative shift of λc during several hours.

References:
[1] P. J. Lemaire *et al.*, Elect. Lett., 29, 1990, pp. 1191-1192.
[2] N. Koshlyakov *et al.*, North-Holland Pub. Comp., 1964.
[3] P. J. Lemaire, Opt. Eng., Vol. 30, n°6, 1991, pp. 780-789.
[4] C. Vassallo, Eyrolles et CNET-ENST, tome 2, 1985.
[5] B. Malo *et al.*, Elect. Lett., 30, 1994, pp. 442-443.

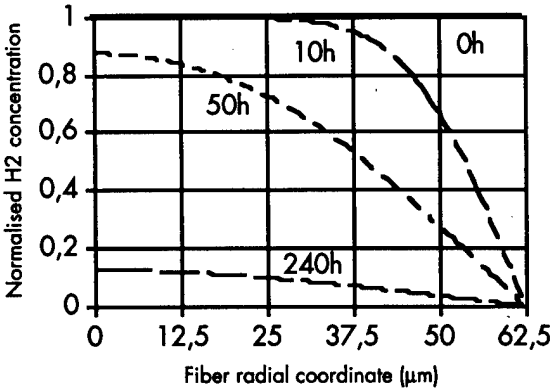

Figure 1a: Out-fiber diffusion of hydrogen at room temperature.

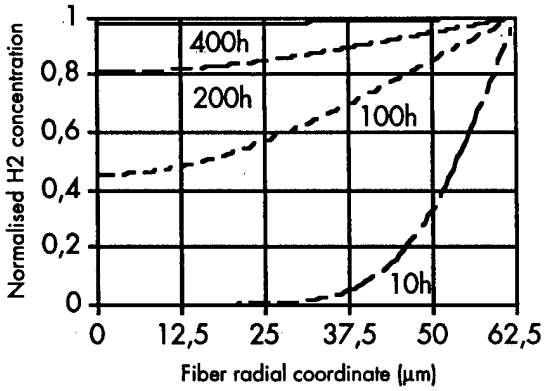

Figure 1b: In-fiber diffusion of hydrogen at room temperature and high pressure.

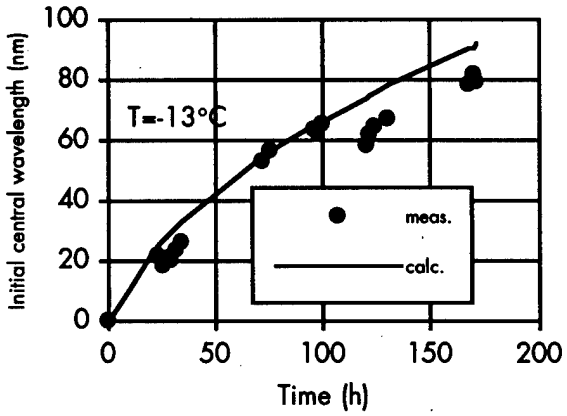

Figure 2: At the writing, increase of the LPG initial λc in function ofH_2 out-fiber diffusion at -13°C

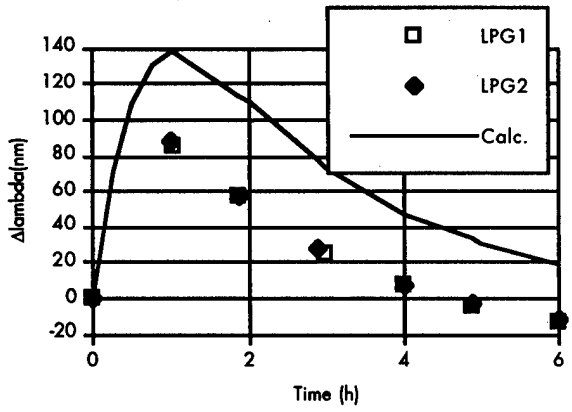

Figure 3: At the begining of the annealing, evolution of λc due to H_2 out-fiber diffusion.

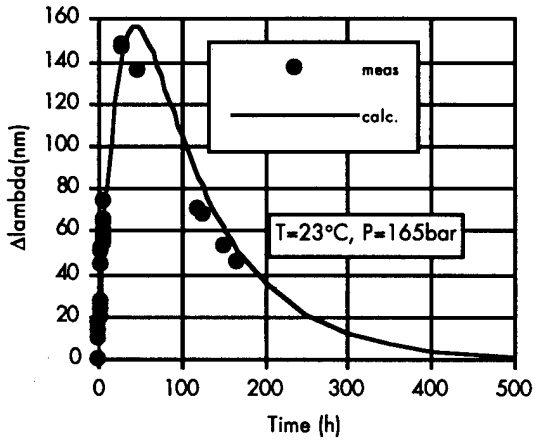

Figure 4: Out-diffusion effect: for a stabilized LPG H_2-loaded at 165 bar, evolution of λc as a function of time at room temperature.

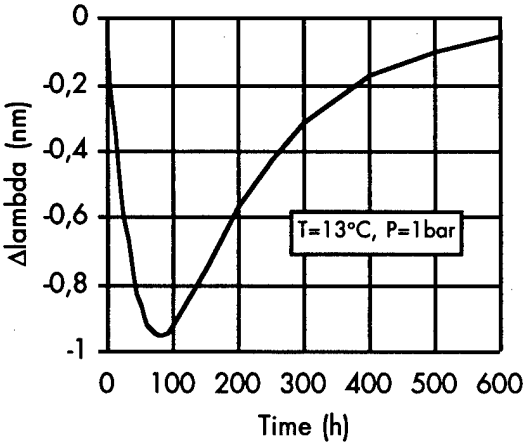

Figure 5: In-diffusion effect: calculated evolution of λc as a function of the time at 13°C and H_2 pressure of 1 bar

A Novel Approach to Fabricate High-Temperature Resistant Fiber Bragg Gratings

Michael A Fokine, Bengt E Sahlgren, and Raoul Stubbe,

Institute of Optical Research
S-100 44 Stockholm, Sweden
Fax: +46-8-791 13 00
Tel: +46-8-789 66 72

Introduction

Ever since the discovery of photosensitivity in optical fibers by Hill *et al.* in 1978 [1] and the development of the transverse holographic writing technique by Meltz *et al.* in 1989 [2] there has been increasing interest in developing gratings with increased temperature stability. The decay of fiber Bragg gratings has been shown to depend on the fabrication process [3,4], the doping [3,5], and the temperature history [6].
In this paper a technique for writing high temperature stable gratings (>800 °C) is presented and a theory for the change in refractive index is proposed. The change is refractive index is believed to result from a reorganization of dopants in the core.

Basic principles

Defining chemical refractive index gratings as periodic variations of the chemical composition, a thermal erasure of these gratings would then require diffusion of the dopants involved. The temperature resistivity would then be limited by the diffusion properties of the specific dopant. The basic idea for fabricating chemical gratings, presented in this paper, is to periodically alter the mobility of one or several dopants by altering the chemical structure in the glass network, i.e. altering their thermal diffusion properties. The problem is that a large change in diffusion properties must be attained in order to avoid erasure of the grating itself during the diffusion process. Here we have used low-temperature hydrogen loaded germanium doped fiber co-doped with fluorine. The germanium dopant is used as a promoter for hydroxyl formation when exposed to UV-radiation [7,8] and the co-dopant fluorine is used due to its chemical interactions with hydroxyls producing hydrogen-fluoride [9]. When the fiber is exposed to spatially varying UV intensity, as in the case of writing Bragg gratings, there will consequently be a spatial variation of the hydroxyl concentration. A subsequent high-temperature annealing process will induce chemical reactions between the hydroxyl groups and fluorine under the formation of hydrogen-fluoride which then diffuses out of the core (or within). The result would then be a fluorine

depletion in the UV exposed regions and consequently a change in refractive index. The process of forming chemical composition gratings is schematically depicted in Fig. 1.

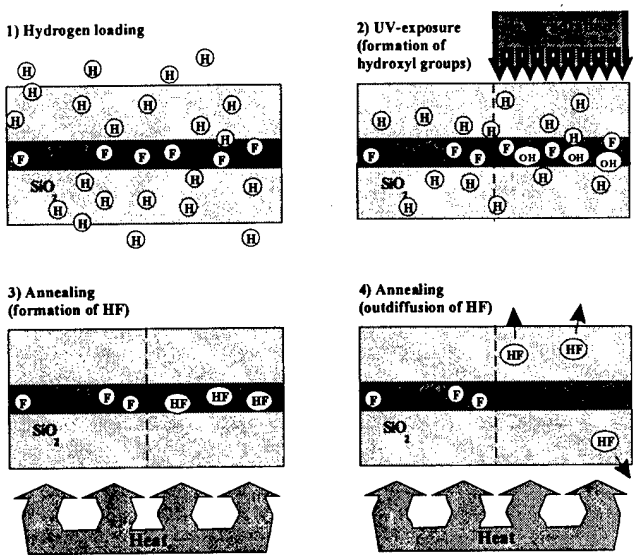

Fig. 1. The process of formation of chemical composition grating.

Experimental results

A silica fiber was developed with an estimated germanium and fluorine content of 10 mol % and ~2 mol % respectively. The fiber was then low-temperature hydrogen loaded at 10 MPa for approximately one week after which the fiber was exposed to UV-radiation at the wavelength of 240 nm to form a Bragg grating by the well-known transverse holographic method [2]. The fiber was then placed in a tube furnace and the grating was monitored using a white-light source and a spectrum analyzer. As the temperature of the furnace was increased at 25 °C/min, the grating reflectivity decreased and the grating was completely erased at approximately 900°C. Very soon after however, the grating reappeared and increased in reflectivity for a few minutes until it saturated at a level of ~ 30 % reflectivity (Fig. 2). The temperature of the furnace was then lowered to 810 °C and held constant at this temperature for approximately 550 hrs. There was no significant change in reflectivity of the grating after nearly 550 hrs at 810°C.

Discussion

The grating in this experiment show a grating behavior not resembling any results from Bragg gratings previously reported, which suggest that a new type of Bragg grating has been observed. Type II gratings have been reported [4] to be rather stable up to 800°C, but a transmission spectrum shows that the grating in our experiment resembles a type I grating. The experiments performed so far can not definitely confirm the proposed theory, however the grating is subject to a temperature of 1000 °C for several minutes during the development process without being erased. To get an understanding of the diffusion behavior of fluorine at 1000 °C one can calculate

the characteristic time $t=l^2/4D$ it takes for fluorine to diffuse a distance l, where D is the diffusion coefficient. By using the diffusion coefficients of fluorine at 1000 °C, derived by Kirchhof et al. [10], an approximate value of 29 minutes is attained for fluorine to diffuse a distance of half a grating period (~ 0,25 μm). Further experiments concerning temperature stability and the proposed theory are currently under evaluation and will be presented at the meeting.

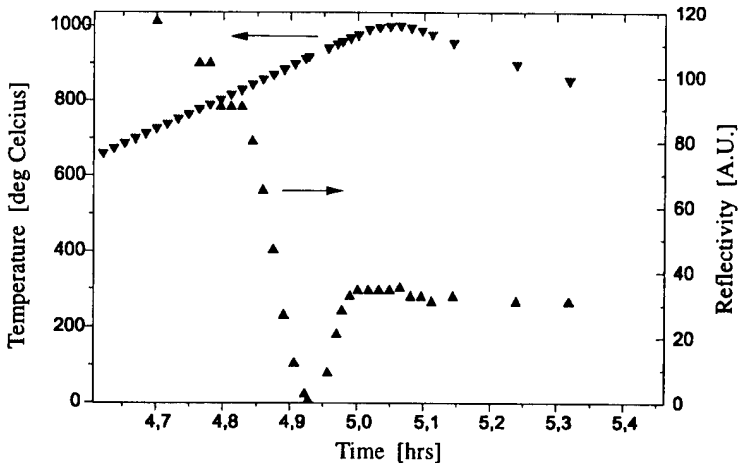

Fig. 2. Development of the grating

References

[1] K. O. Hill, Y. Fujii, D. J. Johnson, and B. S. Kawasaki, "Photosensitivity in optical fiber waveguides:
application to reflection filter fabrication", Appl. Phys. Lett., 32, 647, (1978).

[2] G. Meltz, W. W. Morey, and W. H. Glenn, "Formation of Bragg gratings in optical fibers by transverse holographic method", Opt. Lett., 823, (1989)

[3] I. Riant, S. Borne, and P. Sansonetti, "Dependence of fiber Bragg grating thermal stability on fabrication process", in OFC'96 Vol. 2, 1996 OSA Tech. Dig. Series, paper TuO5.

[4] J.-L. Archambault, L. Reekie, and P. St. J. Russel, "100 % reflectivity Bragg reflectors produced in optical fibres by single excimer laser pulses", Electron. Lett., **29**, 453, (1993).

[5] L. Dong, J. L. Cruz, L. Reekie, M. G. Xu, and D. N. Payne, "Enhanced photosensitivity in tin-codoped germanosilicate optical fibers", Photon. Technol. Lett., 7, 1048, (1995).

[6] T. Erdogan, V. Mizrahi, P. J. Lemaire, and D. Monroe, "Decay of ultraviolet-induced fiber Bragg gratings", J. Appl. Phys., **76**, 73, (1994).

[7] P. J. Lemaire, R. M. Atkins, V. Mizrahi, and W. A. Reed, "High pressure H_2 loading as a technique for achieving ultrahigh UV photosensitivity and thermal sensitivity in GeO_2 doped optical fibres", Electron. Lett., 29, 1191, (1993).

[8] K. Awazu, H. Hosono, and H. Kawazoe, "Chemical reactions of Ge-related species in SiO2:GeO2 optical fibers", in Proc. SPIE, **2044**, 78, (1993)

[9] J. Kirchhof, S. Unger, H. –J. Pißler, and B. Knappe, "Hydrogen-induced hydroxyl profiles in doped silica layers", in OFC'95 Vol. 8, 1995 OSA Tech. Dig. Series, paper WP9.

[10] J. Kirchhof, S. Unger, K.-F. Klein, B. Knappe, "Diffusion behaviour of fluorine in silica glass", J. Non-Crystalline Solids, 181, 266, (1995).

Bragg Gratings, Photosensitivity, and Poling in Glass Fibers and Waveguides: Applications and Fundamentals

Linear and Nonlinear Optical Phenomena in Glass GOMD/BGPP Joint Poster Session

Sunday, October 26, 1997

JSuE
5:30pm–7:00pm
Adams Room

270 nm absorption and 432 nm luminescence bands in doped silica glasses.

B. Poumellec[1], V.M. Mashinsky[2].

1 CNRS URA 446 Thermodynamique et Physico-chimie des Matériaux, Université de Paris Sud, 91405 Orsay Cedex, France. Tel. 33 01 69 15 63 51 Fax: 33 01 69 15 48 19. e-mail: bp@phebus.isma.u-psud.fr
2 FORC at General Physics Institut, 38 Vavilov street, 117942, Moscow, Russia. Tel 7 095 132 82 93 Fax 7 095 135 81 39 vmm@fo.gpi.ac.ru

Introduction

There are a lot of structure defects known more or less in pure and doped silica[1]. They appear either in absorption or in fluorescence or also in EPR. In this paper, we are interested in the occurrence of 270 nm absorption and excitation band. This band was mentioned first in a paper in 1982[2]. In this paper, in synthetic GeO_2-SiO_2 glass containing 0.2 wt% of Ge, the authors have found 270 nm excitation band associated with 435 nm luminescence band. They note that Garrino-Canina[3] have seen a luminescence at 435 nm band but in a much less pure sample. They associate the GeO defect to this band. One year later, Gebala[4] has noticed a 270 nm excitation and 430 nm luminescence band in Ge-P-SiO_2. He has associated this to Ge^{2+} in octahedral coordination.

Here, we come back on the occurrence of this band since it has been detected in samples with various Ge content and elaboration and also not containing Ge.

Experimental details

Two kinds of experiments have been performed: absorption and luminescence measurements. They were obtained from various optical fiber preforms. Figures presented here are just few examples.

Measurements were done in Russia with conventional source and in France with Synchrotron radiation. The set-up contained two monochromators on the synchrotron PAM3 line (LURE-Orsay) and one monochromator and filters or two monochromators in Russia depending on the strength of the luminescence. Resolution on UV spectra is 0.1 nm.

High dosage 248 nm laser irradiation was used to induce absorption and luminescence changes. Preforms with various Ge content were elaborated by MCVD process. For two of them, the cladding was investigated which contained about 0.1 mol% GeO2 with some F- and P-co-doping.

Experimental results

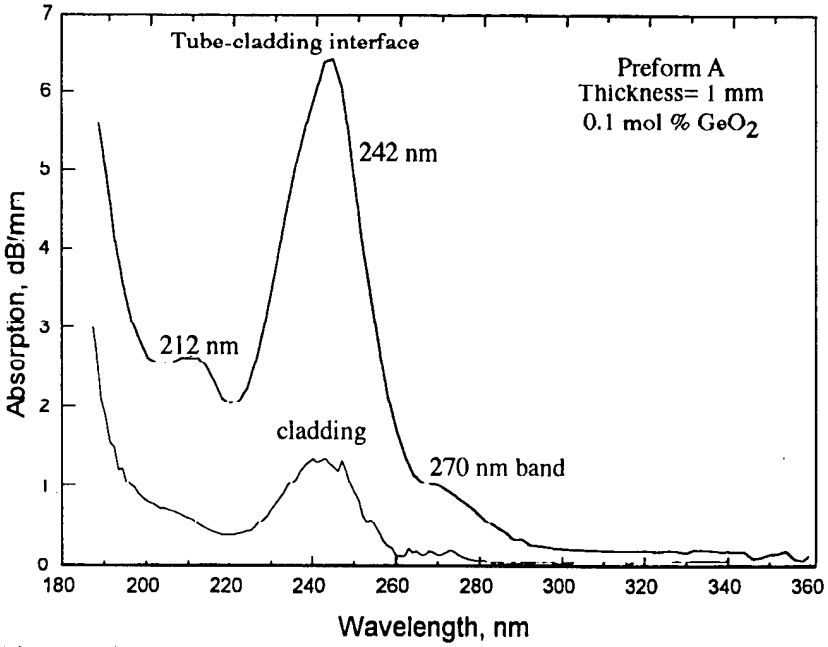

Fig. 1: Absorption spectra recording in the cladding and at the boundary between the tube and the cladding.

Figure 1 shows the absorption spectra in the UV range in two points of the preform A. These two points are situated in the cladding and close to the substrate-tube interface. The absorption spectra are composed of five bands: a tail of a band appearing in the VUV range, a small component situated at around 210 nm, a band near 229 nm strongly overlapping with a larger one peaking at 242 nm and a small one with maximum near 270 nm. Whereas the first four bands are oftenly mentionned in the literature [1], the last one is not subject to attention.

When absorption spectra are recorded across this preform, we find 270 nm only in the cladding, not in the highly Ge doped core. This means this bands is not proportional to Ge

content but depends on another parameter. Moreover, this means that it is not connected to the defects absorbing at 242 nm or at 210 nm or at 229 nm [1] which have another behavior.

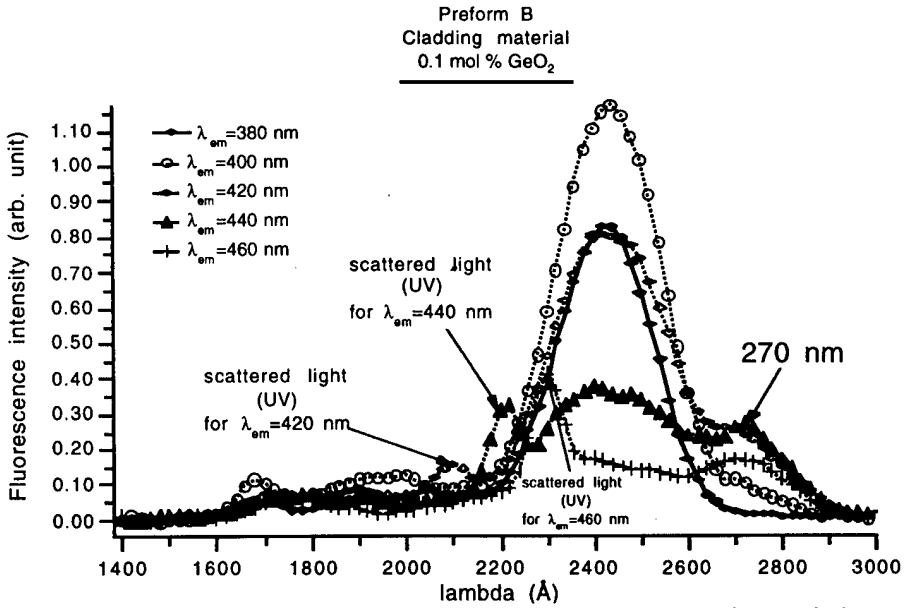

Fig. 2: Fluorescence excitation spectra in cladding material for various emission wavelengths.

Figure 2 shows LE spectra in preform B which is composed uniquely by cladding material. The excitation of luminescence has been achieved by synchrotron radiation. The detection was through the output monochromator with 1 nm resolution. In this figure, we can see that a 270 nm excitation band appears well contrasted for luminescence wavelength situated between 420 and 440 nm. For luminescence around 400 nm, 270 nm band is very weak compared to luminescence from GeODC (242 nm excitation band). In this condition, it is very often masked by the strong 242 nm excited luminescence.

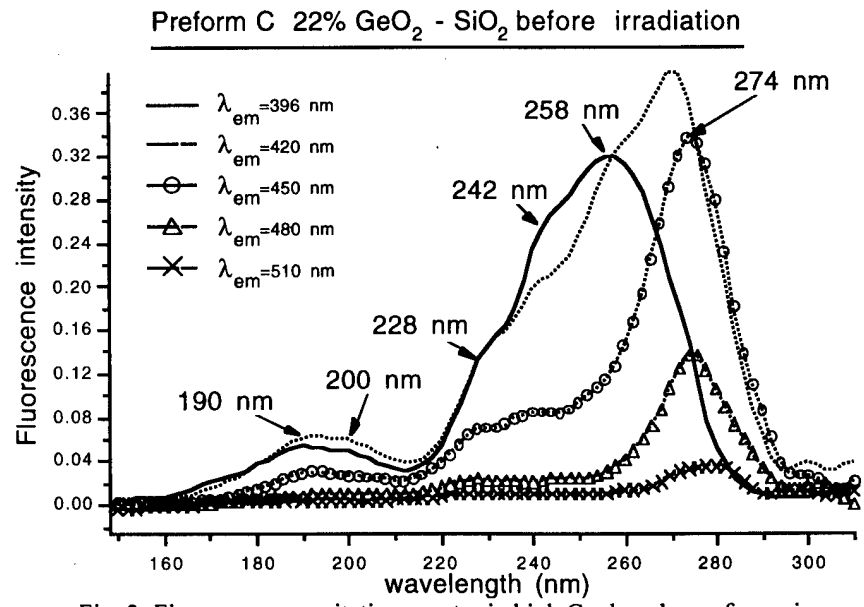

Fig. 3: Fluorescence excitation spectra in high Ge doped core for various wavelengths.

We have found an excitation band in the vicinity of 270 nm in samples containing not only a small amount of GeO_2 but also a large GeO_2 concentration, i.e. larger than 20 mol%. Figure 3 shows LE spectra for various luminescence wavelengths collected from preform C. In that case, a large number of components are detected. When luminescence wavelength is changed, the excitation spectrum is changed non-homothetically. So, for 396 nm luminescence, the spectrum does not show resolved component around 270 nm. On the contrary, for larger luminescence wavelength, e.g. 420 or 450 nm, we see that a component at 274 nm is very strong compared to 258 nm band. From inspection of different curves, it can be deduced that the maximum of luminescence is situated between 420 and 450 nm.

To precise this wavelength several luminescence spectra were recorded for luminescence wavelengths ranging between 200 and 700 nm. Measurements we have made show that the maximum is at 432±2 nm. In addition, for excitation at 280±1 nm no other luminescence band is detected on the investigated emission wavelength range (200-700 nm). This allows to attribute the 432 nm luminescence to the 270 nm excitation band.

We have found excitation bands at around 270 nm in a lot of preforms when detection wavelength is around 432 nm. Different preforms with various GeO_2 content between 4 to 30 mol% have been investigated. Sometimes, this band exists, sometimes does not. It is not possible to make correlation for the moment but this confirms that it is not proportional to the Ge content anyway. A strong absorption band at 270 nm and an associated luminescence band at 430 nm was observed in nitrogen-doped germanosilicate glass prepared by SPCVD method [5]. But, an absorption band at around 270 nm has been detected also in N-doped silica glass without Ge prepared by the same method [6]. So, we can deduced that the correspondingf defect has no Ge atom in its structure.

Behaviour under 248 nm laser irradiation

It is known that performing a UV laser irradiation, the 242 nm band is bleached partly and that absorption around it increases[1] [7]. Fittings made by Neustreuev et al [1] and Fertein [8] has shown that absorption bands at 280-290 nm appear. This is confirmed here. In preform C, after an exposure corresponding to a dose of 12 K J/cm2, a lot of excitation bands are bleached especially the band appearing at 274 nm in the figure 3. Measurement of luminescence spectra in this irradiated preform does not show component at wavelengths larger than about 400 nm anymore.

In N-doped germanosilicate glass, the effect of 244 nm laser irradiation results in a bleaching of 270 nm band (about 20% for dose 5 KJ/cm7 [5]. However, we know other examples which show that sometimes this band increases under 248 nm irradiation. So, it is careful to say that the defect absorbing at around 270 nm is not a primary photosensitive defect but rather it is involved in a secondary reaction. So, using 244-248 nm lasers, this band appears to be stable or bleached or even increases.

Conclusion

We describe the occurrence of an absorption band at 270 nm associated with a luminescence peaking at 432 ± 2 nm. Clearly this band is not dependent on the Ge content but required reduced conditions. It is probable that it is caused by a defect belonging to the silica network and produced by the elaboration process. On the contrary, it has not been detected in fused silica nor in MCVD cladding containing P/F but without Ge codoping. Anisotropy luminescence, decay kinetics measurements as well as irradiation effect of a laser at 266 nm are necessary to perform for increasing our understanding.

References

1. V.B. Neustruev, Sov. Lightwave Commun., 1991. **1**: p. 177-195.
2. O.K. Bilan, N.G. Cheranda, and A.V. Shendrik, *Intrinsic and radiation-induced defects in silicon dioxide doped with germanium.*, in *Electron processes and defects structure in glassy systems.* 1982, Proceedings of Latvian State University. p. 59-66.
3. V. Garino-Canina, Comptes rendus de l'Académie des Sciences., 1954. **239**: p. 875.
4. S. Gebala, Optica Applicata, 1983. **13**(3): p. 257-264.
5. E.M. Dianov, K.M. Golant, R.R. Khrapko, V.M. Mashinsky, O.I. Medvedkov, I.V. Nikolin, O.D. Sazhin, and S.A. Vasiliev. *UV absorption and luminescence in bulk nitrogen-doped germanosilicate glass prpared by SPCVD.* in *ECOC.* 1997.
6. E.M. Dianov, K.M. Golant, R.R. Khrapko, O.I. Medvedkov, A.L. Tomashuk, and S.A. Vasilev, Optical Materials, 1996. **5**(3): p. 169-173.
7. R.M. Atkins, V. Mizrahi, and T. Erdogan, Electronics Letters, 1993. **29**(4): p. 385-387.
8. E. Fertein, *Contribution à l'étude des mécanismes de la photoréfractivité dans des fibres optiques dopées à l'oxyde de germanium.*, . 1994, Lille/Flandres.

UV-induced reaction of H_2 with the core of germanosilicate and aluminosilicate fiber preforms

Caroline Dalle, Patrick Cordier, Christophe Depecker

Laboratoire de Structure et Propriétés de l'Etat Solide - URA CNRS 234

Université des Sciences et Technologies de Lille - UFR de Physique

59655 Villeneuve d'Ascq Cedex - France

Pascal Bernage, Marc Douay, Pierre Niay

Laboratoire de Dynamique Moléculaire et Photonique - URA CNRS 779

Centre d'Etudes et de Recherches Lasers et Applications

Université des Sciences et Technologies de Lille - UFR de Physique

59655 Villeneuve d'Ascq Cedex - France

Jean-François Bayon

France Telecom, CNET-Lannion, Technopole Anticipa

22301 Cedex - France

Liang Dong

Optoelectronics Research Centre, The University of Southampton

Southampton S0171BJ - UK

Aim of the study

The photosensitivity of glasses can be significantly enhanced by high-pressure low-temperature hydrogen loading prior to UV exposure. The chemical reactions that occur between hydrogen and glass under UV exposure are thus of primary importance for the understanding of the mechanisms of H_2 photosensitivity enhancement.

We have used infrared spectroscopy to characterize the microstructural modifications in H_2-loaded optical fiber preform cores exposed to UV laser light. Infrared spectroscopy in the 3 μm range is very well adapted to such a characterization because it is highly sensitive to hydroxyl groups.

Experimental procedure

We have thus studied three germanosilicate preforms: one from the CNET laboratory (BPG286) and two preforms from the University of Southampton which

are codoped with boron (B) and tin (Sn). We have also studied one Ce-doped aluminosilicate preform from the CNET laboratory (FPA630Ce).

The cores of the preforms were exposed to UV fringeless light from a XeCl pumped frequency doubled dye laser at λ_p = 244 nm and a pulse frequency rate of 50 Hz. The number of pulses and the fluence per pulse are given in the table below.

Preform	Core doping	Core diameter	Treatment	Preform thickness	Exposure conditions (248 nm)
BPG286	GeO_2 7-8 mol%	700 µm	H_2	300 µm	F = 175 mJ/cm^2 50.000 pulses/side
			D_2	300 µm	F = 175 mJ/cm^2 50.000 pulses/side
HD 239	GeO_2 20 mol% SnO_2 5 mol%	500 µm	H_2	100 µm	F = 160 mJ/cm^2 55.000 pulses/side
HD 240	GeO_2 27 mol% B_2O_3 6 mol%	500 µm	H_2	100 µm	F = 160 mJ/cm^2 55.000 pulses/side
FPA630Ce	Al_2O_3:10 mol% Ce: 5000 - 8000 ppm	750 µm	H_2	200 µm	F = 150 mJ/cm^2 60.000 pulses/side

Results

The infrared spectra of germanosilicate preforms are dominated by a OH band at 3600 cm^{-1} which corresponds to Ge-OH (Fig. 1). A Ge-H peak is also detected at 2180 cm^{-1}. This shows that reaction with hydrogen occurs mostly on Ge sites. The presence of boron or tin does not change this behavior significantly. One notes also the growth after UV exposure of a broad band at ≈ 3300 cm^{-1} which can be attributed to molecular water (Fig. 1). Experiments have been carried out on deuterated preforms to make sure that this waterformation is not due to some surface reaction with the atmosphere (Fig. 2). This occurence of molecular water shows that the glass has been reduced upon UV irradiation.

Ce-doped aluminosilicate preforms exhibit a similar behavior (Fig. 3). In that case, the hydroxyl groups peak at 3550 cm^{-1} which suggests that OH is associated with Ce. Molecular water is formed too. A further evidence for glass reduction is given by the growth of Ce^{+3} peaks.

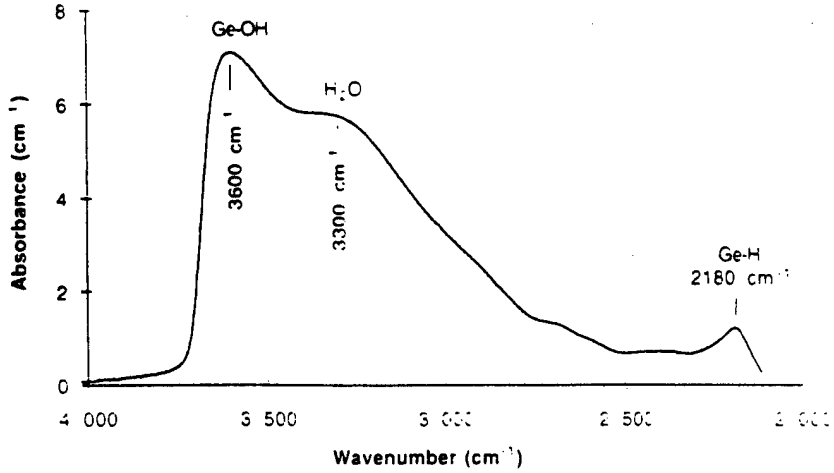

Figure 1
Difference spectrum for a H_2-loaded, BPG 286 sample before and after irradiation.

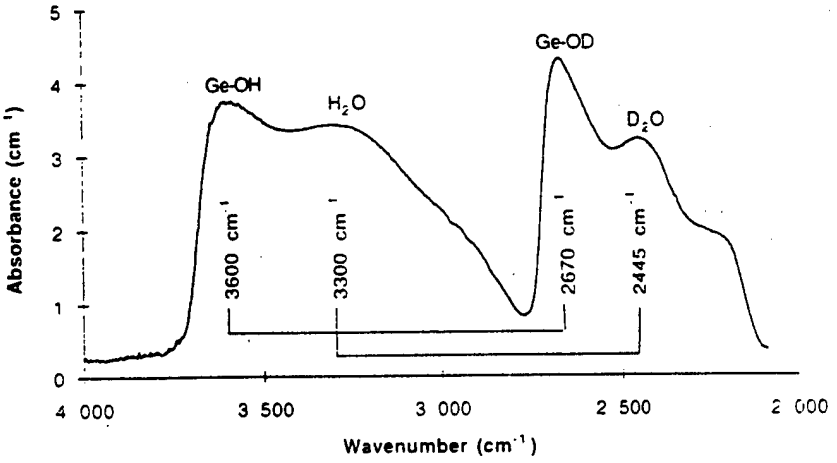

Figure 2
Difference spectrum for a D_2-loaded, BPG 286 sample before and after irradiation.

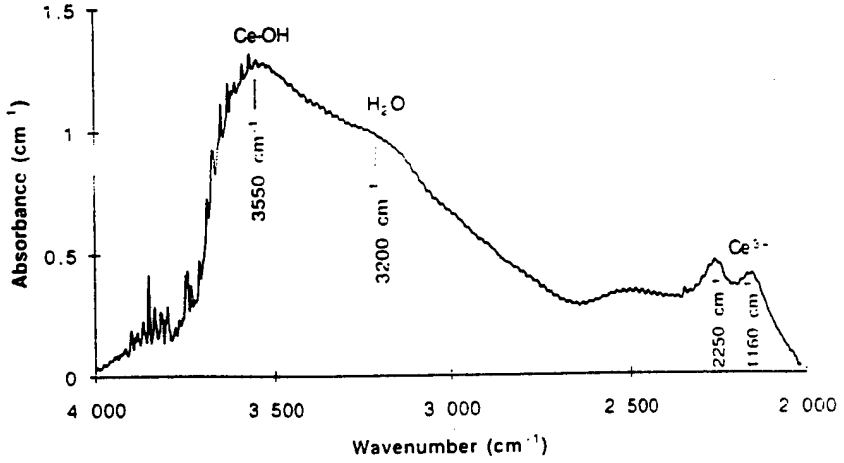

Figure 3
Difference spectrum for a H_2-loaded, FPA 630 Ce sample before and after irradiation.

Effects of molecular hydrogen on low-intensity UV photochemistry of germanosilicate glasses.

V. N. Bagratashvili [a], S. I. Tsypina [a], P. V. Chernov [b], A. O. Rybaltovskii [b], Yu. V. Zavorotny [b], L. Dong [c]

[a] Science-Research Center for Technological Lasers of Rus. Academy of Sci., Pionerskaya 2, Troitsk, Moscow Region, 142092, Russia; tel/fax +7(095)3340342.
[b] Science-Research Institute of Nuclear Physics of Moscow State University, Moscow, 119899, Russia; tel. +7(095)9394395; fax +7(095)9392673.
[c] Optoelectronics Research Centre, the University of Southampton, Southampton SO17 1BJ, UK; tel. +44(1703)593083; fax +44(1703)593149.

Introduction.

Germanosilicate glasses are known to posesses photorefractive (photosensitive) properties [1], that allows to fabricate refractive index gratings in germanosilicate optical fibers [2]. Hydrogen loading silica and germanosilicate glasses enhances its photosensitivity significantly [3-6]. Since the germanium-oxygen deficient center (GODC) is the main photosensitive defect in germanosilicate glasses, it is of particulary importance to reveal the role of molecular H_2 in the processes of GODC phototransformation. In this work, we study the influece of molecular hydrogen impregnated into the glass network on the triplet decay time τ_T, luminescence intensity (T_1 - S_0, λ_{max}=397 nm) and efficiency of GODC photodecay when excited with low-intensity UV light.

Experimental.

The triplet lunminescence kinetics was recorded as follows. The pulse radiation of nitrogen laser (λ=337 nm, $\tau_{pulse}=10^{-8}$ s, f=100 Hz) was focused on preliminary cleaned optical fiber, the maximum irradiation density was 0.23 J/cm^2. A peace of the fiber to be irradiated was fixed in a thermostate with variable temperature (from 90 to 600 K).

In measurements of temperature dependence of triplet photoluminescence intensity I_T for GODC excited into the singlet absorption band (transition S_0-S_1), we used the same apparatus, but with a deuterium lamp serving as a source of irradiation. Besides, for the high- and low-intensity UV irradiation the KrF excimer laser has been used.

All the optical fibers studied were drawn from preforms produced by the MCVD method. For ESR measurements the MCVD germanosilicate films were used.

The fibers ans films were treated in a hydrogen atmosphere at room temperature in a chamber under a gas pressure of 24 atm for 2 weeks. The hydrogen concentration was about 5×10^{19} cm^{-3} in the core of single mode fiber and 3×10^{19} cm^{-3} in the film.

The ESR measurements of irradiated samples were performed with RE-1306 radiospectrometer working in the X-range (f=9.4 GHz).

Results and Discussion.

The presence of molecular hydrogen in the network of germanosilicate glass strongly affects the temperature dependences of the decay time of the excited state T_1. Figure 1a displays the temperature dependences of τ_T for the unloaded (curves 1-3) and H_2-loaded (curves 4) optical fibers with various GeO_2 concentratios in fiber core. Measurements were carried out routinely for a week. As hydrogen escapes from the fiber core, i.e., with a decrease in the hydrogen concentration, the curves 4 $\tau_T(T)$ become similar in shape to curve 1-3 for the hydrogen-free sample.

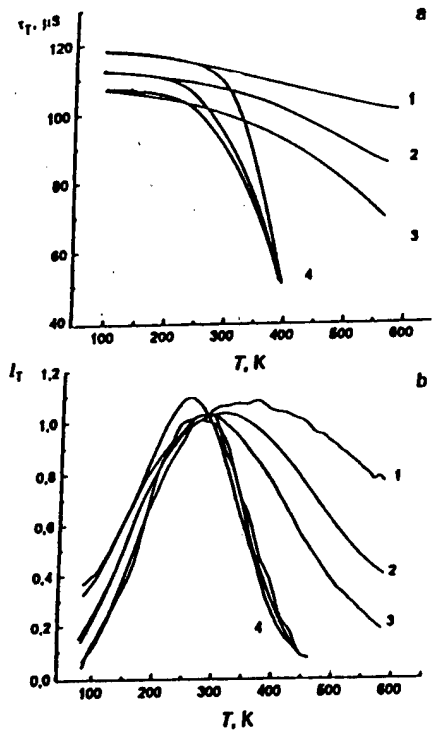

Fig.1. Temperature dependences of triplet lifetime (a) and intensity of tiplet luminescence (b) in fibers with 2.3 (1),11(2) and 23 mol.% GeO_2 (3); H_2-loaded fibers (4).

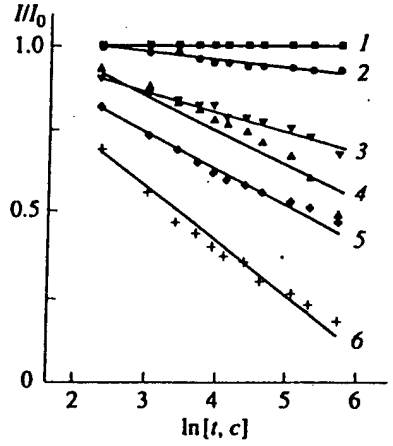

Fig.2.Dependence of the intensity of triplet photoluminescence in fiber with 23 mol.% GeO_2 on the laser irradiation dose (λ=337 nm) at fixed irradiation temperatures T, K: (1) 290, (2) 390 and (3) 480 for the initial samples; and (4) 90, (5) 290, and (6) 390 for H_2-loaded samples.

Such a decrease in the decay time τ_T in optical fibers saturated with hydrogen should manifest itself in the dependences $I_T(T)$, specifically at temperature higher than room temperature. Indeed, comparison of curves 1-3 and 4 in fig.1b shows that, at all germanium concentrations, the presence of molecular hydrogen in glasses leads to a strong decrease in $I_T(T)$ with temperature. The maximum of hydrogen effect on $I_T(T)$ appears in the fiber at the minimum GeO_2 concentration, and eventually the high-temperature wings of curves 4 in Figs.1a and 1b turn out to be close to each other. This indicate that the presence of hydrogen molecules at high concentration almost completely determines the temperature behavior of the intensity of triplet photoluminescence of GODC, irrespective of the germanium concentration.

From our viewpoint, the results obtained from the hydrogen-contaning fibers are explained by the participation of H_2 in photochemical reactions of GODC in the excited T_1 state. Note that the efficiency of these reactions increases with an increase in temperature of irradiation samples. We observed an increase in the efficiency of GODC decay in the H_2-loaded samples, which is a direct confirmation of the above reactions. The experimental data for hydrogen-containing samples with 23 mol.% GeO_2 show photodecay efficiency of GODC considerably increases with an increase in the irradiation temperature. This manifests itself in a rise of the slope of the $I_T(lnt)$ dependences as the irradiation temperature increases (Fig.2).

It is seen from Fig.2 that no decay of GODC occures in the hydrogen-free samples at room temperature and only at T>300 K, the efficiency of decay markedly increases. For H_2-loaded samples, the photodecay of GODC occurs even at temperature close to that of liquid nitrogen (Fig.2, curve 4); i.e., H_2 molecule interact with electron-excited GODC even at 90 K. No such effect is observed in similar processes in pure silica glasses [3]. This is caused by the fact, at liquid nitrogen temperatures, the diffusion of H_2 molecules over the network of amorphous SiO_2 appears to be "frozen", and at

rather small concentration of silicon ODC (10^{16} cm^{-3}), their nearest environment $r<10^{-8}$ cm does not exhibit H_2 molecules at the instant of photoexcitation. An estimated concentration of GODC in germanosilicate glasses is as high as 10^{19}-10^{20} cm^{-3}. Because of excitation migration over GODC, there can appear some chance for frozen H_2 molecules to be located in the nearest environment of GODC excited in T_1 state. It is quite probable that the presence of hydrogen in the immediate vicinity of the excited center affects the efficiency of its decay.

The activation energy of the photodecay of the GODC was estimated from the experimental dependences $\tau_T(T)$ and $I_T(T)$ for the initial and H_2-loaded optical fibers. The activation energies E_a^{τ} and E_a^{I} odtained from Arrhenius dependences $ln[1/\tau_T^{H}-1/\tau_T]$ and $ln[I_T/I_T^{H}-1]$ as functions $1000/T$ are given in table:

C, mol.% GeO_2	E_a^{τ}, eV	E_a^{I}, eV	E_a^{R}, eV
2.3	0.37±0.05	0.36±0.05	0.03
11	0.22±0.05	0.36±0.05	0.05
23	0.25±0.05	0.37±0.05	0.05

The activation energy of the reaction of GODC with hydrogen E_a^{R} can roughly be estimated from the experimental dependences of photodecay of GODC by analysis of their initial portions at the temperatures of 290 and 390 K (see Fig.2 and table).

One could expect the coincidence of activation energies E_a^{τ}, E_a^{I} and E_a^{R}, becaise in principle, they describe the same physical process: the interaction of molecular hydrogen with GODC in the metastable triplet T_1 state. In our opinion, the activation energy E_a^{τ} obtained from the temperature dependences of T_1 state life time is closest to the realistic value. It is noteworthy that the activation energy E_a^{R} obtained from measurements of the photodecay yield is significantly less than E_a^{τ} and E_a^{I}. This is because the E_a^{R} quantity is representative of some overall process in which the recombination (including both photo-stimulated processes and those after pulse), leading to the recovery of GODC, plays an important part. In addition, these processes are termally activated.

It is known that at high-intensity laser irradiation of H_2-loaded silica glasses (two-quantum photochemisrty of ODC) the passivation with hydrogen of laser induced radicals takes place [3]. The same situation is realized for germanosilicate glasses at $F>$ 200 mJ/cm^2. Some of laser induced Ge(n) radicals interacts with H_2 molecules, creating a new stable optically unactive products.

The low-intensity UV irradiation (Hg-lamp; KrF laser, F=2 mJ/cm^2) of GODC leads to formation of paramagnetic Ge(n) and H(II) centers as well. In contradistinction to the case of high-intensity laser irradiation the contribution of Ge(3) centers in total concentration of Ge(n) is increased, but the value [Ge(n)]/Δ[GeOGC] is decreased. Thus, the one-quantum photoreactions of triplet excited GODC with H_2 molecules gives quite different composition of paramagnetic products.

1. K. O. Hill, B. Malo, F. Bilodeau, D. C. Johnson, Ann. Rev. Mat. Sci. 23 (1993) 125.
2. R. Kashyap, Opt. Fiber Technology **1**, 17 (1994).
3. V. A. Radzig, V. N. Bagratashvili, S. I. Tsypina, P. V. Chernov, A. O. Rybaltovskii, J. Phys. Chem. 99 (1995) 6640.
4. P.J.Lemaire, R.M. Atkins, V. Mizrahi, W.A. Reed, Electron. Lett. 29 (1993) 1191.
5. D.S. Starodubov, E.M.Dianov et al. SPIE Proc. 2998 (1997) 11.
6. Yu.S. Zavorotny, A.O. Rybaltovskii, P.V. Chernov, V.N. Bagratashvili, S.I. Tsypina, L. Dong, Glass Phys. and Chem. 23 (1997) 67.

The potentialities of the plasmachemical technology for fabrication of silica-based photosensitive optical fibers.

K.M.Golant, E.M.Dianov

Fiber Optics Research Centre at the General Physics Institute of the Russian Academy of Sciences, 38 Vavilov St., 117942 Moscow, RUSSIA
Tel. +7 (095) 132 -82-54, Fax +7 (095) 135 81-39, e-mail golant@fo.gpi.ac.ru

Irreversible refractive index changes in silica-based optical fibers under the action of UV radiation (photorefractive effect) are associated with the presence of oxygen vacancies in the core glass (Si-ODC & Ge-ODC). Although the microscopic mechanism of the photorefractive effect has not been established in detail, it is Ge-ODC that ensure UV light delivery into the fiber core owing to their strong absorption band centered at 242 nm. Naturally, one of the ways of increasing photosensitivity of silica-based fibers is optimization of the preform fabrication regimes with a view to maximize the Ge-ODC concentration.

In the case of non-plasma processes of preform fabrication, the glass is synthesized through chemical transformation in a heated mixture of $SiCl_4$, $GeCl_4$, and O_2. In such processes the Ge-ODC concentration is governed by thermodynamic equilibrium in the glass-gas system which can be schematically represented as follows:

$$(Si_{1-x}Ge_xO_{2-y})_{glass} \overset{T=T_s}{\leftrightarrow} O_2\uparrow, \qquad (1).$$

Thus, the combined concentration of Si-ODC and Ge-ODC expressed in units of y is determined by the partial pressure of molecular oxygen and temperature T_s. In OVD and VAD processes, where the glass is at first formed through flame hydrolysis of chlorides as a porous preform, T_s is the temperature of the subsequent glass sintering. In MCVD process the glass is synthesized by pirolytic oxidation of chlorides, then the porous material deposits on the inner wall of the substrate tube and is fused by an external torch. In this case T_s is the fusion temperature. In addition, the deposited glass is heat-treated at the collapsing stage.

By varying the partial pressure of O_2 and by properly choosing the thermal regimes, it is possible to control, within certain limits, the Ge-ODC concentration. Experiments [1,2] showed that increasing T_s and/or decreasing the partial pressure of O_2 did enhance the Ge-ODC concentration. Besides, the composition of the inert atmosphere surrounding the glass and the presence of softening codopants in the glass during the heat treatment significantly affect the Ge-ODC concentration. In particular, collapsing MCVD preforms in an oxygen-free helium atmosphere with a small addition of deuterium increases the intensity of the Ge-ODC absorption band by a factor of seven, whereas introduction of phosphorus into the glass suppresses it by an order of magnitude [2].

The fundamental problem limiting the maximum ODC concentration in non-plasma technologies is that it is difficult to control glass stoichiometry at the stage of chlorides conversion into dioxides. Heat treatment of the previously synthesized glass

in an oxygen-free atmosphere and at elevated temperatures is practically the only means. It is worth noting, however, that with increasing T_s the glass loses not only oxygen, but also germanium, to diminish the desired effect.

Plasmachemical technologies provide great scope for controlling stoichiometry in the SiO_2-GeO_2 system. In this case, silica glass is synthesized within a silica substrate tube in the conditions of reduced-pressure non-equilibrium discharge in a gas mixture at a comparatively low temperature (~ 1000 °C). Chemical reactions occur owing to 'hot' electrons which collide with the gas mixture molecules to produce chemically active radicals. In this way 'hot' electrons ensure efficient conversion of chlorides into oxides. An essential distinction of technologies, such as PCVD, from the non-plasma technologies discussed above is incomplete oxidation of silicon and germanium chlorides in the rarefied gas with subsequent complete oxidation of deposited monooxidies on the substrate tube wall through heterogeneous reactions of the following type:

$$(Si_{1-x}Ge_xO)_{solid} + (1-y)O \overset{T=T_{wall}}{\leftrightarrow} (Si_{1-x}Ge_xO_{2-y})_{solid}, \quad (2)$$

where T_{wall} is the tube wall temperature. Here one has a wider range of possibilities to control glass composition and stoichiometry: relation (2) governs oxidation, whereas relation (1), reduction. Moreover, in (2), y may vary from 0 to 1. Finally, partial replacement of oxygen with another, less strong oxidizer ensures its incorporation into the glass concurrent with oxygen, in accordance with (2). In particular, it is this pathway that Ge-free N-doped silica fibers came into being [3].

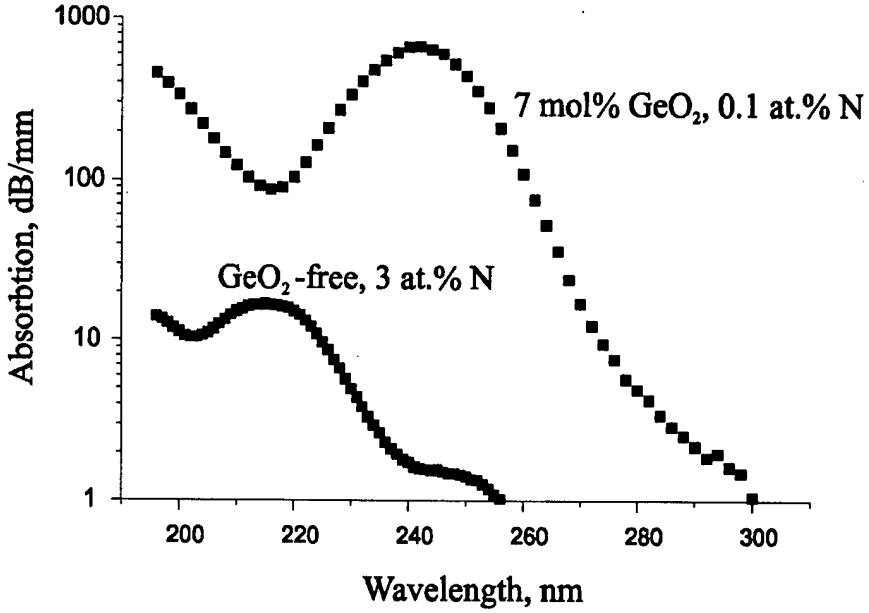

Absorption spectra measured in different glasses fabricated under oxygen-deficient conditions by the SPCVD-technology.

Figure shows absorption spectra of two types of silica glasses fabricated by SPCVD [4] under oxygen-deficient conditions and in the presence of molecular

nitrogen in the gas mixture. The measurements were performed on transverse slices of preforms which were collapsed in an oxygen atmosphere at a pressure slightly above atmospheric pressure. Even with such oxidizing conditions during the collapsing process the germanosilicate glass exhibited a Ge-ODC absorption intensity as great as ~700 dB/mm. This value is nearly three times greater than the maximal value cited in [2] for MCVD germanosilicate preforms collapsed in reduced conditions. N-codoped germanosilicate fibers showed record values of photoinduced refractive index change of up to 10^{-2} of nitrogen in forming Ge-ODC is yet to be understood. Nitrogen was added to the gas mixture for purely technological reasons, as an oxidizer competing with chlorine in the glass-forming reactions (see (2)). This made it possible to reduce the amount of chlorine in the glass layer being synthesized and thereby to collapse preforms without bubbling (otherwise, chlorine readily entering into silica under oxygen-deficient conditions produces strong gas emission at elevated temperatures).

Ge-free N-doped silica preforms can be fabricated by SPCVD under much more stringent reduced conditions. In this case, nitrogen enters into the glass net in amounts sufficient to yield the required refractive index profile of the final fiber. Ge-free N-doped silica thus obtained features different UV absorption bands (see Figure). Some of them are supposed to be due to a nitrogen-modified Si-ODC [6]. Such fibers exhibit a strong photorefractive effect when exposed to 193 nm light [7]. An interesting and important peculiarity of refractive index gratings written in N-doped silica fibers is their high resistance to prolonged thermal treatment at temperatures of up to 900 °C [8].

To sum up, the plasmachemical technology is a new and promising tool for producing highly photosensitive silica glasses and fibers. Optimization of the glass deposition and thermal regimes under oxygen-deficient conditions in the gas mixture is the immediate task of our research.

References.

1. K.MUTA, A.KASHIWAZAKI, H.KAWAZOE, Diffusion and Defect Data, **53-54** (1987) 93-98.
2. I.DONG, J.PINKSTONE, P.ST.RUSSELL, D.N.PAYNE, J. Opt. Soc. Am. B, **11** (1994) 2106-2111.
3. E.M. DIANOV, K.M. GOLANT, A.S KURKOV, R.R., KHRAPKO, A.L TOMASHUK, J. Lightwave Technol., 1 , (1995), 1471-1474.
4. D.PAVY, M.MOISAN, S.SAADA, P.CHOLLET, P.LEPRINCE, J.MARREC, Proc. ECOC'86, Barcelona, (1986) 19-22
5. E.M. DIANOV, K.M. GOLANT, V.M. MASHINSKY, O.I. MEDVEDKOV, I.V. NIKOLIN, O.D. SAZHIN, S.A. VASILIEV, Electron. Lett., **33** (1997), to be published.
6. E.M.DIANOV, K.M.GOLANT, R.R. KHRAPKO, O.I. MEDVEDKOV, A.L. TOMASHUK, S.A VASILIEV, Opt. Mat. **5**, 1996) 169-173.
7. E.M. DIANOV, K.M. GOLANT, R.R. KHRAPKO, A.S KURKOV,
8. M.DOUAY, P.NIAY, Electron. Lett., **33** (1997), 236.
   E.M. DIANOV, K.M. GOLANT, R.R. KHRAPKO, A.S KURKOV, M.DOUAY, P.NIAY, Proc. OFC'97, Dallas, PD5.

Direct characterization of ultraviolet-light-induced refractive index structures by scanning near-field optical microscopy

M. Svalgaard, S. Madsen*, J. M. Hvam and M. Kristensen

Microelectronics Center, Bldg. 345 east,
Technical University of Denmark, DK-2800 Lyngby, Denmark
*also at: Danish Micro Engineering A/S, Herlev, Denmark

Introduction: In recent years high-resolution microscopy has experienced the application of probe-based scanning techniques such as the scanning near field optical microscope[1] (SNOM). In contrast to conventional optical far-field imaging, the SNOM utilizes a non-propagating (evanescent) near-field, whereby the achievable lateral resolution overcomes the far-field diffraction limit of $\lambda/2$ where λ is the wavelength of the imaging light.

Such an instrument may be useful for investigation of ultraviolet (UV) induced reactions in germania-doped silica which lead to permanent changes of the refractive index. We have previously used these reactions to induce planar waveguide structures in the photo-sensitive, germania-doped core layer of glass films deposited on a silicon substrate by plasma-enhanced chemical vapor deposition (PECVD) [2,3]. Up to now the UV-induced reactions have mostly been probed indirectly by monitoring UV absorption spectra and spectral properties of photo-induced Bragg gratings. However, the geometry of planar glass samples permits a more direct characterization with high spatial resolution using probe-based scanning techniques. In the following, we present a novel technique employing a reflection SNOM to directly probe the topography and refractive index of UV-written structures in planar glass samples.

Experiments: The SNOM instrument[4] used in this work employs a tapered uncoated fiber probe which acts both as a sub-wavelength sized light source and detector. Linearly polarized light from a He-Ne laser (λ=633 nm, 5 mW) is coupled into the fiber where it propagates towards the tapered probe. Most of the incident light is coupled out through the side walls of the uncoated probe and thereby largely lost from the optical detection path. However, a small fraction reaches the probe tip, creating a sub-wavelength sized light source. The refractive index of the probe tip is n=1.461 at λ=633 nm. The scattered light at the probe tip, which is highly spatially confined[5] interacts with the sample, producing a small change in the reflected signal which excites a counter-propagating mode in the fiber probe. The optical image is formed by detecting these changes in the reflected signal while raster scanning the sample. To avoid reflections from the fiber input facet only the polarization component orthogonal to that of the incident light is detected. The probe-to-sample distance is approximately 1 nm during scanning and is kept constant using shear-force distance regulation.

We have applied the reflection SNOM to image linear structures UV-written in a photo-sensitive thin film with varying fluences. The sample consisted of a single layer, 3.3 μm thick, germanosilica film (12 mole % GeO_2, n=1.472 at λ=633 nm) on a silicon substrate. Refractive index structures were photo-induced by exposing the sample to a 244 nm, focused beam from a frequency-doubled argon-ion laser. The incident UV power was ~17 mW and the beam full width at half maximum (FWHM) on the sample was ~4 μm, leading to an average power density of 140 kW/cm^2. The UV writing was carried out by scanning the sample relative to the UV beam using two-dimensional DC translation stages. The stages have an absolute precision and repeatability of 0.1 μm. The UV-written structure consisted of parallel lines written with varying scan speed resulting in an applied fluence ranging from 1.1 kJ/cm^2 to 110 kJ/cm^2. The adjacent line spacing was set to increase from 15 μm to 23 μm hence permitting the applied fluences for a given pair of lines to be derived from the observed spacing.

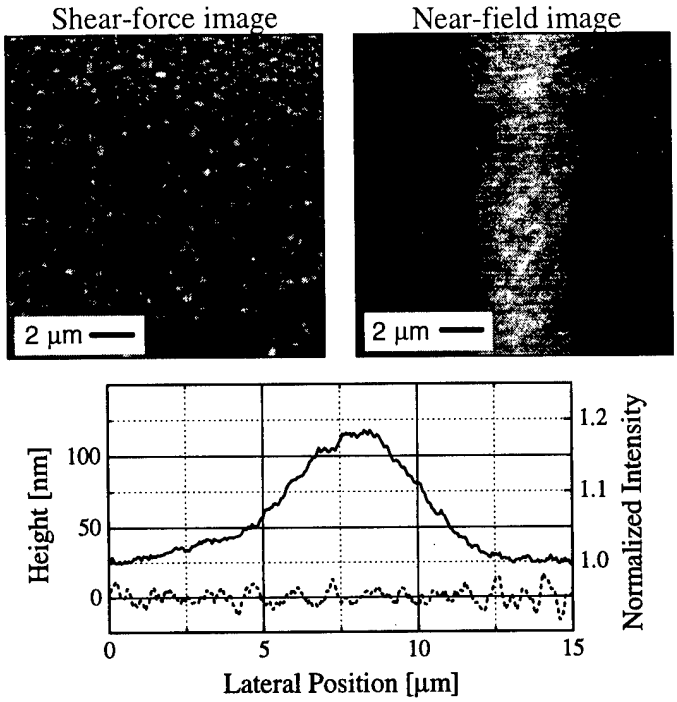

Fig. 1: Shear-force and near-field images of a UV-written line in a germanosilica film on silicon. The lower graphs show cross-sectional profiles of the shear-force (dotted line) and near-field (solid line) images. The profiles are calculated as an average of 256 scan lines.

Results and discussion: A set of images covering a 15×15 μm^2 area around the strongest line (F≈110 kJ/cm^2) are shown in Fig. 1. Brighter shading corresponds to elevated surface features and higher reflected signal in the shear-force and near-field images, respectively. The signal-to-noise ratio may be improved by averaging all the scan lines perpendicular to the UV-written line, as shown in the two cross-sectional profiles in the lower part of Fig. 1. The averaged near-field signal is normalized to the signal detected at the unexposed surface. As seen, there is no sign of the UV-written line in the shear-force image, indicating that possible UV-induced densification has changed the surface height by less than ~10 nm. The shear-force image reveals a rough surface consisting of clusters with lateral dimensions in the 0.1-0.3 μm range and a vertical elevation of about one order of magnitude less. The UV-written line is clearly visible in the near-field image, having a FWHM of 5.1 μm. The maximum relative change in the reflected intensity is 18%. A rough estimation of the UV-induced index change expected to cause such a response may be obtained from the Fresnel equations derived for propagating fields. Hence, for normal incidence we have $R=(n_1-n_2)^2/(n_1+n_2)^2$ where n_1 and n_2 are the refractive indices describing the interface. Since the probe-to-sample separation is only ~1 nm it seems appropriate to use the refractive indices of the fiber probe and the germanosilica film, disregarding the refractive index of the medium between the probe and sample. Thus, according to this estimation, the observed change in reflectance corresponds to a UV induced index change of about 1×10^{-3}, which is in good agreement with the values expected from our previous work with planar waveguide fabrication in other samples having a composition similar to that used here[2]. Hence, the reflection SNOM technique is well suited for direct characterization of refractive index profiles of silica-based planar waveguide structures.

The near-field images of the remaining UV-written lines were qualitatively similar to those shown in Fig. 1, with a peak signal steadily decreasing for lower fluences, as expected from the index dynamics observed in optical fibers and thin film waveguides. The peak near-field signal, as derived from averaged raster scans, is plotted versus the UV fluence in Fig. 2(a). The three weakest lines were below the detection limit of approximately 1%, roughly corresponding to a UV induced index change in the 10^{-5} range, as derived from the Fresnel equation mentioned earlier. The near-field signal

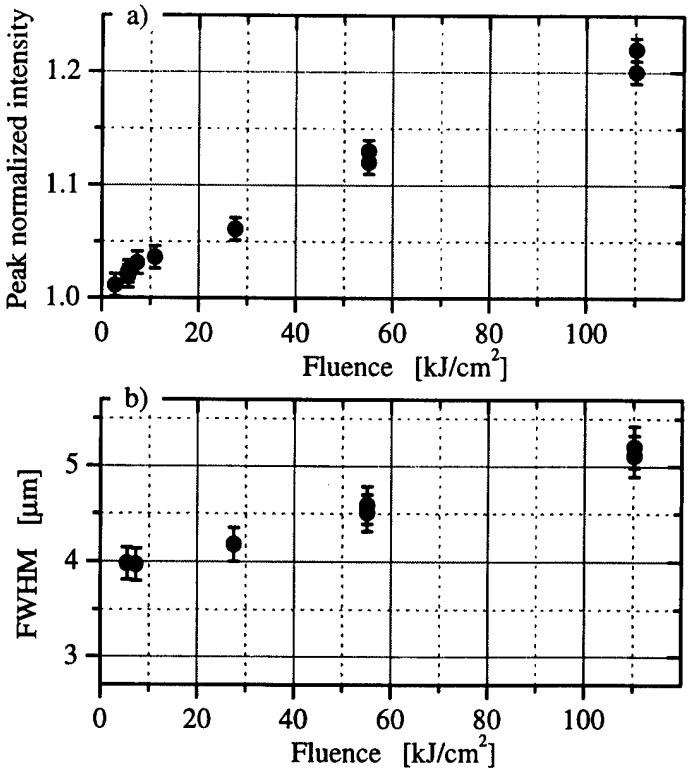

Fig. 2: The peak normalized reflected intensity (a) and the FWHM of the UV-induced refractive index profile (b) versus applied UV fluence.

increases steadily with fluence in a sub-linear fashion, without saturating. From the imaged UV-written lines, the FWHM of the transverse index distribution is plotted versus the fluence in Fig. 2(b). For the weakest detectable line ($F \approx 2.8$ kJ/cm^2) the width is 4.0 µm. The width is seen to increase in a linear fashion with the near-field signal, reaching 5.1 µm for $F \approx 110$ kJ/cm^2. This behavior is interpreted as a non-linear response of the induced index change to the UV intensity and should be taken into account for numerical modeling of the guided mode profile and when designing optical devices such as directional couplers.

Conclusion: We have demonstrated that UV-induced refractive index changes in a germanosilica film can be directly imaged with a lateral resolution better than ~0.1 µm using a reflection SNOM configuration. The magnitude of the observed UV-induced index changes are in the 10^{-5}-10^{-3} range with no observable changes in surface topography. The proposed technique is well suited for direct characterization of topographical and optical properties of silica-based optical waveguides and as a tool for improving our understanding of the photolytic reactions leading to UV-induced refractive index changes.

1. D.W. Pohl, W. Denk and M. Lanz, Appl. Phys. Lett. 44, 651 (1984).

2. M. Svalgaard, C.V. Poulsen, A. Bjarklev and O. Poulsen, Electron. Lett. 30, 1401 (1994).

3. M. Svalgaard and M. Kristensen, Electron. Lett. 33, 861 (1997).

4. DME - Rasterscope SNOM, DME - Danish Micro Engineering A/S, Herlev, Denmark.

5. S. Madsen, S.I. Bozhevolnyi, K. Birkelund, M. Müllenborn, J.M. Hvam and F. Grey, J. Appl. Phys., to be published (1997).

Permanent refractive-index changes in pure GeO_2 glass slabs induced by irradiation with below-gap light.

Yuichi Watanabe*, Junji Nishii[a)], Hiroyuki Moriwaki, Genjiro Furuhashi,

Hideo Hosono[b)], and Hiroshi Kawazoe[b)]

Dept. of Materials Science and Technology, Science University of Tokyo,
2641 Yamazaki, Noda, Chiba 278 JAPAN
a)Dept. of Optical Materials, Osaka National Research Institute, AIST,
1-8-31, Midorigaoka, Ikeda, Osaka 563 JAPAN
b)Materials and Structure Laboratory, Tokyo Institute of Technology,
Nagatsuta, 4259, Midori-ku, Yokohama 227 JAPAN.
* corresponding author,
Phone:+81-471-24-1501, Fax:+81-471-23-9362, e-mail:ywlabo@rs.noda.sut. ac.jp

Here we report on the permanent positive refractive-index changes in pure GeO_2 glass slabs induced by illumination of light having the photon energy far below than the fundamental absorption edge. The mechanism for the formation of permanent refractive-index change is explained tentatively as a consequence of Kramers-Kronig principle for an additional absorption band induced in the glass via two-competitive photochemical reactions.

Pure GeO_2 glass was prepared by the conventional melt-quenching method[1)]. The sample glass was cut and polished into a slab of 2.3mm-thick. For the observation of formation of permanent refractive-index change, we applied the z-scan technique[2)]. In practice, third-harmonic light ($h\nu$=3.51eV) of a Q-switched Nd:YAG laser was focused with a lens. At the focus, radius of the Gaussian beam was evaluated to be ~14μm. First, closed-aperture (S=0.5) z-scan measurement was carried out with the UV light at a low irradiance level. Then, the sample was placed at the focus and was irradiated with UV light at high irradiance level. After the irradiation, closed aperture z-scan transmittance was remeasured at the low irradiance level. Consequently, formation of permanent refractive-index change was observed as the changes in z-scan transmittance before and after UV-irradiation. It should be noted that the photon energy of the UV light irradiated, 3.51eV is far below than the energy gap of GeO_2 glass, 5.63eV[3)]. The UV-exposure conditions were pulse energy 7μJ per pulse, pulse repetition frequency 10Hz, pulse duration 4ns(FWHM), and exposure time 1-30min, whereas for the z-scan measurement, pulse energy was lowered to 1μJ.

Figure 1 shows the results of closed-aperture z-scan measurements. The minimum transmittance at the pre-focal position followed by the post-focal maximum indicates that positive refractive index changes are induced in the glass through UV-irradiation. As seen in Fig.1, difference between minimum and maximum transmittance increased with increasing irradiation time.

Theoretical calculation for the z-scan transmittance was carried out on the assumption that the spatial profile of induced refractive-index change is proportional to the n-th power of beam irradiance of the Gaussian beam, i.e.,

$$\Delta n(r) = C \left[I_0 \exp\left(\frac{-2r^2}{\omega_0^2} \right) \right]^n \qquad (1)$$

,where I_0 and ω_0 represent peak irradiance and radius of the Gaussian beam at the focal plane, respectively. In Eq.(1), the n-th power of irradiance of Gaussian beam represents the factor for the refractive-index changes induced by a single light pulse, while the factor C represents the cumulative effect associated with the total number of light pulses irradiated. Experimental z-scan transmittances could be reproduced satisfactorily, as represented by solid lines in Fig.1, by taking the exponent n=3. Induced changes in refractive indices could be evaluated from the theoretical fits. Figure 2 shows the induced refractive index change Δn at the center of Gaussian beam as a function of irradiation time. As seen in Fig.2, Δn is proportional to the irradiation time less than 10min. Prolonged irradiation caused further increase in Δn, being saturated at about 10^{-4} after irradiation for 30min.

Here we discuss the mechanism for formation of permanent refractive-index changes in pure GeO_2 glass on the basis of a representative model: In the K-K model[4,5], the changes in refractive-index are explained as a consequence of the Kramers-Kronig relationship for the appearance of an additional absorption band due to photo-induced color centers in glass. For this model, we confirmed the formation of paramagnetic defect, Ge-E' center in the UV-irradiated glass: The density of Ge-E' center was evaluated to be $3.1X10^{18}$spins/cm^3 at the peak of Gaussain beam for the glass irradiated with UV-light for 10min. We have already reported that the Ge-E' center gives rise to an absorption band centered at 6.3eV with the FWHM of 1.1eV[6]: absorption coefficient (α) at the center of the band is proportional to the density (N) of Ge-E', i.e., $\alpha/N=7.2X10^{-17}$cm^2. By substituting the above factors into the formula proposed by Hand, et al.[7], in which the refractive index change is evaluated from the changes in absorption coefficient through the Kramers-Kronig principle, refractive-index change for irradiated glass is deduced to be $1.0X10^{-4}$. The value is comparable with that observed in z-scan measurement, i.e., $\Delta n=3.2X10^{-5}$ for the glass irradiated for 7.5min. Thus we recognize that the color center model is valid semiquantitatively for the present observations.

With regard to the formation of Ge-E' center by irradiation of below gap light, it should be noted that the spatial profile of Δn assumed in Eq.(1) is proportional to

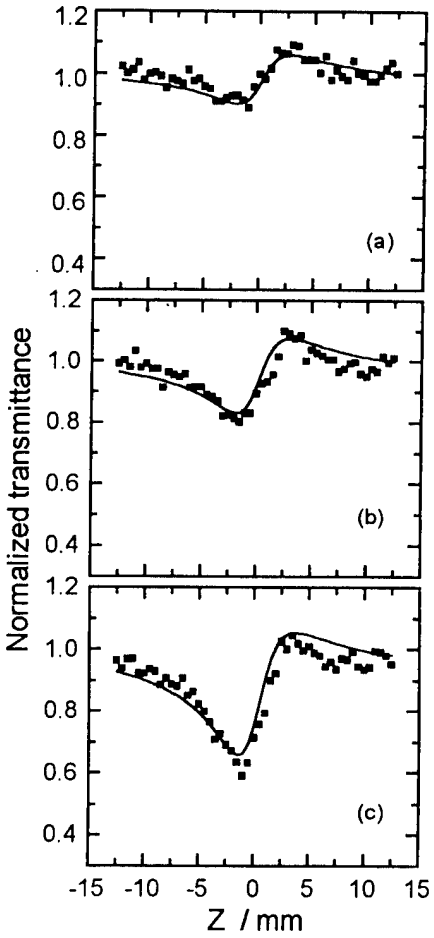

Fig.2 Z-scan transmittace for GeO_2 glass irradiated with UV-light for (a) 3.5min, (b) 7.5min, and (c) 15.5min.

the third power of the irradiance. This can be explained by assuming that the Ge-E' center is generated via two-competitive photochemical reactions[8] under UV-irradiation: One reaction is formation of metastable defect species associated with Ge via two-photon absorption(TPA) process, while the other is structural relaxation of the metastable defect into Ge-E' center through one-photon absorption process. For the metastable defect associated with Ge, GEC is the possible candidate because i) the defect is known to be relaxed into GeE' center through thermal-stabilization process[9]. ii) GEC has been known to show an absorption band centered at 4.4eV with FWHM=1.97eV[10]. Then, UV-light irradiated (3.51eV) should absorbed by GEC. iii) GEC is the dominant defect species in GeO_2:SiO_2 glass irradiated with ArF excimer laser[11]: the photon energy of ArF, hν=6.5eV is comparable to the two-photon energy, 2X3.51eV=7.02eV for the light used in the present study. These facts are consistent with the two-competitive photochemical reaction model for the formation of Ge-E' center, resulting in a formation of permanent positive refractive index changes in GeO_2 glass. Further investigation is ongoing now.

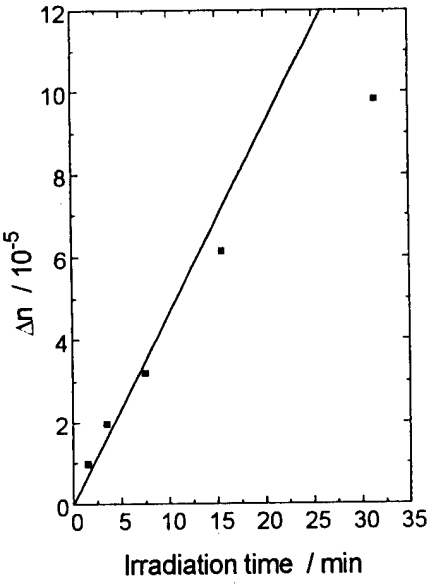

Fig.2 Refractive-index change Δn versus irradiation time.

References

1) J. W. Fleming, Appl. Opt., 23, 4486(1984).
2) M. Sheik-Bahae, A.A.Said, T. Wei, D.J. Hagan, E.W.Van Stryland, IEEE J. Quantum Electron., 26, 760(1990).
3) N.M.Ravindra, R. A. Weeks, and D.L.Kinser, Phys. Rev. B, 36, 6132(1987).
4) R. M. Atkins and V. Mizrahi, Electron. Lett., 28, 1743(1992).
5)H. Hosono, Y. Abe, D.L.Kinser, R. A. Weeks, K. Muta, and H. Kawazoe, Phys. Rev. B, 46, 11445(1992).
6)H. Hosono, M. Mizuguchi, H. Kawazoe, J. Nishii, Jpn. J. Appl. Phys., 35, L234(1996).
7) D.P.Hand and P.St.J.Russell, Opt. Lett., 15, 102(1990).
8)Y.Watanabe, Y.Kikuchi,K.Imanishi,and T.Tsuchiya, accepted for pulication in J. Mat. Sci. Eng.. B.
9)Y.Watanabe,H.Kawazoe,K.Shibuya, and K.Muta, Jpn.J.Appl.Phys.,25,425(1986).
10) E.J.Friebele, in "Optical Properties of Glass", p.205, ed. D.R.Uhlmann and N.J.Kreidl, Am. Ceram. Soc.(1991).
11)H.Hosono, H.Kawazoe,J.Nishii, Phys. Rev. B, 53, R11921(1996).

Defect population in Ge doped silica studied by fluorescence spectroscopy.

B. Poumellec[1], H. Cens[1], A. Trukhin[2], J. C. Krupa[3], B. Leconte[4], M. Bubnov[5]

1 CNRS URA446, Thermodynamique et Physico-Chimie des matériaux, Bât. 415, UPS Orsay, 91405 Orsay, Cedex, France. Tel 33 01 69 15 63 51 Fax 33 01 69 15 48 19 e-mail bp@phebus.isma.u-psud.fr
2 Institute of Solid State Physics, University of Latvia, Kengaraga St. 8, LV-1063 Riga, Latvia. Tel. 371 72 60 686. Fax. 371 71 12 583. e-mail: truhins@acad.latnet.lv
3 Institut de Physique Nucléaire, Bât. 100, UPS Orsay, 91405 Orsay, Cedex, France. Tel. 33 01 69 15 7152. e-mail: krupa@frcpn11.in2p3.fr
4 CNRS URA 779, Dynamique moléculaire et photonique, Bât. P5, Université des Sciences et Techniques de Lille, 59655 Villeneuve d'Ascq Cédex, France. Tel. 33 03 20 44 84 Fax. 33 03 20 43 40 84 e-mail: Bruno.Leconte@univ-lille1.fr
5 Fiber Optics Research Center at General Physics Institute, 38 Vavilov street, 117942, Moscow, Russia. e-mail: bubnov@fo.gpi.ar.ru.

The interest for Ge doped SiO_2 properties is revived by the search of optimisation of photorefractivity. The first step of the mechanism is an absorption at around 240-250 nm or 193 nm. Next step of the transformation leads to index change . Whatever it is connected to a special defect or not, the study of the defect population increases our understanding on that subject and for other applications (fiber line attenuation, non-linear effect). In this paper, we show that UV spectrum of MCVD doped silica is composed of several gaussian components which appear at the same position and with the same width but varie in intensity depending on the samples. We try to systematize this population.

Experimental details

Excitation and luminescence spectra have been recorded at LURE-Orsay on PAM3 station (SA61) with two monochromators. The resolution for the excitation wavelength is 0.1 nm and 1 nm for the emission wavelength. Spectra are corrected from the response of the line using sodium salicylate.

A series of fiber preforms with different concentration of germanium in the core as well as additional phosphorus and boron in some samples have been studied. As an examples of low concentration of germanium the data of fused Ge doped crystalline quartz were taken from [1]. The samples preparation corresponds to reduced conditions.

A gaussian analysis of the excitation spectra have been achieved practicing a multiloop process. First step, objective gaussian analysis with all parameters free. This gives the position of the main components and the most frequent widths. These data are input for a second loop. Process is stopped when correlations are statisfactory.

Two types of correlation has been made according to the emission wavelength and to the Ge content.

Results

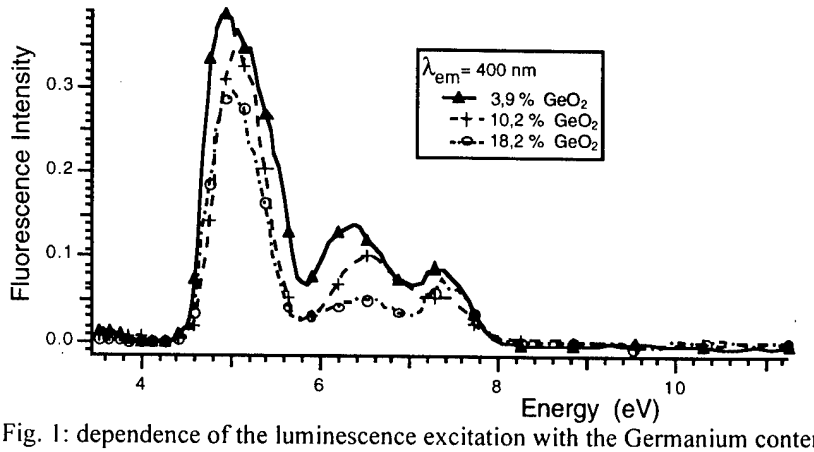

Fig. 1: dependence of the luminescence excitation with the Germanium content.

Fig. 1 shows the variation of luminescence excitation spectrum according the Ge content for three samples. It is worthnoticing that the intensity decreases whatever the wavelength when Ge concentration increases. Measurement of the absorption spectrum in similar samples shows an increase. So, there is a levelling off of the fluorescence as it was already mentioned in [2, 3] but also we deduce that either there is an increase of non-fluorescent defect population or a decrease of the quantum yield.

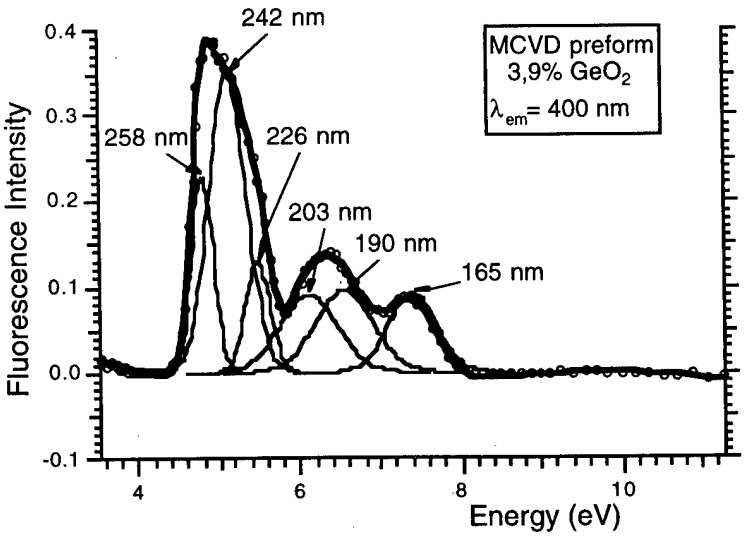

Fig. 2: various gaussian components in an example spectrum

Fig. 2 is an example of gaussian fit showing the main components we have deduced. The broad band around 5 eV is composed by 4.8 eV (256-258 nm), 5.12-5.16 eV (242 nm), 5.48 eV (226-228 nm). Other bands are 6.09-6.11 eV (203 nm), 6.55-6.72 eV (185-190 nm), 7.2-7.49 eV (165-172 nm). This decomposition has been chosen in order to be consistent with other spectra for which bands are resolved. From this study, the following table has been deduced (Table 1).

Table 1: Gaussian components used to decompose the luminescence excitation spectra.

position (nm)	256-258	242	226-228	217	203	185-190	180	172	165-168
energy (eV)	4.8	5.12-5.16	5.48	5.7	6.09-6.11	6.55-6.72	6.86	7.21	7.32-7.49
width (eV)	0.19	0.29-0.33	0.19-0.21	0.25-0.38	0.39-0.54	0.36-0.57	0.58	0.26-0.30	0.36-0.42
associated luminescence (nm)	415	403	392		405	405			406

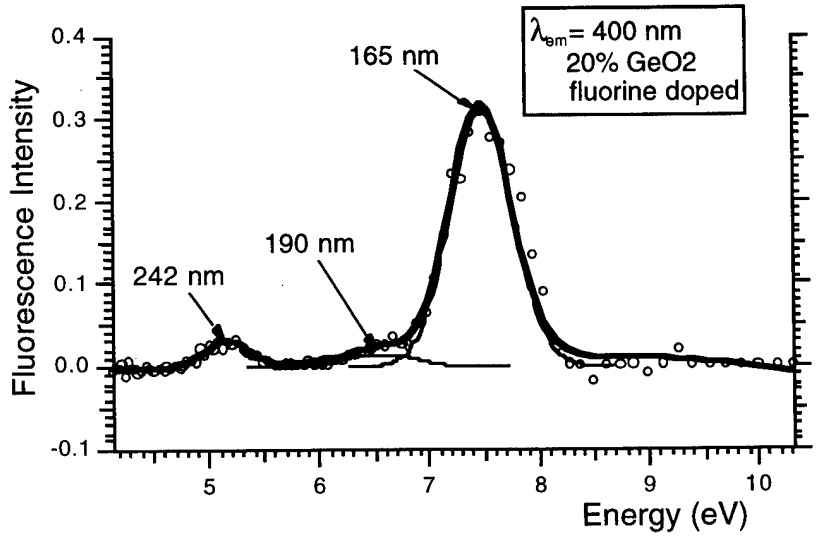

Fig. 3: With fluorine, the 7.5 eV band is enhanced.

Concerning the variations with the Ge content, we have found similar variations of 242, 203, 190 nm bands except when Ge is very weak in presence of phosphorus. 165 nm exhibits a more independant behavior disappearing with phosphorus or increasing dramatically with fluorine (fig. 3).

Discussion

The many bands found in excitation spectra corresponds mainly to luminescence bands around 400 nm (3.1 eV) as shown in the table. In fig. 4, we relate a result from paper [1] about correlative measurement of luminescence and absorption in a 1 mol % GeO_2 doped silica. We find again the same features than above with a band at 242 nm, a small one at 203 nm, a large one at 190 nm and a strong one at 168 nm. The striking feature is the constancy of the quantum yield between 4.8 and 6.8 eV (258 nm et 182 nm). Therefore 242, 203, 190 nm

bands belong to the same defect. The fluorescence peaks at 404±1 nm. The disappearance of 190 nm band with phosphorus can be attributed to a quenching. Let us call this defect $GeODC_{I-2}$. Hosono et al. have seen here two defects having the first 182 and 242-245 nm absorption bands and the second having 207 and 240 nm bands. Sensivity of these two defects to 248 nm irradiation is not the same. Decay constant of the blue fluorescence is around 100-110 μs.

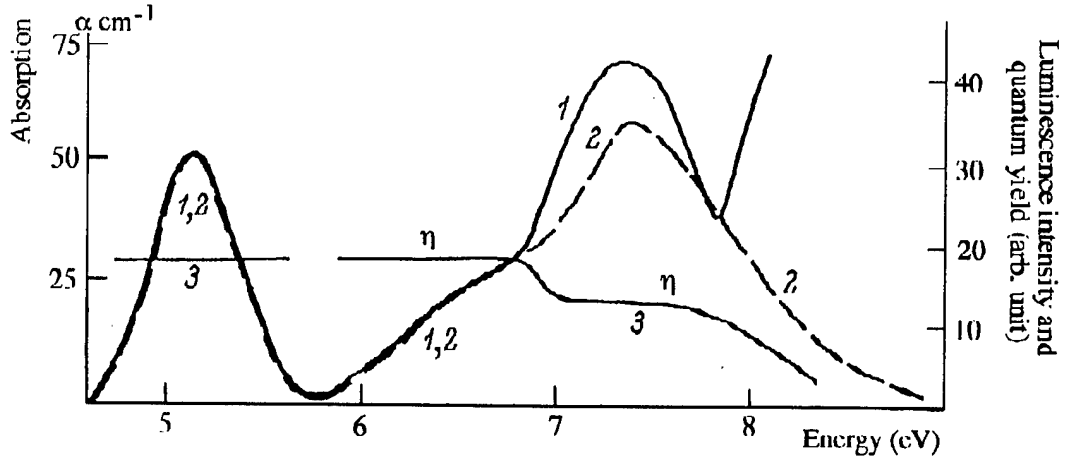

Fig. 4: Optical properties of Ge doped fused quartz. Absorption spectrum (1), excitation spectrum for luminescence band at 3.1 eV (400 nm) (2), relative quantum yield η (3).

There is a defect mentioned by Neustreuev having two UV absorption bands at 230 and 185 nm. This is probably corresponding to our 226-228 and 185-190 nm bands. Let us call this defect $GeODC_3$.

Other excitation bands are also detected: 258-256 nm with a luminescence peaking at 415 nm, 226-228 nm with luminesence at 392 nm, 270 nm for a luminescence at 435 nm which belong probably to the silica network as it is detailed in another paper of the conference[4], 217 nm which is connected to a Boron defect probably and 180 nm to an Sn defect. in samples doped with corresponding elements.

Next question is about 168 nm band. The bands near this wavelength show a complicated behaviour. The quantum yield (only relative values were determined) is strongly dependent on sample preparation history. Therefore we think that 168 and 172 nm bands are probably from polytypes of the same defect, because they do not appear in the same time. They are more or less independant of the 242 nm band. They are suppressed with Sn or phosphorus codoping or pronounced a little with boron or dramatically with fluorine. The smaller yield around 170 nm can be interpreted in several manners. A first solution is that this band belongs to another defect. A second one is that it is an excited state of the $GeODC_{I-2}$ because the emission wavelength and the decay time is the same. In this case, the decrease is explained by quenching but how to explain the large intensity of 165 nm band in fluorine doped sample. Another solution could be ionisation of a polytype center having a core similar to $GeODC_{I-2}$. The last one corresponds well to observation of the 7.6 eV excited thermostimulated 3.1 eV luminescence in the sample $90SiO_2$-$10GeO_2$. Therefore the bands at 7.6 eV could be ascribed to a charge transfer transitions from core of the luminescent center to surrounding host material atoms.

Conclusion

The fluorescence spectroscopy is a useful tool bringing a lot of information on the defect population. Specifically in preform, where we observe several types of Ge related luminescence centers, we develop a first approach of systematisation of these population. We have found that the UV excitation bands show the existence of concentration quenching. We suggest that highest energy bands below optical gap of silica are connected to a direct ionization of a center. Its nature can be ascribed to transitions from core of the center to surrounding host material analogous to charge transfer transition for impurity centers in crystals.

References

1. A.N.Trukhin, A.G.Boganov, A.M.Praulins Soviet Physics and Chemistry of Glasses (Fizika i Khimiya Stekla) 5 (1979) 346-353.

2. A.N.Trukhin J. N. Crystalline Solids 189 (1995) 291-296)1. A.N. Trukhin, A.G. Boganov, and A.M. Praulins, Soviet Physics and Chemistry of Glasses, 1979. **5**: p. 346-353.

2. F. Ouellette, R.J. Campbell, D.L. Williams, and R. Kashyap, Optics Communication, 1993. **103**: p. 85-88.

3. F. Ouellette. *Spectral, temporal and spatial study of UV-induced luminescence in Ge-doped fiber preform.* 1993: SPIE.

4. B. Poumellec, V.M. Mashinsky, and P. Guénot. *270 nm absorption and 432 nm luminescence bands in doped silica glasses.* in *BGPP*. 1997. Williamsburg.

JSuE8 ■ The role of extrinsic species on the nonlinear absorption of bulk and thin film sulfide glasses, T. Cardinal, K.A. Richardson, H. Shin, G.I. Stegeman, L. Glebov, *Center for Research and Education in Optics and Lasers (CREOL), Univ. Central Florida, 4000 Central Florida Blvd., Orlando, FL 32816-2700, (407) 823-6822;* J.F. Viens, A. Villeneuve, *COPL, Univ. Laval, Canada, G1K7P4.* Commercial arsenic sulfide glasses have been prepared with different levels of purification. Linear and nonlinear absorption of both bulk and thin film materials have been measured. Analysis of the components of absorption edge and dependence on purification is discussed. Nonlinear photoinduced absorption measurements were made using femtosecond pulses in the spectral region of 1.5 μm from an optical parametric amplifier. The behavior of glasses prepared by melting or thermal evaporation techniques are compared.

JSuE9 ■ Formation and photosensitivity of defects in Se implanted silica, R.H. Magruder, III, *Dept. of Physics, Belmont University, Nashville, TN 37212;* R.A. Weeks, *Dept. of Applied and Engineering Sciences, Vanderbilt University, Nashville, TN 37235;* R.A. Zuhr, *Solid State Division, Oak Ridge National Laboratory, Oak Ridge, TN 37831.* Ion implantation in silica has been shown to form photosensitive materials that can be used to form photoinduced gratings. The purpose of this work is to ascertain the photosensitivity of optically active defects in Se implanted silica. Se was chosen because of its chemical similarity to oxygen. The two sources of photosensitive responses in ion implanted glass are defects induced by the ionization and atom displacements during implantation and defects induced by the chemical reaction of the implanted ion species with the host. Silica was implanted with 4 MeV Se ions with nominal doses of 0.1 to 1.0×10^{16} ions/cm^2. Only bands at 5.85 and 5 eV are resolved in the absorption spectra in all samples. The bleaching of the bands with KrF irradiation is dose dependent. The sample implanted with 0.3×10^{16} ions/cm^2 exhibits an increase in the absorption at 5.85 eV and only a small decrease at 5 eV while the 1.0×10^{16} ions/cm^2 sample exhibits a decrease in absorption at 5.85 eV and a 33% decrease at 5 eV.

JSuE10 ■ Refractive index dispersion of gallium lanthanum sulfide and oxysulfide glasses, H. Yayama, S. Fujino, H. Takebe, K. Morinaga, *Department of Materials Sciences and Technology, Graduate School of Engineering Sciences, Kyushu University, Fukuoka 816, Japan;* D.W. Hewak, *Optoelectronics Research Centre, University of Southampton, Southampton SO17 1BJ, U.K.* Gallium lanthanum sulfide-based glasses are attractive for new laser and nonlinear optical applications at near infrared region. Refractive indexes were measured for Ga_2S_3-La_2S_3 and Ga_2S_3-La_2O_3 glasses in the range of 0.5 and 1.7 μm using the minimum deviation method. Data is analyzed by Wemple and Didomenico equation. These glasses have relatively large average electronic bandgaps E_0 and electronic oscillator strengths E_d in comparison with other chalcogenide glasses. Possible origins of these features are discussed.

JSuE11 ■ Volume grating recording in fluorinated silicate glasses, L. Glebov, L. Glebova, M.G. Moharam, K. Richardson, V. Smirnov, *Center for Research and Education in Optics and Lasers, UCF, Orlando, FL 32816.* Sodium-zinc-aluminum-silicate glasses doped with silver, cerium, fluorine, and bromine were melted in 100 cc fused silica crucibles in an electrical furnace. The polished glass plates were exposed to UV radiation of a He-Cd laser at 325 nm. Spatial frequencies of the interference patterns written ranged from 500 to 700 l/mm. Exposed samples under went heat treatment at temperatures from 500 to 520 °C to produce photoinduced crystallization. The thickness of gratings formed were from 1 mm to 10 mm. High diffraction efficiencies up to 75% and losses less than 10% have been obtained in these glasses for exposure doses of 100 mJ/cm^2. The dependence of the grating properties on glass composition and thermodevelopment schedule is studied.

JSuE12 ■ Bragg gratings inscription in rare earth doped fluoride glasses, F. Smektala, R. Sramek, J. Lucas, *Laboratoire des Verres et Ceramiques, Universite de Rennes I, 35000 Rennes, France;* W. Xie, P. Bernage, P. Niay, *Laboratorie de Dynamique Moleculaire et Photonique, Universite de Lille I, 59655 Villeneuve D'Ascq, France.* Bragg gratings inscription experiments have been performed on fluorozirconate glasses (ZBLA) doped with Ho^{3+}, as well as on fluorozirconate planar waveguides realized by chlorine ion exchange and doped with Ce^{3+} and Er^{3+}. Both 244 nm and 260 nm light were used. The inscription wasn't possible in any case in the Ce^{3+} doped planar waveguide. Gratings were written in the Er^{3+} doped planar waveguide at 260 nm only. In the case of Ho^{3+} doped fluorozirconate bulk, the inscription was possible at both wavelengths. These results are discussed.

JSuE13 ■ Comparing the effect for second harmonic generation by electron beam scanning and α-beam irradiating on glass, Mingxin Qiu, *Department of Electronics, Kyushu Institute of Technology, 1-1 Sensui-cho, Tobata-ku, 804 Kitakyushu, Japan;* F. Pi, G. Orriols, *Dpt. de Fisica, Universitat Autonoma de Barcelona, 08193 Barcelona, Spain.* We study the mechanism of second harmonics generation in lead silica scanned with an electron beam. Firstly, we found to use α-beam irradiating on either silica or lead silica there is not any second harmonic signal. The electric field in the layer can not be produced by positive particle. Secondly we change lead component, 47%, 51%, 61% and 71% by using F_2, SF_2, SF_{11}, and ZF_7 lead silica, respectively. The second harmonic signal increases linearly with the lead ratio. Thirdly we found there is a saturated signal at an optimum scanning values of total electron charge. This is due to the threshold of inner electric field beneath the glass surface to cause breakdown. Fourthly we obtain the coefficients for Bohr-Bethe electron penetration formula in lead silica.

JSuE14 ■ Photosensitivity as it relates with glass macroproperties, A.V. Cardoso, *CETEC, Belo Horizonte, CEP31, 170-000, PO Box 2306, MG, Brazil, acardoso@oraculo.lcc.ufmg,br.* Since Pelouze [1], it has been proposed that photosensitivity is a glass composition interacted property. Recent developments in Bragg grating technology have confirmed this analysis and indicated the importance of glass composition to improve glass photosensitivity as well as to measure the strength of the grating produced. Other important fact is the occurrence of high temperatures during the process of writing Bragg gratings which is usually mentioned in the literature.

In the present work, the modulation of the refractive index inside the monomode optical fibers is studied in terms of their interdependence with glass composition, viscous flow and density fluctuations associated with high temperatures achieved inside the fiber core. Also, a considerable number of dopants and codopants have been already tested on the production of Bragg gratings and the role of oxidizing and reducing agents added to the core fiber is discussed.

[1] W.A. Weyl, "Coloured Glasses", SGT, Sheffield, U.K. (1951).

JSuE15 ■ Periodic structures in photo-thermo-refractive glasses induced by homogeneous UV irradiation, L. Glebov, V. Smirnov, *Center for Research and Education in Optics and Lasers, UCF, Orlando, FL 32816.* Samples of photo-thermo-refractive glasses were exposed to a homogeneous collimated beam of a He-Cd laser at 325 nm. A refractive index change is observed in the exposed glass upon thermodevelopment due to photoinduced crystallization. A periodic structure was observed inside this exposed area by optical microscopy. This structure is a system of parallel continuous aligned filaments having widths of ten's of microns oriented along the direction of light propagation. Variation of incident light polarization direction does not effect the resulting structure.

JSuE16 (Invited) ■ Photosensitive thin film materials and devices, K. Simmons-Potter, B.G. Potter, Jr., M.B. Sinclair, D.C. Meister, *Sandia National Laboratories, Albuquerque, NM 87185-1423.* Planarization of photosensitive device technology promises to significantly expand the application options for this type of material. Current use of hydrogen techniques have successfully produced strongly photosensitive thin-films, but require complex manufacturing processes and preclude *in-situ* writing of optical interconnects. We will report on the production of highly photosensitive thin films, without the use of post-deposition processing, which promise compatibility and integrability with III-V and Si processing. We will demonstrate a number of device structures with unique optical functionality in our films.

This work was supported by the United States Department of Energy under contract DE-AC04-94AL85000. Sandia is a multiprogram laboratory operated by Sandia Corporation, a Lockheed Martin Company, for the United States Department of Energy.

JSuE17(Invited) ■ Processing-induced defects in optical waveguide materials, G.H. Sigel, Jr., J.W. Lee, *Fiber Optic Materials Research Program, Rutgers, The State University of New Jersey, Piscataway, NJ 08855, sigel@alumina.rutgers.edu.* There is continuing concern with regard to the impact of fiber drawing conditions on the optical properties of silica as both preform sizes as well as drawing speeds increase to meet the demands of production. This paper reports recent work conducted on fiber drawing induced defects using our fabrication facility. Specific topics to be presented include the spatial distribution of defect centers generated in synthetic silica fibers, the photosensitivity of drawn fibers to ultraviolet light, photoluminescence of fibers compared to preforms or bulk rods from which they are drawn and the impact of accelerated cooling on defect center generation in silica fibers. These studies have been conducted over a variety of drawing conditions including drawing speed, drawing temperature and fiber tension.

JSuE18 ■ Photosensitivity in multi-valent rare earth ion doped aluminosilicate glass optical fiber, K. Oh, U.C. Paek, *Kwangju Institute of Science and Tech., 572 Sangam-dong Kwangsan-ku, Kwangju 506-712, Korea;* T.F. Morse, *Division of Engineering, Brown University, Providence, RI 012912.* Multivalent rare earth ion, Sm^{+2}/Sm^{+3} was incorporated into aluminosilicate glass fiber using an aerosol delivery technique. Co-doping of trivalent and divalent states of the ions has been spectroscopically confirmed. Irradiated by multi-line CW Ar ion laser of 1 Watt, the fiber showed photoinduced refractive change of 7.6×10^{-5}. Bleaching of Sm^{+2} absorption band was also observed. Photoionization of Sm^{+2} is believed to be a main cause of the photosensitivity.

JSuE19 (Invited) ■ Material and fiber device aspects of poled fused silica, S.R.J. Brueck, T.G. Alley, R.A. Myers, X.-C. Long, *Center for High Technology Materials, University of New Mexico, Albuquerque, NM 87106.* Since the discovery[1] of a large, stable second-order $\chi^{(2)}$ nonlinearity in temperature/electric field poled fused silica, there have been intensive efforts both to understand the microscopic mechanisms leading to the nonlinearity and to exploit the nonlinearity for planar waveguide and fiber devices. This paper will review the present status of both the fundamental studies and the device applications.

We show the importance of ion dynamics, both transport and exchange in forming the nonlinearity. Ionic hydrogen species are shown to play a large role in the long time development of the nonlinearity.

A large signal (π) electrooptic phase shift is induced in a 12-cm long fiber segment with an applied voltage of 75 V. The nonlinearity shows less than a 10% decay with storage at an elevated temperature of 90 °C for 1050 hours (3 months). Prospects for reducing this voltage-length product are discussed.

1. R.A. Myers, N. Mukherjee and S.R.J. Brueck, Opt. Lett. Opt. Lett. **16**, 1732-1734 (1991).

Present address, Physics Department, University of Auckland, Auckland, New Zealand.

JSuE20 ■ Report on second harmonic generation in soda-lime glass and relative new phenomena, Mingxin Qiu, *Department of Electronics, Kyushu Institute of Technology, 1-1 Sensui-cho, Tobata-ku, 804 Kitakyushu, Japan;* F. Pi, G. Orriols, M. Bibiche, *Dpt. de Fisica, Universitat Autonoma de Barcelona, 08193 Barcelona, Spain.* We report the second-harmonic generation in soda-lime glass for the first time. During poling some white material coated on the glass surface on cathode side. By ESCA analysis the white material is mainly a compound of sodium, which is the first evidence to prove the supposition that sodium captions move towards the cathode in the glass during the poling. This may help us to understand the mechanism of second-harmonic generation in the poled glass. We found the signal of second harmonics decreases with time after poling and the damping rate depends on the surrounding temperature. The signal decay in fact is the decay of the electric field and the charged particle inside glass. There is a residual signal after damping for one week, which does not change for months. The residual signal depends on the poling temperature. Thus we have to assume that there are two kinds of negative particles in the poling process in soda-lime glass.

JSuE21 ■ Refractive index changes in Ge-doped silica glass induced by a KrF excimer laser irradiation, H. Nishikawa, Y. Miyake, E. Watanabe, D. Ito, *Department of Electrical Engineering, Tokyo Metropolitan University, 1-1 Minami Osawa, Hachioji-shi, Tokyo 192-08, Japan.* Refractive-index changes (Δn) in Ge-doped silica glass exposed to KrF excimer laser were studied by the measurements of the diffraction efficiency from a grating formed using a phase mask. The Δn of 3.2×10^{-3} was observed for a hydrogen-treated (150 atm, 2 weeks, room temperature) sample after a KrF laser irradiation (25 Hz, 0.5 J/cm^2/pulse, 27 kJ/cm^2), while the Δn obtained for a non-treated sample is less than 10^{-4}. The depth profile of the Δn for the hydrogen-treated sample is limited by the distribution in the hydrogen concentration inside the sample, while it is determined by the attenuation of the ultraviolet light for the non-treated sample. Ultraviolet (UV) optical absorption measurements show that the decrease at a 5.1 eV band and the increase at ~6 eV are stronger in the hydrogen treated sample than in the non-treated one. Correlation between the observed refractive index change and UV absorption change will be discussed. Also, the role of hydrogen on the enhanced photosensitivity will be discussed.

JSuE22 ■ Yellow/blue luminescences of Dy^{3+} doped borate glasses and their anomalous temperature variations, S. Tanabe, T. Hanada, *Faculty of Integrated Studies, Kyoto University, Japan;* J. Kang, N. Soga, *Faculty of Engineering, Kyoto University, Kyoto 606-01, Japan, Tel: +81-75-753-6821, E-mail: tanabe@chem.h.kyoto-u.ac.jp.* Dysprosium-doped borate glasses were prepared and their physical properties, optical absorption and fluorescence characteristics were investigated. Among three Judd-Ofelt parameters, the O_2 increased and the O_6 decreased with an increasing Na_2O content. The Branching ratio of blue/yellow emission from the $^4F_{9/2}$ level increased and its lifetime decreased with Na_2O content. The lifetime of the $^4F_{9/2}$ level increased with increasing temperature, which is unusual for most rare earth levels. Moreover, the branching ratio of blue/yellow emissions also changed with temperature. These behaviors could be explained by considering the temperature change of local structure and radiative transition probability of Dy^{3+} ions in the borate glasses.

JSuE23 (Invited) ■ Er^{3+} doped phosphate glasses and lasers, Shibin Jiang, Nasser Peyghambarian, *Optical Sciences Center, University of Arizona, Tucson, AZ 85721;* Michael Myers, *Kigre Inc., Hilton Head, SC 29926.* Erbium laser glasses have attracted much attention due to their capability for emission of radiation at the "eye-safe" wavelength of 1.54 μm. This paper describes the development of a new Erbium phosphate laser glass, the optimizing process of doping concentrations of Er^{3+} ions and sensitizers Cr^{3+} ion and Yb^{3+} ion, ion-exchange chemical strengthening of this new glass, pumping energy dynamics as well as laser resonator design to achieve high average power and high repetition rate operations.

By utilizing this chemically strengthened laser glass, 5 mJ single mode laser output was achieved with a 60 ns pulse width at a repetition rate of 15 Hz. A high average output power of 20 W at 1.54 μm was demonstrated pumped with flashlamp. Both the values of the repetition rates for Q-switched laser and the average output power at 1.54 μm represent an increase of several times compared to previously reported Er^{3+} glass lasers.

JSuE24 ■ Photochromic/photoconductive effects in cadmium-alumino fluorosilicates, L.K. Cornelius, P.A. Tick, N.F. Borelli, *Corning Incorporated, Corning, NY 14830.* A novel interaction was observed in cadmium-alumino fluorosilicate glasses when exposed to near UV radiation. Glasses high in cadmium were observed to be photochromic. Accompanying the darkening process was a change of up to five orders of magnitude in the DC conductivity. The process involved the formation of the cadmous ion (Cd+1) as an electron trap. A thin, transparent conductive skin could also be formed by appropriate heat treatments.

JSuE25 ■ Pr^{3+} and Dy^{3+}-doped Ge-S-I glasses suitable for active fiber optic devices, V.M. Krasteva, G.H. Sigel, Jr., *Fiber Optic Materials Research Program, Rutgers, The State University of NJ, Piscataway, NJ 08855;* S.L. Semjonov, M.M. Bubnov, *Fiber Optics Research Center at General Physics Institute, 38 Vavilov Str., Moscow 117942, Russia.* Pr^{3+} and Dy^{3+}-doped Ge-S-I glasses were synthesized and their optical properties studied for active photonic device

applications, such as optical fiber amplifiers at 1.31 μm and mid-IR fiber lasers. Absorption and emission spectra in the near-IR, recorded in doped Ge-S-I samples, are very similar to these observed in Ge-Ga-S glasses. Judd-Ofelt analysis of Dy^{3+}-doped Ge-S-I glasses was used to evaluate their radiative properties. The measured high quantum efficiencies of 1.31 μm transitions (82% for Pr^{3+}-doped and 17% for Dy^{3+}-doped Ge-S-I bulk glass samples) place them among the glass candidates with best emission parameters. Thermal analysis data have been utilized to identify compositions with suitable stability against crystallization during drawing process. Fibers with losses of 3 dB/m at 1.31 μm have been successfully fabricated from Pr^{3+}-doped Ge-S-I glasses.

JSuE26 ■ Spectroscopy and quantum efficiency of halide-modified gallium-lanthanum sulfide glasses doped with praseodymium, J.R. Hector, J. Wang, D. Brady, M. Kluth, D.W. Hewak, W.S. Brocklesby, D.N. Payne, *Optoelectronics Research Centre, University of Southampton, Southampton, SO17 1BJ, U.K.* Gallium-lanthanum sulfide (GLS) glasses are one of the most promising candidates for use in efficient 1.3 μm optical fiber amplifiers. In this paper we present a study of the optical properties of Pr^{3+}-doped GLS, modified using alkali halides. It has previously been shown that the addition of halide modifiers to GLS has a beneficial effect on the glass-forming and bulk optical properties. In this paper we show that the optical emission properties of the Pr^{3+} dopants are altered by the addition of halide modifiers, but are still considerably better than either ZBLAN or oxide-modified GLS. The quantum efficiency of the $^1G_4$–$^3H_5$ 1.3 μm transition, which is the most important parameter for efficient amplification, has been measured at 55% for these glasses, compared to 65% in pure GLS. We will present studies of the effect of compositional changes on the Raman spectrum of the glass, and on the radiative and non-radiative decay of the Pr^{3+} ion, and show how these are related to changes in the structure of the glass.

JSuE27 ■ Optical absorption and magnetic circular dichroism of $ER^{(3+)}$-doped aluminosilicate glasses, D.E. Johnson, D.P. Poulios, N.P. Bigelow, *University of Rochester, Rochester, NY 14627;* J.P. Spoonhower, *Eastman Kodak Company, Rochester, NY 14650.* The magnetic circular dichroism (MCD) and optical absorption spectra are reported for varying $erbium^{(3+)}$ concentrations in aluminosilicate glasses. Visible MCD data are obtained at a field strength of 1.8 Tesla and at a base temperature of 1.7 K. The temperature dependence in the range up to 300 K is also studied. A striking result of this work is the drastic change in both shape and position of many of the MCD absorption bands with $erbium^{(3+)}$ concentration. These changes give insight into the nature of the erbium ion's crystal field and thus its local environment. The MCD (or Faraday) parameters are determined via the method of moments.

JSuE28 ■ Rare earth doped PZG fluoride glass channel waveguides: spectroscopy and signal amplification, E.C. Lebrasseur, *UCBL-UMR-CNRS no 5620, Villeurbanne, France 69622, 33 472448321;* B. Jacquier, *UCBL-UMR-CNRS no. 5620, Villeurbanne, France 69622, 33 472448336;* B. Boulard, *LF-URA CNRS, 449 Univ. du Maine, Le Mans, France, 72 017, 33 243833370;* R. Rimet, *LEMO/INPG UMR CNRS no. 5530, Grenoble, France, 38016, 33 476856028.* Laser spectroscopy of R.E. doped fluoride waveguides elaborated by PVD technique on ZBLAN or CaF_2 substrate is presented. Channel waveguides of the PZG composition were obtained photolithography process on the substrate before deposition. Nd^{3+} fluorescence at 1.5 μm as well as erbium fluorescence at 1.55 μm are reported including decay time dependence with R.E. concentration. Finally, we have measured a signal amplification of 3.8 dB/cm at 1.05 μm in a 1 at% Nd-doped PZG waveguide. However, losses are too large to obtain a positive net gain, at the present time. Modelization of the optical amplifier has been developed, indicating the excellent theoretical performances of such device as soon as losses introduced in the deposition process will be removed, as it has been shown for undoped PZG planar layer.

JSuE29 ■ Rare-earth-doped glass thin films for integrated photonics, Allan J. Bruce, *Lucent Technologies, 700 Mountain Ave., Murray Hill, NJ 07974, ajb@lucent.com.* Applications for which rare earth doped planar waveguide devices can be a viable alternative to fiber based devices will be considered. Erbium doped planar waveguide amplifiers for 1.5 micron amplification will be considered in detail and used to highlight issues of host material selection, luminescence quenching, codoping, waveguide design, fabrication, performance, integration and packaging.

JSuE30 ■ Preparation and nonlinear optical properties of Au/glass composite thin films, I. Tanahashi, T. Tohda, *CRL Matsushita Electric Ind. Co., Ltd., Kyoto, Japan;* H. Inouye, *ERATO, Kyoto, Japan;* A. Mito, *NRL of Meterology, Tsukuba, Japan.* Small metal particles embedded in glasses have been widely studied as resonant type third-order nonlinear optical materials for photonic devices. We have prepared Au/SiO_2, Au/Al_2O_3, Au/TiO_2 composite thin films by a multitarget sputtering method. The $\chi^{(3)}$ and τ of the composite thin films were investigated by means of femtosecond Z-scan and pump-probe experiment, respectively. In the optical-absorption spectra of the three types of the films, the clear absorption peak due to the surface plasmon resonance of Au particles is observed. The imaginary part of $\chi^{(3)}$ and τ for the Au/TiO_2 film were -3.6×10^{-7} esu and ~2 ps, respectively. The $\chi^{(3)}$ of Au/SiO_2, Au/Al_2O_3, Au/TiO_2 films increased in that order.

JSuE31 ■ Nonlinear response of gold nanoparticles embedded in glass matrix, H. Inouye, *Hirao Active Glass Project, ERATO, Kyoto, Japan;* K. Tanaka, *Kyoto Univ., Kyoto, Japan;* I. Tanahashi, *CRL Matsushita Electric Ind. Co., Ltd., Kyoto, Japan;* K. Hirao, *Kyoto Univ., Kyoto, Japan.* Small

metal particles embedded in glass matrix has been investigated energetically both in the application research field and in the basic research field, since the strong enhancement of the third-order nonlinear optical susceptibility is observed around the peak of the surface-plasmon resonance. The mechanism of the nonlinear response, however, has not been clarified yet. We measured transient absorption spectra to investigate the nonlinear response of the gold nanoparticle system by the femtosecond pump-probe method. It is concluded that the nonlinear response originates mainly from the hot electron which is raised by the incidence of the pump pulse in sub-picosecond region. In the long time-scale region, where the time resolution is longer than 5~ps, transient change of the lattice temperature plays an important roll of the nonlinear response.

JSuE32 ■ Nonlinear index of refraction of germanium selenide glass at 10.6 μm, C.R. Schardt, J.H. Simmons, *University of Florida, Gainesville, FL 32611;* L. LeNeindre, P. Lucas, J. Lucas, *University of Rennes, Rennes, France.* We report on the nonlinear index of refraction in germanium selenide glasses at the CO_2 laser wavelength of 10.6 μm. This frequency is near the low frequency edge of the germanium selenide infrared window. The nonlinear index is measured by the z-scan technique probed with a CO_2 laser. The measurements were done with the laser operating in both continuous and pulsed modes. Compositions of germanium selenide glasses varying from 2 to 40 at. % germanium are studied and the data is compared to the structure and infrared spectra of these glasses.

JSuE33 ■ Chalcogenide glasses with high nonlinear refractive index, F. Smektala, C. Quemard, L. LeNeindre, J. Lucas, *Laboratorie des Verres et Ceramiques, Universite de Rennes I, 35000 Rennes, France;* A. Barthelemy, *Institute de Recherches en Communications Optiques et Microondes, Universite de Limoges, 87060 Limoges, France;* C. De Angelis, *Dipartimento di Elettronica e Informatica, Universita de Padova, 35131 Padova, Italy.* Nonlinear refractive index and nonlinear absorption of several chalcogenide glasses have been measured by the Z-scan method at 1.05 μm in order to evaluate their capability to be used in telecommunication all optical ultrafast switching devices. Value obtained for the reference glass As_2S_3, well known to present nonlinearities several orders of magnitude higher than silica glass, agree to those found in the literature. Glasses in the GeSe and GeSeAs systems have been characterized. Values of nonlinear refractive index four times higher than those of As_2S_3 have been obtained for a GeSeAs glass.

JSuE34 ■ Solarization of soda-lime-silicate glass containing manganese, B.T. Long, Lyle J. Peters, Henry D. Schreiber, *Chemistry Department, Virginia Military Institute, Lexington, VA 24450.* Soda-lime-silicate glasses containing different amounts of Mn^{2+} and Mn^{3+} (in concert with varying concentrations of iron or antimony) were exposed to high-intensity ultraviolet light. After solarization, the manganese did not appear to change valency from the reduced Mn^{2+} back to the colored Mn^{3+} state. However, most glasses exhibited an increase in the background absorption in the visible and ultraviolet spectrum from 800 to 300 nm, probably attributable to the degradation of the glass surface by the ultraviolet radiation.

JSuE35 (Invited) ■ Mid-IR high power transmission through chalcogenide glass fibers, L.E. Busse, J.S. Sanghera, I.D. Aggarwal, *Naval Research Laboratory, Code 5606, Washington, DC 20375.* Chalcogenide fibers which are being developed at the Naval Research Laboratory have low optical loss and good mechanical strength, making them practical for use in a variety of mid-infrared applications, including fiber-coupled laser threat warning systems and fiber optic chemical sensors. Current results for both CW and pulsed laser transmission through these chalcogenide fibers in the 2–11 micron wavelength region will be presented. Results and predictions for laser induced optical damage thresholds for glass and fiber will also be discussed. Important issues for optimum infrared power delivery will be addressed, including a novel fiber end termination method and antireflection coatings for the fiber endfaces.

JSuE36 ■ Optical properties of gold (and other precious metals) in acetate glasses, N.R. Wilk, Jr., H.D. Schreiber, *Chemistry Department, Virginia Military Institute, Lexington, VA 24450.* Colors of gold ruby glasses are variable, depending in part on the size of the gold particulates dispersed in the colloidal state. In order to understand more fully the optical properties due to Au and other precious metals (Ag, Pd, Rh, Ru, Re) in silicate glasses, this study reports on the inclusion of such metals into analogous, low-melting acetate liquids and glasses. For example, the color imparted by gold in Na-K-Ca-acetate glasses versus Li-Pb-acetate glasses changes from pink to purple, as the nature of the colloidal dispersion is affected by the structure of the acetate system. Other precious metals can be incorporated into the acetates as colloidal dispersions or as ions, with the resulting colors controlled by the nature of the metal and the structure of the acetate system.

JSuE37 ■ Fluorescent cooling of ytterbium-doped heavy metal fluoride hosts, M.T. Murtagh, G.H. Sigel, Jr., *Rutgers University, Piscataway, NJ 08855-0909;* J.C. Fajardo, *Corning Incorporated, Corning, NY 14831;* B.C. Edwards, R.I. Epstein, *Los Alamos National Laboratory, Los Alamos, NM, Phone: (732) 445-4526.* As first discussed by Pringsheim in 1929, continual cooling of a material may occur via anti-Stokes luminescence. However, not until recently was net cooling actually observed experimentally in a solid. By pumping Yb^{3+} to the lower Stark levels of the $^2F_{5/2}$ manifold, followed by population redistribution across this manifold and fluorescence to the ground state, removal of heat from a ZBLAN-derived fluoride host was achieved. The Yb-doped ZBLANP host demonstrated a temperature drop of 0.33 K at 1008 nm via infrared evaluation. Photothermal deflection spectroscopy (PTDS) was employed to measure the relative

cooling efficiency (DC laser power to cooling power), which was determined to be 2.03%. Due to constraints on the doping levels in ZBLAN-derived hosts, other high rare earth concentration fluoride hosts are presently being investigated as potential coolers. BIZYT-derived hosts, with Yb concentrations as high as 26%, have been shown to contain similar spectral characteristics to that of ZBLAN, and thus sufficient spectral overlap for anti-Stokes fluorescent behavior. In general, the potential for high levels of net cooling in Yb-doped fluoride glasses makes these hosts attractive candidates for the development of a first-generation optical cryocooler for astronomical remote sensing applications.

JSuE38 ■ NMR and IR study of the functionality of electrode glasses, C. Jäger, *Friedrich Schiller University, PATF, Max Wien Platz 1, 07743 Jena, Germany;* K. Glock, B. Thomas, *University of Mining and Technology, Institute of Analytical Chemistry, Leipziger Str. 49, 09596 Freiberg/Sa., Germany.* During conditioning of glass electrodes in aqueous solutions a hydrated layer is formed, which is responsible for the pNa^+ sensitivity. For a detailed understanding of this effect the structure of the bulk glass as well as of the hydrated layer is of particular importance. ^{27}Al and ^{11}B MAS NMR were used to investigate Na_2O-Al_2O_3-SiO_2 and Na_2O-B_2O_3-SiO_2 glasses. The ^{27}Al MAS spectra can be interpreted in terms of two different structural units. We can distinguish between AlO_4 tetrahedra connected to Q^4 groups only and AlO_4 tetrahedra linked to Q^3_m groups. In a similar way two BO_4 units can be detected which are linked to SiO_4 units or BO_3. In both cases only one of the two structural units is removed during the reaction in hydrous solution which can easily be concluded from the changes of the ^{11}B and ^{27}Al MAS lineshape. In summary criteria for a good pNa+ sensitivity could formulate in terms of certain structural units which must be present in the bulk glass. Also, the swelling layer must contain a large content of Q^4 and the H_2O/SiOH ratio must be sufficiently high.

JSuE39 ■ Possibilities of 119-Tin NMR for the characterization of glasses, M. Braun, C. Jäger, *Friedrich Schiller University, Max-Wien-Platz 1, 07743 Jena, Germany;* D. Ehrt, A. Daniel, *Otto-Schott Institut für Glaschemie Fraunhoferstr. 6, 07743 Jena, Germany.* Besides the study of inorganic oxide glasses using traditional MAS NMR of abundant nuclei (e.g. phosphorus, aluminium) the measurement of less common nuclei (e.g. Tin) provide important structural information. The experimental setup is more complicated due to the low natural abundance (8.5%), large chemical shift anisotropies (up to 1000 ppm), and long relaxation times of these nuclei (up to 500 s). Results will be presented for 119-Tin MAS NMR measurements of P_2O_5–SnO_2 glasses. We have found a large change of T_g and phosphorus coordination at different Tin content.

JSuE40 ■ Ion-exchange processes in silicate glasses: the role of oxygen, V.I. Belostotsky, *on leave Institute of General and Inorganic Chemistry of Russian Academy of Sciences, Moscow, Russia. Present address: 5503 Halpine Place #A, Rockville, MD 20851, USA, Phone: (301) 984-7865.* Potassium and oxygen concentration profiles in soda-lime-silica glass subjected to an ion exchange in molten potassium nitrate at a temperature below the strain point of the glass were obtained by Auger electron spectroscopy. Measurement showed the excess of oxygen in the modified layer of glass and the similarity of the shapes of potassium and oxygen concentration profiles in the most part of the modified layer. Consequently, the replacement of smaller sodium ions by larger potassium ions is accompanied by oxygen diffusion from molten salt into glass. On the basis of these results, a microscopic model of ion-exchange processes in silicate glasses, including mixed alkali effect, was proposed.

JSuE41 ■ Residual stresses due to refractory inclusions in silica glass, D.J. Wissuchek, *Corning Inc., Corning, NY 14845.* Residual stresses due to thermal expansion mismatch for refractory particles on high purity silica glass were studied. Finite element analysis was used to determine the stresses around ZrO_2, Cr_3O_4, SiC and graphite particles in contact with a SiO_2 substrate. Results were obtained for both fully and half submerged particles. Results were compared to existing analytical models for fully submerged particles where applicable. Effects of particle aspect ratio for elongated particles were studied. ZrO_2, Cr_3O_4 and SiC were modeled as isotropic materials. All exhibited tensile radial stresses, with ZrO_2 displaying the highest stress levels. The stresses at the SiO_2 surface reached a maximum a short distance from the particle/matrix interface. Peak radial stress increased with increasing particle aspect ratio. Maximum tensile stress for elongated particles was located at the tip of the particle, corresponding to fracture origins noted for these particles. Graphite particles were modeled as anisotropic structures and the stresses were determined for different crystalline orientations. Unlike the other refractories, the maximum tensile stress for a graphite particle in one of its possible orientations was located at the edge of the particle. This corresponds to fracture origins noted on silica glass with graphite particle surface flaws. The stress field results are discussed in a fracture mechanics framework, and the effect of residual stress on material reliability is presented.

INVESTIGATION OF OPTICAL AND RADIATION PROPERTIES OF OXYGEN DEFICIENT SILICA GLASSES

A.N.Trukhin[a] and H.-J.Fitting[b]
[a]Institute of Solid State Physics, University of Latvia, Kengaraga St.8, LV-1063 Riga, Latvia
phone: (371)7260686, fax: (371)7112583, e-mail: truhins@acad.latnet.lv
[b]Physics Department, Rostock University, Universitätsplatz 3, D-18051 Rostock, Germany
phone: (++49) (381) 4981668 , fax: (++49) (381) 4981667 ,
e-mail: hans-joachim.fitting@physik.uni-rostock.de

Silica samples with different level of oxygen deficit have been studied with the aim to investigate the properties related to the 7.6 eV absorption and excitation band. The high purity KS-4V silica was prepared by electrofusion of cristobalitised silicon dioxide. The deficit of oxygen at the level of 10^{-2} wt% was provided by reaction of cristobalite with silicon, [1].

In Fig.1 the main measured optical spectra of silica with different levels of oxygen deficit are presented. The two main absorption and excitation bands at 5 eV and 7.6 eV can be observed. The intensities of these bands are proportional to the deficit of oxygen. The absorption band at 5 eV possesses an intensity of about 2 cm^{-1} for the level of O-deficit of about $1.5 \cdot 10^{-2}$ wt %. This band is due to a singlet-singlet allowed transition, [3,4]. The two photoluminescence (PL) bands at 4.4 eV and 2.7 eV are excited via both absorption bands.

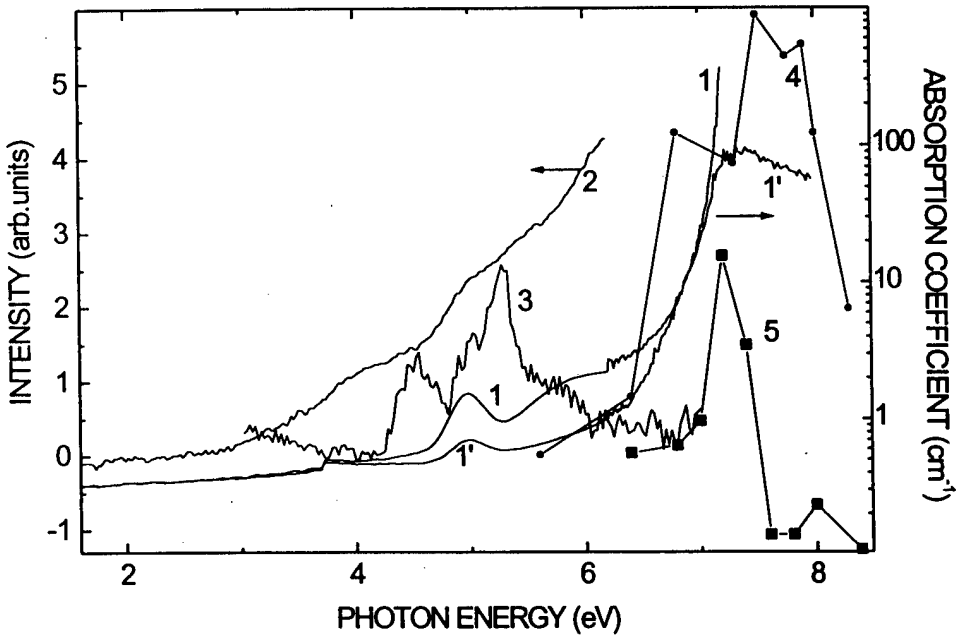

Fig.1. KS-4V silica with excess silicon (1 - $1.5 \cdot 10^{-2}$ wt% ; 1' - $0.7 \cdot 10^{-2}$ wt%).
Spectra: 1- photoabsorption at 290 K; 2 - photoinduced absorption (x20) at 290 K; 3 - photo-stimulation of the blue 2.7eV luminescence after X-ray irradiation at 80 K; 4 - photoexcitation of the 400 K TSL peak ; 5 - photoelectric response.

Taking into account the 4.4 eV band life time with 4 ns [4] we may estimate the oscillator strength of about 0.15 and then, according Smakula's formula, the center concentration. We got a value of 10^{18} cm^{-3} for 5 eV absorption band and this approximately corresponds to 10^{-2} wt % of excess silicon. A second manifestation of oxygen deficit in as received non-irradiated silicas is

connected with the 7.6 eV absoption band which intensity is higher than 100 cm^{-1} for the same concentration of excess silicon. For this band the estimation of concentration with the same value of oscillator strength after Smakula's formula gives a value of about 10^{20} cm^{-3} which strongly exceeds the level of excess silicon. Probably, the excess silicon produces some structural compounds which perturbate the states of the main glass network and the 7.6 eV band can be assumed as a composite of several host material defects, as it was predicted before [2].

In the range of the7.6 eV absorption band the photoelectric response as well as the thermostimulated luminescence (TSL) peaks are excited too. That indicates a photoinduced transformation of primary defects. In Fig.2 TSL curves are presented. It is seen that all curves are practically similar for silica of KS-4V type. The intensity of TSL is proportional to the deficit of oxygen. The spectral nature of the TSL is the same as that of the X-ray excited luminescence. There is a blue band at 2.7 eV as well as an additional band at 3.2 eV and a spread UV band at 4.4 eV. Many TSL peaks point at different kinds of defects appearing as a consequence of phototransformation. The intensity of TSL shows the recombining defect concentration.

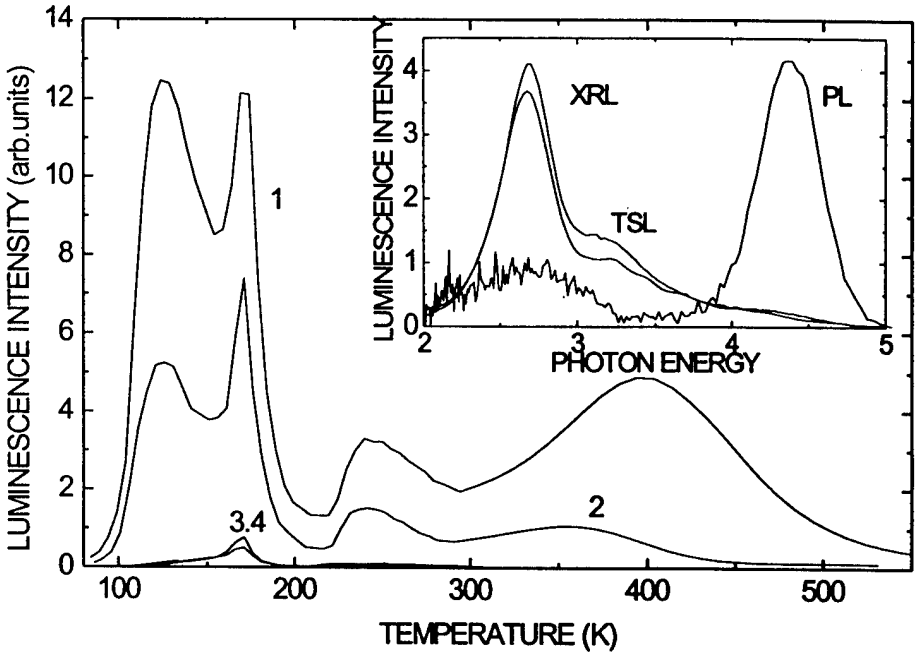

Fig. 2. X-ray excited TSL of the 2.7 eV luminescence band in KS-4V silica with excess silicon, 1 - $1.5 \cdot 10^{-2}$ wt.% ; 2 - $0.7 \cdot 10^{-2}$ wt.% ; 3 ; 4 - without doping.
Insert : different luminescence spectra (PL excited at 7.7 eV)

The TSL existence together with afterglow correlate with the existence of photostimulated luminescence (PSL) for the blue band. The PSL excitation spectrum is presented in Fig.1. This spectrum well corresponds to the induced absorption spectrum, where the bands at 4.5; 5.2 and 5.7 eV were observed. The induced absorption bands are similar at 80 K and 290 K.

The intensity of the peak at 400 K, excited at 290 K with white light of a deuterium lamp in vacuum, grows sublinear over a time of 2 hours, see Fig.3. Under the same condition we got an ESR signal in the range of the E' center, see insert of Fig.3 . The intensity of this signal saturates in few minutes of excitation with VUV light, therefore, there is no correlation to the TSL peak at 400 K which intensity is still growing even after several hours. The ESR signal disappears afterheating.Thus the photoreconstruction related to the 7.6 eV defect is very complicated as it was

also obtained before for silica of low level deficit, [6]. Four TSL peaks at least, a complex photoinduced absorption spectrum, and additionally an ESR signal which does not correlate in growth with TSL do underline that. The photoinduced defect nature is still unknown., however,

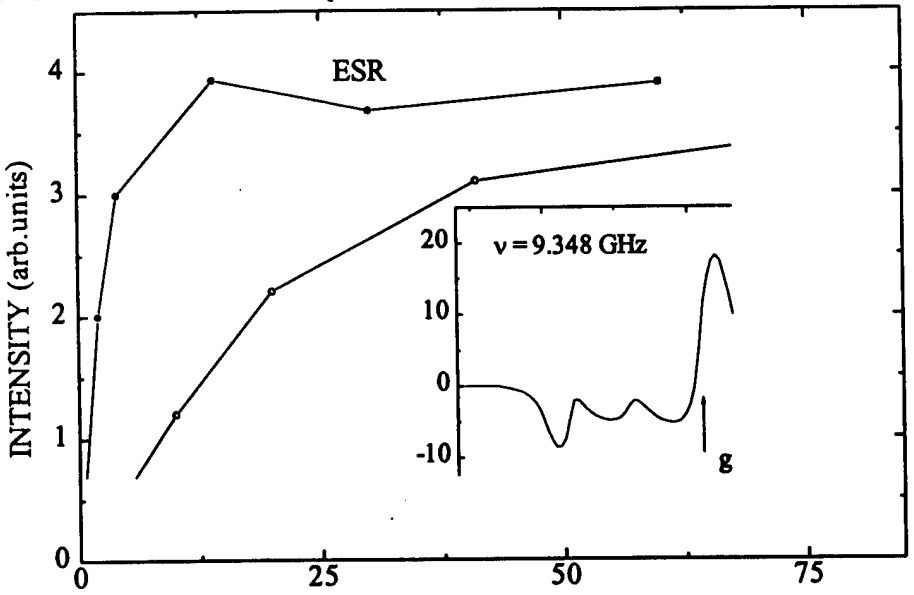

Fig. 3. Excitation kinetics of KS-4V silica with excess silicon $1.5 \cdot 10^{-2}$ wt.% : TSL peak at 400 K and the ESR intensity , both after photoexcitation at T=290 K

the recombination process always involves the blue luminescence of the twofold-coordinated silicon center. Another well-known defect is the E'-center which signal appears under photoreconstruction in accordance with previous studies [5,7]. However, its concentration is saturated much faster than the TSL intensity does, therefore, E'-center precursors may be related only partly to the defects studied and so we can not agree with the assumption in [7] that the band at 7.6 eV is related to the Si-Si bond only. The continuation of TSL growth still after E'-center saturation points at other defects involved. The complex induced absorption also indicates creation of different products in consequence of defect reconstruction responsible for the 7.6 eV absorption and excitation band.

A next step of studies can be done by means of ODMR using the triplet-singlet nature of the 2.7 eV band belonging to twofold-coordinated silicon. This band is the main one in TSL and afterglow. It should be underlined that there is no red NBOHC luminescence, therefore, this defect is not created in photoreconstruction. As a consequence of the data obtained, we may state that the nature of the band at 7.6 eV can not be explained as a single point defect .

This work was supported by the grant 96.0665 of the Scientific Society of Latvia. The authors are grateful to A.V.Shendrik for ESR measurements.

[1] A.N.Trukhin, A.G.Boganov, A.M.Praulinsh, Phys.Chem. Glass.(Sov.) 6 (1979) 346.
[2] A.N.Trukhin, L.N.Skuja, A.G.Boganov, V.S.Rudenko, J.Non-Cryst.Sol.149 (1992) 96
[3] L.N.Skuja, A.N.Streletsky, A.B.Pakovich, Solid State Commun. 50 (1984) 1069.
[4] L.N.Skuja J.Non-Crystalline Solids 167 (1994) 229-238
[5] H.Imai, K.Arai, H.Imagawa, H.Hosono, Y.Abe Phys. Rev. B 38 (1988) 12772 -12775.
[6] Trukhin A.N. J.Non-Crystalline Solids 189 (1995) 1-15.
[7] H.Imai, K.Arai, H.Hosono, Y.Abe, T.Arai, H.Imagawa, Phys. Rev. B 44 (1991) 4812 -4818.

Bragg Gratings, Photosensitivity, and Poling in Glass Fibers and Waveguides: Applications and Fundamentals

Joint Symposium on Vitreous Silica and Related Material

Joint Session on Hydrogen in Glass and Fibers

Monday, October 27, 1997

David Griscom, U.S. Naval Research Laboratory
Presider

JMA
8:00am–10:30am
Auditorium

Radiation-induced density and absorption changes in fused silica

T.P. Seward III, C. Smith, N.F. Borrelli, D.C Allan and R.J. Araujo
Corning Incorporated, Sullivan Park, Corning, NY 14831
Tel: 607-974-3724; Fax: 607-974-3675

A major growing application for fused silica is as microlithography lenses for integrated circuit manufacture using deep ultraviolet excimer laser radiation at 248 nm (KrF) and 193 nm (ArF) wavelengths. Such short wavelength radiation, while allowing higher image resolution, can cause structural changes in the glass which can adversely affect lens performance. These changes are manifest as color centers and glass densification.

That fused silica undergoes such changes, namely color center formation and densification, upon prolonged exposure to high energy radiation is well documented, whether that radiation be electrons, x-rays, gamma-rays, neutrons, or deep ultraviolet photons. A peculiar aspect of short wavelength excimer lasers is the absorption process itself. These sources are pulsed, and while average power is modest, the peak power is very high. (Peak intensities of the order of 10MW/cm^2 are not unusual.) A consequence of the high peak power is the role two-photon absorption (TPA) can play. While the energy from the highest occupied bonding orbital of SiO_2 to the first unoccupied non-bonding orbital is of the order of 10 eV, this transition can be reached by TPA under irradiation at 248 nm (5.0 eV) or 193 nm (6.4 eV).

Induced Absorption - The induced absorptions of concern for the microlithography applications include absorption bands centered approximately at 215 nm and at 260 nm. The 215 band is generally attributed to the E' center [1,2]. The 260 band has been attributed to NBOHCs (non-bridging oxygen hole centers) [3] and, in fused silicas with excess oxygen, to interstitial ozone [4].

For fused silicas exposed to either 248 nm or 193 nm irradiation, the induced absorption tends to diminish in varying degrees when the irradiation ceases; i.e. the absorptions tend to partially fade. To study these changes quantitatively requires monitoring the glass transmittance during as well as after exposure. We did this using a uv probe beam through the exposed region of the sample at right angles to the laser beam direction.

We demonstrated dissolved molecular hydrogen (H_2) to be an important composition variable controlling the rates of darkening and recovery. For example, samples of synthetic fused silica containing approximately 10e17 molecules of H_2 per cm^3 of glass were treated a) so as to remove dissolved molecular hydrogen to a level less than 10e16 and b) so as to increase the level to greater than 10e19. Darkening and fading kinetics of the three samples were studied. The low H_2-containing glass tends to darken rapidly (at 215 nm) and recover extremely slowly. The high H_2-containing glass behaves conversely. A kinetic model based on reaction of the dissolved molecular hydrogen with photogenerated species, such as the E' center and the NBOHC, is being developed. In its present form, it fits the darkening behavior of the high and low H_2-containing glass and qualitatively predicts the intermediate behavior.

Densification - Under excimer laser irradiation, the resulting densification is often less than ten parts per million. Since there is no direct way to measure such small densification, it is necessary to expose only a region of the sample and to measure the densification differentially, using interferometry and/or stress birefringence [5,6,7]. The ultimate distortion produced by the laser densification depends on the exposure arrangement, including the size and geometry of the sample, the size and geometry of the damaged region, and the illumination intensity profile. These all must be taken into account in order to make a meaningful interpretation of the densification. Interpretation of the interferometric or birefringence measurements in terms of changes in density requires elastic theory analysis. We used finite element analysis (FEA) techniques to determine the fractional densification, $\delta\rho/\rho$, that the exposed region of the glass would have experienced had it not been surrounded by unexposed glass. We refer to this as the "unconstrained" densification.

We have shown that the densification, $\delta\rho/\rho$, as a function of dose, which we define as I^2N, where I is the energy density of the radiation in mJ/cm^2/pulse, and N is the number of pulses, generally follows a power law of the form $\delta\rho/\rho = a(I^2N)^b$. Measurements of different silica samples, with different thermal histories, yielded fits with the exponent b ranging between 0.5 and 0.7. For a sample of Corning HPFS^{tm} (containing about 800 ppm OH by weight) irradiated at 193 nm (by a Lumonics Excimer 600 laser having a 16 ns pulse duration, FWHM) we find the following densification:

$$\delta\rho/\rho = 91 \times 10^6 \, (I^2N)^{0.53}$$

where I is measured at the peak of the laser intensity profile.

Data for exposures at different pulse fluences, ranging from greater than 50 mJ/cm^2 to less than 0.6 mJ/cm^3, fall on the same curve, thus establishing reciprocity between energy-density-squared and number of pulses for a given glass. The use of I^2 results from the two-photon nature of the absorption events. For irradiation at 248 nm, the same form of equation holds, with the same exponent, but the pre-exponential factor is about 13x smaller. The same exponent is to be expected since the damage mechanism is the same at both wavelengths. The difference in pre-exponential factor reflects the difference in TPA coefficients at the two wavelengths.

The mechanisms of both induced absorption and densification depend upon breaking or weakening of structural bonds via two-photon ionization events. As has been suggested by others [e.g. 8], the breaking or weakening of bonds permits structural rearrangements that could lead to higher density. Complete cleavage of an Si-O-Si structure leads to the well-known Si E' center - NBOHC pair, responsible for the optical absorptions at 215 nm and 260 nm, as discussed above. These absorbances are seen in varying degrees in different types of silica, or in the same silica under different exposure conditions, often independently of the degree of induced densification. In particular, as a consequence of the role of dissolved molecular hydrogen and the associated tendency for the induced absorption to fade, plots of induced absorption versus dose (where dose is number of pulses times some function of the pulse energy density) lie on different curves, depending on the pulse energy density used for the exposure. Unlike for densification, there is no demonstrated reciprocity between any function of the pulse energy and the number of pulses. This confirms that the mechanisms of induced absorption and densification are not identical.

1. D.L. Griscom, J. Non-Cryst. Solids 73 (1985) 51

2. K. Arai, H. Imai, H. Hosono, Y. Abe, and H. Imagawa, Appl. Phys. Lett. 53 (1988) 3584

3. J. Stathis and M.A. Kastner, Phys. Rev. B35 (1987) 2972

4. K. Awazu and H. Kawazoe, J. Appl. Phys. 68 (1990) 3584

5. R. Schenker, F. Piao, and W.G. Oldham, Proc. SPIE 2726 (1996) 698

6. D.C. Allan, C. Smith, N.F. Borrelli, and T.P. Seward III, Opt. Lett. 21 (1996) 1960

7. N.F. Borrelli, C. Smith, D.C. Allan, and T.P. Seward III, JOSA B, scheduled for publication, July, 1997

8. W. Primak, The Compacted States of Vitreous Silica, Vol. 4 of Studies in Radiation Effects in Solids, edited by G.J. Dienes and L.T. Chadderton (Gordon and Breach, 1975), esp. pp. 91-102

Hydrogen, defects, and compaction of pure and doped vitreous silica

J.E. Shelby, M.S. Bergomi
NYS College of Ceramics, Alfred University, Alfred, NY 14802

Irradiation of vitreous silica results in the formation of optical defects and the compaction of the glass. Irradiation of silica doped with germanium or titanium results in the formation of many more defects, accompanied by compaction. Irradiation of undoped vitreous silica containing large quantities of dissolved molecular hydrogen eliminates the optical defects and reverses the compaction process so that the glass actually expands. Irradiation of hydrogen soaked silica doped with 4% germania results in increased optical absorption, but still leads to expansion of the glass. On the other hand, irradiation of hydrogen soaked silica which contains 3 to 8% titania leads to dramatic increases in optical absorption and to increased compaction of the glass.

Irradiation of all of these glasses results in the formation of bound hydrogen species when the glass contains a high concentration of dissolved molecular hydrogen during irradiation. The species formed and their concentrations vary dramatically with dopant.

Possible models for the defects formed in these glasses during irradiation with and without dissolved hydrogen will be discussed. These models are based on the formation of reduced germanium and titanium ions when hydrogen is present during irradiation.

Mechanisms of Index Change Induced by Near-UV Light In Hydrogen-Loaded Fibers

V. Grubsky, D. S. Starodubov*, and J. Feinberg
Department of Physics
University of Southern California
Los Angeles, CA 90089-0484
(213) 740-1134; Fax (213) 740-6653

* Permanent address: Fiber Optics Research Center, General Physics Institute of the Russian Academy of Science, Moscow, Russia.

Bragg Gratings in optical fibers have been formed using a wide variety of writing wavelengths ranging from the visible at 488 nm (using 2 photon excitation) to the vacuum-UV at 157 nm. [1-4]. Recently fiber gratings were fabricated by a one-photon process with near-UV light [5-8]. However results with near UV fabrication are contradictory: no Bragg grating was observed in the fibers in the absence of hydrogen loading [5,6], gratings in hydrogen-loaded fibers were transient [6], stable Bragg gratings were demonstrated with and without hydrogen loading [7,8]. Here we present the data that can help to explain these apparently contradictory results.

In our first set of experiments we fabricated fiber Bragg gratings using different UV lines of a cw Ar laser from 275 nm to 364 nm. The near-UV light was focused on the fiber core by a 3 cm focal length cylindrical lens to a writing intensity 1–3 kW/cm^2. For hydrogen-free fiber the spectral dependence of photosensitivity mimicked the known excitation spectrum of the triplet state of germanium oxygen-deficient centers (GODC) [5], giving the shoulder at 3.7 eV as shown in Fig. 1. It means that the index change is related to triplet state excitation either directly or through intermediate singlet state of GODC.

However, if we first soaked the fiber for 2 days in 300 atm. of molecular hydrogen, the photosensitivity spectrum significantly changed. The maximum shifted to ~ 4.5 eV, indicating that excitation of GODC triplet state is no longer the key index changing mechanism in hydrogen-loaded fibers. At 351 nm (~3.5 eV) the hydrogen-loaded fibers were relatively insensitive, in agreement with the results of Atkins and Espindola [6]. However the writing speed increased dramatically (by 2-3 orders of magnitude) with shorter wavelengths.

We note that (to the limit of our available laser wavelengths), the photosensitivity of our hydrogen-loaded fibers was maximum at 4.5 eV, which is the dissociation energy of a hydrogen molecule. However, because the initial and final states have the same symmetry, 4.5 eV light itself probably cannot directly break the H-H bond. We suggest instead that there is a resonant energy transfer from some photoexcited Ge-related species in the glass to the hydrogen molecule, causing it to split. For example, light can excite GODC or Ge(1) center, which could transfer the energy to the hydrogen molecule to form new bonds with germanium (Ge-H) or oxygen (O-H). This hypothesis is supported by luminescence studies that show a decrease in the lifetime of the excited triplet state of GODC in hydrogen-loaded fibers [9] compared to hydrogen-free fibers.

We determined how the photosensitivity at 302 nm depended on the Ge concentration while keeping the hydrogen concentration fixed. Figure 2 shows that in the initial stage of writing, when hydrogen was not yet depleted, the rate of index change increase depended linearly on Ge concentration. This implies that the hydrogen interacts mainly with germanium-related sites. However, the *saturated* index change was almost independent of Ge concentration, and reached $\Delta n = 1.1 \times 10^{-2}$ with ~2.7 mol. % of H_2.

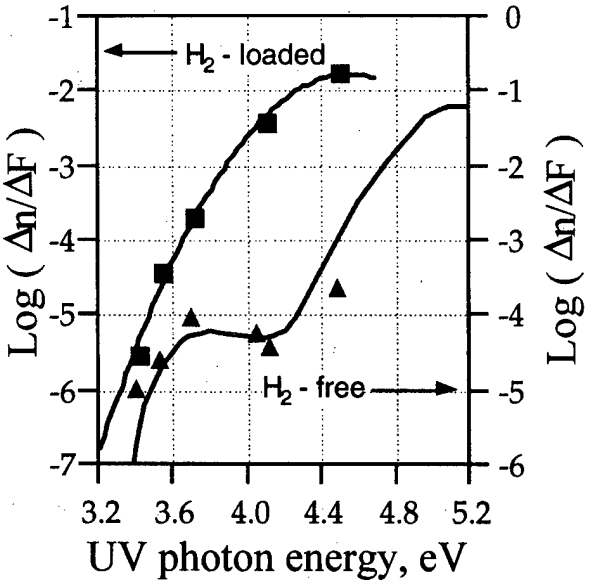

Fig. 1. Log of the H_2-loaded fiber's photosensitivity ($\Delta n/\Delta F$) vs. UV writing energy (squares) approximated by a Gaussian fit. For comparison, we also show data for a H_2-free fiber (arb. units): the normalized by fluence F index change (triangles) and the known absorption spectrum of GODC (solid line).

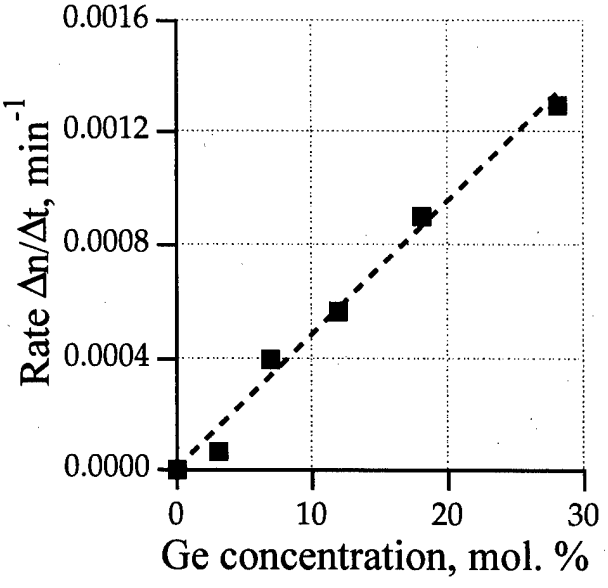

Fig. 2. Index change rate in H_2-loaded fibers vs. Ge content of the fiber.

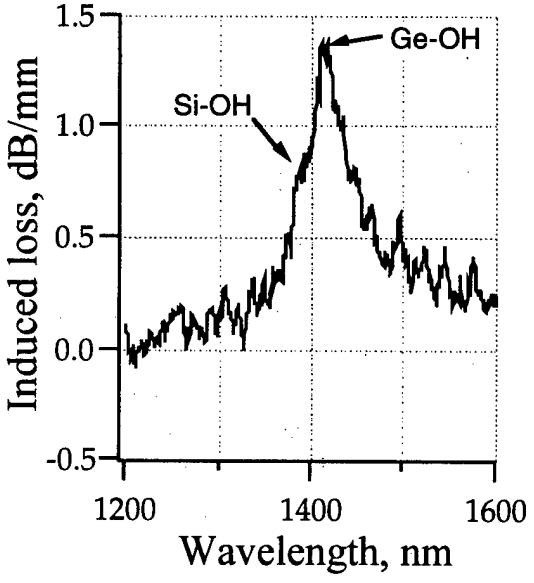

Fig. 3. OH absorption is clearly seen in a H_2-loaded fiber after illumination with 334 nm light. Clearly visible is the Ge-OH peak at 1410 nm. A weaker peak from Si-OH can be seen at 1390 nm.

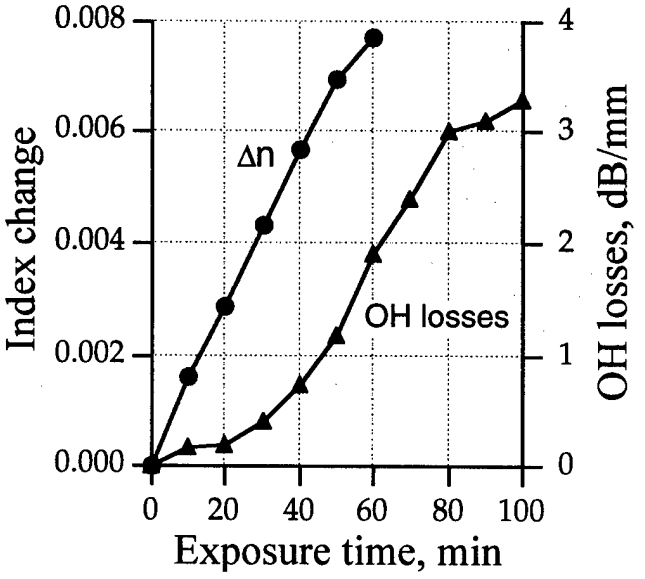

Fig. 4. Light-induced index change and OH loss vs. time in a fiber with 26 mol.% Ge irradiated by 0.4 W of 334 nm light.

We studied the products of the hydrogen/glass reaction in more detail. As in previous work on grating fabrication by mid-UV (240 nm) light [10], in our near-UV experiments we detected the efficient formation of OH bonds, mainly GeOH bonds (see Fig. 3). The saturated concentration of OH bonds was approximately twice the initial concentration of molecular hydrogen H_2 as was also seen with 240 nm excitation [10]. This result suggests that in glass with a high concentration of H_2, most of the hydrogen forms OH bonds rather than GeH or GeH_2 defects [11].

We found that diffusion of hydrogen from the cladding into the core of a fiber [12] has an influence on the index change dynamics. The time constant of this process at room temperature is of the order of a few minutes. This diffusion of hydrogen can be responsible for transient processes in hydrogen-loaded fibers and for the enhancement of fabrication efficiencies at higher temperatures. Also, the replenishment of hydrogen in the core by diffusion from the cladding can maintain a relatively constant core hydrogen concentration at low light intensities; in that case the photosensitivity remains constant and the refractive index of the core increases linearly with fluence.

Figure 4 shows that although the OH bonds concentration grows in strength as the induced index change increases, it obeys an almost quadratic time dependence while the index changes linearly with time, indicating that at low exposures a mechanism other than simply OH bond formation is causing the observed index change.

In conclusion, we have investigated the effect of near-UV light on germanosilicate fibers with and without hydrogen. In hydrogen-free fibers the induced index change is connected with excitation of GODC's triplet state. In hydrogen-loaded fibers the photosensitivity is peaking at ~4.5 eV, supposing the importance of dissociation of hydrogen molecule. The rate of index change in hydrogen-loaded fibers depends linearly on Ge concentration, while saturation depends mainly on hydrogen concentration. The predominant product of the near-UV induced reaction in fibers with high germanium contents are GeOH bonds.

References

1. K. O. Hill, Y. Fujii, D. C. Johnson, and B. S. Kawasaki, Appl. Phys. Lett. **32**, 647 (1978).
2. G. Meltz, W. W. Morey, and W. H. Glenn, Opt. Lett. **14** , 823 (1989).
3. J. Albert, B. Malo, F. Bilodeau, D. C. Johnson, K. O. Hill, Y. Hibino, and M. Kawachi, Opt. Lett. **19**, 387 (1994).
4. K. Beckley, P. Herman, CLEO'97 Proceedings, 1997 OSA Tech,. Digest Series, Vol. 11, paper CTuN3, 107 (1997).
5. E. M. Dianov, D. S. Starodubov, S. A. Vasiliev , A. A. Frolov, and O. I. Medvedkov, Opt. Lett. **21**, 221 (1997).
6. R. M. Atkins and R. P. Espindola, Appl. Phys. Lett. **70**, 1068 (1997).
7. D. S. Starodubov, V. Grubsky, J. Feinberg, B. Kobrin, S. Juma, Opt. Lett. **21**, 1086 (1997).
8. D. S. Starodubov, V. Grubsky, J. Feinberg and T. Erdogan, CLEO'97 Postdeadline paper CPD24.
9. Yu. S. Zavorotnii, A. O. Rybaltovskii, P. V. Chernov, V. N. Bagratashvili, S. I. Tsipina and L. Dong, to be published
10. P. J. Lemaire, R. M. Atkins, V. Mizrahi and W. A. Reed, Electron. Lett. **29**, 1191 (1993).
11. B. J. Greene, D. M. Krol, S. G. Kosinski, P. J. Lemaire, P. N. Saeta, J. Non-Cryst. Solids **168**, 195 (1994).
12. B. Malo, J. Albert, K. O. Hill, F. Bilodeau, D. C. Johnson, Electron. Lett. **30**, 442 (1994).

Kinetics of defect centers formation and photosensitivity in Ge-SiO_2 fibers of various compositions

Tsung-Ein Tsai
Code 5612, Naval Research Laboratory, Washington, DC 20375 and Fiber & Electro-Optics Research Center
Virginia Polytechnic Institute
Blacksburg, VA 24061
Tel.: (202) 767-9515, Fax: (202) 767-6370

E. Joseph Friebele
Code 5612, Naval Research Laboratory, Washington, DC 20375
Tel: (202) 767-2270, Fax: (202)404-7085

It was reported that the Ge E' center is related to second harmonic generation (SHG) in Ge-SiO_2[1]. Since the Ge E' center is known as hole-trapping center, this suggests that the positive charge trapping sites for SHG in Ge-SiO_2 are Ge E' centers. However, in a later, detailed thermal stability study, we reported[2] that only a *variant* of the Ge E' center, i.e., Ge E'_{d1}, has thermal stability similar to SHG. This suggests that not all of the observed Ge E' centers are charged.

The growths of the photoinduced Ge E'_{d1} center concentrations in several types of Ge-SiO_2 fibers and preforms are shown in Fig. 1.

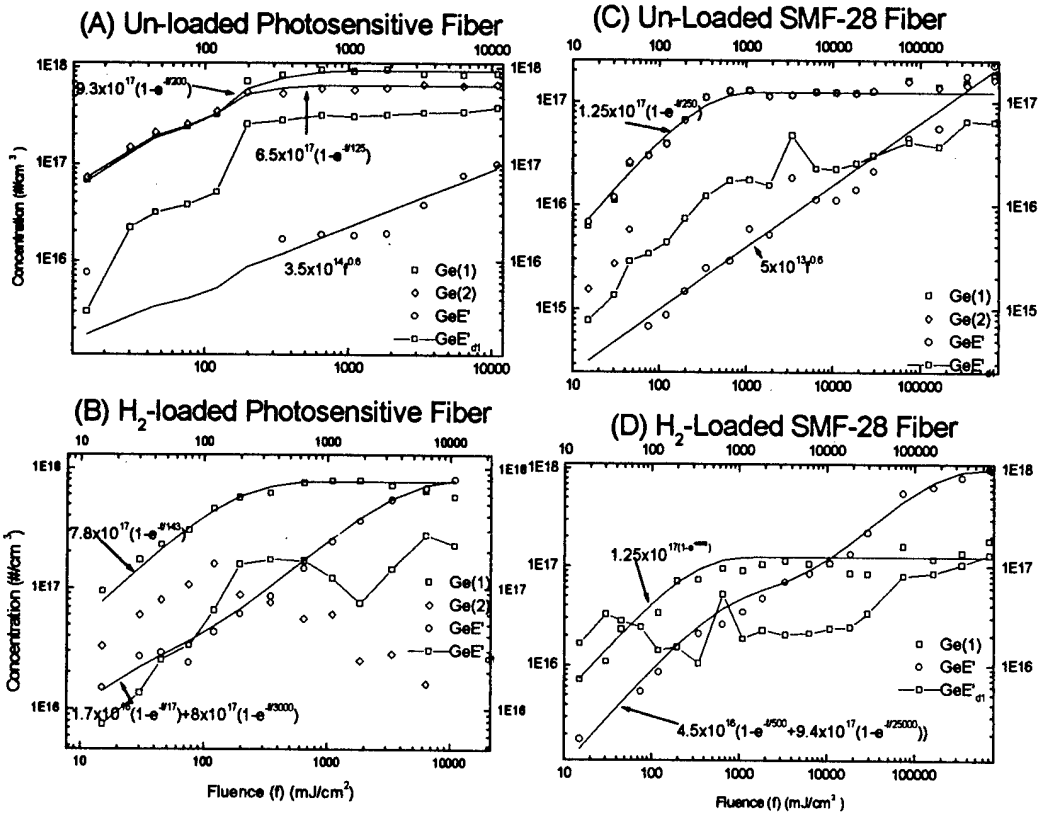

Figure 1. Growth of the Ge-related defect center concentrations in hydrogen loaded and unloaded fibers.

The data show that in all samples the photoinduced Ge E'_{d1} centers are correlated with electron trapping by Ge(1) and Ge(2) centers. These results further support the identification of photoinduced the Ge E'_{d1} center as a positive charge trapping site for SHG in Ge-SiO_2.

The index structure of fiber Bragg gratings (FBG's) in Ge-SiO_2 core optical fibers was recently reported[3] to consist of Ge E' centers, GeH centers, and photoinduced densification, in agreement with the previous report[2] that the thermal stability of FBG's is correlated with that of Ge E' centers. The enhanced formation of Ge E' centers in the presence of H_2 was proposed[4] to be due to the conversion of the 2-coordinated Ge oxygen vacancy defect, which has a 240 nm optical absorption band, to Ge E' centers. It is then expected that the photoinduced Ge E' center concentrations will be much greater in H_2-loaded fibers, which have a higher 240 nm band. In contrast, it is observed in Fig. 1 that similar concentrations of Ge E' centers are induced in both the photosensitive and SMF-28 H_2-loaded fibers even though the 240 nm band in SMF-28 is an order of magnitude less than in the photosensitive fiber. This result is evidence that the formation of Ge E' centers in H_2-loaded Ge-SiO_2 is not primarily from the bleaching of the 240 nm band. This, along with the photo-*generation* of Ge E' centers in H_2-loaded fibers at low fluence (in contrast to the photo-*bleaching* in unloaded fibers), suggests that Ge E' centers in H_2-loaded fibers are induced through the photoinduced reaction of H_2 with Ge-SiO_2.

It is then likely that Ge E' centers in H_2-loaded Ge-SiO_2 are mainly generated from GeH formed from the UV-induced reactions of H_2 and Ge-SiO_2. Since the concentration of H_2 can be as high as $10^{21}/cm^3$ fibers loaded at low temperature and, no H_2 diffusion needs to be involved in the photoinduced reaction of H_2 with Ge-SiO_2 to form GeH. It is then expected that the photo-generation of Ge E' centers is non-dispersive in H_2-loaded fibers. This behavior is seen in Fig. 1 where the growth kinetics of the Ge E' centers are non-dispersive and consist of two saturated exponentials. Similarly, as shown in Fig. 2 for the photosensitive, H_2-loaded fibers, the growth of Δn of the FBG's consists of two saturating exponentials with the saturation of the first occurring around 100 mJ/cm^2. This provides additional support for the conclusion that Ge E' centers are responsible for the Δn of FBG's, as we previously reported[2,3].

The contribution of Ge E' centers to Δn of FBG's is believed to be due to their optical absorption in the UV-region through the Kramers-Kronig relationship (color center model). The >2 μm diffusion length of electrons photoinduced by a KrF laser to be reported[5] at the OSA annual meeting (Oct. 12-17, 1997, Long Beach, CA) suggests that Ge(1) and Ge(2) centers contribute through their optical absorption[6] to the uniform component of the index structure of the FBG.

The growth kinetics of Ge(1) and Ge(2) centers are found to be saturated exponentials with similar saturated concentrations in both loaded and unloaded fibers (see Fig.1). This suggests that the generation of Ge(1) and Ge(2) centers has nothing to do with photoinduced reaction of H_2, in agreement with the proposal[7] that Ge(1) and Ge(2) centers result from electron trapping. The non-dispersive generation kinetics and >2 μm diffusion length of electrons to be reported[5] suggests that the electrons are trapped from the conduction band of Ge-SiO_2

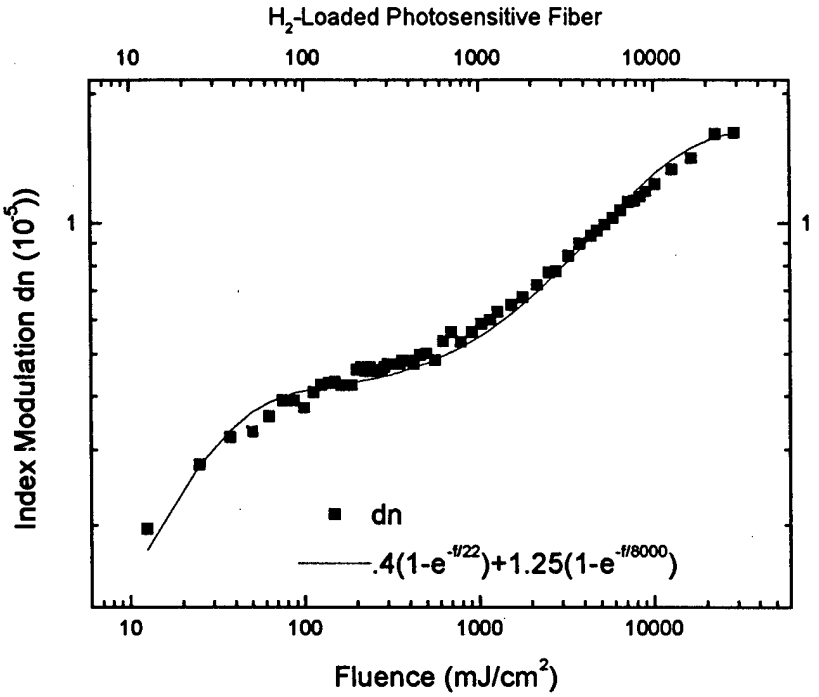

Figure 2. Growth of the index modulation of FBG's in hydrogen-loaded, photosensitive fiber vs. laser fluence (points) and fit of the data to the sum of two saturating exponentials (line).

1. T. E. Tsai, M. A. Saifi, E. J. Friebele, D. L. Griscom and U. Ôsterberg, Opt. Lett. 14, 1023 (1989).

2. T. E. Tsai, E. J. Friebele and D. L. Griscom, Opt. Lett. 18, 935 (1993).

3. T. E. Tsai, G. M. Williams and E. J. Friebele, Opt. Lett. 22, 224 (1997).

4. K. Awazu, H. Onuki, and K. Muta, "Mechanisms of photo-bleaching of 5 eV absorption band in hydrogen loaded Ge-doped SiO_2", paper PMA3-1, Photosensitivity and quadratic nonlinearity in glass waveguides-fundamentals and applications, Optical Society of America, Sept. 9-11, 1995, Portland, Oregon.

5. T. E. Tsai, G. M. Williams and E. J. Friebele, "Uniform component of index structure in Ge-SiO_2 fibers, Oct. 12-17, 1997, OSA Annual Meeting/ILS-XIII, Long Beach, CA.

6. E. J. Friebele and D. L. Griscom, Mat. Res. Soc. Symp. Proc. 61, 319 (1986).

7. T. E. Tsai, D. L. Griscom and E. J. Friebele, Diffusion and Defect Data, 53-54, 469 (1987).

Photosensitivity of oxygen deficient type bulk silica and fibers

J.W. Lee, G.H. Sigel, Jr.
Fiber Optic Materials Research Program, Rutgers, The State University of New Jersey, Piscataway, NJ 08855

Jie Li
SpecTran Specialty Optics Company, Avon, CT 06001, jwlee@rci.rutgers.edu

With the development of fiber gratings, the investigations of optical phenomena induced by UV-laser irradiation such as the photosensitivity of silica-based glasses and optical fibers have been areas of active research. The severe conditions implicit in the fiber fabrication process including high melting temperatures, shear stress, neck down and rapid quenching were found to generate structural defects that are different from those present in bulk rods. Subsequent exposure of the fibers to UV-laser radiation therefore results in the modified photosensitivity of the drawn fibers. In this study, the effects of UV excimer laser (KrF) irradiation on the optical properties of silica fibers are compared to bulk rods from which they have been drawn.

Mode Profile Modification of H Beam-Implanted Waveguides Using UV Processing

J. Canning[1], M. L. von Bibra[2], A. Roberts[2]
[1]*Australian Photonics Cooperative Research Centre, Optical Fibre Technology Centre, University of Sydney, 101 National Innovation Centre, Eveleigh, Sydney, NSW 1430, Australia*
[2]*School of Physics, University of Melbourne, Parkville, Melbourne, Victoria 3052, Australia*

UV photosensitivity in planar waveguides has primarily concentrated on the generation of sufficient oxygen-deficient centres using germanosilicate glass. There exists a wide range of methods fo fabricating such glasses, all with varying degrees of photosensitivity. Empirically, in planar waveguide at least, the degree of photosensitivity seems to be closely related to the defect induced losses such a increased Rayleigh scattering. For example, waveguides fabricated using flame hydrolysis exhibit very low propagation losses indicating a high level of purity of the glass. Consequently, this material requires sensitisation with hydrogen in order to achieve sizeable index changes with uv irradiation [1]. On the other hand, recent developments have allowed the demonstration of ultra-strong Bragg gratings in unsensitised PECVD-based glass [2], although at the expense of significantly higher propagation losses. A somewhat more impressive demonstration of photosensitivity has been the demonstration of direct waveguide writing with a mercury lamp in organically-derived glass using sol-gel methods [3]. By incorporating organic components into the glass silica polymer matrix, index change is achieved through polymerization of the organic ends which is a substantially different mechanism to that relying upon oxygen deficient centre absorptions. Low propagation losses, whilst maintaining a large photosensitivity, have been achieved this way. In addition to these materials, strong uv photosensitivity has also been observed in ion beam implanted material, mainly with Si^{2+} and Ge^{3+} implanted germanosilicate glass [4,5] although some work has been reported on changes in the uv spectra of H^+ implanted germanosilicate waveguides [6].

In this paper, we examine the properties of waveguides made with H^+-implantation of high quality silica glass and subsequently exposed to 193nm light. No germanate species are present. The rationale for previous ion implantation work in silica was to establish a large number of defects through bond breaking as the heavier Si^{2+} and Ge^{3+} ions bombard the glass to form a large number of oxygen deficient centres. This increases the uv absorption which generates, through further bond breaking or bond rearrangement, new defect species that should give rise to large negative index changes via the Kramers-Kronig relations [5]. Despite these large changes no Bragg gratings have been reported, raising the possibility that these negative index changes may not be localised to the irradiated area (on the scale of a micron). If correct this would have significant implications for the proposed mechanism. In order to investigate the requirements for photosensitivity in ion-implanted material, it was decided to examine changes upon irradiation, if any, to the mode profile of waveguides formed by implanting H^+ ions into pure silica glass with very few defects present. The energies of the implanted material are sufficient to induce impact damage. This damage will generate a number of defects, depending on the dosage and energy of the ions. Some of these may be capable of undergoing uv photolysis leading to similar index changes to those reported previously. The magnitude of these changes may be substantially less since the substrate is free of oxygen deficient centres and it is unlikely that the H^+ bombardment will generate quantities equivalent to those expected for the heavier species [4,5]. Further, the absence of germanate glass should result in less photosensitivity [4]. In practice, we have observed a significant index change of ~10% of the core-cladding difference. Further, the difference is more pronounced in the vertical axis of the waveguide suggesting that the uv processing is asymmetric in these samples.

The substrate chosen in this work was Suprasil glass which has negligible absorption in the uv. The ion dosage used was ~$1x10^{16}$ ions/cm^3 which leads to an induced $\Delta n \sim 0.003$ along the 2mm long guides [7]. Generally, these guides tend to have a cross-section where the waveguide width is twice as large as the vertical. An erbium-doped fibre amplifier was used as an unpolarised infrared source. TE and TM light was selected using an in-line fibre polariser providing >25dB contrast. The TE mode profile at 1.5μm, measured by monitoring the near-field profile of the guide on an infrared beam grabbing camera, is shown in figure 1a. The clean circular profiles indicate good single mode propagation with little difference between polarisation states despite the asymmetry of the waveguide cross-section.

The waveguides were subsequently irradiated with 193nm light from an ArF laser whilst the near

field image was monitored. After a fluence of ~1kJ/cm^2 the mode profile (shown in figure 1b) was collected and analysed in detail. Figure 2 shows the observed changes in the waveguide cross-section for both TE and TM light. The most dramatic change is in the vertical axis of the waveguide which may arise from a number of reasons including a greater sensitivity to field overlap since the guide dimensions is smaller along this axis. Alternatively, although most of the ions have passed through the surface during implantation and collected at the point where the ions have lost sufficient momentum to continue passing through the sample, some interaction usually occurs leaving a weak trail of induced change in the glass dielectric response from the surface to the guide. This region itself may also be affected by uv irradiation, leading to a greater decrease in effective index along the vertical direction. Nonetheless, this effect can be used to tailor the mode profile of the light exiting the sample. By designing the waveguide with an appropriate geometry initially (or even by orientating the sample), uv processing can be used to refine the profile into a more symmetric shape.

Since there was an apparent increase in mode size, white light spectra were taken of a similar waveguide sample during irradiation. The spectral resolution is low because of the insertion loss of these particular samples. Figure 3 shows the differential spectra of the sample with increasing fluence (0.02-3kJ/cm^2). The induced attenuation measured is the difference in attenuation between the unprocessed guide and subsequent processing. It is evident that the attenuation in the infrared above the cut-off wavelength, determining single-mode and multi-mode behaviour, has increased substantially. The more tightly confined multi-mode wavelengths below cut-off show very little change although there is an induced weak absorption band centred at 780nm. At this stage the origin of this band is unclear.

From the changes in the mode cross-section it is possible to make estimates of the induced negative index change. For these guides the analytic mode solution matching the intensity profile is best obtained using a inverse cosh fit which describes the shape of the guides [8]. By fitting a 1/cosh^2 profile to the intensity, I (x), the induced index change, Δn, can be related to the average index, n_s, of the guide as [7]:

$$I = \frac{1}{\cosh^{2\eta}(2x/h)} \quad where \quad \eta = \frac{1}{2}(\sqrt{1+v^2}-1), \quad v = kh\sqrt{2n_s\Delta n}$$

n_s is the cladding index, h is the guide width and x is the position along the axis being analysed. Using this approximation, the induced index change is estimated to be as large as 10% of the core/cladding difference. Given reasonably sized index changes, capable of exceeding 10% of Δn, one application of this is to enhance mode matching between imperfect waveguides. An attempt was made to write Bragg gratings through a phase mask using an identical setup to that reported in [2] where gratings exceeding 35dB were easily produced in PECVD glass. No gratings were able to be formed in this material leading us to suspect that the induced index changes may be macroscopic in origin, triggered by localised uv-induced defects. To date, the ability to achieve localised negative index change on the micron scale required for strong Bragg gating formation has only been reported for fibre gratings where a so-called "type IIa" grating phenomena is observed [9]. Consequently, further work needs to be done to establish the reason we have been unable to produce such gratings in our material.

In conclusion, we have demonstrated negative index changes ~10%of the core-cladding refractive index difference in H^+ implanted buried waveguides formed within uv transparent silica glass containing no germanate species and with very few defects present initially. These changes are sufficiently large to allow tailoring of the modes for applications such as mode coupling.

[1] G.D. Maxwell & B.J. Ainslie, Electron Lett., 31, p95, 1995
[2] J. Canning et al., Electron Lett., 32,p1479, 1996
[3] P. Coudray et al., Opt. Eng., 36, (4), p1234, 1997
[4] J. Albert et al., Opt. Lett., 17, p1652, 1992
[5] M. Verhaegen et al., Nuc. Instr. Meth. In Phys. Res. B, (106), p438, 1995
[6] Kyle et al., J. Appl. Phys., 77, p1207, 1995
[7] A. Roberts & M.L. von Bibra, J. Lightwave Tech., 14, p2254, 1996
[8] M.L. von Bibra & A. Roberts, J. Lightwave Tech., Accepted Jun 1997
[9] Xie et al., Opt. Comm., 104, p185, 1994

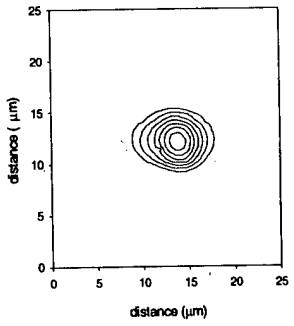

Figure 1a: TE mode profile before 193nm irradiation

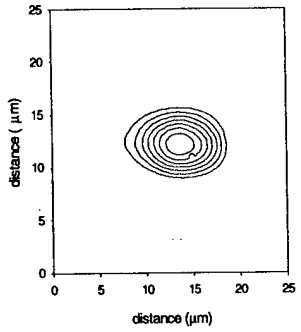

Figure 1b: TE mode profile after uv irradiation.

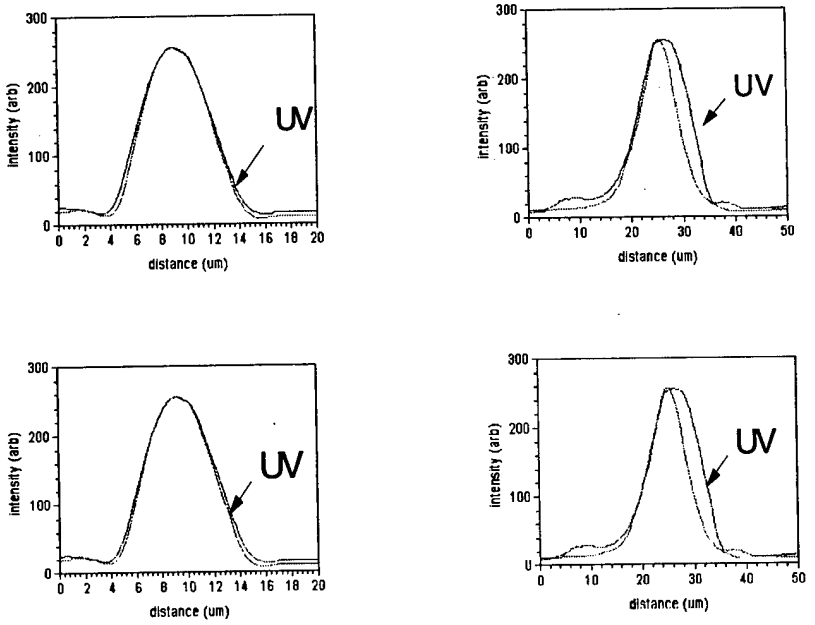

Figure 2: Horizontal (left) and vertical (right) intensity cross-sections of TE (top) and TM (bottom) modes.

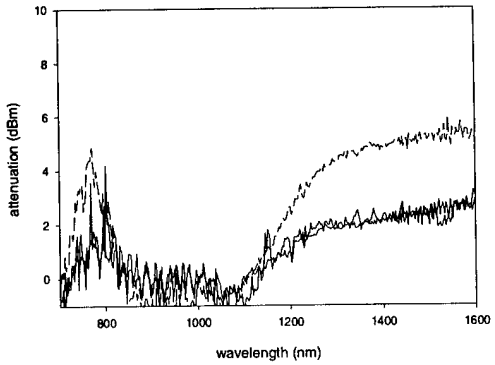

Figure 3: UV-induced attenuation spectrum of H^+ waveguide. Attenuation increases in the infrared.

Large refractive index changes observed in silicon implanted silica exposed to high cumulative doses of ArF laser light

M. Verhaegen, J.L. Brebner

Groupe de recherche en physique et technologie des couches minces, Physics Departement, Université de Montréal, P.O. Box 6128, Station Centre-Ville, Montréal, Québec, H3C 3J7

Tel : (514) 343-6111 (ext. 4209) ; Fax : (514) 343-2071

J. Albert

Communications Research Centre, P.O. Box 11490, Station H, Ottawa, Ontario, K2H 8S2

Tel : (619) 990-7690 ; Fax (613) 993-7139

1. Introduction

Used extensively in optical fibers technology, the change in refractive index produced by ultraviolet light in photosenstive silicate glasses is still not fully understood. Ion implantation is the only technique able to make photosensitive pure silica waveguides by the introduction of bleachable color centers and compaction of the matrix. After 100 pulses of 100mJ/cm^2 of ArF bleaching, changes in the refractive index were found to be in good quantitative agreement with the changes in absorption of the bands induced by implantation between 5 and 8 eV. Index of refraction and absorption measurements of higher cumulative doses of ArF laser light as well as a Kramers-Kronig analysis are reported.

2. Experimental

High purity silica SUPRASIL-2 samples ([OH] : 900-1200 ppm) were implanted with 5MeV silicon ions (Si^{2+}) at room temperature in a vacuum of 10^{-7} Torr using the Université de Montréal 6 MeV Tandem accelerator. Under these conditions the expected range of the ions is 3.3 μm below the surface with a longitudinal straggling of 0.25 μm. In order to minimize the background vacuum ultraviolet optical absorption from the 500 μm thick substrate, all the samples were thinned to 100 μm by chemical etching after implantation. The implanted samples were subsequently exposed to 20 ns pulses of 6.4 eV (193 nm) ArF excimer laser light (Lumonics EX 500) with 100 mJ/cm^2 per pulse. The repetition rate at early stages of bleaching was 1 or 2 pps in order to avoid possible thermal annealing of the implanted material. The optical absorption measurements were carried out in the visible-UV region using a Cary-5 spectrophotometer and in the vacuum UV using a VM-502 spectrophotometer from Acton Research. Index changes in the implanted region were measured at 589 nm using an Abbe refractometer.

3. Results and discussion

Silicon implantation in high purity silica creates optical absorption bands above 3 eV. The major bands $B_2\alpha$ (5.06eV), E'_1 (5.85eV), D (7.15eV) and E (7.6eV) are presented in figure 1. The D_0 (4.8eV) band is responsible for the low energy tail while the high energy tail observed above 8 eV may be due to the change of the absorption edge of silica upon compaction. These absorption bands are almost completely bleached after 5 kJ/cm^2 of ArF laser light. At the same

time a blue shift of the high energy tail is observed. However it is apparent that the ArF bleaching of the E'_1 band is not complete. This effect is most probably due to the creation of E' centers by high cumulative UV doses in the silica substrate of 100 μm. The bleaching of the 7.6eV band with 5 kJ/cm^2 and 15 kJ/cm^2 of ArF laser light is a good indication of a two photon absorption process as the absorption coefficient is zero at 6.4 eV, the laser photon energy.

Defect concentration related to an absorption band can be calculated from the peak amplitude, width, oscillator strength and refractive index using Smakula's equation. The unknown oscillator strength of the 7.15 eV band was assumed to be 1. The peak amplitudes were obtained using a 5 Gaussian lineshape peak fitting procedure with fixed centers and widths. The high energy tail was fitted with a simple exponential function. Figure 2 shows the evolution of the four major defect concentrations with ArF bleaching. Defects related to the $B_2\alpha$ (5.06eV) band, E'_1 (5.85eV) band and D (7.15eV) band are rapidly bleached after 50 J/cm^2 compared to the case of the E (7.6eV) band defects. The creation of E'_1 centers in the silica substrate is most probably responsible for the increase in the numbers of the E' centers above 50 J/cm^2. The bleaching of the unrelaxed oxygen vacancy centers associated with the $B_2\alpha$ band is also strongly correlated with the D band defects.

A Kramers-Kronig analysis was carried out in order to compare the changes of refractive index calculated from absorption measurements with the change of refractive index measured with the Abbe refractometer. Figure 3 shows that the Kramers-Kronig analysis is in good quantitative agreement with the experimental data up to a U.V. light cumulative dose of 50 J/cm^2. The D band is responsible for 46% of the refractve index change while the E'_1 band and the E band produce 22% and 18% index change respectively. At higher doses the measured refractive index change is twice the refractive index estimated by the Kramers-Kronig analysis. The high energy tail of the absorption spectra suggests that this discrepency is due to a change of optical absorption above 8 eV. In particular, the excess measured induced index could be due to bulk relaxation of the glass which would also yield the observed blue shift of the absorption edge. The relaxation would imply a surface height change of 10 nm which is the limit of the precision of our measurements.

4. Conclusion

Up to a cumulative dose of 50 J/cm^2, the Kramers-Kronig analysis based on the optical absorption estimates correctly the measured refractive index changes. For higher cumulative UV light doses, the color centers bleaching cannot explain the observed refractive index changes which must be due to a more fundamental phenomenon like the relaxation of the implanted silica matrix under UV light exposure. These results can be related to the photosensitivity phenomenon in optical fibers that is observed only with high cumulative dose of U.V. light.

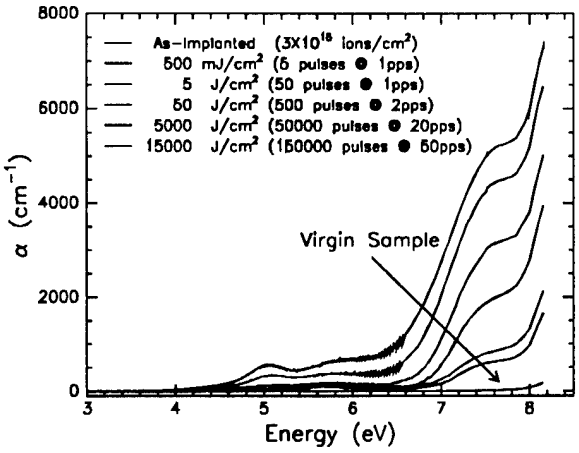

Fig. 1. Absorption spectra of implanted silica at different stages of ArF bleaching. The energies appearing in the legend are the cumulative energies delivered to the samples.

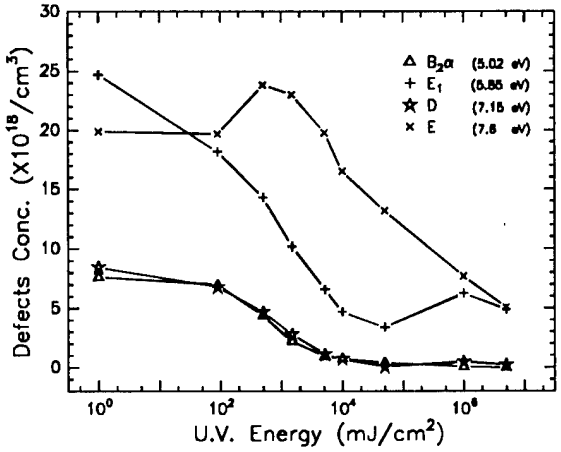

Fig. 2. Defect concentrations associated with the absorption bands as a function of the cumulative energies delivered to the samples. The name and position of corresponding bands appears in the legend.

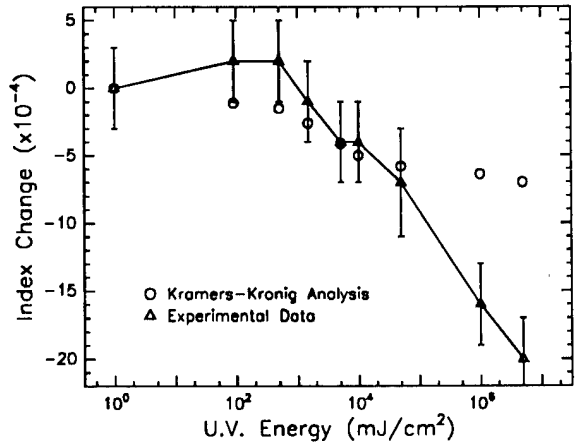

Fig. 3. UV-induced refractive index change measured at 589 nm as a function of the cumulative energy delivered to the samples.

Vacancies in as-grown and electron irradiated α-SiO_2

S. Dannefaer, D. Craigen, D. Kerr
Department of Physics, University of Winnipeg, Winnipeg, Canada R3B 2E9

Positron annihilation is a technique uniquely suited to detect vacancies independent of whether they are EPR active or not. In α-SiO_2 it has long been suspected that EPR inactive precursors should exist for the E' centre. Here we show that vacancies are indeed present in as-grown α-SiO_2 at a concentration of ~10^{17}/cm^3. About 1000 °C these vacancies migrate whereup they form vacancy clusters. 2 MeV electron irradiation introduces additional vacancies but at a highly nonlinear rate. The introduction rate decreases abruptly by a factor of 5 around a dose of $10^{17}e^-$/cm^2. The irradiation-produced vacancies are annealed out at 500 °C well below that for the vacancies in the as-grown α-SiO_2. We ascribe the 500 °C annealing stage to recombination with interstitials closely associated with the irradiation-produced vacancies.

Molecular dynamics simulations of defects and excitons in glasses

L. René Corrales
Environmental Molecular Sciences Laboratory, Pacific Northwest National Laboratory[a]
Richland, WA 99352

The interaction of excited electrons and holes with defects in network semiconducting and insulating glasses is examined. Of particular interest is the diffusion of vacancy sites in oxide materials that can aggregate to form voids and eventually lead to the formation of nanoscale bubbles. This is a process that is known to occur in nuclear waste materials, but the mechanisms remain unclear. A radioactive decay event can release energy in the keV to MeV range that is dispersed amongst the emission of alpha-particles, beta-particles, and gamma rays (depending upon the radionuclide), and into the momentum of the remaining ion. The particle emission lead primarily to electronic excitation energies and self-trapped excitons, whereas the momentum on the ion leads to a recoil cascade. These processes lead to an abundance of bond breaking and topological rearrangement. During the lifetimes of these events, defects such as vacancies, peroxides and E' centers are formed, and also leads to the etching and formation of molecular oxygen. The underlying physics and chemistry of these processes are studied using a semi-empirical methodology specifically designed to examine amorphous networked materials. The method can be implemented in parallel to study large system sizes as required in the simulation of recoil cascades, and contains enough electronic information to model excited states that lead to the formation of excitons. An overview of the model approach and its application for determining the diffusion barriers of defects in the presence of excitons will be discussed.

[a] *Pacific Northwest National Laboratory is a multiprogram national laboratory operated by Battelle Memorial Institute for the U.S. Department of Energy under contract DE-AC06-76RLO 1830.*

Pulse Propagation in Gratings

Monday, October 27, 1997

Ian Bennion, Aston University, U.K.
Presider

BMB
8:00am–9:15am
Washington/Wilson Room

High intensity pulse propagation in fiber Bragg gratings

B. J. Eggleton*, R. E. Slusher, T. A. Strasser

Bell Laboratories, Lucent Technologies, Murray Hill, 07974 New Jersey, USA
*Phone: 908 582 3087, Fax 908 582 3260

C. M. de Sterke
School of Physics, University of Sydney, New South Wales 2006 and Australian Photonics Cooperative Research Centre, Australian Technology Park, New South Wales 1430, Australia.

I. Introduction

Recently we reported the first systematic experiments describing high intensity pulse propagation in fiber Bragg gratings [1-3]. These experiments demonstrated nonlinear pulse compression, and pulse shaping, and also demonstrated the generation and propagation of *grating solitons* [1], which exist because of the balancing of nonlinearity of the glass and the strong dispersion of the grating [4-6]. Possibly the most striking feature of these solitons is that they can travel at velocities between zero and the speed of light in the medium. Indeed initial experimental, which were performed in uniform (unchirped) gratings, indicated that the solitons propagated at about 75% of the speed of light in the uniform medium. In this paper we review the nonlinear optics of fiber gratings and in particular discuss the experimental realization of grating solitons. We also discuss two extensions of this work: launching of slow grating solitons in apodized fiber gratings; and experimental studies of modulational instabilities (MIs) in Bragg gratings. Finally we mention the possibility of soliton engineering, through the design of nonuniform gratings.

II. Experimental considerations

Although nonlinear gratings has attracted mainly theoretical attention for a decade, it has been the remarkable technological advances in fiber gratings that have permitted experimental confirmation. In particular the ability to write long uniform and apodized fiber gratings using the phase mask scanning technique [7,8] has been central to these experiments. The transmission spectrum of a 5cm apodized fiber grating centered at 1052nm is shown in Fig 1(a). Very high intensities are required and thus we used a modelocked/Q-switched YLF laser which generates 100ps pulses at 1053nm with peak powers in excess of 20kW (see Fig 1(b)). Pulses were coupled into the fiber (Area=20μm) using a microscope objective resulting in peak intensities as high as 100GW/cm^2. After propagation the transmitted intensity was spatially filtered removing cladding modes and detected using a fast photodiode (res. 20ps). Given the fixed wavelength of the YLF laser we strain tuned the grating using a precision mechanical translation stage.

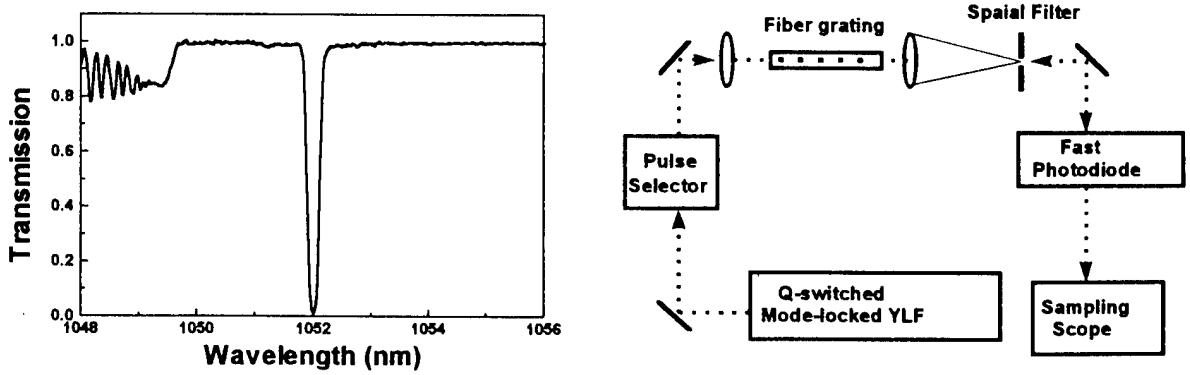

Figure 1: (a) Transmission spectrum of 5cm apodized grating and (b) schematic of nonlinear grating experiment utilizing high power ML/QS YLF laser.

III. Launching slow grating solitons in apodized fiber gratings

Apodization is known to remove sidelobes in the reflection spectrum and is usually thought of in the context of WDM communications [8]. Apodisation leads to reducing in- and out- coupling effects of light into the grating which is highly desirable for launching slow grating solitons. Fig 3(a) shows the transmitted intensity for an input intensity of 40GW/cm^2 when the grating was tuned such that the incident pulses was aligned with the lower edge of the reflection band. The dashed line represents the detuned pulse (FWHM 100ps) and the solid line represent the soliton pulse which is compressed substantially (FWHM 30ps) and retarded by 200ps, corresponding to an average velocity of less than 60% of the speed of light in glass. This represents a significant improvement on our previously published results [1]. Fig 3(b) illustrates the observed nonlinear compression; at low intensities the pulses is dispersed whereas at high intensities the transmitted pulse is significantly compressed associated with the formation of a grating soliton.

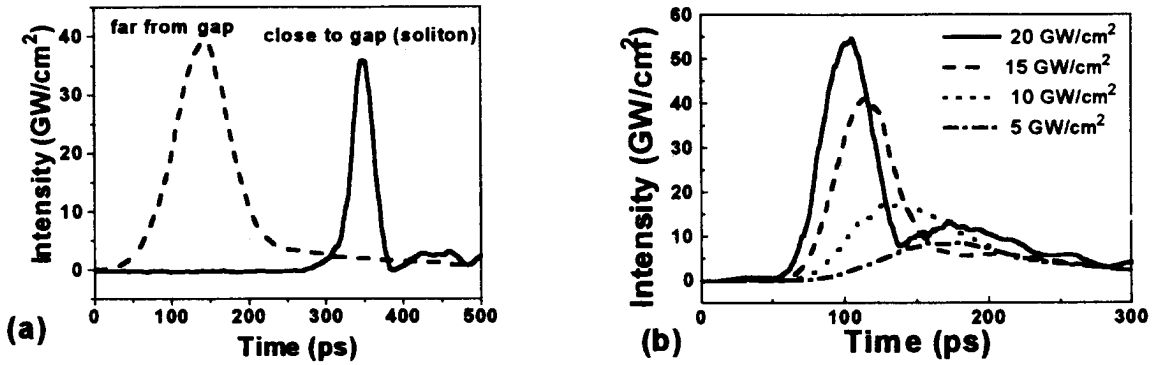

Figure 2: (a) Slow grating soliton propagation, with an average velocity of 60% of the speed of light in glass and (b) transmitted intensity for different input intensities.

IV. Modulational instability in Bragg gratings:

It was found experimentally that at high intensities (I>40GW/cm^2) the output consisted of a train of short pulses as shown in Fig 3; the transmitted intensity consists of a periodically spaced train of soliton-like pulses. Numerical simulation reveal that this is a particular example of the more general behavior of Bragg gratings in which multiple solitons are generated through a MI. Moreover because the dispersion is frequency dependent the number of pulses generated can be varied by adjusting the strain. Such a device could form a key component in future optical communication systems for such applications as short pulse generation.

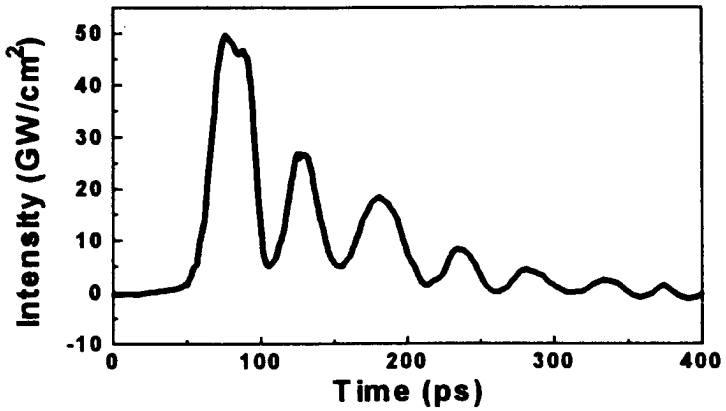

Figure 3: Multiple soliton generation associated with modulational instability (I=50GW/cm^2).

V. Soliton engineering

Thus far we have considered the possibility of propagating grating solitons along gratings in which the dispersion is constant along the grating length. It can be shown that grating solitons act approximately as particles obeying classical Newton like equations; the potential is determined by the grating parameters, e.g. period or strength. This allows one to manipulate the soliton as if it was a charged particle, by suitable grating design; hence the term "soliton engineering." As an example consider a linearly chirped grating, corresponding to an effective potential increasing linearly with position. The behavior of the soliton will depend on the initial conditions. For certain initial conditions the particle (soliton) is reflected, while for others, the particle has sufficient energy to make it over the barrier. This is illustrated in Fig. 4, showing the input (solid) reflected (short dashed) and transmitted (long-dashed) intensity as a function of time. In the top figure a substantial fraction of the incoming light passes the barrier, while in the bottom figure, at a slight different frequency, all light is reflected.

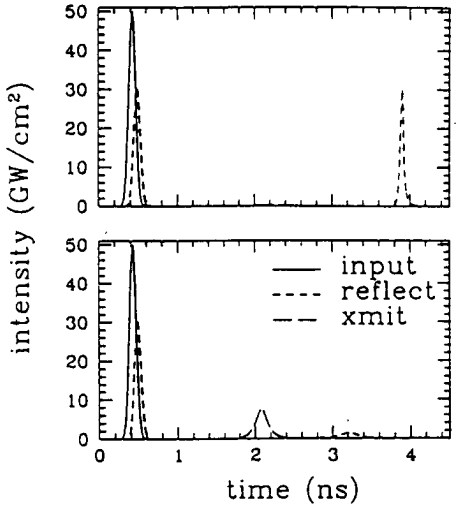

Figure 4. Numerical example of soliton engineering using linearly chirped fiber grating.

VI. Conclusion:

We have presented experimental resulting demonstrating high intensity pulse propagation in fiber gratings. In particular we have demonstrated the propagation of grating solitons with velocities less than 60% of the speed of light. Modulational instabilities in fiber gratings have been studied offering the possibility of a high repetition rate pulsed source. Finally we have considered soliton engineering with the aim of generating even 'slower light' and, through the use of nonuniform gratings, to control the details of its motion.

References:

[1] B. J. Eggleton, R. E. Slusher, C. M. de Sterke, P. A. Krug and J. E. Sipe, *Phys. Rev. Lett.* **76**, pp. 1627 (1996).

[2] B. J. Eggleton, C. M. de Sterke and R. E. Slusher, *Opt. Lett.* **21**, pp. 1223 (1996).

[3] B. J. Eggleton, C. M. de Sterke, R. E. Slusher and J. E. Sipe, *Elect. Lett.* **32**, 2341 (1996).

[4] H. G. Winful, *Appl. Phys. Lett.* **46**, 527 (1985).

[5] C. M. de Sterke and J. E. Sipe, ``Gap solitons," in Progress in Optics XXXIII}, E. Wolf, ed., (Elsevier, Amsterdam, 1994), Chap. III.

[6] A. B. Aceves and S. Wabnitz, *Phys. Lett. A* **141**, 37-42 (1989).

[7] J. Martin and F. Ouellette, *Electron. Lett.* **30**, 811 (1994).

[8] T. A. Strasser *et al.*, OFC'96, Postdeadline paper PD8, 1996.

Ultrashort Pulse Propagation Through Fibre Gratings: Theory and Experiment

L. R. Chen, S. D. Benjamin, P. W. E. Smith, and J. E. Sipe[†]
Department of Electrical and Computer Engineering, University of Toronto and
Ontario Laser and Lightwave Research Center
10 King's College Road
Toronto, Ontario, Canada M5S 3G4
Tel: (416) 978-0602 Fax: (416) 971-3020
[†]Department of Physics, University of Toronto

In-fibre Bragg gratings have numerous applications for optical communications and fibre optic sensors. Typically, grating-based devices and applications involve incoherent broadband sources, narrowband cw sources, or pulsed (quasi-cw) sources where the spectral bandwidth of the input pulse is narrower than that of the grating response. Propagation through fibre gratings for the above cases has been examined and is well understood.[1,2]

In this paper, we review theoretical results from our recent investigations[3] on the linear interaction between (coherent) ultrashort pulses and fibre gratings, for the case where the spectral bandwidth of the incident pulse is larger than that of the grating response, i.e. the ultrashort pulse response of fibre gratings. We also present preliminary measurements which experimentally verify the numerical simulations.

Theoretical calculations reveal that the ultrashort pulse response of fibre gratings is significantly different from and is more complex than the usual cw or quasi-cw cases.[3] In the simulations, we assume transform-limited picosecond (1 - 1.5 ps) Gaussian pulses as the ultrashort inputs (the FWHM bandwidths of the pulses range from 2 to 3.5 nm at 1.55 μm depending on the duration of the pulse and are considerably broader than those of the grating responses considered). Although the input is symmetric, the reflected and transmitted pulses take on different shapes and vary in duration, depending on the grating characteristics (length, index modulation, apodization, chirp, and phase response).

For uniform or linearly chirped gratings with weak index modulations ($\delta n \approx 5\times10^{-5}$), the reflected pulse has a square-like profile with a duration equal to the round-trip propagation time through the grating; no prominent differences between the input and transmitted pulses are observed. On the other hand, for strong index modulations ($\delta n \approx 3\times10^{-4}$), there is considerable shaping of both the reflected and transmitted pulses. Specifically, there is a separation of the reflected pulse into two distinct components, a main reflection peak and transient oscillatory subpulses, that are spaced apart by the round-trip propagation time through the grating. The transmitted pulse also takes on an oscillatory structure that becomes more pronounced for stronger index modulations.

The mathematical calculations to determine the ultrashort pulse response are straightforward; however, they do not provide physical insight into the dynamics of the response. In order to yield such insight, we have qualitatively described the features of the ultrashort pulse response using physical arguments consistent with the properties of the gratings.[3] Many of these features can also be explained by examining the spectral contents in the different components of the reflected (or transmitted) pulse and correlating them with grating properties. For example, for the reflection from uniform or linearly chirped gratings with strong index modulations, the main reflection peak primarily consists of spectral components associated with the stop band of the cw grating response while the transients are composed of the sidelobe frequencies. By examining the reflected delay time versus frequency characteristics for these gratings, we find that frequencies in the grating stop band are reflected well before those in the sidelobes. This explains the separation between the main reflection peak and transient subpulses. The oscillatory nature in the transients

is due to a beating of the sidelobe frequencies which are symmetrically spaced about the Bragg wavelength (small linear chirps result in slight asymmetries of the beating effects). The period of the oscillations slowly increases, corresponding to a beating of frequencies closer to the Bragg wavelength (closer to the grating stop band). This is also consistent with the dispersive or reflected delay time characteristics of the gratings: sidelobe frequencies farther from the stop band travel faster, and hence are reflected before, those closer to the stop band.

We compared the theoretical calculations with experimental measurements for a linearly chirped grating. The grating characterized was fabricated in AT&T Accutether fibre using the phase mask technique and had a peak reflectivity of $R \approx 0.99$ and spectral BW $\Delta\lambda = 0.45$ nm at $\lambda = 1550.9$ nm. From the best-fit curve (obtained using standard coupled-mode theory) to the measured spectral response, we approximate the grating to have a length $L = 10.0$ mm, a peak index modulation of $\delta n = 3.5 \times 10^{-4}$, and a chirp of 0.0195 nm/mm.

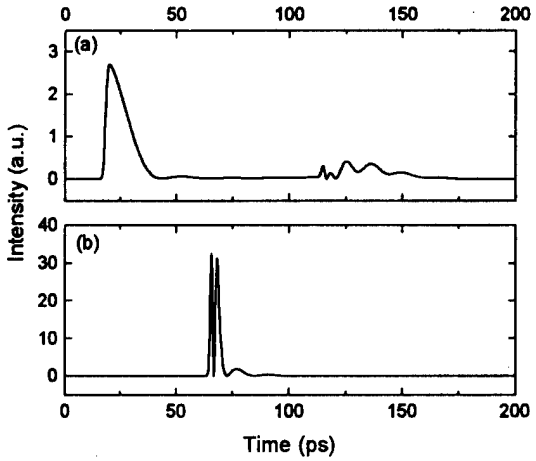

Fig. 1—Calculated (a) reflected and (b) transmitted pulses from grating being characterized. The input is a transform-limited 1.5-ps Gaussian pulse.

Using the above parameters, we calculated the corresponding reflected and transmitted pulses from the grating, depicted in Fig. 1, assuming a transform-limited 1.5 ps Gaussian input pulse tuned to the Bragg wavelength of the grating.

The experimental setup for measuring the reflected and transmitted pulses from the fibre grating is illustrated in Fig. 2. The transform-limited 1.5 ps Gaussian input pulse tunable around 1.55 μm, is generated using a Ti:Sapphire pumped optical parametric oscillator.[4] The reflected or transmitted pulse from the fibre grating is measured by cross-correlation using the picosecond pulse as the reference. Our approach differs from the use of auto-correlation previously reported in Ref. 5 and avoids problems of extracting the reflected pulse duration or shape from the auto-correlation data. Specifically, our measurements clearly show features that are characteristics of the complex nature of the ultrashort pulse response.

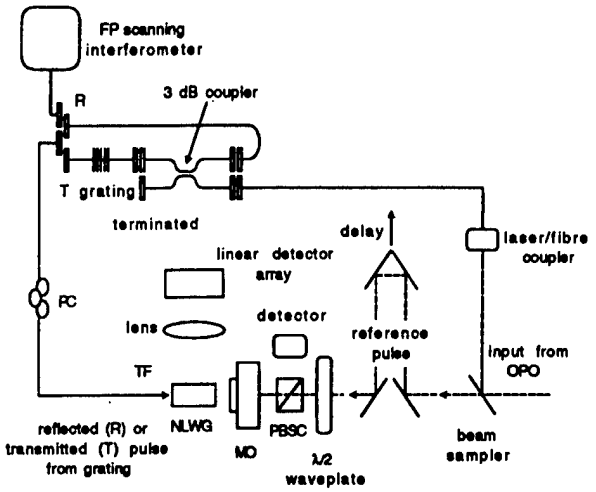

Fig. 2—Experimental configuration for measuring the ultrashort pulse response (TF = tapered-fibre; PC = polarization controller; NLWG = surface-emitting nonlinear waveguide; OPO = optical parametric oscillator; MO = microscope objective; PBSC = polarizing beam splitter cube).

The optical correlator is a surface-emitting semiconductor multi-layer ($Al_{0.8}Ga_{0.2}As/GaAs$) nonlinear waveguide grown on a (100) GaAs substrate.[6] When two cross-polarized counter-propagating signals are launched into the waveguide, they interact through its second-order susceptibility and generate a surface-emitted second harmonic (SH) signal. This SH output describes the cross-correlation of the two input signals with a time compression of 2.[6] The length of the waveguide sample is approximately 5.0 mm which corresponds to a time window of 102 ps, after the time compression factor of 2 is taken into account (the effective mode index of the nonlinear waveguide is 3.077).[6]

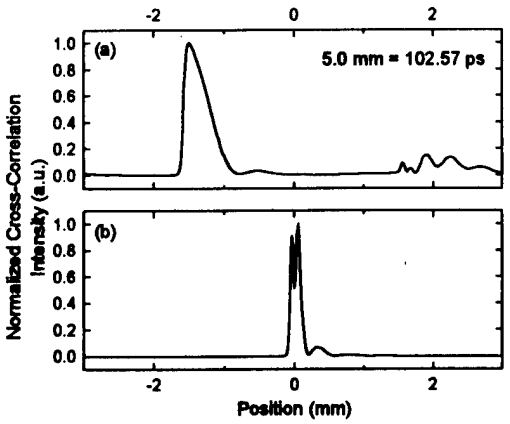

Fig. 3—Calculated cross-correlation with a 1.5-ps Gaussian pulse of (a) reflected and (b) transmitted pulse (i.e. the pulses of Fig.2) from the fibre grating being characterized.

We calculated the cross-correlation of the reflected and transmitted pulses from the fibre grating with the 1.5-ps Gaussian pulse as the reference (see Fig. 3). The experimentally measured reflected and transmitted pulses (with the input pulse tuned to Bragg wavelength of the grating) are shown in Fig. 4. In the experiments, the average power coupled to the fibre grating was less than 5 mW so that no non-linear effects were observed. The measurements are in excellent agreement with the theoretically predicated responses and the main features of the ultrashort pulse response are discernible. For the reflection, there is clearly a transient subpulse which is approximately spaced by the round-trip propagation time through the grating from the main reflection peak, while in transmission, a dip in the main transmitted pulse is apparent in addition to the trailing pulse. However, some finer details are suppressed. Specifically, the oscillatory nature of the transient subpulses in the reflection are not resolved, nor are the two peaks in the transmitted pulse. This is due to the duration of the reference pulse and we expect improved resolution in the cross-correlation if a shorter reference pulse is used.

In summary, we have theoretically and experimentally investigated the ultrashort pulse response of fibre gratings. Measurements of the temporal response of transform-limited picosecond Gaussian pulses reflected and transmitted from a linearly chirped fibre grating are in excellent agreement with theoretical calculations. We are currently measuring the ultrashort pulse response of additional and more complex grating structures.

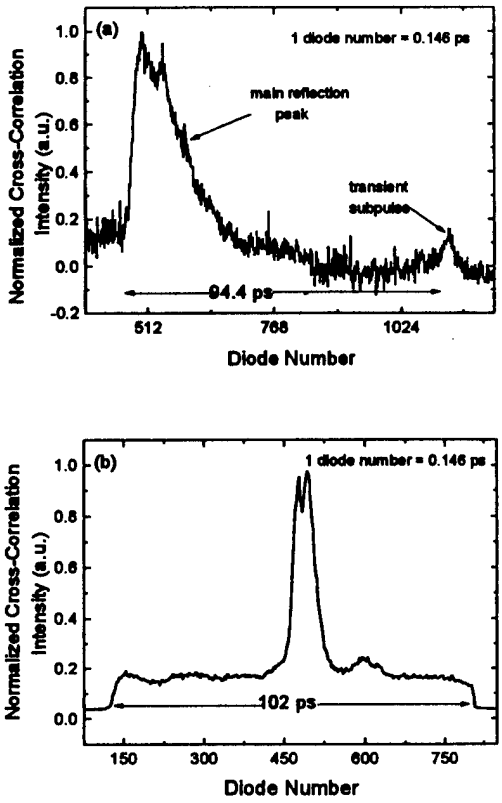

Fig. 4—Experimentally measured (a) reflected and (b) transmitted pulses.

References

1. D. Taverner, D. J. Richardson, J.-L. Archambault, L. Reekie, P. St. J. Russell, and D. N. Payne, Opt. Lett., **20**, 282 (1995).

2. J. E. Sipe, L. Poladian, and C. M. de Sterke, J. Opt. Soc. Amer. A, **11**, 1307 (1994).

3. L. R. Chen, S. D. Benjamin, P. W. E. Smith, and J. E. Sipe, "Ultrashort pulse reflection from fibre gratings: a numerical investigation," IEEE J. Lightwave Technol. (in press, 1997)

4. L. Qian, S. D. Benjamin, and P. W. E. Smith, Opt. Comm., **127**, 173 (1996).

5. K. Rottwitt, M. J. Guy, A. Boskovic, D. U. Noske, J. R. Taylor, and R. Kashyap, Electron. Lett., **30**, 995 (1994).

6. Y. Beaulieu, S. Janz, H. Dai, E. Frlan, C. Fernando, A. Delâge, P. van der Meer, M. Dion, and R. Normandin, Intl. J. Nonlinear Opt. Phys. And Materials, **4**, 393 (1995).

Nonlinear Self-Switching and Multiple Gap Soliton Formation in a Fibre Bragg Grating

D. Taverner, N.G.R. Broderick, D.J. Richardson, M. Ibsen.
Optoelectronics Research Centre, Southampton University, Southampton, SO17 1BJ, UK.
Tel: (UK)+ 1703 594524 Fax: (UK)+ 1703 593142

The interplay of the Kerr-induced nonlinear refractive index changes and dispersion in nonlinear Fiber Bragg Gratings (FBGs) leads to a plethora of nonlinear phenomena, the most striking of which is perhaps the formation and propagation of gap solitons [1]. Whilst a considerable amount of theoretical work has been performed in this area [1,2,3,4] experimental observations of nonlinear grating behaviour are limited, principally by the difficulty in getting sufficiently high power densities within the core of a FBG in a suitable spectral and temporal range. In order to reduce the nonlinear threshold for gap soliton formation one can use the somewhat weaker dispersive properties of FBGs outside of the band gap and indeed recent experiments have yielded the first strong evidence of Bragg grating gap soliton formation by this means [5,6]. However, the strongest and most manifestly nonlinear effects are predicted to occur at wavelengths within the band gap, close to the Bragg wavelength of the grating structure and it is therefore essential to make measurements within this regime. In this paper we report what we believe to be the first clear experimental observation of nonlinearity within the band gap of an FBG, namely nonlinear self-switching and, at higher intensities, multiple gap soliton formation.

Our experiments are made within the quasi-cw regime using nanosecond pulses of a physical length several times that of the FBG. Earlier theoretical work (see Ref[1] and reference therein) show that Bragg gratings under CW excitation should exhibit optical bistability within their band-gap. Stability analysis indicates that under certain operating conditions robust, bistable operation is obtained allowing for optical switching. In other operating regimes instability occurs resulting in the formation of periodic trains of gap solitons, that once formed propagate stably through the grating. The instability has been equated to some form of modulation instability [1,6].

The experimental set-up is shown in Fig.1. High power nanosecond pulses were coupled into a FBG through a polarising beam-splitter and quarter wave-plate arrangement that decoupled the incident and reflected signal pulses, allowing simultaneous measurements of the incident, transmitted and reflected beams. The placement of a $\lambda/2$ waveplate before this PBS allowed control of the power incident on the grating. The transmitted, reflected and incident signals were detected with a single-mode fibre coupled PIN photodiode and sampling oscilloscope. Our temporal resolution was ~50ps. The fibre grating was written into a germanosilicate fibre with a mode-area of $30\mu m^2$ (N.A.=0.25, λ_C=1250nm) using a moving fibre/phase-mask scanning beam technique [7]. The grating was 8cm long, unchirped, with a 0-π sinusoidal apodisation profile along its length. The grating had 98% reflectivity at its peak wavelength of 1536nm and was measured to have a transform-limited, 3dB bandwidth of 3.8GHz. The grating was mounted in a glass capillary and angle polished front and back to remove unwanted reflections from these surfaces. The high power pulses were obtained from a large mode area, erbium doped fibre amplifier chain seeded with ns pulses from a directly-modulated, wavelength-tunable, semiconductor DFB laser [8]. The source was capable of producing nanosecond pulses with energies >100μJ and peak powers >100kW at kHz repetition rates. For the purposes of this experiment the source was operated at 4kHz repetition rate giving 25μJ pulses with ≈2ns duration (see insert Fig.1). Note that the pulse is highly asymmetric due to amplifier saturation effects and has a sharp ~30ps feature on the leading edge due to chirp on the diode seed pulse. This feature becomes more prominent when examining the pulse transmission through the FBG with the pulse spectrum tuned to lie within the band-gap (see Fig 2, trace a). The chirped spike lies outside the band gap and is transmitted whereas the main body of the pulse is reflected (see Fig.3, trace a). Although aesthetically undesirable this feature actually proved a valuable calibration aid, giving a direct measure in the transmitted pulse time domain of the input pulse power. Note that the corresponding physical pulse lengths were significantly longer than the grating, we were therefore well within the quasi-cw regime and anticipated clean switching and the potential to

generate a significant number of gap soliton pulses. The pulse spectrum at the FBG input was measured to have a 3dB spectral bandwidth of 1.2 GHz, considerably less than the FBG bandwidth. The central wavelength of the source could be continuously and accurately temperature-tuned to wavelengths in and around the FBG band gap.

We set the source wavelength close to the short wavelength side of the center of the bandgap and examined the grating pulse transmission and reflection characteristics as a function of increasing peak power. The transmission results are summarised in Fig. 2. At low powers (Fig.2 trace a) the pulse is seen to be almost completely reflected from the grating other than our chirped rising edge marker. However as the pulse peak power is increased strong pulse reshaping becomes apparent. Fig.2 traces b-d show various stages in the growth of the nonlinearly transmitted pulses. Initially one gap soliton is formed (around 3kW peak power), however as the intensity is increased more solitons are generated. Each subsequent pulse then narrows to ~100ps and moves forward allowing additional pulses to form at the rear of the bunch. We observed the generation of up to 5 gap solitons in our experiments (Fig.2, trace d). Note that the absence of Raman scattering or other nonlinear spectral distortion was confirmed by direct spectral measurements. The corresponding effects of the pulse formation are readily observed in the reflected domain, see Fig.3 traces a-d where progressively larger 'chunks' of energy are seen to be switched from the front of the pulse.

We evaluated the percentage energy transmittance of the FBG as a function of peak power both by integration of the transmitted pulse forms and through direct measurements of the incident, transmitted and reflected average powers. Good agreement was obtained between the two approaches. The results are shown in Fig.4 where it is seen that the transmission switches from about 3% in the linear regime to a saturated level of about 40% for peak powers of ~4kW and above, representing ~11dB switching contrast. Note that the data presented in Fig.4 has been processed to eliminate the contribution of the chirped leading spike to the calculated total transmission.

In conclusion, we report the first observation of optical switching and multiple gap soliton generation within the bandgap of a FBG. Switching from 3% to 40% of the pulse energy is obtained for nanosecond pulses at internal field strengths of order 10-15 GW/cm^2. At higher intensities multiple gap solitons were obtained. We have experimentally observed the formation of up to 5 gap soliton with durations in the range 100-500ps. We believe these results to represent a significant step in the study of nonlinear FBG effects and indicate that the combination of high power fiber based 1550 nm sources, coupled to recent improvements in FBG fabrication techniques should allow for further advancements in such studies.

References:

[1] C.Martijn de Sterke, J.E. Sipe:'Gap Solitons', Progress in OpticsXXXIII, 1994, E. Wolf, ed., pp203-260, (Elsevier, Amsterdam, 1994).

[2] H.G. Winful, J.H. Marburger, E. Garmire: 'Theory of bistability in nonlinear distributed feedback structures', Appl. Phys. Lett., 1979, 35, 5, 379-381.

[3] W. Chen, D.L. Mills: 'Gap solitons and the nonlinear optical response of superlattices', Phys. Rev. Lett., 1987, 58, 2, 160-163.

[4] C.M. de Sterke, J.E. Sipe: 'Envelope-function approach for the electrodynamics of nonlinear periodic structures', Phys. Rev. A, 1988, 38, 10, 5149-5165.

[5] U. Mohideen, R.E. Slusher, V. Mizrahi, T. Erdogan, J.E. Sipe, M. Gonokami, P.J. Lemaire, C.M. de Sterke, N.G.R. Broderick: 'Gap soliton propagation in optical fiber gratings', Opt. Lett., 1995, 20, 1674-1676.

[6] B.J. Eggleton, C.M. de Sterke, R.E. Slusher, J.E.Sipe: 'Distributed feedback pulse generator based on nonlinear fibre grating', Electron. Lett., 1996, 32, 25, 2341-2342.

[7] M.J. Cole, W.H. Loh, R.I. Laming, M.N. Zervas, S. Barcelos: 'Moving fibre/phase mask-scanning beam technique for enhanced flexibility in producing fibre gratings with uniform phase mask', Electron. Lett., 1995, 31, 17, 1488-1490.

[8] D.Taverner, D.J. Richardson, L.Dong, J.E. Caplen, K.Williams, R.V. Penty: '158μJ pulses from a single transverse mode, large mode-area EDFA', Opt. Lett., 1997, 22, 6, 378-380

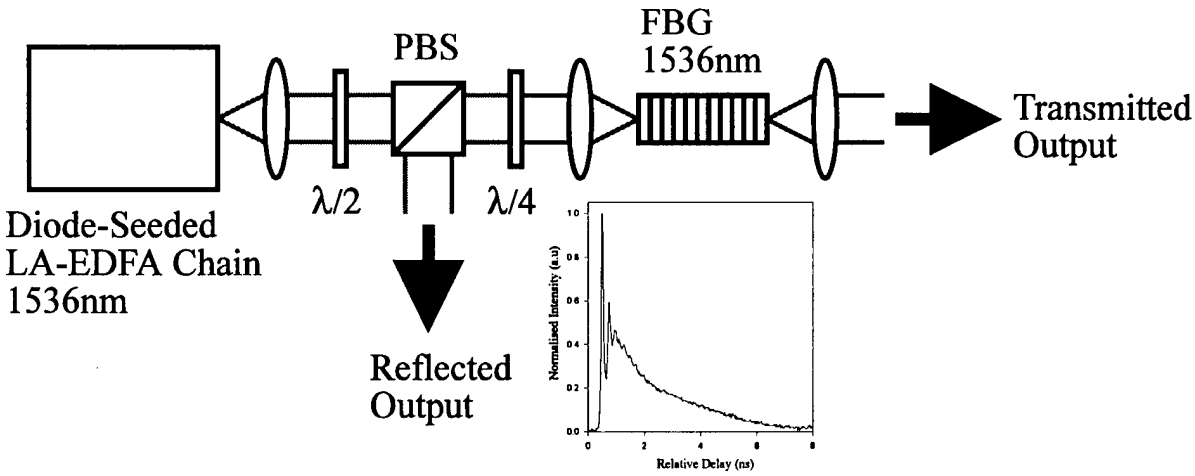

Figure 1: Experimental setup. LA-EDFA: Large mode-area erbium-doped fibre amplifier. PBS: Polarisation beamsplitter. FBG: Fibre Bragg grating. The pulse intensity profile incident on the grating is shown inset.

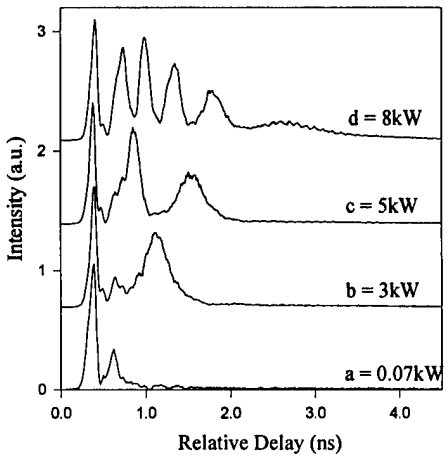

Figure 2: Transmitted pulse intensity profiles with increasing launched peak power from a-d. Each trace is normalised to a peak of 1.

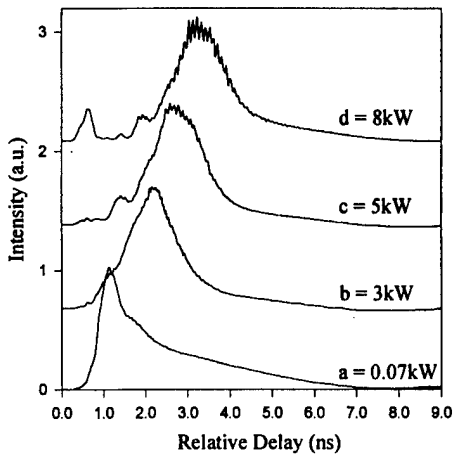

Figure 3: Reflected pulse intensity profiles with increasing launched peak power from a-d. Each trace is normalised to a peak of 1.

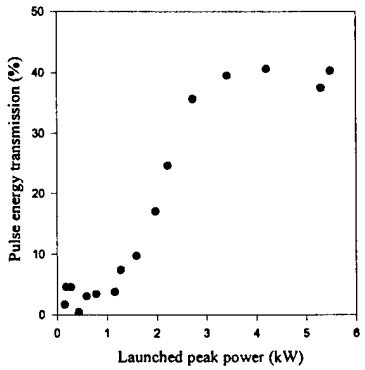

Figure 4: Percentage of pulse energy transmitted through grating.

The Optical Pushbroom in action

N. G. R. Broderick, D. Taverner, D. J. Richardson, M. Ibsen and R. I. Laming
Optoelectronics Research Centre, University of Southampton, Southampton, SO17 1BJ, UK.
Phone: +44 (0)1703 593144, Fax: +44 (0)1703 593142, email: ngb@orc.soton.ac.uk

1. Introduction

The area of nonlinear pulse interactions in Bragg grating structures, although largely unexplored, contains many interesting and novel effects. Perhaps the simplest of these is the CW switching of a weak probe by a strong pump. Recall that a Bragg grating reflects strongly around the Bragg resonance frequency ω_0 which is inversely proportion to the average refractive index. In a nonlinear medium the presence of a strong pump alters the refractive index, and thus frequencies which were reflected (or transmitted) by the grating can be transmitted (or reflected). This effect was first seen by LaRochelle *et al.* in 1990[1] and to date this is the only experimental work done in this area. However since then considerable theoretical work has been done onpulse interactions[2] in fibre Bragg gratings (FBGs). Also experimental reports of nonlinear propagation in FBGs have started appearing in the literature[3,4]. A major factor in this upsurge of interest has been the development of techniques for writing long gratings at arbitrary wavelengths using the side illumination of fibres with UV light. This fact coupled with the latest generation of high power fibre sources allows the exploration of pulse interactions in FBGs in great detail.

The CW switching of a probe beam can be generalised by considering the effects of a strong pump pulse on a weak CW probe – the so-called optical pushbroom[2] effect, demonstrated experimentally here for the first time. The optical pushbroom utilises the frequency shift induced through the cross-phase modulation (XPM) of a CW probe by a strong pump beam to compress and sweep out the probe from the grating. As this frequency shift is proportional to the gradient of the pump beam it is intrinsically a pulse effect and although it compresses the probe it does not exchange energy between the two beams. The operation of the optical pushbroom has been explained in detail before[2,6] and so we give only a brief description here.

The central element of the pushbroom is of course the Bragg grating, which couples the forward and backward propagating modes resulting in a photonic bandgap centred at the Bragg frequency ω_0. For frequencies ω just outside this region, light can propagate but at a significantly reduced velocity. Fig. 1a shows the group velocity as a function of frequency, for frequencies just below the bandgap (which extends from -1 to 1). Consider a low intensity CW probe with a frequency and group velocity indicated by the open circle in Fig. 1a. The electric field inside the grating at this frequency has a resonance structure allowing significant energy to be stored in the grating[5]. The high intensity pump beam, tuned well away from the Bragg resonance, propagates undisturbed through the grating. As the pump pulse propagates through the grating it first lowers the frequency of the back of the probe beam due to XPM. Lowering the frequency of the back of the probe causes its group velocity to increases and thus it catches up with the front of the probe as yet uneffected by the pump. This differential frequency shift thus compresses the probe and sweeps all of the energy out of the grating. The final frequency of the probe is shown by the solid square in Fig. 1a.

In transmission one would then expect to see a narrow peak containing a significant fraction of the energy stored in the grating followed by long dip while the CW field distribution in the grating is restored. These features can be clearly seen in Fig. 1b which shows the results of a numerical simulation of the optical pushbroom for system parameters matched to those of our experiment as detailed below. The solid line gives the probe's intensity as a function of time while the dashed line indicates the pump's profile – on a different vertical scale. The probe's intensity has been normalised to unity since the grating is perfectly transmitting in the linear regime for this frequency. The insert shows an expanded view of the spike in transmission which has a FWHM of approximately 50ps.

2. Experimental Results

Our experimental setup is shown in Fig. 2. High power pump pulses at 1550nm are used to switch a low-power (1mW) , narrow-linewidth (< 10 MHz) probe beam that could be precisely temperature tuned

to wavelengths in and around the bandgap of a FBG centered at 1536.1nm. The pump pulses, derived from a directly modulated DFB laser, were amplified to high power (> 10 kW) in an erbium doped fibre amplifier cascade based on large mode area erbium doped fiber and had a repetition frequency of 4KHz. The pump pulse shape was asymmetric due to gain saturation effects within the amplifier chain and exhibited a 30ps rise time and a 3ns halfwidth (see Fig.3). Note that, as the optical pushbroom relies on the intensity gradient of the pump, the strength of our interaction is stronger than what would be achieved using a transform limited pulse of the same FWHM and energy. The spectral halfwidth of the pulses at the grating input was measured to be 1.2 GHz as defined by the chirp on the input seed pulses.

The pump and probe were polarisation coupled into the FBG and were thus orthogonally polarised within the FBG. A half-wave plate was included within the system allowing us to orient the beam along the grating birefringence axes. Both the reflected and transmitted probe signal could be measured in our experimental system using a fiberised detection system based on a tunable, narrow-band (< 1nm) optical filter with >80 dB differential loss between pump and probe (sufficient to extinquish the high intensity pump signal), a low noise pre-amplifier, a fast optical detector and sampling scope. The temporal resolution of our probe beam measurements was ≈50ps.

The FBG was centred at 1536.1 nm and was 8 cm long with an apodised profile resulting in the complete suppression of the side-lobes. The grating had a peak reflectivity of 98% and a measured width of less than 4 GHz. The grating was mounted in a section of capillary tube and angle polished at both ends so as to eliminate reflections from the grating end faces and was appropriately coated to strip cladding modes.

In Fig. 3a the optical pushbroom can be seen in action for the first time, the line styles and the insert are the same as for Fig. 1b. The initial frequency of the probe in this instance is tuned to just below the bandgap where the linear transmission is close to 100%. The peak intensity of the pump within the FBG is set to 20 GW/cm^2. The transmitted probe is clearly seen to have developed a sharp (≈ 70 ps FWHM) spike in intensity, co-located in time with the peak of the pump pulse. The grating transmission then drops well below unity for a considerable length of time – note that even 10ns after the arrival of the pump pulse the transmission has still not fully recovered. The parameters used in the numerical model in Fig. 1 match the actual experimental parameters, and as can be seen excellent agreement between the experimental and the numerical results is obtained. Experimental results were taken for a wide range of system parameters in both the transmission and reflection directions, full processing of the data and full numerical simulations of the system are currently underway.

3. Conclusion

We have experimentally demonstrated the optical pushbroom effect for the first time. The robustness of the effect is demonstrated by the fact that it was so readily and cleanly observed despite the fact that we were working with an un-optimised measurement geometry. Lower switching powers should readily be achieved through the use of non-apodised FBGs with co-polarised pump and probe beams. Indeed these results are probably the clearest manifestation of a nonlinear effects in a Bragg grating presented to date. Finally the results illustrate the potential of the powerful combination of versatile, high-power, erbium fiber sources with convenient, high-performance communication componentry and FBG fabrication technology for the study of the nonlinear optics of Bragg gratings.

---

1. S. LaRochelle *et al.*, Electron. Lett. **26** 1459 (1990)
2. C. M. de Sterke, "Optical push broom," Optics Letters **17**, 914–916 (1992).
3. U. Mohideen *et al.* , "Gap Soliton Propagation in Optical Fiber Gratings," Opt. Lett. 20 (1995).
4. B. J. Eggleton, *et al.* , "Bragg grating solitons," Physics Review Letters **76**, 1627 (1996).
5. C. M. de Sterke *et al.* , "Nonlinear Optics in Fiber Gratings," Optical Fiber Technology **2**, 253–268 (1996).
6. M. J. Steel and C. M. de Sterke, "Schrödinger equation description for cross-phase modulation in grating structures," Physics Review A **49**, 5048–5055 (1994).
7. D. Taverner *et al.*, "158 μJ pulses from a single transverse mode, large mode-area EDFA," Opt. Lett., **22** (6) 378–380 (1997)

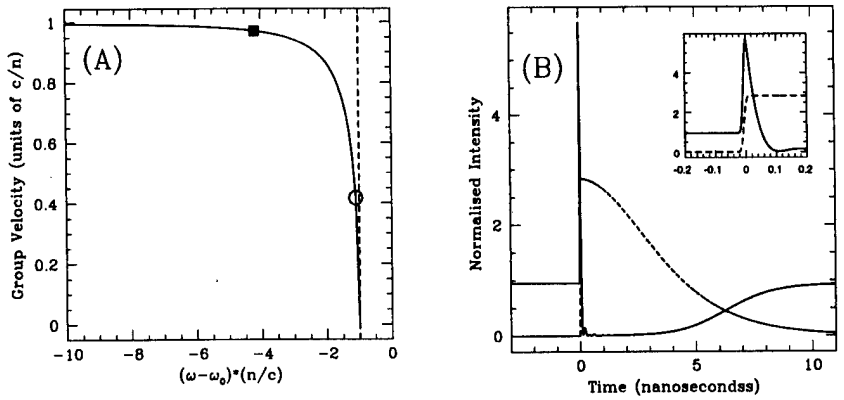

Fig. 1. (A) Group velocity as a function of frequency for a Bragg grating. The dashed vertical line shows the edge of the bandgap. The initial position of the pump is indicated by the open circle, while the solid square shows its final position. The solid line in Fig. B is a theoretical trace showing the transmitted probe intensity as a function of time, while the dashed line shows the pump profile. The insert is a blowup of the front spike in the transmission.

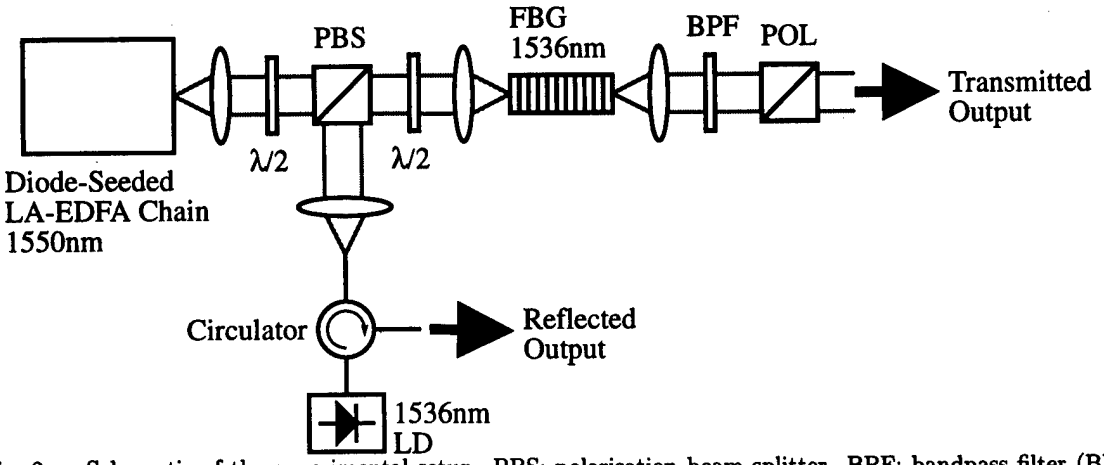

Fig. 2. Schematic of the experimental setup. PBS: polarisation beam splitter. BPF: bandpass filter (BPF) with a width of < 1 nm, see the text for more details.

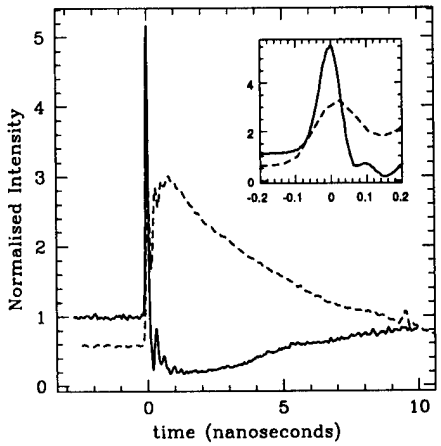

Fig. 3. Experimental trace of the pushbroom. The solid line shows the intensity of the probe beam normalised so that the linear transmitted power is unity. The dashed line shows the heavily filtered pump beam. The inset shows a expanded view of the front peak.

Bragg Gratings, Photosensitivity, and Poling in Glass Fibers and Waveguides: Applications and Fundamentals

Fiber Lasers

Monday, October 27, 1997

Jean-Luc Archambault, Ciena Corporation
Presider

BMC
9:15am–10:15am
Washington/Wilson Room

Cascaded Raman Fiber Lasers and Amplifiers

Stephen G. Grubb
SDL Inc.

The recent availability of high power cladding pumped fiber lasers and low loss fiber resonators enabled with fiber Bragg grating technology, have made efficient CW Raman frequency conversion extremely efficient. The technology of cascaded Raman lasers and amplifiers will be reviewed.

Novel High Power 1.24 μm And 1.48 μm Raman Lasers Based On Phosphosilicate Fiber

E.M.Dianov, M.V.Grekov, I.A.Bufetov, S.A.Vasiliev, O.I.Medvedkov, G.A.Ivanov, A.V.Belov, V.G.Plotnichenko, V.V.Koltashev, A.M.Prokhorov

Fiber Optics Research Center at the General Physics Institute of the Russian Academy of Sciences,
38 Vavilov Street, Moscow 117942, Russia
Phone: (095)135 05 66. Fax: (095)135 81 39. E-mail:dianov@fo.gpi.ac.ru

At present cascaded Raman fiber lasers pumped by Nd or Yb fiber lasers have found wide application. The growing interest in such lasers has been caused by the possibility to generate the high power CW radiation at the wavelengths of 1.24 and 1.48 μm.

In 1993 we suggested and used for the first time the CW third Stokes order at 1.24 μm as a pump radiation for a 1.3 μm Raman fiber amplifier. This radiation was obtained by cascaded stimulated Raman scattering of Nd:YAG laser light (1.064 μm) in a high Ge-doped fiber [1]. This approach for 1.3 μm Raman amplifier pumping turned out to be very successful. Using a diode-pumped Nd cladding-pumped fiber laser and fiber Bragg gratings an efficient resonant conversion of 1.06 μm radiation to the Raman third Stokes was achieved [2].

High power 1.48 μm radiation can be used to pump high power and remotely pumped erbium amplifiers [3].

However, germanosilicate fibers have a small Stokes frequency shift of ~ 440 cm^{-1}. This leads to the necessity of using the third and sixth Stokes orders to obtain the radiation with the wavelengths of 1.24 and 1.48 μm correspondingly. Because of this the structure of a cascaded Raman fiber laser consists of three and six pairs of Bragg gratings for 1.24 and 1.48 μm.

Besides the complexity and high cost of such cascaded Raman fiber lasers, the conversion efficiency is reduced with the growth of the Stokes order. The best option is a fiber with a large enough Stokes frequency shift to obtain 1.24 μm and 1.48 μm radiation corresponding to Stokes lines of low order. Besides, the fiber should be photosensitive enough to get highly reflecting Bragg gratings written directly in it.

It turned out that a phosphosilicate fiber satisfies these requirements. The Raman spectrum of a phosphosilicate fiber shows a strong line shifted by 1330 cm^{-1} [4]. Pumping by Nd laser radiation one can get the first and the second Stokes orders at 1.24 and 1.48 μm. In addition, it has been shown that it is possible to write Bragg gratings directly in a phosphosilicate fiber using 193 nm radiation [5].

All mentioned above make it possible to create simple and efficient Raman fiber lasers generating high power radiation at these important wavelengths.

We have fabricated a single-mode P-doped low-loss silica fiber with $\Delta n = 0.011$ [6]. Fig.1 shows the Raman spectrum of the fiber. One can see a strong Raman scattering line shifted by 1350 cm^{-1}. Using this fiber we have carried out experiments on conversion of 1.06 μm CW radiation to the first and second Stokes frequencies.

Fig.2 shows the schematic of the first order (1.24 μm) (a) and the second order (1.48 μm) (b) Raman fiber laser. As a pump we used 1.06 μm CW radiation of

Nd:YAG laser (Coherent, Antares). The lengths of the fiber were 0.5-1.2 km. The results obtained have shown the efficient conversion of 1.06 μm CW radiation by Raman shifting to 1.24 and 1.48 μm by utilizing resonant Raman cavities.

Using a phosphosilicate fiber and Bragg gratings with nonoptimized parameters we have obtained an output power of about 3 W at 1.24 μm and more than 1 W at 1.48 μm for about 7 W of coupled pump power.

In conclusion, we have reported the first demonstration of resonant conversion of 1.06 μm CW radiation to the first (1.24 μm) and second (1.48 μm) Raman Stokes in a phosphosilicate fiber. The results show that efficient CW generation at these wavelengths is also obtainable with diode-pumped Nd fiber laser as a pump source.

References

1. Annual report of the General Physics Institute of the Russian Academy of Sciences for 1993, Section "Optical fiber communication, integrated optics", p.7, January 1994.
E.M.Dianov et al., Quantum Electronics, vol.24, 749-751, 1994.
2. S.G.Grubb et al., Proc. Optical Amplifiers and Their Applications, paper PD-3, August 3-5, Breckenridge, Co, 1994.
3. S.G.Grubb et al., Proc.Optical Amplifiers and Their Applications, paper Sa A4, Davos, 1995.
4. V.V.Grigoryants et al., Optical and Quantum Electronics, vol.9, 351, 1977.
5. J.Canning, R.Pasman, M.G.Sceats, Topical Meeting "Photosensitivity and Quadratic Nonlinearity in Glass Waveguides. Fundamentals and Applications", paper SuA6, Portland, September 9-11, 1995.
6. E.M.Dianov et al., Conference "High Purity Substances And Materials For IR Optics", Nizhnii Novgorod, June 2-5, 1997.

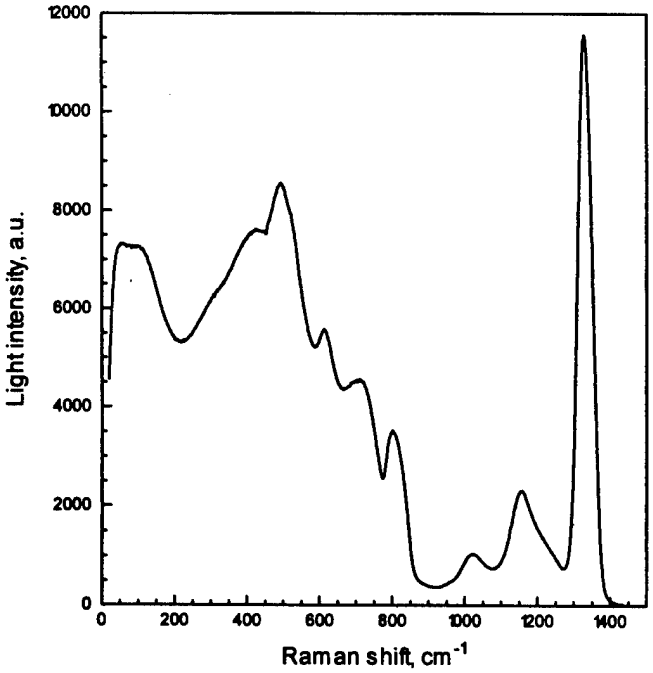

Figure 1.

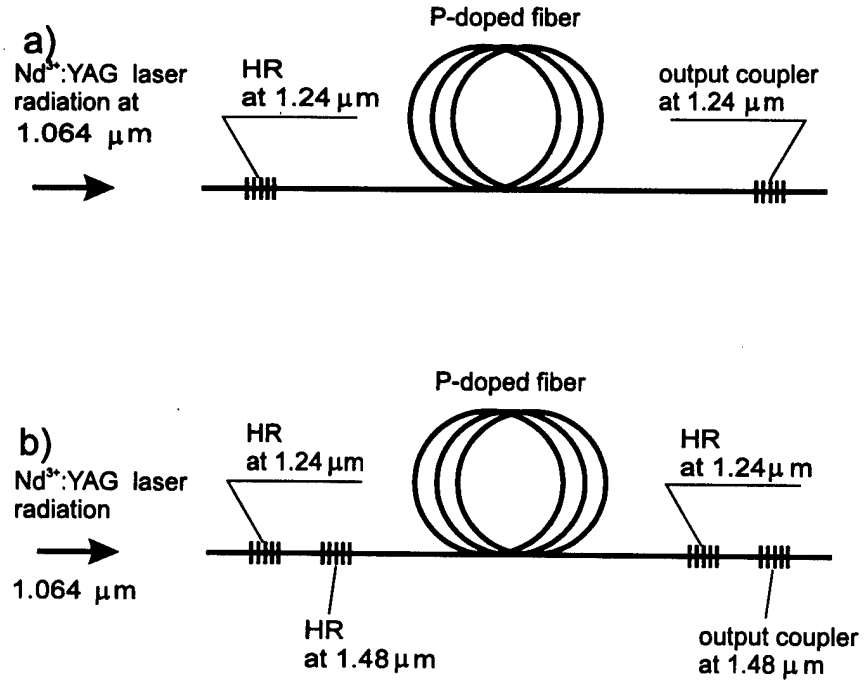

Figure 2.

Performance Characteristics of Single Frequency Er^{3+}:Yb^{3+} Codoped Fiber Lasers

W. H. Loh, B. N. Samson, L. Dong, G. J. Cowle and K. Hsu*

Optoelectronics Research Centre
University of Southampton
Southampton SO17 1BJ, UK

*Micron Optics Inc.
2801 Buford Hwy, Suite 140
Atlanta, Georgia 30329, USA

For much of this decade, interest has been sustained in developing high performance single frequency Er^{3+}-fiber lasers[1-3]. For robust single frequency operation, these lasers need to be only centimeters long. Early grating-based fiber lasers relied on Er-germanosilicate fibers, but lasing powers were low - μW typically[1,2], due to low pump absorption in the short cavity. Increasing the Er-concentration to increase absorption is however difficult. Germanosilicate fibers are prone to ion clustering, which degrades the efficiency and destablises[4,5] the laser. Thus the need to amplify the laser power to useful levels of a mW or more is a drawback where low noise sources are desired.

Considerable effort has been put into investigating solutions for increasing the power from short cavity fiber lasers[3,6]. While the absorption can be increased by changing the pump wavelength[6], this is unlikely to be fully practical till the arrival of green laser diodes. On the other hand, Er^{3+}:Yb^{3+} fibers are mature. With this scheme, the 980 nm absorption can be increased up to 2 orders of magnitude, with corresponding increases in output power.

However, two problems stood in the way. One was the low photosensitivity in these fibers. In addition, the lasers were observed to operate in 2 polarised modes[7], unattractive for many applications. Recently, a Er^{3+}:Yb^{3+} fiber with a photosensitive annular region surrounding the core enabled strong gratings to be written. Also, the resulting lasers were observed to lase in a single polarisation state[8]. We report here on the characteristics of these lasers, and show their potential as high performance low noise narrow linewidth sources.

We first present the performance of a 5 cm distributed feedback (DFB) fiber laser, fabricated by scanning a 100 mW, 244 nm beam across a phase mask. The DFB laser, placed on an aluminium plate without temperature control, is spliced directly to a fiber WDM, which couples the pump from a 40 mW 980 nm laser diode. The 1550 nm arm of the WDM is spliced to a pigtailed isolator. The laser power measured out of the isolator is 4 mW.

At this power, the optical SNR is 65 dB. A scanning F-P interferometer confirmed stable single frequency and single polarisation operation. The optical linewidth, measured with the delayed self-heterodyne technique, is 18 kHz. The RIN is $<$ -153 dB/Hz for frequencies $>$ 10 MHz. The peak RIN of -118 dB/Hz, at the relaxation oscillation frequency of 0.6 MHz, is lower than previous fiber lasers using feedback noise reduction circuits[1].

Estimating the side mode suppression ratio (SMSR) is more involved. The side modes for a 5 cm DFB laser would be GHz away, too close for an optical spectrum analyser with 0.1 nm resolution. We estimate the SMSR from the rf frequency spectrum during the self-heterodyne measurement, in the 1-7 GHz frequency range. Any side modes should show up as a beat signal (with the main mode) in that range. No such beat signals were observed. From the main mode beat signal level, we conclude that neighbouring side modes are $<$ 50

Output Power	4 mW
Optical Linewidth	18 kHz
Optical Signal-to-Noise Ratio	65 dB
Relative Intensity Noise, RIN (> 10 MHz)	< -153 dB/Hz
Peak RIN (at 0.6 MHz)	-118 dB/Hz
Side Mode Suppression Ratio (SMSR)	< -50 dB
Single Polarisation State Purity	50 dB
Wavelength Stability	0.01 nm/°C

Table 1. DFB fiber laser device characteristics

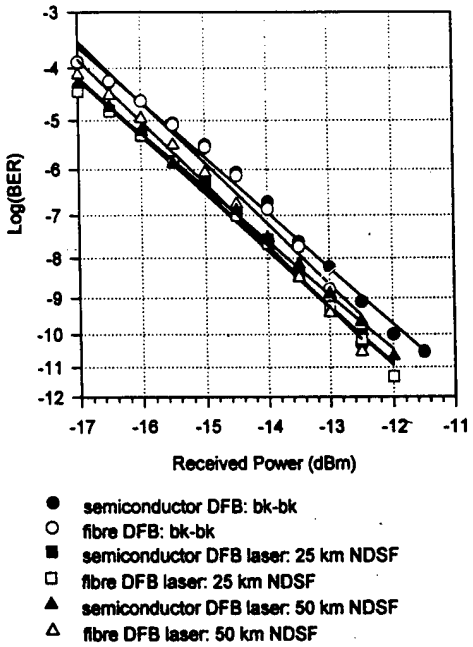

Fig. 1 (Top right) Comparison of BER performance of DFB fiber and semiconductor lasers

dB below the main mode, resolution limited by the noise floor.

To determine the single polarisation state purity, the laser output was connected to a polarisation controller and a polariser. By adjusting the polarisation controller, the output from the polariser was reduced by 50 dB. The 2nd polarisation mode is thus effectively nonexistent. Table 1 summarises the device characteristics of the Er^{3+}:Yb^{3+} DFB fiber laser.

Finally, transmission tests were performed in a 10 Gb/s NRZ system over 50 km of standard fiber. A diode DFB laser (with 8 MHz optical linewidth) was also similarly tested for comparison. Fig. 1 show the plots of the Bit Error Rate (BER) performances, establishing that no problems or penalties are incurred in using the fiber laser.

These findings show that Er^{3+}:Yb^{3+} DFB fiber lasers are excellent for applications requiring single frequency low noise sources. However, some applications, e.g. CATV, require more power. Unfortunately, at high pump powers, these lasers invariably fall off in power[8]. These behaviours, repeatable and occurring over time scales of many seconds, are attributed to thermal effects, changing the refractive index and dephasing the grating. However, high power single frequency operation can be achieved, as described below.

Fig. 2(a) shows the configuration of a Er^{3+}:Yb^{3+} fiber Bragg grating laser (FBGL). One end consists of a dielectric mirror (R=99.86% at 1.55 μm), while the other end is a centimeter long Bragg grating (R=98% at 1536 nm) written directly in the doped fiber, and situated a few mm away from the dielectric mirror. The entire laser is < 1.5 cm in length.

Fig. 2(b) shows the lasing characteristic of the FBGL. A maximum power of 58 mW (at the output of the isolator) is obtained for 500 mW pump power. A scanning F-P interferometer confirmed single frequency operation. The RIN is < -168 dB/Hz for frequencies > 10 MHz, with a peak RIN value of just -133 dB/Hz at the relaxation oscillation frequency of 2.8 MHz. The optical linewidth was measured to be 500 kHz. Single polarisation state purity was confirmed to be better than 50 dB.

The 60 mW FBGL has a reasonable net efficiency of 12% with respect to pump power, but it is clear that the efficiency is much better at lower pump powers. This is due to the 'bottleneck' effect, arising from the finite energy transfer rate from excited Yb^{3+} to Er^{3+} ions. As the transfer rate is a strong function of the ion separation, optimising the Yb^{3+} and Er^{3+} concentrations and their ratio may enable output powers exceeding 100 mW. It was recently argued that the Yb^{3+}-Er^{3+} energy transfer can usefully act as a low-frequency filter,

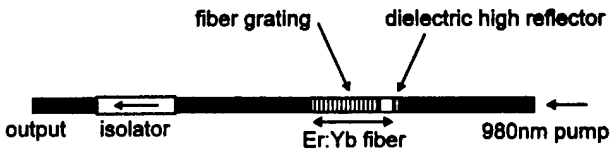

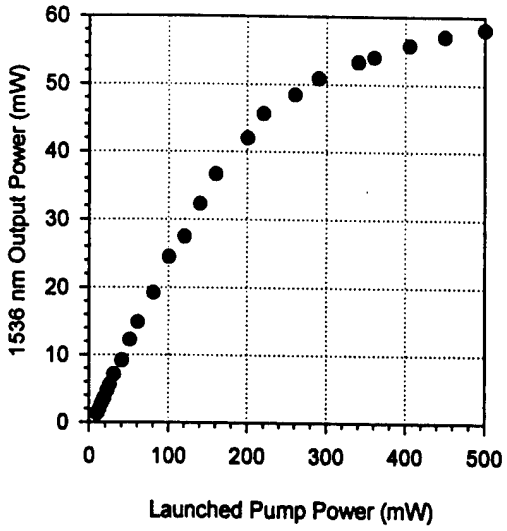

Fig. 2 (a) Configuration of FBGL.
(b) Lasing Characteristic of FBGL.

buffering Er^{3+}:Yb^{3+} lasers against pump noise[9]. However, as this also leads to the 'bottleneck' problem, the degradation in laser efficiency at high pump powers would appear to outweigh the advantage of any limited immunity against pump fluctuations.

The results clearly show that high performance single frequency short cavity fiber lasers are finally a realistic option. They are now capable of producing reasonable output powers, and possess excellent low noise characteristics under free-running conditions. Only centimeters long, they are compact, easy to fabricate and package. In 10 Gb/s NRZ transmission tests over standard fiber, they perform equally well compared to a diode DFB laser. Although the fiber lasers are not necessarily superior in digital transmission tests, they may hold advantages over DFB diodes. Apart from ease of fabrication, fiber lasers have a wavelength insensitivity to temperature at least an order of magnitude better, which could be attractive in dense WDM systems requiring tight wavelength tolerances. Also, as WDM transmitters, fiber lasers may afford better reliability, e.g. for a 16-channel WDM transmitter, by first combining the pump powers from all the pump diodes before redistributing them to each of the fiber lasers, a failure in any one laser (pump) diode will simply result in only a small reduction in the transmitter power of each channel.

References

1. G. A. Ball, C. E. Holton, G. Hull-Allen and W. W. Morey, IEEE Photon. Technol. Lett., **17**, 420-422 (1992).
2. J. L. Zyskind, V. Mizrahi, D. J. DiGiovanni and J. W. Sulhoff, Electron. Lett. **28**, 1385-1387 (1992).
3. J. T. Kringlebotn, J.-L. Archambault, L. Reekie, J. E. Townsend, G. G. Vienne and D. N. Payne, Electron. Lett., **30**, 972-973 (1994).
4. F. Sanchez, P. Le Boudec, P.-L. Francois and G. Stephan, Phys. Rev. A., **48**, 2220-2229 (1993).
5. W. H. Loh and J. P. de Sandro, Opt. Lett., **21**, 1475-1477 (1996).
6. W. H. Loh, S. D. Butterworth and W. A. Clarkson, Electron. Lett., **32**, 2088-2089 (1996).
7. W. H. Loh, L. Dong and J. E. Caplen, Appl. Phys. Lett., **69**, 2151-2153 (1996).
8. L. Dong, W. H. Loh, J. E. Caplen, J. D. Minelly, K. Hsu and L. Reekie, Opt. Lett. **22**, 694-696 (1997).
9. S. Taccheo, P. Laporta, O. Svelto and G. DeGeronimo, Opt. Lett., **21**, 1747-1749 (1996).

Bragg Gratings, Photosensitivity, and Poling in Glass Fibers and Waveguides: Applications and Fundamentals

Joint Symposium on Vitreous Silica and Related Materials

Joint Session on Fundamental Mechanisms

Monday, October 27, 1997

Tsung Tsai, U.S. Naval Research Laboratory
Presider

JMD
11:00am–12:30pm
Auditorium

Dielectric Characteristics of Silica and Inference of Related Defects

Minoru Tomozawa and Dong-Wook Shin[+]

Rensselaer Polytechnic Institute, Troy, New York, 12180-3590, USA

[+] Now Smsung Electronics Co. Ltd, Suwon, Korea

I. Introduction.

There are various types of silica glasses made by different methods. They contain, in general, different levels of impurities such as sodium oxide, alumina and hydroxyls and have different fictive temperatures. Some investigators [1-3] reported anomalous electric and dielectric properties of silica glasses and attributed these anomalies to impurities. In order to resolve the cause of these anomalies, electric and dielectric properties of various silica glasses were measured as a function of temperatures [4-6].

Large second harmonic generation (SHG) has been reported [7] for poled silica glasses and it is believed that the phenomenon is related to the space charge polarization of silica glasses. The other objective of this paper, therefore, is to compare the observed polarization with the reported SHG.

II. Experimental Procedure

Thin plate samples with Au or Au/Pd evaporated film electrodes were used and the DC absorption current method was employed to determine DC conductivity as well as dielectric characteristics. In order to vary water contents and fictive temperatures of the silica glasses, samples were pre-treated by heating at various temperatures under various water vapor pressures. The water content was determined from the IR absorbance near 3600 cm^{-1} while the fictive temperature was determined from the IR reflection peak position near 1200 cm^{-1}. Often the fictive temperature of silica glasses changed while water was introduced into the glass. The effect of water content was separated from that of the fictive temperature by using specimens heat-treated in a dry atmosphere and assuming that the effects of water content and fictive temperature on the activation energies are additive. In order to separate the bulk electrical phenomena from the interface-related phenomena, same glass specimens with different thickness was examined.

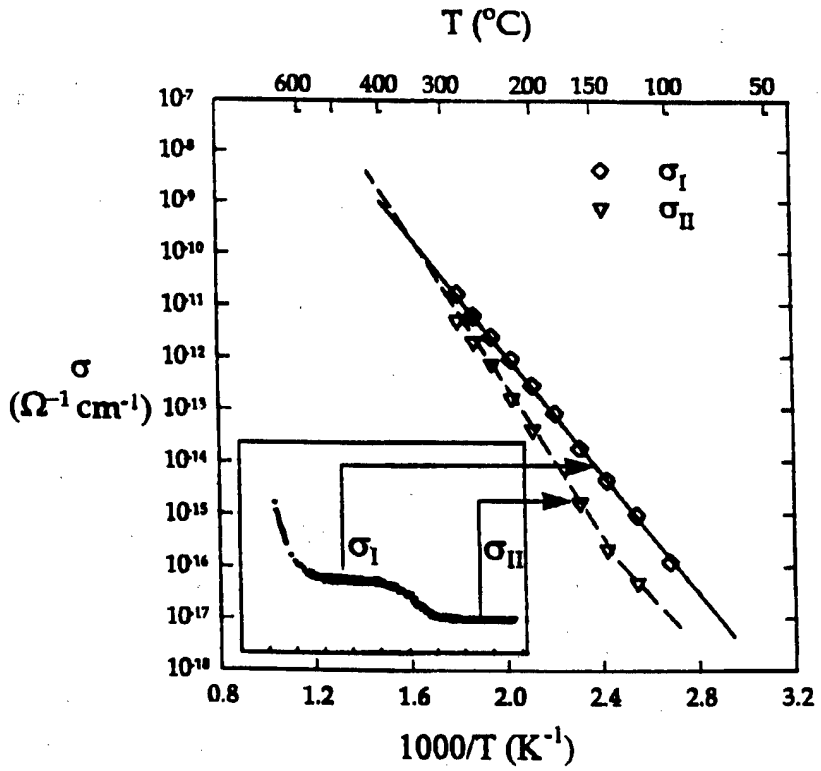

Figure 1. Temperature dependence of dc conductivity of a synthetic silica glass (Heraeus Suprasil 2-type III). σ_I was obtained taking the first plateau while σ_{II} was obtained taking the second plateau. From the thickness dependence σ_I was found to be the bulk value while σ_{II} was not. The inset is the schematic representation of the apparent conductivity vs. charging time.

References

1. A.E. Owen and R.W. Douglas, J. Soc., Glass Technology, 43 (1959) 159.
2. K. Yamamoto and H. Namikawa, J. Ceram. Soc., Jpn 102 (1994) 658.
3. K. Yamamoto and H. Namikawa, J. Ceram. Soc., Jpn 103 (1995) 910.
4. D.W. Shin and M. Tomozawa, J. Non-Cryst. Solids, 163 (1993) 203.
5. D.W. Shin and M. Tomozawa, J. Non-Cryst. Solids, 203 (1993) 262.
6. D.W. Shin and M. Tomozawa, J. Non-Cryst. Solids, 211 (1993) 237.
7. R.A. Meyers, X. Long and S.R.J. Brueck, SPIE 2289 (1994) 98.
8. J.H. Beaumont and P.W. Jacobs, J. Phys. Chem. Solids, 28 91967) 657.

III. Results and Discussions

The DC current under a constant voltage exhibited two plateaus at two different times, indicating the existence of two separate polarization processes in silica glasses, with one appearing at a shorter time than the other. From the thickness dependence of the dielectric properties, the shorter time (or higher frequency) polarization (I) was found to be a bulk phenomenon, while the longer time (or lower frequency) polarization (II) was a surface phenomenon, i.e. electrode polarization. When the conductivity was determined taking the first plateau immediately after the first polarization, the conductivity, σ_I, followed Arrhenius relation. On the other hand the apparent conductivity, σ_{II}, after the second polarization exhibited a kink in a similar plot, as shown in Figure 1. Apparently, the similar kink for DC conductivity of some silica glasses reported in literature was caused by mistaking the interfacial phenomenon as the bulk phenomenon.

The effect of water content on DC conductivity of silica glasses depended upon the type of silica glasses; conductivity increased and activation energy decreased with increasing water content for fused silica glasses, while conductivity decreased and activation energy increased with increasing water content for synthetic silica glass. The increasing fictive temperature caused reduction of DC conductivity for both types of silica glasses.

The polarization II was successfully explained by the space charge polarization mechanism [8] with partial blocking at the glass-electrode interface, and its magnitude varied with fictive temperature as well as water content of the specimens and correlated well with the reported trend of SHG.

IV. Conclusions

Two separate types of polarization were observed. The shorter time polarization was due to the bulk phenomenon while the longer time relaxation was due to interfacial phenomenon. The latter was due to the space charge polarization and was found correlated with the reported SHG of silica glasses.

Determination of the Visible-Range Optical Absorption Spectrum of Peroxy Radicals in Gamma-Irradiated Fused Silica

David L. Griscom[a] and Masafumi Mizuguchi[b]

[a]*Optical Sciences Division, Naval Research Laboratory, Washington, DC 20375, USA*
Phone: (202) 404-7087, FAX: (202) 404-8114, e-mail: griscom@nrl.navy.mil
[b]*Interdisciplinary Graduate School of Science and Engineering, Tokyo Institute of Technology, Yokohama, Japan, Phone: +81 45 924-5628, FAX: +81 45 922-5169*

The most fundamental defect centers induced by high-energy radiations (x rays, γ rays, electrons, protons, neutrons, or intense UV light) in amorphous silicon dioxide are E′ centers (≡Si·), nonbridging-oxygen hole centers (NBOHCs: ≡Si-O·), peroxy radicals (PORs: ≡Si-O-O·), and self-trapped holes (STHs), where the notation "≡" represents three bonds with other oxygens in the glass network and "·" denotes an unpaired electron. The structures of these defects are known from electron spin resonance (ESR) studies (see, e.g., ref. 1). The E′ center has a strong optical absorption in the UV at 215 nm and no known absorptions in the visible range. Both the NBOHC and the POR are believed to have absorption bands near 260 nm, and the former exhibits a low-oscillator-strength band ($f \approx 4 - 8 \times 10^{-4}$) near 600 nm.[1-5] On fundamental grounds, the POR would be expected to have a corresponding transition near the same wavelength. Based on data for drawing-induced defects in optical fibers,[4] the likely existence of such a band was previously inferred,[1] but proof has been lacking. We report here unambigous spectral resolution of a POR absorption band near 630 nm, based on ESR and differential-optical isochronal-anneal studies of γ-irradiated high-purity silicas in bulk and optical-fiber forms, respectively.

Optical measurements in the range ~400 - 1000 nm were carried out at the Naval Research Laboratory (NRL) by means of a prism-based CCD-camera spectrometer described elsewhere.[6] Both fibers for the present study had 200-μm core diameters, 240-μm-diameter claddings of F-doped silica, and aluminum jackets. The core materials were (1) Russian-developed KS-4V silica containing <200 ppb OH and <20 ppm Cl and (2) a VAD silica of Japanese origin containing 0.54 mass% F and ~4 ppm OH. One-meter lengths of fibers (1) and (2) were coiled to diameters of 62 mm and simultaneously exposed to ^{60}Co γ rays at a dose rate of 1.0 Gy(Si)/s at 27 C in the dark to an accumulated dose of 13 MGy(Si). Four-meter lengths of the same fibers had been previously studied[6] during γ irradiation at a dose rate of 5.6 Gy(Si)/s to a total dose of 12 MGy(Si) but were not subjected to thermal annealing until after a subsequent reactor irradiation. Samples for the present ESR measurements comprised three high-purity bulk silicas, including a piece of F-doped silica cut from the same core rod as was used to draw fiber (2); these had been γ irradiated simultaneously with the 4-m fiber lengths (rate 5.6 Gy(Si)/s). Room-temperature X-band ESR spectra were recorded at Tokyo Institute of Technology (TIT). At both NRL and TIT, 7-minute isochronal anneals were performed in tube furnaces. Only the fibers γ irradiated at 1.0 Gy(Si)/s were annealed. At TIT, the partially overlapping spectra of E′ centers, NBOHCs, and PORs were separated at certain stages of the anneals by making use of differing microwave power levels. These were numerically integrated and compared with a copper sulfate standard sample to determine absolute spin concentrations. At other temperatures, relative changes in the three spectral types were determined from their amplitudes in regions of minimum spectral overlap and were normalized to the cases where absolute calibrations were possible.

Figure 1 displays the isochronal-anneal *difference* spectra, $L(\lambda, T_{ann}) - L(\lambda, T_{RT})$, for the F-doped-core fiber, where T_{ann} is the isochronal anneal temperature and T_{RT} denotes no anneal.

These spectra reveal for the first time the presence of a band near 630 nm *which grows in consequence of post-irradiation heat treatment* (here growth continues to T_{ann} ~500 C). Figure 1(c) illustrates an indisputably transparent 2-component Gaussian decomposition of spectrum 6 of Fig. 1(a) corresponding to T_{ann}=400 C. Here the sharp band centered at E_0=1.97 eV (width W=0.175 eV) is ascribed to the POR on the basis of the ESR data of Fig. 2 (and many similar data in the literature)[1,7] which show the POR to be the only fundamental defect to *increase* significantly in numbers upon annealing above ~100 C. The broader fitted band (E_0=2.19 eV, W=0.505 eV) is ascribed to NBOHCs. Figure 1(d) shows that an additional NBOHC band (E_0=2.08 eV, W=0.325 eV) is required to fit the difference spectrum for T_{ann}=600 C. Data for the KS-4V pure-silica-core fiber (not shown) were qualitatively similar except that (i) the 2.19-eV NBOHC band and the POR band were both weaker by a factor of ~3, (ii) the band(s) centered ≥2.5 eV (not fitted) were stronger by a factor of ~3, and (iii) the 2.08-eV NBOHC band was essentially absent. Based on this result, the 2.08-eV band is suggested to arise from NBOHCs deriving from the removal of hydrogens from hydroxyl groups (present at 4 ppm in the F-doped silica but essentially absent in KS-4V). Apropos, it should be noted that fluorine doping is not expected to contribute to the radiation sensitivity of a-SiO_2, and evidence has been given that F doping levels ~0.5 - 1.0 mass% actually reduce the radiation yields of E' centers and NBOHCs by about an order of magnitude.[8]

While qualitatively similar, the isochronal anneal data of Fig. 2 obtained by ESR (symbols) and optical means (bold curves), exhibit profound differences. In particular, the thermal bleaching of NBOHCs and concomitant increases in PORs take place at lower values of T_{ann} in the ESR experiment than in the optical study. This unexpected outcome is deemed most likely an effect of the factor-of-six difference in dose rates experienced by the ESR and optical samples. Given this assessment, oscillator strengths were calculated based on Gaussian fits (not shown) of the previously measured spectra[6] of 4-m fiber lengths γ irradiated *at the same dose rate* and to the same total dose as the ESR samples (but not subjected to annealing). The component bands used in these fits were constrained to closely match those which optimized the fits of Fig. 1(c, d). Smakula's relation for Gaussian line shapes was employed in the form

$$N \cdot f = (8.7 \times 10^{16}) \cdot n \cdot \Sigma_i (\alpha_i \cdot W_i)/(n^2+2)^2,$$

where N is the defect concentration measured by ESR in spins/cm^3, n is the index of refraction of the material, W_i is the full width of the i^{th} sub-band in eV, and α_i is its absorption coefficient in cm^{-1} (=$2.303 \times 10^6 \cdot$ L(dB/km)). The combined oscillator strength of the two resolved NBOHC sub-bands is found to be $f = (6.86 \pm 0.10) \times 10^{-4}$, in good agreement with earlier work.[2,4] Assuming that the POR gives rise to the band with $E_0 \approx 1.97$ eV and $W \approx 0.175$ eV which grows with increasing T_{ann}, its oscillator strength is determined as $f = (6.0 \pm 1.0) \times 10^{-4}$--essentially equal to that of the NBOHC. The surprisingly large dose-rate effects apparent in the data of Fig. 2 likely have significant implications regarding the mechanisms of radiation damage in amorphous silicon dioxide exposed to high-dose-rate environments, including focussed excimer laser light.[9]

1. D.L. Griscom, J. Cer. Soc. Jpn. **99**, 923 (1991).
2. E.J. Friebele, D.L. Griscom, and M.J. Marrone, J. Non-Cryst. Solids **71**, 133 (1985).
3. K. Nagasawa, Y Hoshi, Y. Ohki and K. Yahagi, Jpn. J. Appl. Phys. **25**, 464 (1986).
4. Y. Hibino and H. Hanafusa, J. Appl. Phys. **60**, 1797 (1986).
5. L. Skuja, J. Non-Cryst. Solids **179**, 51 (1994).
6. D.L. Griscom, J. Appl. Phys. **80**, 2142 (1996).
7. M. Stapelbroek, D.L. Griscom, E.J. Friebele, and G.H. Sigel, Jr., J. Non-Cryst. Solids **32**, 313 (1979)
8. K. Arai, H. Imai, J. Isoya, H. Hosono, Y. Abe, and H. Imagawa, Phys. Rev. **B45**, 10818 (1992).
9. T.E. Tsai and D.L. Griscom, Phys. Rev. Lett. **67**, 2517 (1991).

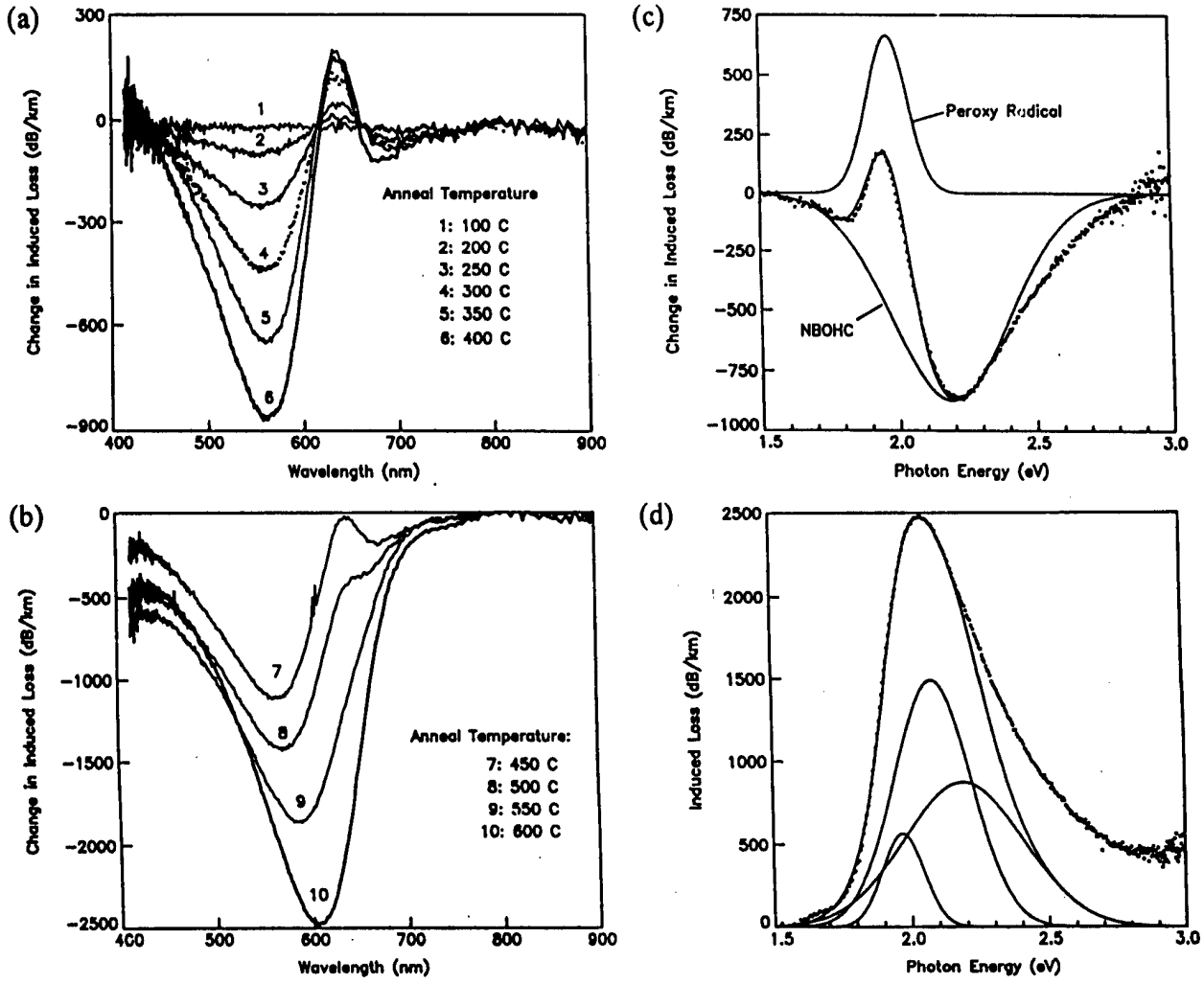

Figure 1. (a, b) Changes in γ-ray-induced optical absorption in an F-doped-silica-core fiber effected by 7-min isochronal anneals to the indicated temperatures. (c, d) Gaussian resolutions of spectra 6 and 10 from (a) and (b), respectively.

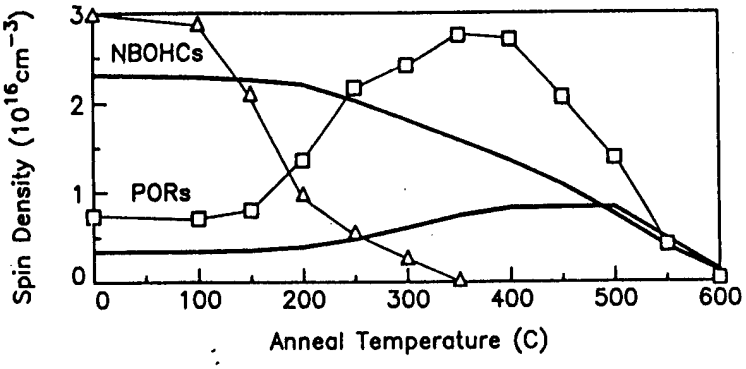

Figure 2. Isochronal anneal behaviors of defects induced in an F-doped fused silica by ~12 MGy γ irradiations. Symbols: ESR data for NBOHCs and PORs in bulk samples (dose rate 5.6 Gy/s). Bold curves: concentrations of the same two defects in an optical fiber (dose rate 1.0 Gy/s), determined from the induced optical losses by means of oscillator strengths derived in this paper.

The Point Defects with Low-Coordinated Si or Ge Atoms on Vitreous Silica Surface. Surface and Bulk Centers Comparison

Victor A. Radzig

Semenov Institute of Chemical Physics, Russian Academy of Sciences,
Kosigina street 4, Moscow, 117977 Russia
Fax: (095) 938 2156
Phone: (095) 939-74-01
E-mail: radzig@center.chph.ras.ru

Until recently, investigations of the surface and bulk defects in silica glass have developed virtually independent. Only in [1,2] some properties of the surface and bulk defects in vitreous silica were compared. Identification of the structure of defects in the bulk of silica glass is a considerably more complicated problem. This is explained by a wide variety of methods, which can be used to identify the structure of surface defects and reveal the mechanisms of their transformations under the action of different external factors (temperature, UV and γ-irradiation, reactions with different impurity molecules, the so-called technological impurities, etc.).

The surface centers can be involved in different reactions with molecules of the surroundings to implement *purposeful* chemical modification of the structure of a surface defect. By this means, the surface center can be transformed to new forms. On the one hand, this enables the data on the reactivity of the center with respect to different compounds to be obtained, and on the other, the results of experimental investigations into a modified center by IR, and ESR spectroscopy, optical techniques, calorimetry, etc. can prove to be more informative. These opportunities are severely restricted for the bulk defects. Here, information provided by the studies of surface defects also can appear to be useful [1-5].

The results of the studies of the nature of different types of point defects stabilised on the activated surface of vitreous silica are presented. Mechanical, chemical and thermal techniques of surface activation were used. Concentration of the active centers in solids with a developed specific surface (10-100 m^2/g) falls in the range 10^{18}-10^{19} g^{-1}. These ammounts are large enough to be reliably recorded by different spectral methods.

Structure, spectral characteristics and reactivity of the main types of uncharged defects, Si or Ge atoms of which are connected with two or three lattice oxygens, are studied using FTIR, ESP and optical (absorption and luminescence) spectroscopy. Ab initio calculations are used for the interpretation of the experimental data.

The majority of vitreous silica defects can be considered as paramagnetic or diamagnetic products of chemical modification of main defect centres: (≡Si-O)$_3$Si$^{\cdot}$, (≡Si-O)$_3$Ge$^{\cdot}$, (≡Si-O)$_2$Si:, (≡Si-O)$_2$Ge:. The simplest examples of such type of the centres are paramagnetic ((≡Si-O)$_3$Si-O$^{\cdot}$, (≡Si-O)$_3$Si-O-O$^{\cdot}$, (≡Si-O)$_2$Si$^{\cdot}$-H(D), (≡Si-O)$_2$Ge$^{\cdot}$-H(D)) and diamagnetic ((≡Si-O)$_3$Si-H(D), (≡Si-O)$_3$Ge-H(D), (≡Si-O)$_2$Si=O, (≡Si-O)$_2$Ge=O, (≡Si-O)$_2$Si<H$_2$(D$_2$), (≡Si-O)$_2$Ge<H$_2$(D$_2$)) groups. The electronic structure and geometry, nature of the electronic transitions responsible for observed optical properties of above mentioned and some other defects are analysed. The reactivity of the centres those include two-coordinated Si and Ge atoms in their electronically excited states (lowest triplet and first singlet) is studied using different experimental and theoretical approaches. The scale of possible differences in spectral properties and reactivity of defects with similar chemical surrounding but with different geometry is analysed. The available experimental data indicate that the wavefunctions of defect states in SiO_2 and GeO_2/SiO_2 systems are spatially localized and predominantly concentrated in the neighborhood of a "defective" atom. This is true for both paramagnetic and diamagnetic intrinsic defects in SiO_2 and GeO_2/SiO_2 systems. The formation of the above states is generally attended by a decrease in the coordination number of the "defective" atom, i.e., by breaking and reconstruction of part of its chemical bonds with the neighboring atoms.

Taking into account the structural features of vitreous silica glass and the directed character of siloxan bond, one can expect that centers identical in their chemical structure and stabilized on the surface or in the bulk of silica glass will exhibit similar spectral characteristics. The distinctions between the surface and bulk centers can be attributed to different arrangements of the substituents in the coordination sphere of the defect. It can be supposed that, for a defect stabilized on the surface of solids, the environment hinders changes (relaxation) in its geometric structure to a lesser degree. In this situation, the energy level corresponding to the ground state of the surface should lie lower than that of the bulk center similar in its structure. Stabilization of the ground state is generally accompanied by an increase in the energy of the excited state. Therefore, one can anticipate that, compared to bulk centers, the surface centers will show a short-wavelength shift of the optical absorption bands.

The available experimental data confirm these conclusions. The basic types of defects in silicon dioxide, i.e. paramagnetic centers (so-called E'-centers, nonbridging oxygen centers, and peroxy radicals) and diamagnetic centers (so-called oxygen deficient centers) are found both in the bulk and on surface of silica glass. The optical properties of silicon-centered paramagnetic sites (≡Si-O)$_3$Si$^{\cdot}$ can be compared to illustrate the scale of the differences observed. The maxima of the optical absorption bands of the bulk and surface centers are observed at 5.9 eV and 6.2 eV respectively. The same tendency is also revealed for diamagnetic defects. For example, the optical absorption bands of the surface defects containing twofold-coordinated silicon and germanium

atoms are observed at 5.3 and 5.4 eV, respectively; whereas the centers, which have, in our opinion, the same structure and the stabilized in the bulk of silica glass, exhibit the optical absorption bands at 5.0 and 5.1 eV, respectively.

An analysis of the bulk defects and processes with their participation is given based on above described results of surface sites. Special attention is paid to the discussion of the structure of so called oxygen-deficient centres in pure and Ge-doped vitreous silicas.

1. L.N.Skuja, A.N.Streletsky, A.B.Pakovich, Solid State Commun., 1984, v.50, n.12, p.1069.
2. V.A.Radtsig, A.A.Bobyshev, Phys. Status Solidi B, 1986, v.133, p.621.
3. V.A.Radzig, Chem.Phys. Reports, 1995, v.14(8), p.1206.
4. V.N.Bagratashvili, S.I.Tsypina, V.A.Radtsig, A.O.Rybaltovskii, P.V.Chernov, S.S.Alimpiev, Y.O.Simanovskii, J. Non-Crystalline Solids, 1995, v.180, p.221.
5. V.A.Radzig, V.N.Bagratashvili, S.I.Tsypina, P.V.Chernov, A.O.Rybaltovskii, J. Phys. Chem., 1995, v.99, n.17, p.6640.

Relationship between Ge lone pair center and Ge electron center

Koichi Awazu
Groupe de recherche physique et technolgie des Couches Minces (GCM),
Département de Physique, Université de Montréal, P.O. Box 6128,
succursale "Centre-Ville", Montréal, Québec H3C 3J7, Canada
TEL (514) 343-6111 FAX (514) 343-2071

Yuichi Morishita, and Ken-ichi Muta
Showa Electric Wire and Cable Co. Ltd.,
Minami-Hashimoto, Sagamihara, 229, Japan
Tel (427) 74-8208 FAX (427) 73-3967

Introduction

Recently, material science on Bragg gratings are well studied, yet, there is still much room for investigation. For example, whether the 5eV optical absorption band in Ge doped silica is essential for the photo-sensitivity or not is highly debatable point. One of the reasons why photo-sensitive phenomena are complicate is that different light sources and samples have been used in each reports. Even if laser power for excitation is very week, two-photon process might not be negligible. For instance, Ge electron center (GEC)[1] is induced in the Ge-doped silica with UV illumination at 5eV by KrF excimer laser, in contrast, it is not observed in the sample illuminated at 5eV using Xe/Hg discharged lamp.[2] In this article, relationship between intensity at 5eV and GEC was examined. Secondly, relation between GEC generation and excitation photon energy was also examined.

Experimental procedure

$1GeO_2$:$9SiO_2$ glass rod was prepared by the vapor-phase axial deposition (VAD) method. More than 50 polished plates with 0.5mm thickness are made from the same rod. To examine the relation between the optical absorption at 5eV and the generation efficiency of GEC, the intensity of the 5eV band is controlled by the heat treatment in the O_2 or H_2 environment or by the high pressure treatment at 150atm in H_2 at room temperature. UV illumination was performed with a Xe/Hg discharged lamp, whose emission peak was at 5eV or undulator radiation at room temperature. The peak energy of the beam emitted from the undulator was tuned at 5.78eV or 6.4eV. Optical absorption and ESR were measured on each samples before and after illumination.

Results and Discussion

Fig.1 shows the optical absorption of $1GeO_2$:$9SiO_2$ plate before and after 5eV illumination using Xe/Hg discharged lamp. In the virgin sample (spectrum (a)), absorption band at 5.14eV and the absorption tail from the VUV absorption band can be observed. Both absorption bands are assigned to Ge lone pair center (GLPC).[3] In addition to these bands, 5.06eV band having week intensity might exist. After illumination (spectrum (b)), peak intensity at 5.06eV (not 5.14eV) decreased, on the other hand, peak intensity at 6.2eV increased. In the illuminated samples, ESR signal assigned to Ge-E' center is observed. Spectrum (c) denotes the UV illuminated one after H_2 loading at room temperature, under 150atm, and for two weeks. Intensity at 5.14eV (not 5.06eV) decreased with illumination. Spectrum (d) shows the sample heated in H_2 atmosphere at 400°C. Absorption intensities in the region above 5.4eV as well as at 5.14eV increase with the treatment. Dotted line (e) denotes the spectrum of the plate after UV illumination with Xe/Hg discharged lamp. Intensity at 5.14eV decreased, on the other hand, two absorption bands at 4.5eV and 5.8eV, which are assigned to GEC, were generated after illumination. GEC signal was observed in only H_2

treated Ge-doped silicas with UV illumination. GEC was not observed in virgin sample with UV illumination.

Fig.2 shows the absorption change at 4.5eV, which is assigned to GEC, as a function of photon number during illumination. Open circles, squares, and closed circles denote the illuminated samples with Xe/Hg discharged lamp emitted at 5eV, undulator at 5.8eV, and 6.4eV, respectively. When the photon energy for excitation is below 5eV, 4.5eV band assigned to GEC was not generated, the intensity at 4.5eV increased with illumination at 5.8eV and 6.4eV with increase of photon number. GEC signal in ESR was observed in virgin sample illuminated with UV above 5.8eV without any H_2 treatments.

Fig.3 shows the relationship between GLPC concentration and GEC concentration. GLPC concentration was estimated from the absorption coefficient at 5eV using value of the absorption cross section ($4\times10^{-18}cm^{-2}$).[3] GEC concentration was determined from the ESR measurement. Circles show the 5eV illuminated samples for 1,3, and 7 hours after heated H_2 treatment at 400°C. Squares denotes samples for 1 and 3 hours after heated H_2 treatment at 400°C. When one GLPC tunes to be one GEC, data will be on the solid line.

Conclusion

1. GEC was not observed in the Ge-doped silicas illuminated with Xe/Hg discharged lamp emitting at 5eV. In contrast, GEC generates in Ge-doped silicas illuminated with the Xe/Hg discharged lamp after heating in H_2 or putting into high pressure H_2 atmosphere.
2. GEC was also generates in Ge-doped silicas with illumination above 5.8eV without any H_2 treatment. Reaction modes were shown in Fig.4.

References

1. H.Kawazoe, Jpn.J.Appl.Phys., 71, 231 (1985).
2. K.Awazu and K.Muta, J.Non-cryst. Solids, 211, 158 (1997).
3. K.Awazu and H.Kawazoe, J.Appl.Phys., 68, 2713 (1990).

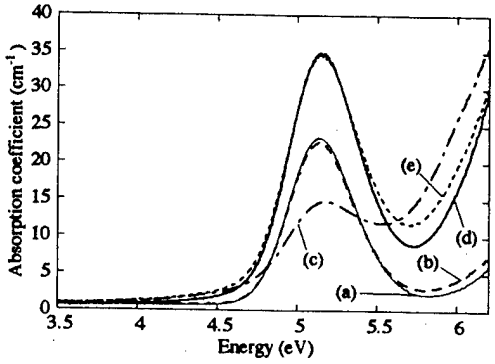

Fig.1 Optical absorption spectrum of $1GeO_2$:$9SiO_2$ plate. Spectrum (a) denotes virgin sample and H_2 loaded one. Both contours are almost same. Spectrum (b) is the UV illuminated sample without any H_2 treatment. Spectrum (c) denotes the UV illuminated one after H_2 loading at room temperature, under 150atm, and for two weeks. Spectrum (d) denotes the sample annealed in H_2 at 400°C. Spectrum (e) is the UV illuminated sample after the heated H_2 treatment. Xe/Hg discharged lamp which emits a broad UV light peaking at 5eV was used with photon number of $2.8\times10^{20}cm^{-2}$ for illumination. To remove the IR and deep UV light simultaneously emitted from the lamp, H_2O filter was used. Details on the technique was shown in ref.3.

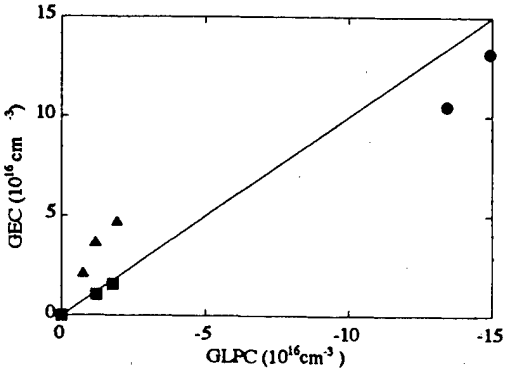

Fig.2 Relationship between GLPC concentration and GEC concentration. GLPC concentration was estimated from the absorption coefficient at 5eV

using value of the absorption cross section ($4\times10^{-18}cm^{-2}$). GEC concentration was determined from the ESR measurement. Circles show the 5eV illuminated samples for 1, 3, and 7 hours after heated H_2 treatment at 400°C. Squares denotes samples for 1 and 3 hours after heated H_2 treatment at 400°C. When one GLPC tunes to be one GEC, data will be on the solid line.

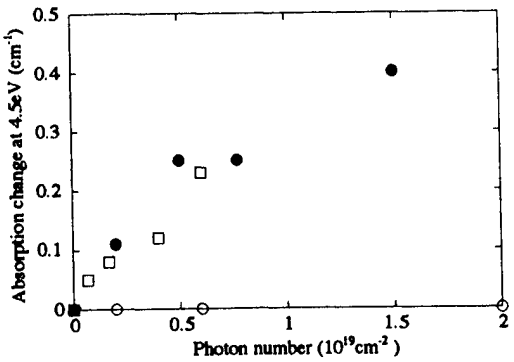

Fig.3 Absorption coefficient at 4.5eV band assigned to GEC as a function of photon number during UV illumination. The 5eV illumination was done with Xe/Hg discharged lamp, the 5.8eV and 6.4eV illumination was performed with undulator radiation.

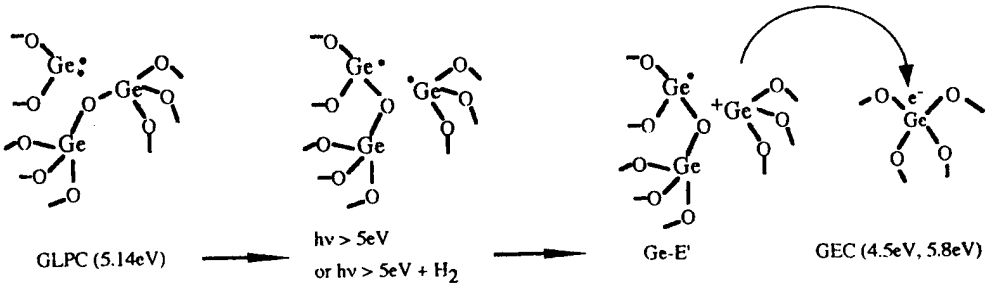

Fig.4 Chemical reaction models in Ge-doped silicas.

Bragg Gratings, Photosensitivity, and Poling in Glass Fibers and Waveguides: Applications and Fundamentals

Novel Grating Materials and Fabrication Methods

Monday, October 27, 1997

Charles Askins, U.S. Naval Research Laboratory
Presider

BME
11:00am–12:30pm
Washington/Wilson Room

Bragg Grating Fabrication in Fibers by Near-UV Light

D. S. Starodubov, V. Grubsky, J. Feinberg

The photosensitivity of germanosilicate fibers has been tied to the presence of germanium oxygen-deficient defects (GODC) [1,2]. These defects are identified by a strong absorption peak at 240 nm and a weaker absorption peak at 330 nm (Fig. 1) [3]. The microscopic model of these defects is still debated [4-7]; however, the three-level model of the defect shown in Fig. 2 nicely explains the defect's main spectroscopic features [4]. It was thought that color center formation due to photoionization of defects by 240 nm light was the principal mechanism of index change (through the Kramers-Kronig relation) [8]. However recent tension measurements and observations of glass densification after UV exposure suggest that a structural transformation of the glass occurs [9,10].

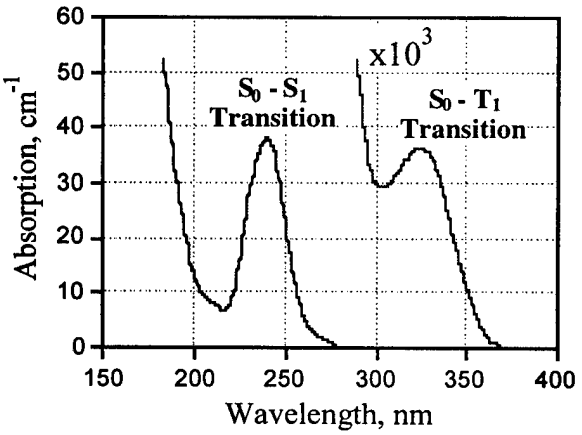

Fig. 1. The absorption spectrum of a germanium oxygen-deficient center (GODC) in silica glass has an absorption band at 240 nm (singlet to singlet) and a much weaker band at 330 nm (singlet to triplet) [3].

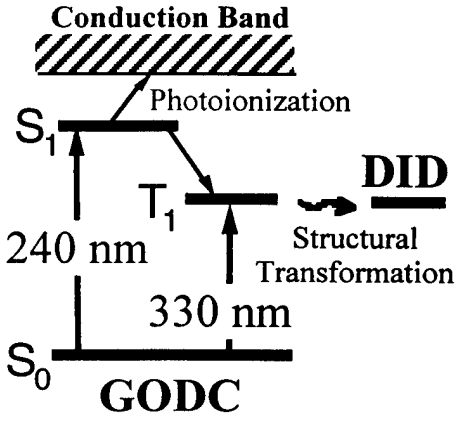

Fig. 2. Level diagram of a GODC showing two paths for its destruction by light: photoionization from the excited singlet state or structural transformation from the triplet state [14].

First near-UV experiments

Indirect signs of the possibility of an index change by near-UV light in glass were noticed before any grating fabrication experiments. In 1986 Noguchi et al. exposed multimode germanosilicate fiber with 20 mW of near-UV light at 351 nm at an intensity ~10^3 W/cm^2 and reported the formation of a luminescence band at 650 nm and a UV-induced absorption band at 630 nm [11]. The authors showed that the observed changes are due to Ge doping, but ascribed the induced luminescence to non-bridging oxygen hole centers and did not further investigate this unusual phenomenon. In 1992 Driscoll and Lawandy reported a significant and stable enhancement of photoinduced second-harmonic generation in fibers that had been previously exposed to near-UV light from an argon laser at 351 nm or 364 nm [12]. This result indicated that a new defect had been created by near-UV light. In 1993 Poirier et al. studied the bleaching dynamics of 400 nm luminescence in germanosilicate fibers and noticed that this blue luminescence decreased with time as a stretched exponential [13]. The authors suggested that a triplet-state related photochemical reaction was responsible for this behavior. Dianov and Starodubov proposed a simple experimental test of this idea: if triplet-state excitation is involved in the photosensitivity of germanosilicate glass, then direct excitation of the triplet state by near-UV 330 nm light should produce the same changes in the glass as 240 nm radiation [14]. An important difference between excitation with 330 nm light and 240 nm light is that the longer wavelength does not directly ionize the defect. Dianov and Starodubov also showed that 351 nm radiation bleaches GODC blue luminescence, produced 650 nm red luminescence [15,16], and causes partial erasure and tuning of long period index grating, implying a near-UV induced index change ~10^{-5} [14]. More direct proof of a near-UV induced index change in glass was reported in 1996 with the fabrication of a long-period grating in a Ge-doped glass fiber [17], although attempts of Bragg grating fabrication were not very successful [18,19].

How to write a Bragg grating with near-UV light

Because the absorption of a GODC is ~1000 times weaker with near-UV compared to mid-UV light, it is necessary to use a high writing intensity, typically a few kW/cm^2 to obtain an index change in a reasonable amount of time. Hundreds of milliwatts of near-UV light from an Ar laser focused by a cylindrical lens onto a fiber core will create a Bragg grating within a minute. Note that pulsed near-UV lasers with high peak power are less efficient for producing an index change than cw lasers because their high peak intensity damages the fiber, as with 157 nm writing [20]. The near-UV sensitivity of an ordinary Ge-doped fiber has a maximum at ~330 nm [19], and in hydrogen-loaded fiber this maximum shifts to even shorter wavelengths. Therefore, Ar laser lines at 334 nm are the optimal choice for most near-UV experiments.

Properties of near-UV fabricated Bragg gratings

We fabricated fiber Bragg gratings using a phase mask from Bragg Photonics. The obtained index change was ~10^{-4} and varied approximately linearly with the fiber's Ge concentration [21], as shown in Fig. 3. This indicates that the defect responsible for near-UV photosensitivity contains only 1 Ge atom (a Ge-Si wrong bond or a twofold coordinated Ge). We also studied germanosilicate fibers with Ce co-doping to see if an efficient donor of electrons such as Ce would enhance the glass's near-UV photosensitivity. It did not, which indicates that photoionization is not the principal mechanism for the refractive index change induced by near-UV light. However, we found that fibers co-doped with boron had an increased photosensitivity, which supports the idea that a structural transformation is enhanced in this type of fiber [22].

Annealing experiments of near-UV induced gratings show that their temperature stability is basically the same as that of gratings fabricated with mid-UV light. Near-UV light makes type I gratings, and does not damage the core-cladding interface [19,21]. These features make 330 nm light a reasonable alternative to 240 nm light for fabricating gratings in fibers.

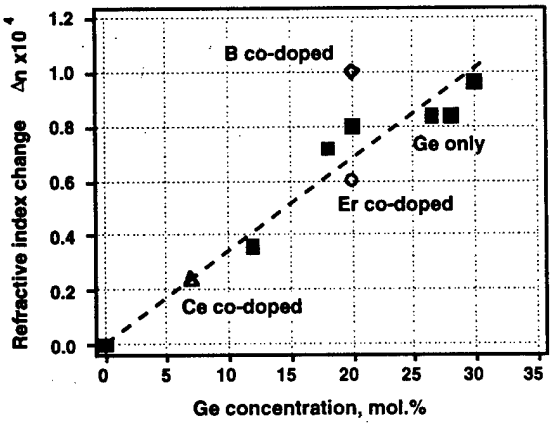

Fig. 3. Index change induced by near-UV light vs. Ge concentration in the glass fiber. Note that co-doping with B enhanced the index change while co-doping with Ce or Er did not [21].

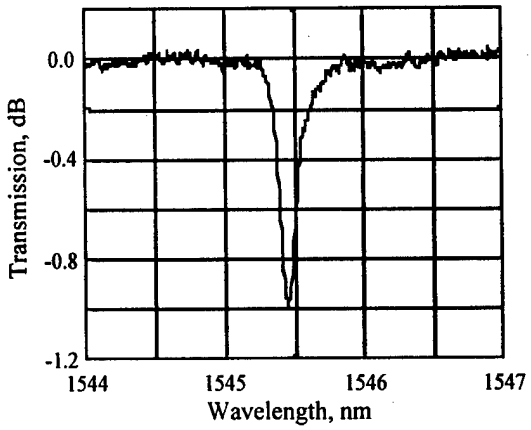

Fig. 4. Spectrum of a Bragg grating fabricated in a B co-doped fiber without hydrogen loading through a standard polymer jacket using 334 nm light [23].

Writing gratings through the polymer jacket

The standard polymer jackets of most fibers absorb light at 240 nm, so the jacket must be stripped before such light can write a grating in the fiber from the side. However, fiber jackets are reasonably transparent to 330 nm light. We used this fact to fabricate a Bragg grating in the fiber's core by writing right through a standard 63 μm-thick polymer jacket [23] (see Fig. 4). The main mechanism of polymer degradation from near-UV light is heating, and this degradation is faster for thicker coatings. However this degradation does not change the shape of the grating spectrum. Although using thin (40 μm-thick) and specially designed polymers makes it possible to fabricate

gratings with mid-UV 257 nm light, the resulting grating spectrum is distorted [24]. Therefore the near-UV technique seems more promising for the side writing through the polymer coating.

By hydrogen loading [25,26] our fibers we are able to produce enormous index changes up to 10^{-2} [27].

Conclusions

Near-UV light at 330 nm produces the same index gratings in fibers as mid-UV light at 240 nm, but due to the lower absorption with near-UV light damage of the fiber's core/cladding interface is avoided. Although near-UV light requires a higher writing power, this power is readily available from Ar lasers, which have better beam quality and coherence than 240 nm excimer lasers (and are less expensive and finicky than 240 nm frequency-doubled argon lasers). Photoionization of defects in the glass is not required to make a refractive index change. Instead, exciting the triplet state of the germanium oxygen-deficient defect appears to activate structural transformation in the glass matrix. The transparency of a number of polymer fiber coatings starting from 300 nm makes it possible to fabricate fiber gratings right through the jacket of the fiber. Hydrogen sensitizing of the glass is very efficient with near-UV writing, and allows fabrication of strong index gratings with $\Delta n > 10^{-2}$.

References

1. K. O. Hill, Y. Fujii, D. C. Johnson, B. S. Kawasaki, Appl. Phys. Lett. 32, 647 (1978).
2. G. Meltz, W. W. Morey, and W. H. Glenn, Opt. Lett. **14**, 823 (1989).
3. M. J. Yuen, Appl. Opt. **21**, 136 (1982).
4. L. S. Skuja, J. Non-Cryst. Solids **149**, 77 (1992).
5. H. Hosono, Y. Abe, D. L. Kinser, R. A. Weeks, K. Muta, H. Kawazoe, Phys. Rev. B **46**, 11445 (1992).
6. M. Gallagher, U. Osterberg, J. Appl. Phys. **74**, 2771 (1993).
7. V. B. Neustruev, J. Phys. Condens. Matter, **6**, 6901 (1994).
8. L. Dong, J. L. Archambault, L. Reekie, P. St. J. Russell, D. N. Payne, Appl. Opt. **34**, 3436 (1995).
9. P. Y. Fonjallaz, H. G. Limberger, R. P. Salathe, F. Cochet, B. Leuenberger, Opt. Lett. **20**, 1346 (1995).
10. B. Poumellec, P. Guenot, I. Riant, P. Sansonetti, P. Niay, P. Bernage, J. F. Bayon, Opt. Materials **4**, 441 (1995).
11. K. Noguchi, N. Uesugi, K. Suzuki, Electron. Lett. **22**, 519 (1986).
12. T. J. Driscoll, N. M. Lawandy, Opt. Lett. **17**, 571 (1992).
13. M. Poirier, S. Thibault, J. Lauzon, F. Ouellette, Opt. Lett. **18**, 870 (1993).
14. E. M. Dianov, D. S. Starodubov, Proc. SPIE **2777**, 60 (1995).
15. E. M. Dianov, D. S. Starodubov, Opt. Lett. **21**, 635 (1996).
16. E. M. Dianov, D. S. Starodubov, A. A. Frolov, Electron. Lett. **32**, 246 (1996).
17. E. M. Dianov, D. S. Starodubov, S. A. Vasiliev, A. A. Frolov, O. I. Medvedkov, Vol. 1 of LEOS'96 Annual Meeting Proc., paper TuCC2, 374 (1996).
18. R. M. Atkins and R. P. Espindola, Appl. Phys. Lett. **70**, 1068 (1997).
19. E. M. Dianov, D. S. Starodubov, S. A. Vasiliev, A. A. Frolov, O. I. Medvedkov, Opt. Lett. **21**, 221 (1997).
20. K. Beckley, P. Herman, CLEO'97 Proc., 1997 OSA Tech. Dig. Ser. **11**, CTuN3, 107 (1997).
21. D. S. Starodubov, V. Grubsky, J. Feinberg, B. Kobrin, S. Juma, Opt. Lett. **22**, 1086 (1997).
22. D. L. Williams, B. J. Ainslie, J. R. Armitage, R. Kashyap, R. Campbell, Electron.Lett. **29**, 45 (1993).
23. D. S. Starodubov, V. Grubsky, J. Feinberg, Electron. Lett. **33**, in press (1997).
24. R. P. Espindola, R. M. Atkins, D. A. Simoff, K. T. Nelson, and M. A. Paczkowski, OFC'97 Tech. Dig., Postdeadline paper PD-4.
25 P. J. Lemaire, R. M. Atkins, V. Mizrahi, W. A. Reed, Electron. Lett. **29**, 1191 (1993).
26. D. S. Starodubov, E. M. Dianov, S. A. Vasiliev, A. A. Frolov, O. I. Medvedkov, A. O. Rybaltovskii, V. A. Titova, Proc. SPIE **2998**, 111 (1997).
27. D. S. Starodubov, V. Grubsky, J. Feinberg, T. Erdogan, CLEO'97 Tech. Dig., Postdeadline paper CPD-24.

Highly Photosensitive Germanosilicate Fibre Codoped with Nitrogen

E.M.Dianov, K.M.Golant, V.M.Mashinsky, O.I.Medvedkov, I.V.Nikolin, O.D.Sazhin, S.A.Vasiliev.

Fiber Optics Research Center at the General Physics Institute, Russian Academy of Sciences,

38, Vavilov Str., 117942, Moscow, Russia.

Tel.: 7-095-1328306, Fax: 7-095-1358139, E-mail:sav@fo.gpi.ac.ru

INTRODUCTION

In-fiber grating writing based on the photorefractive effect is now attracting considerable interest [1]. However, photosensitivity of standard germanosilicate fibres with a moderate concentration of germanium in the core (5 ÷ 7 mol.% GeO_2) is not large and does not allow efficient writing of refractive index gratings. To increase the writing efficiency, one has to increase the germanium concentration and/or load the fibre with hydrogen [2]. Increasing the germanium concentration results in a reduction of the mode spot size and in additional losses when the fibre is spliced with a standard telecommunication fibre. Hydrogen loading complicates the grating technology and raises losses in the IR region owing to the OH-group absorption. Therefore, optimization of the grating writing technology and development of novel types of photosensitive fibres are now high on the agenda.

It was shown in [3] for the films synthesized on silica substrates by plasmachemical deposition (PECVD) that doping germanosilicate glass with nitrogen increases its photosensitivity. Clearly, fabrication of such a glass by using a fibre preform technology and investigation of the final fibres would be of great practical interest.

With the help of a hydrogen-free plasmachemical technology we have fabricated, for the first time, a preform and a fibre with a silica core codoped with nitrogen and germanium. This paper deals with UV absorption spectra of the core glass and photosensitivity of the fiber.

SAMPLE PREPARATION AND EXPERIMENTS

The fibre preform was fabricated by the SPCVD process [4]. Doping silica with nitrogen was performed under the conditions described in [5]. The preform core contained ~7 mol.% GeO_2 and ~0.1 at.% N, and the core/cladding index difference was $\Delta n \approx 0.01$. For comparison, we used nitrogen-free germanosilicate fibres prepared by the standard MCVD process.

The UV absorption spectra were measured on transverse preform slices of about 100 μm in thickness. The dynamics of refractive index change under the action of cw radiation of a frequency doubled Ar^+-laser (λ = 244 nm, I~13 kW/cm^2) was measured by the interferometric technique [6]. For this purpose two long-period 3 dB gratings were written in

the fibre under test to form a Mach-Zehnder interferometer. By measuring the evolution of the transmission spectrum of the interferometer in the process of side irradiation of the fibre section between the gratings it was possible to determine the induced refractive index of the fiber core: $\Delta n_{ind} \approx \lambda\Delta\varphi_{ind}/(2\pi L\eta)$, where λ is the probe light wavelength, $\Delta\varphi_{ind}$ is UV-induced phase differencebetween core and cladding modes, L is the length of the fibre section being irradiated, η is the share of the fundamental mode power propagating in the core.

RESULTS AND DISCUSSION

The UV absorption spectrum in the Ge- and N-codoped silica is similar to that in N-free germanosilicate glass (Fig.1): we see the 242 nm singlet-to-singlet absorption band of the germanium oxygen-deficient centre (Ge-ODC) and a short wavelength absorption edge ($\lambda < 210$ nm). Note that the bands observed earlier in Ge-free N-doped silica [7] are absent. The amplitude of the Ge-ODC absorption band in the Ge- and N-codoped silica amounted to 670 dB/mm, which far exceeds the values commonly observed in germanosilicate glass with 7 mol.% GeO_2 fabricated by the MCVD process. In the latter case the ratio of the absorption at 242 nm to the concentration of germanium dioxide $k = \alpha_{242} / C_{GeO_2}$ lies in the range 10 ÷ 40 dB/(mm×mol.% GeO_2) [8], whereas in the Ge- and N-codoped silica this ratio turned out to be 100 dB/(mm×mol.% GeO_2). Thus, the addition of nitrogen strongly increases the Ge-ODC concentration. The luminescence spectrum of the Ge- and N-codoped silica excited at 242 nm exhibited only the two well-known bands of Ge-ODC (290 and 395 nm).

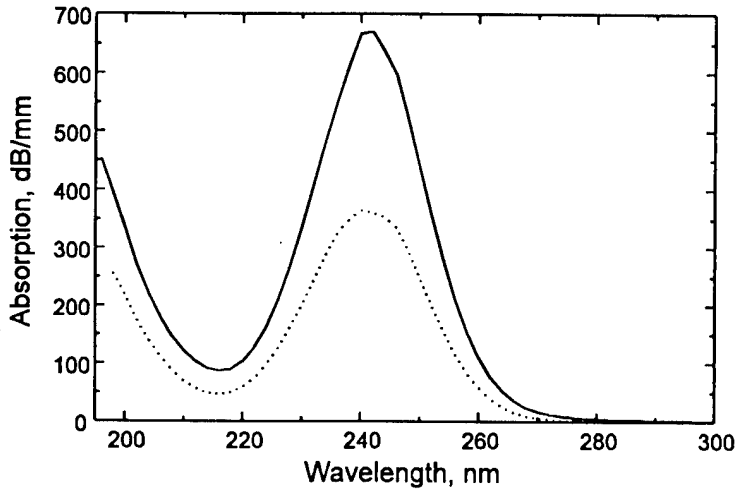

Fig.1. Absorption spectra of silica glass doped with:
——— *7 mol.% GeO_2 and 0.1 at.% N (SPCVD-technology);*
····· *20 mol.% GeO_2 (MCVD-technology).*

The dose dependencies of photoinduced refractive index in different fibres are shown in Fig.2. The Ge- and N-codoped fibre showed a greater photosensitivity than an N-free fiber with 12 mol.% GeO_2. The induced refractive index in the N-and Ge-codoped fibre amounted to 2.8×10^{-3} without hydrogen loading and 1×10^{-2} in a fibre piece treated in hydrogen at a pressure of 200 atm during two weeks. It is noteworthy that the induced refractive index in the N-codoped fibre rose up to doses of about 300 kJ/cm² (type I photosensitivity), whereas an N-free germanosilicate fibre with 20 mol.% GeO_2 demonstrated the type IIa photosensitivity [9] at a dose of ~50 kJ/cm².

The isochronal annealing of Bragg gratings written in the N-codoped fibre have shown that their high-temperature stability is approximately the same as that of gratings imprinted in an N-free fibre. This fact confirms a suggestion that high photorefractivity of the Ge- and N-codoped fiber is governed mainly by a Ge-ODC concentration change.

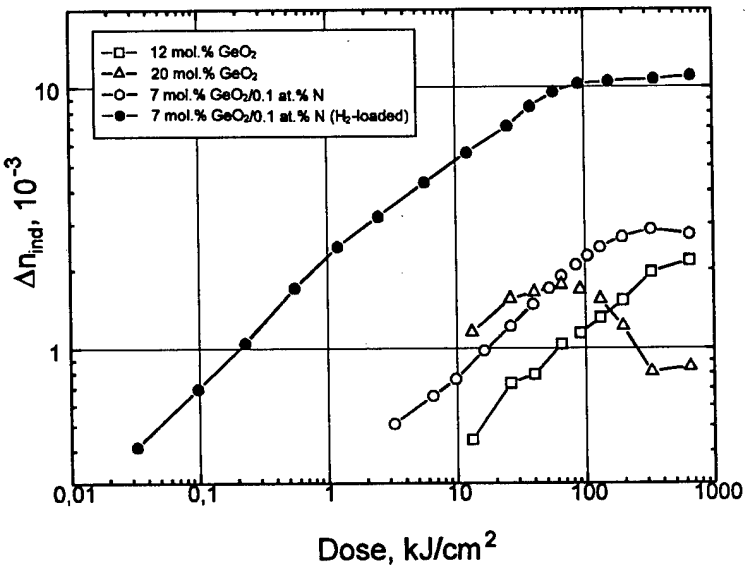

Fig.2. Dose dependencies of induced index change in different germanosilicate fibres and in a Ge- and N-codoped fibre.

CONCLUSION

The novel nitrogen-doped germanosilicate fibre prepared by SPCVD has been found to be much more photosensitive than similar N-free fibres. The increase in photosensitivity is believed due to an increase in the concentration of the germanium oxygen-deficient centres in this glass. Hydrogen loading magnifies photosensitivity of N-doped germanosilicate fibres. Because the waveguide parameters of such fibres can be made very close to those of standard telecommunication fibres, gratings written in N-doped germanosilicate fibres may find wide application in fibre-optic communication.

REFERENCES

1. R.Kashyap: *Opt. Fib. Technol.*, 1994, **1**, pp.17-34.
2. P. J.Lemaire, R. M.Atkins, V.Mizrahi, W. A.Reed: *Electron. Lett.*, 1993, **29**, pp.1191-1193.
3. C.V.Poulsen, T.Storgaard-Larsen, J.Hubner, O.Leistiko: Proc. SPIE'97, San Jose, 1997, **2998**, pp.132-141.
4. D.Pavy, M.Moisan, S.Saada, P.Chollet, P.Leprince, J.Marrec: *Proc. ECOC'86*, Barcelona, 1986, pp.19-22.
5. E.M.Dianov, K.M.Golant, A.S.Kurkov, R.R.Khrapko, A.L.Tomashuk: *J. Lightwave Technol.*, 1995, **13** (7), pp.1471-1474.
6. E.M.Dianov, S.A.Vasiliev, A.S.Kurkov, O.I.Medvedkov, V.N.Protopopov: *Proc. ECOC'96*, Oslo, Norway, 1996, **1**, pp.65-68.
7. E.M.Dianov, K.M.Golant, R.R.Khrapko, O.I.Medvedkov, A.L.Tomashuk, S.A.Vasiliev: *Opt. Mat.*, 1996, **5**, pp.169-173.
8. L.Dong, J.Pinkstone, P.St.J.Russell, D.N.Payne: *J. Opt. Soc. Amer. B*, 1994, **11**, pp.2106-2111.
9. W.X.Xie, P.Niay, P.Bernage, M.Douay, J.F.Bayon, T.Georges, M.Monerie, B.Poumellec: *Optics Commun.*, 1993, **104**, pp.185-195.

Wide Range and Linearity of Near-UV Induced Index Change in Hydrogen-Loaded Fibers: Applications for Bragg Grating Fabrication

V. Grubsky, D. S. Starodubov*, and J. Feinberg
Department of Physics
University of Southern California
Los Angeles, CA 90089-0484
(213) 740-1134; Fax (213) 740-6653

* Permanent address: Fiber Optics Research Center, General Physics Institute of the Russian Academy of Science, Moscow, Russia.

Because of their potential applications in fiber communication systems, there is a considerable interest and possible profit in exploring new techniques for fabricating fiber Bragg gratings. For example, the photosensitivity of Ge-doped fiber to mid-UV (240 nm) light can be substantially improved by loading the fiber with molecular hydrogen before writing [1-3]. However, the strong absorption of 240 nm light in the fiber's core causes the induced index change across the core to be non-uniform [4]. Also, strong absorption of 240 nm light can heat the core and cause a thermal reaction with molecular hydrogen [3] that saturates the index change and substantially reduces the contrast of the final grating.

Fortunately, germanosilicate glass is also sensitive to light in the near UV (at 330 nm) where the absorption is smaller [5], so the core stays cooler during writing. Hydrogen loading of the fiber increases the index induced by near-UV light [6], making it possible to fabricate strong Bragg gratings ($\Delta n = 3 \times 10^{-3}$) [7].

In this paper we show that a refractive index change as large as 10^{-2} can be obtained in high-pressure, hydrogen-loaded fibers using near-UV exposure. The index change is found to be linear with fluence over almost the entire range of index variation. The observed linearity of the process is used to tune an existing grating over a large (~ 5 nm) tuning range by uniform, post-fabrication exposure. We can also overlap gratings in the same physical region of the fiber making low dispersion fiber grating devices.

We fabricated fiber Bragg gratings using the phase mask technique [2]. Our 1-cm long silica phase mask was made by QPS Technology and had a period of 1.06 microns. It was optimized for the near-UV wavelength region. We illuminated the fiber through the mask with light from an argon-ion laser operating on a single, near-UV line (334 nm) with the aid of an intracavity prism. The laser light was focused on the fiber core by a 3-cm focal length cylindrical lens of fused silica to a typical writing intensity of ~ 2×10^3 W/cm^2. All grating spectra were measured in transmission with an optical spectrum analyzer (Ando AQ 6315A).

Our germanosilicate fiber was made in Fiber Optics Research Center, Moscow and had a Ge concentration ~26 mol.% in the core. We loaded our fiber in a high-pressure (~300 atm.) chamber at 50°C for 2 days.

Figure 1 shows the time dependence of the index change induced by near-UV light in the fiber with hydrogen loading. We measured Δn by first writing a 50% reflectivity grating in the fiber and then exposing it to uniform near-UV light and measuring the resulting shift in the grating resonance. While in fibers without hydrogen the index change saturated at ~10^{-4}, in our hydrogen-loaded fiber the index change grew linearly with fluence to saturate at a value 100 times larger.

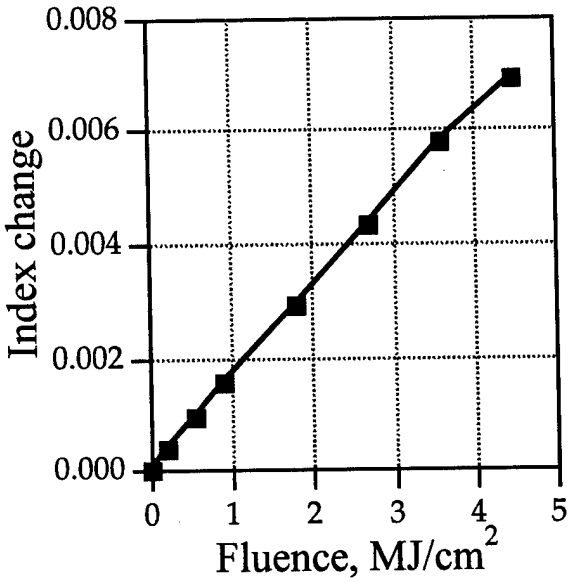

Fig. 1. Change in the refractive index vs. near-UV fluence in a hydrogen loaded fiber. The index change saturates at 10^{-2} at a fluence of ~15 MJ/cm^2.

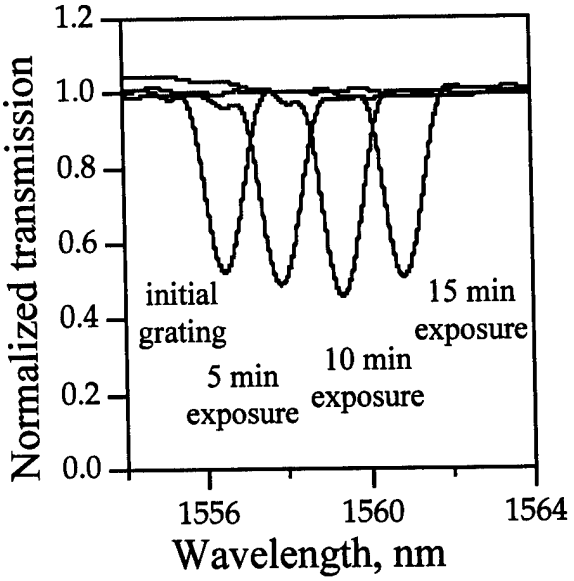

Fig. 2. Tuning of a fiber Bragg grating by uniform, near-UV exposure. Tuning over the 4.4 nm range shown here caused only a ±6% variation in the grating strength.

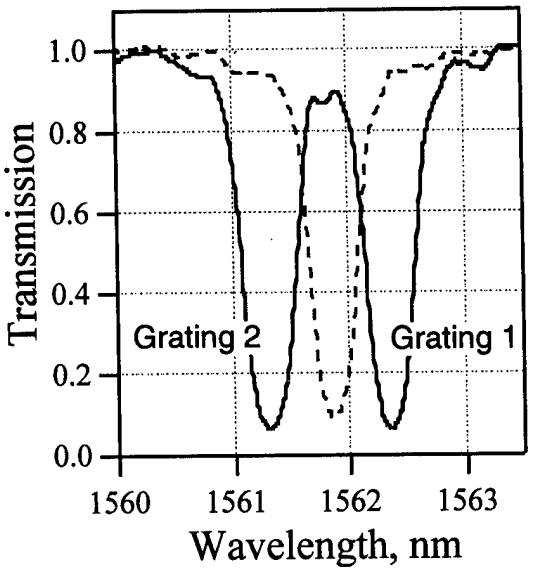

Fig. 3. Transmission spectrum of two Bragg gratings written in the *same* 3-mm long section of a hydrogen-loaded fiber. The dotted line is the spectrum of the first grating alone. The solid line is the spectrum with both gratings in place. The shift of grating 1 to longer wavelengths after grating 2 is written is due to the increase in the core's average refractive index.

Exposure of a fiber before or after grating fabrication to change the average index is a useful technique for fabricating chirped gratings [8,9]. By changing the average refractive index one can change the resonance wavelength of a fiber grating. To demonstrate this we first fabricated a 1-mm long Bragg grating with 50% reflectivity. Figure 2 shows that the central wavelength of the grating could be tuned over a 4.4 nm range with only ±6% variation in the grating strength by subsequent exposure of the fiber to uniform, near-UV light. (Actually, we achieved more than a 10 nm tuning range, but only at the cost of a decrease in the grating's reflectivity.)

Figure 3 shows the spectrum of two gratings written sequentially in the same 3 mm-long physical region of the fiber. We first uniformly exposed a 3-mm section of fiber to near-UV light to push the fiber's response into the linear region shown in Figure 1. We then created a grating by exposing the fiber through the phase mask. Finally, we tilted the phase mask (to change the grating's resonant wavelength) and re-exposed the fiber. Note that here the gratings were superimposed linearly, in contrast to previous work [9].

In summary, a refractive index change as large as 10^{-2} is demonstrated using near-UV light in hydrogen-loaded germanosilicate fiber for the first time to our knowledge. We exploit the linear dependence of this index change on near-UV fluence to accurately and permanently tune the grating resonance over a ~ 5 nm range without significant distortion of the grating spectral shape. We also demonstrate the fabrication of overlapped Bragg gratings in the same physical region of the fiber.

References

1. G. Meltz, W. W. Morey, and W. H. Glenn, "Formation of Bragg gratings in optical fibers by a transverse holographic method," Opt. Lett. **14** (15), 823 (1989).

2. B. Malo, F. Bilodeau, J. Albert, D. C. Johnson, K. O. Hill, Y. Hibino, and M. Abe, "Photosensitivity in optical fiber and silica-on-substrate waveguides," SPIE Proc. **2044**, pp. 42-54 (1993).

3. P. J. Lemaire, R. M. Atkins, V. Mizrahi and W. A. Reed, "High pressure H_2 loading as a technique for achieving ultrahigh UV photosensitivity and thermal sensitivity in GeO_2 doped optical fibers," Electron. Lett. **29** (13), pp. 1191-1193 (1993).

4. A. M. Vengsarkar, Q. Zhong, D. Inniss, W. A. Reed, P. J. Lemare, S. G. Kosinski, "Birefrngence reduction in side-written photoinduced fiber devices by dual-exposure method," Opt. Lett. **19** (16), pp. 1260-1262 (1994).

5. E. M. Dianov and D. S. Starodubov, "Microscopic mechanisms of photosensitivity in germanium-doped silica glass," SPIE Proc. **2777**, pp. 60-70 (1995).

6. D. S. Starodubov, E. M. Dianov, S. A. Vasiliev , A. A. Frolov, O. I. Medvedkov, A. O. Rybaltovskii, and V. A. Titova, "Hydrogen enhancement of near-UV photosensitivity of germanosilicate glass," SPIE Proc. **2998**, pp. 111-121 (1997).

7. D. S. Starodubov, V. Grubsky, J. Feinberg, and T. Erdogan "Near-UV fabrication of ultrastrong Bragg gratings in hydrogen-loaded germanosilicate fibers," CLEO'97 Postdeadline paper CPD24.

8. K. O. Hill, F. Bilodeau, B. Malo, T. Kitagawa, S. Theriault, D. C. Johnson, J. Albert, and K. Takiguchi, "Chirped in-fiber Bragg gratings for compensation of optical fiber dispersion," Opt. Lett. **19** (17), pp. 1314-1316 (1994).

9. K. Sunden, L. A. Everall, J. A. R. Williams, and I. Bennion, "Single and multi-passband Moire filters from dual exposure of uniform -period and chirped phase masks," SPIE Proc. **2998**, pp. 29-34 (1997).

157-nm Photosensitivity in Germanosilicate Waveguides

Peter R. Herman, Keith Beckley, and Sola Ness
Dept. of Electrical & Computer Eng'g, University of Toronto,
10 King's College Rd., Toronto, ON, M5S 3G4, Canada
Tel: 416 978 7722; Fax: 416 971 3020; hermanp@ecf.utoronto.ca

In standard optical communication fiber, low Ge-dopant levels (~3%-GeO_2) preclude strong photosensitivity responses, restricting index-of-refraction changes to 1-4 × 10^{-4} [1,2]. Type II index changes that rely on high laser fluence are less attractive because of material damage [3,4]. Therefore, sensitization techniques such as hydrogen loading [5], high germanium concentration [6], and flame brushing [7] are frequently employed to provide commercially attractive index-of-refraction changes of >10^{-3}. However, this improved sensitivity trades against poor coupling efficiency and inconvenience when exposed fibers are connected into ordinary telecommunication networks.

Vacuum-ultraviolet (VUV; 100-200 nm) laser radiation is a promising source for overcoming the weak photosensitivity responses of low-Ge doped waveguides. Such radiation may access new defect bands, and provide strong linear absorption for above bandgap photons. Hill and coworkers [1] demonstrated a 10-fold improvement in the saturated index modulation (to Δn = ~10^{-3}) of standard telecommunication fiber by shifting from a 248-nm to 193-nm laser source. The authors proposed a two-photon mechanism that accesses states high in the conduction band, making available many more active reaction sites (precursors) for contribution to the index change. However, the inherent weakness of two-photon processes was responsible for a long 15-min. writing time at 50 Hz.

This paper presents new results on the photosensitivity responses of optical fibers and slab waveguides driven by 157-nm radiation from a F_2 laser. Strong photosensitivity responses are anticipated because of the close proximity of 7.9-eV photons to the bandgap of germanosilicate—a 7.1-eV bandgap energy has been reported [8] for 5%-GeO_2 doped silica. Evidence for strong 157-nm interactions in fused silica and germanosilicate has been noted by this laboratory in related VUV ablation studies [9,10]. The 157-nm radiation lowers the ablation threshold, and furnishes smoothly etched surfaces free of debris and microcracks in comparison with 193-nm laser light. An ablation threshold 0.38 J/cm^2 defines an upper exposure limit for the germanosilicate guiding layers while a cladding attenuation of α_{157nm} = 10 cm^{-1} [11] is sufficiently weak to propagate the laser radiation to the fiber core.

The photosensitivity response of two single-mode fiber types were examined: high Ge-doped fiber (8%-GeO_2, JRFTV 1066AITV) and standard telecommunication fiber (3%-GeO_2, Corning SMF-28). Both fiber types were also soaked in 3-atm. hydrogen for >2 weeks to provide a total of four sample types for study. Planar waveguides (PIRI, SMPWL, ~3% Ge) were also examined. Fibers were configured into a Michelson interferometer, and exposed in ambient argon to provide VUV transparency, permitting real-time characterization of the laser-induced index changes at 1.55-μm wavelength. Up to 9,000 exposures were made for single-pulse fluence values of 25, 100 and 450 mJ/cm^2.

Results for the Corning SMF-28 fiber are shown in Fig. 1. Rates of index change are several factors larger at fluences of 100-450 J/cm^2, and orders of magnitude faster at lower fluence than the 193-nm results in Ref. 1. The 157-nm fluence dependence suggests a single-photon dependence of index change in departure with the 2-photon response noted at 193-nm in Ref. 1 for the same fiber type. Further work is in progress to saturate the index change for comparison with the longer-wavelength studies. The 157-nm induced index changes were ~10-fold faster for hydrogen-loaded fiber while higher germanium content had little effect on the rates.

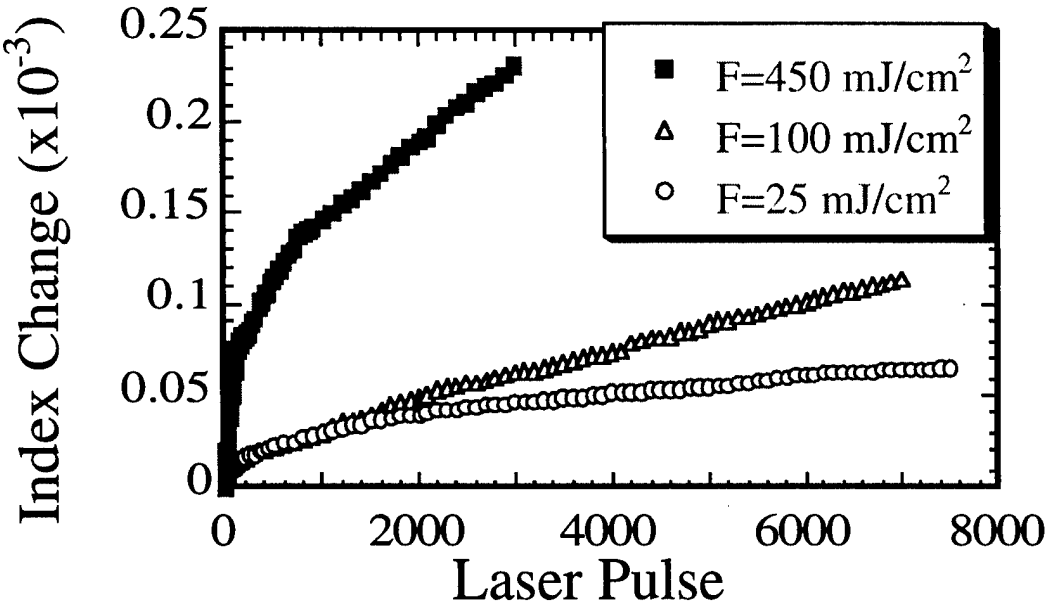

Figure 1 Index of refraction changes observed in Corning SMF-28 fiber exposed to 157-nm radiation. Values were inferred using a Michelson interferometer configuration.

All fiber-types yielded to a non-linear damage mechanism at higher fluence, especially for the highly doped or hydrogen loaded fibers. Such fibers developed milky-colored striations, were brittle, and suffered radiation losses. One approach to avoid cladding damage is to apply such radiation to claddless planar waveguide structures. Current experiments have shown an index change of 2×10^{-4} in hydrogen-soaked PIRI waveguides following an exposure of 5,000 pulses at 80 mJ/cm^2.

Index changes of fibers were also monitored by writing 1.55-μm Bragg gratings using a custom VUV phase-mask. A reflection spectrum is shown in Fig. 2. Values of index change based on reflection and transmission spectra concur with the Michelson interferometer results.

Current experiments are aimed at determining saturated index-of-refraction changes in both fiber and slab waveguides, and assessing the practical limits imposed by the high-fluence damage. This paper will review the current status of our 157-nm photosensitivity studies in germanosilicate waveguide materials.

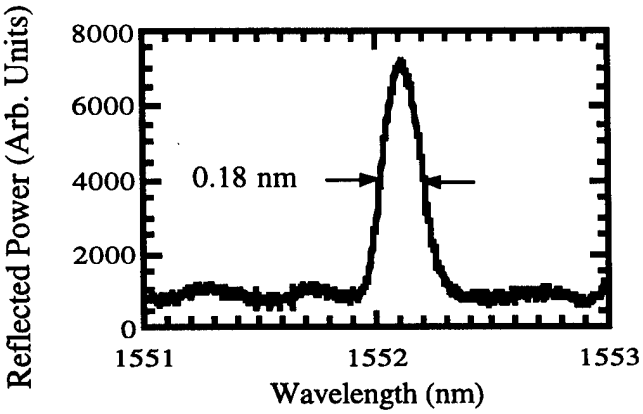

Figure 2 Reflection spectrum of a fiber containing a Bragg-grating written by 157-nm laser radiation. The fiber was exposed through a MgF_2 phasemask to 500 laser pulses at 100 mJ/cm^2 fluence.

---

1. J. Albert, B. Malo, K.O. Hill, F. Bilodeau, D.C. Johnson, and S. Theriault, Appl. Phys. Lett. **67**, pp. 3529-31, 1995.
2. One exception is a low-defect fiber (Philips, DLPC5) which yieled a large value of 1.2×10^{-3} following a long, 30-min exposure (180,000 pulses) at 240 nm: H.G. Limberger, P.Y. Fonjallaz, and R.P. Salathe, Electron. Lett. **29**, pp. 47-49, 1993.
3. J.-L, Archambault, L. Reekie, and P. St. J. Russell, Electron. Lett. **29**, pp. 28-29, 1993; ibid. pp. 453-455.
4. C.G. Askins, T.-E. Tsai, G. M. Williams, M.A. Putnam, M. Bashkansky, and E.J. Friebele, Opt. Lett. **17**, pp.833-835, 1992.
5. P.J. Lemaire, R.M. Atkins, V. Mizrahi, and W.A. Reed, Electron. Lett. **29**, pp. 1191-1193, 1993.
6. E. Fertein, S. Legoubin, M. Douay, S. Canon, P. Bernage, P. Niay, F. Bayon, and T. Georges, Electron. Lett. **20**, pp. 1838-39, 1991.
7. F. Bilodeau, B. Malo, J. Albert, D.C. Johnson, K.O. Hill, Y. Hibino, M. Abe, and M. Kawachi, Opt. Letts. **18**, pp. 953-955, 1993.
8. J. Nishi, N. Kitamura, H. Yamanaka, H. Hosono, and H. Kawazoe, Opt. Lett. **20**, pp. 1184-86, 1995.
9. P.R. Herman, B. Chen, D.J. Moore, and M. Canaga-Retnam, Mat. Res. Soc. Symp. Proc. **236**, pp. 53-58, 1992.
10. P.R. Herman, K. Beckley, B. Jackson, K. Kurosawa, T. Yamanishi, and J. Yang, Processing applications with the 157-nm fluorine excimer laser, in Excimer Lasers, Optics, and Applications, SPIE Proc. **2992**, pp. 86-95, 1997.
11. E.D. Palik, Handbook of Optical Constants of Solids, Academic Press, New York, 1986.

Strong Higher-Order Fiber Bragg Gratings Written with an Amplitude Mask

J. L. Wagener, R. P. Espindola and A. M. Vengsarkar
Bell Laboratories, Lucent Technologies
700 Mountain Avenue, Murray Hill, NJ 07974
Tel: (908) 582-4746, Email: jlw@lucent.com

Reflective Bragg gratings have been written in optical fibers using UV induced index changes. Initial work used a standing wave interference pattern set up by light launched down the fiber core.[1] The more versatile techniques of side-writing using bulk interferometric fringes[2] and phase-masks[3] followed. The field of phase-mask-written Bragg gratings in germano-silicate fibers has matured with the use of specially designed high-photosensitivity fiber and hydrogen loading.[4] While gratings written with these methods can be precisely tailored in spectral shape, bandwidth and strength, a precise mask, a coherent laser, and very stable alignment during the exposure are needed. Multiple grating applications, including weak pump-diode stabilizers, fiber laser mirrors, and grating sensors may not require the high precision gratings produced with the phase mask method, but would benefit from an inexpensive mass production technique. In this paper we demonstrate an amplitude mask exposure technique to create strong higher order Bragg reflectors with minimal optics.

Higher-order Bragg reflectors written with an amplitude mask do not require the laser coherence, alignment stability or mask precision necessary using the phase mask writing technique. The Bragg wavelength is given by $\lambda_b = \frac{2n_{eff}\Lambda}{m}$ where Λ is the grating period and m is the grating order. Higher order reflectors (m = 2, 3, 4 ...) create the same phase matching condition, but with reduced strength due to the reduced number of periodic perturbations in any given grating length. Mihailov and Gower have written moderate strength 6th order gratings using a pulsed KrF laser.[5] They imaged an amplitude mask with a lens onto the fiber to create the grating. However, the maximum strength was limited to 5.5 dB and significant loss due to fiber damage was observed. An exposure technique that does not require mask imaging and does not create significant fiber damage would be desirable. For the gratings described below, we chose amplitude masks with 2.14 μm and 2.68 μm periods (m = 4 & 5) as a compromise between the strong strengths of the low orders, and the ease of fabrication of the higher orders.

A schematic of the grating writing setup is shown in Figure 1. The output of a frequency-doubled Argon laser operating at λ = 257 nm was focused to a broad line using a combination of a 10X beam expander and a 15 cm cylindrical lens. Gratings were observed in multiple fiber types, all deuterium loaded, with the strongest gratings being written in a high-delta high-photosensitive fiber.

The amplitude mask was lithographically-patterned chrome-on-silica. Two masks, one with 1.07 μm slits spaced at 2.14 μm, and another with 1.34 μm slits spaced at 2.68 μm, were made. These spacings correspond to 4th and 5th order gratings at 1560 nm,

compared to the standard spacing of 0.535 μm for a first order grating. Note that the smallest slit is on the order of four UV wavelengths. Each mask was 5 mm long with no known phase errors in the periodicity.

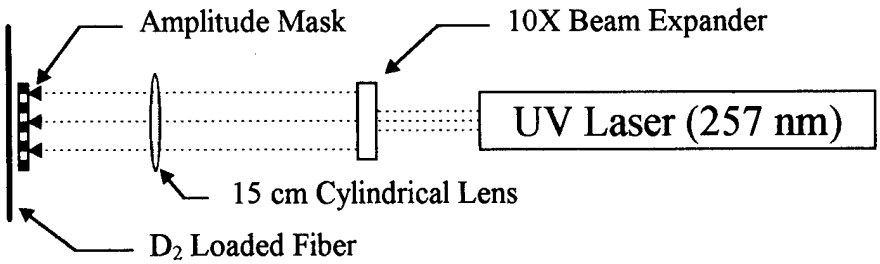

Figure 1: Amplitude mask setup for writing higher order Bragg reflectors.

Figure 2 shows the transmission spectrum of a 4th order Bragg grating 5 mm long, written using the 2.14 μm period mask. A pseudo-gaussian amplitude profile was written across the grating length due to the transverse intensity profile of the laser beam. The grating depth approaches 40 dB with the characteristic Fabry Perot modes on the short wavelength edge along with cladding mode loss starting 7 nm away. While this grating was exposed for 75 minutes, the use of a more tightly focused beam can decrease this writing time significantly. The period of 2.14 μm corresponds to two optical wavelengths at 1560 nm in the fiber core at an n_{eff} of 1.458, slightly higher than the unexposed fiber fundamental mode n_{eff} due to the high DC UV exposure through the amplitude mask. The grating peak wavelength shifts 5 nm during writing and indicates a change in the average n_{eff} of 4.6×10^{-3}. A 5th order reflection 13 dB deep was observed at 1256 nm along with a weak 6th order reflection at 1040 nm.

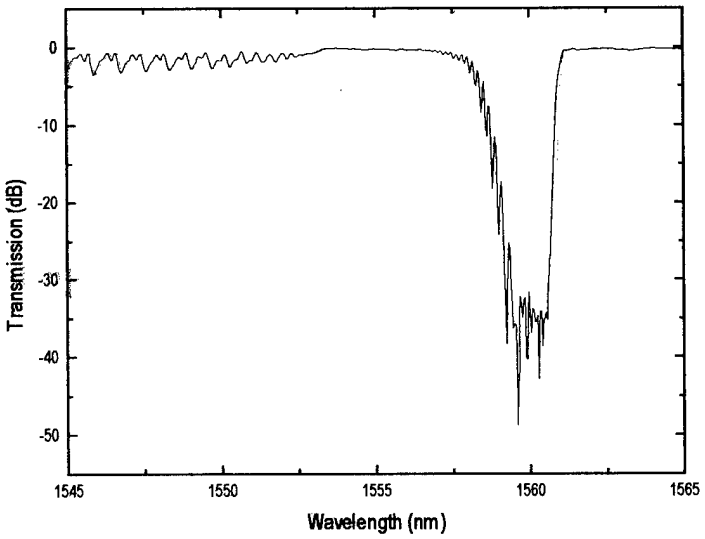

Figure 2: 4th order Bragg reflector 5 mm long written with a 2.14 μm period amplitude mask

Figure 3 shows a 5th order Bragg reflector written in the same fiber with a 2.68 μm mask period. Again, the exposed length was 5mm, but with a reduced exposure time of 40 minutes, yielding a grating 22 dB deep. In this case the mask period of 2.68 μm is equivalent to two and a half wavelengths at 1560 nm with an n_{eff} of 1.455.

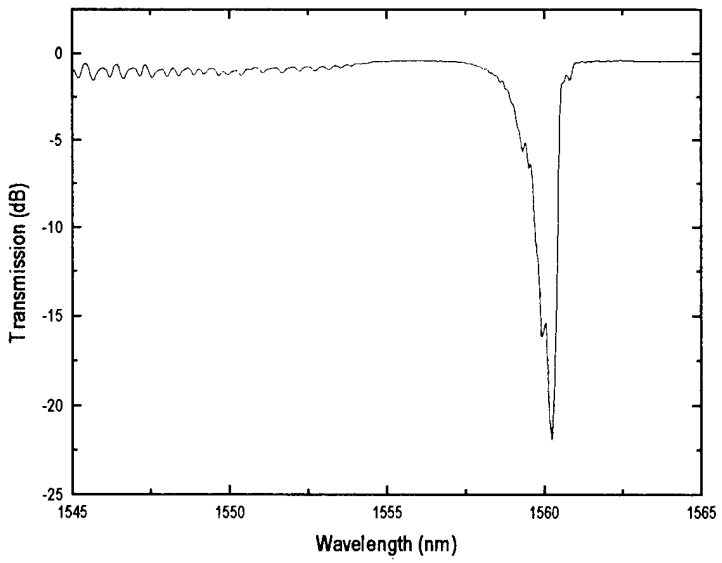

Figure 3: 5th order Bragg reflector similar to that in Fig. 2 but written with a 2.68 μm period amplitude mask.

Both Figs. 2 and 3 show cladding mode loss on the short wavelength side of the grating. Since the gratings are written in identical sections of fiber and at the same wavelength, one would expect the cladding mode loss to be identical if both gratings were written using the phase mask approach. Instead, the cladding mode loss is 1.5 nm farther from the Bragg wavelength in the first grating. The higher core index due to extended UV exposure in the first grating is responsible for this difference.

In this work we have shown that it is practical to write strong multi-order Bragg gratings using a simple amplitude mask. While this technique will not displace phase mask writing due to the longer exposure times needed for deep gratings and the high DC index change associated with the amplitude mask writing, it is useful in the manufacture of low reflectivity gratings where the precision and narrow linewidth of standard Bragg gratings is not required.

1. K. O. Hill, Y. Fujii, D. C. Johnson, and B. S. Kawaski, Appl. Phys. Lett., vol. 32, pp. 647-649, 1978.
2. G. Meltz, W. W. Morey, and W. H. Glenn, Opt. Lett., vol. 14, pp. 823-825, 1989.
3. K. O. Hill, B. Malo, F. Bilodeau, D. C. Johnson, and J. Albert, Appl. Phys. Lett., vol.62, pp.1035-1037, 1993.
4. P. J. Lemaire, R. M. Atkins, V. Mizrahi and W. A. Reed, Electron. Lett., vol. 29, pp. 1191-1193, 1993.
5. S. J. Mihailov and M. C. Gower, Electron. Lett., vol. 30, pp. 707-709, 1994.

Bragg Gratings, Photosensitivity, and Poling in Glass Fibers and Waveguides: Applications and Fundamentals

Joint Symposium on Vitreous Silica and Related Materials

Joint Session on Germanium-Doped Silica

Monday, October 27, 1997

E.J. Friebele, U.S. Naval Research Laboratory
Presider

JMF
1:30pm–3:30pm
Auditorium

Defects Associated with Photosensitivity in GeO_2-SiO_2 Glasses

Hideo HOSONO
Tokyo Institute of Technology, Materials and Structures Laboratory,
Nagatsuta, Midori-ku, Yokohama 226, JAPAN

1. Two types of ODCs in GeO_2-SiO_2 glasses

An absorption band centered at ~5eV in SiO_2:GeO_2 glasses is composed of two components, photobleachable and unbleachable (by one photon process) components, and attributed the former and the latter to a neutral oxygen monovacancy (NOMV) coordinated with two Ge^{4+} ions and a Ge^{2+} (this may be regarded as neutral oxygen divacancy, NODV) coordinated with two oxygens, respectively. The NOMV is converted into a Ge E' center by illumination with 5 eV light or with 488nm Ar laser light. On the other hand, NODV with a lone pair electron occupying the uppermost level emits an intense blue luminescence but does not change chemically with 5 ev-light (at least via one photon process). Therefore, we consider that the presence of the NOMV is essential to emergence of index change by irradiation with 488 Ar laser light. Concentrations of the NOMV and NODV and are $2x10^{16}$ and $2x10^{18}$ cm^{-3} in VAD-$5GeO_2$·$95SiO_2$ glasses (as-delivered) or $6x10^{16}$ and $1x10^{18}$ cm^{-3} in $10GeO_2$·$90SiO_2$ glasses, respectively.

The concentration of the NOMV can be selectively increased by heating at 500 °C in a H_2 atmosphere[2] or ion implantation of protons[3] as summarized in Table 1. It is of interest to note a distinct bleaching behavior between H-implanted SiO_2: GeO_2 glasses and Si or Ge-implanted SiO_2 glasses[4]. Although implantation of each ion induces an intense absorption band at ~5eV, the bleaching behavior of the H-implanted glasses fairly differs from that in other implanted SiO_2 glasses. In the former the 5 eV band was bleached and intense absorptions above 5 eV emerged, whereas in the latter bleaching occurred in the whole uv region.

2. Nanometer-scale heterogeneity in VAD SiO_2-GeO_2 glasses and defect model

TEM observation (Fig.2) on $1GeO_2$-$9SiO_2$ glass preforms prepared by VAD method revealed that nanometer-scale heterogeneity of Ge ions exists[5]. Observation of Ge E' centers in the as-prepared state and proton-implantation-induced nanometer-sized Ge colloid formation in an as-implanted state[6] may be understood by the occurrence of these heterogeneity.

The validity of model of the NOMV , an oxygen vacancy coordinated by two Ge ions, is also justified by this finding. The most probable oxygen vacancy is Ge^{4+} -(vacancy)- Si^{4+} on the assumption that Ge ions are randomly distributed. The electronegativity (1.8 on the Pauling scale) of Ge^{4+} is the same as that (1.8) of Si^{4+}. Thus, it is reasonable to expect that both Si E' and Ge E' centers are created via photochemical reactions in eq.1;

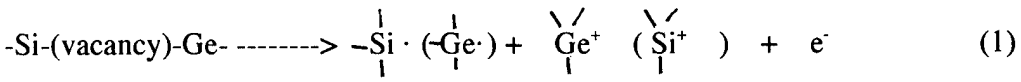

-Si-(vacancy)-Ge- --------> $\equiv Si\cdot$ ($\cdot Ge\equiv$) + Ge^{+} ($Si^{+}\equiv$) + e^{-} (1)

However, only the Ge E' centers are observed experimentally in the glasses after uv-illumination. This discrepancy between the prediction from the random distribution and the result may be understood by the present observation, i.e., the neutral oxygen vacancies occur in the Ge-rich particles and consequently they are coordinated by two Ge ions.

Table 1. Changes in concentrations of NOMV and NODV in $5GeO_2 \cdot 95SiO_2$ glass with H_2 treatment (500 °C for 70 h) or H^+-implantation (1.5 MeV

	NOMV ($x10^{16}$ cm^{-3})	NODV ($x10^{18}$ cm^{-3})	[NOMV] /[NODV]
As-delivered	2.1	1.6	1.3×10^{-2}
After H_2-treatment	16	4.3	3.8×10^{-2}
H^+ ($1x10^{16}$ cm^{-2})	9.6	4.8	2×10^{-2}
H^+ ($1x10^{17}$ cm^{-2})	53	84	$6x10^{-2}$

Fig.1. TEM photo of GeO_2-SiO_2 glass preform prepared by VAD method.

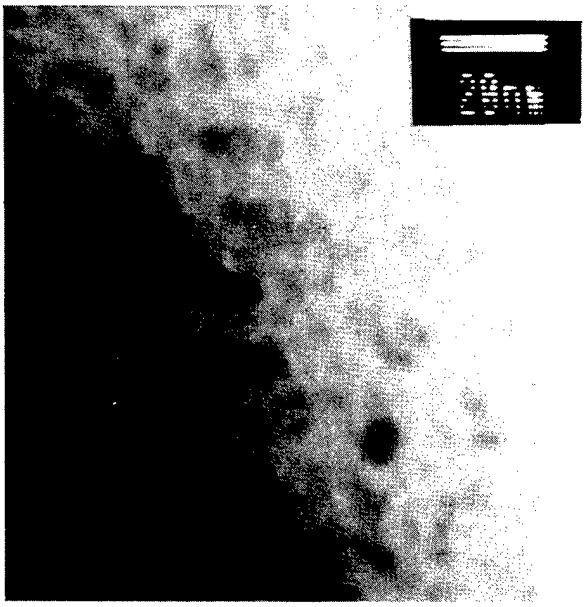

3. Photoreaction [1,7]

Two photochemical reaction channels are ascertained, depending on light source (photon density). The exposure to the Hg lamp radiation (~ 10 mW/cm^2) induced Ge E' centers accompanied by bleaching of the absorption band due to the NOMV and the emergence of an intense band near 6.4 eV(Ge E' center). The irradiation with ArF ($10mJ/cm^2$/pulse, pulse duration 20 ns), KrF and XeCl ($90mJ/cm^2$/pulse) lasers generates Germanium-Electron-Centers (GEC) and a self-trapped hole center (STH). The former and the latter proceed one- and two-photon absorption processes, respectively. Since the latter reaction occurs via band-to-band excitation, no precursor such as oxygen-vacancies is required Table 2 summarizes the properties of two photoreaction channels.

Table 2. Comparison between Hg-lamp and excimer laser light irradiation

Power density	Absorption process	UV source	Excitation	Created Defect	Precursors
~$10mW/cm^2$	1- photon	Hg-lamp	σ-σ^* of Ge--Ge bond	Ge E'	Pre-existing NOMV

0.5~10 MW /cm^2	2-photon	Excimer lasers	band-to-band excitation	GEC (---> Ge E')+ STH	intrinsic structure

4. Structural relaxation of defect - a key to realize a large index change -

Two models have proposed for photo-induced index change, i.e., K-K model and densification model. The former model cannot explain index change of $> \sim 10^{-4}$. Therefore, it is consider that whether densification occur or not is critical to realize a large index change of $> 10^{-4}$. I think that one of the ways to induce photo-induced densification is to utiliuze change in coordination structure around the dopant which traps an electron or a positive hole upon uv-irradiation. A drastic coordination change is anticipated for conversion from tetrahedrally-coordinated state to three-coorinated state as eq.2 (left superscript and right subscript denote formal charge and coordination number of T).

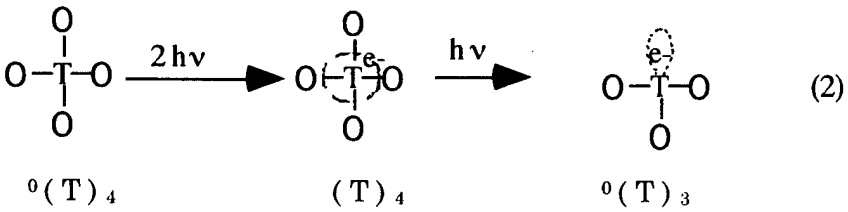

(2)

$^{0}(T)_4$ $(T)_4$ $^{0}(T)_3$

Relaxation of GEC to Ge E' center observed in prolonged irradiation with KrF laser light just corresponds to this type of coordination change[8]. The driving force of this relaxation , i.e., $\cdot(T)_4$ to $^{0}(T)_3$, is an electrostatic repulsion and the local electroneutrality around T is recovered by detaching a non-bridging oxygen carrying a negative charge from the coordination sphere. When $\cdot(T)_4$ center may be decomposed into $^{0}(T)_3$ by light excitation with , photo-induced coordionation change will occurs. VI group elements taking tetrahedral coordination such as P^{5+} and As^{5+} are candidates which meets the above requirements because they can trap an electron without changing coordination number. Phosphorus-doped silica glasses also exhibit a large index-changes by irradiation with ArF excimer laser light[9]. Since phosphorus-electron center can be converted into P E' center by uv illumination[10], the present hypothesis is consistent with this result. An analogous change will be expected for As-doped silica glasses.

References

1. H.Hosono et al. Phys.Rev.B 46, 11445(1992). 2. H.Hosono et al. Appl.Phys.Lett. 63, 479(1993). 3. H.Hosono et al. J.Phys.: Condens. Matter 7, L343(1995), 4. J.Albert et al. Opt.Lett. 17, 1652(1992), 5. H.Hosono et al. J.Appl.Phys. 80, 3115(1996). 6. K.Kawamura et al. ibid, 89, 1357(1996). 7. J.Nishii et al.Phys.Rev.B52, 1661(1995). 8. H.Hosono et al. Jap.J.Appl.Phys. 35, L234(1996). 9. B.Malo et al. Appl.Phys.Lett. 65, 394(1994). 10. H.Hosono et al. J.Non-Cryst.Sol. 71, 261(1985).

Local Kramers-Kronig analysis of UV induced absorption changes: Dynamics of excess loss induced by exposure to light at 248 nm or 193 nm in Ge:SiO_2 preforms.

B. Leconte, W. X. Xie, M. Douay, P. Bernage, P. Niay
Laboratoire de Dynamique Moléculaire et Photonique, Centre d'Etudes et de Recherches Lasers et Applications
Université de Lille I, 59655 Villeneuve d'Ascq cedex - France

J.F. Bayon, E. Delevaque, H. Poignant
Laboratoire DTD / TSO, France Telecom CNET, Technopole Anticipa, 22301 Lannion cedex - France

INTRODUCTION

It is well known that exposure of a germanosilicate glass to light at 248 nm or 193 nm leads to a permanent change in the refractive index and in the absorption spectra at wavelength shorter than 350 nm. The changes in absorption spectra are assumed to result either from the creation of point defects (color center model)[1,2] and/or from light induced structure changes in the glass (densification model)[3,4]. A Kramers-Kronig (KK) transformation of the changes in absorption enables one to determine the related changes in refractive index which in turn can be compared with those measured at the time of a grating inscription. However using this process is rather tricky since ideally the comparison requires that when writing a grating within a fiber, one measures the UV induced excess loss spectrum at each exposure time and at each place along the grating wavevector on the spectral range within which the absorption changes are observed. As the above mentioned procedure cannot be strictly followed, we suggested a simplified method[5] for performing the KK analysis. We use this method to compare the index changes which can be ascribed to absorption changes occurring in the spectral range (220 - 350 nm) at the time of a grating inscription through exposure of a germanosilicate fiber either to a fringe pattern at 193 nm or 248 nm.

METHOD AND EXPERIMENTAL DETAILS

The experiments were carried out on a 7-mol % germanium doped core preform, (cladding dopants P and B) prepared by the M.C.V.D. process at the C. N. E. T. laboratory in Lannion. Some samples were H_2 loaded for 15 days at 100 atm at room temperature. Light from a deuterium lamp was used to probe the UV induced absorption change, and after dispersion, was detected by an intensified silicon photodiode array processed by a computerized acquisition system. Exposures were performed by using an excimer laser operating at 248 nm (KrF laser) or at 193 nm (ArF laser). During the irradiation, spectra were recorded after a time delay of 1 ms by reference to the time of the laser pulse in order to minimize a possible spoiling of the absorption spectra by laser induced fluorescence.

The evolution of the refractive index changes have been obtained through our recently proposed procedure[5]. It is assumed that the changes in absorption spectra are identical in preforms and fibers cores[6]. The method consists in recording the dynamics of excess loss spectra during exposure of the preform core to spatially uniform UV light at various pulse energy densities (50 - 500 mJ/cm^2). These densities sample those within the fringe pattern used to write the grating. A KK transformation (Eq. (1)) is then used to calculate the numerical values of the changes in refractive index $\Delta n^{KK}(t, F)$ versus the exposure time and the pulse energy density. The index profiles $\Delta n^{KK}(t, z)$ are deduced from $\Delta n^{KK}(t, F)$ and F(z). The different terms of the Fourier series expansion of $\Delta n^{KK}(t, z)$ have then been calculated and compared at each exposure time with the corresponding ones deduced from the measurement of the grating spectrum.

EXPERIMENTAL RESULTS AND DATA ANALYSIS

Fig. 1(a) shows typical UV induced loss spectra recorded in a H_2 free sample during exposure to light at 248 nm. As shown in Fig. 1(a), a few pulses of UV light impinging on this sample, led to a strong attenuation from a UV band tail with a broad dip which corresponds to the partial bleaching of the GODC band.[7] No further significant change in the absorption spectra could be observed from $4x10^4$ pulses to $1.2x10^5$ pulses. Fig. 1(b) shows excess loss spectra obtained under conditions similar to those in Fig. 1(a) except that the sample is now H_2 loaded. Up to $1.4x10^5$ pulses the UV induced losses increased monotonously leveling off at this time at a higher level than this in the unloaded sample.

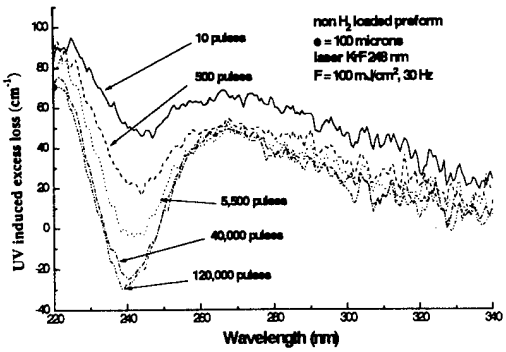

Fig. 1(a) Excess loss spectra measured in the unloaded germanosilicate preform core (7% mole GeO_2 doped) after exposure to 248 nm UV pulses at 100 mJ/cm^2.

Fig 2(a) shows a typical result obtained when exposing the H_2 free sample to 193 nm light. There is no UV induced bleaching of the GODC band. The UV induced losses increased monotonously as a function of exposure time up to $5x10^4$ pulses. No significant change could be detected from $5x10^4$ to $1x10^5$ pulses. Fig. 2(b) shows spectra recorded when exposing the H_2 loaded sample to light at 193 nm. The evolution of the UV induced excess loss as a function of exposure time looks like this for the H_2 free sample with however a level of losses significantly higher. This result differs from this reported by Albert et al[8]. Indeed these authors observed a lower level of loss under exposure at 193 nm for the H_2 loaded samples than at 248 nm. Nevertheless this higher level of induced loss is consistent with the higher refractive index change that can be achieved by using exposure at 193 nm.

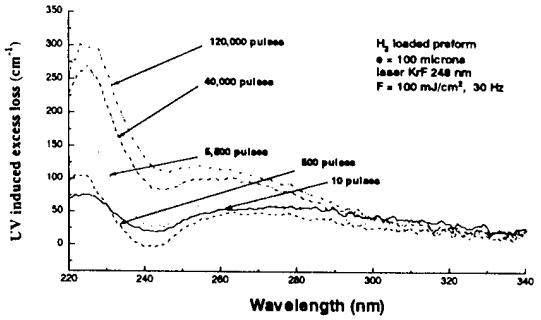

Fig. 1(b) Excess loss spectra measured in the H_2 loaded germanosilicate preform core (7% mole GeO_2 doped) after exposure to 248 nm UV pulses at 100 mJ/cm².

The above-mentioned KK analysis[5] of the excess loss spectra $\Delta\alpha(\lambda, F, N)$ was then carried out through Eq. (1)[9] to derive the magnitude of the refractive index change $\Delta n^{KK}(\lambda', F, N)$ as a function of the number of pulses (N) impinging on the core of the preform plate. In (1), λ_1 and λ_2 are the boundaries of the spectral range within which absorption changes are taken into account, λ' is the wavelength at which the refractive index change was calculated. Eq. (1) is valid for $\lambda' >> \lambda_2 > \lambda_1$. The values of λ', λ_2 and λ_1 were set at 1500, 350, 220 nm respectively.

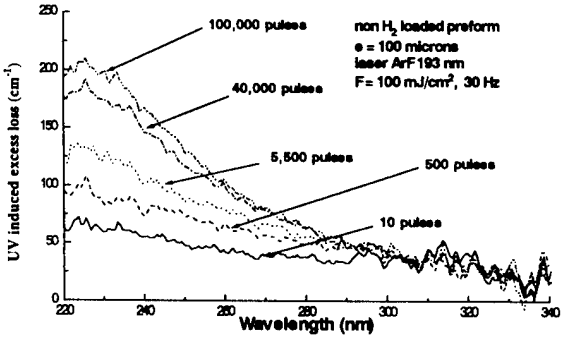

Fig. 2(a) Excess loss spectra measured in the unloaded germanosilicate preform core (7% mole GeO_2 doped) after exposure to 193 nm UV pulses at 100 mJ/cm².

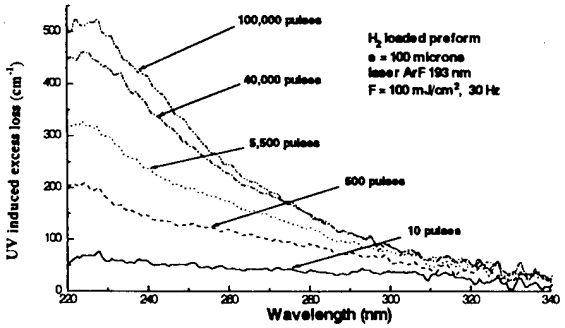

Fig. 2(b) Excess loss spectra measured in the H_2 loaded germanosilicate preform core (7% mole GeO_2 doped) after exposure to 193 nm UV pulses at 100 mJ/cm².

$$\Delta n^{KK}(\lambda', F, N) = \frac{1}{2\pi^2}\int_{\lambda 1}^{\lambda 2} \Delta\alpha(\lambda, F, N)\cdot\left[1-\left(\frac{\lambda}{\lambda'}\right)^2\right]^{-1}\cdot d\lambda \qquad (1)$$

The result of the simulation is shown in Fig. 3(a). The evolution of Δn^{KK} is plotted as a function of F after various exposure times for the H_2 free sample exposed to 248 nm light. As shown in Fig. 3(a), the change in refractive index Δn^{KK} was observed to decrease as a function of exposure time after few pulses of UV light. This decrease contrasts with the rise in refractive index corresponding to the grating growth. It is an artifact which comes from the system detection limited small size of analyzed spectral range. Indeed, within the spectral range (220 - 350 nm) the change in refractive index is governed by the bleaching of the Ge-Si wrong bond band at 243 nm. This bleaching contributes negatively to the refractive index change. The evolution of Δn^{KK} for the H_2 loaded sample is shown in Fig. 3(b). One can note that Δn^{KK} saturates as a function of the exposure time and shows a non-linear dependence on the fluence per pulse. A calculus performed on samples exposed to 193 nm light (H_2 loaded and unloaded) leads to results similar to those in Fig. 3(b).

Accordingly, it appears that, when writing a grating using either 248 nm or 193 nm light, although the irradiance distribution could be perfectly sinusoidal along ***Oz***, a distortion of the refractive index profile along ***Oz*** comes from saturation effects. Fig. 4 shows the shape of the refractive index change as calculated from (1) along ***Oz*** for the H_2 loaded sample exposed to 248 nm light. The refractive index profile is no more sinusoidal at high pulse energy density (the same result was obtained for the unloaded sample). The evolutions of the first terms Δn^{KK}_{mean} and Δn^{KK}_{mod} of the Fourier series expansion of $\Delta n^{KK}(z, N)$ have been calculated as a function of N using relation (2). Mostly due to the distortion noticeable in Fig. 4, Δn^{KK}_{mean} is significantly higher, for $F > 150$ mJ/cm², than Δn^{KK}_{mod} whatever the number of pulses may be. Similar results were obtained for samples exposed to 193 nm light.

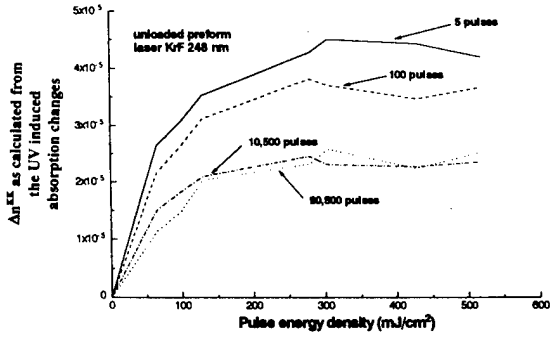

Fig. 3(a). Change in refractive index Δn^{KK} for unloaded samples as a function of the 248 nm UV pulse energy density. The change was calculated from UV induced loss spectra similar to those displayed in Fig. 1(a).

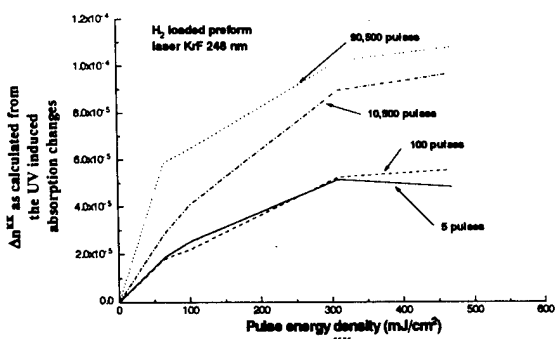

Fig. 3(b). Change in refractive index Δn^{KK} for H_2 loaded samples as a function of the 248 nm UV pulse energy density. The change was calculated from UV induced loss spectra similar to those displayed in Fig. 1(b).

$$\Delta n^{KK}(z, N) = \Delta n^{KK}_{mean} + \Delta n^{KK}_{mod} \cos\left(\frac{2\pi z}{\Lambda}\right) + \ldots \quad (2)$$

Fonjallaz et al.[10] have recently shown that the tension in the core of single-mode germanosilicate fibers is strongly increased by the formation of a Bragg grating. The phenomenon was explained by a structural change of the glass in the fiber core into a more compact configuration. They reported[11] that, after exposure of germanosilicate fibers to accumulated fluence of 35 kJ/cm^2, the total mean index change Δn_{mean} was at least 20% smaller than the total index modulation Δn_{mod}. Thus, the situation seems somewhat complicated. Total mean refractive index changes smaller or higher than refractive index modulation can be observed when writing a grating. It depends on the fringe visibility, the exposure time, the pulse energy density and the mechanism of photosensitivity.

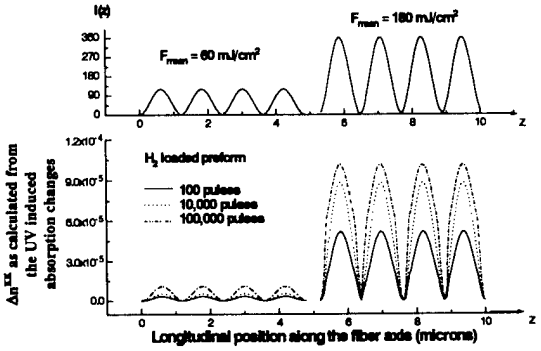

Fig. 4. Change in refractive index as a function of the position along the fiber axis, under 248 nm exposure. The graphs correspond to two mean fluence per pulse (F = 60 and 180 mJ/cm^2). They were obtained with the changes displayed in Fig. 1(b) for the H_2 loaded preform, under the assumption that the fringe visibility V = 1.

CONCLUSION

The behavior of UV induced excess loss in germanosilicate glass using both 248 nm KrF excimer laser or 193 nm ArF excimer laser was investigated. Induced losses are shown to be significantly higher under 193 nm than under 248 nm laser light. The evolutions of the UV induced changes in refractive index, that can be attributed to defects absorbing between 220 nm and 350 nm have been calculated through a Kramers-Kronig analysis of the excess loss spectra in preform cores. The refractive index changes have proved to be non linear as a function of both the UV fluence per pulse and the exposure time. This implicates that the value of mean index change is higher than this for the index modulation. Accordingly significant difference in thermal behavior between the average index and the amplitude of index modulation can be observed. This will be shown at the conference.

REFERENCES

1 L. Dong, J.L. Archambault, L. Reekie, P.St.J. Russell and D.N. Payne, Appl. Opt. 34, 3436-3440 (1995).
2 R.M. Atkins, V. Mizrahi and T. Erdogan, Electron. Lett. 29, 385-387 (1993).
3 E.M. Golant,V.M. Mashinsky, V.B. Neustruev, O.D. Sazhin, V.V. Brazhkin, OFC'97 Technical Digest, Vol.6 of 1997, TuB4.
4 P. Cordier, J.C. Doukhan, E. Fertein, P. Bernage, P. Niay, J.F. Bayon and T. Georges, Opt. Comm. 111, 269-275 (1994).
5 B. Leconte, W. X.Xie, M. Douay, P. Bernage, P. Niay, J.F. Bayon, E. Delevaque, H. Poignant, accepted in Applied Opt.
6 R.M. Atkins, Opt. Lett. 17, 469-471 (1992).
7 D.L. Williams, S.T. Davey, R. Kashyap, J.R. Armitage and B.J. Ainslie, Electron. Lett. 28, 369-371 (1992).
8 J. Albert, B. Malo, F. Bilodeau, D. C. Johnson, K. O Hill, Y. Hibino, M. Kawachi, Opt Lett, 19,387-389, (1994).
9 J.E. Roman and K.A. Winick, Opt. Lett. 18, 808-810 (1993).
10 P.Y. Fonjallaz, H.G. Limberger, R.P. Salathé, F. Cohet and B. Lauenberger, Opt. Lett. 20, 1346-1348 (1995).
11 H.G. Limberger, P.Y. Fonjallaz, R.P. Salathé and F. Cochet, Appl. Phys. Lett. 68, 3069-3071 (1996).

Rise and Decay of 3.15 eV Luminescence in Germanosilicate Glass: Influence of Glass Densification

E. M. Dianov, V. M. Mashinsky, V. B. Neustruev, O. D. Sazhin

Fiber Optics Research Center at the General Physics Institute, Russian Academy of Sciences
38 Vavilov Street, Moscow, 117942, Russia, tel. (095)132-8293, fax (095)135-8139

V. A. Sidorov

Institute of High Pressure Physics, Russian Academy of Sciences
Troitsk, Moscow Region, 142092, Russia

Introduction

A wide variety of defects in germanosilicate glass observed in absorption and in luminescence spectra results in the energy transfer from some defects to others. Such a process was directly demonstrated by Gallagher and Osterberg[1] and Bagratashvili *et al.*[2] when 3.15 eV luminescence of germanium oxygen-deficient center (GODC) was excited by 5 eV photons. Along with usually observed decay of luminescence with about 100 μs lifetime they observed an initial rise of the luminescence with time of about 10 μs. To explain this phenomenon, Gallagher and Osterberg added to the commonly accepted scheme of GODC's states (S_0, S_1 and T_1) one more energy state of another defect. This state can nonradiatively transfer its excitation to the triplet state of GODC and this results in the rise of triplet-to-singlet luminescence. In this case the rate of the rise is governed by the lifetime of additional state.

We have found that about 20% densification of germanosilicate glass in the process of hydrostatic pressurization strongly (up to 3 times) decreases the intensity of blue (3.15 eV) luminescence while UV luminescence (4.28 eV) is not influenced by the densification.[3] The conclusion was made that these luminescence bands belong to different centers.

Luminescence kinetics is also expected to vary in the process of glass densification. In this paper we present the results of investigation of 3.15 eV luminescence kinetics i) at both 5.0 and 3.68 eV excitation and ii) in as-made and densified germanosilicate fiber preforms.

Experimental details

Samples of germanosilicate glass prepared by MCVD and VAD methods (GeO_2 concentration 10 and 7 mol%, absorption coefficient at 5.0 eV 180 and 30 dB/mm, respectively) were hydrostatically pressurized at a pressure of 9 GPa and a temperature of 300°C during 15 minutes. As a result, residual isotropic densification of 16% (MCVD) and 19% (VAD) was achieved.

Luminescence was excited by the radiation of KrF- (5 eV photons) and N_2-lasers (3.68 eV photons) with pulse duration of about 20 ns. Two registration methods were used in accordance with the intensity of luminescence. In the first case (5.0 eV), measurements were performed by digital oscilloscope Tektronix 7612D with the setup rise time of about 20 ns. In the second case (3.68 eV), luminescence intensity was weak and averaging of a signal with boxcar integrator (Stanford Research Systems SR 250) was used with the setup rise time of about 500 ns.

Results

3.15 eV luminescence kinetics was recorded during 300 μs. Figure 1 shows fragments of this kinetics at 5.0 and 3.68 eV excitation in MCVD glass, before and after its densification. In all cases luminescence rises first, reaches maximum at 2 to 8 μs and then decreases. Behavior of luminescence in VAD glass was the same.

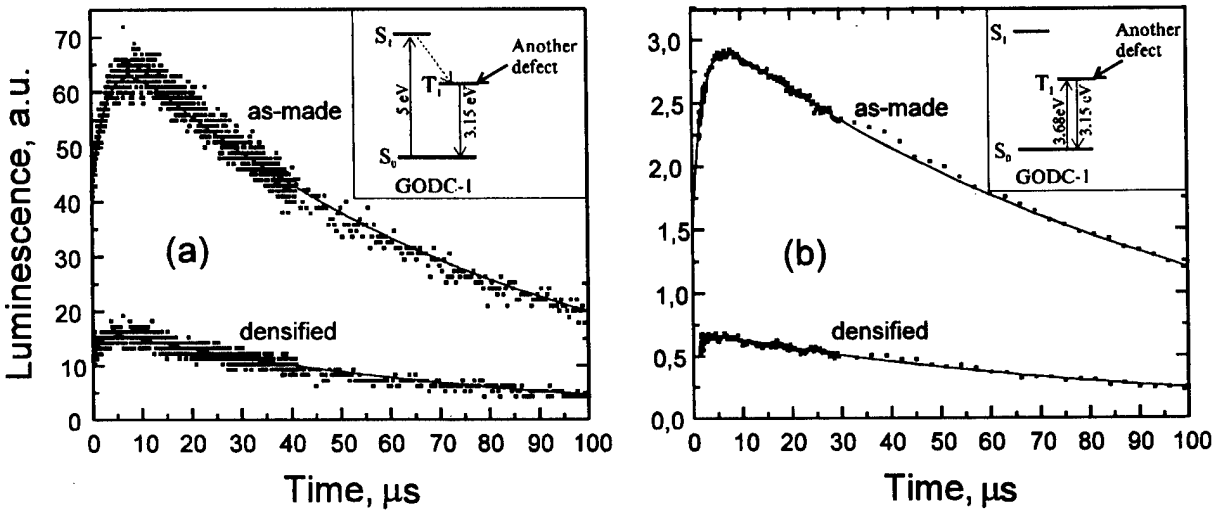

Figure 1. Kinetics of 3.15 eV luminescence excited by 5.0 (a) and 3.68 eV (b) photons in as-made and densified MCVD germanosilicate glass. In the insets: diagrams of GODC's T_1 state excitation including energy transfer from another defect.

We fitted the obtained curves by two exponential following paper[1]

$$I_{lum} = A_1 exp(-t/\tau_1) - A_2 exp(-t/\tau_2).$$

The first term means conventional decay of T_1 state with extrapolated initial intensity of A_1 at t=0. The second term means delayed excitation of T_1 state owing to an energy transfer from another defect. Thus, (A_1-A_2) value corresponds to the initial population of T_1 state and the ratio $(A_1-A_2)/A_1$ is a measure of GODC's own luminescence in the total luminescence. Parameters of fitting are listed in Table.

Table. Parameters of two-exponential fit of luminescence kinetics

	Excitation 5.0 eV					Excitation 3.68 eV				
Sample	A_1	τ_1	A_2	τ_2	$(A_1-A_2)/A_1$	A_1	τ_1	A_2	τ_2	$(A_1-A_2)/A_1$
MCVD, as-made	72	78	30	3.2	0.58	3.2	103	1.6	2.2	0.5
MCVD, densified	17	77	5.3	1.9	0.69	0.67	87	0.24	1.4	0.64
VAD, as-made	48	85	22	3.1	0.54	0.89	111	0.33	3.6	0.63
VAD, densified	11	83	2.6	3.2	0.76	0.21	89	0.06	6.0	0.71

Discussion

Thus, it was shown for the first time that the rise of 3.15 eV luminescence takes place at 3.68 eV excitation. This rise is very similar to the rise at 5.0 eV excitation. This seems to

indicate that at both excitations energy transfer occurs between the same states of two defects.

Initial luminescence intensity (at t=0) forms 50-60% from the maximum value in as-made glass. The other part, 40-50%, is transferred from another defect. In densified glass a portion of transferred energy decreases to about 30% and simultaneously the total luminescence decreases about 4 times. Absorption decrease at 5.0 eV does not explain this luminescence lowering. [3]

We could suppose that the real value of A_2 is higher than the obtained in this work (because of the insufficient setup rise time and S/N ratio) and greater portion of excitation is transferred from another defect. High susceptibility of this process to the glass densification can be evidently explained by changes of distances between the defects and of the height of barriers between the states. However, in this interpretation it is not clear why T_1 state being a good transformer of any excitation to 3.15 eV luminescence has low quantum yield for its own excitation directly to T_1 state.

On the other hand, if the obtained values of A_2 are correct, 3.15 eV luminescence is not due to $T_1 \rightarrow S_0$ transition in GODC because of strong dependence of its intensity on the glass densification, the lifetime being practically independent. Thus, these results, together with the results published earlier,[3] call into question the validity of the known transition scheme in GODC and allow to assume that the absorption band at 3.76 eV (330 nm) belongs not only to $S_0 \rightarrow T_1$ transition in GODC.

In principle, the rise of luminescence could be explained by the burning of T_1 state population because of excited-state absorption.[4] However, by varying of 5.0 eV excitation intensity we found no effect of excited-state absorption on the luminescence rise.

It should be noted that the annealing of densified samples at 1000°C recovered luminescence kinetics, together with the recovering of absorption spectrum.[3]

The unsufficient accuracy of measurements does not permit to state that τ_2 changes at densification of glass. But the difference of our values (1.4 to 6 μs) from data[1] (9 to 12.5 μs) is clearly seen. This means that τ_2 can be sensitive to a composition and history of glass samples. More accurate measurements are required to find the correlations here.

Conclusion

The rise of 3.15 eV luminescence during 2 to 8 μs at 3.68 eV excitation is found in germanosilicate glass (similarly to the 5 eV excitation). This points to the effective (more than 40%) energy transfer to GODC from another defect. Densification of glass reduces this energy transfer and decreases the luminescence intensity. Well known energy scheme of GODC explains no more than about 25% of 3.15 eV luminescence intensity.

References

1. M. Gallagher and U. Osterberg, *Appl. Pys. Lett.*, **63**, 2987, 1993.
2. V.N.Bagratashvili, V.K.Popov, S.I.Tsypina, P.V.Chernov and A.O.Rybaltovskii, *Opt. Lett.*, **20**, 1619, 1995.
3. E.M.Dianov, V.M.Mashinsky, V.B.Neustruev, O.D.Sazhin, V.V.Brazhkin and V.A.Sidorov, *Opt. Lett.*, **22**, 1089, 1997.
4. M.Fujimaki, K.S.Seol and Y.Ohki, *J. Appl. Phys.*, **81**, 2913, 1997.

Germanosilicate Glass Refractive Index Change Under Singlet and Triplet Excitation of Germanium Oxygen Deficient Centers

E.M.Dianov, S.A.Vasiliev, A.A.Frolov, O.I.Medvedkov

Fiber Optics Research Center at the General Physics Institute, Russian Academy of Sciences
38, Vavilov Str., 117942, Moscow, Russia
Tel.: 7-095-1328306, Fax: 7-095-1358139, E-mail: sav@fo.gpi.ac.ru

INTRODUCTION

Although in-fiber photoinduced structures are widely used in practical applications [1] the nature and the microscopic mechanisms of glass photosensitivity is still unclear. To explain the phenomena observed in fibers under UV-irradiation, several models have been suggested: color center transformation [2], initial stress relief [3], UV-induced glass densification [4]. However these models are not in complete agreement with the experiments. It is well known that germanium oxygen deficient centers (GODCs) play an important role, at least at the initial stage of photoinduced glass transformation. As a rule, the intense GODC absorption band centered at 242 nm is used to write refractive index gratings in germanosilicate fibers.

In our previous works it was found that direct photoexcitation of the GODC triplet state T_1 leads to similar processes as in the case of excitation of the singlet state S_1 [5, 6]. Significant decay of the blue triplet luminescence, an increase of the red luminescence, and GeE' center formation accompany powerful near-UV irradiation of Ge-doped glass in the triplet band. We have also shown that the near-UV radiation can induce a refractive index change, high enough to write in-fiber gratings [7]. Such gratings exhibit a similar temperature stability as those written by a KrF laser. The main conclusion that can be drawn from the above observations is that the long-lived T_1 state of GODC is directly involved in the photorefractive effect. A possible microscopic mechanism of GODC transformation to describe the glass index change was proposed in [8]. By calculating the energy diagram of GODC it was shown that a triplet-state GODC can overcome a small energy barrier (~ 0.2 eV) to convert into a stable "puckered" state which is accompanied with compaction of the glass.

In this work we compare quantitatively the refractive index induced in a Ge-doped-silica-core fiber by direct photoexcitation of GODC in the singlet and triplet absorption bands.

RESULTS AND DISCUSSION

We used a Ge-doped fiber with a step-index profile ($\Delta n \approx 0.02$), a cut-off wavelength of 1.04 μm, and a cladding diameter of 125 μm. To investigate the refractive index evolution, we used the interferometric

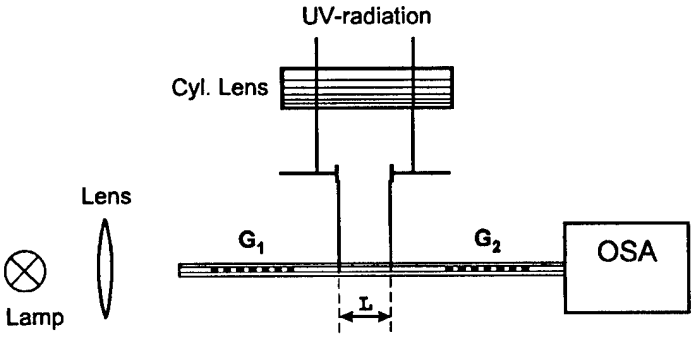

Fig.1. Experimental setup for measuring refractive index change in the fiber core.

technique that was proposed in [9]. A Mach-Zehnder interferometer based on a pair of long-period gratings was written in the fiber tested. In measuring the induced index change, a part of the fiber (L ~ 5 mm) localized between the gratings was uniformly irradiated (fig.1). The measurements were performed using two CW lasers: a frequency doubled Ar^+-laser (λ = 244 nm, I ~ 100 mW) and an Ar^+-laser generating several wavelengths in the near-UV spectral range (λ = 333 - 364 nm, I ~ 500 mW). Radiation of the latter laser consisted of three lines with an intensity ratio $I_{333}/I_{351}/I_{364}$ = 0.12/0.47/0.41. The spectral shift of the interference pattern $\Delta\lambda$ (fig.2) was related to the UV-induced index as $\Delta n_{ind} \approx \lambda\Delta\lambda/(L\Lambda\eta)$, where λ is the probe wavelength, Λ is the interference period, and η is the share of the fundamental mode power propagating in the fiber core.

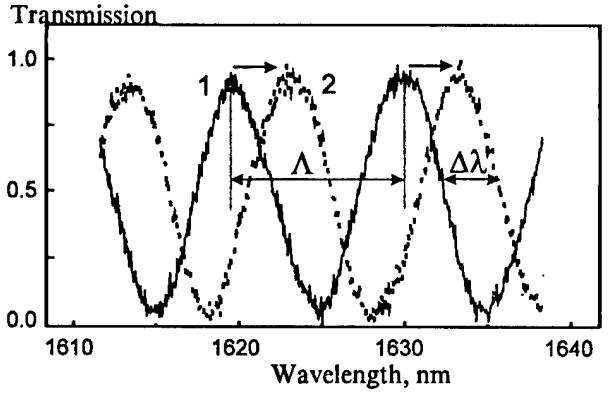

Fig.2. Transmission spectra of interferometer before (1) and after (2) UV-irradiation.

To clarify the role of the T_1 state of GODC in the photorefractive effect, we compared the efficiencies of index changes induced by exciting the triplet and the singlet states separately. We determined the laser light intensities at the wavelengths of 244 nm and 333 - 364 nm that led to an equal magnitude I_0 of the blue triplet luminescence, i. e. to the same populations of state T_1 during the both types of irradiation. In doing so, equal lengths of the fiber (2 mm) were irradiated. The luminescence signal was detected at the fiber output at the wavelength of 400 nm. The intensities of irradiations were sufficiently small to prevent luminescence decay and enhancement of induced absorption during the measurements. Then the irradiation intensities were increased to I_{244} ~ 80 mW/cm², $I_{333\text{-}364}$ ~ 300 W/cm², their ratio remaining the same as in the above experiment, to measure the dose dependencies of the induced refractive index in the fiber core. At such intensities we can neglect fiber heating due to light absorption and two photon processes. Therefore, we assumed that these irradiation conditions provided the same populations of state T_1 both in singlet and triplet excitations. Fig.3 gives the dependencies of the induced index on the

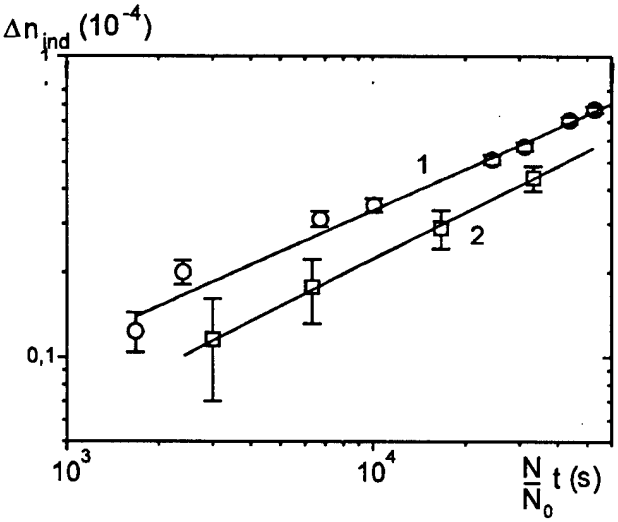

Fig.3. The dependencies of the induced index on the total number of photons incident on the fiber and normalized to the photon density per unit time N_0: 244 nm (1) and 333 - 364 nm (2).

total number of photons incident on the fiber normalized to the photon density N_0 per unit time (N_0 produced the reference signal of luminescence I_0). One can see that both curves are well approximated by a straight line on logarithm-logarithm scale; that is the dose dependencies of the induced index are described by a power low $\Delta n_{ind} \sim D^b$. Moreover, the powers are close to each other ($b_{244} \approx 0.49$, $b_{333\text{-}364} \approx 0.54$), which demonstrates a similarity of the both processes under investigation. Obviously, under singlet photoexcitation, at least 2/3 of the induced index results from state T_1. Two factors can be proposed to explain more efficient index formation in the case of 244 nm excitation: 1) the presence of the second channel of GODC photodestruction (for example, GODC photoionization from singlet state S_1) which also leads to the increase of the refractive index; 2) a shift of dynamic equilibrium of creation and destruction of Ge-DID centers under triplet excitation.

CONCLUSION

Thus we have compared the dose dependencies of the refractive index change induced in a Ge-doped silica core fiber under singlet and triplet photoexcitation of the GODC. The measurements were performed with the help of Mach-Zehnder interferometer based on a pair of long-period gratings and showed that the prevailing microscopic mechanism of the index change under the action of a CW low-intensity laser radiation is a transformation of GODC from the excited triplet state. The results obtained confirm the possibility of refractive index induction via a transition of GODC into the "puckered" state.

REFERENCES

1. R. Kashyap, Opt. Fib. Techn. **1**, 17 (1994).
2. D. P. Hand and P. St. J. Russel, Opt. Lett. **15**, 102 (1990).
3. M. G. Sceats, G. R. Atkins, and S. B. Poole, Annual Rev. Mat. Sci. **23**, 381 (1993).
4. B. Poumellec, P. Guenot, I. Riant, P. Sansonetti, P. Niay, P. Bernage, and J. F. Bayon, Opt. Mat. **4**, 441 (1995).
5. E. M. Dianov, D. S. Starodubov, and A. A. Frolov, Electron. Lett. **32**, 246 (1996).
6. D. S. Starodubov, E. M. Dianov, S. A. Vasiliev, A. A. Frolov, O. I. Medvedkov, A. O. Rybaltovskii, and V. A. Titova, in Proc. SPIE, **2998**, 111 (1997).
7. E. M. Dianov, D. S. Starodubov, S. A. Vasiliev, A. A. Frolov, O. I. Medvedkov, in Proc. SPIE, **2998**, 154 (1997).
8. V. B. Sulimov, V. O. Sokolov, E. M. Dianov, and B. Poumellec, in *Photosensitivity and quadratic nonlinearity in glass waveguides: fundamentals and applications*, Vol.22 of OSA Technical Digest Series (Optical Society of America, Washington, D.C., 1995) Postdeadline paper PD3.
9. E. M. Dianov, S. A. Vasiliev, A. S. Kurkov, O. I. Medvedkov, and V. N. Protopopov, in Proc. *22nd European Conference on Optical Communication*, ECOC'96, **1**, 65 (1996).

Links between writing and erasing (or stability) of Bragg gratings in disordered media.

B. Poumellec

CNRS URA 446 Thermodynamique et Physico-chimie des Matériaux, Université de Paris Sud, 91405 Orsay Cedex, France. Tel. 33 01 69 15 63 51 Fax 33 01 69 15 48 19 E-mail: bp@phebus.isma.u-psud.fr

A lot of experiments have been performed to measure the stability of Bragg gratings in silica based optical fibers for various temperatures. The most famous one is from Erdogan et al. [6, 7] who show a law like $\frac{1}{1+at^{\alpha}}$ with α increasing on the temperature. Applying this mathematical function systematically, various authors have found other variations. Furthermore, some stability measurements have been made according the writing conditions and in some glasses this has been found mutually dependent [1, 2].

Here, in this paper, we propose a link between writing and erasing of Bragg grating using a first order reversible physico-chemical reaction.

I - The physico-chemical reaction, VAREPA model for the writing.

Let assume that the change of index is achieved by the production of a species B from a species A and proportional to it. A is an UV absorbing species and as I already mentioned elsewhere [3], the way to B is complex but can be assumed to be simple exponential at least for intermediate time. Mechanism for passing A to B can be color center formation (type 0 for H_2 loaded sample [4]) or densification (type I) or stress induced index change or also ionic migration.

Three assumptions define our model called VAREPA

1) the reaction $A \xrightarrow{k_1} B$ is achieved with a distributed activation energy E_1, $k_1 = k_1^0 \exp\left(-\frac{E_1}{k_B T}\right)$. An activation energy is assumed since the grating writing rate is dependent on the temperature [5]. This energy varies from site to site (it is distributed) as the glass is disordered, the reaction pathways are variable (VAREPA).

2) the distribution function is called $g_1(E_1)$ and can be chosen normalized. It is the fraction of pathways having the energy E_1. $\int_0^{\infty} g_1(E_1)dE_1 = 1$. We note $x(E_1,t)$ the degree of advancement of the reaction having activation energy E_1.

Thus, the number of B per unit volume is: $[B](t) = A_0 \int_0^{\infty} g_1(E_1) x(E_1,t) dE_1$

We can observed, now, that x=0 for all E_1 at t=0 and x=1 for all E_1 at t=+∞. For intermediate time, we make the third assumption that $x(E_1)_t$ is a steep function i.e. below a defined energy E_d, x=1 and above E_d, x=0. To properly define $E_d(t)$, a demarcation energy, we will state $x(E_d,t)=1-1/e$. This third assumption is essential for the simplification of the integral but it is always fulfilled for exponential kinetics (behavior $\exp(-t/\tau)$ e.g. first order kinetics). For a simple exponential reaction, $x=1-\exp(-k_1 t)$ and $E_d = k_B T \ln(k_1^0 t)$.

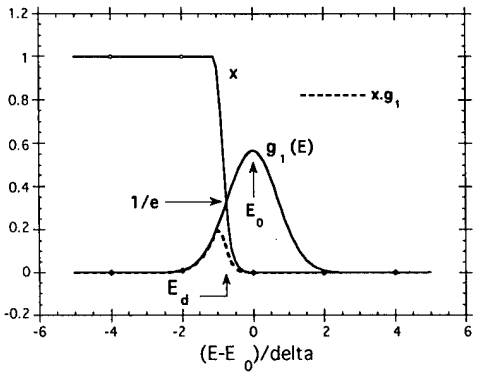

Fig. 1: plot of the distribution function and of the degree of advancement.

The main feature of this model is the loss of ergodicity. Pathways are sorted according to their activation energy. As time is increasing, more difficult pathways are concerned (fig. 1). E_d moves up as the time increases.

Thus, we get: $[B](t) = A_0 \int_0^{E_d(t)} g_1(E_1) dE_1$

It is worthnoticing that the time dependence is defined by $g_1(E)$

and $E_d(t)$. g(E) is relevant of the disorder structure of the glass whereas $E_d(t)$ is only function of the type of kinetics. The advantage of such an approach is to split these two functions. The distribution function can be studied through the derivative of [B](t), we have: $\left.\frac{d[B](t)}{dE_d}\right)_t = A_0 g_1(E_d(t))$

Several cases for $g_1(E)$ can be investigated. For instance, I have used gaussian distribution some in other papers [3] [4]. Here I consider the distribution already used by Erdogan et al. in order to emphasize the connection between writing and erasing.

Erdogan distribution

From an empirical approach, Erdogan et al. [6, 7] have found the following distribution function for Bragg erasure description. We take again this function for writing. It is a bell shape function centered on E_0 and of width $\approx 3k_BT_0$.

$g_1(E) = \frac{1}{k_BT_0}\frac{\exp\left(\frac{E_1-E_0}{k_BT_0}\right)}{\left[1+\exp\left(\frac{E_1-E_0}{k_BT_0}\right)\right]^2}$. We obtain $[B](t) = A_0\int_0^{E_d(t)} g_1(E_1)dE_1 \approx A_0\frac{\exp\left(\frac{E_d-E_0}{k_BT_0}\right)}{1+\exp\left(\frac{E_d-E_0}{k_BT_0}\right)} = A_0\frac{\left(k_1^0 t\right)^{T/T_0}\exp\left(\frac{-E_0}{k_BT_0}\right)}{1+\left(k_1^0 t\right)^{T/T_0}\exp\left(\frac{-E_0}{k_BT_0}\right)}$

using $E_d = k_BT\ln(k_1^0 t)$.

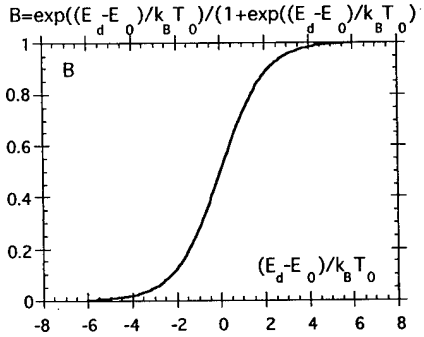

The bound 0 of the integral has been shifted to $-\infty$ assuming $E_0 > 3k_BT_0$. If it is not the case, a renormalisation is required. Let us call $\bar{g}$ the renormalised distribution. We have to use $\bar{g}_1(E) = \frac{g_1(E)}{\left(1-\int_{-\infty}^{0} g_1(E)dE\right)}$

A power law appers for small times with the exponent depending linearly on the temperature. For γ=0.15-0.2 and T=300K realistic values are $3\kappa_BT_0$=0.75 eV and E_0=few eV.

Fig. 2: plot of B concentration against $(E_d - E)/\Delta$

II The erasure

$$B \xrightarrow{k_{-1}} A \qquad k_{-1} = k_{-1}^0 \exp\left(-\frac{E_{-1}}{k_BT}\right)$$

We have to consider here that there exists a distribution of B (B^0) at the beginning of the erasure produced through the forward chemical pathways with activation energy E_1 during the grating writing:

$B^0(E_{+1},t_w) = A_0 x_{+1}(E_{+1},t_w)$, where t_W is the duration of the writing. The remaining number of B is:

$$[B](t) = \int_0^{\infty} g_{-1}(E_{-1})\left(1-x_{+1}(E_{-1},t)\right)B^0(E_{+1},t_w)dE_{-1} \text{ or } [B](t) = A_0\int_0^{\infty} g_{-1}(E_{-1})\left[1-x_{-1}(E_{-1},t)\right]x_{+1}(E_{+1},t_w)dE_{-1}$$

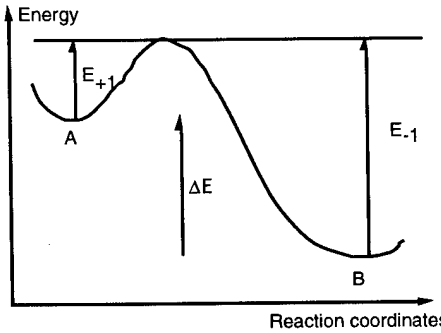

Fig. 3: Reaction pathway

Here we make the assumption that the forward and backward pathways are the same and that only the energy of the saddle point is distributed. We have:

$$\Rightarrow \begin{cases} E_{-1} - E_{+1} = \Delta E_{B\to ODC} = \Delta E > 0 \\ g_{-1}(E_{-1}) = g_{+1}(E_{+1}) \\ E_d^+ = k_BT_W \ln\left(k_1^0 t_w\right) + \Delta E \text{ in } E_{-1} \text{ scale} \\ E_d^- = k_BT\ln\left(k_{-1}^0 t\right) \text{ in } E_{-1} \text{ scale} \end{cases}$$

So, for $\begin{matrix} x_{+1}\left(E_{-1} < E_d^+\right) = 1 \\ x_{+1}\left(E_{-1} > E_d^+\right) = 0 \end{matrix}$ we obtain $[B](t) = A_0\int_0^{E_d^+} g_{-1}(E_{-1})\left[1-x_{-1}(E_{-1},t)\right]dE_{-1}$

Then, for $\begin{matrix} x_{-1}\left(E_{-1} < E_d^-\right) = 1 \\ x_{-1}\left(E_{-1} > E_d^-\right) = 0 \end{matrix}$ and we obtain $[B](t) = A_0\int_{E_d^-}^{E_d^+} g_{-1}(E_{-1})dE_{-1}$

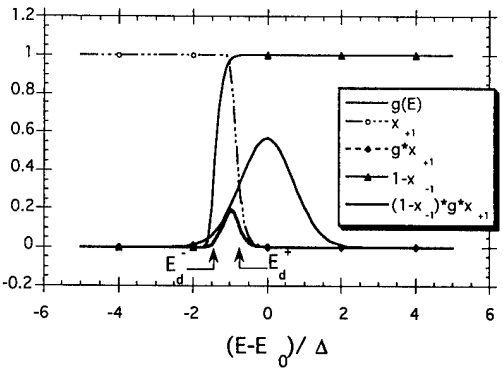

Fig. 4: Plot of distribution function and the forward and backward degrees of advancement of the reaction.

So, effect of writing and erasing can be accounted for by means of demarcation energies. E_d^+ increases on time and on temperature i.e. pathways having larger activation energies are used. This fixes the upper limit of the initial distribution B^0. E_d^- shifts on time and on temperature also in the same direction than E_d^+. It moves upwards, erasing the easiest pathways till E_d^+. Beyond that, the grating is completely bleached.

Erdogan distribution

Using expression of $g_1(E)$ in section I, we have:

$$[B](t) = A_0 \int_{E_d^- - \Delta E = k_B T \ln(k_{-1}^0 t) - \Delta E}^{E_d^+ - \Delta E = k_B T_w \ln(k_1^0 t)} g_1(E_1)dE_1 = A_0 \left[-\frac{1}{1+\exp\left(\frac{E-E_0}{k_B T_0}\right)} \right]_{k_B T \ln(k_{-1}^0 t) - \Delta E}^{k_B T_w \ln(k_1^0 t_w)}$$

And finally,, the stability is defined by the following function:

$$\frac{[B](t)}{B_0} = \frac{1 - \frac{\left(k_{-1}^0 t\right)^{\frac{T}{T_0}} \exp\left(\frac{-\Delta E}{k_B T_0}\right)}{\left(k_1^0 t_w\right)^{\frac{T_w}{T_0}}}}{1+\left(k_{-1}^0 t\right)^{\frac{T}{T_0}} \exp\left(\frac{-\Delta E - E_0}{k_B T_0}\right)}$$

When writing is saturated, we get: $[B](t) = \frac{A_0}{1+\left(k_{-1}^0 t\right)^{\frac{T}{T_0}} \exp\left(\frac{-\Delta E - E_0}{k_B T_0}\right)}$ which is just the Erdogan function used in [7]. we observe that, when the grating is not saturated, the stability increases on the writing time and temperature. This effect can explain some experiments [5]. On the other hand, an annealing rubs out the less stable species i.e. the species produced through the pathways having the smallest activation energy, incresing thus the stability.

III Conclusion

I make here the first link between the writing and the erasure of the Bragg grating i.e. between the elaboration and the stability. When the distribution function is not dependent on the temperature and the grating not saturated, the stability increases with the writing time and temperature. If the distribution changes on temperature for instance if there is a linear broadening of the widh of the distribution then the stability is independent on the writing parameters. This could account for some experimental observations [5]. Furthermore, other types of distribution can be considered, this will be detailed elsewhere along with the writing when reversible reaction is working (high temperature or low laser power density). Also the model can be complexified on the same basis to account for different exponents between writing and erasing.

References

1. T. Taunay, *Contribution à l'étude des mécanismes de la photosensibilité de verres et de fibres dopés par des ions de terre rare ou par de l'oxyde de germanium.*, . 1997, Université des Sciences et Techniques de Lille, France.
2. E. Fertein, *Contribution à l'étude des mécanismes de la photoréfractivité dans des fibres optiques dopées à l'oxyde de germanium.*, . 1994, Lille/Flandres.
3. B. Poumellec, P. Niay, and T. Taunay. *Stress dependent kinetics of UV induced refractive index change in germanosilicate fibers.* in *Photosensitive optical Materials and Devices.* 1997. San José, Ca, USA: SPIE.
4. B. Poumellec, P. Bernage, and I. Riant. *Mechanisms of refractive index change under UV irradiation in some SiO2 core optical fibers.* in *Doped Fiber Devices and systems II.* 1996. Denver, Colorado, USA: SPIE.
5. P. Bernage, T. Taunay, B. Leconte, M. Douay, P. Niay, J.F. Bayon, H. Poignant, H. Herlemont, J. Legrand, and B. Poumellec. *Inscription kinetics and thermal stability of Bragg gratings written within heated fibers.* in *Doped Fiber Devices and systems II.* 1996. Denver, Colorado, USA: SPIE.
6. T. Erdogan, V. Mizrahi, P.J. Lemaire, and D. Monroe. *Decay of U.V. -induced fiber Bragg gratings.* in *Optical Fiber Communication'94.* 1994. San Jose, California, USA: Optical Society of America, Washington, D.C. USA.
7. T. Erdogan, V. Mizrahi, P.J. Lemaire, and D. Monroe, J. Appl. Phys., 1994. **76**(1): p. 73-80.

Growth Kinetics Of Photoinduced Gratings And Paramagnetic Centers In High NA, Heavily Ge-Doped Silica Optical Fibers

T. Taunay*, T.E. Tsai*, and E.J. Friebele
Naval Research Laboratory, Washington DC, 20375
Tel. 202-404-2560, FAX 202-404-8114
P. Niay
LDMP, URA CNRS 779
Centre d'Etudes et de Recherches sur les Lasers et Applications
Université Des Sciences et Technologies de Lille, 59655 Villeneuve d'Ascq Cédex, France
Tel. 33-2-20-43-47-62, FAX 33-3-20-43-48-84
J.F. Bayon
LAB/RIO/TSO, France Télécom, CNET Lannion B
22307 Lannion Cédex , France
Tel. 33-2-96-05-21-89 FAX 33-2-96-05-13-07

The achievement of UV photoinduced refractive index changes in germanosilicate fibers paved the way for the development of fiber Bragg grating (FBG) based optical devices (e.g., filters, fiber lasers, sensors). Although the mechanisms underlying the UV photosensitivity are not fully understood, it is now well established that the refractive index changes are associated with a partial bleaching of an absorption band around 5 eV, arising from the Germanium Oxygen Defect Center (GODC). Several mechanisms have been proposed to explain the photosensitivity in germanosilicate fibers: color centers [1], stress relief [2] and compaction [3]. Depending on the Ge concentration and the experimental conditions used to write the gratings, three types of photosensitivity, type 1, type IIa and type 2 have been identified in unloaded Ge-doped silica fibers. The most commonly observed, type 1, arises in standard fibers ([GeO_2] < 20 mol%) under either pulsed or cw UV exposure in the low fluence regime. Type 1 photosensitivity is characterized by a monotonic increase of both the mean refractive index $<\Delta n_{eff}>$ and the induced refractive index modulation Δn_{mod} under UV exposure. Unlike type 1, the most relevant feature of type IIa photosensitivity ([GeO_2] > 25 mol%, $\phi_c \approx 2\mu m$) is the complex behavior of $<\Delta n_{eff}>$ and Δn_{mod} as a function of exposure time [4]. Indeed, with increasing UV exposure time, a partial or total bleaching of the saturated type 1 grating is followed by the formation of a new grating spectrum. At the time of the second grating growth, the shift experienced by the Bragg grating wavelength is nulled or slightly negative, indicating a negative refractive index change. Moreover, a noticeable difference between type 1 and type IIa photosensitivities is their markedly different thermal behavior. Type 1 gratings begin to anneal at temperatures as low as 300 C and are no longer observed at 550 C while type IIa gratings experience no annealing at temperatures below 450-500 C; a rapid decay is then observed at annealing temperatures ~600-700 C. Recent experiments have shown that the formation dynamics of type 1/IIa grating spectra are strongly affected when the gratings are written in strained fibers [5]. Using the "Photoelastic densification" model and stress dependence kinetics, it has been demonstrated that, under the assumption of a decrease in densification rate, stretching the fiber will in turn decrease the type 1 index modulation [3], [6]. Nevertheless the origin of type IIa photosensitivity in high NA Ge-doped silica fibers still remains unresolved.

Correlation between the thermal stabilities of type IIa gratings and Ge *E'* centers support the hypothesis that these two are closely related [7]. In this paper, the behavior of the photoinduced defect center concentrations in high NA, heavily Ge-doped fibers was compared with the complex dynamics of the refractive index changes associated with FBG's written in the same fiber. We found that stretching the fiber leads to significant changes in the accumulated fluence dependence of the photoinduced defect center concentrations.

The single mode fiber used for the experiments, which was manufactured by the CNET laboratory Lannion-France, had the following parameters: core diameter 1.8 μm, $\Delta n = 42 \times 10^{-3}$, core [$GeO_2$] ~28 mol %, λ_c = 0.8 μm. For all experiments, the fiber was exposed to a KrF excimer laser (Lambda Physik Model EMG103; λ_p= 245 nm, E= 5 eV, $\tau \approx 20$ ns). A phase mask (grating pitch Λ= 1.078 μm, Bragg wavelength ~1560 nm, L=8 mm)

from Lasiris Corp. was used to produce the fiber Bragg gratings. After being clamped on two supports, one of which was mounted to a precision translation stage, the fiber was held into contact with the phase mask. A precision gauge allowed an accurate measurement of the strain applied to the fiber. The grating reflectivity and the Bragg wavelength were monitored in real time in the course of the writing the gratings using a broad band Er-doped superluminescent source and an optical spectral analyzer (AQ-6315A, ANDO). For the study of the UV-induced defect centers, 20-cm lengths of fiber of total length 60 cm were uniformly UV-exposed with the same fluence per pulse as that used to write the FBG's. The paramagnetic defect centers were studied by X-band electron-spin resonance (~9.4 GHz) spectroscopy using a Bruker ER 200D-SRC spectrometer in second-harmonic mode operation, field modulated at 50 kHz with an amplitude of 6.3 G and a microwave power of 20 mw.

Typical time evolutions of the refractive index modulation derived from the grating reflectivity are displayed in Fig. 1 for four gratings. The mean fluence per pulse used to write the gratings was 375 mJ/cm^2. The repetition rate was increased from 2 Hz (at the early stages of grating formation) up to 20 Hz during the inscription of the type IIa gratings. The behavior of the gratings written in strained fiber ($\Delta L/L = 0.39 \times 10^{-3}$) is typical for fibers where types 1 and IIa were observed. After the index modulation achieves a maximum value at about 1 kJ/cm^2, it decreased quickly toward zero. Then, when the exposure time was further increased (F > 1.9 kJ/ cm^2), Δn_{mod} exhibited a monotonic growth. As shown in Fig. 1, when $\Delta L/L$ increased from 0.39×10^{-3} to 9.85×10^{-3}, no type 1 grating could be observed, whereas the efficiency of type IIa increased. The negative Bragg wavelength shift experienced by the grating ($\Delta\lambda_B \approx -0.25$ nm) in the fiber strained to 9.85×10^{-3} is proof that the observed dynamics corresponds to type IIa gratings. The features of Fig. 1 are similar to those previously reported in [5].

The concentrations of the observed paramagnetic defect centers (Ge *E'* and Ge(1)+Ge(2)) as a function of accumulated UV fluence on the fiber are shown in Fig. 2. The data of the unstrained fiber are drawn in open symbols while those of the strained fiber are shown with filled symbols. We find that the concentration of the UV-induced Ge *E'* centers increases with fluence, in agreement with [8], while that of Ge(1) and Ge(2) centers saturates quickly ($F_t < 400$ J/cm^2) and bleaches Nevertheless, one can note that bleaching occurs for an accumulated fluence one order of magnitude less than in the data reported by Tsai *et al.*[8]. Furthermore, the ESR spectra of strained and unstrained fibers show that the fluence dependence and the total concentration of the UV induced Ge *E'* centers are greater in the former case. Indeed, in the unstrained fiber the concentration of Ge *E'* centers appears to be noticeable only for accumulated fluence = 800 J/cm^2. At these fluences, the efficiency of the type 1 Δn_{mod} saturates and then decreases. On the other hand, note that straining the fiber induces an assisted bleaching of the Ge(1,2) defect centers, since their concentration saturates at 3.3×10^{18}/cm^3 for F_t = 38 J/cm^2 (vs. 5.3×10^{18} for the unstrained case), and these centers are no longer observed for F_t > 2 kJ/cm^2. Poumellec & al [6] proposed that straining the fiber decreases the rate of the densification process. Thus the enhanced disappearance of type I gratings in strained fibers can be understood by the increase rate of photobleaching of Ge(1,2) centers observed in the study and the decreased rate of densification[1]. The [Ge E'] is much greater in the strained fiber as is the higher type IIa photosensitivity. However, this result does not imply that Ge *E'*-type defects are directly responsible for type IIa gratings since the saturating exponential growth of the Ge *E'* centers in both the strained and unstrained fibers does not follow the growth of the type IIa index modulation at high accumulated fluence.

Formation and photobleaching of paramagnetic defect centers in high NA, heavily Ge-doped SiO_2 fibers exposed under various strains were examined and compared with that of the refractive index modulation associated with gratings inscriptions. A conspicuous increase of the Ge *E'* concentration was observed in strained fibers. However, the temporal behavior of the Ge *E'* centers does not match that of the gratings for high cumulative fluences, which prevents us from ascertaining a direct correlation between Ge *E'* centers and type IIa gratings (although their thermal annealing behavior is similar). Further details and comments, together with similar experiments realized in standard fibers, will be presented at the conference.

[1] D.P. Hand, and P. St. J. Russell, "Photoinduced refractive index changes in germanosilicate fibers," Opt. Lett., vol. 15, p.102-104 (1990).
[2] M.G. Sceats, G.R. Atkins, and S.B. Poole, "Photolytic index changes in optical fibers," Ann. Rev. Mater. Sci.,

[1] Note that this result obtained for high fluence, e.g. ≥1 kJ/cm2, is different from the correlation of GeE' centers with type I gratings reported by Tsai & al for fluences <12 J/cm2

vol. 23, p. 381-410 (1993).

[3] B. Poumellec, P. Niay, M. Douay, J.F. Bayon, "UV index refractive index changes in Ge:SiO_2 preforms: additional CW experiments and macroscopic origin of the index change," J.Phys. D: Applied Physics, vol. 29, p. 1842-1856 (1996).

[4] M. Douay, W.X. Xie, E. Fertein, P. Bernage, P. Niay, J.F. Bayon, and T. Georges, "Behaviors of spectral transmission of photorefractive filters written in germania-doped fibers: writing and erasure experiments," Proc. SPIE, vol. 2044, p. 88-112 (1993).

[5] P. Niay, P.Bernage, T. Taunay, W.X. Xie, G. Martinelli, J.F. Bayon, H. Poignant, and E. Delevaque, "Bragg gratings photoinscription within various type of fibers and glasses," vol.22 of 1995 OSA Technical Digest Series (Optical Society of America, Washington DC, 1995) paper SW A1-1, p. 66-69.

[6] B. Poumellec, P. Niay, T. Taunay, "Stress dependence kinetics of UV induced refractive index changes in germanosilicate fibers," Proc. SPIE, col. 2998, p. 36-48 (1997).

[7] T.E. Tsai, E.J. Friebele, and D.L. Griscom, "Thermal stability of photoinduced gratings and paramagnetic centers in Ge- and Ge/P-doped silica optical fibers," Opt. Lett., vol. 18, No 12, p. 935-937 (1993).

[8] T.E. Tsai, E.J. Friebele, D.L. Griscom, and M. Saifi, "Defect centers induced by harmonic wavelength of 1.06 μm light in Ge/P-dope fibers," Electro-optics & non linear-optics optics, vol. 14, p. 127-136 (1990).

[9] T.E. Tsai, G.M. Williams, and E.J. Friebele, "Index structures of fiber Bragg gratings in Ge-SiO2 fibers" Opt. Let., vol. 22, N° 4, p. 224-226, (1997)

* Also with Fiber & Electro-Optics Research Center, Virginia Polytechnic Institue , Blacksburg, Virginia 24061

Figures

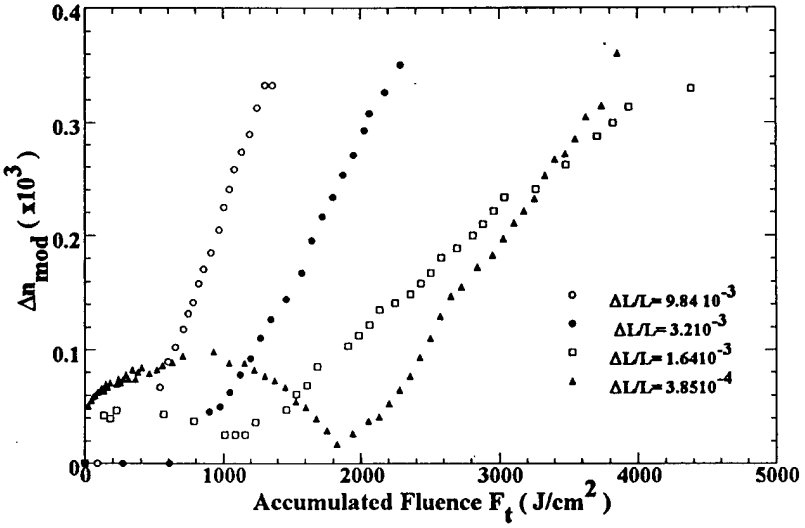

Figure 1: Growth of the UV induced refractive index modulation as a function of the accumulated fluence for gratings written in fibers put under various strains

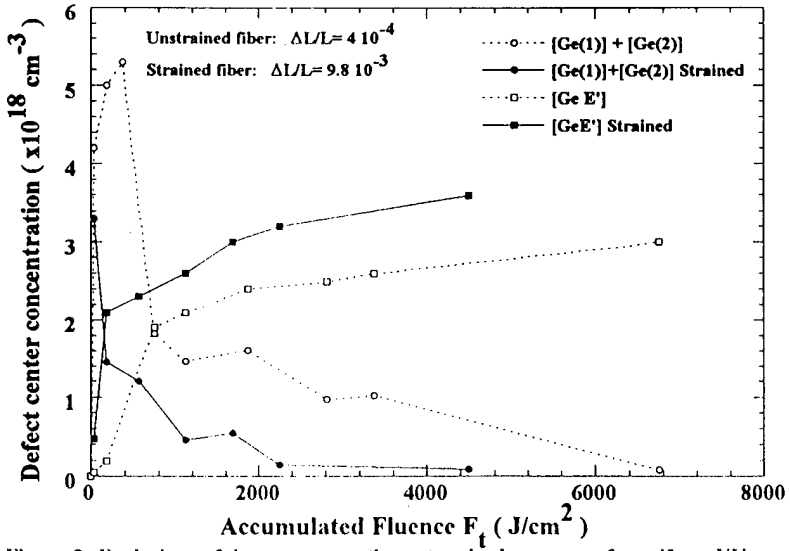

Figure 2: Evolutions of the paramagnetic centers in the course of a uniform UV exposure.

Two Types of Photosensitivity Observed in Hollow Cathode PECVD Germanosilica Planar Waveguides.

M. V. Bazylenko* & D. Moss
Optical Fibre Technology Centre, 101 National Innovation Centre
Australian Technology Park, Eveleigh, NSW 1430, Australia
(ph: + 61-2 9351 1900, fax: + 61-2 9351 1910)
* on secondment to Electrical Engineering, University of New South Wales, Sydney, NSW, 2052, Australia.
(ph: +-61-2-9385-4027, fax: +-61-2-9385-5993)

Introduction.

Plasma enhanced chemical vapour deposition (PECVD) is a promising technique for growing intrinsically UV-photosensitive germanosilica waveguides. Conventional PECVD techniques have been used to fabricate low-loss waveguide devices since the late 1980's [1], but it is only recently that work has started on the development of UV-photosensitive PECVD glasses for direct writing, bragg gratings and UV-tuning applications [2]. Although high intrinsic photosensitivity in conventional PECVD germanosilica has been reported [3], its practical use has been limited by the high loss of this material due to N-H related absorption and film porosity. The loss can be reduced by high temperature annealing which, however, deletes the intrinsic photosensitivity, thus negating its potential advantage of PECVD over the more mainstream, flamehydrolysis technique.

In overcoming the problems experienced by conventional PECVD, a novel hollow cathode PECVD (HCPECVD) technique has been developed which is capable of producing low loss waveguides [4], highly photosensitive germanium doped silica [5] (with negative UV-induced index changes of $|n|>0.006$), and low loss Ge doped buried waveguides [unpublished work]. In this paper we demonstrate that effects previously observed in optical fibers, where the photoinduced index change undergoes a change in sign (from positive to negative) with increasing fluence, is also observed in our material, except an order of magnitude larger. We attribute this to competition between a change in material density and microscopic polarizability.

Experimental.

The high plasma density Hollow Cathode PECVD (HC-PECVD) system is described in detail elsewhere [6]. Briefly, it consists of two parallel electrodes both connected to the same radio frequency (rf) power supply (13.56MHz) and surrounded by a grounded chamber. This differs from a conventional PECVD system, where only one of the electrodes is rf powered, and the chamber and the other electrode are grounded. The use of a hollow cathode rf system allows for a significant increase in the process parameter space since the system is capable of maintaining a high intensity discharge outside the parameter space of a conventional rf system. For example, it can operate at pressures two orders of magnitude lower than those used in conventional rf systems, allowing for the use of O_2 instead of N_2O as an oxidant for silane to overcome the problem of N-H related absorption in conventional PECVD silica [4]. The level of ion bombardment is also significantly higher in the hollow cathode system compared to conventional PECVD, which is important for obtaining homogeneous, porosity free germanosilica [7].

Germanosilica waveguides with 20 mol.% of GeO_2 and a thickness of 3μm were deposited from a mixture of silane and oxygen with additions of germane (GeH_4) at a temperature of 400°C following the deposition of a 10 μm thick undoped lower cladding layer on a 4" silicon substrate. After deposition the above bilayers were consecutively exposed to 193 nm radiation from an ArF excimer laser at 17 mJ/cm^2 pulse energy and 20 Hz repetition rate. The refractive indices were measured after each exposure at the same point on the sample using the prism coupling technique at 633 nm. To investigate the thermal stability of the UV-induced refractive index changes the exposed samples were repeatedly annealed for one hour at increasing temperature.

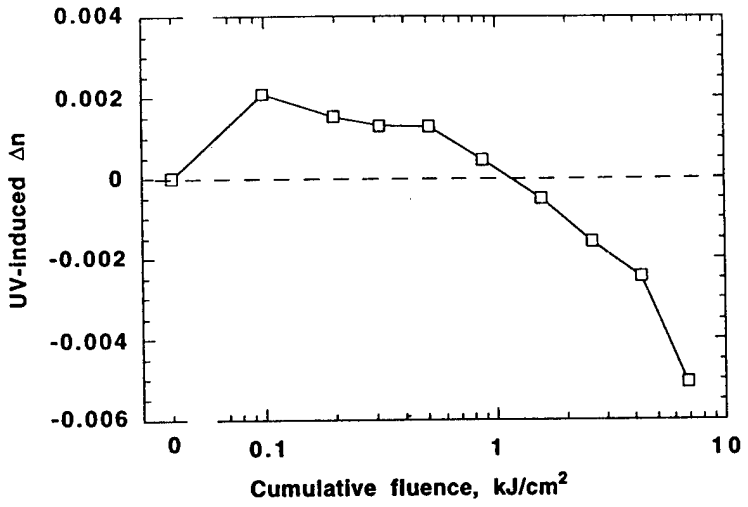

Figure 1. UV-induced change in refractive index (Δn) of germanosilica (20 mol%) planar waveguide as a function of cumulative UV fluence. Irradiation conditions: 193nm, 17mJ/cm² per pulse, 20Hz.

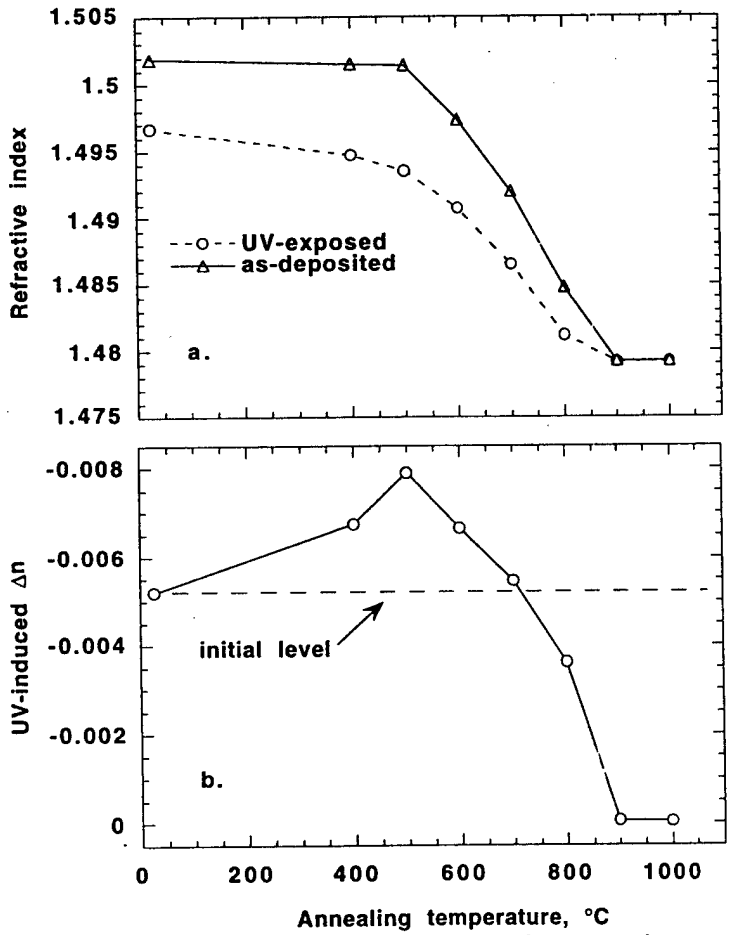

Figure 2. (a) Refractive index in UV-exposed and unexposed areas of the same sample, (b) refractive index difference between UV-exposed and unexposed areas (Δn), as a function of concecutive annealing temperature.

Results.

Figure 1 shows the UV-induced Δn as a function of the cumulative fluence. Following the initial increase of 0.0021, Δn decreases and changes sign at around 1 kJ/cm^2 cumulative fluence and then becomes increasingly negative. A maximum index change (unsaturated) of -0.0051 is obtained for a total exposure of 6.8 kJ/cm^2.

The annealing behaviour of the refractive index in the exposed and unexposed areas and their difference are shown in Fig. 2a and 2b, respectively. Up to 500°C the refractive index of the unexposed material remains unchanged while the refractive index of the exposed area decreases, giving rise to a maximum Δn of -0.0080. At higher temperatures the refractive index in the unexposed area also begins to fall (but at a higher rate) causing a gradual decrease in Δn. The Δn is fully annealed at 900°C.

Discussion.

Similar photosensitive and annealing behaviour has been previously observed in fibres with high germanium content for both pulsed and cw 244nm [8] and pulsed 193nm [9] irradiation. The positive part of the Δn curve has been termed photosensitivity type I and the negative part, photosensitivity type IIA [8]. Here, however, we observe an order of magnitude stronger effect for both positive and negative parts. We also note a higher thermal stability of the negative refractive index change obtained here, which is completely annealed out only at 900°C, while the negative Δn gratings in fibers become undetectable at temperatures below 800°C.

In the previous work we established that as-deposited

HCPECVD silica is denser than fused silica and the negative refractive index changes in this material is the result of a decrease in its density through UV-induced structural dilation [7]. The higher refractive index (and the higher density) of HCPECVD silica can also be reduced by high temperature annealing. The overall reduction in refractive index during annealing in Fig. 2a illustrates this effect. Note also that the unsaturated UV-induced negative index change at high fluence obtained here is less than 1/3 of the index change due to annealing (of the unexposed material) alone, implying that even larger UV-induced index changes may be possible.
A refractive index change Δn can result not only from a change in material density but also from a change in its polarizability, which are related through differential form of the Lorenz-Lorenz equation:

$$\Delta n = \frac{(n^2 - 1)(n^2 + 2)}{6n^2} \left(\frac{\Delta\alpha}{\alpha} - \frac{\Delta V}{V}\right) \qquad (1),$$

where $\Delta\alpha/\alpha$ and $\Delta V/V$ are the relative changes in material polarizability and volume, respectively. One can see from Eq.(1) that $\Delta\alpha/\alpha$ competes with $\Delta V/V$ in its effect on refractive index, so that, for example, the refractive index decrease caused by a volume expansion (or decrease in density) should be larger in the absence of a simultaneous polarizability increase. Previously [7], we have shown that, by using Eq(1) in conjunction with measurements of Δn and film thickness for a fixed, high fluence ($5kJ/cm^2$), the contribution to the induced index change in this material due to a change in polarizability alone is $\Delta n \approx +0.002$. Here we can see from Fig. 1 that this increase occurs at smaller fluences and counteracts the negative index change due to structural dilation at higher fluences, thus reducing the overall index change. When this polarizability increase is annealed out (Fig. 2) the structural dilation can manifest itself fully, leading to a net maximum index change of $\Delta n = -0.008$. The origin of the polarizability increase, and the corresponding positive refractive index change, is not clear at this stage. One can note, however, that it is an order of magnitude larger than the type I photosensitivity observed in fibers. This may be due to a much higher density of wrong (Si-)Ge-Ge bonds in HCPECVD germanosilica and therefore a higher defect density produced by UV irradiation. The presence of a higher density of wrong bonds (and potentially other lattice defects) in the HCPECVD material is supported by its extremely high absorption in the UV region (up to 3dB/μm at 193 nm) and can be attributed to the non-equilibrium nature of the plasma-surface interactions intrinsic to plasma assisted deposition at low temperatures.

Conclusion.

Germanosilica bilayers have been deposited by hollow cathode PECVD - a novel deposition technique which, as opposed to conventional PECVD, is capable of producing germanosilica waveguides with both high intrinsic photosensitivity and low loss. During consecutive exposure to 193nm UV light, positive index changes peaking at +0.0021, followed by negative index change of -0.0051 (unsaturated), have been observed. These photosensitive effects are similar to type I and type IIA photosensitivity observed in optical fibers, but an order of magnitude stronger. The positive index change is annealed at 500°C, while the negative index change is fully annealed out at 900°C.

References.

1. G. Grand, J.P. Jadot, H. Danis, S. Valette, A. Fournier, A. M. Grouillet, Electron. Lett. **26**, 2135 (1990).
2. M. Svalgaard, C. V. Poulsen, A. Bjarklev and O. Poulsen, Electron. Lett. **30**, 1401 (1994).
3. J. Canning, D. Moss, M. Faith, P. Leech, P.Kemeny, C. V. Poulsen, O.Leistiko, Electron. Lett. **32** 1479 (1996).
4. M.V. Bazylenko, M. Gross, P. M. Allen and P. L. Chu, IEEE Photonics Technol. Lett. **7**, 774 (1995).
5. M. V. Bazylenko, M. Gross, P. L. Chu and D. Moss, Electron. Lett. **32**, 1198 (1996).
6. M. V. Bazylenko, M. Gross, A. Simonian, and P. L. Chu, J. Vac. Sci. Technol. **14**, 336 (1996).
7. M. V. Bazylenko, M. Gross and D. Moss, J. Appl. Phys. **81**, 7497 (1997).
8. P. Niay, P. Bernage, S. Legoubin, M. Douay, W. X. Xie, J.F. Bayon, T. Georges, M. Monerie, B. Poumellec, Opt. Comm. **113**, 176 (1994).
9. L. Dong, W. F. Liu and L. Reekie, Opt. Lett. **21**, 2032 (1996).

Bragg Gratings, Photosensitivity, and Poling in Glass Fibers and Waveguides: Applications and Fundamentals

Poster Session II

Monday, October 27, 1997

BMG
3:30pm–4:30pm
The Promenade

Widely Wavelength Tunable External Cavity Laser by Using Fiber Bragg Grating Embedded Optical Switch

Masakazu Shigehara, Hiroshi Kohda, Kazuhito Saito and Hiroo Kanamori

Yokohama Research Laboratories, Sumitomo Electric Industries, Ltd.
1, Taya-cho, Sakae-ku, Yokohama, 244 Japan
Tel: +81-45-853-7167, Fax: +81-45-851-5300, E-mail: m-shige@yklab.sei.co.jp

1.Introduction

A fiber Bragg grating(FBG) external cavity laser(ECL) has been of great interest for a variety of applications in wavelength division multiplexing systems such as a transmitter[1],[2], a pumping laser of an erbium-doped fiber amplifier[3], a low coherency light source for an optical time domain reflectometer(OTDR)[4], and so forth.

On the other hand, wavelength tunability is an attractive feature for a light source in a specific application. A wavelength tunable distributed Bragg reflector laser for wavelength division multiplexing(WDM) communication systems were demonstrated[5].

In this paper, we propose a widely wavelength tunable FBG-ECL employing a fiber transfer type optical switch, and oscillation of four different wavelength applicable to WDM networks is demonstrated.

2.Structure of wavelength tunable FBG-ECL

A basic structure of a FBG-ECL is shown in Fig. 1. It consists of a semiconductor optical amplifier(SOA) and an FBG for an external cavity mirror. A high reflection coating(reflectivity more than 90%) and an anti-reflection coating(less than 0.3%) are employed on a back and a front facet of the SOA, respectively, so that an optical resonator is formed between the back facet of the SOA and the FBG.

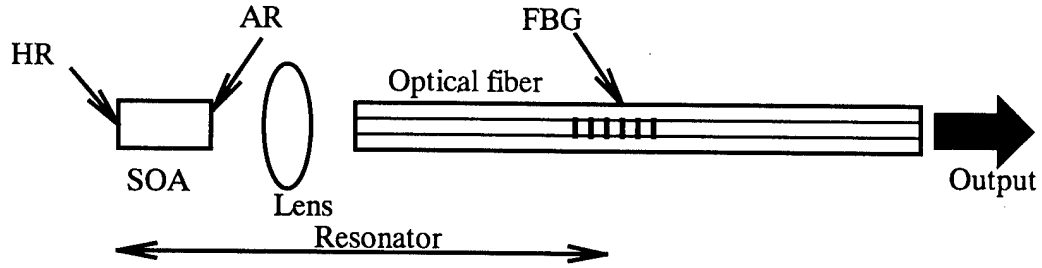

Fig. 1, Schematic diagram of FBG-ECL

Since an oscillation wavelength of an FBG-ECL is determined by the Bragg wavelength of the FBG, it is stable against temperature variation owing to low temperature sensitivity of an FBG(0.01nm/°C). In addition, it would possibly have a wide wavelength tunable range because of a wide gain spectrum region of the SOA over 40nm, if the Bragg wavelength of the FBG is changed. So we propose a wavelength tunable FBG-ECL, which consists of an SOA and a fiber transfer type optical switch, as schematically shown in Fig. 2. By selecting an FBG with the switch, the oscillation wavelength can be changed. This switch features large scale (up to 2×800) and low loss as well as compact size[6],[7]. It is, therefore, possible to accommodate hundreds optical fibers in a fiber array, number of oscillation

wavelengths could be more than 100.

The switching mechanism is shown in Fig. 3. V-grooves are formed parallel every 0.25mm on a silicon plate, and optical fibers are arrayed and glued on each groove. The FBGs have been already written on the fibers in the V-grooves. Mobile optical fibers are fixed obliquely on a head chip and pressed against the V-groove so as to be coupled with confronting fibers fixed in the array. The gap between the optical fibers is kept within 20μm and filled with index matching oil resulting in an optical connection loss less than 0.3dB. As shown in Fig. 2, two mobile fibers are used. One is led to the SOA, and the other is an output optical fiber. In the optical fiber array, the optical fibers with the FBGs are looped so that the SOA is linked to the output fiber through the FBG with a desired Bragg wavelength. Thus, by operating the optical switch, one FBG is selected. A switching speed of the switch is as fast as 1sec. Side mode could be suppressed by inserting a band path filter in the fiber loop.

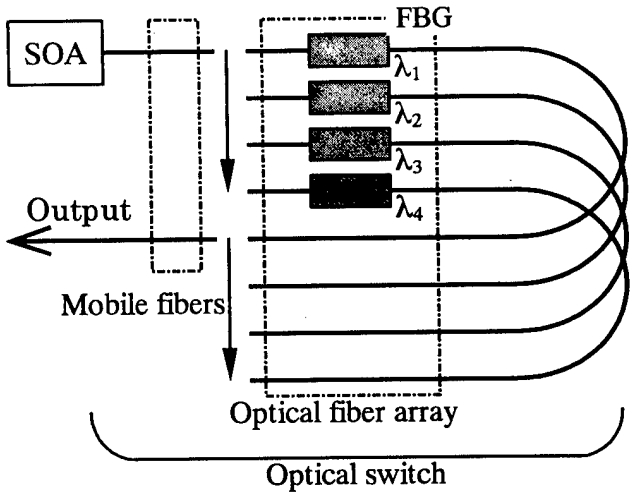

Fig. 2, Schematic diagram of wavelength tunable laser

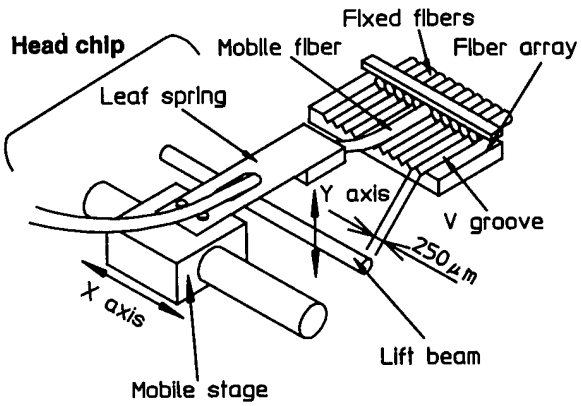

Fig. 3, Switching principle of optical switch

3.Experiment

We experimentally fabricated a four different wavelength FBG-ECL. The wavelengths are 5nm spaced, between 1540 and 1555nm. An optical path length between the back facet of the SOA and the FBG was about 300mm. The cw oscillation characteristics are shown in Table 1 and the cw oscillation spectra of the SOA and the wavelength tunable laser are shown in Fig. 4. It was confirmed that each oscillation wavelength corresponds with the Bragg wavelength of each FBG, and that the obtained spectrum does not overlap each other in the region above -20dB from the maximum power level, if the wavelengths spacing are 0.8nm apart. It indicates that the bandwidths of the emitted lights from the fabricated FBG-ECL are suitable for the WDM light source.

Table. 1, Oscillation characteristics

	Bragg wavelength of FBG[nm]	Center of oscillation wavelength[nm]	Oscillation bandwidth at -20dB[nm]
1	1540.02	1540.16	0.32
2	1545.10	1545.13	0.28
3	1549.82	1549.88	0.27
4	1555.03	1555.10	0.31

In the spectra shown in Fig. 4, there still remains a Fabry-Perot mode noise around a center wavelength of the SOA. It could be improved by decreasing the reflectivity of the anti-reflection coating on the front facet of the SOA.

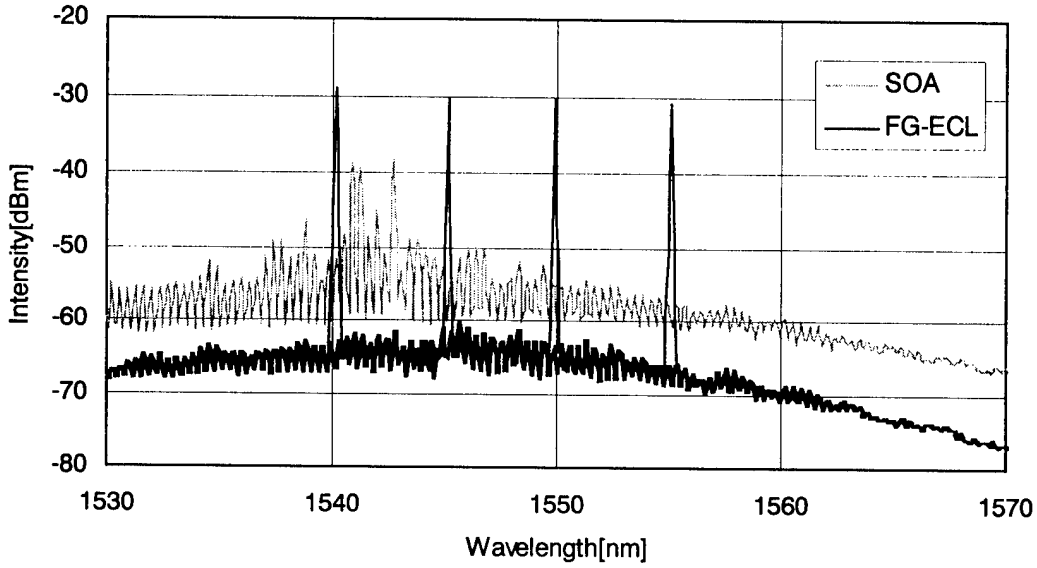

Fig. 4, Oscillation spectra of SOA and wavelength tunable laser

4.Conclusion

We have proposed the discrete type wavelength tunable laser by using the FBGs as the external cavity mirror, embedded in a fiber transfer type optical switch. We fabricated a four wavelength FBG-ECL and demonstrated oscillation of four wavelengths which are decided by the Bragg wavelength of the FBG in a fiber array of the optical switch.

References

[1] F. N. Timofeev, *et al.*, in OFC'97 Technical Digest, ThM1, 1997
[2] A. Hamakawa, *et al.*, in OFC'97 Technical Digest, ThM3, 1997
[3] A. Hamakawa, *et al.*, in ECOC'96 Technical Digest, MoC.3.6, 1996
[4] M. Shigehara, *et al.*, in OECC'97 Technical Digest, 9D1-3, 1997
[5] B. Mason, *et al.*, in OFC'97 Technical Digest, ThM2, 1997
[6] S. Furukawa, *et al.*, Technical Digest in 1994 Spring Meet., IEICE Japan, B-986, 1994, in Japanese
[7] M. Tamura, *et al.*, in OECC'97 Technical Digest, 9EP-15, 1997

Narrow Transmission Bandpass Filters Using Bragg Grating-Assisted Mode Conversion

J. Canning, D. Moss
Australian Photonics Cooperative Research Centre (APCRC), 101 National Innovation Centre, Eveleigh, Sydney, NSW, 1430, Australia

Fibre Bragg gratings are proving to be instrumental in enabling the introduction of WDM systems. They offer highly selective bandpass filtering needed for the transmission of multiple closely-spaced wavelengths. These gratings, however, tend to work in reflection since the large k-vector allows coupling from forward travelling modes to backward travelling modes. This has proved to be a major disadvantage since to operate in transmission requires the use of optical recirculators. However, gratings which operate using phase-matching in the forward direction tend to have long periods, determined by the beat length between two modes. Fundamental mode conversion [1,2] requires stripping of the higher order mode to achieve a loss bandpass. This is more readily achieved when conversion is to cladding modes [3]. Whilst these filters have very low reflections, they operate as loss filters and not transmission bandpass devices. Further, the loss bandwidth tends to be broad, on the order of 20nm, because of the small differences in modal dispersion [1-3]. On the other hand, grating dispersion has been used to achieve mode conversion in reflection over a small wavelength range [4]. In all these cases transmission notch filters are generally produced, whereas in most cases the opposite - a transmission bandpass filter - is desired.

In this paper, it is shown that Bragg gratings can be used to achieve mode-coupling in a manner where narrow transmission bandpass filtering is obtained. This is possible because at the Bragg grating resonances light coupled into a backward travelling mode is re-coupled into a forward travelling mode. Previously, Bragg grating dispersion has been used to detune the phase-matching condition in a fibre coupler to generate a narrow peak in one of the transmission arms [5]. In this work, experimental results are presented which illustrate the use of this principle to couple light from one mode to another in a planar waveguide device selected to be lossy at all modes except the desired output mode. Loss for the unwanted modes is achieved using multi-moded tapered guides with single-mode input and output fibres. A transmission bandpass ~1nm wide with a 15dB signal-to-noise level is demonstrated. Hence, the resonant properties of a Bragg grating can be used to generate narrow transmission bandpass filters which have spectral widths determined by the dispersion bandwidths of the grating.

Experimental:

A germanosilicate (20%GeO_2) tapered rib waveguide fabricated in PECVD material [6] was used in these experiments. The taper dimensions [7] were 1mm wide at one end and 10μm at the other end thus supporting a large number of modes. The rib height was ~0.5μm and the length 1cm. PECVD-based glass was used because of the inherently high photosensitivity which allowed the fabrication of Bragg gratings well in excess of 35dB [8]. However, ribs made from this material have a large birefringence splitting arising both from form geometry and stress effects which are not easily compensated [9]. Using the 193nm output from an ArF laser, a Bragg grating was written across the taper length (fluence: 400J/cm^2) resulting in several chirped grating peaks whose spectral position is dependent on the particular mode into which launched light is coupled.

Figure 1 shows the setup used to obtain narrow pass peaks. By adjusting both launch and collection ends it is possible to couple into a lossy mode within the initial part of the taper which is not supported at the other end. Thus very little light couples out. However, the grating is able to couple some of this light into a mode which is coupled out into the single-mode fibre.

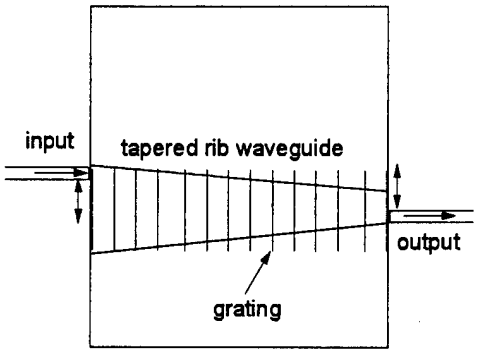

Figure 1. Setup for generating narrow bandpass peaks. Principle also valid for launched input light from output end above.

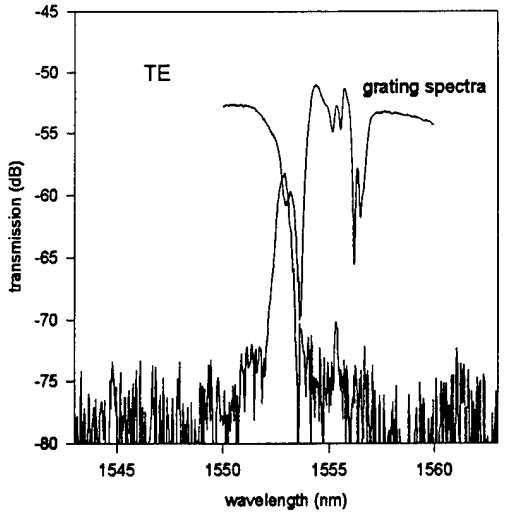

Figure 2. Optimised TE transmission bandpass. Also shown is the corresponding grating spectrum.

Those wavelengths which satisfy the phase-matching condition, determined by the beat length between the modes, are effectively coupled across resulting in the generation of a highly dispersive narrow bandpass. This peak was not able to be generated without the presence of a grating. If the waveguide was uniform, some modal interference, similar to that previously used as a fibre interferometer [10], can be detected. Light from an EDFA is polarised using two in-line polarisers. The TE results of these experiments are shown in figure 2 where it can be seen that the peak only occurs at the grating edge. Also shown is the corresponding grating peak when the input light couples directly to the output fibre. The transmission peak lies on one edge of the grating spectrum. By varying the input coupling it is possible to generate a similar peak on the other side of the bandgap whilst suppressing the other. Further, by adjusting polarisation inputs, both TE and TM peaks can be generated (figure 3). In this case the TE bandpass is on the long wavelength side. This very much depends on the adjustment of input and output fibre coupling. The birefringence splitting, determined by the peak separation of the transmission bandpass for TE and TM, is ~1.2nm.

Figure 2 shows the optimised result using TE light. The narrow bandpass is ~1nm wide and the signal to noise level ~15dB over a measured range of 1530 to 1550nm. Although the signal peak is ~7dB below the optimised background transmission signal, this can be significantly improved by optimising the design of the waveguide shape as well as optimising the grating profile.

In order to ensure that coupling was not dependent on the waveguide dimensions the experiment was repeated for several available tapers where one end width is fixed at 10μm and the other ranges from 20μm up to 1mm. It was found that similar narrow transmission bands could be generated and the only difference was the effectiveness of the broadband suppression of light coupling into the output fibre. The larger the taper the greater the loss contrast between the launched and output modes, ensuring that very little of the launched mode can couple out the other end.

Discussion:

The experiments clearly indicate that the grating is able to fulfill phase-matching conditions in the forward direction. The effective period for coupling is determined by the number of cavity round-trips in the grating necessary to introduce the desired phase delay (i.e. the delay is proportional to the cavity Q). Since the round-trip involves both forward and backward travelling waves variable phase-matching in both forward and reverse directions should be possible. Thus the grating can act as a powerful variable delay element by either tuning the wavelength or by tuning the grating itself. Since the optimum results were obtained by adjusting the input and output coupling, it was not possible to identify with certainty the particular modes coupled. However, if the grating is assumed azimuthally uniform, then coupling must occur between two symmetric modes. Otherwise, an asymmetry is present, either as blaze in the grating or non-uniformity in the taper.

Since the coupling relies on the grating dispersion, these filters can be used to generate pre-chirped bandpass peaks which take into account any fibre dispersion experienced later in a WDM system. This pre-chirp can be tailored by selecting which side of the grating coupling is achieved (to control the sign of the dispersion) and by optimising the grating chirp. In the experimental setup described above the large mode-selection range available by adjusting input and output coupling can also allow some tunability. Alternatively, some post-dispersion compensation is available at the other end of a WDM system. By generating and chirping signals simultaneously, the problem of maintaining grating dispersion compensator compatibility with the incoming signal is to a great extent alleviated.

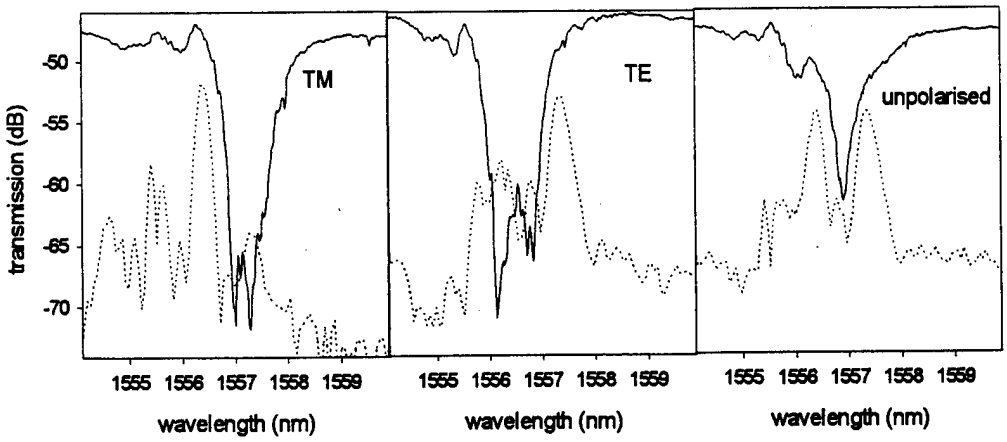

Figure 3. Transmission bandpass peaks for TE, TM and unpolarised light. Also shown are the corresponding grating notches when the input mode is the same as the output mode.

Improvements in background light suppression may be achieved by optimising the integrated waveguide shape or by using loss elements such as mode strippers or specially designed long period gratings similar to those used for gain flattening [4]. Alternatively, such filters may be used to equalise a series of transmission peaks which cover the entire EDFA spectrum. In this case, sampled grating structures may be used to generate multiple peaks with close to equal spacings.

Another application might be as a polarisation converter. It should be possible to adjust the coupling condition such that one polarisation state can be coupled into the other. The beat length will be determined by the birefringence splitting. Further, polarisation mixing may be possible if there is incomplete power transfer.

Although the above principles are independent of the form of waveguide used, integrated optics have distinct advantages including a greater ease of reproducibility on the one wafer as well as being more tolerant to environmental instabilities. In addition, concatenation and parallel operation can be performed on the one packaged element.

Conclusions:

Narrow bandpass transmission peaks have been generated in PECVD-based tapered planar waveguides using Bragg gratings. Improved signal contrast can be achieved with an optimised design of the waveguide filtering shape. Further work is necessary to allow modelling and design of such optimised filters.

References:

[1] H.G. Park, B.Y. Kim, Electron Lett., 25, 797-799, 1989

[2] C.D. Poole, C.D. Townsend, K.T. Nelson, J. Lightwave Tech., 9, (5), 598-604, 1991

[3] A.M. Vengsarkar, P.J. Lemaire, J.B. Judkins, V. Bhatia, T. Erdogan, J.E. Sipe, J. Lightwave Tech., 14, (1), 58-65, 1996

[4] K. Hill, B. Malo, K. Vineburg, F. Bilodeau, D. Johnson, I. Skinnner, Electron. Lett., 26, 1270-1272, 1990

[5] J. Archambault, P. St. Russell, S. Barcelos, P. Hua, L. Reekie, Opt. Lett., 19, (3), 180-182,1994

[6] PECVD material was supplied by the Mikroelektronik Centret, Danish Technical University, Denmark

[7] Tapers were etched at the Telstra Research Laboratories, Melbourne, Australia

[8] J. Canning, D.J. Moss, M. Faith, P. Leech, P. Kemeny, C.V. Poulsen, O. Leistiko, Electron. Lett., 32, (16), 1479-1480, 1996

[9] J. Canning, D. Moss, M. Faith, P. Kemeny, C.V. Poulsen, O. Leistiko, post-deadline paper PD2-6, First Optoelectronics and Communications Conference (OECC'96), Makuhari Messe, Japan, 1996

[10] J. Canning, A.L.G. Carter, Opt. Lett., 22, (8), 561-563, 1997

Rapid Thermal Annealing of Chalcogenide glasses for Photodarkened Waveguide and Grating Applications

S. Ramachandran and S. G. Bishop

Center for Optoelectronic Science and Technology,
Microelectronics Laboratory,
Department of Electrical and Computer Engineering
University of Illinois
Urbana, IL 61801

Optical elements for applications in communications and interconnections such as waveguides and grating devices can be patterned in chalcogenide glasses by illumination with above band gap light, which causes photodarkening[1]. Photodarkening is a photo-induced red shift of the optical absorption edge and is accompanied by an increase in the index of refraction in the transparent spectral range below the absorption edge. A configurational model[2] describes photodarkening as an illumination induced transformation from a stable configuration to a quasi-stable configuration via an electronically excited state. Annealing close to the glass transition temperature (T_g) causes a direct structural relaxation from the quasi-stable to stable state.

A sputtered or evaporated thin film of chalcogenide glass is in a quasi-stable state in the as-grown form and closely corresponds to the photodarkened (PD) state. To utilize the photodarkening property and fabricate photonic devices, it is necessary to first change the film to its stable state from the as-grown, PD state. This transition may be induced by either direct thermal annealing under an inert atmosphere[3] or by illuminating the film with high intensity light that causes local heating to give the same effect[3,4], called photobleaching. The optical annealing process will require uniform high intensity illumination over the film and is not technologically feasible. More importantly, illumination also contributes to photodarkening and thus competes with the photobleaching process. Chalcogenide glasses have high coefficients of thermal expansion (CTE) and thus thermal annealing must be performed with very low temperature gradients in order to avoid cracking the films due to thermal stress. Still, the quality of the film will depend on the CTE of the substrate, limiting the integration of these films with other opto-electronic devices.

We have demonstrated the use of Rapid thermal annealing (RTA) in obtaining high quality films of sputtered $Ge_{10}As_{40}Se_{25}S_{25}$ glasses. Bertolotti *et. al.*[4] have demonstrated that the electronic relaxation process has a 1-2 second time scale and thus a thermal anneal process of only a very short duration is needed for relaxing the glass structure. RTA has the advantage of

providing just this kind of a thermal spike without allowing time for thermal expansion to set in, eliminating the thermal stress problems with conventionally annealed chalcogenide glass films.

Fig. 1 contrasts SEM micrographs of a conventionally annealed chalcogenide film (Fig. 1(a)) with that of an RTA sample (Fig. 1(b)). The glass cracks under thermal stress and then reflows to trap air bubbles in the film when conventionally annealed, as shown in Fig. 1(a), while RTA yields excellent surface smoothness (Fig. 1(b)).

Transmission measurements on these glasses are used to compute the index of refraction as a function of wavelength in the transparent region. Index measurements shown in Fig. 2 reveal that the index change between as-grown (PD state) and annealed films is as high as 5%. This is twice the maximum change reported by Tada *et. al.*[5] and we attribute the difference to a more stable, lower index film due to RTA. The large index changes indicate that these glasses are good candidates for high density optical interconnects.

Films grown on cover glass substrates were used to characterize the efficiency of the PD process by holographic grating exposures. Spatially collimated light from an Argon ion laser at 514.5 nm was split and recombined at the film surface to fabricate 1 μm period gratings. Fig. 3 is a plot of the diffraction efficiency versus exposure time and we find that an index change of 0.001 (0.05%) is achieved with a 1 min. exposure. Fig. 3 indicates that longer exposures decrease the modulation depth of the gratings, possibly due to vibrations in the holographic set up and back reflection problems. Since up to 5% index changes are possible in RTA films of $Ge_{10}As_{40}Se_{25}S_{25}$ glass, the use of a phase mask and appropriate substrate will make possible the fabrication of much stronger gratings.

Channel waveguides were fabricated in the RTA films by exposing them to spatially uniform light from an Argon ion laser through an appropriately patterned mask. The existence of the waveguides was confirmed by end-fire launching 980 nm light and observing the output facet. Fig. 4(a) is a near field image of the 5 μm by 1 μm channel waveguide and Fig. 4(b) shows the intensity profile in the lateral direction. The waveguide should be multimoded at this wavelength but the focused gaussian input beam selectively excites only the fundamental mode, as shown in the figure. Fig. 5 is a top view of the excited waveguide and the absence of strong out of plane scattering suggests that RTA yields high quality thin films of chalcogenide glasses for waveguide and grating applications.

This work is supported by DARPA under the Center for Optoelectronic Science and Technology (Grant #MDA972-94-1-0004) Program.

References

1. Y. Utsugi and Y. Mizumisha, *Jpn. J. Appl. Phys.* **31**, Pt. 1, 3922 (1992).
2. G. Pfeiffer, M.A. Paesler and S.C. Agarwal, *J. Non-Cryst. Solids* **130**, 111 (1991).

3. T. Igo and Y. Toyoshima, *Supplement J. Jpn. Soc. Appl. Phys.* **43**, 106 (1974)
4. M. Bertolotti, F. Michelotti, V. Chumash, P. Cherbari, M. Popescu and S. Zamfira, *J. Non-Crystalline Sol.* **192&193**, 657 (1995).
5. K. Tada, N. Tanino, T. Murai, M. Aoki, *Thin Solid Films* **96**, 141 (1982).

Fig. 1

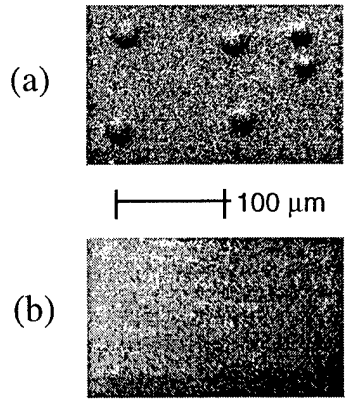

Fig.2

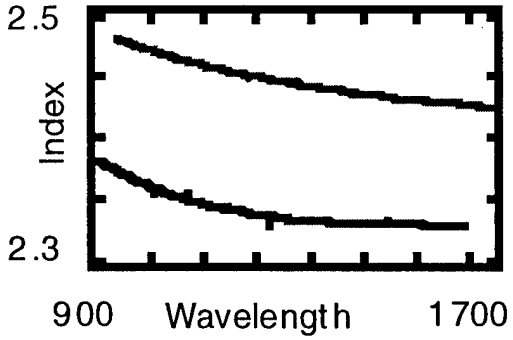

Fig. 3

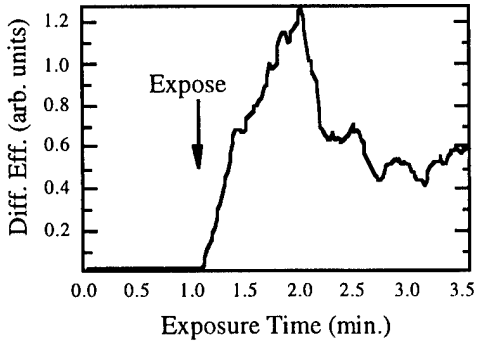

Fig. 4

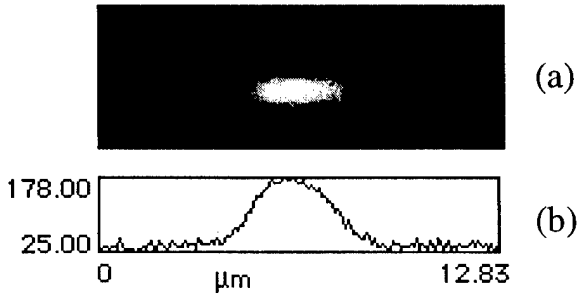

Fig. 5

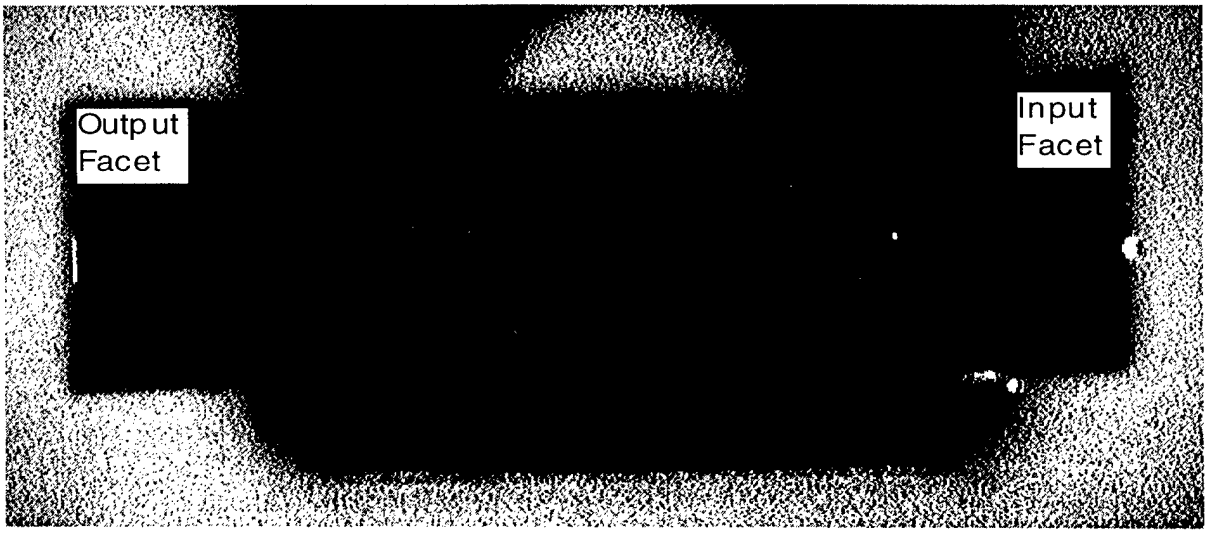

Z-SCAN STUDY OF THIN CHALCOGENIDE As_2S_3 GLASS FILMS AND HOLOGRAPHIC FABRICATION OF MICROLENS NETWORKS

A. Saliminia, T. V. Galstyan, A. Villeneuve
Université Laval, Centre d'Optique, Photonique et Laser,
Cité Universitaire, Pavillon A.-Vachon, Québec, Canada, G1K 7P4
Phone:(418)-656-2025, Fax:(418)-656-2623, E-mail: galstian@phy.ulaval.ca

Kathleen Richardson
CREOL, University of Central Florida
Orlando, FL, USA

Chalcogenide glasses (ChG) have been shown to be very promising candidates for optical information storage and infrared communication systems [1]. The high photosensitivity of these materials in the visible (near bandgap for ChG) spectral band allows the fabrication of various photoinduced structures for integrated optical circuits [2]. The characterization of the light-induced complex refractive index changes (Δn) in ChG and the realization of new applications represent the goal of the present work. Namely, we report, we believe for the first time, the dynamic separation of different photoexcitation modes in ChG, and the holographic fabrication of one (1D) and two (2D) dimensional microlens networks. We study the ChG film refractive index (n), absorption (α) and thickness (d) photomodulation processes, both in steady state and in transient excitation regimes. We use dynamic holography [3] and Z-scan techniques [4] for this study. These techniques provide important information concerning both the dynamical and the steady-state excitation behavior of our ChG films. Different physical and photochemical mechanisms are responsible for the complex behavior of ChG [3] and their understanding and control is an important challenge for the possible applications.

Our ChG samples are fabricated by thermal vaporization on a microscope glass slide. They have high optical quality, and thickness (d) varying from d=1 to d=5 μm. The 488 and 514.5 *nm* lines of a CW Argon laser were used (separately) as excitation wavelengths. These wavelengths are near the bandgap (λ_g = 527 nm or $E_g \approx 2.35$ eV) for our ChG films.

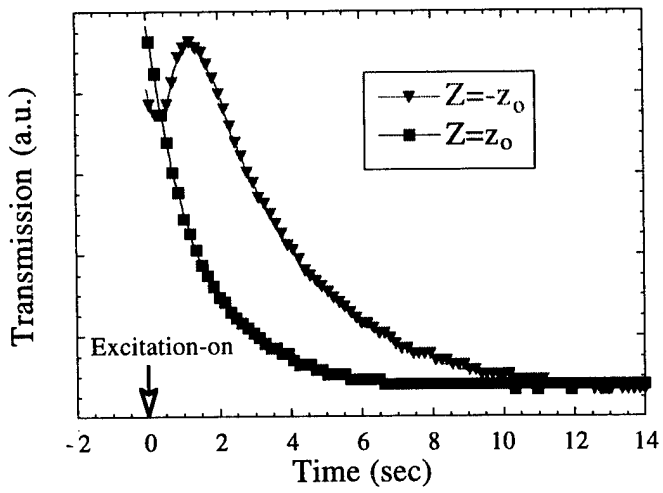

Figure 1. Non symmetrical kinetics of the light transmission through a limiting aperture in the far field.

The steady state excitation data obtained by Z-scan measurements show that the total Δn and absorption changes ($\Delta\alpha$) are positive, as one could expect. However, results of time resolved Z-scan study show that there is a summation (very likely, a complex coupling) of different mechanisms. In particular, we are capable of clearly distinguishing the characteristic times of two phenomenon - namely the Δn and $\Delta\alpha$ - by using the time resolved Z-scan. Thus, the dynamics of the intensity change ΔI^{NL} behind the limited aperture (the light transmission) in the far field shows a quite different behavior for the two symmetrical (with respect to the focal plane) $Z=z_0$ and $Z=-z_0$ positions (Figure 1). We have a monotonic decrease of the intensity for $Z=z_0$ and a non monotonic behaviour for $Z=-z_0$ position. Note that the contribution in ΔI^{NL} due to Δn is changing its sign when moving from z_0 to $-z_0$, while the contribution of the absorption in ΔI^{NL} always has the same sign. This demonstrates that these two phenomenon have different characteristic time constants. Thus, the absorption and refractive index changes at excitation wavelength are not directly related, as it should be according to the Kramers-Kronig formula in the case of one component excitation.

The strong dispersion of our experimental data and the discovery of strong surface relief modulation effects in thin ChG films in the same experimental conditions [3] suggested the presence and the influence of thickness modulation on the Z-scan data. The analyses of the Z-scan processed surfaces by a surface profilometer (Dektak) revealed (Figure 2) very strong surface modulations in spite the fact that we have used μW power level! The surface of the film is

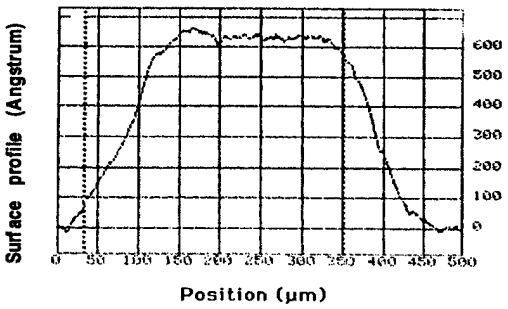

Figure 2 (a). Saturated photoexpansion.

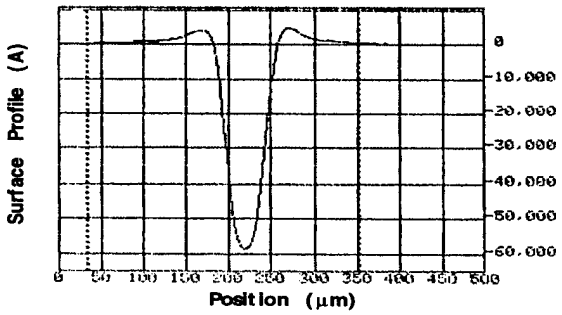

Figure 2 (b) Expansion and depression

differently modulated depending upon its position with respect to the focal plane of the focusing lens (for the same total power of the input beam). We observe a quasi gaussian expansion shape when the film is far from the focal plane, saturated step-like expansion shape in an intermediate position (Figure 2 (a)) and a complex, crater-like shape (with both expansion and depression) near to the focal plane (Figure 2 (b)). Thus, we have to significantly decrease the intensities used (already in the μW range) to get correct Z-scan data.

We can estimate the temperature rise due to the light absorption in the ChG film. The temperature variation in the stationary regime could be estimated as $\delta T=\alpha x I(L/\pi)^2 k^{-1}$ [5] where α - is the absorption coefficient of ChG at excitation wavelength ($2\cdot10^3$ cm^{-1}), x - is the quantum yield of non radiative relaxation of photoexcited electrons, I - is the light intensity and k - is the thermal conductivity of the ChG, $k=3\cdot10^{-2}$ $W(cm\ K)^{-1}$. We obtained only several degrees of heating for experimental parameters used in the present work, which is much less than the glass transition temperature reported so far for bulk ChG materials (T_g=180°C). Obviously, the light induced heating is much smaller (more than an order of magnitude) than the softening or evaporation temperatures [2]. We emphasize that the characteristics we use are taken for bulk elements, while

surface tension and interaction with the substrates may be also important [6]. Thus, the microscopic origins of such giant thickness modulations are not yet clear.

In spite of that, the obtained experimental results already allow for several applications. An interesting example of such application of this photoexpansion phenomenon is the fabrication of microlens structures. Single beam illumination (with an out of bandgap wavelength) has been used to directly fabricate a single microlens [2]. One can also fabricate 1D (cylindrical) or 2D network of microlenses systems using a corresponding mask or x-y stages [7,8]. We have proposed and realized a new, holographic, technique for microlens fabrication, taking into account the data we have obtained both by holographic technique [3] and by Z-scan for near bandgap illumination of thin ChG films (Figure 3). These data allow the control of the fabrication processes and the realization of high modulation efficiency. Namely, with a proper choice of the holographic exposition geometry, intensity and duration we are capable of fabricating high quality 1D and 2D microlens structures. The fabrication process is a single (for 1D network) or double (with rotated at 90 degree film, to obtain 2D, crossed microlenses network) holographic exposition (Figure 3). The choice of crossing angle between excitation beams, their intensity and exposition allows the fabrication of microlenses with largely variable optical parameters. As we noted, the knowledge of the expansion and/or depression behavior detected in Z-scan study facilitate the correct choice of these parameters.

In summary, we have shown that single, near bandgap beam illumination of the ChG film leads to a local refractive index change in the bulk of the film as well as a thickness variation. The refractive index change includes the modulation of the film absorption, refractive index, and of the induced birefringence. The thickness modulation may be positive (photoexpansion) as well as negative (depression), with variation of the initial thickness by up to 30% for the expansion and by 100 % for the depression. We use this property to fabricate 1D and 2D microlens structures with easily controllable parameters via holographic exposition.

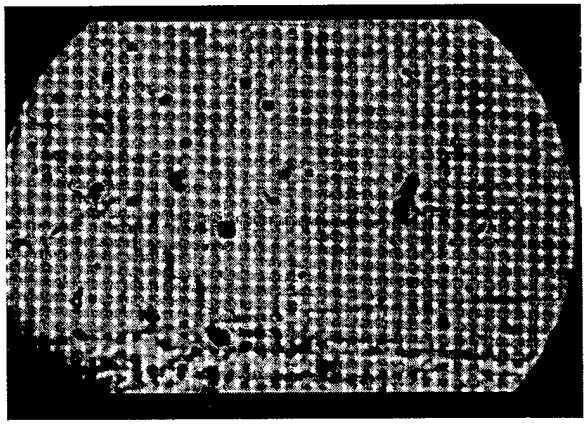

Figure 3. Microscope photography of the microlens 2D network obtained via two consecutive holographic expositions (with horizontally and then vertically oriented ChG film). The grating period is 38 μm, and the thickness of the film is 3 μm.

References

1. M. Asobe, T. Kanamori, and K. Kubodera, IEEE J. Q.E., Vol.29, No 8, p. 2325 (1993).
2. H. Hisakuni, K. Tanaka, Optics Letters, V. 20, No 9, 958-960 (1995); Appl.Phys.Lett., V.65 (23), 2925(1994); A. Sasaki, T. Baba, K. Iga, Jpn. J. Appl. Phys.,V.31,1611(1992) Pt.1.No 5B.
3. T.V. Galstyan, J.-F. Viens, A. Villeneuve, M. Duguay, K. Richardson, Special Issue of the IEEE/OSA Journal of Lightwave Technology on Applications of Photosensitivity and Quadratic Nonlinearity in Glasses (to be published in August 97).
4. M. Sheik Bahae et al. IEEE Journ. Quant. Electr., Vol. 26, No. 4, 760-769 (1990).
5. T.V. Galstyan, Sov. Journal of Quantum Electronics, V.19, No.10, p.1035 (1992).
6. We thank Professor Dana Anderson (from JILA) for drawing our attention on this fact.
7. G. Beadie, et al., Technical Digest of CLEO'97, Baltimore, paper CTuX3
8. A. Y. Smuk, et al., Ibid, paper CTuX4

Analysis of an optical frequency-hop encoder with strain-tuned Bragg gratings

H. Fathallah, S. LaRochelle and L. A. Rusch
(http://www.gel.ulaval.ca/~copgel)
Département de génie électrique et de génie informatique
Université Laval, Sainte-Foy, Québec, Canada, G1K 7P4

Introduction

In optical communication systems, fiber gratings have been used to perform chromatic dispersion compensation, gain equalization, pulse compression, soliton pulse shaping, add/drop switching and channel filtering for wavelength division multiplexing (WDM) systems [1,2]. Recently Chen *et al.* studied a multiple grating structure that could be used to achieve spectral slicing in WDM and CDMA systems [3]. In this paper we propose a tunable multiple-grating fiber for frequency-hop encoding-decoding operations. To our knowledge, this is the first proposal for frequency-hop code division multiple access (FH-CDMA) in optical fiber local area networks.

CDMA techniques fall into four broad categories: direct sequence (DS), frequency encoded (FE), time hopping (TH) and frequency hopping (FH). Optical CDMA systems have been proposed for the first three [4-6]. The agility of modern radio transmitters to quickly change transmission frequencies for FH-CDMA has no obvious corollary in optics. The use of multiple Bragg gratings, however, has the effect of introducing a delay among reflected frequencies (depending on the position of the Bragg grating) that can be interpreted as a FH-CDMA "hopping" pattern. By use of piezo-electric devices, the order of the center frequencies of the Bragg gratings can be changed, effectively changing the hop pattern and therefore allowing for programmable codes (Figure 1). An important feature of every CDMA system is the architecture of the encoder/decoder pair, the functionality of which should provide for an efficient encoding and correlation of the code sequences. In this paper, we present the tradeoffs involved in the design of the encoder-decoder pairs. We first select a family of suitable codes for simulation of the FH-CDMA communication system. We then address the design issues of the encoding device. Apodization of the Bragg gratings is required to perform accurate and dense spectrum slicing. Optimization of code performance and spectrum utilization is performed. Finally, the achievable performance is evaluated in term of auto- cross-correlation properties.

Frequency-hop signal

In FH-CDMA communications each information bit from user m is encoded into a signal $c_m(\omega, t)$ that corresponds to a code sequence of N chips (or pulses) representing the address of that user. The k^{th} pulse is thus modulated with frequency f_k about the carrier frequency f_c;

$$f_k = y(k)\frac{B}{N} \qquad k = 1,\ldots,N \qquad (1)$$

where B is the signal bandwidth, y(k) is the placement operator (also called the frequency hop pattern). The placement operator is a sequence of N ordered integers determining the placement of frequencies in various time slots. A convenient way of representing a frequency hop pattern is through a NxN matrix representing the time and frequency axis (Figure 2). We adopt the hyperbolic codes [7], derived based on congruence theory for satellite and mobile FH-CDMA communications systems, having the following placement operator

$$y_{l,a} \equiv \frac{l}{k} + a(\mathrm{mod}\,N) \quad \text{for } k,l,a = 1,2,\ldots,N-1 \qquad (2)$$

where k denotes the frequency bin number; and the pair (l, a) defines the user code, leading to (N-1)x(N-1) independent codes. Thus, with N=11, 100 independent codes can be obtained with first two placement operators given by $y_{1,1}$=[1 2 7 5 4 10 3 9 8 6 11] (user 1) and $y_{2,1}$=[1 3 2 9 7 8 5 6 4 11 10] (user 2).

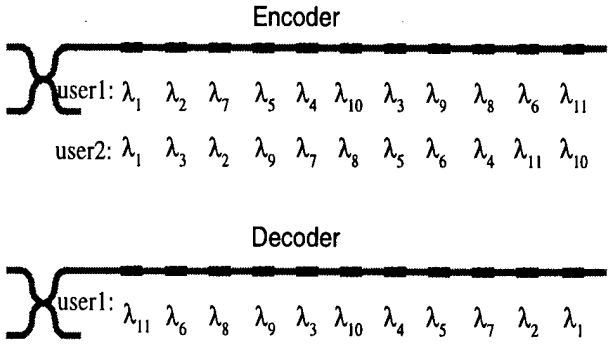

Figure 1: The encoder/decoder.

As in any CDMA system, the selected users' codes must satisfy the following three funda-

mental conditions. Firstly, the peak of the auto-correlation function

$$R_{c_m}(s)=\sum_{i=0}^{N} c_m(i)c_m(i-s) \quad -N+1\le s\le N-1 \quad (3)$$

should be maximized for each code. Secondly, the side-lobes of this function should be minimized. Finally, the cross-correlation function

$$R_{c_m,c_p}(s)=\sum_{i=0}^{N} c_m(i)c_p(i-s) \quad -N+1\le s\le N-1 \quad (4)$$

of each pair of sequences c_m and c_p should be minimized. These conditions constrain the physical positioning of the gratings on the fiber as well as their bandwidth. The relative distances between the gratings must be chosen to satisfy a given level of auto- and cross-correlation between the codes. This distance in turn determines the achievable bit rate. Equations (3) and (4) will be used later to evaluate the auto- and cross-correlations for the proposed devices.

The encoding device

The encoding device consists of a series Bragg gratings all written at the same wavelength λ_B. Each grating can be tuned independently using piezo-electric devices to adjust the Bragg wavelength from λ_B to a given wavelength defined by the corresponding placement operator. The advantage of this approach is that only one phase mask is needed to write any encoder or decoder. The tuning of each device will determine the code used.

As an example, user two will tune the first grating to λ_1, the second to λ_3, ..., and the eleventh to λ_9 (see Figure 1). The gratings will spectrally and temporally slice an incoming broadband pulse into several components as demonstrated by Chen *et al.* [3]. In the decoder, the peak wavelengths would be placed in reverse order to achieve the decoding function (matched filtering). The reflected pulses are equally spaced in time, which is precisely the round-trip propagation time between two gratings. The time spacing, the chip duration, and the number of gratings will limit the data bit rate of the system, *i.e.* all reflections should exit the fiber before the next bit enters.

For uniform gratings, the optical fiber is required to stretch approximately $\Delta L=2N\lambda_B$, or 34 μm for N=11. Tuning Bragg gratings with typical strains of 0.5% results in a nominal spacing of L_0=1cm between the beginning of successive gratings. The total round trip time in the grating structure will therefore be $2(N-1)L_0n_0/c$ leading to a maximum transmission frequency of 1 Gbs.

Each grating bandwidth must however be such that the time overlap of the reflected pulses does not degrade the cross-correlation function. At a 1 Gbs data transmission rate, the chip rate is 11 Gbs. The required grating bandwidth is thus in excess of 25 GHz. Furthermore, in FH-CDMA, the frequency components are assumed to have a rectangular shape. Recently, Helge *et al.* [8] demonstrated a grating with a sinc apodization that approaches the ideal rectangular reflectivity characteristics. To achieve nearly disjoint and high-density frequency slices, several apodization profiles have been simulated in this work.

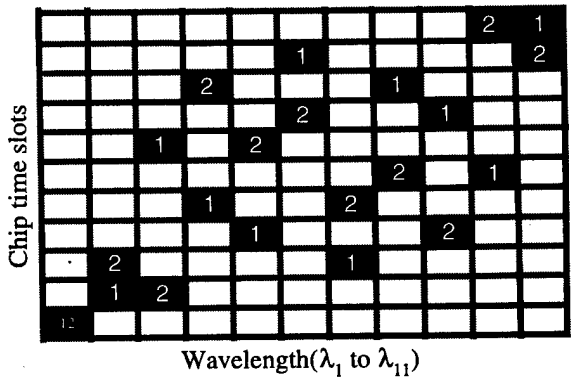

Figure 2: Frequency-hop patterns 1 and 2.

The Gaussian profile performs high main lobe reflectivity, (about 20 dB over the side lobes), but occupies relatively large bandwidth reducing the possible number of slices. The near ideal rectangular reflectivity can be achieved only by using 1) an infinitely long complex grating with a sinc apodization including many side lobes, 2) the inverse Fourier transform of the raised cosine Hamming window or 3) the Blackman window. In our case, the grating length and separation are crucial parameters, limiting the data bit rate.

We found that for finite limited length, the sinc main lobe apodization can outperform the Gaussian apodization, with –25 dB side-lobes. Figure 3a) depicts the reflectivity of 11 main lobe sinc apodized gratings, *i.e.* user code one. The central resonance wavelengths of these gratings are selected allowing the overlapping between the first and the second side lobes of successive gratings. The time delay between the frequency components is presented in the Figure 3c), which clearly represents the frequency-hop pattern of code one (see Figure 2). Note that the horizontal segments in the group delay curves correspond to the central frequency intervals of the reflected slices. It demonstrates that these frequencies are instantaneously reflected, with no appreciable travel time

in the fiber. The side lobes, in contrast, have long delay times, but lower energy (-25dB).

To estimate the performance of the proposed FH-CDMA encoder-decoder we calculate its achievable auto- and cross-correlation functions versus the ideal case. Figure 4 shows that the device can efficiently perform interference rejection. The auto- correlation presents a high peak, and the cross-correlation between codes one and two only slightly exceeds the ideal case. In simulations we observed that the recombination of the auto-correlation peak is sensitive to the inherent delay between the central and near edge frequencies of each grating reflection main lobe [7]. This intra-band delay is the same for the reflection off the encoder and the decoder. This effect is thus amplified by the double reflection, as the encoder-decoder pair are not true conjugates. Chirped gratings are good candidates to compensate for this effect. The auto-correlation nonetheless presents an easily identifiable peak.

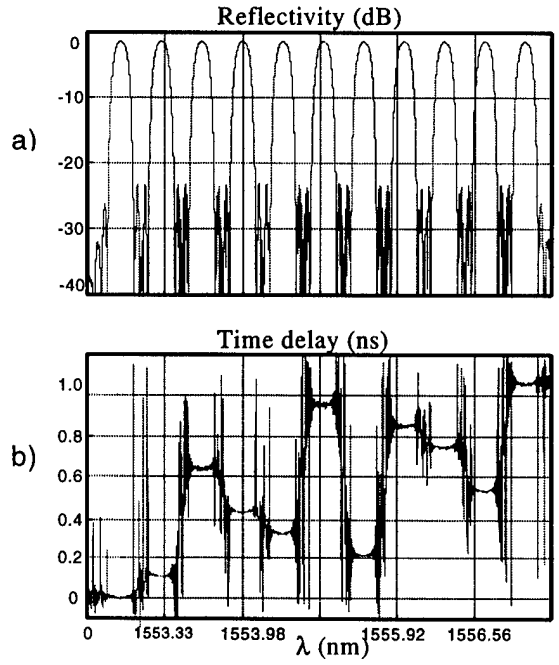

Figure 3: a) Reflectivity, b) group delay

Conclusion:

We proposed and analyzed a novel FH-CDMA encoding device. We selected suitable apodization to perform accurate spectral slicing. Tunable multiple gratings can efficiently detect the desired user, with low cross-correlation (or cross-talk) between the medium sharing users. No chip synchronization is required. The proposed device has the advantage of one design for all encoders and decoders, *i.e.* one fabrication set-up, with programmable codes via piezo-electric tuning.

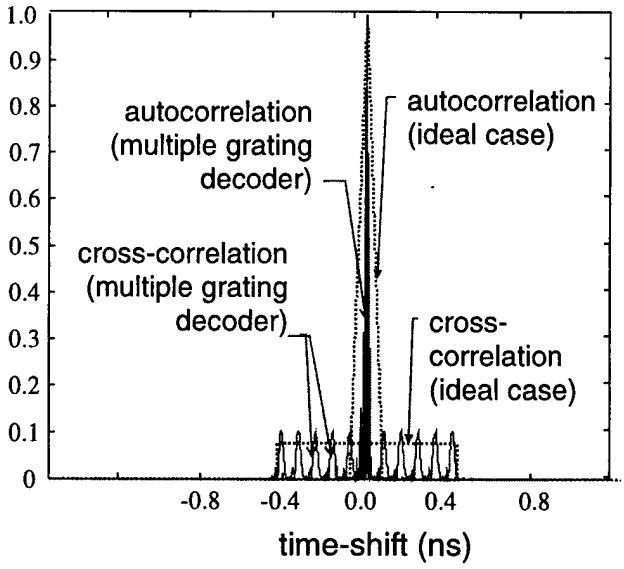

Figure 4: Auto- and cross-correlation.

References:

[1] C. Randy Giles, *Optical Fiber Conference.*, paper TuM, 1997.

[2] K. O. Hill, B. Malo, F. Bilodeau, and D. C. Johnson, *Ann. Rev. Mat. Sci.,*. vol. 23, no. 125, 1993.

[3] L. Chen, S. Benjamin, P. Smith, J. Sipe, to be published *IEEE Journal of Lightwave Technology, 1997.*

[4] R. Chung, J. Salehi, and V. Wei, *IEEE Transactions on Information Theory*, vol. 35, no. 3, pp. 595-604, May 1989.

[5] A. Wiener, J. Heritage, and E. Kirschner, *Journal Opt. Soc. Am. B*, vol. 5, no. 8, pp. 1563-1572, August 1988.

[6] J. Salehi, A. Weiner, and J. Heritage, *IEEE Journal of Lightwave Technology,* vol.8, no. 3, pp. 478-491, March 1990.

[7] S. V. Maric, and E. L. Titlebaum, *IEEE Transactions on Communications*, vol. 36, no. 8, Aug. 1992.

[8] H. Shoroy, H. E. Engan, B. Sahgren and R. Stubbe, *Optics Letters,* vol. 22, no. 11, June 1, 1997.

Effects of doping of H_2O and Na on second-order nonlinearity in poled silica glass

Hiroaki Imai, Suguru Horinouchi, Naoko Asakuma, Kazuhiro Fukao,
Daizaburo Matsuki, Hiroshi Hirashima, and Keisuke Sasaki

Faculty of Science and Technology, Keio University
3-14-1 Hiyoshi, Kohoku, Yokohama 223, Japan

Large second-order nonlinearity was reported to be induced in the near-surface region of commercial fused silica[1] and in the whole region of sol-gel derived silica glass[2] by thermal poling. The origin of the nonlinearity was suggested to be diffusion of Na^+ for the former and OH groups for the later. To control the nonlinearity of silica glass and clarify the effects of the impurities, we investigated second harmonic generation (SHG) from silica glass doped with H_2O and Na.

Doping of H_2O into synthetic silica glass (type III, [OH]~600 ppm) was performed by exposure of the glass plates (thickness: 0.5-1.0 mm) to purified water using an autoclave at 150°-220℃ for 6-96 hrs. Introduction of Na was carried out by coating of PMMA films containing a trace amount of Na_2CO_3 (1-1000 ppm). The samples were poled at 150°-250℃ for 1-12 h using corona discharge at 3-10 kV. Then, the SHG intensity was measured by the Maker-fringe method with a Q-switched Nd:YAG laser.

The exposure of the glass plate to water increased the SHG intensity induced by the thermal poling. As shown in Fig. 1, oscillation is clearly observed in the Maker-fringe pattern for the treated silica glass. The similarity of the calculated pattern indicates that the nonlinearity was induced in the whole region of the glass plate. Change in infrared absorption around 3600 cm^{-1} shows an increase of OH groups and H_2O molecules in the treated glass. Thus, the doped OH groups and/or H_2O molecules are deduced to increase the nonlinearity in the whole region of the silica glass plate. However, the penetration depth of H_2O molecules is estimated to be less than 10 μm and the induced SHG was reduced by etching of the surface. Moreover, the doping of H_2O into low-OH silica glass was not effective in the SHG intensity. Therefore, the increase in the nonlinearity is attributed to charge formation at the anode and the cathode surface regions. These results suggest that the doped H_2O molecules or OH groups and the originally contained OH groups are related to the charge separation. Coating of PMMA films containing Na_2CO_3 on silica glass also increased the SHG intensity. However, broad fringe patterns were observed. In this case, diffusion of Na ions from the PMMA films was inferred to promote formation of the nonlinearity in the near-surface region. Thus, the nonlinearity in the whole region promoted by the H_2O doping is suggested to be formed through a different process from the diffusion of Na ions.

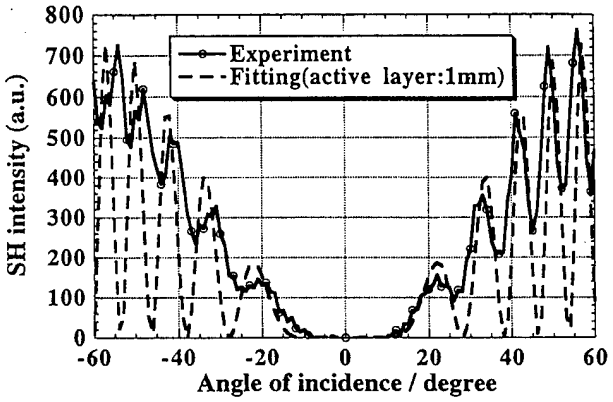

Fig. 1. Maker-fringe patterns obtained by experiment and calculation for the silica glass exposed to water at 180℃ for 96 hrs. (Poling condition: 200℃, 10 kV, 2 hrs.)

References

1. R.A. Mayers, N. Mukherjee, and S.R.J. Brueck, Opt. Lett. 16, 1732 (1991).
2. H. Nasu, H. Okamoto, K. Kurachi, J. Matsuoka, K. Kamiya, A. Mito, and H. Hosono, J. Opt. Soc. Am. B 12, 644 (1995).

A Thermally Poled Electrooptic Fiber

X.-C. Long and S. R. J. Brueck
Center for High Technology Materials, University of New Mexico
1313 Goddard, SE, Albuquerque, NM 87106
Tel: (505)272-7800
Fax: (505)272-7801

We have reported[1] previously on a planarized fiber-poling structure which allows us to apply a high field across a polished fiber and results in a linear electrooptic coefficient as high as 0.3 pm/V using a commercially available D-fiber. This fabrication technique has several advantages including: low cost volume manufacturing capability; planar structure to allow lithographic definition of high-speed circuits; and fiber ends unaffected by the processing to provide low-cost packaging and integration with fiber systems.

A single-mode polarization-maintaining germanosilicate D-fiber designed for 1.3 μm was used. The core is 1.25 x 2.5 μm^2 with 18 wt% Ge doping, and the thickness, *d* of the fused silica cladding is 14.25 μm on the flat ("D") side of the fiber. The total thickness of the fiber, D, from the flat to the opposite side of the cladding is 70 μm. The first fabrication step is to mechanically polish the D-side of the fiber to reduce the *d* value down to less than 5 μm (Fig. 1.i). The fiber was then remounted D-side down and layers of polyimide were spun and cured to a total thickness of ~ 70 μm fully encapsulating the fiber. A layer of metal film was deposited on top of fiber by e-beam. The resulting fiber structure was poled by applying -5 kV between the top electrode and Si bottom anode at 255 °C for ~10 minutes (Fig. 1.ii). The final step in the fabrication is to remove the metal electrode and polish the remaining structure to a final thickness of ~ 13 μm (Fib. 1.iii), thereby increasing the applied field for a fixed voltage during device operation. A top electrode is formed using a conducting liquid solution.

Using this planar fiber poling structure (Fig. 1), we observed[2] a half-wave (π) phase shift in these poled fibers with a driving voltage as low as 75 V applied over a 12-cm active length ($V_\pi l$ = 900 V-cm) using a free-space Mach-Zehnder optical configuration. A sinusoidal input was applied to the poled fiber. The Mach-Zehnder output is a first-order Bessel function of the driving voltage. A lock-in amplifier, extracts the first harmonic component of the signal as shown in Fig. 2. The fit to the Bessel function is also shown in Fig. 2. The reference signal for calibrating the nonlinearity using the longitudinal electrooptic effect in a $LiNbO_3$ wafer is also shown. The $LiNbO_3$ signal is weaker because of the much shorter active path length (500-μm longitudinal geometry) and lower applied fields.

Excellent thermal stability is observed for the fiber nonlinearity. The induced linear electrooptic coefficient shows no decay at room temperature for over four months, and only a ~ 10% decay after heating to 90°C for 1000 hours. This is in contrast to a recent report[3] of a ~280 day 1/e decay time-constant for UV-poled GeO_2-SiO_2 glass held at 15 °C.

A difficulty with the present fabrication process is that the fiber is poled before the final polishing step. After the polishing, it is no longer possible to e-beam or sputter deposit an electrode structure without heating the fiber to a significant extent and losing some of the nonlinear-

ity. Here, we report an improved fabrication technique to address this issue. After polishing the D-side of the fiber to reduce the cladding thickness, the fiber was affixed, D-side down, to a silicon wafer using a thin layer of polyimide. Additional layers of polyimide were spun on and cured until the fiber was totally surrounded by polyimide. Then the total thickness was polished down to less than 10 μm. A microstrip line metal electrode was deposited on the fiber by standard lithography. Another layer of polyimide was spun on and cured. A high voltage was applied between top microstrip line electrode and bottom ground electrode(silicon wafer) at 255 °C to pole the fiber. The detailed fabrication technique, the measurement of half-wave voltage and modulation speed will be presented.

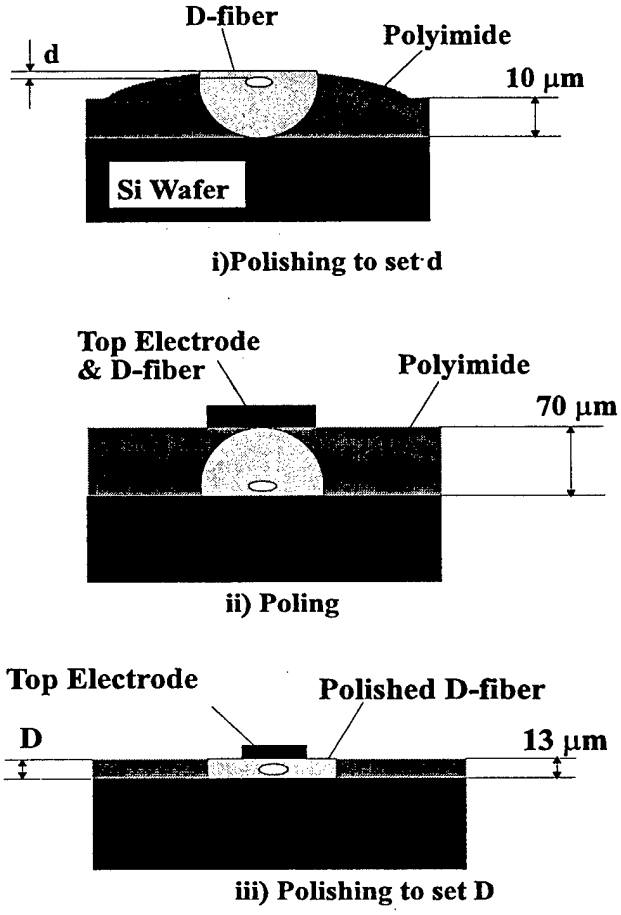

Fig. 1: The cross section of planarized fiber-poling structure: i) polish "d" (the distance from the surface to core-cladding interface) down to 5 μm; ii) pole the fiber by -5 kV at 255 °C for 10 minutes; iii)polish the total thickness "D" value of the fiber down to 13 μm and application of a top electrode.

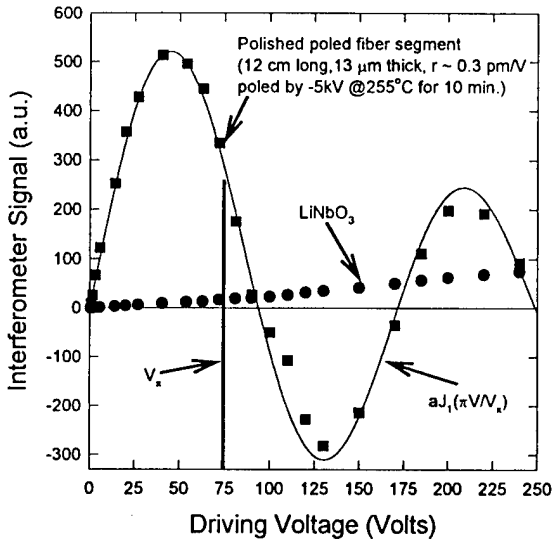

Fig. 2: Interferometer fundamental frequency response for voltages applied to poled fiber and to a $LiNbO_3$ reference sample in a Mach-Zehnder interferometer. The solid curve is a fit to a first order-Bessel function giving a half-wave driving voltage V_π=75 V for the poled fiber structure. The $LiNbO_3$ reference sample is a 0.5-mm thick sample in a longitudinal geometry with ITO electrodes.

References

1. X.-C. Long, R. A. Myers and S. R. J. Brueck, " A poled electrooptic fiber" IEEE Photon. Tech. Lett. **8**, 227-229 (1996).
2. X.-C. Long, and S. R. J. Brueck, " Large-signal phase retardation with a poled electrooptic fiber" IEEE Photon. Tech. Lett. **9** 767-769 (1997).
3. T. Fujiwara, M. Takahashi and A. J. Ikushima, "Decay behavior of second-order nonlinearity in GeO_2-SiO_2 glass poled with UV-irradiation," Electron. Lett. **33**, 980-981 (1997).

UV and thermal poling of germanosilicate fibre

Y. Quiquempois, G. Martinelli, P. Bernage, M. Douay, P. Niay

Laboratoire de Dynamique Moléculaire et Photonique
URA 779, Centre d'Etude des Lasers et Applications
Université de Lille, 59655 Villeneuve d'Ascq Cedex

E. Delevaque, H. Poignant, B. Loisel, J.F. Bayon

Laboratoire DTD/TSO et DTD/PIH, CNET Lannion
Technopole Anticipa, 22307 Lannion Cedex

I) Introduction

The non-zero second order susceptibility obtained by poling a glass is generally explained by the creation of a permanent frozen electric field E_{DC} which breaks the centro-symmetry of the glass. Multiplying the third order susceptibility tensor terms by E_{DC} gives rise to second order non zero terms according to the relation (1)

$$\chi^{(2)} = \chi^{(3)} \cdot E_{DC} \qquad (1)$$

So, after a poling process applied to a fiber, a linear (Pockels) non-zero electro-optic coefficient r_{333} appears.

In this study, two technics for poling the fiber have been investigated : the thermally - assisted electrical poling [1,2] and the UV-assisted electrical poling [3].

II) Thermally - assisted electrical poling : process and result

The fiber under test is a special fiber elaborated in the CNET Lannion laboratories. The electrodes (aluminum wires) are introduced into the holes as shown fig. 1. Two identical Bragg gratings are photowritten within the core of the fiber for obtaining a Fabry-Perot interferometer. The resonant wavelength for the two gratings is usually 1.53 µm.

Scheme of a Bragg-grating based Fabry-Perot interferometer with a poled area

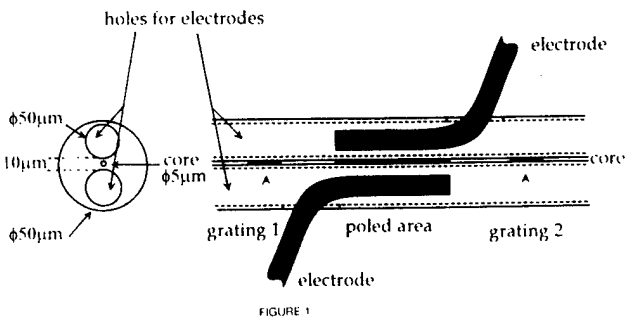

FIGURE 1

During the poling, the fiber is heated by using a CO_2 laser. Two ZnSe lenses allow the laser spot size adjustement for obtaining a fiber temperature between the room-temperature and 800 °C. All the measurements are made by using a tunable laser source (TUNICS laser source from PHOTONETICS). Before poling the fiber, the spectral shift in the Fabry-Perot peak wavelengths induced by the application of a voltage between the electrodes is measured. This shift results from the quadratic (Kerr) electo-optic coefficient of the glass.

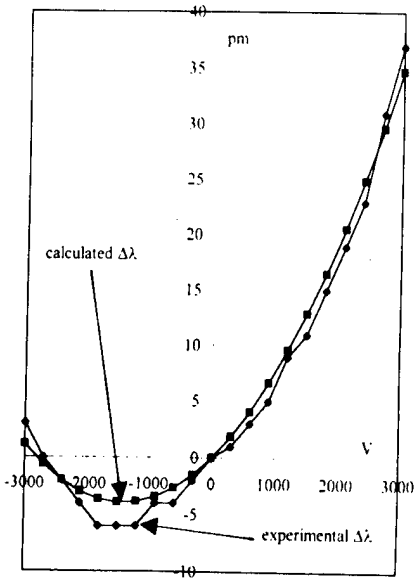

FIGURE 2

After this first measurement, the voltage applied to the electrodes was fixed at 2000 V and a 1 cm long part of the fiber was heated at 400 °C during one hour. The spectral shift in the F. P. peak wavelengths versus the applied voltage was then measured at room temperature . The results are given fig. 2 together with the calculated shift $\Delta\lambda$ resulting from a quadratic least square routine.

The linear electro-optic coefficient induced by the poling process is proportional to the slope at origin of the plot which represents the spectral shift in the wavelength versus voltage.

From this value, we can deduce the electro-optic r_{333} coefficient by using the relations (2) and (3) :

$$\frac{dn}{n} = \left(\frac{\ell}{\ell'}\right)\frac{d\lambda}{\lambda} \qquad (2) \quad ; \quad r_{333} = \frac{2d}{n^3}\left(\frac{dn}{dV}\right)_{V=0} \qquad (3)$$

In (2), ℓ is for F. P. cavity length, ℓ' for the poled length. In (3), d represents the hole (electrode) separation. The position of the poled area (which probably don't lie in the middle of the separation d, but near the anode [3]) is not known. So, the overlap between the poled area and the guided mode cannot be determined, and the given value is only an effective value. (r_{333} = +0.06 pm/V).

III) UV - assisted electrical poling : process and result

In order to check the difference between the thermally-assisted and the UV-assisted polings, we have realized an other component in the same fiber as before. This fiber was hydrogen loaded at high pressure and room temperature

(100 atm, 1 month). A 25 mm long part of the fiber was uniformely irradiated by using the 193 nm radiation from an ArF excimer laser (non-polarized beam, fluence : 100 mJ/cm^2, 10^5 pulses). During this poling process, the applied voltage was 900 V. For measuring the electro-optic coefficient, a 25 mm long grating was photowritten in the poling area by using a 244 nm frequency-doubled dye laser. A thousand of pulses at a fluence 100 mJ/cm^2 was sufficient to obtain a sharp grating with 10% in reflectivity. During this inscription the voltage was maintained at the previous value 900 V. The slope at origine for the plot which represents the post-processing wavelength shift versus the applied voltage (not shown here) is negative with respect to the sign of the applied voltage during the poling. So, the effective electro-optic coefficient is negative : $r_{333} = - 0.014$ pm/V.

IV) Discussion and Conclusion

The australian group [3] has already reported a similar observation : after the UV poling of a fiber without H_2 loading, an increase in the refractive index resulted from a post - poling negative applied voltage.

So the experiments made by this group and this new experiment demonstrate that the poling effects are quite different according to the process used : the signs of the electro-optic coefficients created by the two processes are opposite. This result seems to indicate that the orientation of the frozen electric fields are opposite [4].

References

[1] M.V. Bergot, M.C Farries, M.E. Fermann, L. Li, J. Poyntz-Wright, P.St. J. Russell and A. Smithson
Opt. Lett. 13, 7 (1988).

[2] V. Mizrahi, V. Osterberg, C. Krautshick, G. I. Stegeman, J. E. Spie and T. F. Morse
Appl. Phys. Lett. 53, 557 (1988).

[3] S.C. Fleming, T. Fujiwara and D. Wong,
O.S.A. Technical Digest Series., 22, 180 (1995).

[4] P. G. Kazansky, A. R. Smith, and P. St. J. Russell,
O.S.A. Technical Digest Series., 22, 175-178, Portland, U.S.A. (1995).

The Influence of Phase Mask Stitch Errors on the Performance of UV-written Bragg Gratings

X. Liu, R. M. De La Rue, P. V. S. Marques[a], S. Thoms, J. S. Aitchison
Department of Electronic and Electrical Engineering,
University of Glasgow,
Glasgow G12 8QQ, UK

Telephone: +44-0141-330 6022 Fax: +44-0141-330 4907

E-mail: x.liu@elec.gla.ac.uk

L. A. Everall, J. A. R. Williams and I. Bennion
Department of Electronic Engineering and Applied Physics,
Aston University,
Aston Triangle,
Birmingham B4 7ET, UK.

a) Also with Centro de Física do Porto, Rua do Campo Alegre, 687
4150 Porto, Portugal

Bragg gratings produced by direct UV exposure are finding wide-spread applications in fields ranging from telecommunications to optical sensing. In order to produce such fibre gratings a great deal of research has been directed to the use of electron beam lithography for direct writing of the phase masks [1]. The technique allows very precise structures (grating period < 100 nm) to be defined over large areas up to 140 × 140 mm^2. Phase mask are generated by stitching small (400 μm × 400 μm) electron beam fields together. It is therefore important to understand the nature of the various stitching errors which can occur and their effect on the corresponding UV written fibre grating spectra. Here we report the spectroscopic effect of one sign stitching errors which has the characteristic of shifting the grating in a field to one direction (left or right) only along the grating axis.

We have previously shown that, using an optimised writing strategy for a uniform phase mask, these errors are random in both direction and value within a range of mean + 3σ < 40 nm [2]. The fibre gratings produce using these phase masks showed no evidence of ghost peaks, or asymmetry. For chirped gratings, or gratings which require phase shifts, stitching errors can play a significant role. These errors can occur in regions where there is either a discrete change in period, or phase. Due to the fact that field distortion produces a regular trapezoid of a stitching field rather than an ideal square, or a completely random shape, stitching errors produced by this kind of systematic fault have a random value but occur in a single direction. We use the term one sign stitching errors. An example of the one sign large abnormal stitching error is shown in fig. 1. In this extreme case, the period of the phase mask is 726 nm, the axial stitching errors causes the gratings in the field on the right hand side of the stitching shift ~ 20 - 25% of a period in a single direction: the right of the stitch at all stitches in the phase mask. Such large stitching errors in phase mask produce field wide repeated large phase errors in fibre gratings which is characterised by ghost peaks at both side of the main reflection peak in the reflection spectra as can be clearly seen in fig. 1.

Many stitching errors caused by systematic fault of the electron beam lithography have the typical one sign characteristic shown above. It is therefore possible to simulate its effect on spectra of the fibre grating with a deliberately made, multi small shift phase mask. To perform a more detailed characterisation of the stitching errors, a series of phase masks with varying stitches of known size was fabricated. The stitch size varied from 50 nm up to 537.5 nm, or half a period of the phase mask.

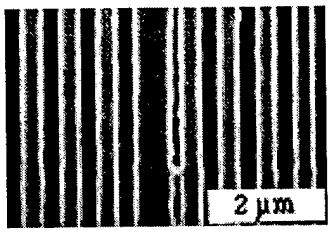

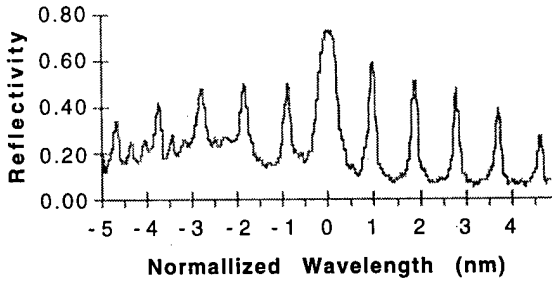

(a) SEM of a stitch in the mask with abnormal stitching errors

(b) Reflection spectra of UV written fibre gratings using the mask shown on the left

Fig. 1. Large stitching error in a 726 nm phase mask (a) and the corresponding fibre reflection spectra (b).

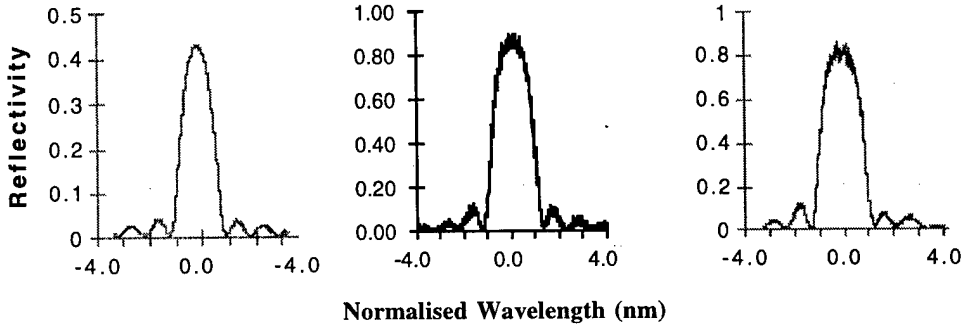

(a) No phase shift

(b) 50 nm

(c) 107 nm (1/10 period)

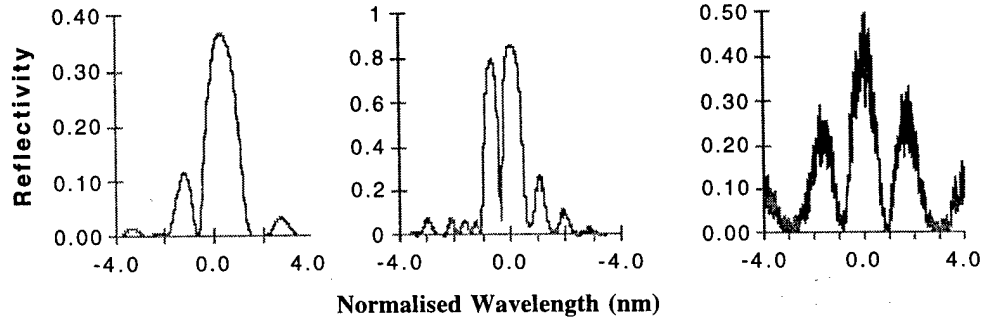

(d) 134 nm (1/8 period)

(e) 269 nm (1/4 period)

(f) 537.5 nm (1/2 period)

Fig. 2. The reflection spectra for fibre gratings produced using phase masks with varying stitching errors, for 800 µm long gratings.

Gratings were written into the hydrogen loaded core of a standard fibre. From fig. 2. it can be seen that using phase masks with relatively small stitching errors (50 and 107 nm (1/10 of the period)) has only a minimal effect on the fibre grating response. The basic shape, particularly the symmetry, of the spectra remain unchanged. Larger stitching error begin to introduce an

asymmetry into the spectra, starting from that of 1/8 of the period and changing the spectra dramatically afterwards such as those shown in fig. 2 (d), (e) and (f). Such large phase shifts have previously been used to produce narrow band transmission filters [3-5].

We have also investigated the effect of multiple stitching errors within a phase mask. Figure 4 shows the reflection spectra obtained from a grating written using a phase mask with seven 50 nm (1/21 of the period, 1075 nm) stitching errors, each of them shift the right hand grating block to the right to the designed distance. The stitching errors were separated by 100 periods of the mask gratings. As can be seen multiple stitching errors of this size also produce an negligible effect in the reflection spectra. We believe that the reason for this is the shift diffusion effect of the UV exposure procedure in relevance to the distance between the phase mask and the fibre core as have been described before [4-5].

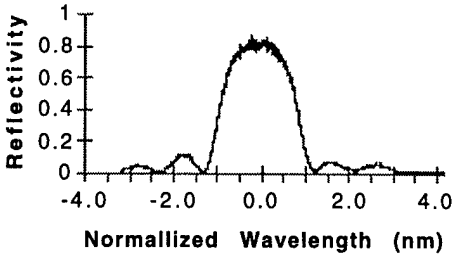

Fig. 3. Reflection spectra produced using a 800 μm long phase mask with seven 50 nm stitching errors.

In conclusion we have presented results on the reflection spectra of fibre gratings, written using phase masks with deliberate small step phase shifts. From our results if the stitching error is < 100 nm, or 10 % of the period of the phase mask there is negligible effect on the reflection band. Multiple small stitching errors were also found not to degrade the reflection spectra of the fibre grating.

Reference

[1] Malo, F. Bilodeau, J. Albert, D.C. Johnson, K.O. Hill, 'Photosensitivity in optical fibre and silica-on-substrate waveguides', Proc. SPIE, vol. 2044, pp. 42-54.

[2] X Liu, J S Aitchison, R M De La Rue, S Thoms, L Zhang, J A R Williams, I Bennion, 'Electron beam lithography of phase mask gratings for near-field holographic production of optical fibre gratings', Microelectronic Engineering, **35**, 1997, pp 345-348.

[3] R. Zengerle and O. Leminger, 'Phase-shifted Bragg grating filters with improved transmission characteristics', J. Lightwave Technol., vol. LT-13, pp. 2354-2358, 1995.

[4] J A R Williams, X Liu, L A Everall, I Bennion, J. S. Aitchison, S, Thoms, R M De La Rue, 'The effect of phase steps in e-beam written phase masks used for fibre grating fabrication by near-field holography', accepted in ECOC,1997.

[5] X Liu, J S Aitchison, R M De La Rue, J A R Williams, L Everall, I Bennion, 'Design and fabrication of specific filter responses in photosensitive fibre gratings produced by UV holographic exposure', Conf on Lasers and Electro-Optics (CLEO'97), Baltimore, Maryland, May 1997, CThL57.

Dynamics of Coupling Peaks by H_2 Diffusion in Long-Period Grating Filters

Joo-Nyung Jang, and Kyung-Ho Kwack

Telecom. R&D Center at Samsung Electronics Co., Ltd., Suwon P.O. Box 105, Kyungki-Do Korea 440-600

Tel : +82-331-280-1854, Fax : +82-331-280-9639

Sang-Bae Lee, and Sang-Sam Choi

Korea Institute of Science and Technology, P.O.Box 131, Cheongryang, Seoul, Korea, 130-650

Tel : +82-2-958-5714, Fax : +82-2-958-5709

Introduction

It is now well known that germanium-doped silica fibers exhibits excellent photosensitivity. A UV source changes the refractive index of the core that contains germanium. A common type of defect formed in germanium-doped silica is GeO or oxygen deficient germania related defect [1], which is bonded to three oxygen atoms, and one bond is made to a silicon/germanium atom. This has been identified as giving rise to absorption centered around 240 nm. But, typically UV induced index changes have been limited to $3x10^{-5}$ for standard single mode fibers doped with 3% germania [2]. Increasing GeO_2 doping concentration and reducing the amount of oxygen used in the fabrication of the preform also enhance the fiber photosensitivity [2]. In this case, the peak index changes are usually about $5x10^{-4}$ or less. More recently, two techniques have been proposed to enhance the photosensitivity of germanium-doped silica fibers : exposure of the material to the flame of an oxygen-hydrogen burner(flame brushing method) [3], and hydrogen loading at low temperature and high pressures [4]. Lemaire [4] showed $5.9x10^{-3}$ peak-to-peak index change in the case of 3% GeO_2 loaded with 3.3% H_2. In long-period grating filter fabrication, hydrogen treatment is needed to get high Δn for coupling a fundamental guided mode to the cladding leaky modes efficiently. Hydrogen treated germano-silicate fiber is unstable because of H_2 diffusion process. We present the growth and decay behavior of the coupling peaks induced by H_2 diffusion and annealing process for stabilization.

Experiments

The fiber used in this experiment was a standard single-mode fiber treated in a H_2 chamber at temperature ranging from $80^{o}C$ to $90^{o}C$ and pressure around 120 atm for 2 - 12 days. We used the fiber immediately after removing it out of the H_2 gas chamber because the hydrogen starts to diffuse out quickly. A 248 nm KrF excimer laser was used as a UV source, and its beam was focused through a cylindrical lens in order to get a rectangular beam profile. The length of the fiber exposed to the excimer laser was 2.5 cm, and the transmission spectrum was *in situ* monitored with an optical spectrum analyzer.

Results and Discussions

Figure 1 shows the general growth behavior of a long-period grating filter during the exposure of the UV source at various conditions. The coupling peaks moves toward longer wavelengths and the extinction ratio varies with

exposure time. The larger the pulse energy and/or the repetition rate are, the more quickly the wavelength moves.

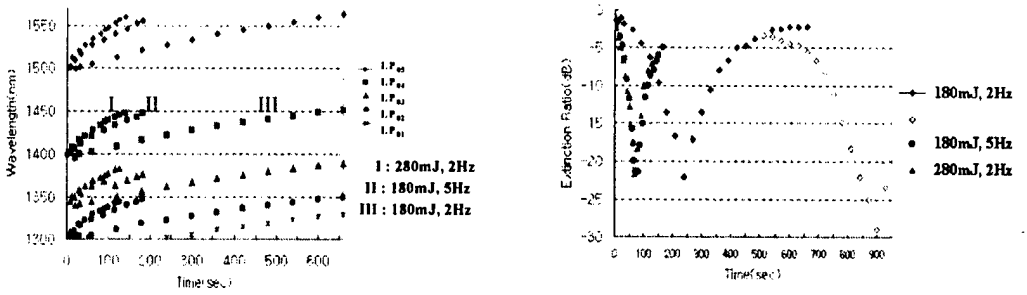

(a) (b)

Fig. 1. (a)Wavelength shift of LP_{0m} modes and (b)extinction ratio behavior of LP_{05} modes(b) with exposure time at various conditions

At first, the speed of the wavelength shift is linear with time and decreases continuously because of saturation of defect centers. Extinction ratio increased to 22 dB and decreased to 0 dB. New coupling peaks arise and grow to overlap (open diamond in Fig. 1(b)). In order to understand growth behavior of coupling peaks by the hydrogen diffusion, we fixed other variables except for the exposure time and *in situ* monitored the transmission spectrum during and after UV exposure (Fig. 2 and Fig. 3). Coupling started at 1523 nm in both cases and the UV pulse laser was turned off after 2 and 8 minutes, respectively. Shortly after the 2 minutes exposure, the center wavelength of LP_{05} cladding mode is 1545 nm and extinction ratio is 7 dB, and it moved continuously toward a long wavelength although the UV source was turned off. We measured 20 nm shift from 1545 nm to 1565 nm for about 11 hours and then it started to shift to a short wavelength direction. Extinction ratio also increased as wavelength shift to a long wavelength and decreased after 11 hours.

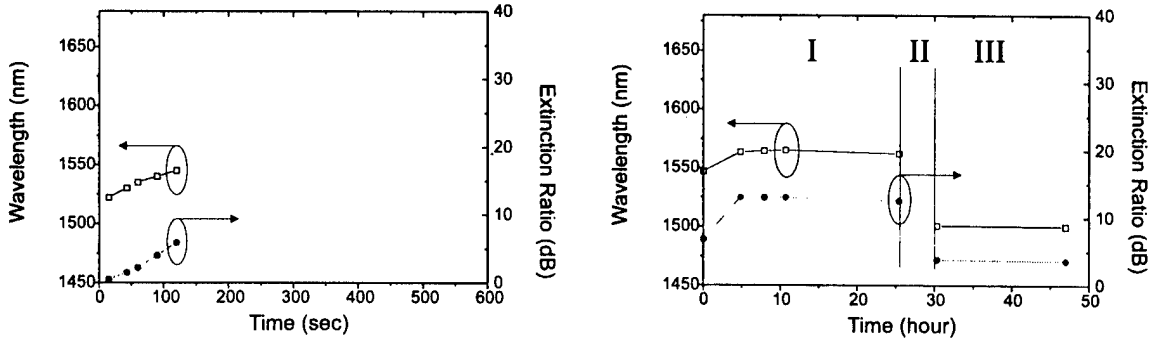

(a) (b)

Fig. 2. Coupling peak behavior vs exposure time for 2 minutes(a), and after exposure(I), annealing(II), stabilization(III) process (b).

If the fiber is in the equilibrium state after H_2 treatment, hydrogen molecules are dissolved uniformly in the entire region of the fiber. The UV source induces dissociation of the hydrogen molecules into hydrogen atoms and subsequent reaction with oxygen-deficient germanium defect sites to form GeOH bonds[5]. This reaction doesn't occur in the cladding region because there are no defect sites. So this reaction induces hydrogen-molecule- concentration difference between core and cladding, and this concentration difference acts as a driving force for diffusion of hydrogen molecules into the core. The coupling peaks moves toward a long wavelength during the period of hydrogen molecule diffusion to the core. After a long time, the driving force is formed between fiber and air, and hydrogen molecules diffuse out of the fiber. We found a 44 nm wavelength-shift from

1500 nm to 1544 nm after re-loading hydrogen into the stabilized grating. The degradation process occurs very slowly at room temperature, so it needs annealing treatment at high temperature, which is expected to cause the defect site with a small energy barrier empty and return to the ground state. In the case of the fiber exposed for 2 minutes, we obtained the results ; coupling to LP_{05} mode starts at 1523 nm with 0.1 dB extinction ratio and ended with 1500 nm with 4.3dB after annealing ; 20nm shift from 1545nm to 1565nm after UV exposure. This results show that the coupling behavior is not reversible between growth and annealing process even with same Δn ($=n_{co} - n_{cl}^{(n)}$) which means the same coupling wavelength from the phase matching condition.

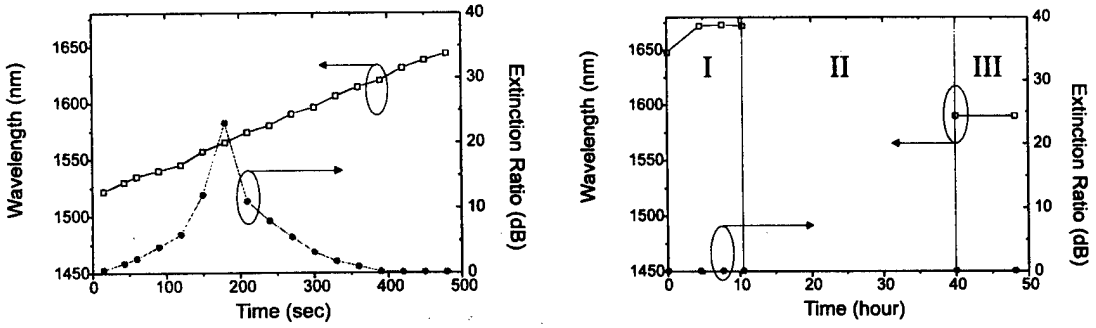

Fig. 3. Coupling peak behavior vs exposure time for 8 minutes(a), and after exposure(I), annealing(II), stabilization(III) process(b).

Figure 3 shows the growth behavior of the grating with 8 minutes exposure. The trend is very similar to Fig. 1 but the amount of shift to the long wavelength after exposure is about 29 nm, larger compared to the case of 2 minutes exposure. It might be explained by the fact that the difference of the hydrogen molecule concentration between core and cladding is large in longer time exposure. In this case, coupling to LP_{05} mode starts at 1523 nm with 0.1 dB extinction ratio and ends at 1590 nm with 0.1 dB extinction ratio after annealing (5dB in the writing process) ; 29nm shift from 1644nm to 1673nm after UV exposure.

Conclusion

We have shown the dynamics of the coupling peaks induced by H_2 diffusion and annealing process for stabilization. The coupling peaks shifted toward the longer wavelength for about 11 hours after exposure of the UV source and then returned back by H_2 diffusion behavior. We found the growth and decay behavior was not reversible.

References

1. M. J. Yuen, 1982, Appl. Opt., 21, 136
2. D. L. Williams, B. J. Ainslie, J. R. Armitage, and R. Kashyap, 1992, Proc. European Conf. On Optical Communication, ECOC'92, 425
3. F. Bilodeau, B. Malo, J. Albert, D. C. Johnson, K. O. Hill, Y. Hibino, M. Abe, and M. Kawachi, 1993, Opt. Lett., 18, 953
4. P. J. Lemaire, R. M. Atkins, V. Mizrahi, and W. A. Reed, 1993, Electron. Lett., 29, 1191
5. I. Greene, D. M. Krol, S. G. Kosinski, P. J. Lemaire, and P. N. Saeta, 1994, Proc. Conference on Optical Fiber Communications, OFC'94, 48

Analysis of Narrow Depressed-Cladding Fibers for Minimization of Cladding and Radiation Mode Losses in Fiber Bragg Gratings

C.W. Haggans[1], H. Singh[2], W.F. Varner[1], and J-.S. Wang[3]

[1]3M Fiber Optics Laboratory,3M Center, Bldg. 260-5B-08
St. Paul, MN 55144, Ph. (612)-737-1556
FAX (612)-736-8140, cwhaggans@mmm.com
[2]3M Bragg Grating Technologies
206 West Newberry Road, Bloomfield, CT 06002
[3]3M Specialty Optical Fibers
420 Frontage Road, West Haven, CT 06516

Undesirable losses in highly reflective fiber Bragg gratings due to coupling to bound cladding modes or lossy radiation modes are well documented[1-5]. Several approaches have been proposed for reducing this coupling, including high LP_{01} mode confinement fibers (high numerical aperture single-mode fibers[6] and two-mode fibers[7]), fibers with equally photosensitive core and cladding regions[8], and, recently, fibers with wide depressed cladding regions[5]. However, the solution detailed by Komukai, et al.[6] is undesirable due to mode-field mismatch losses when splicing to conventional single-mode telecommunication fibers operated at 1550 nm (e.g, Corning SMF-28) and the solution of Okude, et al.[7] requires advanced fabrication techniques. Additionally, while the solutions detailed by Dong, et al.[5] and Delevaque, et al.[8] reduce cladding mode losses for gratings with no variation of the photoinduced index transverse to the fiber axis, it is well known that strong asymmetries in the transverse photoinduced index profile can occur in Type I[9] and Type II[10] gratings due to the sidewriting process. In fact, elaborate writing schemes have been proposed to reduce this asymmetry[11-12]. Additionally, in practice, small tilts of the grating fringe planes can be introduced during fabrication due to mask-fiber misalignment. It is demonstrated in this paper that the solutions detailed by Dong, et al.[5] and Delevaque, et al.[8] are not optimum for azimuthally asymmetric transverse photoinduced index distributions, and a new narrow depressed cladding fiber design that has superior loss suppression characteristics for moderate grating asymmetries is presented.

Azimuthal grating asymmetry due to a physical tilt of the grating fringe planes can be characterized by the angle of that tilt in the fiber, θ_{tilt}. Other small azimuthal asymmetries can be approximated by an "effective grating tilt", θ_{eff}, where this value is defined as the value of θ_{tilt} that experimentally gives cladding-mode loss equivalent to the loss observed when the azimuthal asymmetry in question is present in the grating.

In general, reduction of cladding mode coupling can be obtained for moderate grating asymmetries ($\sim 0.25° < \theta_{eff} < \sim 1.5°$) for core radius (A) to depressed inner cladding radius (AB) ratios (C=A/AB) of C>0.6 and moderate index depressions ($0.003 < \Delta n\_ < 0.012$) due to the balancing of two effects (See Fig. 1 for fiber parameter definitions):

1. For this fiber geometry range, the LP_{11} hybrid mode field distribution[4] does not strongly duplicate the field distribution of a core LP_{11} mode. This limits the strength of the allowed asymmetric mode coupling (principally the LP_{1m} mode set for small grating asymmetries).
2. The presence of the inner depressed clad changes the boundary conditions that must be satisfied by the LP_{0m} cladding mode set at the inner and outer boundaries of the depressed cladding. The weak "pinning" effect due to the presence of the narrow barrier reduces the cladding mode field amplitude in the core region as compared to the cladding mode field amplitude in a matched-cladding fiber of the same mode-field diameter. Thus, coupling to the LP_{0m} mode set is reduced compared to the coupling for a matched-clad fiber with an identical mode-field diameter.

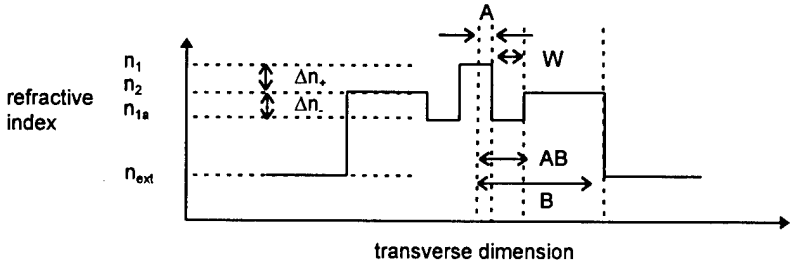

Fig 1. Definition of depressed inner clad fiber geometry.

The effect of azimuthal asymmetry on cladding mode losses can be understood from Figs. 2a-d. These figures are simulated transmission spectra for moderately strong gratings written in the four fiber types under consideration for suppression: 1) SMF-28, 2) the wide barrier design proposed by Dong et al.[5], 3) SMF-28 with an equally photosensitive cladding (corresponding to the design approach of Delevaque, et al.[8] and 4) a fiber representative of the narrow-barrier design region proposed in this paper with C=0.86. In generating these plots, an effective grating tilt in the fiber of 0.6 deg is used to reproduce the cladding mode losses that we have observed using certain exposure processes. These plots were generated using a coupled-mode simulation similar to that of Archambault[2]. The grating simulated was 10mm in length and unapodized with a peak-to-peak photoinduced index modulation of ~0.00044 (the exact index modulation value was adjusted to give equal peak rejection for each grating).

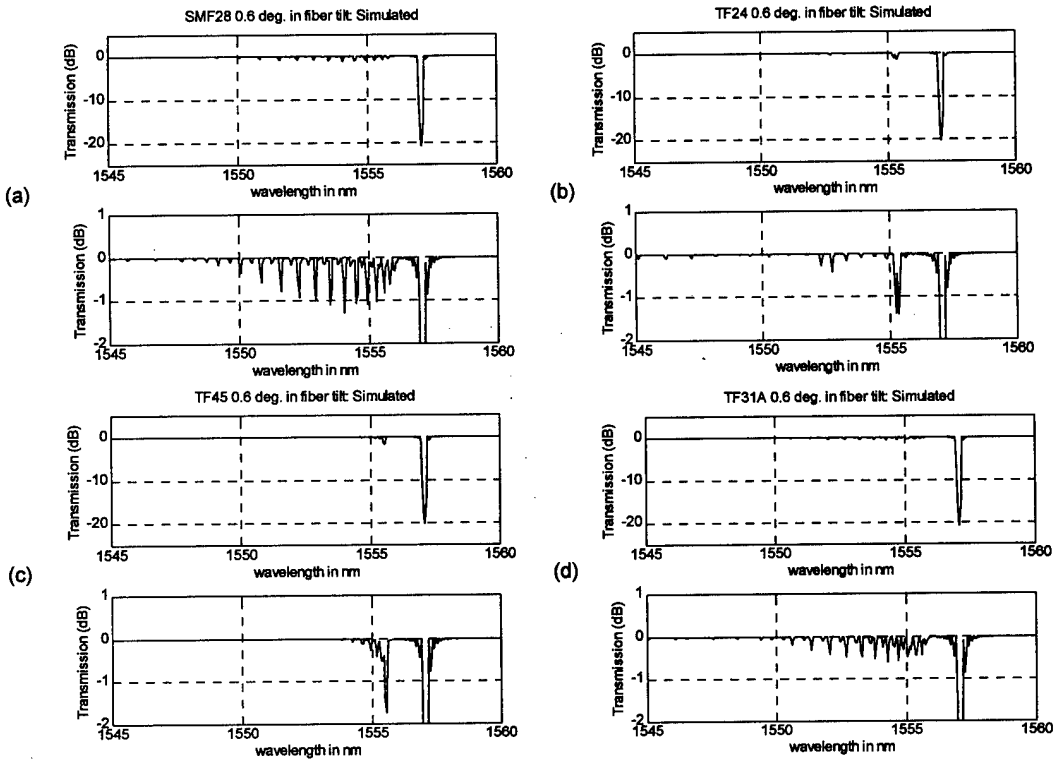

Fig.2. Simulated transmission spectra for 4 fiber types. λ_B=1550nm ,n_{clad}=1.4446, $n_{external}$=1.0, B=62.5μm, θ_{eff}=0.6°. (a) SMF-28-like matched clad fiber: A=4.15μm, MFD=10.5 μm, Δn_+=0.0046, (b) Wider depressed-clad fiber design: Same parameters as (a) with A=5.86 μm, AB=9.71μm, Δn+=0.0038, Δn_-=0.0064, MFD=9.5 μm (c) SMF-28-like fiber with a photosensitive inner cladding: Same parameters as (a) except $\Delta n_{inner\ clad}=\Delta n_{core}$ extending to a radius of 2A (9.4 μm), A=4.7 μm, MFD=10.1 μm. (d). Proposed narrow depressed clad fiber: Same parameters as (a) with Δn_+=0.0052, Δn_- =0.0059, A=4.65 μm, AB=5.4 μm, MFD=9.85 μm.

Note from Figs 2a-d that at this effective grating tilt value (θ_{eff}=0.6), the peak cladding mode losses are minimized for the proposed narrow design (Fig. 3d).

Figs. 3a-c are measured spectra for gratings written in fibers similar to those detailed in Fig. 2a,b, and d and were fabricated with θ_{tilt}=1°. Figs. 4a-c are corresponding simulated spectra for θ_{eff}=1.2°. Note the excellent qualitative agreement between the measured and simulated spectra, which suggests that a small sidewriting asymmetry was introduced to the grating during exposure. Additionally note that even for this relatively large azimuthal asymmetry, the narrow depressed clad design of Figs. 3c and 4c gives improved performance over the other two fibers.

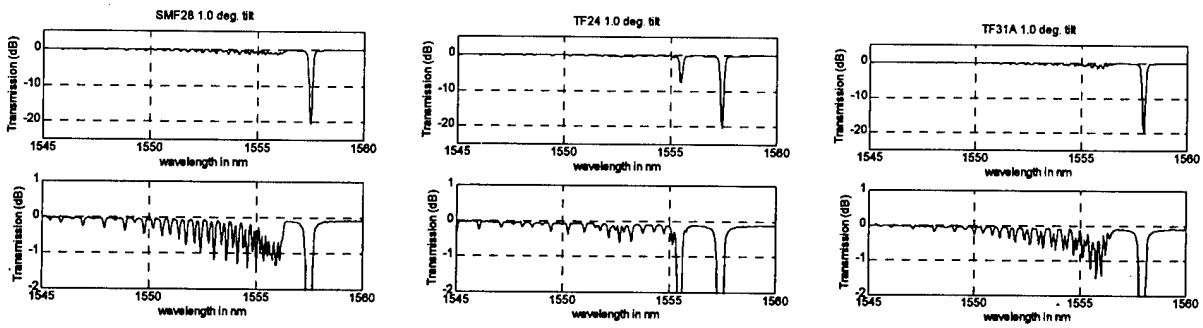

Fig. 3a-c. Measured grating spectra with geometrical parameters similar to those simulated in Fig. 2a, 2b, and 2d for θ_{tilt}=1.0°. (a) SMF-28. (b) Wide depressed clad design. (c) Narrow depressed clad design.

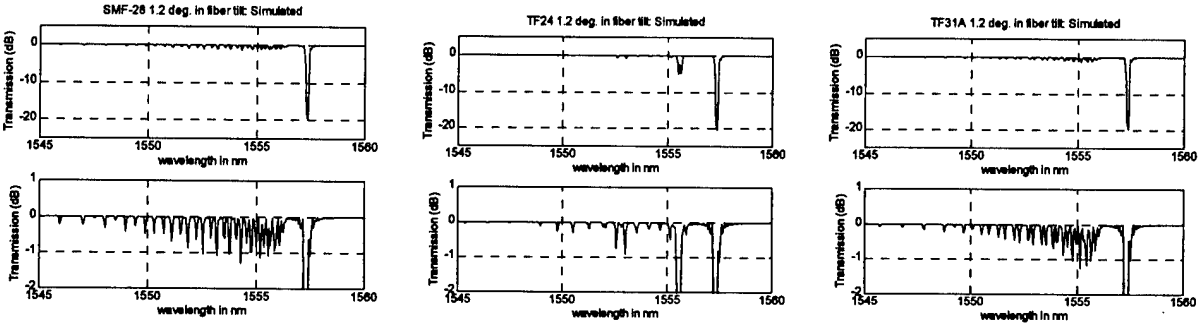

Fig. 4a-c. Simulated grating spectra corresponding to the experimental spectra of Figs. 3a-c for θ_{eff}=1.2°. (a) SMF-28. (b) Wide depressed clad design. (c) Narrow depressed clad design

In conclusion, the optimum fiber design for cladding mode loss suppression is dependent on the azimuthal asymmetry present in a given grating writing process. For large effective grating tilts (θ_{eff}>~1.5°), a matched clad design such as SMF-28 is superior, and for negligible tilt or the equivalent asymmetry (θ_{eff}<~0.25°), the approach of Dong et al.[5] and Delavaque et al. [8] give superior suppression of the cladding mode losses. However, for intermediate asymmetries which may desirable for volume manufacturing processes, a narrow depressed inner cladding fiber has been shown to be superior to conventional matched clad telecommunication fiber, matched photosensitive clad fiber, and wide depressed inner clad fiber.

References

1. V. Mizrahi and J. Sipe, J. Lightwave Tech. 11, 1513 (1993).
2. J.L. Archambault, PhD. thesis, University of Southampton, Chapter 2 (1994).
3. T. Erdogan and J. E. Sipe, Opt. Lett. 20, 1838 (1995).
4. S. J. Hewlett, et al., Opt. Quantum Electron. 28, 1641 (1996).
5. L. Dong, et al., IEEE Photon. Tech. Lett. 9, 64 (1997).
6. T. Komukai and M. Nakazawa, Jpn. J. Appl. Phys. 34 L1286, Part 2, No 10A (1995).
7. S. Okude, et al., European Patent Application Serial Number 0770890A1.
8. E. Delevaque, et al, in Opt. Fiber. Commun. Conf. Proc., 1995, paper PD5.
9. D. Inniss, et al., Appl. Phys. Lett. 65, 1528 (1994).
10. B. Malo, et al., Opt. Lett. 18, 1277 (1993).
11. D. Inniss, et al, US Patent Serial Number 5559907.
12. S. R. Baker, et al., UK Patent Application Serial Number 2298287A.
13. Snyder and Love, Optical Waveguide Theory, (Chapman and Hall , London, 1983), Ch. 13.

Strong LP_{11}-Mode Splitting in UV Side-Written Tilted Fiber Gratings

Dietmar Johlen, Peter Klose, Hagen Renner, Ernst Brinkmeyer
Technische Universität Hamburg-Harburg, Arbeitsbereich Optik und Meßtechnik
21071 Hamburg, Germany
e-mail: renner@tu-harburg.d400.de, Tel.: +40 7718 3342, Fax.: +40 7718 2860

Dual-mode fiber gratings are promising components for mode converters and reflectionless band filters. In order to be able to use standard telecommunication fibers, which are single-moded at the wavelengths of interest, one can increase the refractive index by UV laser-beam side-writing such that higher modes propagate through the grating region. We show here that UV side-writing is an efficient method to increase the refractive index to allow higher modes to propagate. In addition, the problems of multiple resonant peaks due to weakly broken higher-mode degeneracy [1] is circumvented by breaking the degeneracy such strongly that the resonant peaks are spectrally widely separated.

Figure 1 shows the transmission spectrum of a UV-written tilted fiber Bragg grating. The fiber used is single-mode at $\lambda = 1550$ nm. A length of 20 mm is pre-illuminated with UV light to raise the refractive index. Afterwards a 10 mm long tilted grating is written into the fiber by using a phase mask with a design Bragg wavelength of 1550 nm. In the core, the grating tilt angle is 3°.

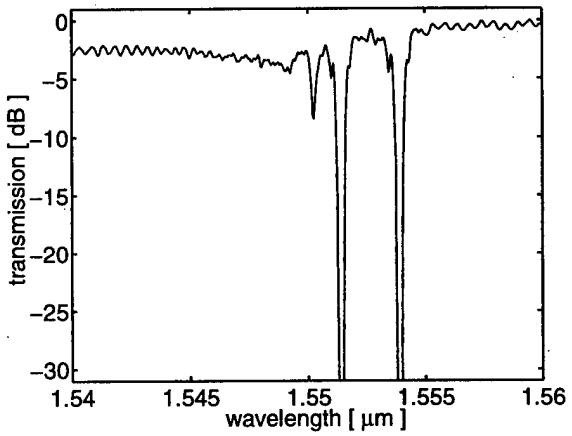

Figure 1: Transmission spectrum of a tilted Bragg grating

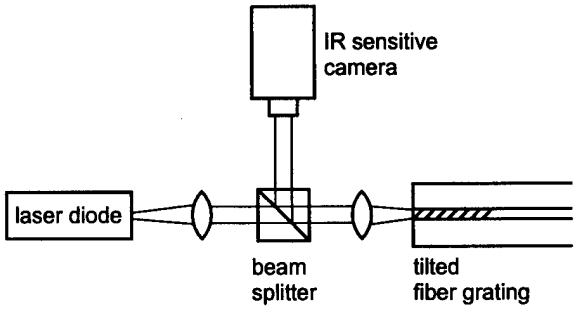

Figure 2: Observation of the near fields of the reflected modes.

The aim of using a tilted grating is to achieve a contra-directional coupling between the LP_{01} and LP_{11} modes. With the chosen tilt angle the coupling strengths between LP_{01}-LP_{01} modes and between LP_{01}-LP_{11} modes are nearly the same.

In order to measure near-field intensities of the reflected modes, light from a tunable laser is coupled through a beam splitter into the fiber which is cut at one end of the Bragg grating (Fig. 2). The incident beam is focused to excite the fundamental LP_{01} mode of the fiber. The near field of the light reflected by the Bragg grating can be observed with an IR sensitive camera.

At the wavelength $\lambda = 1553.7$ nm the Bragg condition for contra-directional coupling between the forward and backward LP_{01} modes is met. The mode conversion efficiency is stronger than 30 dB. The near field of the reflected LP_{01} mode taken by the camera is shown in Fig. 4. It exhibits the typical, nearly circular, intensity distribution. A second strong transmission dip of more than 30

dB depth is caused by contra-directional coupling of the input LP_{01} mode to one of the two possible LP_{11} modes at $\lambda = 1551.6$ nm. Since the Bragg grating was written from above with the UV beam into the negative y direction as illustrated in Fig. 3, the grating elements are tilted about the y axis. Thus the even LP_{11} mode with a field distribution nearly antisymmetric with respect to the y axis is reflected. Fig. 5 shows the intensity distribution of this mode as expected. The small orientational deviation by an azimuthal angle ϕ is due to some uncertainty in marking the angle from which the grating was written, but it is the same for all modes studied here.

A third, but smaller, transmission dip of 6 dB depth occurs at $\lambda =$ 1550.3 nm. The near-field intensity distribution shown in Fig. 6 reveals that the odd LP_{11} mode with a field nearly symmetric to the y axis is reflected. The contra-directional coupling of the input LP_{01} mode to the backward odd LP_{11} mode can be explained as follows. Both the constant increase of the refractive index along the grating and the grating itself have been UV side-written from above (Fig. 3). Since the UV-laser beam is partially absorbed when passing through the fiber core, the UV-induced refractive-index increase is strongest at the upper boundary of the core and decays in the negative y direction [2,3] as indicated by the hatched region in Fig. 3. Thus the grating elements are not only tilted about the y axis but are also non-symmetric in the y direction. Further, the modal field of the odd LP_{11} is perceptably distorted by the non-symmetric refractive-index increase as can be seen in Fig. 6. Similarly to modes in graded-index planar waveguides [4], the upper field lobe in the region of the higher index is smaller both in strength and in transverse extension than the lower lobe in the region of lower index [5].

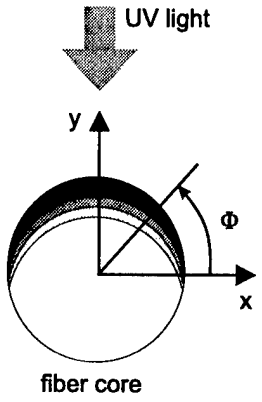

Figure 3: Non-homogeneous UV-induced refractive-index distribution

Both asymmetries cause contra-directional coupling between the forward LP_{01} mode and the backward odd LP_{11} mode. The strong asymmetries both of the UV-induced refractive-index distribution and of the modal field are in accord with the strong break-up of the degeneracy of the two LP_{11} modes obvious from Fig. 1. The separation of the two pronounced short-wavelength transmission dips is as large as 1.3 nm. Assuming a UV-induced refractive-index increase that decays exponentially in the negative y direction inside the core, it can be shown that, for strong asymmetries, the propagation constant of the even LP_{11} mode is larger than that of the odd LP_{11} mode [5] in agreement with the spectral succession of the transmission dips in Fig. 1. All three transmission dips mentioned above represent contra-directional coupling into truely guided modes, since the dip shapes remained unchanged when the fiber was immersed in various index-matching fluids, for which the typical modulation in the spectrum below $\lambda = 1549.5$ nm caused by coupling to the cladding modes was smoothed out.

In conclusion we have demonstrated that UV-side writing can break up the LP_{11} mode degeneracy so strongly that the two LP_{01}-LP_{11} resonances of fiber gratings can be used separately.

References:

[1] K. O. Hill et al., Electron. Lett **26**, 1270 (1990)

[2] P. J. Lemaire, A. M. Vengsarkar, W. A. Reed and D. J. DiGiovanni, OFC '95, Technical Digest, paper WN1, 158 (1995).

[3] M. Janos, J. Canning and M. G. Sceats, Opt. Lett. **21**, 1827 (1996).

[4] E. M. Conwell, Appl. Phys. Lett. **23**, 328 (1973).

[5] H. Renner, 'Break-up of LP_{11} mode degeneracy in UV side-written optical fibers', in preparation.

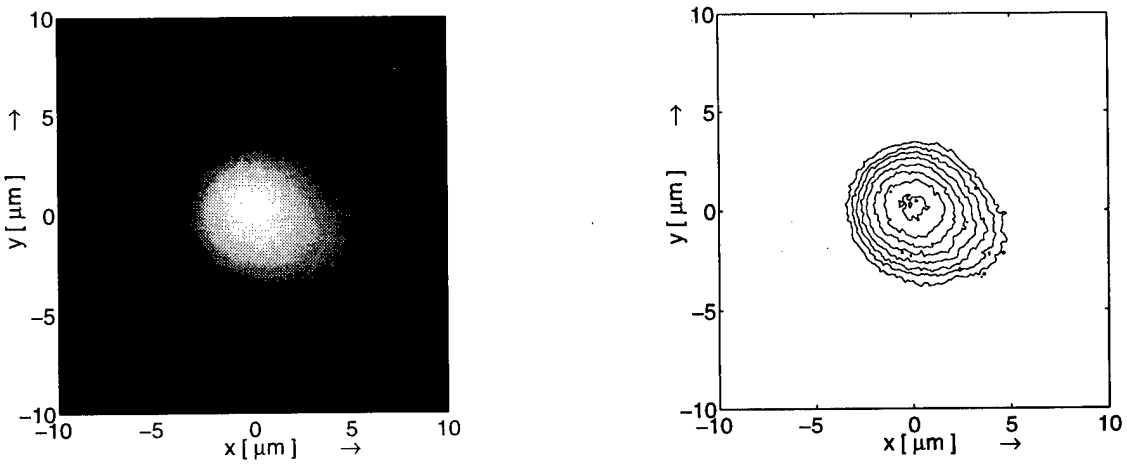

Figure 4: Fundamental LP_{01} mode

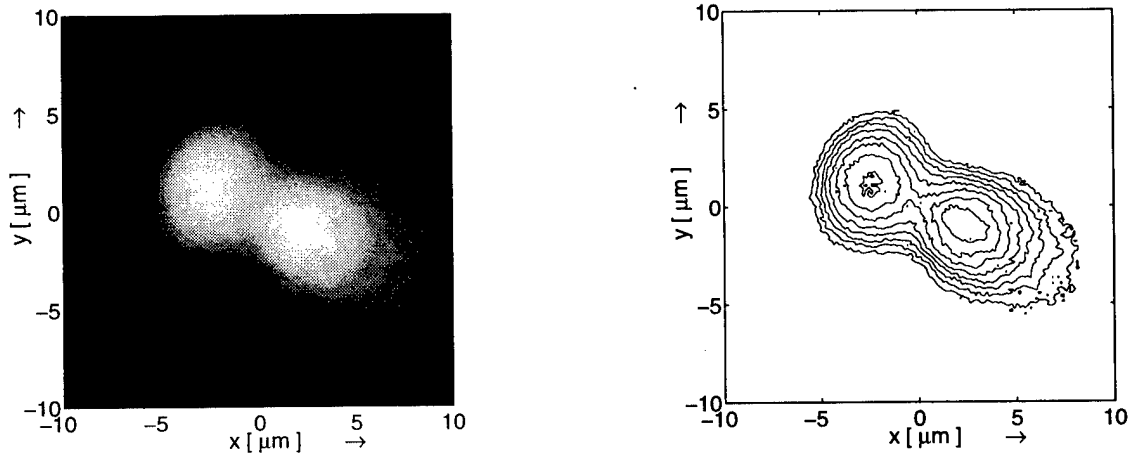

Figure 5: Even LP_{11} mode

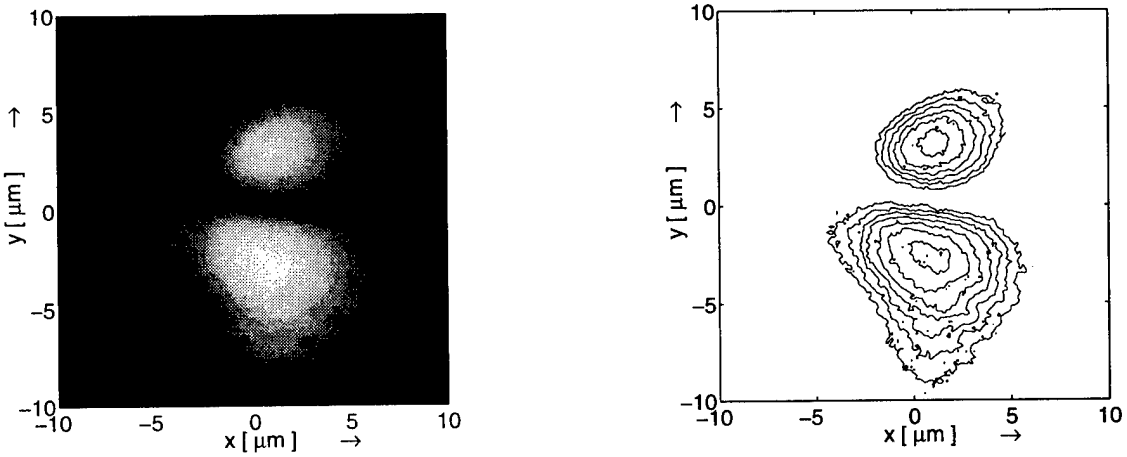

Figure 6: Odd LP_{11} mode

THE EFFECT OF PROFILE NOISE ON THE SPECTRAL RESPONSE OF FIBER GRATINGS

François Ouellette, Kromafibre inc.
1501 Ampère, suite 112, Boucherville (Québec), Canada J4B 5Z5
Ph. (514) 641-1414, Fax (514) 641-4062, e-mail: f.ouellette@kromafibre.com

Fiber Bragg gratings are now finding more and more commercial applications, particularly in Wavelength-Division-Multiplexed (WDM) optical communication systems. For such systems, the fiber grating response must meet stringent requirements of wavelength accuracy, stability, bandwidth, channel isolation and, for dispersion compensators, group delay ripple. It is important for fiber grating manufacturers to understand the factors that can degrade the response of a fiber grating, and what tolerances this places on the manufacturing system.

We have investigated the effect that noise on the spatial profile of a fiber grating has on its spectral response. We have looked at noise on either the coupling coefficient or the grating period. We present here results on two cases of interest: short, gaussian-apodized gratings typical of bandpass filters, and long apodized chirped gratings for dispersion compensation. The grating response was calculated with a transfer matrix method, where the grating is subdivided into a number of short, uniform gratings, each characterized by a 2X2 matrix, the total response being the product of all individual matrices [1]. Noise was introduced as gaussian white noise, with average amplitude defined as a fraction of the local coupling coefficient, or a deviation from the local period. We also used different cut-off frequencies for the spatial variation of the noise.

The short gratings have a gaussian spatial profile with a FWHM of 8 mm, a maximum coupling coefficient κ_0=6 cm^{-1}, and a total length of 20 mm. We have found that the main reflection peak of the grating suffers minimally from the noise on the profile, and is

therefore not a good indicator of the quality of the spatial profile. However, around the main peak, where reflection is small, one observes the appearance of a non-negligible background, that grows rapidly with noise amplitude such that, at nearby wavelengths, reflection can eventually exceed the specifications for channel isolation. Figure 1 shows the profile and reflection spectrum for a grating with 10% noise on the coupling coefficient, and a 1 mm^{-1} cut-off spatial frequency (full line). The spectrum of the un-noisy grating is shown as a dashed line. Noise on the grating period of only about 0.02 nm, and the same cut-off frequency, has qualitatively the same effect.

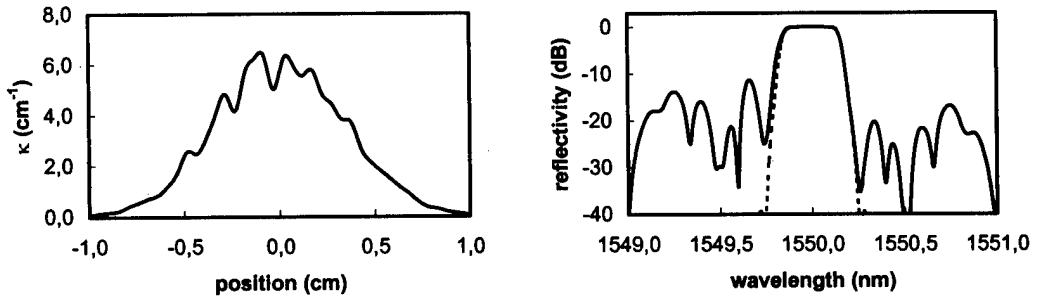

(a) **(b)**

Fig. 1 (a) Spatial profile and (b) reflection spectrum of gaussian-apodized grating with noise on the coupling coefficient. Dashed line in (b) is spectrum of un-noisy grating.

For a chirped grating, the most striking effect of spatial profile noise is on the group delay response. Fig. 2 shows the spatial profile and reflection spectrum for a 12 cm long chirped grating, with a super-gaussian profile [1] of exponent 8, with a FWHM of 9 cm, and a maximum coupling coefficient κ_0=2 cm^{-1}, with 7.5% noise on the coupling coefficient and a cut-off spatial frequency of 1 mm^{-1}. Again, the reflection spectrum is hardly affected. However a strong group delay ripple appears approaching +/-50ps, as seen in Figure 3, where the group delay, and its deviation from a linear fit are shown. The un-noisy grating only has a maximum ripple of +/- 5 ps. A similar result is obtained when the noise is on the grating period with an average amplitude of about 0.03 nm. Given that such ripple rapidly deteriorates the performance of the grating for dispersion compensation, it is essential that the manufacturing process have very good control on all the factors that can cause noise on the profile during fabrication.

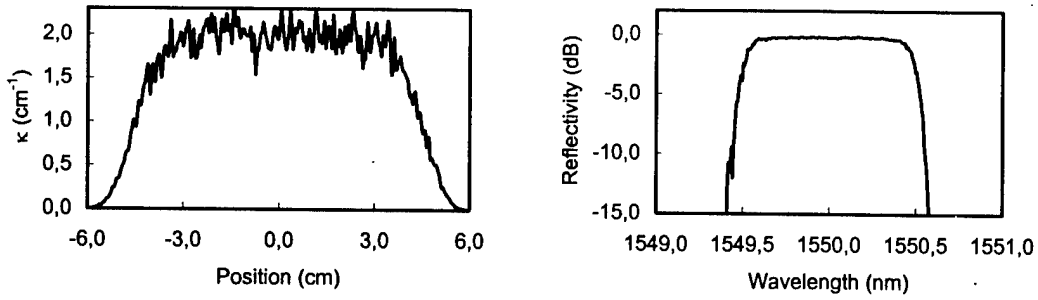

(a) **(b)**

Figure 2: (a) Spatial profile; **(b)** reflection spectrum of apodized, chirped grating with 7.5% noise on the coupling coefficient.

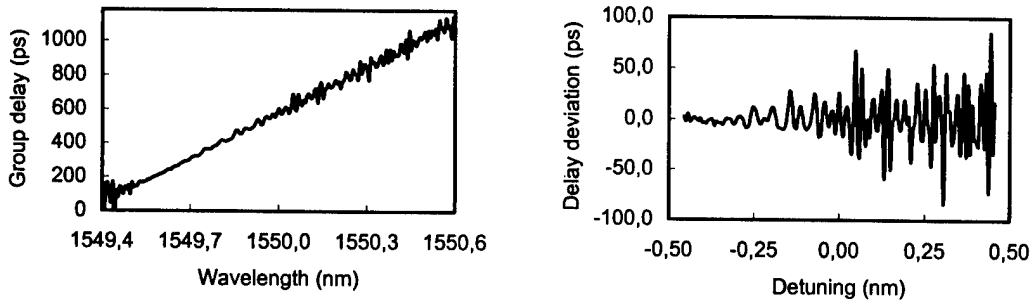

(a) **(b)**

Figure 3: (a) Group delay versus wavelength ; **(b)** deviation of group delay from the best linear fit for the grating of Figure 2.

In conclusion, we have shown that spatial profile noise can have a detrimental effect on the response of gratings, even though it does not affect the main reflection peak. For short, gaussian-apodized gratings, it causes a stronger reflection background outside the main reflection peak. For long, chirped and apodized gratings, it worsens the group delay ripple.

References

[1] F. Ouellette, J.-F. Cliche, S. Gagnon, J. Lightwave Technol. Vol.12, p. 1728 (1994).

Thermal stabilities of strong UV written gratings in sol-gel germanosilicate planar waveguides.

A. D. RAZAFIMAHATRATRA*, M. BENATSOU**, M. BOUAZAOUI**, W. X. XIE*, C. MATHIEU***, A. DACOSTA*** and M. DOUAY*.

*LDMP, URA 779 CNRS, **LSH, URA CNRS n° 249
Centre d'Etudes et de Recherches Lasers et Applications, Université Lille I, 59655 Villeneuve d'Ascq Cedex, FRANCE.

*** Centre de Recherches de l'Université d'Artois à Lens. Faculté J. Perrin, rue Jean Souvraz, S.P. 18 62307Lens Cedex, FRANCE.

Introduction

Bragg gratings inscriptions or UV direct patterning of single mode channel waveguides are key issues for the achievement of new integrated components. Photosensitivity was reported in planar waveguides elaborated by different processes: FHD [1], PECVD [2], sol-gel [3], ion implantation [4], sputtering [5]. The sol-gel approach allows to prepare planar waveguides at low cost and low temperature. Hence, this process can be easily applied to industrial procedure. Photoinduced refractive index of 3 10^{-5} was already reported in H_2 loaded sol-gel germanosilicate waveguides using the 488nm of an argon ion laser [3]. Recently, UV light imprinted Bragg grating with 97% reflectivity was imprinted in an hybrid sol-gel silica glass waveguide on silicon [6].

This work reports first on the UV photosensitivity of sol-gel germanosilicate waveguides densified at 700°C and second on the thermal stability of the photoinduced refractive index modulation imprinted in the guide. The waveguide surface has been investigated using Atomic Force Microscopy (AFM) and profilometry to enlighten the photosensitivity involved in these materials during the UV irradiation and after the thermal annealing.

Waveguide preparation and characterization

Germanosilicate thin films were deposited by using standard dip-coating technique [7]. The thin films deposited on a synthetic fused silica (suprasil 1) were heat treated at 700°C under oxygen flow to remove the organic residues and ensure the densification of the film. An index value of 1.532 ± 0.001 was measured using the M-line method for 50%SiO2-50%GeO2 planar waveguides. The propagation losses were found to be equal to 0.3 and 0.6 dB/cm respectively for films with thicknesses of 0.36 and 0.9 μm. Raman measurements performed on these waveguides show that no organic compounds were detectable after the heat-treatment process. Therefore, these sol-gel films are expected to have a very good long term aging.

Photosensitivity

The sol-gel films were exposed to a fringe pattern (λ = 244 nm) in order to write Bragg gratings through the conventional external holographic method [8]. The grating pitch were fixed to 5μm. The irradiation were performed using a cw or a pulsed laser at a wavelength of 244 nm. Irradiations were performed on H_2 loaded and unloaded samples.

The thin films were H_2 loaded at a temperature of 450°C under a flowing H_2/N_2 (1:10 volume ratio) for 120 min.

Photoinduced refractive index modulation was calculated using the Bragg grating diffraction efficiency which was measured using a He-Ne laser at 632.8 nm. The stability of the gratings was studied through 30 min. isochronal annealing experiments. The surface's corrugations (figure 1a and 1b) and the hologram diffraction efficiencies were then measured after each step of temperature. This procedure was carried out for a temperature until 500°C (figure 2a and 2b).

Discussion and conclusion

The measurements' accuracy of the diffraction efficiencies was less than 10^{-5}. No diffraction efficiency was observed in the unloaded samples. For the H_2 loaded samples, the diffraction efficiencies were 10^{-1} and 10^{-4} respectively for pulsed and cw UV exposures.

The microscopic inspections of all the gratings written in the H_2 loaded sol-gel films have shown corrugations of the surfaces. Figures 1a and 1b give quantitative informations on the corrugation for a grating written during 60 seconds (respectively 100 pulses) at a mean irradiance of 70 W/cm^2 (respectively a fluence per pulse 90 mJ/cm2) using cw (respectively pulsed) exposure. Figure 1b exhibits a strong corrugation of the sol-gel surface due to the pulsed exposure. A peak to peak modulation as high as 1 nm (respectively 70 nm) can be measured for the cw (respectively pulsed) exposure. The evolution of the surface corrugation as a function of the pulsed number and/or the UV fluence was not monotonous: the corrugations show an expansion of the waveguide in the beginning of the irradiation, then a photoablation and/or a densification of the material lead to the reported profile in figure 1b. The corrugation was too large (70 nm) to perform a correct estimation of the photoinduced refractive index modulation using the diffraction efficiency of the grating.

The thermal annealings show that the gratings imprinted using cw exposure are stable up to a temperature of 400°C and then decrease rapidly. The comparison between the diffraction efficiencies and the surface's corrugation during the annealing process shows that the pulsed irradiation produced photoablation and that the cw exposure produced almost no photoablation. In this latter case, the variation of the diffraction efficiency during thermal annealing is attributed to the change of photoinduced refractive index and found to be equal to $5\ 10^{-3}$. The thermal erasure of gratings (Type I) written in germanosilicate fiber begins at 200-300°C, whereas it begins at 400°C in the case of a cw exposures of the sol-gel films (figure 2a). This thermal evolution suggests a long term aging of gratings written in the sol-gel germanosilicate waveguides better than ones (type I) written in germanosilicate fibers.

References

/1/ G. D. Maxwell et al., Elec. Lett., 28, 1992, pp 2106-2107

/2/ M. Svalgaard et al., Elec.Lett. 30(17), 1994, pp 1401-1405

/3/ K.D. Simmons et al., Opt.Lett. 18, 1993, pp 25-27

/4/ F.Bilodeau et al., Opt.Lett. 18, 1993, pp 953

/5/ Zhong-Yi Yin et al., Appl.Opt. 21, 1982, pp 4324

/6/ M.A. Fardad et al., Elec.Lett. 33(12), 1997, pp 1069-1070

/7/ B.G.Potter et al., Opt.Lett. 17, 1992, pp 1349

/8/ G.Meltz et al., Opt.Lett. 14, 1989, pp 823-825

Surfaces and profiles of gratings written in germanosilicate sol-gel (figure 1)

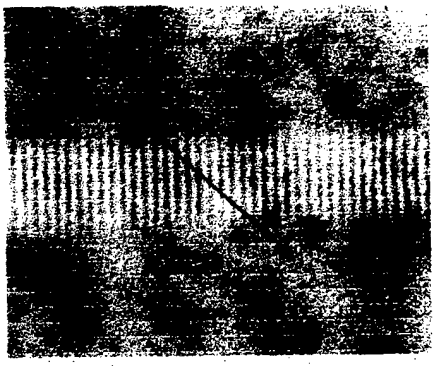

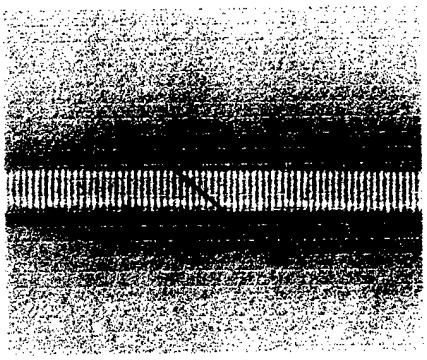

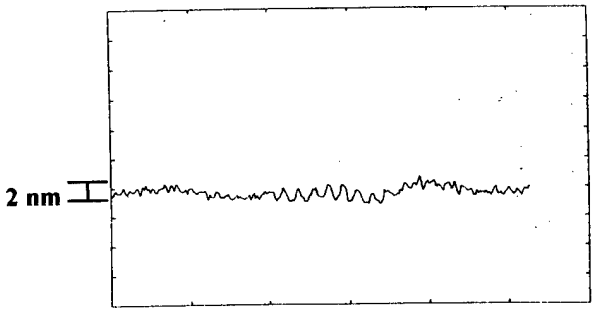

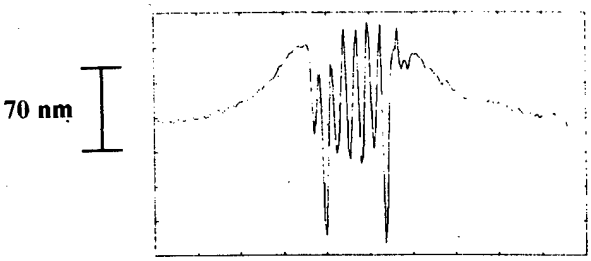

figure 1a: cw UV exposure (244 nm)
grating pitch= 5µm, Ir= 70 W/cm^2
irradiation time= 60 s

figure 1b: pulsed UV exposure (244 nm)
grating pitch= 5µm, Fluence per pulse= 93 mJ/ cm^2
number of pulses= 100

isochronal annealing experiments of Bragg gratings written in sol-gel (figure 2)

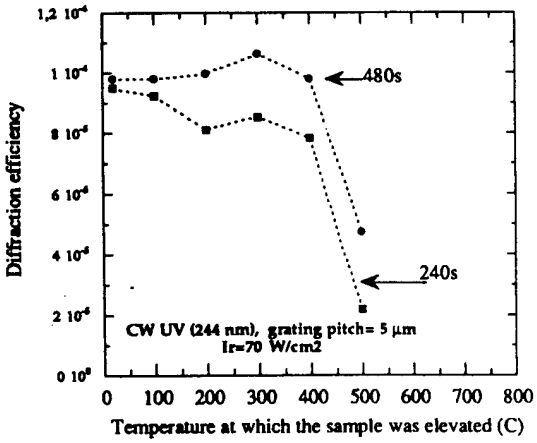

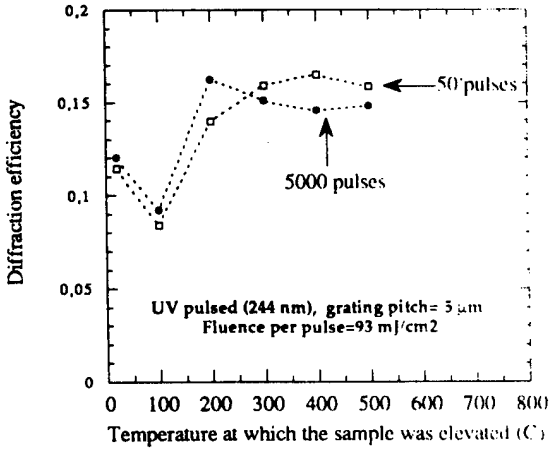

figure 2a: cw UV irradiation

figure 2b: pulsed UV irradiation

FABRICATION OF IN-FIBRE MOIRÉ FILTERS USING A 5CM NON-DEDICATED CHIRPED PHASE MASK

L A Everall, K Sugden, J A R Williams, I Bennion

Dept. Electronic Engineering and Applied Physics, Aston University, Aston Triangle, Birmingham, B4 7ET, UK.

Tel: 44 121 359 3611, Fax: 44 121 359 0156

X Liu, J S Aitchison, R M De La Rue

Dept. Electronic and Electrical Engineering, University of Glasgow, Glasgow, G12 8QQ, UK.

Tel: 44 141 330 6022, Fax: 44 141 330 4907

INTRODUCTION

Since the initial observation of photoinduced refractive index changes in optical fibres[1], the area of application of fibre Bragg gratings has broadened from simple wavelength dependent reflectors to noise filtering, wavelength selection and as sensors.

The concept of a Moiré filters is well understood and they have been fabricated previously in uniform period surface relief structures[2] and uniform period in-fibre gratings[3]. The introduction of chirped in-fibre Moiré gratings[4] overcame the limitation on the maximum stopband that could be achieved with high reflectivity.

The development of the near-field holographic (NFH) approach to fabricating in-fibre Bragg gratings[5] brought with it the potential for the mass-production of gratings due to the intrinsic reproducibility of the fabrication process. Uniform period Moiré filters have been fabricated either by introducing a phase shift during the inscription process[6], or by using a dedicated phase mask containing a single phase shift[7]. More recently, the Moiré technique has been incorporated into the phase mask fabrication process, with the resulting phase mask producing an apodised Bragg grating[8].

We have previously reported a technique to fabricate in-fibre multiple passband Moiré structures using the dual scan of a uniform period phase mask[9]. In this paper, we report on the extension of this idea, to include the use of a non-dedicated 5cm chirped phase mask. This enables the fabrication of much stronger Moiré filters, with rejection ratios far exceeding those previously reported.

EXPERIMENT

The fabrication process involved the dual exposure of a 5cm chirped phase mask. The mask had a total chirp along its length of 0.692nm, which produced a grating of bandwidth 1nm, at 1550nm. The first chirped Bragg grating was written into fibre using a computer controlled scan of a frequency doubled argon-ion laser. The fibre was then placed under an increased tension and a second grating was written on top of the first. The increase in fibre tension induces a wavelength shift in the second grating with respect to the first. This results in a grating with a rapidly varying component of period $\Lambda_s(z)$ and a slowly varying envelope of period $\Lambda_e(z)$. Each crossover point of the beat produces a passband in the resulting grating response. The number of passbands contained within the grating structure is dependent on the difference in periodicities of the two chirped gratings.

After fabrication the filters were characterised using a narrow linewidth tunable laser. This enabled the fine structure of each device to be resolved.

Figure 1 (a) shows a 5cm filter was written into hydrogen-loaded boron/germania co-doped fibre, with a inter-scan stretch of 17μm. This stretch is equivalent to a 0.01% change in grating length. The resulting Moiré structure has 5 passbands contained within its structure and has a stopband which rejects ~20dB.

Figure 1(b) shows a stronger 5cm Moiré structure, having an inter-scan stretch of 8μm which is equivalent to a 0.005% change in length. The resulting filter has a single passband within a stopband of 35dB rejection. The

bandwidth of the passband is 0.001nm, which corresponds to the smallest wavelength step achievable by the tunable laser. The features of the grating do not appear to be fully resolved and the bandwidth of the passband is likely to be narrower than it appears to be in Figure 1(b).

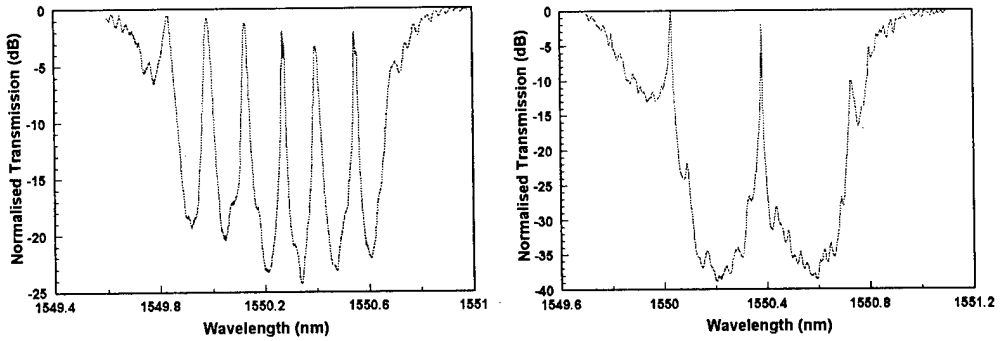

Figure 1: (a) Chirped Moiré filter of length 5cm, (b) Single passband chirped Moiré structure

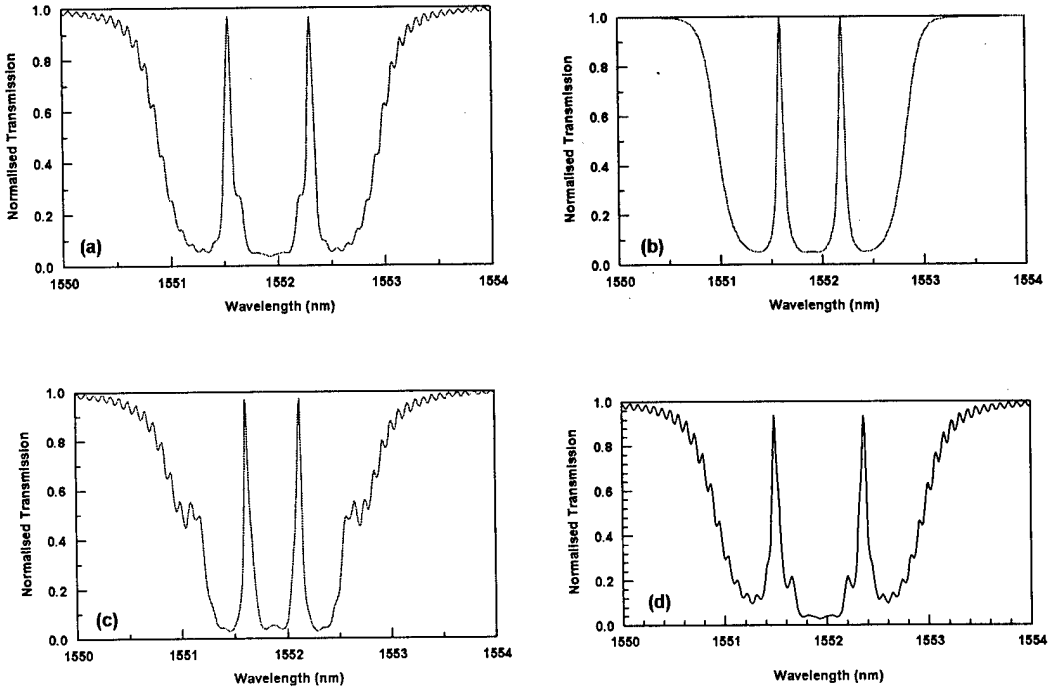

Figure 2: Modelled Moiré filters; (a) wavelength separation 0.165nm; (b) filter was wavelength separation 0.25nm; (c) separation 0f 0.29nm; (d) comparison of modelled and experimental non-optimised Moiré filter. (Dark line: model, grey line: experiment)

The magnitude of the inter-scan stretch is crucial if a smooth filter profile is to be obtained. The effect of varying the inter-scan stretch, for a filter with a chosen number of passbands can be seen in Figure 2. The modelled results

were obtained using the transfer matrix technique, for a Moiré filter, of length 1cm and bandwidth 2nm which contained two passbands within its stopband. The effect of incrementally increasing the relative wavelength shift between the two chirped gratings was examined. Figure 2(a) shows a Moiré consisting of two gratings separated by a wavelength of 0.165nm. Although we have achieved a two-passband structure, there are some obvious additional features produced and these are due to the non-optimised wavelength separation. The Moiré filter in Figure 2(b) has an increased wavelength separation of 0.24nm which produces a smoother filter response. This appears to the optimum value of wavelength separation for a Moiré filter with no ripple. Figure 2(c) shows a filter with a 0.29nm wavelength separation but again the additional features are apparent. The ripples occurring in the modelled Moiré filter are replicated in the corresponding experimental response. Figure 2(d) shows this comparison between modelled and experimental results for a non-optimised 1cm Moiré grating. The resulting features of the modelled and experimental filter can be seen to match very closely.

CONCLUSIONS

Multiple passband Moiré resonators have been fabricated using the superposition of two gratings, both fabricated with a 5cm chirped phase mask. The bandwidth of the resulting Moiré filter is determined by that of the chosen phase mask, so theoretically large bandwidth filters are achievable by choosing a suitable phase mask. This technique demonstrates the flexibility of a non-dedicated chirped phase mask in the fabrication of passband filters. The introduction of a mask of length 5cm allowed the fabrication of far stronger Moiré structures than have previously been reported.

References

[1] K. O.Hill, Y.Fuji, D. C.Johnson and B. S.Kawasaki, Appl. Phys. Lett.,**32**, no. 10, pp. 647—649, 1978.

[2] D.C.J.Reid, C.M.Ragdale, I.Bennion, D.J.Robbins, W.J.Stewart, Electron. Lett.,**26**,12, (1990)

[3] S.Legoubin, E.Fertein, M.Douay, P.Bernage, P.Niay, F.Bayon, T.Georges, Electron. Lett. **27**, 1945, (1991)

[4] L.Zhang, K.Sugden, I.Bennion, and A.Molony, Electron. Lett. **31**, 477, (1995)

[5] K.O.Hill, B.Malo, F.Bilodeau, D.C.Johnson and J.Albert, Appl, Phys. Lett.,**62**,(1993) 1035

[6] W.H. Loh, M.J.Cole, M.N.Zervas, S.Barcelos, R.J.Laming, Opt. Lett. **20**, 2051, (1995)

[7] R.Kashyap, P.F McKee, D.Armes, Electron. Lett. **30**, 1977 (1994)

[8] J.Albert, K.O.Hill, D.C. Johnson, F.Bilodeau, M.J.Rooks, Electron. Lett. **32**, 2260, (1996)

[9] K.Sugden, L.A.Everall, J.A.R.Williams, I.Bennion, SPIE Proc. **2998**, 29, (1997)

Equalisation of Spectral Non-Uniformities in Broad-Band Chirped Fibre Gratings

Michael K. Durkin, Morten Ibsen, and Richard I. Laming
Optoelectronics Research Centre, University of Southampton, Southampton, SO17 1BJ, England

Valeria Gusmeroli
Pirelli Cavi SpA, Viale Sarca 222, Milan. Italy

e-mail: md@orc.soton.ac.uk tel: +44 (0) 1703 593136 fax: +44 (0) 1703 593142

Introduction

The use of chirped fibre Bragg gratings (FBGs) in a dispersion compensating role has been shown to be a successful technology with great promise for future network upgrades [1, 2]. A natural consequence of using FBGs in a negative dispersion sense is that although the structure is designed to phase-match forward- and backward- propagating LP_{01} modes, the phase-matching condition for coupling from the forward propagating fundamental mode to a higher order cladding-mode is also met for wavelengths just below that of the fundamental Bragg reflection. Because propagation in cladding-modes is extremely lossy there is a significant out-coupling of this shorter wavelength light. The chirped nature of FBGs designed for broad-band (> 5 nm) dispersion compensation means that this cladding-mode loss is integrated along the length of the grating with the result that the reflection spectrum has a slope extending from the short wavelength edge of the useable bandwidth. In a practical transmission system this in-band variation of reflectivity is unacceptable. In this paper the authors present for the first time a demonstration of spectral equalisation of cladding-mode losses by exercising control over local apodisation along the length of a 8.5 nm 75 cm long continuously-written chirped FBG. No post-processing was used.

Experiment

The longitudinal distribution of the spatial frequencies that comprise the structure of a chirped FBG means that a localised change of coupling constant coverts directly to a narrow-band modulation of spectral response. Although it is possible to temper the coupling constant by regulating the fluence of the UV writing beam, this leads to a change in background refractive index and hence induces an undesirable chirping effect. The technique of apodisation [3], in contrast, allows the direct control over the index modulation of a FBG *without* altering the background index and hence the dispersion characteristic of the device remains unaffected. In this paper the authors describe an experiment where the dispersion-friendly process of apodisation is turned to face and overcome the problem of non-uniform spectral response in chirped FBGs caused by short-wavelength cladding-mode losses.

Figure 1 shows the effect of cladding-mode loss on a 8.5 nm 75 cm long high-quality chirped FBG designed to compensate 50 km of step index fibre with a dispersion of 17 ps/nm/km when characterised in a negative dispersion sense. The grating was fabricated with the 100 mW 244 nm output of a CW laser in a fibre of ~ 0.2 N.A. using a variation on the moving-fibre/phase-mask scanning technique [3] and was characterised with 5 pm steps using a wavemeter accurate to 0.15 pm. The loss induced as a result of coupling to cladding modes is ~ 2.5 dB, with the first cladding mode (associated with longest structural period) observed at a wavelength approximately 3 nm short of the corresponding Bragg phase-matching condition.

By using a suitable apodisation profile it is possible to reduce the coupling constant of the grating at the long wavelength end and thus both lower the coupling of short wavelengths to lossy cladding-modes and compensate for any remaining spectral non-uniformity. Figure 2 shows a 8.5 nm 75 cm long chirped FBG made with an apodisation profile designed to counteract the effects of cladding-mode loss when the

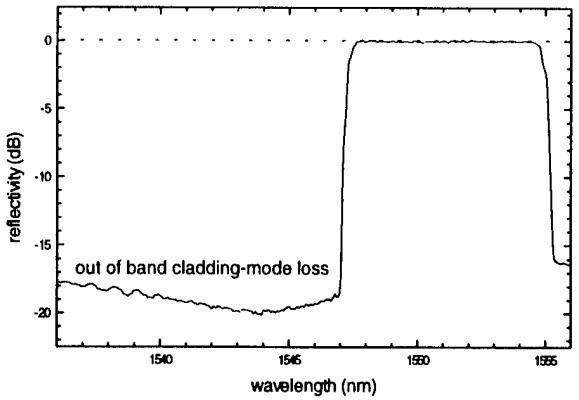

a) reflection form the short wavelength end showing the flat-top response of the grating without the effect of cladding-mode loss

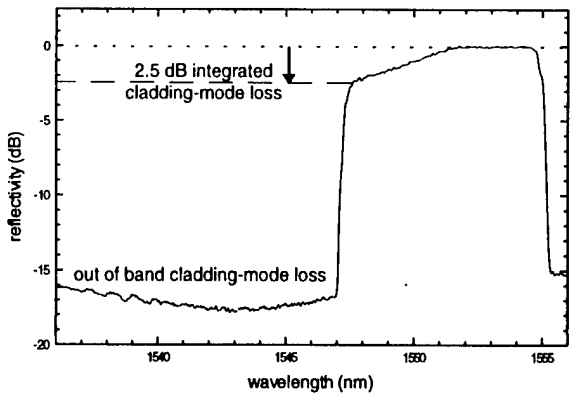

b) reflection from the long wavelength end showing the effects of integrated cladding-mode loss

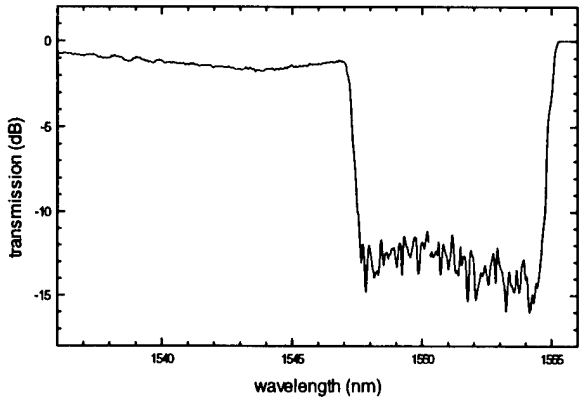

c) transmission spectrum of the grating

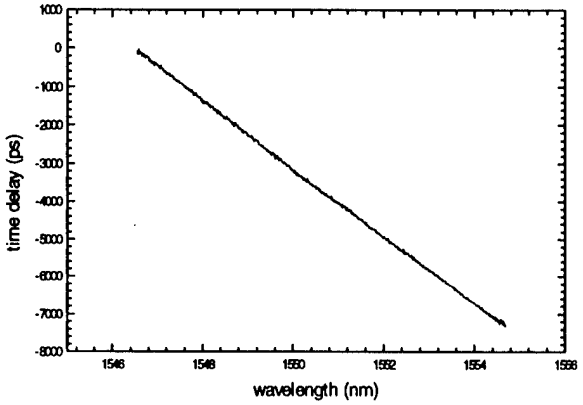

d) time delay from the long wavelength end

Figure 1. A 8.5 nm 75 cm long chirped FBG clearly shows strong cladding-mode losses when used in a negative dispersion sense (b) compared to the positive dispersion case (a).

grating is used in a negative dispersion sense; it is clear that the effects of short wavelength cladding-mode loss have been successfully equalised. This figure also confirms that the dispersion is not unduly affected when apodisation is used to locally vary the coupling constant of a grating.

The use of apodisation to vary the local coupling constant of the grating inevitably means that there will be a decrease of maximum reflectivity, but in many applications the demand for spectral uniformity outweighs the need for very low insertion losses. The fibre used in this experiment exhibited undesirably strong coupling to cladding-modes and hence the insertion loss of the spectrally-equalised device is more than would be ideal; the use of fibre with a higher N.A. or depressed cladding would help minimise this effect by suppressing the coupling to cladding-modes somewhat [4].

Summary

This demonstration of spectral equalisation of cladding-mode effects shows that the use of apodisation should not just be considered as a tool to reduce unwanted coherence effects, but rather as a method of tailoring the spectral response of FBGs without affecting their dispersion. The successful flattening of a broad-band chirped FBG will be crucial for dispersion compensation in fibre link where there is either significant drift of the carrier wavelength or several WDM channels. The application of apodisation to spectral shaping is not just limited to this example and, by the time of the conference, the authors hope to show spectral flattening of FBGs designed for combined 2nd and 3rd order dispersion compensation [5], and also FBG devices for combined dispersion compensation and EDFA gain flattening.

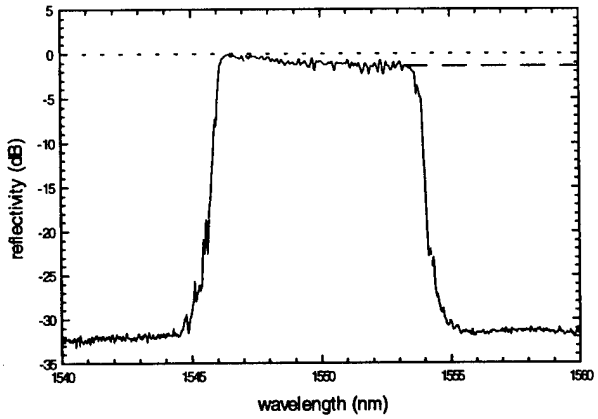

a) reflection from the long wavelength end showing the shape of the grating without the effect of cladding-modes

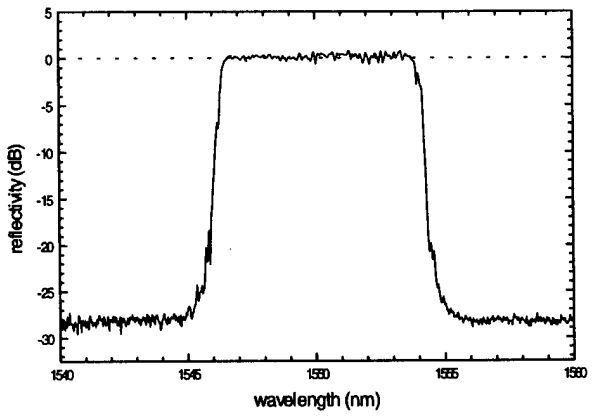

b) reflection from the short wavelength end showing that the effects of cladding-mode loss have been equalised

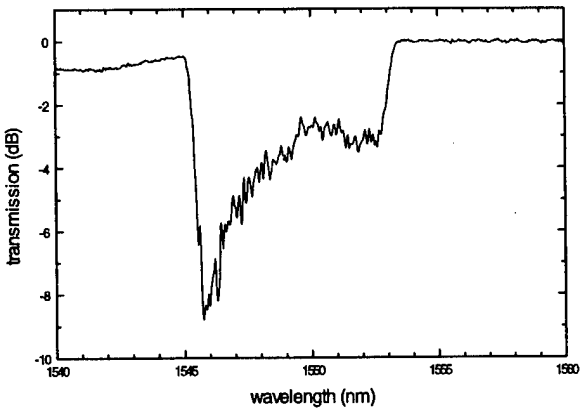

c) transmission spectrum showing the profile of the grating

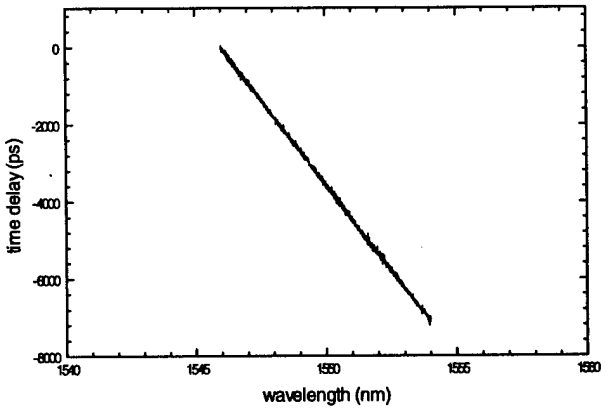

d) time delay from the long wavelength end

Figure 2. A chirped FBG fabricated with an apodisation profile designed to compensate for the effects of cladding-modes can be seen to have a flat reflection spectrum when used in a negative dispersion sense (b). The shaping of the grating is evident when viewed it transmission (c) and the dispersion is still clearly linear (d).

References

1. Hill, K. O., Bilodeau, F., Malo, B., Kitagawa, T., Therlault, S., Johnson, D. C., and Albert, J., 'Chirped In-Fibre Bragg Gratings for Compensation of Optical-Fibre Dispersion', *Optics Letters,* 1994, **19**, (17), pp. 1314-1316

2. Dong, L., Cole, M. J., Ellis, A. D., Durkin, M, Ibsen, M., Gusmeroli, V., and Laming, R. I., '40 Gbit/s 1.55 μm Transmission Over 109 km of Non-Dispersion Shifted Fibre with Long Continuously Chirped Fibre Gratings', *Proc. OFC'97*, PD6, San Jose, USA, 1997

3. Cole, M. J., Loh, W. H., Laming, R. I., Zervas, M. N., and Barcelos, S., 'Moving Fibre/Phase Mask Scanning Beam Technique for Enhanced Flexibility in Producing fibre Gratings with Uniform Phase Mask', *Electronics Letters*, 1995, **31**, (17), pp. 1488-1490

4. Dong, L., Reekie, L., Cruz, J. L., Caplen, J. E., de Sandro, J. P., and Payne, D. N., 'Optical Fibers with Depressed Claddings for Suppression of Coupling into Cladding Modes in Fiber Bragg gratings', *IEEE Photonics Technology Letters*, 1997, **9**, (1), pp. 64-66

5. Durkin, M. K., Ibsen, M., Cole, M. J., and Laming, R. I., '1m Long Continuously Written Fibre Bragg Gratings for Combined 2nd and 3rd Order Dispersion Compensation', *submitted to Electronics Letters April 1997*

Long Period Gratings Formed in Depressed Cladding Fibres

Liang Dong, Laurence Reekie and Jose L. Cruz

Optoelectronics Research Centre,
The University of Southampton,
Southampton SO17 1BJ, UK.
Tel: +44 1703 593163, Fax: +44 1703 593149
Email: ld@orc.soton.ac.uk

There has been a significant interest in long period gratings, primarily due to their applications in gain-flattened erbium doped fibre amplifiers [1]. Up till now, cladding modes supported by the glass-air interface of an optical fibre have been used in a forward mode coupling scheme involving also the guided fundamental mode of the optical fibre. Here we propose an alternative technique. In a single mode depressed cladding fibre of an appropriate design (an example is given in fig.1), the higher order LP11 mode can be made to be a leaky mode in such a structure, i.e. it can propagate for a short length before being stripped off the high index region beyond the depressed cladding. This enables coupling between the guided fundamental LP01 and leaky LP11 modes, despite the fact that the optical fibre is single-moded. This coupling was first observed in [2], where a Bragg grating caused strong coupling into the backward-propagating leaky LP11 mode and much weaker coupling into a series of cladding modes. In a forward coupling scheme with a long period gratings (several hundred micrometres pitch), the LP01 mode can be coupled into the forward propagating leaky LP11 mode, therefore creating a loss peak in the transmission in the same way as when the LP01 mode is coupled into a cladding mode supported by the glass-air interface of the optical fibre which is subsequently stripped off over the coated section of the optical fibre. Two advantages are anticipated, I) potentially much stronger coupling due to the much large modal overlap possible and II), insensitivity to the glass-air interface as the LP11 mode is supported mainly by the core. It must be stressed that as the LP11 mode is an asymmetrical mode, the coupling from LP01 to LP11 will not occur if a circularly

symmetrical grating is written over the core of the fibre, but this is not usually a problem when H_2 or D_2 loading is used, because of the asymmetry of the index change in such gratings due to strong absorption induced at the writing wavelength.

In the design in fig.1, the core will support two modes at 1.55 μm if the depressed region extends all the way to infinity. The presence of the high index region beyond the depressed cladding will strip off the higher order LP11 mode over a short length of fibre. The length over which the LP11 mode will propagate can be controlled by varying the normalised wavelength of the core and the thickness and depth of the depressed cladding, In general, the coupling between the LP01 and LP11 modes can be enhanced by having a large normalised wavelength for the core while keeping the structure single-moded. Also shown in fig.1 is the index profile in a grating written by a 248 nm KrF excimer laser. Such a structure has also been used to demonstrate suppression of coupling into cladding modes [3].

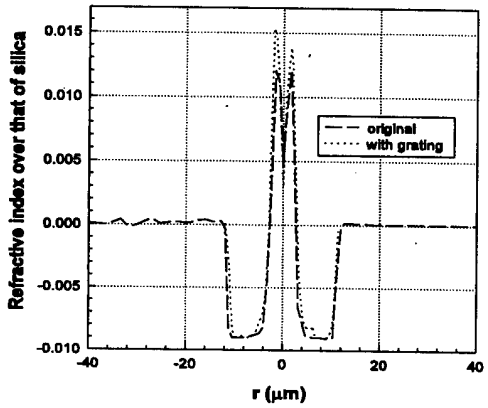

Figure 1 Index profile of a depressed cladding fibre.

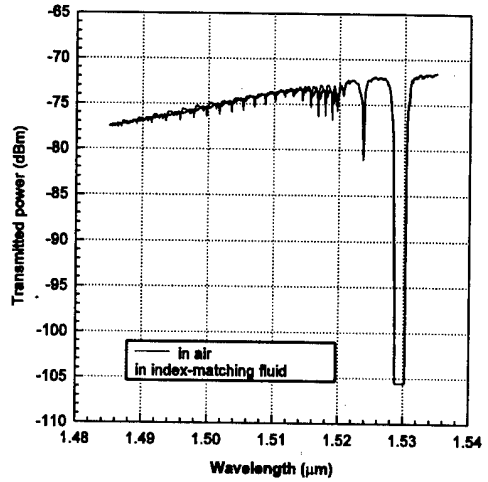

Figure 2 Transmission of a Bragg grating in a depressed cladding fibre.

To demonstrate the two advantages of the LP01/leaky LP11 coupling, a strong Bragg grating was written in a fibre with a similar refractive profile as in fig.1 but 1.26 times larger in

overall dimension. This gives a measured cutoff wavelength of 1.47 μm compared to the 1.16 μm measured in the fibre in fig.1, using a standard bending technique (5 cm diameter). The fibre has a germania doped core and a boron doped depressed cladding. The fibre was H_2-loaded before a grating was written by a ArF excimer laser at 193 nm. Two transmission curves are shown in figure 2. One curve was taken while the fibre was in air and the other was taken while the fibre was in a silica-index matching fluid (n=1.452 at 633 nm). Immediately to the shorter wavelength side of the main Bragg grating band is the peak caused by coupling from LP01 mode to the leaky LP11 mode. Further to the short wavelength side are the coupling peaks caused by coupling from the LP01 mode to the cladding modes supported by the glass-air interface. The thicker line is the transmission taken while the fibre was in index-matching fluid. As can be seen, the coupling peaks for the cladding modes in the index matching fluid case are reduced due to a decrease in guidance and the peak wavelengths move towards longer wavelength due to an increase of the modal effective refractive index. Meanwhile, the peak for coupling into the LP11 mode is not affected by the changing environment of the fibre, strong evidence that this mode is a core mode which has virtually no power distribution at the glass-air interface of the fibre. Coupling into the leaky LP11 mode is also very much stronger than the strongest peak for the cladding mode coupling, ~5 dB in this case. Coupling into the leaky LP11 mode can be further improved by having a grating with strong non-circular symmetry and appropriate fibre design.

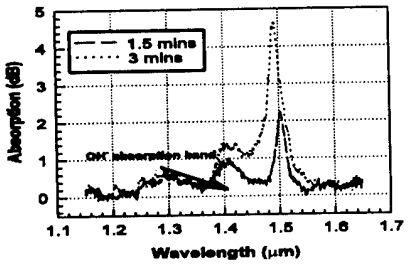

Figure 3 Growth of a long period grating in a depressed cladding fibre.

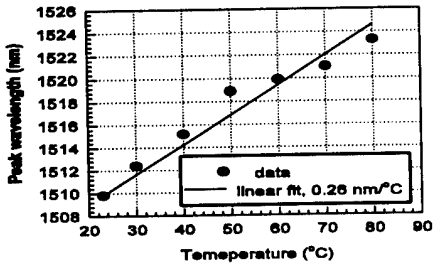

Figure 4 Temperature sensitivity of a long period grating in a depressed cladding fibre.

A long period grating was written into the fibre used above to demonstrate this method. The fibre was H_2-loaded before a ~2 cm grating was written by a 193 nm ArF excimer laser using an amplitude mask. The transmission of the fibre was monitored and then translated into absorption. This is plotted in fig.3. The temperature sensitivity of the grating is also measured and plotted in fig.4. The sensitivity was measured to be 0.26 nm/°C for this grating. This is typical for long period gratings.

To summarise, we have demonstrated a new method for use in long period gratings, which has enhanced coupling strength and is insensitive to the fibre glass-air interface.

Reference:

1. A.M. Vengsakar, J. R. Pedrazzani, J.B. Judkins and P.J. Lemaire: "Long-period fibre gratings based gain equaliser", Optics Letters, **21**, pp.336-338, 1996.

2. S.J. Hewlett, J.D. Love, G. Meltz, T.J. Bailey and W.W. Morey: "Cladding-mode coupling characteristics of Bragg gratings in depressed cladding fibre", electronics Letters, **31**, pp.820-822, 1995.

3. L. Dong, L. Reekie, J.L. Cruz, J.E. Caplen, J.P. De Sandro and D.N. Payne: "Optical fibres with depressed claddings for suppression of coupling into cladding modes in fibre Bragg gratings", IEEE Photonics Technology Letters, **9**, pp.64-66, 1997.

Bragg Gratings, Photosensitivity, and Poling in Glass Fibers and Waveguides: Applications and Fundamentals

Joint Symposium on Vitreous Silica and Related Materials

Joint Session on Photoinduced Effects in Novel Materials

Monday, October 27, 1997

Koichi Awazu, Electrotechnical Laboratory
Presider

JMH
4:30pm–5:30pm
Auditorium

Photosensitivity of tin doped phosphosilicate glasses

P. V. S. Marques[a,b], J. R. Bonar[a], A. Glidle[a], A. McLaughlin[a],
A. M. P. Leite[b], J. S. Aitchison[a]

a) Dept. of Electronics and Electrical Engineering, University of Glasgow
Glasgow G12 8QQ, Scotland, UK
Tel: +44 141 339 8855 Fax: +44 141 330 4907
b) Centro de Física do Porto, Rua do Campo Alegre, 687
4150 Porto, Portugal
Tel: +351 2 6082 623 Fax: +351 2 6082 679

In recent years, there has been a great deal of research into development and application of photosensitive glasses. The changes in refractive index due to the UV exposure has been used for Bragg gratings [1], optical trimming [2] and direct writing of channel waveguides [3]. In particular, Bragg gratings have numerous applications such as narrow-band reflectors for fiber and waveguide lasers, add-drop multiplexers, sensors and dispersion compensation devices.

The majority of this research has concentrated in germanium and germanium-boron doped glasses. However, when the final application demands co-doping with rare earth ions (RE), germanosilicate glasses are not ideal, since the solubility of RE is low in this host. A better host is achieved by doping the silica with phosphorus and small amounts of aluminium [4]; but it is well known that the presence of phosphorus bleaches the absorption band centred around 240 nm, and thus reduces the photo induced index change [5]. Gratings can be written into glass but require high pressure hydrogen loading and a short writing wavelength [6].

In this letter we report the absorption characteristics of tin doped phosphosilicate glasses produced by flame hydrolysis deposition and two different doping techniques - aerosol [7] and solution doping [8].

For aerosol doping a modified four port torch was used, with $SiCl_4$ and $POCl_3$ fed through a common port. An aqueous solution of tin chloride was nebulized in a pneumatic atomizer, using N_2 as the carrier gas. The doping concentration was controlled either by changing the solution strength, or the N_2 flow rate. The advantage of this technique is that allows grow of the phosphosilicate host matrix and simultaneous doping, thus reducing the processing time. The glass was deposited directly onto the quartz substrate and subsequently consolidated at a temperature of 1350 °C.

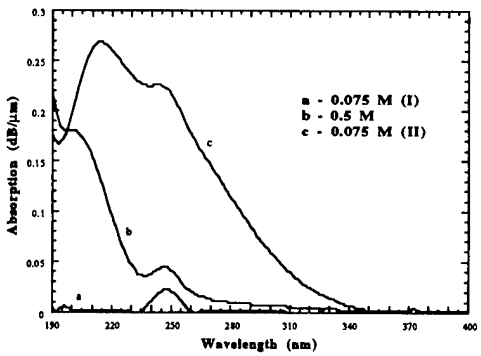

Fig. 1 - Absorption measurements for tin doped phosphosilicate glasses using aerosol doping.

Figure 1 illustrates a typical absorption spectra at short wavelengths for 4.7 μm thick layers. Spectras a) and b) were obtained from different concentrations (0.0075M and 0.5M, respectively) using the same N_2 flow rate (1.8 l/min) to the pneumatic atomizer. Spectra c) was obtained from a 0.075M solution concentration but with an increased N_2 flow rate of 2.8 l/min. The deposited film that corresponds to curve c) exhibits macroscopic clusters on a large scale. The increase in clustering was attributed to the increase of reactants carried to the torch and the associated decrease in flame temperature. It is interesting to note that the absorption spectra have a well defined band around 248 nm similar to the case of germanium doped glass [2] or germanosilicate glasses co-doped with tin [9]. However, Dong et al do not refer this band in phosphosilicate tin doped glass [10]. The optical quality of the films was characterised using prism coupling. The lowest amount of scattering was observed in film a) and the highest in c).

It was noticed that solutions obtained by dissolving tin chloride in water developed precipitates and ageing is quite evident turning the solutions from white to a brown colour. We attribute this to the formation of oxidised Sn^{II} and Sn^{IV} species within the precipitate. This was more evident for stronger concentrations.

Waveguides were defined using photolithography and reactive ion etching. A grating was written using a KrF excimer laser (248 nm) and a quartz phase mask. The reflection band had two peaks, both having a reflectivity of 30%. We attribute the low individual reflectivity and the two peaks to the fact of the waveguides supported two guided modes.

A similar planar sample was exposed to a KrF excimer laser (500 mJ per pulse, 30 Hz for 5 minutes) and the absorption increased for shorter wavelengths around 200 nm but the 248 nm was bleached.

Hydrogenation, using flame brushing, was used in a sample doped from a 0.5M solution, using a oxy-hydrogen flame for 12 minutes. It was clear the increase in the absorption, specially at shorter wavelengths.

Due to the problems of solution stability due to the reactions of tin chloride with water, a solution doping technique was tested using ethanol as a solvent. After the immersion on the respective solutions the samples were dried and a second step of sintering was carried out in order to compact the deposited layers. A batch of samples was prepared using a range of solutions strengths and the same immersion time. The phosphosilicate layer were deposited and partially fused in order to have some mechanical strength that allows the soot to stand the doping process. In this case the doping level depends on solution strength, immersion time and degree of porosity after the first sintering stage. One of the samples was not doped with tin and was used as a reference for the absorption measurements. Even for the low solution strengths used it was clear that the doping levels were quite high. For higher doping levels the losses increased and for the samples obtained from the two strongest solutions a white appearance was noticeable. However, the macroscopic clustering was not evident. That means that under the experimental conditions used solution doping is more efficient than aerosol doping.

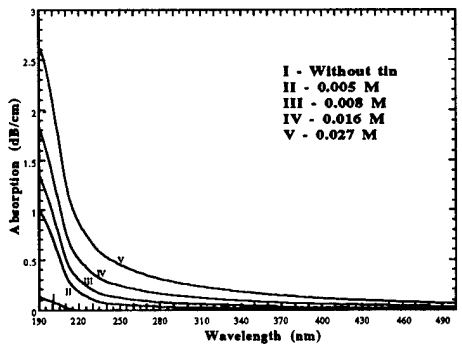

Fig. 2 - Absorption of thin doped planar samples using different doping solution strengths.

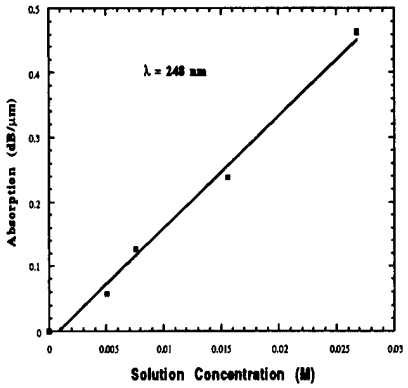

Fig. 3 - Changes of absorption as a function of the doping solution concentration at 248nm.

The results show that the band around 248 nm was not present (figure 2) in agreement with results published by Dong et al [10], and the absorption is proportional to the doping solution concentration. In order to determine the species within the glass that gives rise to this band will be necessary to have some chemical analysis using XPS.

Conclusions

Two doping methods have been used to produce photosensitive phosphosilicate tin doped glass using flame hydrolysis deposition. Solution doping proved to be the best doping method from the two, allowing high tin concentrations without macroscopic clustering formation. Currently we are producing samples with lower tin concentrations to give an optical loss figure and for testing gratings formation in channel waveguides. Quantitative material analysis is desirable, XPS for example, in order to interpretate and associate the material characteristics with the measured absorption bands.

References:

[1] - K. O. Hill et al., Appl. Phys. Lett., vol. 32, No. 10, 647 (1978)
[2] - R. Kasyhap, G. D. Maxwell, B. J. Ainslie, Phot. Tech. Lett., 5 No. 2, 191 (1993)
[3] - M. Svalgaard et al., Elect. Lett., Vol. 30, No. 17, 1401 (1994)
[4] - K. Arai, H. Namikawa, K. Kumata, T. Honda, J. Appl. Phys., 59 (10), 3430 (1986)
[5] - L. Dong, J. Pinkstone, P. Russell, D. N. Payne, J. Opt. Soc. Am. B, 11, 2106 (1994)
[6] - T. Kitagawa et al., Tech. Dig. Opt. Fiber Commun., Paper PD17, 1994.
[7] - J. A. Bebbington et al., Appl. Phys. Lett., 62 (4), 337 (1993)
[8] - J. E. Towsend, S. B. Poole, D. N. Payne, Elec. Lett., Vol. 23, No. 7, 329 (1987)
[9] - L. Dong et al., IEEE Phot. Tech. Lett., Vol. 7, No. 9, 1048 (1995)
[10] - L. Dong. et al., Opt. Lett., Vol. 20, No. 19, 1982 (1995)

Photoinduced integrated optical devices in sulfide chalcogenide glasses

J.-F.Viens, A.Villeneuve, T.Galstian, M.A.Duguay
Centre for Optics, Photonics and Lasers (COPL), Université Laval,
Ste-Foy, Quebec, Canada G1K 7P4.
Tel: 418-656-3568, Fax: 418-656-2623, email: avillene@phy.ulaval.ca

K.A.Cerqua-Richardson, S.Schwartz
CREOL, University of Central Florida, Orlando, USA 32826.

Chalcogenide glasses are known to be optically highly transmitting in the 1-10 μm wavelength region and to have applications in both communication and mid-IR optical systems. Arsenic (S,Se)-based chalcogenide glasses also exhibit a wide variety of photostructural effects. Photostructural changes in amorphous chalcogenides are induced by exposing the material to near bandgap light. Such changes, among others, can be structural [1,2] (e.g. change in the density, photoexpansion) or optical [3] (e.g. photodarkening, refractive index change). Thin films of As-S-(Se) also exhibit photoinduced volume effects similar to those seen in bulk materials. This fact makes the application of the chalcogenide glass films to guided wave optical devices, very attractive. With suitable bandgap light exposure techniques, a variety of photoinduced integrated optical components can be patterned on thin films of chalcogenide glasses.

Two different glass compositions were used for our experiments, namely As_2S_3 and $As_{24}S_{38}Se_{38}$. These chalcogenide materials were selected according to their optical transparency and their large optical nonlinearity [4]. The refractive index at 1.55 μm and the bandgap values of these glasses are 2.4, 2.5, and 2.35 eV, 2.1 eV respectively. The low bandgap value makes the glasses optically opaque to visible light. To make use of the photosensitivity of these glasses, the thin films can be exposed with visible light lasers, such as an Ar ion laser working at a wavelength of 514 nm, closely matching the bandgap of the materials.

The chalcogenide glass thin films were prepared by thermal deposition onto unheated silicon wafers or Corning 7059 SiO_2 glass slides, and subsequently annealed at 130°C for two hours. A 2 μm thick SiO_2 layer on the Si wafers provided a suitable cladding between the high refractive index of the substrate and the chalcogenide films. The wafers were then cleaved to obtain good facet quality, suitable for efficient endfire coupling. There were no further treatments of the films after the laser exposures.

In order to determine the energies to be used for the laser beam exposure, we performed real-time transmission measurements of a 1.5 μm thick As_2S_3 thin film, as it was subjected to photodarkening during laser exposure. The film was deposited on a transparent SiO_2 glass slide and a Si photodiode monitored the intensity of the transmitted writing beam. Figure 1 shows the increase of absorption of the film with increasing exposure energy, up to a saturation level which depends on the exposition wavelength. One consequence of the increase in absorption of the glass is suggested by the connection between absorption coefficient and index of refraction through the Kramers-Kronig relation. Namely, photodarkening is accompanied by a change in refractive index. According to [3], the refractive index change amounts to about +0.1 in As_2S_3 glass when exposed at 514 nm. Figure 1 also suggests that an index change can be induced, to a lesser extent, by illumination with laser wavelengths in the range 514-632 nm. The photodarkening dynamics of the $As_{24}S_{38}Se_{38}$ glass is quite similar to that of the As_2S_3 glass. However, when scalar holographic gratings are written on such films at 514 nm, we observe that the writting beam is more efficiently diffracted in the As_2S_3 glass in comparison to the $As_{24}S_{38}Se_{38}$ glass (figure 2). This suggests that the refractive index change is much lower in the As-S-Se glass. This may be

due to the fact that arsenic concentration in the material plays a role in the extent of photostructural change in the chalcogenide [3], in which an increase of As concentration increases the photosensitivity.

A channel waveguide can easily be fabricated in the chalcogenide film by laser beam exposure at 514 nm. We used a cw Ar laser at 10 mW, and we stretched the beam profile with a cylindrical telescope to cast a long, thin line of light on the films (3 cm x 25 μm). Figure 3 shows the endview output of a 2-cm long As_2S_3 waveguide before and after a 20 second Ar-beam exposure. Light at λ=1.3 μm is confined in the exposed channel. The propagation loss in this As_2S_3 photoinduced waveguide has been measured at 0.9 dB/cm at 1.3 μm, while the $As_{24}S_{38}Se_{38}$ photoinduced waveguides exhibits losses of about 2 dB/cm.

The depth of penetration of a 514 nm beam in the As_2S_3 material is about 30 μm. This value is much larger than the typical thickness of a single-layer waveguide, which is about 2 μm. This enables us to write structures in thicker layers. From this characteristic, we performed Ar laser beam exposures on stacked chalcogenide planar waveguides. The multi-layer structure was composed of 2 μm thick $As_{24}S_{38}Se_{38}$ guiding regions and 3 μm thick As_2S_3 claddings, successively deposited on each other on the same wafer during thermal evaporation. Annealing and cleaving were done as before. Figure 4 shows the double core waveguide output before and after laser beam exposure. Here again, light is confined in the exposed As-S-Se regions and the propagation losses were measured to about 2 dB/cm at λ=1.3 μm. The top view picture of the waveguide (Figure 5) clearly shows the coupling behavior of the light between the two photoinduced cores, hence producing a vertical coupler. The coupler's beating lengths ranged from 2.5 to 5 mm for wavelength of 0.82 to 1.58 μm respectively. Thus, the photosensitivity of the chalcogenide glasses opens new possibilities of fabricating compact integrated devices with optical routing in 3-D space. Easy processing and low fabrication costs are some of the advantages of these optical devices.

In conclusion, we have demonstrated that laser beam writing in arsenic (S,Se)-based chalcogenide glasses makes an attractive and efficient way of fabricating guided wave integrated optical devices. It offers new possibilities of fabricating multi-layer integrated optical devices.

References

[1] S.Ramachandran, S.G.Bishop, J.P.Guo, D.J.Brady *"Fabrication of holographic gratings in As_2S_3 glass by photoexpansion and photodarkening"*, IEEE Photonics Technology Letters, Vol 8, No 8, August 1996.

[2] T.Galstian, J.-F.Viens, A.Villeneuve, M.A.Duguay, K. Richardson, *"Combined relief and volume gratings in thin film As_2S_3 chalcogenide glass"* To be published in Journal of Lightwave Technology, August 1997

[3] A.Zakery, P.J.S.Owen, A.E.Owen, *"Photodarkening in As-S films and its application in grating fabrication."*, J. Non-Cryst. Sol., 198-200 (1996) 769-773

[4] K.A.Cerqua-Richardson, J.M.Mckinley, B.Lawrence, A.Villeneuve, *"Comparison of nonlinear optical properties of sulfide glasses in bulk and thin film form."*, Submitted to J. of Optical Materials.

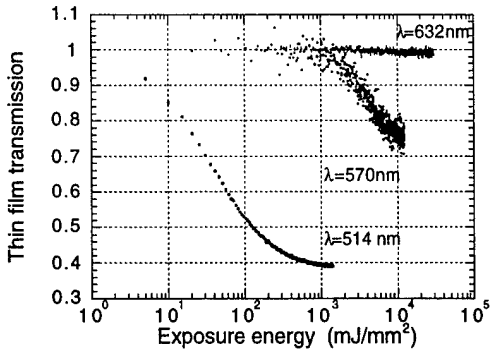

Figure 1: Change of the optical transmission of a 1.5 μm As_2S_3 glass film during laser exposure at 514, 570 and 632 nm. The extent of photo-darkening depends on the exposure energy and the wavelength.

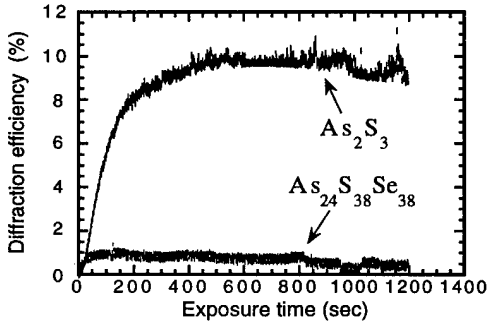

Figure 2: Efficiency of the diffracted writing beam during a scalar hologram exposure using a 10mW Ar laser at 514 nm and 1.5 μm glass films. The diffraction efficiency is one order of magnitude larger in the As_2S_3 glass in comparison to the $As_{24}S_{38}Se_{38}$ glass.

Figure 5 (right): Topview of the photo-induced double core waveguide, showing the vertical coupling process between the two cores. The light at 1.3μm is injected at bottom, and the guide is 12 mm long. The beat-length is 4.7 mm, which means a difference of refractive index of 0.025 between the core and the cladding.

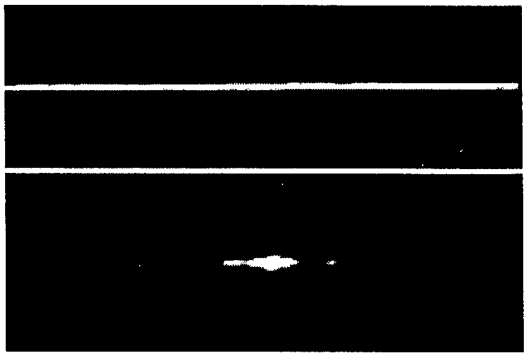

Figure 3: Endview output of a photoinduced As_2S_3 waveguide before (top) and after (bottom) the 20-sec 10 mW Ar laser exposure. The light is confined in the exposed region, thus channeling the waveguide. The guided light is at λ=1.3μm, lateral confinement is 15 μm.

Figure 4: Endview output of a photo-induced, double core $As_{24}S_{38}Se_{38}/As_2S_3$ waveguide before (top) and after (bottom) the 150-sec 10 mW Ar laser exposure. The light at λ=1.3 μm is confined laterally by 25 μm in the As-S-Se regions.

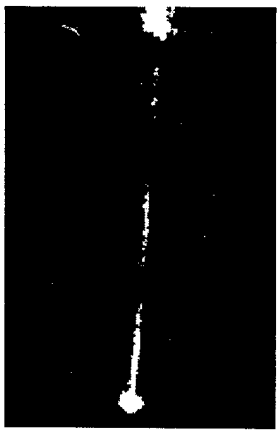

Temperature dependence of UV-induced defects in thulium-doped ZBLAN fibers

Pierre Laperle, Réal Vallée, Alain Chandonnet†, and Sophie LaRochelle

Centre d'optique, photonique et laser, Université Laval
Ste-Foy, Québec, G1K 7P4, Canada
Tel.: (418) 656-2698, FAX: (418) 656-2623

†*Institut national d'optique*
369 rue Franquet, Ste-Foy, Québec, G1P 4N8, Canada
Tel.: (418) 657-7006, FAX: (418) 657-7009

Introduction

The thulium-doped ZBLAN fiber has been identified as a promising candidate for the generation of coherent blue radiation.[1] Yet Tm-ZBLAN blue fiber lasers have been shown to suffer from a progressive deterioration of their performances as they operate for several hours, apparently because of an increase in the absorption of the fiber at the laser wavelength. This problem, which has been clearly observed with a pumping source at 1.12 μm, is thought to be related to the formation of defect centers induced by UV radiation generated as a by-product of the upconversion process occuring in the thulium ions.[2,3] The induced absorption can be bleached by exposure to visible light. However, the observed photobleaching is only temporary and a permanent recovery of the pristine condition of the glass can only be achieved by a thermal treatment. Moreover, the darkening as well as the bleaching processes taking place in these fibers have been shown to be well described by stretched-exponential (S-E) functions.[4] Thus, it appears that a better understanding of these defects, which is crucial for the development of practical Tm-ZBLAN blue fiber lasers, relies on the study of their UV-induced formation as well as their temperature dependence. We report on these two mechanisms and, through an S-E analysis of the temperature dependence of the defects, show to what extent they are related.

Direct UV irradiation

A frequency doubled (R6G) dye laser tunable from 280 to 305 nm and an UV argon laser were used to end-pump one sample of 70 cm of a Tm(1000 ppm)-ZBLAN fiber. The thulium was excited directly to the $^1I_6$ level with 285-nm light and to the $^1D_2$ level with 351 or 364-nm light. Once excited, the thulium ions produced fluorescence bands peaking in the UV at 290, 351, 363 nm and in the visible at 455, 482, 514, and 650 nm. In addition, the Tm-ZBLAN fiber was exposed to 300-nm light, a wavelength which is not resonant with the Tm^{3+} energy levels.

The results of the exposures at the different wavelengths are summarized in Table 1 and show that absorption is induced whether the radiation is resonant or not with the thulium ions. This suggests that the detrimental effects associated with thulium are mainly arising from the UV light that is produced by these ions. From the above results the possibility that the incorporation of the thulium ions in the glass matrix might have other effects on the formation of defects cannot be completely ruled out but is certainly not of major importance. Another interesting observation is that the UV light did not produce any detectable absorption during the exposure. However, as soon as the UV light was blocked, absorption started to grow up and reached an asymptotic value after $\sim$72 hours at room temperature. Such a behavior clearly suggests that the UV light is creating defect centers but simultaneously bleaches them. This is in sharp contrast to what has been observed with pump beams at 1.12 μm.[2,3]

Table 1: Parameters related to the UV-induced absorption in Tm-ZBLAN fibers.

Thulium (ppm)	λ_{pump} (nm)	$Power_{incident}$ (mW)	$Time_{exposure}$ (hrs)	λ_{probe} (nm)	Absorption (dB)	Length (cm)
1000	285	6	1	514	1.4	70
1000	300	6	1	514	1.7	70
1000	351	18	1/2	514	3.6	70
1000	364	18	1/2	514	1.5	70

Temperature dependence of the induced-absorption

To illustrate the transient behavior of the photobleaching as well as the thermal annealing of the photo-induced absorption the following experiment was performed. A first sample of 37 cm of a Tm(1000 ppm)-ZBLAN fiber was exposed to a saturating power level of 700 mW at 1.12 μm resulting in a uniform induced absorption of 85% at 514 nm (measured with a low intensity probe). (Note that with a pump at 1.12 μm the UV photons resulting from upconversion darken the fiber but do not simultaneously photobleach it as was observed to be the case for direct UV irradiation.) The fiber was then heated to 398 K for several hours. A second fiber was darkened in the same manner but subsequently photobleached with a high intensity beam at 514 nm prior to the heat treatment. Fig. 1 shows the time evolution of the induced absorption (normalized to the initial absorption after darkening) of both samples during the heat treatment. The main observation is that both fibers appear to reach the same asymptotic value which suggests that a definite number of defects are removed at a given temperature, irrelevant of the photobleaching. The experimental data in both cases are well fitted by stretched-exponential functions of the form:

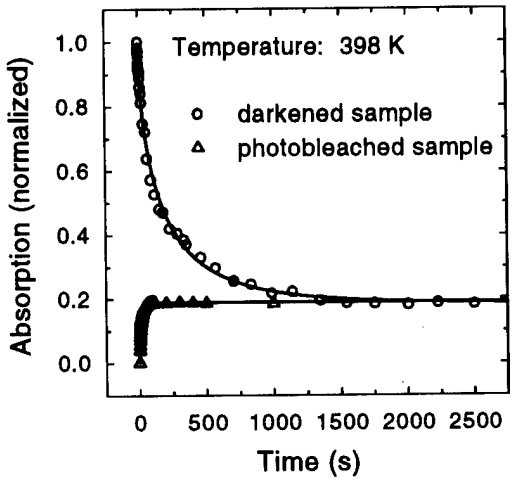

Figure 1: Absorption of a darkened and photobleached Tm-ZBLAN fiber heated to 398 K as a function of time.

$$A(t) = \alpha + (1-\alpha)\exp\left[-(t/\tau)^{\beta}\right] \quad \text{[darkened sample]} \tag{1}$$

$$A(t) = \alpha - \alpha\exp\left[-(t/\tau)^{\beta}\right] \quad \text{[photobleached sample]} \tag{2}$$

where $A(t)$ is the normalized absorption, β is the stretch parameter, τ is the time constant, and α is the normalized absorption at $t \to \infty$.

The same experiment was performed at eight other temperatures in the range 296 to 460 K. The dependence on temperature T of the S-E parameters is illustrated in Fig. 2. The stretch parameter is shown to be the same for both darkened and photobleached fibers and is found equal to $\beta = 0.0016T$. Of particular interest is the fact that the same parameter β which was found previously to be independent of both the exposure intensity and thulium concentration,[4] appears now to depend on the temperature. The inverse time constant is found to be $1/\tau = 7.0 \times 10^{-15}\exp(0.069T)$ for darkened samples and $1/\tau = 9.4 \times 10^{-14}\exp(0.069T)$ for photobleached samples. One notes that although the photobleached sample seems to recover more rapidly (Fig. 1), the argument of the

exponential terms is the same for both samples. It is also interesting to note that β and τ show similar temperature dependences as those previously reported for Ge-defect centers in silica glass fibers.[5] Finally, Fig. 2(c) shows that different asymptotic values of absorption (α) are reached at different temperatures.

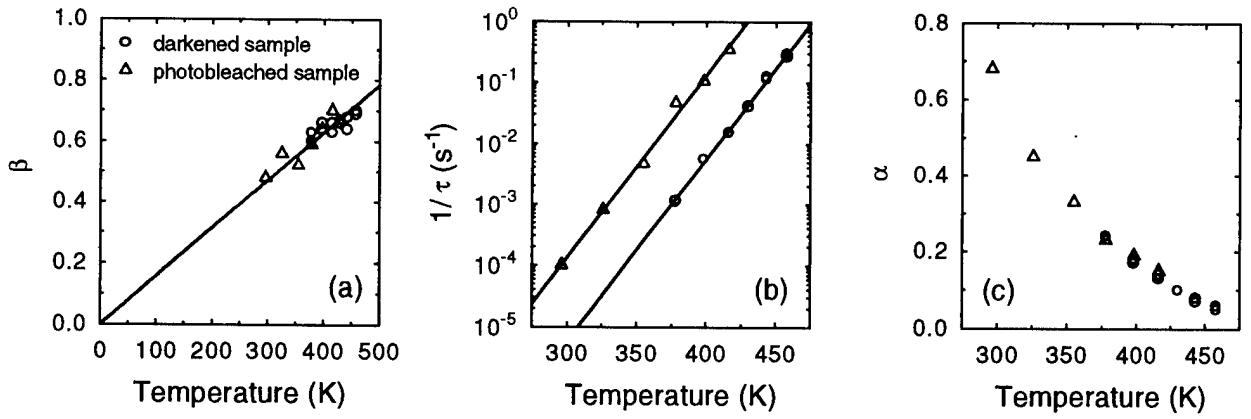

Figure 2: Dependence of β, τ, and α on the temperature.

Discussion and Conclusions

Following exposure to direct UV radiation, ZBLAN fibers exhibit a broadband increase of their absorption. This photo-induced absorption was not found to be significantly enhanced by resonant excitation of Tm^{3+} ions. No real-time absorption change could be measured while the UV radiation was present in the fiber, which suggests that the defect centers are simultaneously photobleached. This was not observed in fibers exposed to so-called indirect UV irradiation produced by thulium ions excited using 1.12 μm. The different dynamics observed in the defect center formation could be related to the presence of the infrared radiation, but the exact contribution of the infrared light to these processes has yet to be determined.

The induced absorption produced by UV or near-infrared irradiation is observed to be modified by photobleaching and thermal annealing. Photobleaching temporarily restores the transmission of the fibers but the defect center populations created during the darkening process eventually recover to their equilibrium level. In fact, in every cases the steady-state absorption depends on the fiber temperature only. This suggests that the defects are characterized by broadband energy distributions and can be partially annealed (up to a certain level which depends on the temperature) by thermal activation. Permanent annealing of the fibers can therefore only be obtained by heating them to moderate temperatures in order to remove most of the defects without altering the glass structure (~200 °C in our case). Furthermore, the annealing dynamics of the darkened and photobleached samples show similar temperature dependence as described by the parameters of their stretched-exponential functions. These observations suggest that a charge transport model may possibly be applied to the defects created in ZBLAN fibers.

References

1. S.G. Grubb, K.W. Bennett, R.S. Cannon, and W.F. Hummer, Electron. Lett. **28,** 1282 (1992).
2. P. Laperle, A. Chandonnet, and R. Vallée, Opt. Lett. **20,** 2484 (1995).
3. P.R. Barber, R. Paschotta, A.C. Tropper, and D.C. Hanna, Opt. Lett. **20,** 2195 (1995).
4. P. Laperle, A. Chandonnet, and R. Vallée, Opt. Lett. **22,** 178 (1997).
5. T. Erdogan, V. Mizrahi, P.J. Lemaire, and D. Monroe, J. Appl. Phys. **76,** 73 (1994).

The origin of photoinduced anisotropy in germanium sulfide based glasses.

V. Tikhomirov [a], P. Hertogen [a], V. Krasteva [b], G. Adriaenssens [a], G. Sigel [b].
[a]Halfgeleiderfysica, KU Leuven, B-3001 Heverlee, Belgium.
[b] Fiber Optics Materials Research Program, Rutgers University, Piscataway, NJ 08855, USA.

Metastable photoinduced anisotropy (PA) generated by linearly polarized sub-bandgap light in Pr-doped Ge-S-I glasses is reported. A PA minimum is observed in undoped $Ge_{34.5}S_{55.5}I_{10}$ composition. PA increases with S content in S-rich glasses. PA increases with Ge content at a constant I content in Ge-rich glasses, while addition of I at a constant S/Ge ratio in Ge-rich glasses decreases the PA. The addition of Pr to about 1000 ppm increases PA in Ge-rich glasses, if no Pr-clustering occurs. The explanation of these compositional trends is based on the coexistence of three different molecular phases (structural units) in these glasses, with their relative contribution varying with varying composition. Microscopic models are proposed for diamagnetic defect centers responsible for PA in S-rich, Ge-rich and stoichiometric glasses.

Photosensitive glasses are of interest for applications in waveguide devices and due to fundamental interest in microscopic mechanisms of photosensitivity. Knowledge of the microscopic mechanisms will allow improvement and optimization of such devices as Bragg-reflectors or rocking filters by a proper choice of glass materials. Metastable photoinduced anisotropy (PA) appears in all chalcogenide glasses [1], as well as in some oxide glasses [2 and ref's therein], after prolonged irradiation by linearly polarized light. The optical axis of PA is parallel to the electric vector of the inducing linearly polarized light [1,2]. Unpolarized light can also produce PA, but then the optical axis will be parallel to the wavevector of the inducing beam [3].

Currently it is necessary to develop rare-earth doped fiber amplifiers (using Pr) operating in the 1.3 μm telecommunication window. Most promising hosts for Pr are sulfide glasses transparent at pump and signal wavelengths. Interest in these glasses follows up to 80 %-efficient luminescence of Pr^{3+} dopants at 1.3 μm and possibility of their fiberization with small optical losses (~3 dB/m) [4].

In this paper we report on PA in undoped and Pr-doped Ge-S-I glasses with varying composition and Pr content. A model for the defect centers responsible for PA is suggested and discussed with respect to the variation of Ge/S ratio at constant I, to the variation of I content at constant Ge/S ratio, and to the variation of Pr content for constant host composition.

The procedure for preparation of Pr-doped Ge-S-I glassy rods is described in [4]. Techniques for measurements of photoinduced dichroism and birefringence, which are manifestations of PA, are described in [1,5].

Fig. 1 shows the dependence of the saturation value of photoinduced dichroism (α_z-α_x) versus parameter p=(y+z/2)/x in $Ge_xS_yI_z$ glasses. Kinetics of dichroism were shown in [5]. Compositional dependencies of the absorption edge and rare-earth solubility in these glasses can be represented with a single parameter p. Glasses with y/x>2 were considered as S-rich and with y/x<2 as Ge-rich ones [4]. Due to the relatively small concentration of iodine (<10 at.%), Ge-S-I glasses considered further can be regarded as a modification of the basic binary Ge_xS_y glasses. Parameter p characterizes the ratio between different molecular phases (structural units).

A typical build-up of photoinduced birefringence in Ga-modified S-rich glass is shown in fig.2.

An example of the effect of Pr content is shown in fig.3.

A microscopic model for PA was proposed [1], based on the intrinsic structurally bistable defect combinations of the valence-alternation pair (VAP's), such as $S_3^+S_1^-$ type, where S stands for a sulfur atom, while super and subscripts designate charge and coordination number of the respective atom.

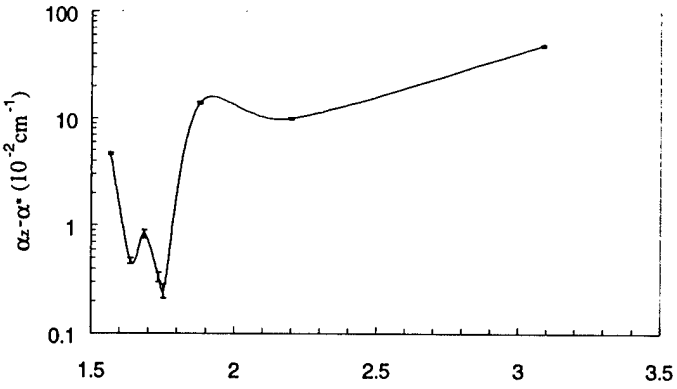

Figure 1: Saturation values of photoinduced dichroism vs $p=(y+z/2)/x$ in $Ge_xS_yI_z$ glasses. Absorption coefficients for inducing and probe beams were about 5 cm^{-1} due to proper choice of generation wavelength of He-Ne or Ar-laser.

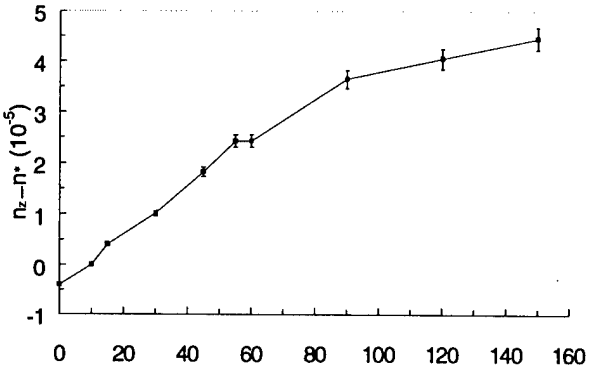

Figure 2: Kinetics of photoinduced birefringence in 1 cm thick bulk glass $Ge_{24.33}Ga_{0.99}S_{74.63}$ generated with an Ar laser beam (α=3 cm^{-1}, λ=515 nm, P=1.2 W/cm^2) and measured ellipsometrically with the unabsorbed beam of a He-Ne laser (λ=633 nm).

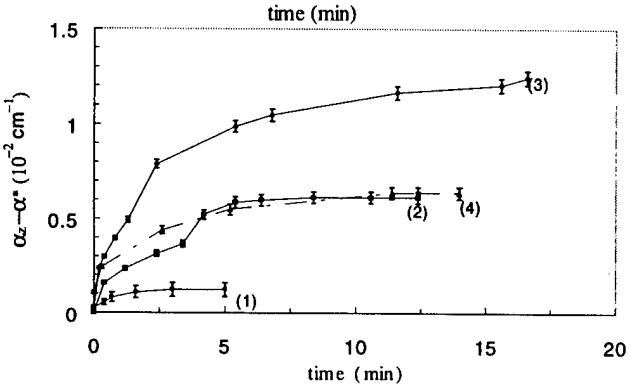

Figure 3: Kinetics of photoinduced dichroism in bulk glasses $Ge_{34.5}S_{55.5}I_{10}$ (p=1.75): (1) undoped, (2) doped with 500 ppm Pr, (3) doped with 1000 ppm Pr and (4) doped with 2000 ppm Pr. The dichroism was generated and measured with a He-Ne laser (λ=633 nm, P=200 mW/cm^2)

A diamagnetic pyramid $S_3^+S_1^-S_2^0S_2^0$ (fig.4a) can be used as the key structural element responsible for PA in S-rich glasses [1,5]. Optical excitation of a S_1^- electron and subsequent trapping of the electron by the positively charged S_3^+ nearby will produce an unstable $S_3^0S_1^0$ pair with an antibonding electron localized near the S_3^0 (shown by the dashed circle in fig.4a). It is seen that the pyramid $S_3^0S_1^0S_2^0S_2^0$ is unstable now, since (i) the antibonding electron weakens the bonds of the S_3^0 atom, (ii) the S_1^0 atom has only one (weakened) bond and no electrostatic forces as in the $S_3^+S_1^-$ case, and (iii) a void should exist near S_1^- atom to accord with its onefold coordination . This means that the S_3^0 atom can tunnel into a position S_{3m}^0 which is its mirror image with respect to plane defined by $S_1^0S_2^0S_2^0$ (shown by the dash-dot lines in Fig.4a), from where its antibonding electron can return to the S_1^0 atom, thus restoring the charged VAP, but with a modified direction of its dipole moment.

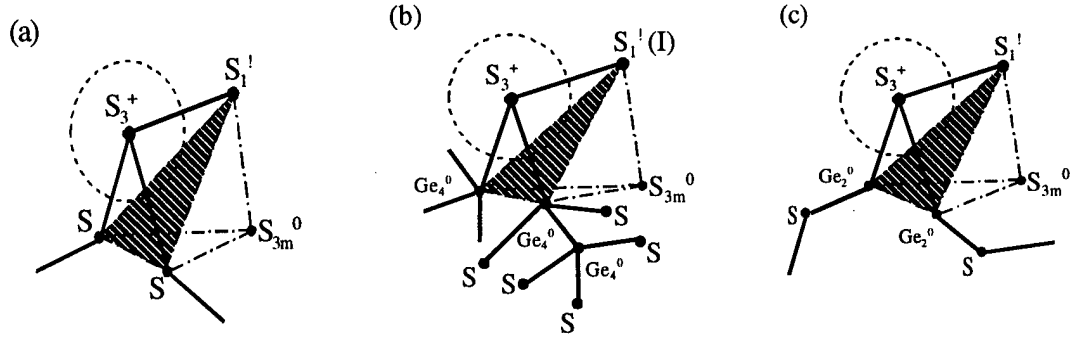

Figure 4: Model for PA in S-rich (a) , in stoichiometric (b) and Ge-rich (c) Ge-S-I glasses. Solid lines represent chemical bonds.

Consequently, the flip of the $S_3^+S_1^-S_2^0S_2^0$ pyramid is accompanied by a change of its anisotropy and chirality producing linear and circular dichroism/birefringence (observed in chalcogenide glasses [6]), respectively [1].

The PA centers in Ge-rich glasses would generally contain non-chalcogen atoms, as suggested in fig.4b, but would still have a $S_3^+S_1^-$ dipole as the crucial component. A shallow minimum of PA is observed around the stoichiometric composition, characterized by tetrahedral GeS_4 units (A-phase, p=2 [7]). This minimum can be due to increased rigidity of $S_3^+S_1^-Ge_4^0Ge_4^0$ pyramid (fig. 4b). A much more pronounced minimum is observed around $Ge_{34.5}S_{55.5}I_{10}$ which corresponds to B-phase characterized by ethane-like units [7] where Ge_4^0-Ge_4^0 bonds appear (fig.4b). In this case the pyramid $S_3^+S_1^-Ge_4^0Ge_4^0$ becomes even more rigid as compared to stoichiometric composition thus preventing PA.

The coordination (valence) of the Ge atom is changed from 4 (Ge_4^0) to 2 (Ge_2^0) in Ge-rich compositions [4], where rock-salt C-phase appears [7]. This explains the increase of PA with Ge-content in Ge-rich glasses when Ge_4^0 atoms are replaced by Ge_2^0 ones, allowing larger flexibility of the configuration illustrated in fig.4c, similar to that in S-rich glasses (fig.4a).

A deep minimum in fig.1 is splitted in two minima corresponding to I-rich (10 at.%) compositions, indicating that I influences VAP's, e.g. by substitution of S_1^- (fig. 4b) and decreasing dipole moments of centers responsible for PA. In contrast, Pr^{3+} increases PA (fig.3) indicating that positive Pr^{3+} ion, being placed close to negative S_1^-, increases VAP's dipole moments.

1. V.K. Tikhomirov, G.J. Adriaenssens and S.R. Elliott, Phys. Rev. B 55 (1997) R660
2. K.O. Hill, F. Bilodeau, B. Malo and D.C. Johnson, Electron. Lett. 27 (1991) 1548.
3. V.K. Tikhomirov and S.R. Elliott, Phys. Rev. B 49 (1994) 17476.
4. V. Krasteva, D. Hensley, and G. Sigel, J. Non-Cryst. Solids, at print.
5. V. Tikhomirov, V. Krasteva, P. Hertogen, G. Adriaessens, G. Sigel, J.Non-Cryst. Solids, at print
6. V. Tikhomirov and M. Chervinskii, Sov. Phys. Solid State 35, 566 (1993).
7. P. Boolchand, J. Groathaus, M. Tenhover, M.A. Hazle, and R. Grasseli, Phys. Rev. B 33 (1986) 5421

Bragg Gratings, Photosensitivity, and Poling in Glass Fibers and Waveguides: Applications and Fundamentals

WDM Applications

Tuesday, October 28, 1997

Gary Ball, Uniphase Telecom Products
Presider

BTuA
8:00am–10:15am
Room 18

Fiber Grating Devices for WDM Communication Systems

Thomas A. Strasser

Bell Laboratories, Lucent Technologies
600 Mountain Avenue, Murray Hill, NJ 07974, USA
Phone (908) 582-3894, Fax (908) 582-2559

Introduction

UV-induced fiber phase gratings [1,2] have become a very active area of research and development in recent years. This interest is in large part due to properties of these devices which make them an enabling technology for numerous high-performance devices. Perhaps the broadest range of devices developed to date is for fiber communications technology, where current and future devices will undoubtedly play a major role in implementing Wavelength Division Multiplexing (WDM) systems, as well as future, complex, optical networks based on such systems.

Fiber Grating Properties

A number of properties define fiber gratings as unique optical filtering devices. First and foremost is the integration of the device within the core of a fiber, making low-loss, low-cost, reliable interconnection with optical fiber systems a reality. Hydrogen-loading [3] can be utilized to sensitize virtually any fiber, enabling large index changes [>0.001] without special fibers, which is important to allow freedom to choose optimum device fibers for reasons other than UV-photosensitivity (*e.g.* low splice loss). The UV-induced index changes also add minimal insertion loss (~0.05 dB/cm @1.5 μm), have a low birefringence of 1-2% [4], and have excellent long term stability after appropriate annealing [5].

An additional advantage is a well-defined Bragg condition ($\lambda_B = 2\, n_{eff}\, \Lambda$), where the effective index of the fiber (n_{eff}), and the periodicity of the grating (Λ) are well controlled. This enables excellent wavelength accuracy and reproducibility. When this accuracy is combined with well-controlled UV exposure, it enables the fabrication of precise apodization profiles with corresponding reflection filtering characteristics that have significantly sharper spectral response than alternate technologies [6]. These apodized filters are critical to avoid Fabry-Perot resonances [7] which can severely degrade resonant signal channels incident in an Add/Drop filtering application.

Although the above advantages are described in terms of reflective Bragg gratings, similar advantages are shared for Long Period Gratings (LPGs). These gratings perform spectrally-selective coupling from a guided mode to lossy cladding modes [8], and have been employed extensively to produce flat-gain optical amplifiers. Their

primary advantage over Bragg gratings is a high return loss, an important characteristic for components within an optical amplifier.

WDM Applications

The advantageous properties described above have been utilized in a number of devices targeted at new WDM systems.

LPG filters were used to create a conventional Er fiber amplifier with > 40 nm of flat gain bandwidth [9]. Sharp, broadband Bragg gratings improve bandwidth utilization when extending this approach to achieve > 80 nm of amplifier gain bandwidth with a new design utilizing a parallel second stage [10].

WDM amplifiers with such broad bandwidth will require large pump powers (>500 mW) when used with as many as 100 channels. One practical means for obtaining very high powers with high reliability is the use of a Cladding-Pumped Cascaded Raman Laser (CP-CRL). These devices utilize very low-loss fiber resonators defined by Bragg gratings to efficiently convert high powers from Yb cladding-pumped lasers near 1.1 μm (> 20W, [11]), to high powers at 1.48 μm for pumping Er amplifiers (> 9W, [11,12]). Er fiber amplifiers pumped with a CP-CRL have been shown to be very efficient, with no signs of saturation with up to 5W of signal output power in a single channel [12]. Additionally, CP-CRL Raman gain in a transmission fiber has been used to increase the power budget of a transmission system, enabling the upgrade of an installed single channel system to a 4 channel WDM system with no changes to the outside plant [13].

Finally, techniques will be described to use Bragg gratings as a wavelength-dependent tap with resolution and functionality comparable to an optical spectrum analyzer. Such a functionality may be critical for monitoring in future optical networks to supervise network configuration and transmission quality [14].

References

1. K. O. Hill *et al.*, Appl. Phys. Lett. **32**, 647 (1978).
2. G. Meltz *et al.*, Opt. Lett. **14**, 823 (1989).
3. P. J. Lemaire *et al.*, Elect. Lett. **29**, 1191 (1993).
4. T. Erdogan and V. Mizrahi, JOSA B: Optical Physics **11,** 2100 (1994).
5. T. Erdogan *et al.*, J. Appl. Phys. **76**, 73 (1994).
6. T. A. Strasser *et al.*, OSA Technical Digest Series, OFC '96, San Jose, CA, PD-8.
7. V. Mizrahi and J. Sipe, J. Light. Tech. **11**, 1513 (1993).
8. A. M. Vengsarkar *et al.*, J. Lightwave Tech. **14**, 1, 58-65 (1996).
9. P. F. Wysocki *et al.*, OSA Tech. Digest Series, OFC '97, Dallas, TX, paper PD-2.
10. Y. Sun , OSA Technical Digest Series, OAA '97, Victoria, Canada, paper PD-2.
11. D. Inniss *et al.*, CLEO '97 Proceedings, Baltimore, MD, paper PD31-2.
12. G. Jacobovitz-Veselka *et al.*, OSA Tech. Dig., OAA '97, Victoria, Canada, PD-3.
13. P. B. Hansen *et al.*, Proc. ECOC '96, Oslo, Norway, Vol. 2, paper TuD.1.4.
14. F. Heismann, Proc. ECOC '96, Oslo, Norway, Vol. 3, paper WeB.2.2.

An All-Fiber, Zero Insertion Loss, Add/Drop Filter for Wavelength Division Multiplexing

Anthony S. Kewitsch, George A. Rakuljic, Phil A. Willems and Amnon Yariv*

Arroyo Optics, Inc.
1646 17th Street
Santa Monica, CA 90404

Tel: 310-452-4004
Fax: 310-452-7686

Numerous optical filter concepts have been proposed for dense wavelength division multiplexing (WDM) applications.[1-7] For the lowest insertion loss and most reliably packaged device, an all-fiber solution is preferred. The present filter is based on grating assisted mode conversion and backwards coupling in the merged region of two dissimilar waveguides formed by adiabatically tapering and strongly fusing two single-mode optical fibers. From the theory of adiabatic following,[8] the modes of the input fibers will evolve on a one-to-one basis into the first two eigenmodes of the merged region. These eigenmodes will propagate through the waist independently of one another, transform back into their original modes, and exit the device through their respective output fibers. This adiabatic mode evolution is lossless and free of optical crosstalk.

Figure 1(a) illustrates the one-to-one relationship between input modes 1 and 2 in waveguides I and II, and the eigenmodes into which they are transformed. By recording a Bragg grating in the waist of the device, eigenmode 1 can be converted and backwards coupled into eigenmode 2, which will then exit the merged region as mode 2 via waveguide II as shown in Figure 1(b). This transformation will occur only at a specific wavelength λ satisfying the phase matching or Bragg condition

$$\beta_1(\lambda) + \beta_2(\lambda) = 2\pi/\Lambda_g , \qquad (1)$$

where Λ_g is the period of the grating and $\beta_{1,2}$ are the respective modal propagation constants. Since the eigenmodes and the grating fully overlap in the merged region, the coupling coefficient of this device is much larger than that of a grating assisted directional coupler based on evanescent wave coupling. If $\beta_1 + \beta_2 \neq 2\pi/\Lambda_g$, input mode 1 will simply pass through the merged region, unaffected by the grating, and exit waveguide I unattenuated as shown in Figure 1(c). Conversely, if light satisfying the Bragg condition is launched into waveguide II, it will be "added" onto waveguide I by the grating. Thus, this device functions as an efficient, narrow bandwidth, four-port, all-fiber optical add/drop filter.

The structure of the filter that was fabricated is shown in Figure 2. Since identical starting fibers were used, the necessary waveguide dissimilarity was introduced by locally pretapering one of the two fibers before fusion. The Bragg grating in the waist of the device was recorded using an excimer laser.

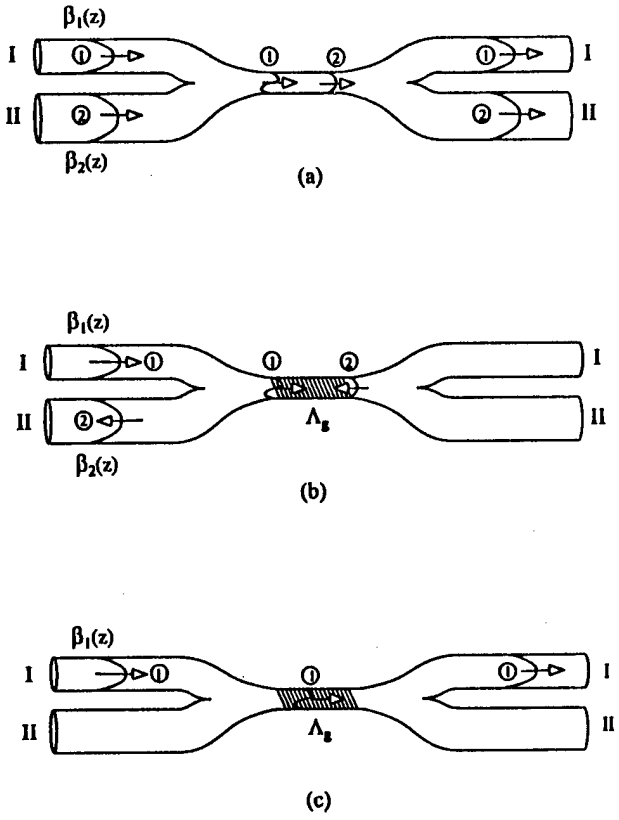

Figure 1: Operating principle of the grating assisted mode converter/coupler: (a) adiabatic mode evolution without grating; (b) mode transformation when $\beta_1 + \beta_2 = 2\pi/\Lambda_g$; (c) mode transformation when $\beta_1 + \beta_2 \neq 2\pi/\Lambda_g$.

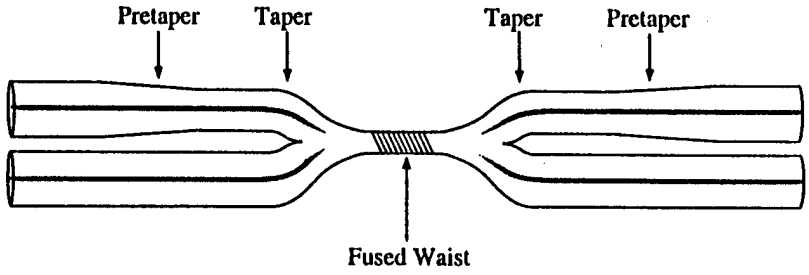

Figure 2: The structure of the add/drop filter that was fabricated.

The out-of-band insertion loss of the filter measured in throughput was ~0.1 dB, including the losses due to splicing, non-adiabaticity of the tapered and merged regions,

and the UV-induced background loss. The spectral response of the filter is shown in Figure 3. A peak add/drop efficiency of ~98% centered at 1547 nm was measured. The FWHM bandwidth of the grating was ~0.7 nm. An unpolarized erbium-doped fiber ASE source and an HP 70950B optical spectrum analyzer were used to obtain the data. The response of the filter was also examined using polarized input light, but no polarization dependence was observed.

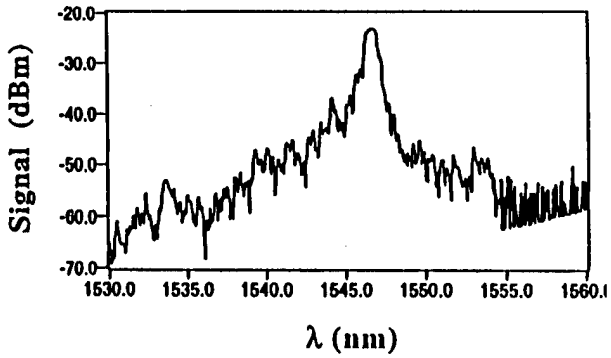

Figure 3: The spectral response of the add/drop filter.

In summary, an all-fiber four-port add/drop filter was developed and fabricated by recording a Bragg grating in the merged region of two adiabatically tapered and fused optical fibers. A device with very low insertion loss, large add/drop efficiency, no polarization dependence, and a narrow spectral bandwidth was demonstrated. Since the operation of the filter does not depend on optical interference or directional coupling, strict optical path length control is not required. This filter is expected to apply to numerous dense WDM applications.

References

1. C. Dragone, *IEEE Photon. Technol. Lett.* **3**, 812 (1991).
2. F. Heismann, L. L. Buhl, B. I. Miller, M. Newkirk, U. Koren, M. G. Young, and R. C. Alferness, *Appl. Phys. Lett.* **64**, 2335 (1994).
3. T. Komukai, Y. Miyajima, and M. Nakazawa, *Jpn. J. Appl. Phys.* **34**, L230 (1995).
4. J.-L. Archambault, P. St. J. Russell, S. Barcelos, P. Hua, and L. Reekie, *Opt. Lett.* **19**, 180 (1994).
5. I. Baumann, J. Seifert, W. Nowak, and M Sauer, *IEEE Photon. Technol. Lett.* **8**, 1331 (1996).
6. F. Bilodeau, D. C. Johnson, S. Theriault, B. Malo, J. Albert, and K. O. Hill, *IEEE Photon. Technol. Lett.* **7**, 388 (1995).
7. M. J. Guy, S. V. Chernikov, J. R. Taylor, and R. Kashyap, *Electron. Lett.* **30**, 1512 (1994).
8. L. I. Schiff, *Quantum Mechanics* (McGraw-Hill, New York, 1968), pp. 213-216.99

Low Crosstalk Optical Add-Drop Multiplexer based on a Planar Silica-on-Silicon Mach-Zehnder Interferometer with UV-induced Bragg Gratings and UV-Trimming.

J.-M. Jouanno, D. Zauner, M. Svalgaard and M. Kristensen
Mikroelektronik Centret -Technical University of Denmark
Bldg 345 East - 2800 Lyngby - Denmark
Phone : +45 45 25 57 23, Fax : +45 45 88 77 62, Email : jmj@mic.dtu.dk

Introduction : Optical Add-Drop Multiplexers (OADM) are key-components of multi-wavelength optical networks. Several techniques and designs may be used in order to achieve this function [1]. UV-induced Bragg gratings are of great interest since they enable construction of compact devices, and when written in the arms of a planar Mach-Zehnder interferometer they realise an OADM device with potentially low crosstalk. Moreover this device drops one channel without altering the other ones enabling cascading of several OADM's. Silica-on-Silicon planar OADM devices based on Mach-Zehnder interferometers have already been reported by other groups [2-5] but they were all limited by a low grating strength leading to a ratio between the -30 dB bandwidth in transmission and the -20 dB bandwidth in reflection, the so-called BandWidth Utilisation parameter (BWU) [6], equal to zero and therefore a high intra-channel crosstalk. We present in this paper a planar OADM with a positive BWU obtained by writing strong gratings in waveguides [7].

Experiments : The waveguides are made by Plasma Enhanced Chemical Vapour Deposition (PECVD) of silica layers on silicon and reactive ion etching. The refractive index difference between the Ge-doped core and the cladding is $7x10^{-3}$ and the waveguide dimensions are 6 μm x 6 μm. The structure of the multiplexer is shown in Fig. 1. It is composed of a 51 mm long symmetric Mach-Zehnder interferometer with identical 3 dB directional couplers.

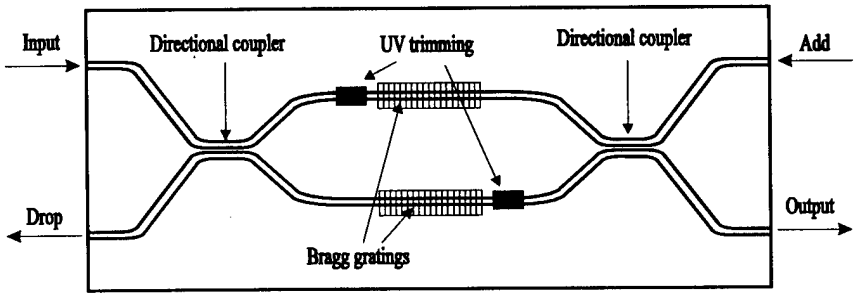

Fig. 1 Schematic of the OADM multiplexer.

The Bragg gratings are simultaneously induced in the two arms of the Mach-Zehnder interferometer by illuminating the waveguides with UV-light through a phase mask. The exposure was performed with a KrF excimer laser operating at 248 nm. Prior to grating fabrication, the photosensitivity was enhanced by loading the sample with around 2 mol%

deuterium at room temperature. The beam of the excimer laser is uniform in one direction and approximately Gaussian in the other dimension which is used for apodising our gratings. The $1/e^2$ radius of the beam is 3.1 mm and the total fluence used for the exposure is 3.9 kJ/cm^2. After exposure the wafer is annealed at 80°C for 10 hours, in order to outdiffuse the deuterium still present in the glass and to stabilise the gratings.

Results and discussion : The device is characterised using a broadband light source around 1550 nm and an optical spectrum analyser. A two-fibre array with fibres fixed in V-grooves on a silicon plate was butted to the multiplexer chip to measure the power at the drop port. The input fibre was also connected to a three-port circulator in order to record the back-reflected signal.
After the post annealing, most of the power was back-reflected to the input port indicating that the signals reflected by the two gratings were experiencing different optical paths. This phase difference can be cancelled by inducing with UV-light a permanent increase of the refractive index in one arm of the Mach-Zehnder. This UV-trimming was realised with a continuous wave frequency doubled argon ion laser delivering 244 nm light. This laser was used instead of the excimer laser because its beam can easily be focused to a few microns. Moreover, the sample was mounted on computer controlled stages (0.1 nm precision) thereby allowing a precise and reproducible tuning [8]. The waveguide was illuminated with a 10 µm FHWM beam having a power of 40 mW. A scanning speed of 0.8 µm/s led to a refractive index change of 8.9×10^{-4} in the non-loaded glass. The back-reflected light at the input port is recorded while trimming. The tuning is stopped when minimum power is reached. In order to keep the phase balance, another UV-trimming is realised on the other arm of the Mach-Zehnder interferometer as shown in Fig. 1.
We then measured the transmitted spectra at all ports. They were normalised by the spectra recorded fibre-to-fibre after removing the sample. Fig. 2 shows the light transmitted from the input to the output port and the signal reflected to the drop port.

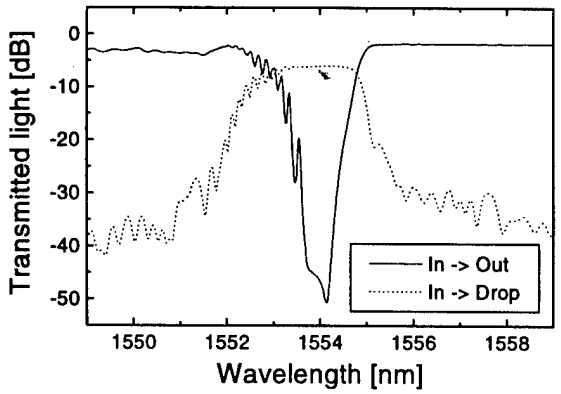

Fig. 2 Spectra at the output (solid line) and drop ports (dotted line) measured with non polarised light.

The 3 dB and 20 dB bandwidths in reflection are 2.3 nm and 3.9 nm respectively. In the case of a multi-wavelength transmission with a 400 GHz spacing, the isolation of the next channel (inter-channel crosstalk) is 28.5 dB. At the Bragg wavelength, the losses are around 5 dB with at least 2 dB due to the misalignment of the fibre array.

The transmission dip is around 50 dB. Its strength determines the isolation between the transmitted and the add channels, the so-called intra-channel crosstalk. Isolation better than -30 dB leads to less than 1 dB penalty in high rate transmission experiments [9]. The -30 dB bandwidth is therefore a very critical parameter when characterising the performance of an OADM component. In our case the -30 dB bandwidth is 0.7 nm leading to a BWU parameter equal to 0.18. The losses in transmission are 1.8 dB for wavelengths higher than the Bragg wavelength. On the short wavelength side, some residual coupling to cladding modes slightly increases this value.
The extinction ratio between the signals at the add and output ports, and between the dropped signal and the back-reflected light at the input port is determined by the coupling coefficient of the directional couplers and the phase variation of the signals propagating in the two arms of the Mach-Zehnder. After UV-trimming this extinction ratio is 20.6 dB indicating a coupling ratio of 46%. Further optimisation of the coupler design will result in performance enhancement.

Conclusion : We present an optical Add-Drop multiplexer based on a symmetrical Mach-Zehnder interferometer with UV-written Bragg gratings in the arms. The device has subsequently been optimised by UV-trimming. The quality of the gratings enabled us to achieve both a low inter-channel and low intra-channel crosstalk resulting in a positive BWU parameter. The -30 dB bandwidth in transmission is 0.7 nm, which is a significant progress in Mach-Zehnder based planar Add-Drop filters enabling utilisation of such devices in multi-wavelength networks.

References :

[1] H. Venghaus, A. Gladisch, B.F. Jørgensen, J.-M. Jouanno, M. Kristensen, R.J. Pedersen, F. Testa, D. Trommer and J.-P. Weber, Proc. Optical Fiber Communication 1997, Paper ThJ1, pp 280-281, 1997.
[2] R. Kashyap, G.D. Maxwell and B.J. Ainslie, IEEE Phot. Tech. Lett., Vol. 5, No. 2, pp 191-194, 1993.
[3] Y. Hibino, T. Kitagawa, K.O. Hill, F. Bilodeau, B. Malo, J, Albert and D.C. Johnson, IEEE Phot. Tech. Lett., Vol. 8, No. 1, pp 84-86, 1996.
[4] G.E. Kohnke, T. Erdogan, T.A. Strasser, A.E. White, M.A. Milbrodt, C.H. Henry and E. J. Laskowski, Proc. Optical Fiber Communication 1996, Paper ThQ6, p 277, 1996.
[5] G.E. Kohnke, C.H. Henry, E.J. Laskowski, M.A. Cappuzzo, T.A. Strasser and A.E. White, Electron. Lett., Vol. 32, No. 17, pp 1579-1580, 1996.
[6] T.A. Strasser, P.J. Chandonnet, J. DeMarco, C.E. Soccolich, J.R.Pedrazzani, D.J. DiGiovanni, M.J. Andrejco and D.S. Shenk, Proc. Optical Fiber Communication 1996, Post-deadline paper 8, 1996.
[7] J.-M. Jouanno, J. Hübner and M. Kristensen, Proc. Optical Fiber Communication 1997, Paper WL60, pp 228-229, 1997.
[8] M. Svalgaard, Ph.D. thesis, Mikroelektronik Centret, DTU, 1997.
[9] R.J. Rune, B.F. Jørgensen, submitted to IEEE Phot. Tech. Lett.

Apodized UV-induced Gratings in Planar Waveguides for Compact Add-Drop Filters

C.K. Madsen, J.J. DeMarco, C.H. Henry, E.J. Laskowski, R.E. Scotti, and T.A. Strasser
Lucent Technologies, Bell Laboratories, 600 Mountain Avenue, Murray Hill, NJ 07974
Tel: (908) 582-6095 Fax: (908) 582-4868 E-mail: cmadsen@lucent.com

Introduction

Add-drop filters are key components for WDM communication systems. Filters with flat passbands, which can separate channels spaced by 100 GHz, are needed to allow many devices to be concatenated without decreasing the available channel bandwidth significantly. A Mach-Zehnder Interferometer (MZI) with UV-induced gratings realized using planar waveguides [1] is an attractive architecture for creating an add-drop filter (see Fig. 1a). To increase the number of devices which can be fabricated on a common substrate, it is desirable to make the overall device as short as possible; however, requirements on the allowable channel crosstalk (typically -20 dB for adjacent channels and -30 dB between the dropped and added channels) places a lower limit on grating length. Previous work has demonstrated Gaussian profile gratings [2] which have sidelobes on the short wavelength side of the Bragg wavelength. A double filtering architecture was reported with a transmitted isolation of -40 dB over the drop channel width and a 3dB width of 1 nm [3]. Such an architecture increases the number of gratings needed for each channel and requires that the two grating passbands be identical or passband narrowing occurs.

UV-induced gratings suffer undesirable losses in transmission resulting from coupling to cladding and radiation modes on the short wavelength side of the Bragg wavelength [4]. The offset between the Bragg wavelength and this coupling determines the number of channels which can be transmitted through the grating. An architecture which avoids this problem and allows shorter gratings to be used is discussed. Experimental results are presented for short gratings in MZIs with apodized profiles which are suitable for 100 GHz channel spacing add-drop filters.

Device Design and Fabrication

An architecture which provides add-drop functionality, avoids radiation and cladding mode coupling problems, and allows shorter gratings to be used by removing requirements on the transmission isolation is proposed. The drop function is shown in Fig. 1b with the gratings ordered by increasing wavelength, so that the shortest wavelength is dropped first. The add functionality is realized by replicating this architecture and reversing the signal directions so that the input is on the right and the longest wavelength is added first. Only the gratings' reflection spectrum is used for filtering and signals transmitting through the gratings are always on the long wavelength side.

The filter quality, i.e. the passband flatness, rolloff and sidelobe level, is determined by the index profile, or apodization. A profile which has good rolloff and sidelobe suppression properties is the raised cosine profile [5]. It has a coupling strength which varies over the grating length as $0.5*[1+\cos(\pi z/L)]$ where L is the grating length and $-L/2<z<L/2$. In contrast to the profile resulting from direct exposure with a Gaussian-shaped UV beam, the raised cosine profile has no chirp across the grating. Such apodization has been reported in optical fibers with gratings lengths of 3 to 4 cm [6]. This paper reports experimental results for apodized gratings in planar waveguide MZI structures with grating lengths of 1 cm.

The waveguides are P_2O_5-doped SiO_2 channel waveguides with a $\Delta=0.6\%$ on silicon substrates which are deuterium loaded prior to grating fabrication to increase their photosensitivity. The arm separation in the MZIs is 30 μm so that both arms can be exposed simultaneously [2].

Any accumulated phase differences between the arms changes the ratio of the transmitted and reflected signals in their respective cross- and bar-state outputs. The gratings were exposed using a zero-order-nulled phase mask and a 193 nm ArF excimer laser. The UV beam was apertured to a 3 mm length and scanned across the waveguide with and without the phase mask to produce the ac and dc portion, respectively, of the raised cosine index profile.

Results

The transmission and reflection spectrum for a 10 mm long grating in a MZI are shown in Fig. 2 measured using an OSA with 0.05 nm resolution. The 3dB width is 0.5 nm and the 20 dB width is 0.8 nm. A grating with this spectrum provides a minimum crosstalk of 25 dB over a channel width of 0.4 nm which is suitable for filtering 100 GHz spaced channels. In this device, phase differences between the MZI arms caused the reflection to be dominantly in the bar state. Compared to theoretical calculations of a raised cosine profile, the 3dB width indicates a peak modulated refractive index change of $1x10^{-3}$. The rolloff is more gradual and the transmission isolation is smaller than the theoretical predictions. Factors which contribute to the spectrum differing from the calculated result are variations in the material's photosensitivity, phase mask transmission, and UV exposure along the grating and across the MZI arms. The polarization dependent wavelength shift of the spectrum is less than 0.1 nm.

A stronger grating in a MZI is shown in Fig. 3. The reflection spectrum has a flat passband with a 1 dB width of 0.7 nm and a transmission isolation of 30 dB over 0.3 nm. This device demonstrates that it is possible to achieve sufficient transmission isolation for stronger gratings with a single stage precluding the need for double filtering.

In conclusion, an architecture was proposed which avoids radiation and cladding mode problems associated with UV-induced gratings and allows shorter gratings to be used to meet a given set of filter requirements. Apodized gratings were written in planar waveguide MZIs, and an apodized grating capable of meeting 100 GHz add-drop requirements was demonstrated.

References

1. R. Kashyap, G. Maxwell, and B. Ainslie, "Laser-Trimmed Four-Port Bandpass Filter Fabricated in Single-Mode Photosensitive Ge-Doped Planar Waveguide," *IEEE Photonics Technol. Lett.*, vol. 5, no. 2, pp. 191-194, 1993.

2. T. Erdogan, T. Strasser, M. Milbrodt, E. Laskowski, C. Henry, and G. Kohnke, "Integrated-Optical Mach-Zehnder Add-Drop Filter Fabricated by a Single UV-Induced Grating Exposure," Optical Fiber Conference. San Jose, CA, Feb., 1996.

3. G. Kohnke, C. Henry, E. Laskowski, M. Cappuzzo, T. Strasser, and A. White, "Silica based Mach-Zehnder add-drop filter fabricated with UV induced gratings," *Electron. Lett.*, vol. 32, no. 17, pp. 1579-1580, 1996.

4. V. Mizrahi and J. Sipe, "Optical Properties of Photosensitive Fiber Phase Gratings," *J. of Lightw. Technol.*, vol. 11, no. 10, pp. 1513-1517, 1993.

5. M. Matsuhara and K. Hill, "Optical-waveguide band-rejection filters: design," *Applied Optics*, vol. 13, no. 12, pp. 2886-2888, 1974.

6. T. Strasser, P. Chandonnet, J. DeMarco, C. Soccolich, J. Pedrazzani, D. DiGiovanni, M. Andrejco, and D. Shenk, "UV-induced Fiber Grating OADM devices for efficient bandwidth utilization," *Optical Fiber Conference*, PD8, 1996.

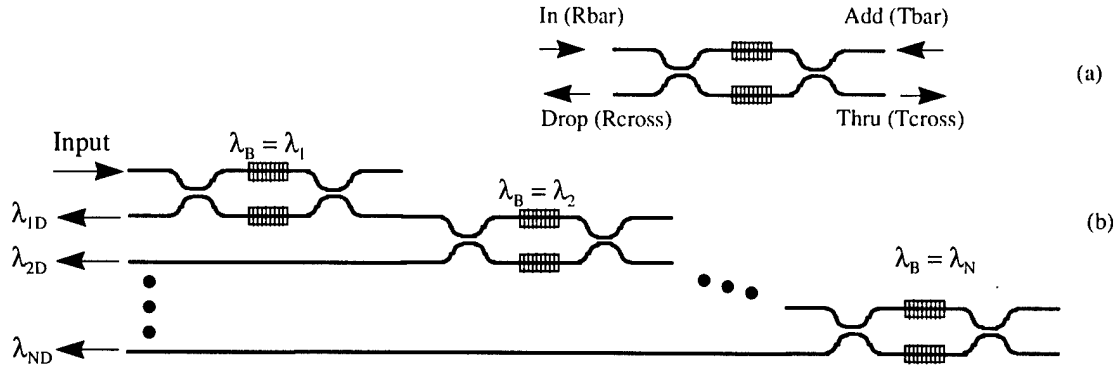

Fig. 1. Schematic of (a) a single-stage MZI add-drop and (b) a proposed multistage add-drop with the drop function shown.

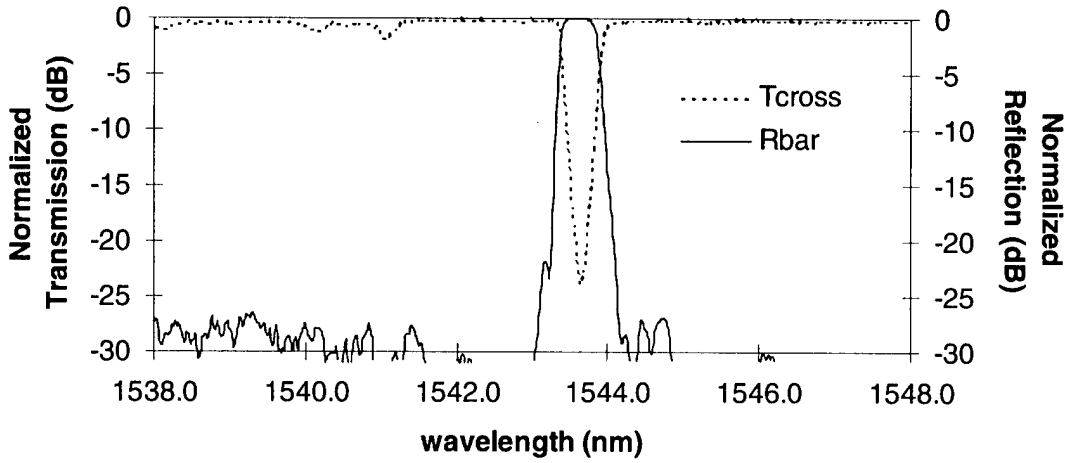

Fig. 2. A 10 mm long grating in a MZI with a 3dB width of 0.5 nm.

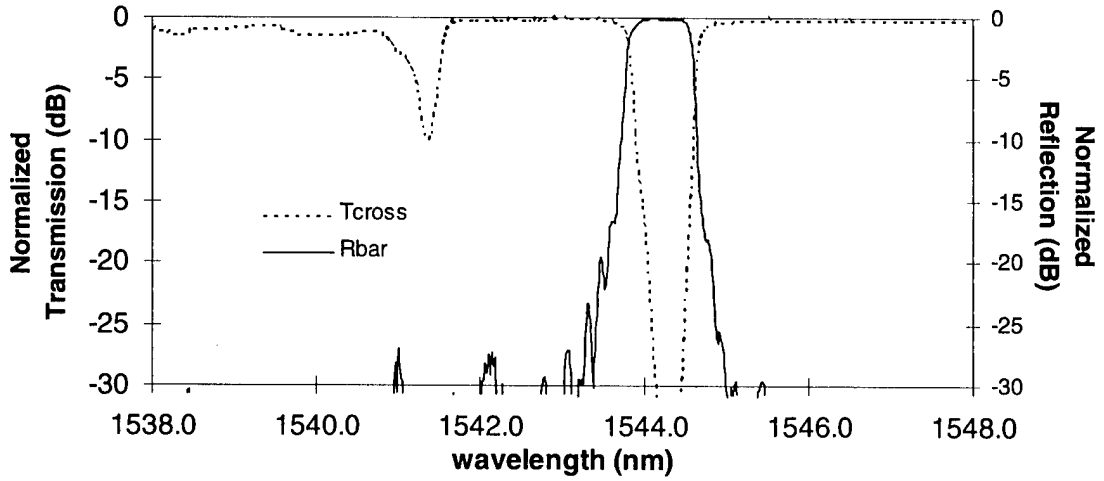

Fig. 3. A 10 mm long grating in a MZI with a 3dB width of 0.8 nm.

Efficient Active Bragg Grating Tunable Filters

H.G. Limberger, N.H. Ky, D.M. Costantini, R. P. Salathé, C.A.P. Müller* and G.R. Fox*

*Institute of Applied Optics, *Laboratory for Ceramics,*
Swiss Federal Institute of Technology, CH-1015 Lausanne, Switzerland.
Tel. +41 21 693 5183 Fax. +41 21 693 6108

Reflection, transmission and loss filters based on fiber Bragg gratings are key components in future wavelength division multiplexing telecommunication networks. A shift of the Bragg wavelength, λ_B, can be achieved by applying a strain or heating the fiber section containing the grating [1]. Here we report on Bragg grating devices that use a thin metallic coating to directly heat the fiber or a piezoelectric coating to strain it. Such integrated tunable filter devices show DC tuning [2-5] and modulation capabilities with promise for enhanced efficiency, reduced size, and low electrical power consumption.

Bragg gratings, 10 mm long, were fabricated in a hydrogenated standard telecommunication fiber using a phase mask and a KrF excimer laser with a pulse energy of 50 mJ/cm^2 and a pulse repetition rate of 50 Hz. The total laser fluence was about 1.5 kJ/cm^2. After laser irradiation, the fiber including the Bragg grating was cut to a 19 cm length and any remaining polymer coating was stripped away. For the thermal fiber Bragg grating (TFBG) device, DC sputtering was used to deposit radially symmetric fiber coatings of Ti and Pt with 40 and 300 nm thicknesses, respectively. The length of the coated fiber section was 22 mm with the grating centered under the coating. Electrical connections were realized at the ends of the coated section resulting in a total resistance of about 38 Ω. The conductive layer and the fiber were heated by a current passed through the metal layer [2-5]. The piezoelectric fiber Bragg grating (PFBG) modulator was fabricated using DC sputtering of ZnO. The fabrication process is similar to that used for the fabrication of piezoelectric fiber optic modulators [5, 6]. The Cr/Au bottom and top electrodes have thicknesses of 13/130 nm and 25/300 nm, respectively, whereas the ZnO coating is 18 μm thick [5]. The grating was centered under the 14 mm long top electrode of the device.

The DC tuning and modulation capabilities of TFBG and PFBG have been investigated. For the TFBG device, the Bragg wavelength shift has been measured as a function of electrical power. The TFBG device shows a linear dependence of the wavelength shift on the DC electrical input power with an efficiency of 4.1 nm/W (Fig. 1) [2-5].

Modulation was achieved by applying a sinusoidal voltage of frequency f to the electrodes. To measure the wavelength modulation (WM), the output wavelength of a laser was placed at the half maximum of the low wavelength side of the reflection peak. This wavelength position is in the linear region of the spectrum. For the PFBG, the WM signal follows directly the driving frequency, f, whereas for the TFBG, the WM output signal has a 2 f frequency like the electrical input power. Figure 2 shows the frequency dependence of the TFBG-WM amplitude for different driving powers. The 3dB cut-off frequency is about 3 Hz. Above this frequency, a $1/f$ frequency dependence of the

WM amplitude is observed. Modeling of the temperature behavior shows that the cut-off frequency and the frequency dependence of the device is governed by heat conduction [7]. Figure 3 shows the TFBG wavelength modulation amplitude as a function of driving power at different frequencies. The modulation amplitude depends linearly on the driving power with an efficiency that reduces with increasing frequency. A maximum efficiency of 4.0 nm/W was observed at 0.2 Hz which is close to the DC value.

Figure 4 shows the WM amplitude of the PFBG device as a function of driving frequency for an applied peak-to-peak voltage of 1 V. Up to 10 resonance peaks were observed between 10 and 320 MHz. The fundamental resonance peak is observed at 15.25 MHz and has a maximum WM amplitude of 10 pm. The next three resonance peaks, separated by about 40 MHz, have still more than 3 pm amplitude. The position of the peaks corresponds to that of the radial resonances of the ZnO coating-fiber structure [8-10].

Figure 5 shows the linear voltage dependence of the PFBG-WM amplitude at different resonance peaks. The WM efficiency decreases from 12 to 3 pm/V with increasing resonance frequencies from 15 to 117 MHz. A linear voltage dependence is also observed for the optical phase shift [9]. Table I summarizes the characteristics and performance of the TFBG and PFBG devices.

In conclusion, novel active Bragg grating devices based on strain and thermal effects have been fabricated and characterized. The thermal device showed a DC tuning efficiency of 4.1 nm/W. Its modulation capability was demonstrated at frequencies below 100 Hz with a WM amplitude proportional to the electrical input power. The piezoelectric device showed a linear voltage dependence of the wavelength modulation amplitude at radial resonances. A WM efficiency of 12 pm/V and a maximum WM amplitude of 18 pm was obtained at 15.25 MHz.

References:

1. W.W. Morey, G. Meltz and W.H. Glenn, SPIE **1169**, 98 (1989).
2. H.G. Limberger, N.H. Ky, D.M. Costantini, R.P. Salathé, C.A.P. Muller, and G.R. Fox, to be published in IEEE Photon. Technol. Lett.
3. N.H. Ky, H.G. Limberger, D.M. Costantini, R.P. Salathé, C.A.P. Muller and G.R. Fox, CLEO'97, in *Conference on Lasers and Electro-Optics,* OSA Technical Digest Series, Vol. 11 of 1997, p. 310, paper CWR2 (1997).
4. G.R. Fox, C.A.P. Muller, C.R. Wüthrich, A.L. Kholkin, N.Setter, D.M. Costantini, N.H. Ky, and H.G. Limberger, in Materials for Smart Systems II (Materials Res. Soc. Proc. **459**, Materials Research Society, Pittsburgh, PA, 1997) p. 25.
5. G.R. Fox, C.-R. Wüthrich, C.A.P. Muller, N. Setter, D.M. Costantini, N.H. Ky, H.G. Limberger, J. Vac. Sci. Technol. **15**, (1997).
6. G.R. Fox, H.G. Limberger, N.Setter, J. Mater. Res. **11**, 2051 (1996).
7. B.J. White, J.P. Davis, L.C. Bobb, H.D. Krumboltz and D.C. Larson, IEEE J. Lightwave Technol. LT-**5**, 1169 (1987).
8. G.R. Fox, C.-R. Wüthrich, C.A.P. Muller, N. Setter, and H.G. Limberger, accepted by Ferroelectrics.
9. N.H. Ky, H.G. Limberger, R.P. Salathé and G.R. Fox, IEEE Photon. Technol. Lett. **8**, 629 (1996).
10. A. Gusarov, N.H. Ky, H.G. Limberger, R.P. Salathé and G.R. Fox, IEEE J. Lightwave Technol. **14**, 2771 (1996).

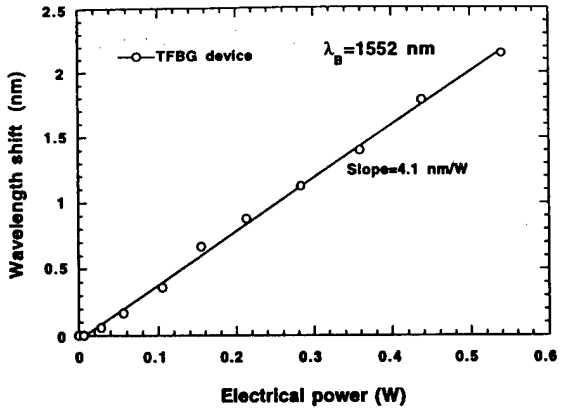

Fig.1: Bragg wavelength shift of TFBG device as a function of electrical input power.

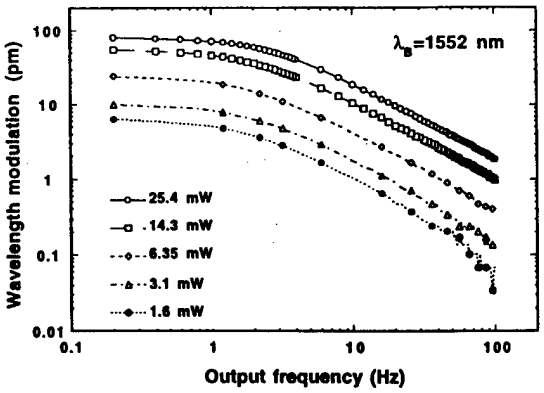

Fig. 2: TFBG wavelength modulation amplitude as a function of output frequency at different driving powers.

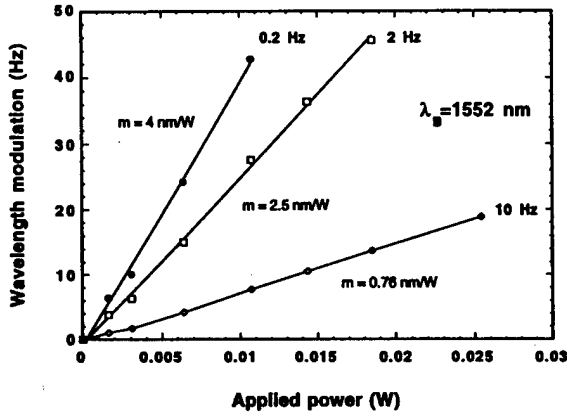

Fig. 3: Driving power dependence of TFBG wavelength modulation amplitude at different frequencies.

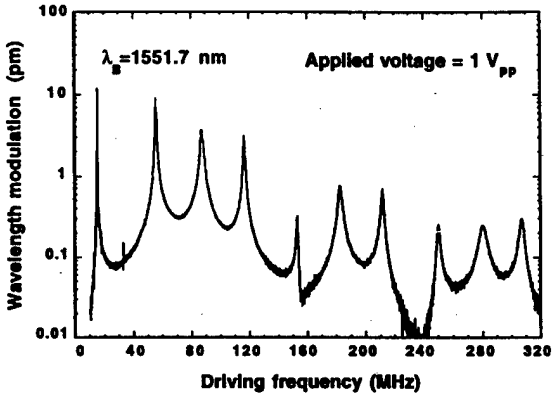

Fig.4: PFBG wavelength modulation amplitude as a function of driving frequency.

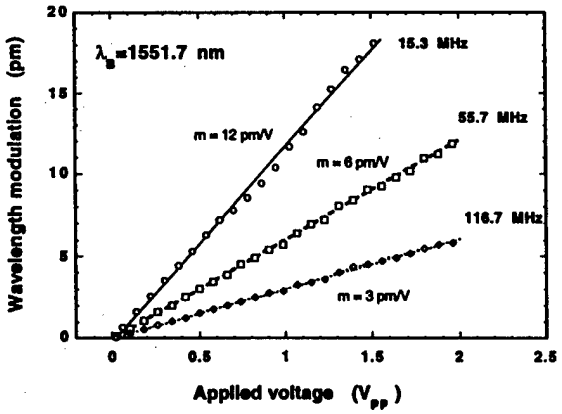

Fig. 5: Driving voltage dependence of PFBG wavelength modulation amplitude at different resonance peaks.

Table I: Characteristics and performance of TFBG and PFBG devices

	TFBG	PFBG
Fiber	H_2 loaded standard telecom	
Grating length (mm)	10	10
λ_B (nm)	1552	1551.7
Reflection (%)	95	90
Coating length (mm)	22	14 (top electrode)
Coating	Pt/Ti/fiber	Au/Cr/ZnO/Au/Cr/fiber
Operation	DC, Mod	Mod
Max. efficiency	4.1 nm/W	12 pm/V

CHIRPED MOIRÉ FIBRE GRATINGS OPERATING ON TWO WAVELENGTH-CHANNELS FOR USE AS DUAL CHANNEL DISPERSION COMPENSATORS

Morten Ibsen, Michael K. Durkin and Richard I. Laming

Optoelectronics Research Centre, University of Southampton,
Southampton SO17 1BJ, UK.

email: mi@orc.soton.ac.uk
Tel: +44 1703 593138
Fax: +44 1703 593142

Introduction:

Dispersion compensation is necessary in order to allow high data rate transmission through the installed standard fibre links. Several dispersion compensation techniques exists, including dispersion compensating fibre, phase conjugation and chirped fibre gratings. Of these, chirped fibre gratings offer many advantages including compactness, low-loss and low non-linearity. Recent error-free 10 Gbit/s and 40 Gbit/s transmission experiments at 1.55 μm over 109 km of standard fibre together with the possibility of simultaneous compensation of 2nd and 3rd order dispersion confirm the potential of this solution [1,2,3].

Interest in wavelength division multiplexing (WDM) has increased markedly over recent years driven by the rapid increase in communication traffic. Different schemes have been suggested to cope with the increased density of information. One is to multiplex the data in time (TDM), another is to wavelength multiplex data (WDM).

Multi-channel chirped gratings have been demonstrated previously using sampled gratings [4] but the lack of reflection equality and bandwidth together with a missing control over the exact number of wavelength channels required may limit the practicality of these devices. Moiré gratings and techniques to manufacture them have also been demonstrated [5,6] but none with clear distinction between the channels. The advantage of multichannel gratings is that they excibit characteristics similar to those of several single-channel gratings but are written within a single length of fibre hence offering higher stability when packaged and lower cost effectivity.

In this paper we demonstrate for the first time chirped Moiré fibre gratings operating on 2 wavelength-channels for use as dual channel dispersion compensators in a WDM scheme. Two devices with dispersion designed to compensate for 1.55 μm transmission through either 100 km or 200 km of standard telecommunication fibre with a dispersion of 17 ps/nm/km are shown. The channel spacing on one of the gratings is designed to match the ITU specifications.

Fabrication technique:

The gratings are made using an extented version of the scanning fibre/phase mask technique developed at the ORC [7]. This technique allows non-uniform grating formation with a uniform phase mask. An intracavity frequency doubled argon ion laser producing 100 mW of 244 nm CW light is employed as UV source. A total fluence of ~0.8 kJ/cm^2 is used to write the gratings. The gratings are written in a Deuterium loaded Ge/Si fibre with an NA ~ 0.2, and the time taken to write each grating is just 30 min. In order to smooth out the time delay ripples the gratings are apodised over 10 % of the total grating length at either end of the grating.

The gratings are characterised for reflectivity and time delay with a wavelength resolution on 2 pm using a tunable laser together with a high precision wavemeter.

Results and discussion:

Fig. 1 shows the reflection and time delay spectra of the two channels in a 1 m long continuously chirped Moiré grating designed to compensate 200 km dispersion in a fibre with a

dispersion of 17 ps/nm/km. The Bragg wavelength of the grating is 1531.9 nm and the grating has a refractive index modulation period of 291 μm leading to a wavelength separation of the two reflection channels by 2.7 nm (338 GHz). The bandwidth of each channel is identical at ~2.7 nm. The two channels both experience a total time delay of 9672 ps where channel I has a dispersion of 3630 ps/nm and channel II a dispersion of 3607 ps/nm a value given by the length of the grating and the channel bandwidth. The grating was also tested in transmission and each dispersion channel showed a transmission loss of ~10 dB indicating a reflectivity of ~ 90 %.

Fig. 2 shows a 35.1 cm long chirped Moiré grating designed to compensate 100 km of dispersion in standard fibre. This grating has a channel separation of 2.4 nm (300 GHz) and each channel in the grating has a bandwidth of ~ 2 nm; this yields a dispersion of ~1770 ps/nm for each channel. In this case the strength of the channels is ~8 dB (~84 %).

From figures 1 and 2 we can see that the two channels are nearly identical in terms of reflectivity and time delay. In both gratings channel I is the weaker, this is due to cladding-mode loss generated by channel II. These results demonstrates full control of the grating parameters available from today's technology. A scan of wavelengths well out of band of the gratings show that no wavelengths other than the two produced by the superstructure are evident.

One advantage of these "non-uniform" chirped fibre Bragg gratings is that the characteristics of several reflection wavelength gratings can be written into the same piece of fibre in one step, and therefore expensive problems such as implementation of several gratings either in series or on different ports of a circulator are avoided. Our results also show that chirped Moiré fibre gratings offer a robust way of achieving equal dispersion characteristics on two and only two channels. In addition they show that the use of chirped Moiré fibre gratings greatly simplifies the dispersion and wavelength matching of gratings where very accurate wavelength separations are required for implementation in the same WDM link.

Conclusion:

We have demonstrated long continouosly chirped Moiré fibre gratings with equal strength and linear dispersion characteristics in two channels designed to compensate the dispersion of 100 km and 200 km of standard telecommunication fibre. These types of gratings could find important applications in WDM systems.

References:

1 COLE, M. J., GEIGER, H., LAMING, R. I., ZERVAS, M. N., LOH, W. H. and GUSMEROLI, V.: 'Broadband Dispersion-Compensation Chirped Fibre Bragg Gratings in a 10 Gbit/s NRZ 110km Standard Step Index Monomode Fibre Link' , *Electron. Lett.*, 1997, **33**, (1), pp.70-71

2 DONG, L., COLE, M. J., ELLIS, A. D., DURKIN, M., IBSEN, M., GUSMEROLI, V. and LAMING, R. I: '40 Gbit/s 1.55 μm transmission over 109 km of non-dispersion shifted fibre with long continuously chirped fibre gratings', in proceedings to *OFC'97*, PD6, San Jose, USA, 1997.

3 IBSEN, M., DURKIN, M. K., ENNSER, K., COLE, M. J., and LAMING, R. I., 'Long continuously chirped fibre Bragg gratings for compensation of linear- and 3rd order-dispersion', Accepted for publication on *ECOC'97,* Edinburgh, 22-25 September 1997.

4 OUELLETTE, F., KRUG, P. A., STEPHENS, T., DHOSI, G. and EGGLETON B.: 'Broadband and WDM dispersion compensation using chirped sampled fibre Bragg gratings', *Electron. Lett.*, 1995, **3** ., (11), pp.899-901.

5 REID, D. C., RAGDALE, C. M., BENNION, I., ROBBINS, D. J., BUUS, J. and STEWART W. J.: 'Phase-shifted Moiré grating fibre resonators', *Electron. Lett.*, 1990, **26**, (1), pp.10-12.

6 LEGOUBIN, S., FERTEIN, E., DOUAY, M., BERNAGE, P., NIAY, P., BAYON, F. and GEORGES, T.: 'Formation of Moiré-grating in core of germanosilicate fibre by transverse holographic double exposure method', *Electron. Lett.*, 1991, **27**, (21), pp.1945-1947.

7 COLE, M. J., LOH, W. H., LAMING, R. I., ZERVAS, M. N. and BARCELOS, S.: 'Moving fibre/phase-mask scanning beam technique for enhanced flexibility in producing fibre gratings with a uniform phase-mask', *Electron. Lett.*, 1995, **31**, (17), pp. 70-71.

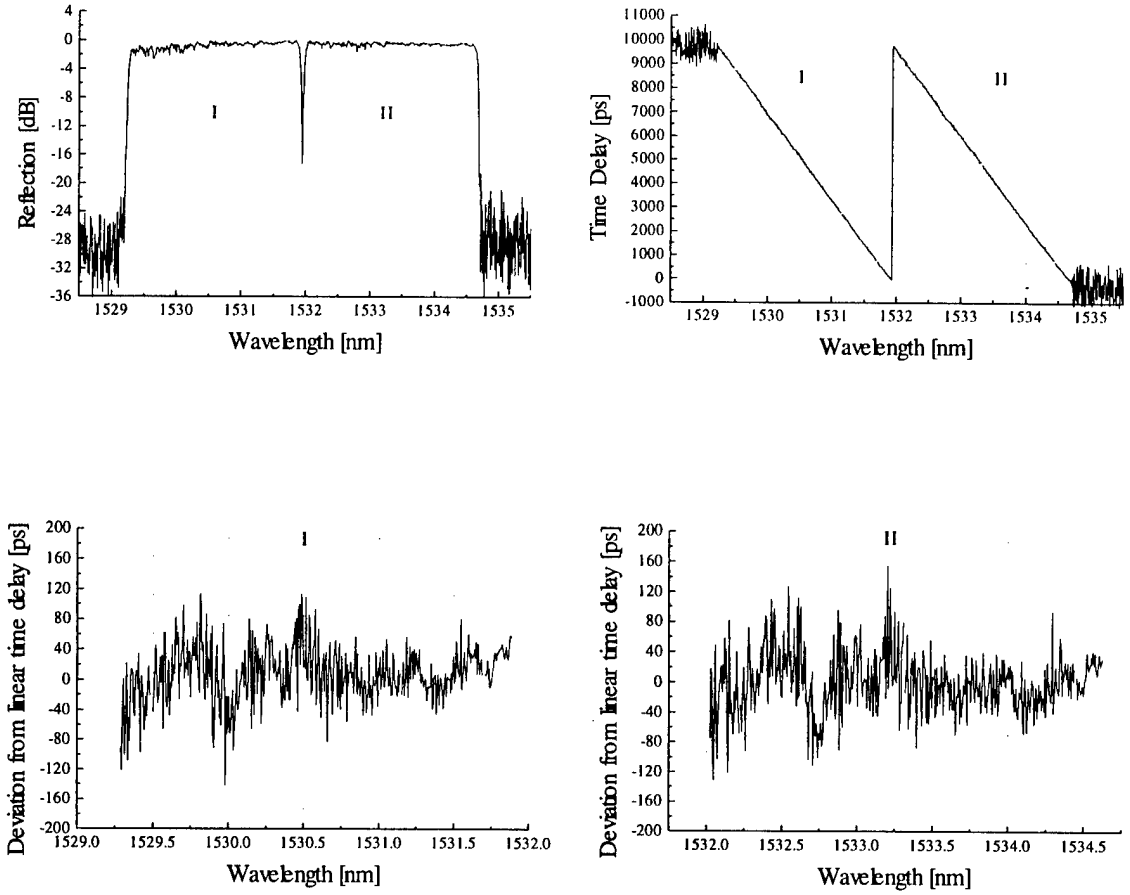

Figure 1 *Reflection and time delay characteristics of a 1 m long chirped Moiré grating with a channel bandwidth of 2.7 nm (338 GHz) and a channel separation of 2.7 nm. The dispersion in the channels is D_I=-3630 ps/nm and D_{II}=-3607 ps/nm.*

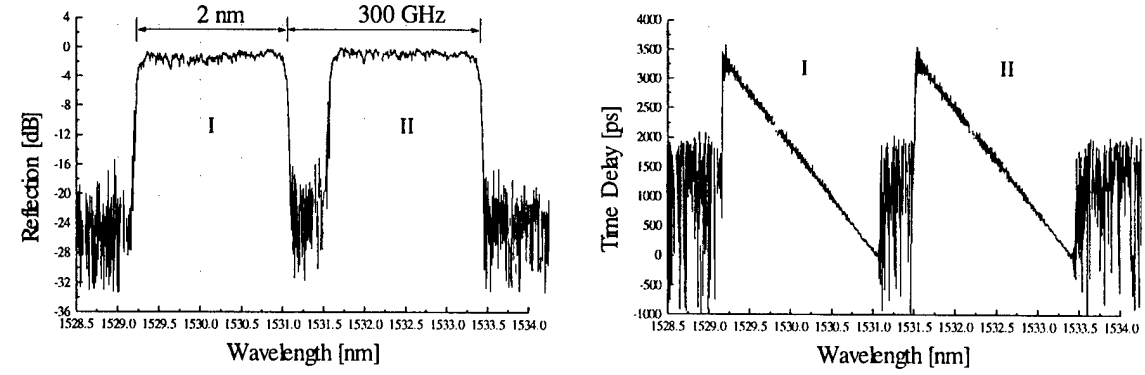

Figure 2 *Reflection and time delay characteristics of a 35.1 cm long chirped Moiré grating with a channel bandwidth of 2.0 nm (250 GHz) and a channel separation of 300 GHz. The dispersion in the channels is D_I=-1772 ps/nm and D_{II}=-1768 ps/nm.*

DISPERSION COMPENSATION GRATINGS

Richard I. Laming, M. Ibsen, M. Durkin, M.J. Cole, M.N. Zervas, K.E. Ennser & [1]V.Gusmeroli.

Optoelectronics Research Centre, University of Southampton, Southampton SO17 1BJ, UK
Tel: +44 1703 592693, Fax: +44 1703 593142

[1]Pirelli Cavi SpA, Milano, Italy

Abstract: Broadband Chirped fibre gratings allow the upgrade of the existing non-dispersion shifted fibre network to high data rate operation within the 1.55μm low-loss window. The design, fabrication, performance and application of these devices is covered.

Summary: Erbium doped fibre amplifiers have effectively eliminated the propagation-loss barrier in modern telecommunication systems, providing high gain and low noise figure operation over a large (30-80nm) bandwidth 1.55μm, and have enabled high-bit-rate data transmission over transoceanic distances. However, to date the majority of the installed fibre shows a zero dispersion at ~1.3μm and exhibits a relatively high dispersion (~ +17ps/nm/km with a slope of +0.07ps/nm^2/km) across the erbium band. This implies that the upgrade of the existing network to make full use of the erbium bandwidth by either TDM or WDM techniques, will be severely limited by the effects of linear and third order dispersion. The dispersion effects become even more adverse when combined with the optical fibre non-linearities.

Efficient dispersion compensation schemes will be of paramount importance in al the future, high capacity optical networks. So far, a number of different dispersion compensation techniques, such as dispersion compensating fibres, linearly chirped fibre gratings and mid-point spectral inversion have been proposed and studied extensively. However, chirped fibre Bragg gratings are proving to be one of the most attractive devices for this application as they are low loss, compact and polarisation insensitive [1]. Additionally, these devices do not suffer from optical non-linearity which is the primary drawback of the main competing technology i.e. dispersion compensating fibre (DCF).

The length of the fibre grating limits the maximum time delay or, equivalently, bandwidth x dispersion product. For example a 10cm grating can compensate for 100km of standard fibre over approximately a 0.5nm bandwidth. To date there have been several techniques reported for producing chirped gratings. These include post-chirping uniform gratings using UV processing [2] or by applying either a linear temperature [3] or strain gradient [4]. Alternatively the chirp can be directly imposed during fabrication [5]. At present all these techniques are limited to gratings ~10cm in length, and thus narrowband compensation, by the length of available phase masks used in production. By employing such narrowband compensators 10Gbit/s transmission distances ranging from 100 to 700km of non-dispersion shifted fibre have been achieved demonstrating the viability of this technology [3,4,6-10]. In the latter case a 0.07nm bandwidth grating in combination with duobinary transmission was employed [10]. Sampling the grating can increase the effective number of channels compensated providing that the laser wavelengths and grating passbands are accurately matched.

Although in the future transmitter wavelength tolerances will improve and thus narrowband gratings may be employed, for present practical applications chirped fibre Bragg gratings must exhibit both high dispersion and large bandwidth. A time delay of around 1700ps/nm would be sufficient to compensate around 100km of standard step index fibre at 1.55μm and a bandwidth of the order 5nm would cover typical semiconductor laser diode wavelength tolerances. This implies the need for long gratings (of ~1m in length) with a constant dispersion profile and broad bandwidth.

Kayshap et al [11] have achieved 1.3 metre gratings by concatenating many shorter gratings. However the stitching errors between section cause time-delay and reflection spectra discontinuities which may limit their usefulness. Taking some of the ideas from our earlier work [5] we have recently developed a continuous fabrication technique capable of producing arbitrary profile fibre gratings of 1 metre at present, ultimately limited by the maximum length of high quality translation stages. The phase shift is continuously added during the entire writing process and hence no glitches are present in the time-delay and/or reflectivity spectrum. Fabrication time for each 1 metre device is typically 10 minutes depending on the photosensitivity of the fibre used. Figures 1(a,b) show the characteristics of a typical linearly chirped 1 metre gratings with apodisation to reduce the time-delay ripples. Theoretical

simulations [12] of the wavelength dependence of the eye opening penalty for a 10Gbit/s NRZ dispersion compensated link are shown in figure 2. The results indicate that their is only a small degradation due to imperfections in the time delay characteristic of the latest gratings. This will improve further in the near future. Results from a 10Gbit/s transmission experiment confirm that the device works across the full bandwidth and confirms chirped gratings as a powerful component for use in networks [13]. Further operation of similar gratings has been demonstrated in a 4 x 10Gbit/s field trial by MCI and in a 40Gbit/s RZ experiment [14]

By periodically modulating the strength of the grating 'sampling' creates multiple reflection gratings for WDM applications [15, see also Ibsen et al at this conference]. The response of the super-structure can potentially be tailored to match/compliment the EDFA gain spectrum and compensate for linear and higher-order dispersion. In fact we have recently achieved 1 metre gratings optimised for third order dispersion [16] as shown in figure 3.

Although fibre gratings can compensate the dispersion of several hundred km's of fibre with one device, numerical simulations have shown that it is preferable to distribute compensators throughout the link to reduce the effects of fibre non-linearity. Employing this approach high-bit-rate error-free transmission over distances in excess of 1000km are predicted using linear transmission [17,18] and further using soliton transmission. Recent experiments confirm this potential [19] as shown in figure 4.

In summary, chirped gratings have been shown to be ideal for upgrading the installed standard fibre network to the 1.55μm wavelength window and high bit-rate operation. This talk will cover various aspects of their design, performance and network application.

References:

1. F. Ouellette, *Opt. Lett.*, vol 12, pp 847-849, 1987
2. K.O. Hill et al, *Opt. Lett.*, vol 19, pp 1314-16, 1994
3. R.I. Laming et al, *IEEE Photonics Technology Letters,* vol 8, pp 428-430, 1996
4. D. Garthe et al, *Elect. Lett.*, vol 30, pp 2159-2160, 1994
5. M.J. Cole et al, *Elect. Lett.*, vol 31, pp 1488-90, 1995
6. K.O. Hill et al, *Elect. Lett.*, vol 30, pp 1755-6, 1994
7. P.A. Krug et al, *Optical Fiber Comm,* paper Pdp27, 1995
8. W.H. Loh et al, *Elect. Lett.*, vol 31, pp 2203-2204, 1995
9. W.H. Loh et al, *IEEE Photonics Technology Letters*, vol 8, pp 944, 1996
10. W.H. Loh et al, *IEEE Photonics Technology Letters*, vol 8, pp1258-60, 1996
11. R. Kayshap et al, postdeadline paper, *ECOC '96, Oslo, Norway*
12. K. Ennser et al, *Proc ECOC '97, Edinburgh*
13. M.J. Cole et al, *Proceedings ECOC '96, Oslo, Norway* pp 5.19-22, postdeadline paper ThB.3.5, 1996
14. L. Dong et al, *postdeadline paper, OFC ' 97, Dallas*
15. F. Ouellette et al, *Elect. Lett.*, vol 31, pp 899-900, 1995
16. M. Ibsen et al, *Proc ECOC '97, Edinburgh*
17. D. Atkinson et al, *IEEE Photonics Technology Letters*, vol 8, pp 1085-87, 1996
18. K. Ennser et al, submitted to *Optical Fibre Technology*
19. A.B. Grudinin et al, to be published.

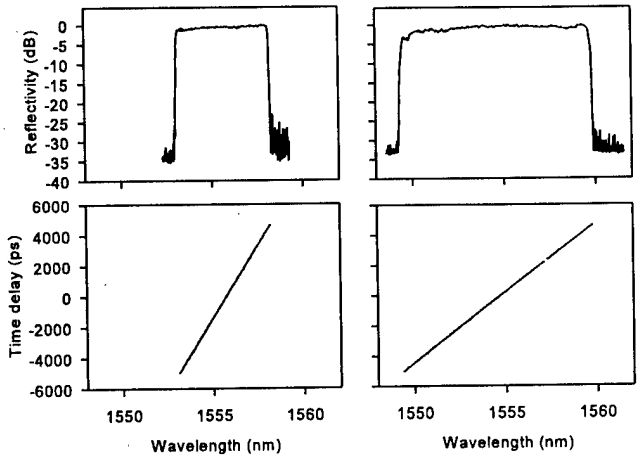

Figure 1. Characteristics of two 1 meter chirped gratings.

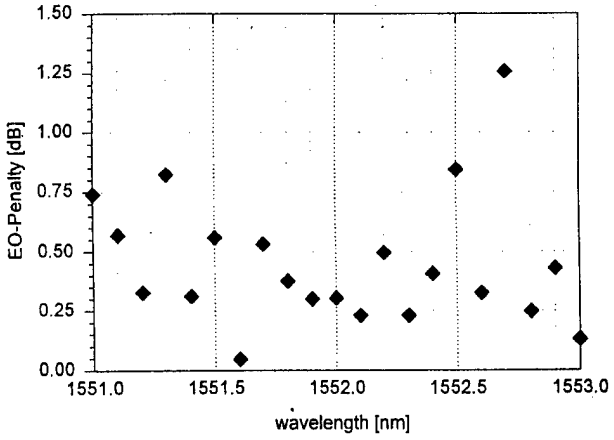

Figure 2. **Simulated EO-penalty for a 1 meter grating operating in a 100km 10Gbit/s dispersion compenated link as a function of transmitter wavelength.**

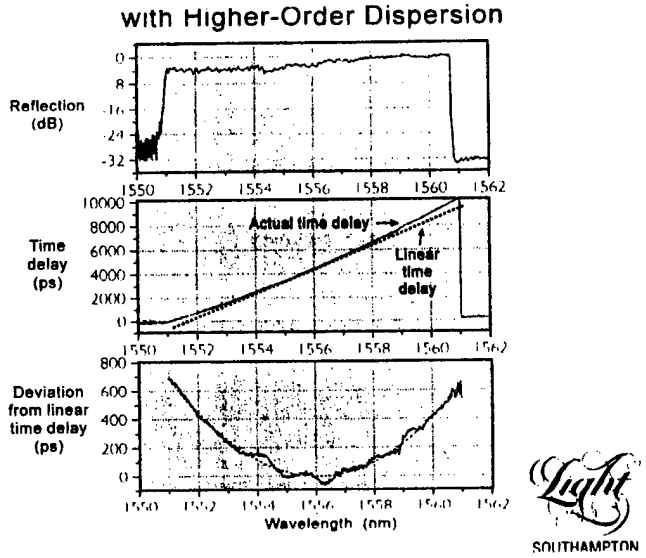

Figure3. **1 metre grating with third order dispersion.**

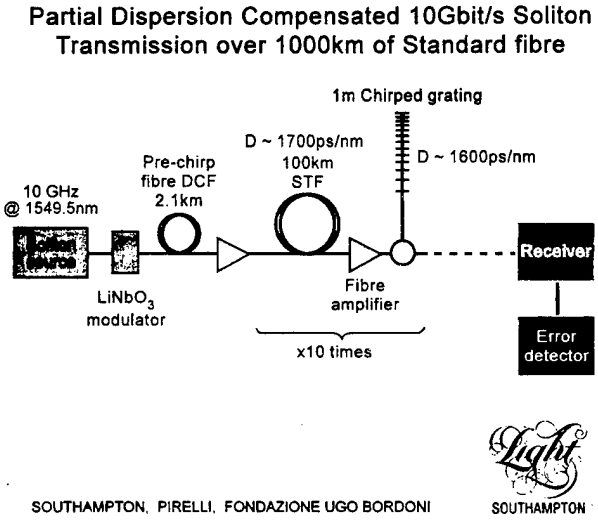

Figure 4. **1000km straight-line 10Gbit/s soliton experiment over standard fibre.**

Bragg Gratings, Photosensitivity, and Poling in Glass Fibers and Waveguides: Applications and Fundamentals

Planar Waveguide Devices

Tuesday, October 28, 1997

Graeme Maxwell, BT Laboratories, U.K.
Presider

BTuB
10:45am–12:15pm
Room 18

Application of photosensitivity in planar silica-on-silicon optical waveguides

Yoshinori Hibino*

Photonic Integration Research, Inc.
2727 Scioto Parkway
Columbus, OH 43221
Tel: (614)771-3747 Fax: (614)876-5726
e-mail: yhibino@piri.com

1. Introduction

Planar lightwave circuit (PLC) devices such as splitters, Mach-Zehnder interferometers and arrayed-waveguide grating (AWG) multiplexers, have been developed using GeO_2-SiO_2 waveguides on Si substrates. Such devices typically have low propagation and fiber-connection losses. Advanced optical communication systems, such as wavelength division multiplexing (WDM) systems, optical switching systems, and optical access networks[1] uses PLC devices. These silica-based planar waveguides are photosensitive[2]. This property can be used to make new types of PLC devices. For instance, photo-induced refractive index changes have been used for trimming the spectral response in the PLCs and forming Bragg gratings in the same way as used for optical fibers [3].

It is important to note, however, that the intrinsic refractive index change observed during irradiation due to Ar^+ laser or KrF irradiation was small because the absorption band at 245 nm is almost negligible. There are three ways to enhance the photosensitivity of the waveguides; consolidation in a reduced atmosphere [4], flame-brushing [5] and H_2 loading sensitization [6]. GeO_2-doped silica waveguides become highly sensitive to UV light at 249 nm after processing with 3 ways. Bragg gratings therefore can easily be formed in the waveguides. From the standpoint of practical application, however, each of three methods have drawbacks. Consolidation in reduced atmosphere differs from ordinary fabrication processes and threfore is inconvenient. Frame brushing technique sometimes changes the optical performance of the circuits, and H_2 loading is a very time-consuming process.

Recently, large index changes have been induced using irradiation at 193 without the need of any enhancements[7]. Presented here are the basic phenomena of refractive index change due to irradiation at 193 nm in silica-based planar waveguide and applications in phase control and device fabrication.

2. Irradiation at 193 nm

Irradiation at 193 nm was first tried to create the grating in Er^{3+}-and P_2O_5-doped waveguides[8]. In addition to germanium, phosphorous is often used as a dopant in the fabrication of high silica waveguides. Duing the investigation, 196 nm laser irradiation, when used with flame brushing and H_2 loading was found to be effective for creation of photosensitive P_2O_5-doped silica waveguides. Although the absorption of the as-deposited films was not observed over 200 nm, a refractive index change of more than $1x10^{-4}$ was created in P_2O_5-doped silica thin films following flame-brush photosensitization and exposure to 193 nm UV light. Using this techniques, the Er^{3+}-doped silica waveguide laser with Bragg gratings integrated has been demonstrated[9].

Irradiation with ArF laser at 193 nm has been tested for GeO_2-doped silica glass. Recently, changes of more than $1x10^{-4}$ have been induced by irradiation at 193 nm in the PLC without any treatment. The change due to irradiation at 193 nm results from the absorption change in lower than 200 nm. These results indicate that the photosensitivity issue is more complicated. Up until the present time, bleaching of the 5.0 eV band has always been held responsible for permanent refractive-index changes at visible and infrared wavelengths. Although further investigation is necessary for clarifying the mechanisms which cause

changes in refractive index, it is still useful to apply irradiation at 193 nm to practical device fabrication.

3. Device application

3.1 Polarization dependent control of waveguide circuits

Photo-induced birefringence is used to compensate for the intrinsic stress-induced birefringence (which occurs during waveguide fabrication), thus allowing fabrication of polarization-insensitive silica-based AWG filters[10]. The basic AWG configuration with GeO_2-doped silica waveguides on Si is shown in Fig. 1. The spectra of the AWG before and after UV irradiation are shown in Fig. 2. Prior to irradiation, the AWG initially has a polarization dependent wavelength shift of about 0.2 nm, which is caused by the intrinsic birefringence in the waveguide. The polarization dependence in the spectra between the TE and TM modes is eliminated after irradiation at 193 nm. This elimination is due to the photo-induced birefringence, which compensated the intrinsic birefringence in the planar compensating effect of the exposure to UV light. The level of irradiation can be reduced by about half by using an ArF laser as compared to a 245 nm laser.

3.2 DBR laser

Another important applications of photosensitive grating is the construction of a laser dioade (LD) cavity in the planar waveguide. External cavity lasers with a UV written grating in silica fiber or planar waveguide show that the oscillation wavelength, which is determined by the Bragg wavelength, is less temperature dependent than single-mode semiconductor laser diodes. Recently, a promising integrated external cavity laser has been demonstrated by integrating a spot-size converted laser diode (SSC-LD) on a PLC platform[11, 12]. The SSC-LD provides high efficiency coupling to a silica waveguide and the fabricated external cavity laser exhibited single-mode and wavelength stable oscillation.

Figure 3 shows the schematic configuration of 4-array integrated external cavity lasers. The lasers consist of SSC-LDs, a GeO_2-doped silica waveguide chip with 4 different Bragg gratings. The 4 mm-long gratings were written by UV irradiation through a phase mask from an ArF excimer laser (193 nm). No photosensitization techniques were used. The SSC-LD output face was anti-reflection coated, and the rear face was high reflection coated. The completed laser was 5 mm x 20 mm in size.

The lasers operate with threshold currents of about 8 mA. Output power of more than 0.8 mW at about 50 mA were obtained for all 4 lasers, resulting from efficient 4 dB coupling between the SSC-LD and the silica waveguide. Figure 4 shows the output spectra of each of the 4-wavelength lasers at 25℃ and 40 mA. The 4-wavelength laser realized 4 simultaneous single-mode oscillations with side-mode suppression of more than 40 dB. None of the lasers had any side modes. The average frequency change was -1.7GHz/℃ which is one eighth of the thermal coefficient in a semiconductor single-mode laser. The intervals between oscillation wavelengths were relatively evenly spaced (2.3, 2.0 and 2.2 nm). It may be possible to tune the wavelength within 0.1 nm by using uniform UV irradiation after forming the gratings.

4. Conclusion

This paper reviewed recent progress on photosensitivity in silica-based planar waveguides. The primary focus was the photosensitivity due to 193 nm irradiation. This is found to induce a large refractive index change in the waveguide without any special treatment. In terms of practical applications, irradiation at 193 nm in planar waveguides has been shown to be useful in order to control the birefringence of PLCs as well as to photo-imprint Bragg gratings in PLCs. These technologies are expected to be implemented in devices used for advanced WDM optical communication systems.

Acknowledgments

The author thanks his coworkers of Communications Research Center and NTT Opto-Electronics Laboratories.

*) On leave from NTT Opto-Electronics Labs., Tokai, Ibaraki 319-11, Japan.

References

[1]M. Kawachi and K. Jinguji, OFC'95, FB-3. [2]Y. Hibino, et al., IEEE Photonics Technol. Lett., 3, 640(1991) [3]R. Kashyap, et al., IEEE Photonics Technol. Lett., 5, 191(1993). [4] Y. Hibino, et al., Electron. Lett., 29, 621(1993). [5] F. Bilodeau, et al., Opt. Lett., 18, 953(1993). [6] P. J. Lemaire, et al., Electron Lett., 29, 1035(1993). [7] J. Albert, wt al., Opt. Lett. 19, 387(1994). [8] B. Maro, et al., Appl. Phys. Lett., 65, 394(1994). [9] T. Kitagawa, et al., Electron. Lett., 30, 1311(1994). [10] M. Abe, et al., to be pyblished. [11] T. Tanaka, et al., Electron. Lett., 32, 1202(1996). [12] T. Tanaka, et al., OECC'97.

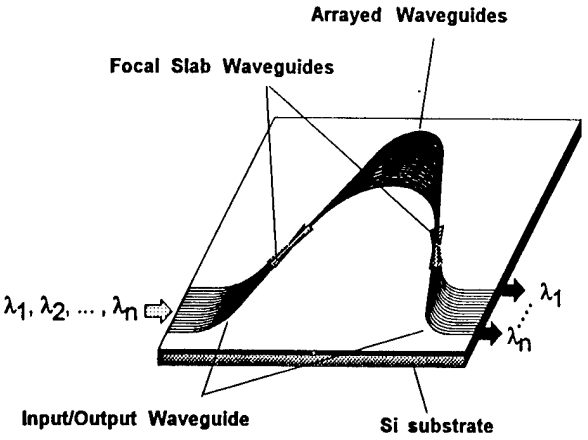

Fig. 1 AWG structure

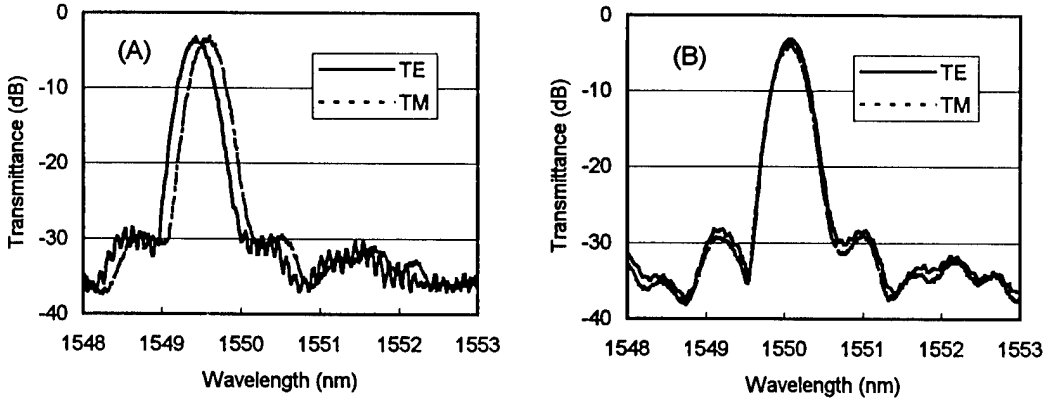

Fig. 2 Polarization dependence of AWG spectra. (A) Before irradiation, and (B) After irradiation.

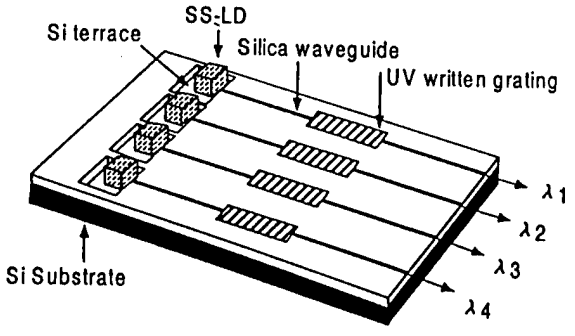

Fig. 3 Configuration of 4-wavelength laser.

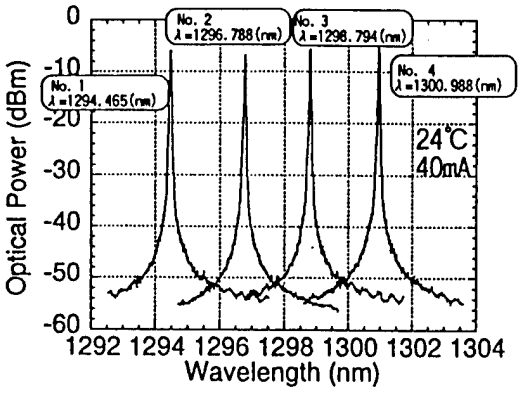

Fig. 4 Oscillation spectra of 4-wavelength laser.

Direct writing of planar waveguide devices using ultraviolet light

Mikael Svalgaard and Martin Kristensen
Microelectronics Center, Bldg. 345 east, Technical University of Denmark, DK-2800 Denmark

Introduction: Ultraviolet (UV) induced Bragg gratings in optical waveguides have been under intense investigation in the past few years, currently leading to commercial applications in fiber based sensor and telecommunication networks. However, the one-dimensional geometry of optical fibers limits the range of possible UV induced index structures and hence also the functionality of devices based hereon. This situation is currently changing, partly due to the large UV induced index changes available when using hydrogen loaded glass[1]. Large index changes permit direct writing of buried waveguide cores directly in planar silica based thin films, hence expanding the regime of UV induced index structures from one to two dimensions. The potential functionality of UV written optical devices is correspondingly increased.

In this paper we present results obtained with direct UV writing of silica based planar waveguide devices on a silicon substrate. Our results indicate that UV writing can yield devices with a performance in terms of loss and functionality similar to or better than those made by much more elaborate techniques relying on photolithography and reactive ion etching to define the waveguides.

Experimental: Planar waveguides have been written into a photosensitive glass film on silicon using a focused 244 nm continuous wave (CW) laser beam and high precision, three dimensional translation stages[2,3]. The sample used here is fabricated using plasma enhanced chemical vapour deposition and consists of a three layer silica film waveguide on silicon containing about 13 mole % GeO_2 in a ~2.5 μm thick core layer. The UV spot diameter on the sample is 5 μm and the incident UV power is ~17 mW. The sample was prior to UV exposure loaded with ~2 mole % of D_2 to increase the photosensitivity. After UV processing the sample is annealed at 80 °C for several days to permit outdiffusion of residual D_2 and to increase the thermal stability of the UV induced index change. For evaluation, light from a 1.54 μm diode laser is coupled in and out from the waveguides using standard single mode fibers, permitting measurement of the insertion loss. The broadband spectral response may be evaluated on a spectrum analyser by replacing the diode laser with a white light source. Replacing the outcoupling fiber with a microscope objective (N.A.=0.68) permits the intensity distribution of the guided mode to be imaged onto a CCD camera.

Linear and curved waveguides: Linear waveguides with a propagation loss below 0.2 dB/cm have been written[3] with a UV fluence of ~3 kJ/cm^2, corresponding to a scan speed of ~150 μm/s. The guided mode intensity profile is somewhat elongated with a full width at half maximum (FWHM) of 4 μm by 10 μm in the vertical and horizontal (i.e. parallel to the silicon substrate) directions, respectively. This is mainly due to differing index steps and waveguide widths in the vertical and horizontal directions. Comparison with effective index calculations suggest that the UV induced index change is ~3×10^{-3}. Higher index changes up to ~7×10^{-3} are derived for fluences of 40 kJ/cm^2. The fiber mode is circular with a FWHM of 10.4 μm; hence the fiber-waveguide coupling loss is rather large, typically ~1.8 dB. This value has since been lowered to 0.6 dB in other samples by increasing the core layer thickness and by lowering the GeO_2 content. Low loss curved waveguides have also been demonstrated[3]. The required index change to obtain low loss is generally larger in a curved waveguide than in a straight waveguide and hence before a bend is written the applied fluence is gradually increased. For s-bends consisting of circular arcs with a radius of curvature of 40 mm and a transverse displacement of 100 μm we routinely measure an excess loss of ~0.2 dB, as compared to a straight waveguide. This is obtained for a fluence of ~15 kJ/cm^2 in the bend, corresponding to a scan velocity of 30 μm/s.

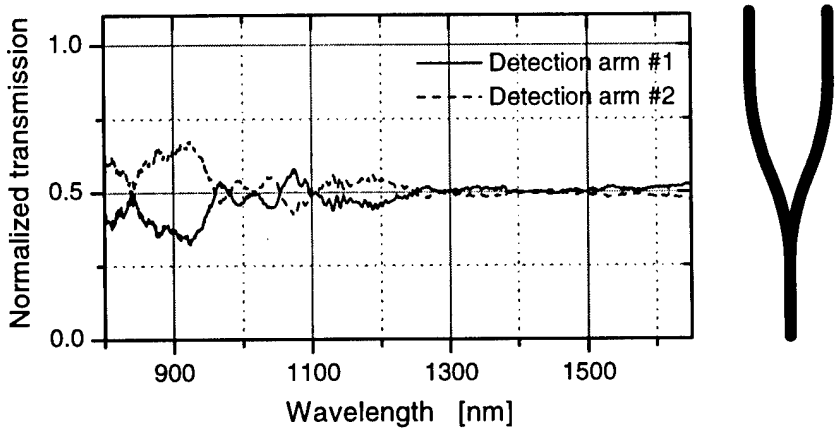

Fig. 1: Spectral response of UV written 1:2 power splitter, having a total length 7.2 mm. The device layout is shown to the right.

Waveguide devices: To test the capabilities of the direct UV writing technique we have made 1:2 power splitters and directional couplers using the results outlined above. Such devices have been demonstrated previously[4,5] using pulsed UV lasers and a metal mask containing the waveguide pattern; however these devices exhibited higher loss than normally obtained with standard techniques.

Although the power splitter is a relatively simple structure it is often difficult to fabricate with standard, etching based techniques due to the sharp inner edge at the branching point. In this respect the direct UV writing technique should be superior, since any pattern, within the limits of the UV spotsize, can be defined by the translation stages. We wrote 1:2 splitters using two scans. During the first scan, the input arm is written with twice as high a scan velocity as normal. After the s-bend, the left-hand splitter arm is written with the usual scan velocity. When the UV beam has passed the edge of the sample it is moved back to the initial position and the process is repeated to make the right-hand arm. Thus the input arm is scanned twice, but with a final fluence equal to that of the remaining circuit. This method becomes unfeasible for splitters consisting of more than one branching point. For such structures a beam shutter should be used to block the writing beam while moving to each new branching point. A number of splitters with an output arm separation of 200 μm have been fabricated. The total splitter length was varied from ~3 mm to ~8 mm, by varying the radius of curvature used in the s-bends. Several straight waveguides, intended for calibration, were also written along with the splitters. The excess loss, defined as the ratio between the total transmitted power through the splitter and that through a straight reference waveguide, is typically less than 0.2 dB. Only for splitter lengths approaching 3 mm did the loss increase above this value, most likely due to increased bending loss since the s-bend radius of curvature here approaches 20 mm. Measurements of the spectral response for λ=0.9-1.65 μm indicate a wavelength dependent splitting ratio for short device lengths. For lengths larger than about 6-7 mm, the splitting ratio was 50% within a few percent over a 400 nm range from 1.25-1.65 μm, as shown in figure 1.

Realisation of directional couplers is an important test of any waveguide fabrication technique since good results can only be achieved with a high spatial accuracy and highly reproducible waveguide propagation constants. Using the direct UV writing technique we have fabricated a number of couplers with a center-to-center core separation of 9 μm and a linear coupling region varying in length from 500 μm to 2600 μm. The port waveguide separation is 200 μm, while the s-bends consist of circular arcs with R=40 mm. The total device length varies from approximately 8 mm to 10 mm. Several straight waveguides, intended for calibration, were written along with the couplers.

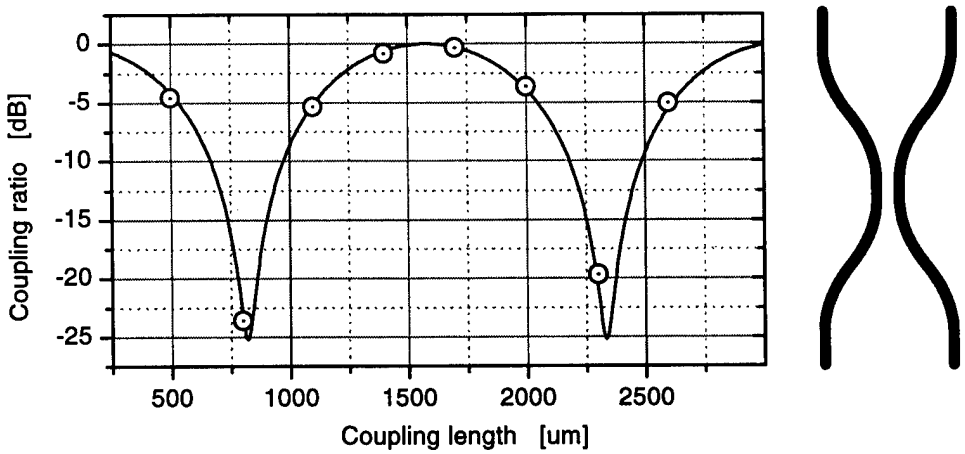

Fig. 2: Measured (circles) and calculated (solid curve) coupling ratio versus the length of the linear region of UV written directional couplers. The device layout is shown to the right.

The couplers were evaluated by measuring the ratio of transferred power to the total transmitted power at 1.54 μm (fig. 2). All the couplers were verified to be symmetrical within the measurement accuracy, i.e. the behaviour does not depend on which waveguide is excited at the input port. The behaviour expected from simple coupled mode theory[6] has been fitted to the measured values with the coupling length, the degree of coupling occurring in the bends and the maximum extinction ratio as free parameters and is included in the figure. In this way we obtain a coupling length of ~760 μm. The maximum extinction ratio is ~25 dB which may be shown to correspond to the propagation constants in each waveguide being identical within ~30 ppm. The measured excess loss of the couplers (defined in terms of the transmission of a straight waveguide) is less than 0.2 dB for linear coupling regions up to ~1500 μm in length, after which it increases to ~0.8 dB.

The UV fabrication time of the devices described here has been about 13 minutes pr. device. Recently, we have increased the amount of incident UV power by a factor of four, leading to a corresponding reduction in fabrication time to ~3 minutes pr. device.

Conclusion: Direct UV writing using a focused UV laser beam has been shown to yield planar waveguides with a propagation loss below 0.2 dB/cm as well as low loss curved waveguides. Using this technique we have fabricated 1:2 power splitters and directional couplers. These devices exhibit low excess loss (<0.2 dB), good spectral characteristics and have a fabrication time of just a few minutes. These results indicate that direct UV writing is a realistic alternative for high volume production of planar waveguide devices.

1. P.J. Lemaire, R.M. Atkins, V. Mizrahi and W.A. Reed, Electron. Lett. 29, 1191 (1993).

2. M. Svalgaard, C.V. Poulsen, A. Bjarklev and O. Poulsen, Electron. Lett. 30, 1401 (1994).

3. M. Svalgaard and M. Kristensen, Electron. Lett. 33, 861 (1997).

4. G.D. Maxwell and B.J. Ainslie, Electron. Lett. 31, 95 (1995).

5. J. Hübner, C.V. Poulsen, J.E. Pedersen, M.R. Poulsen, T. Feuchter, M. Kristensen, Conference on Lasers and Integrated Optoelectronics, SPIE 2695A-11, 98 (1996).

6. A.W. Snyder and J.D. Love, "Optical Waveguide Theory", Chapman & Hall (1983).

Self-writing in photosensitive materials: theory and experiment

Tanya M. Monro[1,2], D. Moss[2],
C. Martijn de Sterke[1,2] and L. Poladian[2]
Dept Theoretical Physics, School of Physics,
University of Sydney, NSW 2006 Australia[1] and
Australian Photonics CRC, Optical Fibre Technology Centre,
University of Sydney, 101 National Innovation Centre,
Australian Technology Park, Eveleigh NSW 1430, Australia[2]
Email: T.Monro@physics.usyd.edu.au Ph: +61 2 9351 5799 Fax: +61 2 9351 7726

1. Introduction

Theoretical models predict that a channel waveguide can be self-written in a planar photosensitive material using a beam of light.[1,2] We present here the first experimental observation consistent with this self-writing process in germano-silicate glass, and describe the theoretical analysis of the process.

Consider a Gaussian beam incident on a planar photosensitive material. Initially the beam diffracts freely. Photosensitvity causes the refractive index to increase, and it increases most where the intensity is highest. Hence the refractive index change is greatest on the axis of propagation of the beam, and so the beam is guided more strongly along this axis. Theory predicts that this leads to the formation of a channel waveguide in the glass for both one and two-photon photosensitivity processes.[2] We call this a self-writing process because the beam of light which writes the waveguide is simultaneously guided by it. The structure of the resulting waveguide depends on the beam profile. Different choices of the incident beam shape allow the properties of the waveguide to be tailored to suit the desired application.

Waveguides written in this way are likely to have advantages over waveguides written using more conventional methods. In particular, the self-writing process described here is a direct, one-step method, unlike current methods, such as epitaxial growth, diffusion methods and direct writing, which all require several processing steps. Our theoretical results indicate that self-written channel waveguides display no sharp features, and hence would be expected to have low radiation losses.

Other similar self-writing processes have been observed. For example, photopolymerization has been used to create permanent, self-written solid structures in bulk liquid photopolymers.[3,4] The principal difference between photosensitivity and photopolymerization is that in a photopolymer, the index response is delayed relative to the illumination. Tapered waveguides have also been written in UV-cured epoxy using a self-writing process.[5]

2. Model

Two partial differential equations describe self-writing in a planar material. The propagation direction is z, the transverse direction is y, and we assume that the field profile is unaffected in the x direction.[1,2,6] The paraxial wave equation describes light propagation[6,7]

$$ik_0 n_0 \frac{\partial \mathcal{E}}{\partial z} + \frac{1}{2}\frac{\partial^2 \mathcal{E}}{\partial y^2} + k_0^2 n_0 \Delta n \mathcal{E} + \frac{i}{2} k_0 n_0 \alpha \mathcal{E} = 0, \tag{1}$$

where k_0 is the free space wavenumber, n_0 is the initial refractive index, $\Delta n = n - n_0$, where n is the refractive index at time t and $\mathcal{E}$ is the electric field envelope amplitude at time t. We include a constant loss term in Eq. (1), where α is the attenuation coefficient. The loss in decibels per unit length is 4.343α.

A simple phenomenological model describes the photosensitive evolution of the refractive index:[2,8,9]

$$\frac{\partial \Delta n}{\partial t} \propto (\mathcal{E}\mathcal{E}^*)^p. \tag{2}$$

For a one-photon photosensitivity process, $p = 1$, and for a two-photon process $p = 2$. We ignore saturation because typical refractive index changes required for waveguide formation in the planar geometry are small.[10]

No non-trivial exact solutions to Eqs (1) and (2) problem are known. The most straightforward approach is to solve these equations numerically and we have done this using a beam propagation method combined with updates of the refractive index.[1,2]

3. Precursors to waveguide formation

Using the simulation technique described in Section 2, we have solved Eqs (1) and (2) using a Gaussian input beam.[1] The major steps in the evolution

of a waveguide are as follows. The refractive index on axis increases with time and thus the diffraction of the beam decreases. After some time, a maximum in the beam intensity forms (the *primary eye*). A similar maximum also forms in the refractive index. The locations of these maxima change over time. As time passes, additional maxima form in the intensity. These *secondary eyes* result from beating between the lowest two even modes of the self-written waveguide. These eyes change their position rapidly, and so the refractive index does not display these features. As this process continues, the waveguide beyond the primary eye gradually becomes more uniform. Ultimately a channel waveguide is formed beyond the primary eye.

A primary eye forms when the refractive index change in the material is sufficient to overcome the initial diffraction of the beam. The structure has then begun to guide light. Simulations suggest that primary eyes are always precursors to the formation of a waveguide in the material.

Simulations indicate that primary eyes are typically located near the input face. Hence we use series expansions for the intensity and the refractive index in the propagation distance to explore the behavior of these eyes. Using these expansions we can track the paths of the primary eyes in the material over time.

Real materials always exhibit loss, and so we use this technique to study the effect of loss on this process.[10] In particular, we investigate the effect of loss on the experiment described in Section 4. Hence we take the beam width to be $8\,\mu$m, and use the two-photon wavelength of 488 nm. Using the intensity series expansion we can analyse the behavior of the eye. The solid line in Fig. 1 is the position of the primary eye in the absence of loss as a function of time. After the primary eye has formed, there is a local minimum in the intensity at the input face. We find that loss causes a maximum and a minimum to form a finite distance into the sample, rather than at the input face. The dashed line in Fig. 1 shows the motion of the maximum and minimum pair for $5\,\mathrm{dB\,cm^{-1}}$ loss, which is the loss in the material used in our experiment. This figure shows that the minimum moves towards the input face, and the maximum moves away, as it does in the absence of loss.

Figure 1 demonstrates that $5\,\mathrm{dB\,cm^{-1}}$ loss only significantly changes the behaviour of the primary eye in a small region near the input face. We find that by the time a channel waveguide has formed in the material, the effect of the loss on the waveguide is negligible outside this region. As the bilayer we are using in the experiment described in Section 4 is 1 cm long, the presence of $5\,\mathrm{dB\,cm^{-1}}$ of loss has little effect on the properties of the waveguide as measured at the output edge of the bilayer.

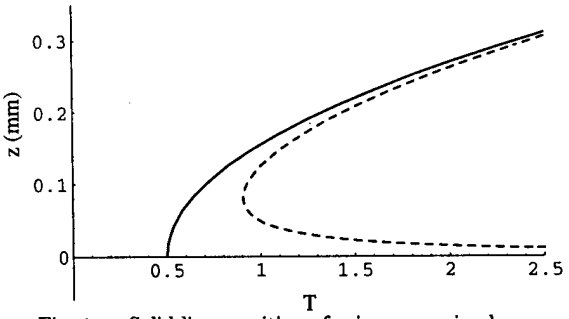

Fig. 1. Solid line: position of primary eye in absence of loss vs time (arbitrary units). Dashed Line: position of max/min pair with $5\,\mathrm{dB\,cm^{-1}}$ loss vs time.

4. Experimental results

We have conducted an experiment to demonstrate this self-writing process, and the experimental setup is shown in Fig. 2.

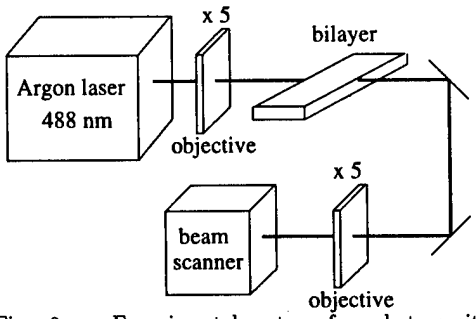

Fig. 2. Experimental setup for photosensitive self-writing experiment

We use a bilayer on a silicon substrate: the buffer layer ($n = 1.458$) is $10.5\,\mu$m thick, the core layer ($n = 1.485$) is $3.1\,\mu$m thick. In our experiment the laser beam is vertically polarized, and this bilayer supports two even TM modes. The bilayer is approximately 1 cm long, and the core layer contains 20% Ge. The structure was grown at the Danish Technical University using Plasma Enhanced Chemical Vapour Deposition (PECVD). The loss in this bilayer is $\approx 3 - 5\,\mathrm{dB\,cm^{-1}}$, and so our analysis in Section 3 indicates that a channel waveguide should form. We use the two-photon photosensitivity pro-

cess at 488 nm because there is less absorption at this wavelength than at the one-photon wavelength of 244 nm. The laser output power 1 W. A microscope objective (×5) is used to focus the Gaussian beam to a spot size of 8 μm incident on the Ge-doped layer at the edge of the bilayer. Another microscope objective (×5) is used to image the beam at the output side of the bilayer onto a PHOTON BeamScan beam profiler.

We infer that the refractive index is evolving by monitoring the change in the width and peak intensity of the beam at the output edge of the bilayer as measured by the beam profiler. As a channel begins to form, more light is guided along the central axis, and so we expect the peak intensity to increase. Also, as the waveguide evolves, the index change counteracts the diffraction of the input beam, and so we expect the width of the beam at the output end of the bilayer to decrease over time.

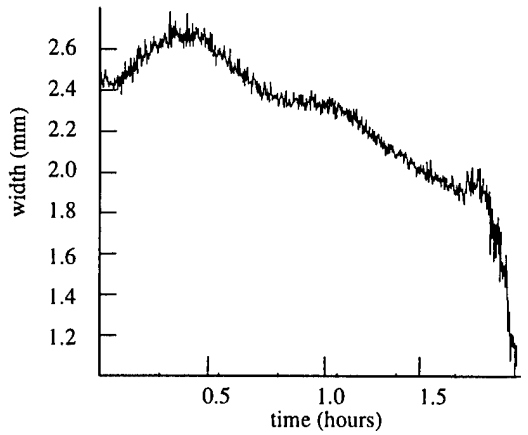

Fig. 3. The Gaussian-fitted FWHM of the beam at the output end of the bilayer as a function of time.

Figure 3 shows the Gaussian fit to the full width at half maximum (FWHM) of the beam (in mm) at the output end of the bilayer as a function of time (hours). The shape of the output beam did not change significantly in the first 1.5 hrs. After this, the peak intensity grew rapidly, and hence the FWHM decreased dramatically, this can be seen in Fig. 3. We do not know why this dramatic change occurs at this time, but the rapid increase in the peak intensity suggests that waveguide is becoming much more strongly guiding. Figure 3 indicates that the width decreases by just over a factor of 2 in two hours, which is consistent with the self-writing process described here.

We interpret the oscillations in Fig. 3 to be caused by the secondary eyes. As described in Section 3, these eyes are caused by the beating of modes of the waveguide forming in the glass. Since secondary eyes are maxima, when they pass through the output edge of the sample, the width at this position decreases. As more secondary eyes pass, we expect the width to oscillate, a minimum occurring whenever a secondary eye passes the output edge. When combined with the overall decrease in width caused by the creation of a channel waveguide, we expect a width profile of the type shown in in Fig. 3.

5. Conclusions

Preliminary experimental results suggest that we have made the first experimental observation of self-writing in a photosensitive material. Further experiments are underway to verify important aspects of this self-writing process. For example, we need to confirm that we are creating a permanent waveguide in the glass, and that the speed of the process depends on the intensity of the incident beam in the expected way.

The structure of a self-written waveguide depends both the input beam profile and the material properties. Our analytical series expansion technique is a useful tool in determining how these factors affect the waveguides which can be self-written in a photosensitive material.

1. T.M. Monro, C.M. de Sterke and L. Poladian, Opt. Comm. **119**, 523 (1995).
2. T.M. Monro, C.M. de Sterke and L. Poladian, J. Opt. Soc. Am. B **13** (12), 2824 (1996).
3. A.S. Kewitsch and A. Yariv, Opt. Lett. **21**, 24 (1996).
4. A.S. Kewitsch and A. Yariv, Appl. Phys. Lett. **68**, 455 (1996).
5. S.J. Frisken, Opt. Lett. **18**, 1035 (1993).
6. C. M. de Sterke and J.E. Sipe, J. Opt. Soc. Am. A **7**, 636 (1990).
7. A.E. Siegman, *Lasers* (University Science Books, Mill Valley, 1986), Ch 16.
8. V. Mizrahi, S. LaRochelle, G.I. Stegeman and J.E. Sipe, Phys. Rev. A **43**, 433 (1991).
9. C.M. de Sterke, S. An and J.E. Sipe, Opt. Comm. **83**, 315 (1991).
10. T. M. Monro, L. Poladian and C.M. de Sterke, Phys. Rev. E (submitted) (1997).

Writing Waveguides and Gratings in Silica and Related Materials by Femto-Second Laser

K.Hirao
Kyoto Univ. and ERATO, Hirao Active Glass Project of JST, Japan
Department of Material Chemistry, Graduate School of Engineering, Kyoto University, Sakyo-ku, Kyoto 606-01, Japan

With the goal of being able to create various optical glass devices for the telecommunications industry, the effects of 810 nm, femto-second laser radiation on various glasses were investigated. By focusing the laser beam via a microscope objective, transparent but visible, round-elliptical damage lines were successfully written inside high silica, borate, soda-lime-silicate, fluoride and chalcogenide bulk glasses. Micro-ellipsometer measurements of the damaged region in pure and Ge-doped silica glasses showed a 0.01-0.035 refractive index increase, depending on the radiation dose. The formation of several types of defects including Si'E or Ge'E centers, non-bridging oxygen hole centers, and peroxy radicals was also detected. These results suggest that multi-photon interactions are occurring in the glasses and that it is possible to write three dimensional optical circuits in bulk glasses via such a focused laser beam technique. The following is the technique to create waveguides.

A regeneratively amplified, 810 nm, Ti:Saphire laser which emits 120 fs, 200 kHz, mode locked pulses and delivers an average power of 975 mW was utilized for our study. The 5 mm diameter beam was focused via 5-20 X microscope objectives and injected into polished plates of dry and wet silica, Ge-doped silica, borate, soda-lime-silicate and ZBLAN glasses (Fig.1). The average power of the laser beam at the sample location was controlled between approximately 40 and 800 mW via neutral density filters which were inserted between the laser and microscope objective. With the help of an XYZ stage, the samples were translated at rates of 100-10,000 m/s either parallel or perpendicular to the incident laser beam, thus, creating damage lines inside of the glasses.

For all translation speeds and directions, structural changes were induced along the path transversed by the focal point of the laser, and colorless, transparent, linear damage marks were produced inside glasses such as silica. Ge-doped silica, soda-lime-silicate, borate, fluoride and chalcogenide glasses. These persistent damage lines and

their cross-sections are clearly visible using transmitted light optical microscopy (Fig.2) and are stable at room temperature.

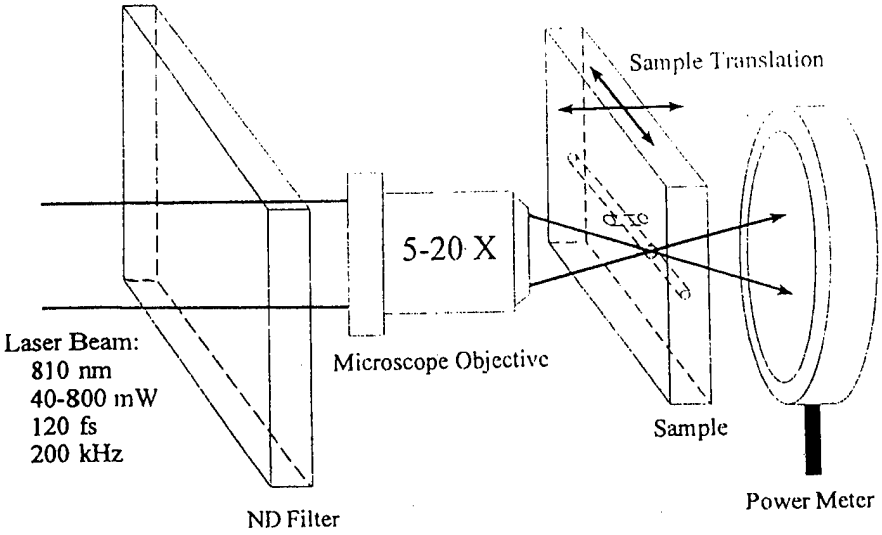

Fig.1. Experimental setup for writing waveguides

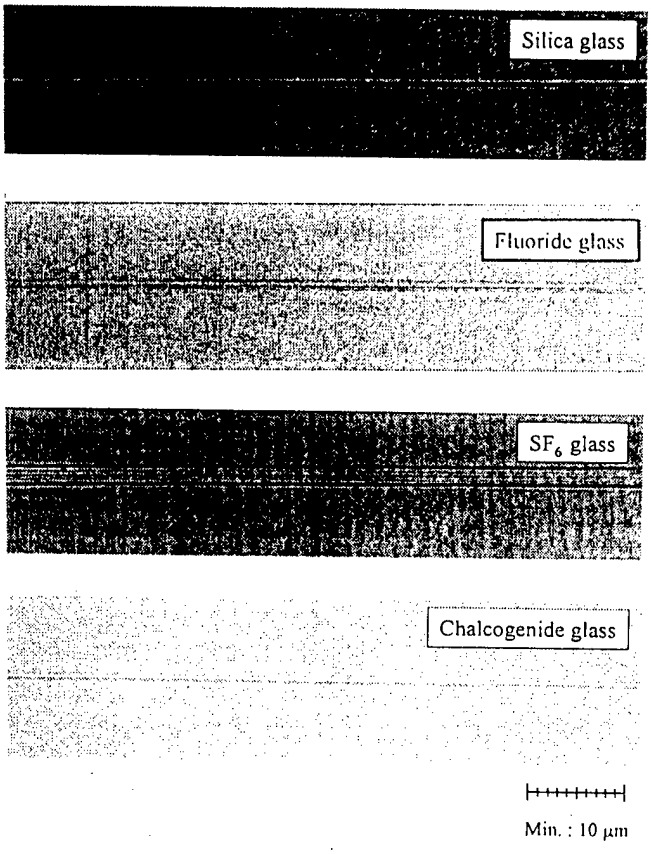

Fig.2. Waveguides written in various kinds of glasses

Using a micro-ellipsometer, refractive index profiles were measured across the cross-sections of damage lines formed perpendicular to the laser beam. After ten passes of the laser, the refractive index at the center of the damage was approximately 0.035 higher than the surrounding glass in the case of Ge-doped silica. The refractive indices of the as-received glasses vary by less than 0.0005 across the probed region according to the manufacturers specifications and the error in the ellipsometer measurements is less than 0.01 .

In addition, the followings were also examined : Pulse width, average power and scanning numbers of the laser dependence of refractive index variation and core size of the optical waveguides. These results showed that the control of the relative index difference and core diameter of the waveguide were possible by the adjustment of the writing condition. At present, we do not have the clear answer on the mechanism of the refractive index variation. However, by the atomic force microscope (AFM), the elaboration of a silica glass was observed in the laser irradiation region(Fig.3). The ultrafast energy deposition such as the excitation by the femtosecond laser pulses generates high temperatures and pressures inside the glass. Therefore, a likely mechanism for the change of the refractive index is due to the densification that occurs inside the glass by the femtosecond laser pulses.

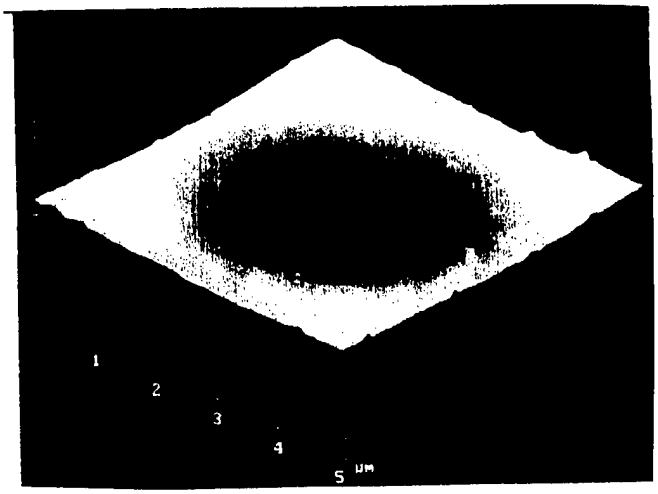

Fig.3. AFM profile of the damage spot.

According to ESR (Fig.4) spectroscopic measurements for the damage spot, the silica glass showed an increase in the concentrations of Si E'centers, while the Ge-doped

silica glass exhibited an increase in the concentration of Ge E'centers. The formation of peroxy-radicals POR) and non-bridging oxygen hole centers (NBOHC) was also observed in both glasses. The UV difference spectra are in agreement with these assignments, but also show a possible decrease in the concentration of neutral oxygen monovacancies (NOMV) in the Ge-doped glass. In addition, unidentified broad absorption bands running from 320 to 700 nm are formed in both glasses.

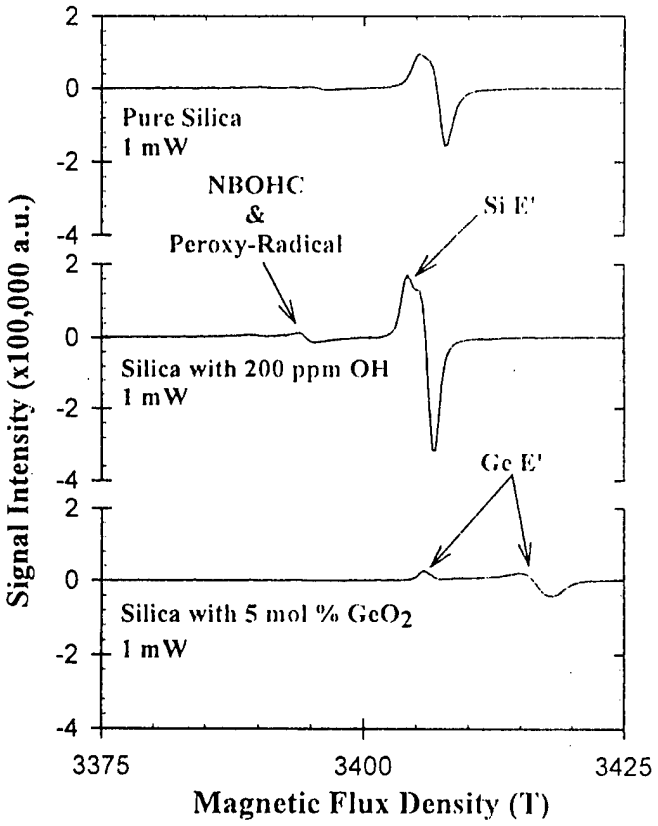

Fig.4. ESR spectra of high silica glasses

The creation of defects in the high silica glasses via 810 nm radiation suggests that the damage mechanism involves a multi-photon process. To our knowledge, such damage at this wavelength has not been previously reported, and it is suspected that the high pulse energy of the femto-second laser is responsible for the effect. The photo-induced refractive index increase in pure silica glass also appears to be a new observation.

With the elucidation of the mechanism, writing of the three-dimensional optical waveguide and function enhancement of the optical waveguide will be advanced in future.

Bragg Gratings, Photosensitivity, and Poling in Glass Fibers and Waveguides: Applications and Fundamentals

Poling I

Tuesday, October 28, 1997

Roger Stolen, AT&T Labs-Research
Presider

BTuC
1:15pm–3:15pm
Room 18

Large SHG in UV-Poled Silica Glass

Takumi FUJIWARA, Masahide TAKAHASHI*, and Akira J. IKUSHIMA

Frontier Materials Laboratory, Toyota Technological Institute
2-12-1 Hisakata, Tempaku, Nagoya 468, Japan
phone : +81 52 809 1881
fax : +81 52 809 1884
e-mail : fujiwara@toyota-ti.ac.jp

A number of work have been reported on enhancement of the second-order nonlinearity in silica-related glasses, e.g. poling at elevated temperatures (200~500 ℃) in bulk fused-silica [1], in sol-gel films [2], and in those of waveguide- and fiber-forms, in addition [3,4]. Recently, a significant increase of the effective electro-optic (EO) coefficient in a germanosilicate fiber was reported [5], where UV irradiation was applied along with an intense electric poling field. The EO coefficient measured in the fiber poled in that way was comparable to r_{22} in $LiNbO_3$. This "UV-poling" method has a further advantage of spatial resolution, which is useful to create periodically poled structures for the quasi phase-matching SHG and the EO-tunable Bragg gratings [6].

To clarify origin of the induced nonlinearity is the most important subject to realize a glass with hopefully a larger second-order nonlinearity, but systematic and quantitative studies are still scarce. In this paper we report, to our best knowledge, the first observation of induced SHG in a "UV-poled" germanosilicate glass. We have performed quantitative measurements of the SHG coefficient, d, as a function of poling electric-field strength and polarization of fundamental light. Furthermore, we will discuss origin of the induced nonlinearity.

A Ge-doped SiO_2 glass (15.7 GeO_2-84.3 SiO_2 in mol.%) fabricated by VAD method as a fiber preform was used in this experiment. Samples were cut from the preform and polished to the dimension of 10x10 mm with 1 mm thick, and two grooves for electrodes were fabricated on both sides of faces to insert electrodes for poling. To eliminate the breakdown of air, we have performed a method of poling, the same as that in Ref. [7], and the method provides poling electric-field strength up to 3×10^5 V/cm, which is at least one-order of magnitude higher than those ever reported with bulk glasses.

With a poling electric-field up to 3×10^5 V/cm across the electrodes, glass samples were irradiated by a

*Present affiliation: *Venture Business Laboratory, Kobe University, Nada, Kobe 657 JAPAN*
phone: +81 78 803 0593 fax: +81 78 803 0722 e-mail: masahide@kobe-u.ac.jp

pulsed ArF excimer laser. The excimer laser used had the wavelength of 193 nm, an energy density of 100 mJ/cm^2, and a pulse repetition rate of 10 pps. Total number of the shots in this experiment was 10^4 for all poling electric-field strengths.

For measuring the induced SHG (d coefficient) in the UV-poled glasses, the Maker-fringe patterns were obtained by using Q-switched Nd:YAG laser pulses operating at 1064 nm. The rotational axis in the UV-poled glass samples was chosen to be parallel to the direction of the poling electric-field. Upon each polarization (s- and p-polarizations) in fundamental light, the SHG signals were measured for s-polarization.

Fitting curves to analyze the Maker-fringe patterns are given by

$$I_{2\omega}(\theta) = R(\theta)\,\frac{A}{n_{2\omega}\,n_{\omega}^{2}\,\Delta n^{2}}\,\sin^{2}\left(\frac{2\pi\,\Delta n}{\lambda_{\omega}}\,\frac{L_e}{\cos\theta}\right), \quad (1)$$

where $I_{2\omega}(\theta)$ is the intensity of SH light as a function of the angle of incidence, θ, $R(\theta)$ is the reflectivity at the input and output faces of the samples, n_{ω} and $n_{2\omega}$ are the refractive indices for fundamental and SH lights, respectively, $\Delta n = n_{2\omega} - n_{\omega}$, A is amplitude of the SH fringe including d coefficient, and L_e is the effective path length of UV-light in glass samples. Since the absorption coefficient in the germanosilicate glass used in this work is about 45 cm^{-1} at 193 nm, region with the second-order nonlinearity induced by the UV-poling should be located in the vicinity of incident surface. L_e is defined by $L_e = \eta L$, where L is path length of sample and close by surface. η is the correction factor taking into account the absorption coefficient at 193 nm; that is,

$$\eta = \frac{1}{L}\int_0^L e^{-\alpha x}\,dx = \frac{1}{\alpha L}\left(1 - e^{-\alpha L}\right), \quad (2)$$

where α is the absorption coefficient.

We obtained excellent fits to Eq. (1) with fitting parameters, A, n_{ω}, $n_{2\omega}$, and Δn. Y-cut quartz with $d_{qz} = 0.51$ pm/V [8] was used as a reference sample to obtain the absolute value of d coefficient. The induced d coefficients as a function of poling electric-field strengths are shown in Fig.1. The d_{33} and d_{31} coefficients in Fig.1 were obtained from s-s and p-s polarization dependences of SHG, respectively [9].

Both d_{33} and d_{31} increase with increasing the poling field up to about 1.5x10^5 V/cm, and then the value saturates. The largest values are 3.4 $\pm$0.3 pm/V for d_{33} and 1.1$\pm$0.2 pm/V for d_{31}. The value of d_{33} is exactly 3 times as large as that of d_{31} for poling electric-field strengths in our experiment.

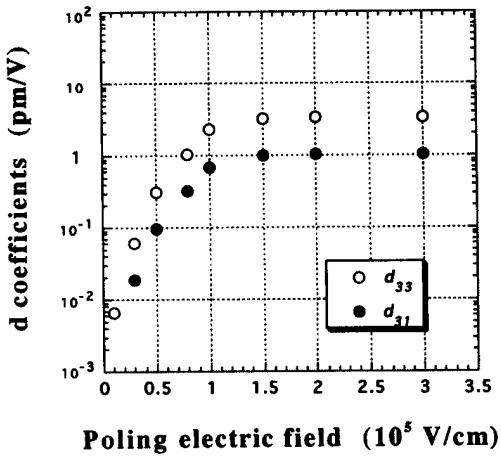

Fig.1 Poling electric field dependence of induced d coefficients

Moreover, the largest value of d_{33} should be compared with d_{22} ~ 2.6

pm/V in $LiNbO_3$. We believe that the SHG present result is the highest coefficient ever reported in silica-related bulk glasses.

From the dependence of SHG on polarization of fundamental light, the refractive indices of fundamental light are plotted in Fig.2 as a function of poling electric-field strength. n_ω^e and n_ω^o are the extraordinary and ordinary refractive indices of fundamental light, corresponding to s- and p-polarizations, respectively.

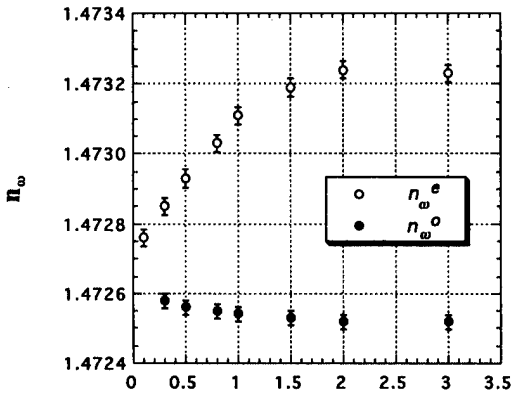

Fig.2 Poling electric field dependence of refractive indices of fundamental light

n_ω^e increases with increasing the poling electric-field strength up to approximately 1.5×10^5 V/cm, and then saturates. n_ω^o, on the other hand, decreases with increasing the poling field, in contrast with the increase of n_ω^e. We are not aware of any reported results as a direct experimental evidence of inversion-symmetry breaking in glasses induced by poling.

In summary, in a UV-poled germanosilicate glass we have found remarkable results regarding the induced SHG: 1) A large d coefficient exceeding d_{22} of $LiNbO_3$, was induced, 2) An anisotropic refractive index was observed, which is a direct evidence of inversion-symmetry breaking.

The "UV-poling" is one of the promising ways to obtain a novel photonic glass with an appreciable second-order nonlinearity, comparable to that in crystals. Quantitative measurements are still significantly necessary to understand basic mechanisms of thus induced nonlinearity.

Acknowledgments: The authors are grateful to Dr. Kazuya Saito of Toyota Technological Institute for fruitful discussions.

References

[1] R. A. Myers, N. Mukherjee, and S. R. J. Brueck, *Opt. Lett.* 16, 1732 (1991).
[2] T. Hirama, H. Muto, O. Sugihara, and N. Okamoto, *Opt. Rev.* 3, 17 (1996).
[3] A. C. Liu, M. J. F. Digonnet, and G. S. Kino, *Opt. Lett.* 19, 466 (1994).
[4] P. G. Kazansky, L. Dong, and P. St. J. Russell, *Opt. Lett.* 19, 701 (1994).
[5] T. Fujiwara, D. Wong, Y. Zhao, S. Fleming, S. Poole, and M. Sceats, *Electron. Lett.* 31, 573 (1995).
[6] T. Fujiwara, D. Wong, Y. Zhao, S. Fleming, V. Grishina, and S. Poole, Tech. Dig. of OFC, (San Diego, CA) 1995, paper PD-6
[7] T. Fujiwara, M. Takahashi, and A. J. Ikushima, *Electron. Lett.* 33, 980 (1997)
[8] B. F. Levine, *Phys. Rev. Lett.* 25, 440 (1970)
[9] T. Fujiwara, M. Takahashi, and A. J. Ikushima, accepted for publication in *Appl. Phys. Lett.*

An Ion Exchange Model for Extended-Duration Thermal Poling of Bulk Fused Silica

Thomas G. Alley, Richard A. Myers* , and S. R. J. Brueck
Center for High Technology Materials, University of New Mexico
1313 Goddard SE, Albuquerque, NM 87106
Tel: (505) 272-7800, Fax: (505) 272-7801

Thermal poling induces a strong second-order nonlinearity in bulk fused silica.[1] The nonlinearity occurs on the anode side of the poled glass; various measurements have shown that the nonlinear region is ~ 5 to 15 μm thick; and that the nonlinearity scales linearly with the applied poling voltage. The formation of the nonlinearity is a dynamic process involving mobile ionic charge carriers.[2] We present experimental observations of additional aspects of this dynamic process along with a model that demonstrates that ion exchange can play a role in the formation of the nonlinearity.

The creation of the nonlinearity is typically explained by the establishment of a strong electric field in the anodic region of the sample resulting from depletion of a positively charged mobile ionic carrier such as sodium, a common impurity in bulk fused silicas, under the applied field[1]. When the sample is heated to a temperature of $\gtrsim 200°C$, sodium ions become mobile, and migrate to screen an applied external field. The anodic region, now depleted of sodium, contains negatively charged centers still affixed in the glass matrix. The charge motion reaches equilibrium once a wide enough depletion region is established to reduce the total field to zero in the bulk of the sample. This screening results in a very large ~ 10^6-10^7 V/cm electric field, dropping essentially the entire applied voltage across this depletion region. This electric field breaks the macroscopic inversion symmetry of the glass, and a second order nonlinearity ($\chi^{(2)}$) results: either through the third order nonlinearity ($\chi^{(2)} = 3\,\chi^{(3)}E_{dc}$) and/or through dipole orientation (for example, singly-bonded oxygen defects) resulting from the large electric field.

There is, however, evidence that the dynamics of the formation of the nonlinearity are not fully explained by a simple single charge carrier model. There have been reports[3,4,5] of varying nonlinear region depths. Alternating layers of charge on the anodic surface have been reported.[6] Here we report experiments that demonstrate that a second, much slower charge transport process also impacts the formation of the nonlinearity in bulk silica glasses. Since this process occurs on time scales of 10 min to several hours, it can be responsible for many of the sample dependent and hysteretic effects that have been reported. Variables such as time duration

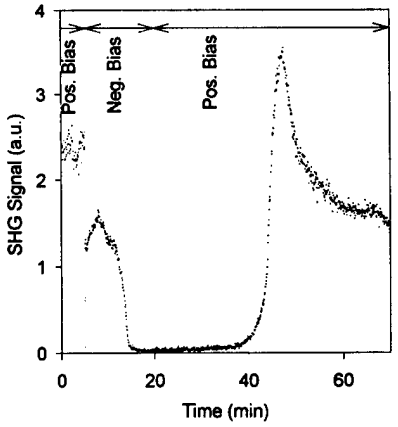

Figure 1. Field reversal behavior of second harmonic signal generated under top electrode. Positive bias was 5 kV, negative bias was -5 kV.

* Present address: Dept. of Physics, University of Auckland, Auckland, New Zealand

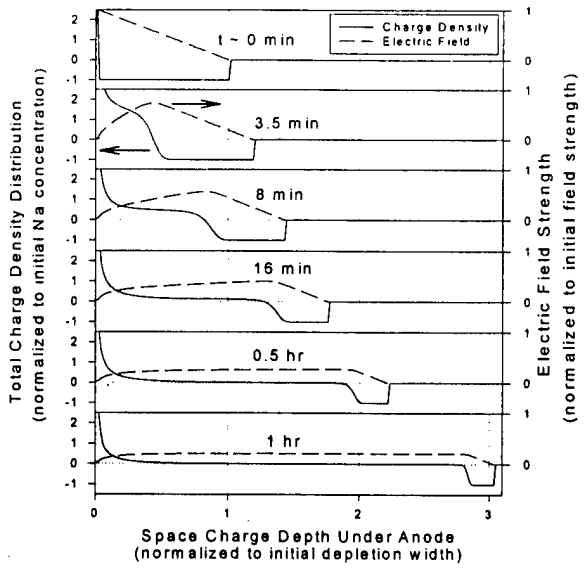

Figure 2. Modeled development of the space charge region with poling time under the positively biased electrode with the presence of moisture at the surface. Zero on the x axis represents the anode surface and unity depletion width (scaled to the depletion width for a single mobile charge carrier) is approximately 10 μm.

of the poling, poling atmosphere, and polarity of applied electric field all contribute to the observed dynamics of the formation of the nonlinearity.

Second harmonic generation experiments (mode-locked 1.06 μm source) were carried out using 0.6 and 1-cm thick bulk silica samples (Herasil™) maintained in a controlled atmosphere with optical access for monitoring the dynamics of the nonlinearity during poling. An indium-tin-oxide top electrode allowed optical access. The fundamental radiation was focused to a ~ 1-mm depth-of-field to isolate the nonlinearity arising from a single surface region.

Under certain conditions, reversing the applied field leads to a transient nonlinearity on the cathode side (fig. 1) as well as the dominant anode side nonlinearity. This is consistent with some, hitherto unexplained, reports of Maker fringes with a period corresponding to the full thickness of the sample.[7,8] Following a second (and subsequent) field reversals, long delays (~ 20 min) are observed before growth of the signal (fig. 1). These observations cannot be explained by the simple, single charge carrier, depletion region model.

We propose that water, present either on or already diffused into the glass, coupled with the strong fields provides a source of hydrogenated ions such as H_3O^+ that are injected into the glass and contribute to the space-charge formation. A numerical simulation is presented that tracks the movement of these ions into the depletion region. Because of the large difference (approximately 10^4) between the mobility of sodium ions and that of hydronium ions, the usual charge neutrality assumptions for charge exchange processes are not valid and the hydrogenated ions accumulate and develop a region of positive charge, pushing the negative depletion region further into the sample, diminishing its width, and lowering the electric field within the region (fig. 2). The positive charges localized at the anode result in a reduced field at the surface and eventually reach a limit where further injection is prevented. This ex-

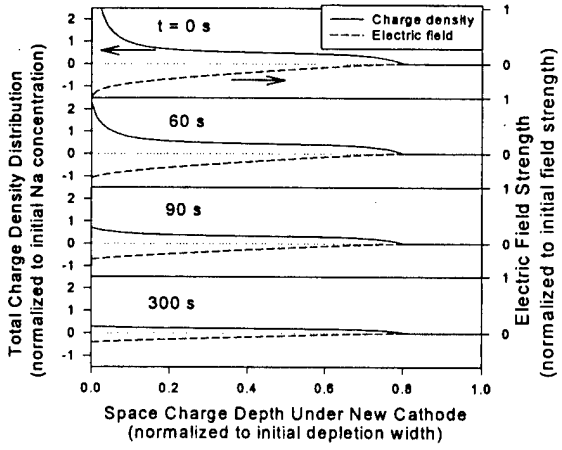

Figure 3. Evolution of space charge region with poling time under negatively biased electrode after field reversal. Zero on the x axis represents the new cathode surface and unity depletion width (scaled to the depletion width for the single charge carrier model) is ~ 10 μm.

plains why one might measure a dipole charge distribution.

When the applied voltage is reversed, there is an electric field in the (new) cathode region associated with the positive charge accumulation. The electric field diminishes in strength until the hydrogenated ions are eliminated from the sample (fig. 3). This can explain why a second harmonic signal is observed after field reversal under the cathode. Further, the long time scale associated with reversing the hydronium charge can be associated with the observed delay in re-establishing the nonlinearity for multiple poling cycles.

Reports of various nonlinear region depths, alternating charge layers, and our observation of a dynamic process on the order of 10's of minutes, show that there are additional contributing factors in the formation of the $\chi^{(2)}$ in bulk fused silica, beyond the simple single charge carrier model. Our model, based on ion exchange of hydrogenated ions, is helpful in understanding the mechanisms underlying these observations.

References:

[1] R.A. Myers, N. Mukherjee, and S.R.J. Brueck, "Large second-order nonlinearity in poled fused silica," Opt. Lett. **15**, 1733 (1991).

[2] N. Mukerjee, R. A. Myers and S. R. J. Brueck, "Dynamics of second-harmonic generation in fused silica," Jour. Opt. Soc. Amer. **B665** (1994).

[3] R.A. Myers, *Large Second-Order Nonlinearity in Amorphous SiO_2 Using Temperature/Electric-Field Poling*, Ph.D. Dissertation, University of New Mexico (1995).

[4] P.G. Kazansky, A. Kamal and P.St.J. Russell, "Erasure of thermally poled second-order nonlinearity in fused silica by electron implantation," Optics Lett. **18**, 1141 (1993).

[5] W. Margulis and F. Laurell, "Interferometric study of poled glass under etching," Opt. Lett **21**, 1786 (1996).

[6] P.G. Kazansky, A.R. Smith, P.St.J. Russell, G.M. Yang, and G.M. Sessler, "Thermally poled silica glass: Laser-induced pressure pulse probe of charge-distribution," Appl. Phys. Lett. **68**, 269 (1996).

[7] H. Nasu, H. Okamota, M. Mito, J. Matsuoka, and K. Kimiya, "Influence of the OH content on second harmonic generation from electrically polarized SiO_2 glasses," Jpn. J. Appl. Phys. **32**, L406 (1993).

[8] L.J. Henry, A.D. DeVilbiss, and T.E. Tsai, "Effect of preannealing on the level of second-harmonic generation and defect sites achieved in poled low-water fused silica," J. Opt. Soc. Amer. **B12**, 2037 (1995).

Effect of Minority Species on Thermal Poling of Fused Silica Glasses

Noriyuki Wada and Kenji Morinaga
Department of Materials Science and Technology, Graduate School of Engineering Sciences, Kyushu University, Fukuoka 816, Japan

Hiromichi Takebe*, Valerio Pruneri and Peter G. Kazansky
Optoelectronics Research Centre, University of Southampton, SO17 1 BJ, United Kingdom
*Visiting Research Fellow from Kyushu University
Tel +44-1703-593954, Fax +44-1703-593149, E-mail ht@orc.soton.ac.uk

High second-order nonlinearity (SON) in poled silica glasses [1] is of great interest for the development of linear electro-optic modulators and frequency converters monolithically integrated into optical fibres or planar glass waveguides. However, its origin [1, 2] is not fully understood. The extrinsic effects of poling time and voltage on second-harmonic (SH) generation in thermally-poled silica glass have been studied [1, 3]. In particular the quadratic dependence of the maximum SH signal on the applied voltage indicated linear dependence of the SON on internal electric field [3]. There are several studies on intrinsic effects associated with defects [1, 4] and minority species such as OH [1, 5] and Na [1, 6] in thermal poling of silica glasses. In this work we carried out a systematic analysis of oxygen related defects and impurities (OH and Na) in commercial fused silica glasses (without relying on their catalogue data) and discuss their effects on SON.

Table 1 shows the sample characterizations and the results of SH signal measurements in commercial fused silica glasses. We used three types of fused silica glasses, as in previous work [1, 4, 6]: electrically-fused quartz glass (type I), quartz glass fused in a H_2-O_2 flame (type II) and silica glass synthesized from $SiCl_4$ in a H_2-O_2 flame (type III). Two types of oxygen defects: oxygen deficient centre (ODC, ≡Si···Si≡) for type I and III silica and silicon lone-pair centre (SLPC, =Si:) for type II silica can be identified from the absorption bands near 5 eV [7]. The latter defect in Herasil 1 samples could be annealed out at 1000°C, which agrees with previous work [7]. The concentrations of OH were determined from the intensity of an infrared absorption peak at 3600 cm^{-1} using a molar extinction coefficient 86 $L \cdot mol^{-1} \cdot cm^{-1}$ for OH [8]. The concentrations of Na were analysed by the inductively coupled plasma (ICP)-mass method.

SH signal measurements were performed in bulk samples (15 x 15 x 3 mm) poled in air by applying 4 kV at 280°C for 60 min [3]. Q-switched and mode-locked Nd: YAG laser pulsed radiation at 1064 nm with an average power of 850 mW was used as the pump source. Laser radiation was passing through the samples at a Brewster angle of 60°. SH signals were detected by a Si detector and the value of SH signal in poled Herasil 1 samples was ~ 4.5 nW and the minimum detectable value of SH signals was about 0.1 nW. Our results in type I and type II silica glasses agree with previous results [1, 4-6]. However, no SH signal was observed in type III synthesized silica, contrary to previous studies [1, 6],where type III showed ~ 10 % of SH signal with respect to type I and II. Myers et al. [1] suggested that there is no obvious correlation between SON and Na or OH concentrations. Nasu et al. [5] concluded that the SH intensity is linearly dependent on OH concentration in all of the following three types of silica glasses: fused quartz, synthesized silica and sol-gel derived silica. Our results show that the SH signals are

independent of OH concentration and are observed only in fused quartz glasses (Infrasil 1 and Herasil 1) containing Na impurities in relatively-high concentrations, ≥ 0.4 ppm, according to the ICP-mass analysis.

Henry [4] showed that by using EPR analysis the SH signal in type I silica glass was independent of the relative concentration of Ge impurity E' defects sites, but that in type II silica glass was linearly dependent on this concentration. From our results in as-received (with the absorption band) and annealed (without the absorption band) Herasil 1 samples, one can infer that SLPC is not directly related to the SON in type II silica glasses.

Table 1 Impurity characterizations and SH signals in commercial fused silica glasses.

Type	Commercial Name	Defect	OH (ppm) catalogue	OH (ppm) analysis	Na (ppm) catalogue	Na (ppm) analysis	SH signals (a. u.)
I	Infrasil 1*	ODC	< 8	5	1	0.52	1.5
	IR**	None	8	<1	4	0.06	Not observed
II	Herasil 1*						
	As-received	SLPC	130~200	117	1	0.39	1
	Annealed	None		102			0.8
III	Suprasil 1*	ODC	1200	511	0.04	0.04	Not observed

* Heraseus, **Nippon Silica glass.

The effect of Na impurities on DC current measured during thermal poling processes was also studied. For this purpose circular electrodes of Au paste were formed and fired on both sides of the glass samples (10 x 10 x 3 mm). An Au grounded ring electrode was also formed on the cathodic surface to prevent effects associated with surface current.

Fig. 1 shows the DC current variation as a function of poling time at 280°C and 4 kV in type II silica, as-received Herasil 1, and in type III silica, Suprasil 1. The current in the former glass, which shows SON, decreases continuously and after ~30 min becomes approximately constant (Type I is similar to type II). This behaviour is similar to the electrical conduction attributed to trap filling processes in poling of nonlinear optical side chain polymers [8]. The type III silica glass, without detectable SON, has a similar behaviour; however, the magnitude of the DC current is about ten times smaller than that in type II silica glass. The difference between these two types of silica can be explained through the different concentration of Na impurities.

SH signals were observed in type I and II silica glasses poled above 200°C, with a maximum signal at ~ 280°C, in good agreement with previous results [1]. Fig. 2 shows the current variation during poling at two different temperatures (200 and 280°C) and 4 kV applied voltage for type II silica glass, as-received Herasil 1. The current at 200°C is small and constant in time. Therefore, the initial current decrease at 280°C is probably related to migration of mobile Na ions and formation of Na depletion region (poled layer). The relaxation time of current in Herasil

1 is consistent with the fact that the SH signal in this glass saturates after 45 min up to 180 min from the beginning of the poling process [3]. Our studies indicate that Na impurities play a key role in thermal poling of bulk fused silica.

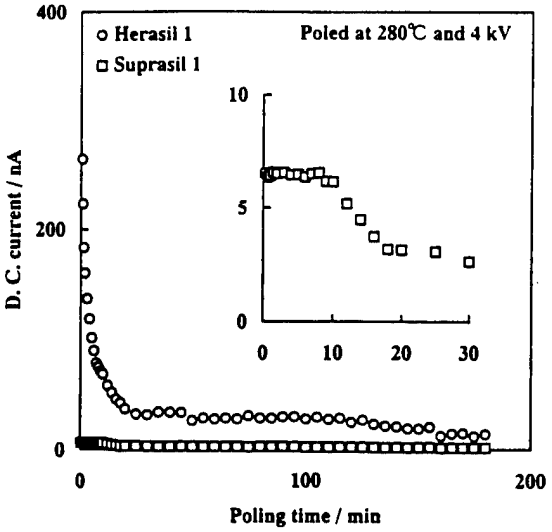

Fig. 1 DC current versus poling time in type II fused quartz and type III synthesized silica glasses at 280°C and 4 kV.

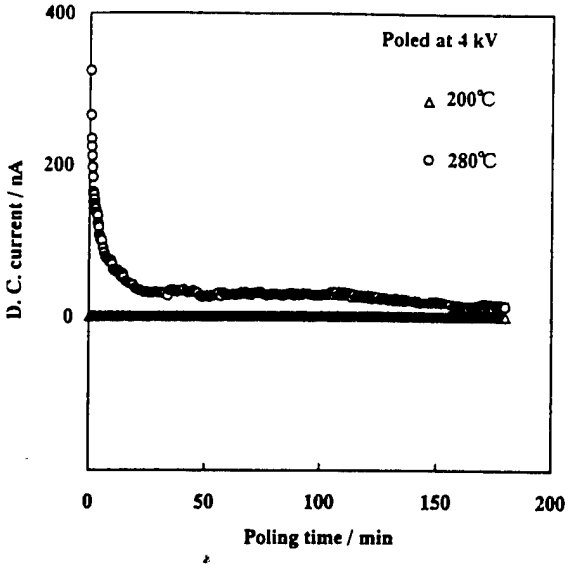

Fig. 2 DC current versus poling time in type II fused quartz glass, Herasil 1 at 200 or 280°C and 4 kV.

References

1. R. A. Myers, N. Mukherjee and S. R. J. Brueck, Opt. Lett. **16**, 1732 (1991); N. Mukherjee, R. A. Myers and S. R. J. Brueck, J. Opt. Soc. Am. B **11**, 665 (1994); R. A. Myers, X. Long and S. R. Brueck, Proc. SPIE **2289**, 98 (1994).
2. P. G. Kazansky and P. St. J. Russell, Opt. Commun. **110**, 611 (1994).
3. H. Takebe, P. G. Kazansky, P. St. J. Russell and K. Morinaga, Opt. Lett. **21**, 468 (1996).
4. L. J. Henry, Opt. Lett. **20**, 1592 (1995).
5. H. Nasu, H. Okamoto, K. Kurachi, J. Matsuoka and K. Kamiya, J. Opt. Soc. Am. B **12**, 644 (1995).
6. J. M. Dell and M. J. Joyce, "Second Harmonic Generation in Electric Field Poled Glasses"; "Erasure of Poling Induced Second Order Optical Nonlinearities in Silica by UV exposure", presented at the Australian Optical Society (1993).
7. N. Kuzuu and M. Murahara, Phys. Rev. B **47**, 3083 (1992).
8. J. P. Williams, Y. -S. Su, W. R. Strzegowski, B. L. Butler, H. L. Hoover and V. O. Altemose, Am. Ceram. Soc. Bull. **55**, 524 (1976).
9. M. Eich, R. Blum, M. Sprave, Procs.of Inter. Conf. on Organic Nonlinear Optics 3, Marco Island, Florida, USA, December, 1996, pp. 92-93.

Absolute Prism-Assisted Maker Fringe Measurements of the Nonlinear Profile in Thermally Poled Silica

D. Pureur*, A. C. Liu, M. J. F. Digonnet, and G. S. Kino
E. L. Ginzton Laboratory, Stanford University, Stanford, CA, USA
** on leave from Laboratoire de Dynamique Moléculaire et Photonique, Université des Sciences et Technologies de Lille, FRANCE*
Tel: 415-723-2893, Fax: 415-725-7509, Email: alice@macro.stanford.edu

I. INTRODUCTION

Since the first measurements of a sizeable nonlinearity in thermally poled silica [1] were reported, there has been considerable interest in developing silica-based frequency converters and electrooptic devices. It is generally well accepted that the nonlinearity in thermally poled silica is confined to a thin (1-15 μm) layer on the glass sample that was exposed to the anode side during poling. However, reports differ markedly as to the shape (exponential [1], or Gaussian [2]) and thickness (a few to 10 μm and even 700 μm) [1–3] of this nonlinear region. In practical waveguide devices, a precise knowledge of these parameters is critical to understand and maximize the spatial overlap between this region and the optical mode. Yet to date, no standard method is available to measure these quantities reliably. Earlier, we made initial measurements of the nonlinearity using a prism pair [4]. Difficulties with the homogeneity of the poled region limited the maximum angle that could be explored, and a profile could not be definitively inferred. In this paper we describe 1) improvements in this prism-assisted Maker fringe technique and 2) a theoretical analysis that permits the first absolute measurement of the nonlinearity profile in poled silica.

II. EXPERIMENTAL DESCRIPTION

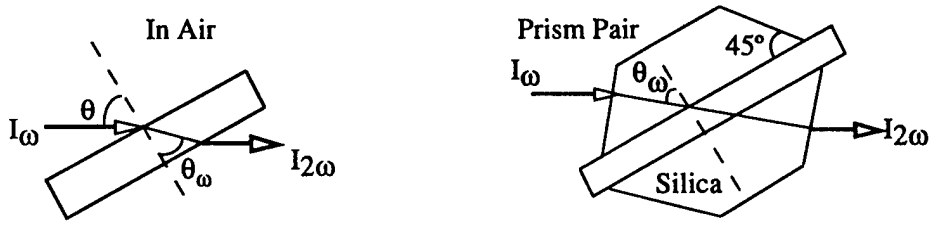

FIG. 1. Sample orientation in SH measurement

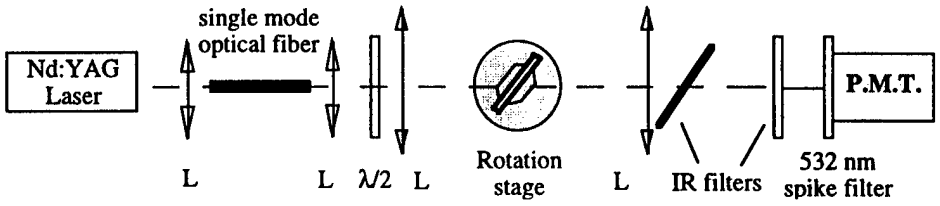

FIG. 2. Experimental setup for an absolute SH conversion efficiency measurement.

A common technique for the measurement of the nonlinear coefficient d of a thin nonlinear region is a relative Maker fringe measurement using a known standard material such as $LiNbO_3$ or quartz [5]. The angular variation of the second harmonic (SH) can be used to determine the thickness of the region. However, when the induced nonlinearity is not a step profile, as may be the case for poled silica, such a relative measurement is not reliable , and an absolute SH measurement is required. Furthermore, since the region is expected to be thin, Maker fringes are not observed in poled silica unless the fundamental beam propagates near grazing incidence. When the sample is tested in air, the maximum possible propagation angle of the fundamental beam inside the sample θ_ω is limited by total internal reflection (TIR) of the SH beam at the glass-air output interface of the sample (see Fig. 1). For silica, this angle is $\approx 43.2°$, which is much too small

to observe even the first fringe for nonlinear regions only a few microns thick. As a remedy, we proposed to place a matched pair of silica prisms against the input and output faces of the sample [4], as shown in Fig. 1. In the measurements reported, we used 45° prisms, which in principle allows testing the sample up to angles approaching 90°.

The sample we tested was a 1.6 mm thick silica substrate (Herasil 1) prepared in the manner described in Ref. [1]. The poling parameters used were 270 ℃, 5.26 kV, and 30 min. To produce a homogeneous poling region, n-type silicon wafers (0.1 - 0.9 Ω-cm) were used as the electrodes. The induced nonlinearity was measured using the setup shown in Fig. 2. A single mode optical fiber spatially filtered the output of the Q-switched Nd:YAG laser (200 ns pulse, 1 kHz repetition rate, 1 W average power) to provide the sample with a clean and easily measured spot size at the focus. The polarization of the fiber output was controlled by a Babinet-Soleil compensator and a $\lambda/2$ wave plate. The focused beam ($1/e$ radius $w_0 \approx 30\ \mu m$, 70 mW average power) probed the poled surface of the sample as a rotation stage varied the angle of propagation through the silica. Using calibrated filters, the generated SH was separated from the fundamental beam and measured with a photomultiplier tube. The measured peak power of the fundamental and SH beams were corrected for Fresnel reflections at the input and output face of the sample (or prism), respectively, to obtain the SH and fundamental peak powers inside the sample. The peak intensity of the fundamental beam was determined by dividing the powers by the appropriate measured area. In this manner, we made an absolute measurement of the angular dependence of the intensity conversion efficiency $\eta(\theta_\omega) = I_{2\omega}(\theta_\omega)/I^2_\omega(\theta_\omega)$ at the nonlinear region.

III. EXPERIMENTAL RESULTS AND ANALYSIS

With this setup, we were able to measure the angular dependence of the SH intensity generated by the poled silica sample, as shown in Fig. 3. The prisms can only be used to measure angles down to $\theta_\omega \approx 30°$. To complete the curve at smaller angles, we characterized the sample without the prisms as well. The crosses and open circles represent data taken with and without the prism pair, respectively. The smooth transition between propagation angles probed in air and with the prisms indicates that the sample homogeneity is much improved, and that the various Fresnel correction factors were properly accounted for. We were able to measure the SH signal up to an internal angle of 84°, which let us observe nearly one full fringe.

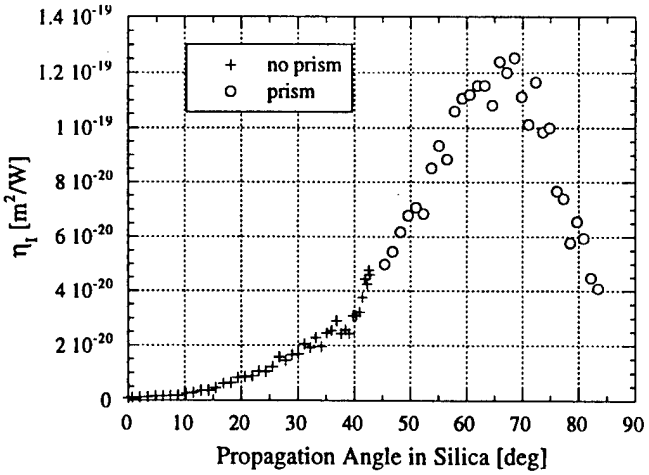

FIG. 3. η_I vs. θ_ω. Comparison of the measured SH conversion efficiency with (o) and without (+) prism pair.

In order to theoretically fit the measured Maker fringe, it is necessary to take into account the induced nonlinearity as a function of the perpendicular penetration distance into the bulk silica $d_{33}(z)$. Using an approximate coupled mode theory, we first define $\Delta k = 4\pi(n_{2\omega} - n_\omega)/\lambda$, where n_ω and $n_{2\omega}$ are the refractive indices of the fundamental and second harmonic waves, respectively, and ω and λ are the fundamental frequency and wavelength. The intensity conversion efficiency η_I as a function of the angle of propagation of the fundamental beam in the sample θ_ω is then given by:

$$\eta_I(\theta_\omega) = \frac{2\omega^2 \tan^2\theta_\omega}{\epsilon_0 c^3 n_\omega^2 n_{2\omega}} \left| \int_0^\infty d_{33}(z)\, e^{j\Delta kz/\cos\theta_\omega}\, \mathrm{dz} \right|^2 \qquad (1)$$

where ϵ_0 and c are the permittivity and speed of light in vacuum. Since the path length of the beam is $z/\cos\theta_\omega$, for the poled silica symmetry the effective nonlinear coefficient is $d_{33}\sin\theta_\omega$. This expression was fitted to the data (see Fig. 3 by varying the magnitude and shape of the nonlinear coefficient $d_{33}(z)$. For a Gaussian profile with an amplitude of 0.34 pm/V, $1/e$ width of 5.5 μm and buried 2.5 μm beneath the surface (shown in the Fig. 4 inset), the solid theoretical curve in Fig. 4 shows good agreement with the experimental data. These values are consistent with those inferred in earlier work by a different technique in similar glass poled under similar conditions [1]. The dashed curve is a theoretical fit for a step profile of similar thickness and amplitude. The ability to propagate at large angles in silica enabled us to distinguish between a step and Gaussian profile.

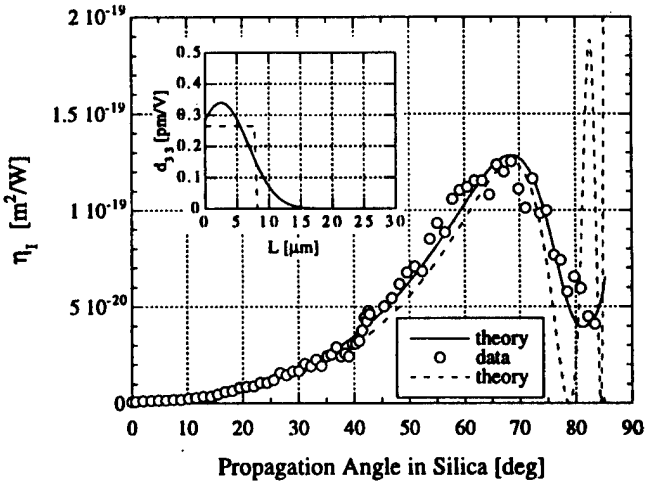

FIG. 4. η_I vs. θ_ω. Solid line is the theoretical fit assuming a Gaussian profile with amplitude = 0.34 pm/V, $1/e$ width = 8 μm, and buried depth = 2.5 μm. Dashed line is the fit assuming a step profile of amplitude 0.33 pm/V and thickness L = 8 μm.

IV. SUMMARY

In this paper we have demonstrated a prism-assisted absolute Maker fringe measurement technique which can be used to characterize the strength of the nonlinear coefficient d_{33} and determine the depth profile of the induced nonlinearity. For a thermally poled silica sample (5.26 kV, 270 ℃), we find the induced second order nonlinearity has a strength of 0.34 pm/V, and a Gaussian profile with a $1/e$ width of 5.5 μm and a buried depth of 2.5 μm. This technique is a powerful tool to characterize thin nonlinear regions, in particular to analyze the effect of poling parameters and material composition, and to gain a better understanding of the poling process.

[1] R. A. Myers, N. Mukherjee, and S. R. J. Brueck, "Large second-order nonlinearity in poled fused silica," *Optics Letters*, vol. 16, no. 22, pp. 1732–1734, 1991.

[2] P. St. J. Russell, P. G. Kazansky, and A. Kamal, "Electron implantation-a new technique for creation and modification of second-order susceptibility in glasses," *Proc. SPIE - Int. Soc. Opt. Eng.*, vol. 2044, no. 192-201, 1993.

[3] H. Nasu, H. Okamoto , A. Mito , J. Matsuoka , and K. Kamiya , "Influence of the OH^- content on second harmonic generation from electrically polarized SiO_2 glasses," *Japanese Journal of Applied Physics*, vol. 32, no. 3B, pp. L406–7, 1993.

[4] A. C. Liu, M. J. F. Digonnet, and G. S. Kino, "Characterization of the second order nonlinearity in poled fused silica," *Proc. SPIE - Int. Soc. Opt. Eng.*, vol. 2289, no. 194-206, 1994.

[5] J. Jerphagnon and S. K. Kurtz, "Maker fringes: A detailed comparison of theory and experiment for isotropic and uniaxial crystals," *Journal of Applied Physics*, vol. 41, no. 4, pp. 1667–1681, 1970.

Improving the Nonlinearity of Silica by Poling at Higher Temperature and Voltage

A. C. Liu, D. Pureur*, M. J. F. Digonnet, and G. S. Kino
E. L. Ginzton Laboratory, Stanford University, Stanford, CA, USA
E. J. Knystautas
Université Laval, Québec, Canada
* *on leave from Laboratoire de Dynamique Moléculaire et Photonique, Université des Sciences et Technologies de Lille, FRANCE*
Tel: 415-723-2893, Fax: 415-725-7509, Email: alice@macro.stanford.edu

I. INTRODUCTION

Thermal poling of silica offers the exciting prospect of achieving, for the first time, low-loss electro-optic switches and modulators in a fiber form, devices that can be fusion spliced to a single mode fiber with negligible loss, unlike any other existing modulator. For this to become possible, both the depth (a few microns) and the nonlinear coefficient (0.5-1 pm/V) of the nonlinear region induced in silica by standard thermal poling must be increased. These objectives may be met by optimizing the glass composition and/or the poling process.

Poling is normally conducted by applying a voltage of 4-5 kV to the glass sample heated in air at around 275 ℃ for a few minutes. [1] This process is based on the observation that for poling voltages around 4-5 kV, a temperature of $\sim$ 275°C maximizes the SH efficiency of the poled sample. [1,2] We suggest here that this decrease in nonlinearity at higher temperatures may result from a competition between two physical mechanisms. Assuming that part of the poling mechanism is associated with dipole orientation model, we surmise that, 1) the greater thermal energy increases the number of available bonds, dipoles or space charges available for orientation by the applied field, and 2) thermal agitation tends to misalign the orientation induced by the applied field. Consequently, we suggest that to produce a poled region with a greater nonlinearity and/or depth than obtained with standard poling one must increase both the poling voltage and the poling temperature. In this paper we describe a 400 ℃ and high voltage poling process and compare it to the standard thermal poling at 275 ℃. We show that 400 ℃ poling can improve the measured second harmonic (SH) intensity conversion efficiency by a factor of 3 over standard thermally poled substrates (defined as 275 ℃ and 4-5 kV).

II. EXPERIMENTAL SETUP

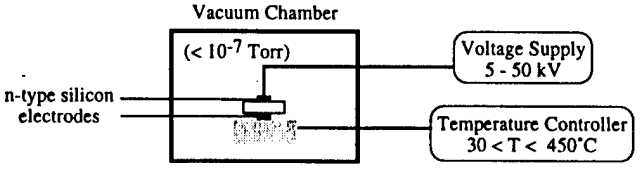

FIG. 1. High Temperature and Voltage Vacuum Poling System

Poling in air at elevated temperature and high voltages is impeded by dielectric breakdown of air around the sample. Whereas standard poling is easy to achieve, poling at higher temperature (400 ℃) and voltages ($\geq$ 10 kV) is difficult because the dielectric breakdown strength of air drops with increasing temperature. To circumvent this problem, we poled our samples in the vacuum system depicted in Fig. 1. The glass samples used were 1.6 mm thick wafers of Infrasil or Herasil (which yield approximately the same poling characteristics). The sample was sandwiched between two n- type silicon wafers and placed on the heater in the vacuum chamber. After the residual air pressure in the chamber reaches 10^{-7} Torr or better, and after the heater has raised the temperature to $\sim$ 400 ℃, the voltage is switched on and maintained for typically 30 minutes. The heater is then turned off and the sample cools off (typically several hours), at which point

the voltage is switched off. The data is limited in extent because this poling process takes several days from start to finish.

III. EXPERIMENTAL RESULTS

The poled samples were characterized by a Maker fringe second harmonic (SH) generation method, described elsewhere [3]. This method involves measuring the dependence of the SH peak power generated by the sample from an infrared (IR) focused beam (1064 nm) on the angle of incidence of the beam on the sample. By probing the SH signal up to large angles and fitting the data to a Maker fringes model, the profile of the poled sample nonlinearity and the peak nonlinearity were inferred. Fig. 2 shows the intensity conversion efficiency η_I measured at a fixed incidence angle as a function of poling voltage measured in a variety of poled samples. The open circles show the results obtained with samples poled at the standard temperature of 275 ℃. As shown by others [2,4], as the voltage is increased η_I, increases rapidly, then reaches a more level plateau above 5 kV. Note, however, that 5 kV is not the optimum poling voltage, but that higher voltages yield stronger SH conversions. The triangle and cross data points show the results obtained with identical samples poled with our improved method, i.e. at higher temperature (400- 440 ℃) and higher voltages (10 kV and 15 kV). It can readily be seen that under these new conditions the SH conversion efficiency is significantly increased, by about a factor of 3 over a sample poled under standard conditions (275 ℃ and 4-5 kV).

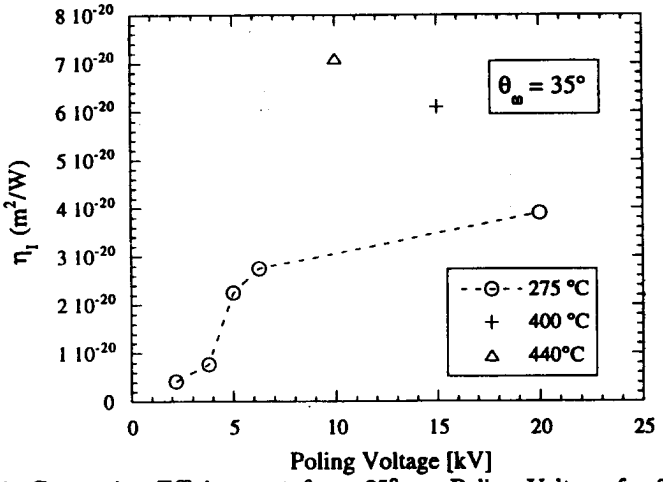

FIG. 2. Second Harmonic Conversion Efficiency at $\theta_\omega = 35°$ vs. Poling Voltage for 275 ℃ and $\geq$ 400 ℃ Poling Temperatures

To further elucidate the effect of the poling conditions on the induced nonlinearity, we fitted the angular dependence of the SH conversion to a model to obtain the nonlinearity profile. In all cases we obtained a buried Gaussian profile. Fig. 3 shows a sample of the d_{33} profiles we inferred by this method where the nonlinear depth represents the dimension perpendicular to the poled surface.

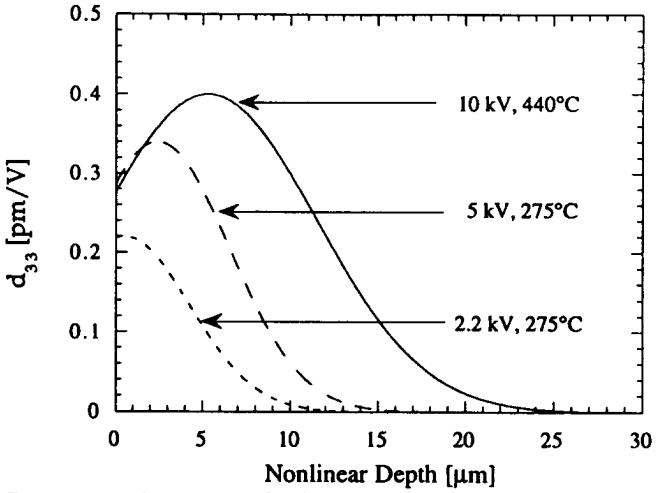

FIG. 3. Inferred Buried Gaussan Profiles for 275 °C (dashed lines) and 440 °C (solid line). The surface in contact with the anode corresponds to 0 μm.

Table 1 summarizes the values of the nonlinear coefficient d_{33} at the peak of the Gaussian, the half width of the Gaussian W, the distance by which its peak is buried, B, and the total depth T=W+B. For a given poling temperature, d_{33} and the half-width of the Gaussian all increase slightly. However, the nonlinear region becomes more deeply buried and the total depth T increases steadily and significantly.

Volt [kV]	Temp [°C]	d_{33} [pm/V]	W [μm]	B [μm]	T [μm]
2.2	275	0.22	5.3	0.5	5.8
3.8	275	0.22	5.7	2.4	8.1
5	275	0.34	5.8	2.4	8.2
20	275	0.33	10	4	14
10	440	0.4	8.7	5.3	14.0

TABLE 1. Inferred Gaussian Profile Parameters d_{33}, W, B, and T for 275 °C and 440 °C Poling Temperature Samples.

IV. SUMMARY

In summary, we have shown that the strength and depth of the nonlinear region induced in silica by thermal poling are increased when both the poling temperature and voltage are raised beyond the values used for standard poling at 5 kV. Detailed Maker fringes analysis shows that in a sample poled at 400 °C and 10 kV, the maximum nonlinear coefficient d_{33} is only slightly higher (0.4 pm/V versus 0.34 pm/V), but the depth of the nonlinear region is nearly doubled (14 μm versus 8.2 μm). This improvement is meritorious when trying to make waveguide devices, in which it is important that the nonlinear region reaches into the generally buried guiding region of the waveguide. This study strongly suggests that futher improvements are expected by poling at even higher temperature and voltage.

[1] R. A. Myers, N. Mukherjee, and S. R. J. Brueck, "Large second-order nonlinearity in poled fused silica," *Optics Letters*, vol. 16, no. 22, pp. 1732–1734, 1991.

[2] H. Takebe, P. G. Kazansky, P. St. J. Russell, and K. Morinaga, "Effect of poling conditions on second-harmonic generation in fused silica," *Optics Letters*, vol. 21, no. 7, pp. 468–70, 1996.

[3] D. Pureur, A. C. Liu, M. J. F. Digonnet, and G. S. Kino, "Absolute prism-assisted Maker fringe measurements of poled silica," to be published.

[4] R. A. Myers, *Large Second-Order Nonlinearity in Amorphous SiO_2 Using Temperature/Electric Field Poling*, Ph.D. thesis, Univerisity of New Mexico, 1995.

FUNDAMENTALS OF GLASS POLING: FROM SELF-ORGANIZATION TO ELECTRIC-FIELD POLING

Peter G. Kazansky and Valerio Pruneri

Optoelectronics Research Centre, University of Southampton,
Southampton SO17 1BJ, United Kingdom

One decade has passed since the discovery of self-organized (photoinduced quasi-phase-matched) second-harmonic generation (SHG) in optical fibers [1-2]. This discovery has attracted considerable interest world-wide [3-16] due to the unusually strong $\chi^{(2)}$ (second-order susceptibility) gratings induced purely by optical fields in glass (10^{-15}-10^{-16} m/V, which were 4-5 orders of magnitude higher than one could explain by known physical processes). In 1991 the value of $\chi^{(2)}$ has been increased to a new level of 1 pm/V by thermal poling [26]. In this paper we discuss fundamentals of glass poling, trying to answer the question: What is the limit of a second-order nonlinearity in glass?

The mystery of photoinduced $\chi^{(2)}$ gratings was finally solved on the basis of a new phenomenon - the coherent photogalvanic effect [6]: quantum interference between the one- and two-photon ionization processes of defect states changes the angular distribution of photoelectrons and excites a phase dependent current (*coherent photocurrent*); this current gives rise to a spatially-oscillating electrostatic field ($E_g \simeq j_{coh}/\sigma$, where E_g is the photogalvanic field, j_{coh} is the *coherent photocurrent*, σ is the photoconductivity); the amplitude of the photogalvanic field E_g in glass is typically $\sim 10^4$-10^5V/cm and this field can induce experimentally observed values of $\chi^{(2)}$, via the third-order susceptibility: $\chi^{(2)} = 3\chi^{(3)} E_g$ (assuming $\chi^{(3)} \simeq 1.8\text{x}10^{-22}$ $(\text{m/V})^2$ for silica glass).

More recently, the interference between different quantum processes has been the subject of considerable attention in many areas of physics (e.g. electromagnetically induced transparency (EIT) and lasers without inversion are based on quantum interference [17]). One of the reasons for this growing interest is that such kinds of interference open a prospect of a new degree of freedom in the control of physical and chemical processes - not only by the intensity or the polarization of light, but also by the phase of light. *Coherent photocurrent* was observed in the experiments on rubidium atoms [18] and photoemission from Sb-Cs photocathodes [19] and in AlGaAs/GaAs quantum well superlattices [20]. However self-organized SHG in glass was the first observed phenomenon where *coherent photocurrent* was involved.

It is possible to interpret the *coherent photocurrent* in glass in terms of electronic wave-functions interference. Indeed, in centrosymmetric media one-photon transition is allowed between states of different parity and two-photon transition between states of the same parity. If the ground state for one- and two-photon transitions is the same, then the parity of the corresponding excited states should be different. The interference of electronic wave- functions of different parity in the continuum of states (conduction band) results in asymmetric wavefunction, leading to photocurrent [20]. The orthogonality of the wave-functions in the excited state of the one-and two-photon transitions in centrosymmetric media leads also to the absence of modulation of the total cross section of ionization (*coherent photoconductivity*) in this process (involving odd number of photons).

However, until recently, two interesting aspects of the quantum interference phenomenon have not been investigated. Firstly, experiments on quantum interference have been carried out only in centrosymmetric media although it was already widely discussed that in media without inversion symmetry the interference between one- and two-photon transitions induced by light at frequencies 2ω and ω can lead to a modulation of the total cross-section for the overall transition [21]. Secondly, the modulation of the total cross-section of ionizing transitions due to quantum interference involving

even number of photons (*coherent photoconductivity*) has been observed only in atomic systems [22-24]. Recently, we reported the observation of efficient SHG in glass subjected to a strong external electrostatic field [25]. The spatial periodic modulation of the applied electric field, responsible for the second harmonic signal, arises from the interaction of the intense light at frequencies ω and 2ω with glass, which has its inversion symmetry broken by the applied field. We achieved ~ 2% conversion efficiencies for peak powers of ~ 1 kW. These values give an amplitude of $\chi^{(2)} \simeq 10^{-14}$m/V, which corresponds to a modulation of ~8% of the applied electric field (~6×10^6 V/cm). The observed phenomenon represents the first evidence of *coherent photoconductivity* in solid state materials.

On the other hand during the past six years a number of glass poling techniques have emerged that produce permanent second-order nonlinearities (independent of the presence of optical fields of ω and 2ω) approaching 1 pm/V (very close to the value of nonlinearity in LBO, which is a crystal widely used for pulsed frequency conversion). These new poling techniques are: thermal poling at 250-300°C under an applied high voltage (the second-order nonlinearity appears in a thin layer just under the anode) [26], corona poling of glass waveguides [27] and charge implantation by exposure to an electron-[28] or proton-beam [29]. Most recently an electro-optic coefficient of ~6 pm/V has been reported in silica fibre poled under UV excitation [30]. However the latter result has not been confirmed by other groups. So far thermal poling is the most promising technique for practical applications: nonlinearity is strong enough and shows no degradation under illumination with intense visible and infrared light [31-50]. It was suggested that a high dc field (~10^7 V/cm) in a thin region (~5-10 μm) depleted of cations under the anodic surface is responsible for this phenomenon [26]. This field can be frozen-in between the two layers of space charge: negatively charged depletion region and positively charged layer created as a result of ionization or diffusion in the high field between the depletion region and the anode [37, 44]. Charged distributions obtained in poled glasses by the laser induced pressure pulse (LIPP) [45] and the etching techniques [46] are in good agreement with this model. More complicated charge distributions (with the inverted charge regions) were also observed by the LIPP technique in poled samples [45]. It is still not clear whether $\chi^{(2)}$ is induced by high dc field via $\chi^{(3)}$ or orientation of dipoles. Indeed with the maximum dc field limited by the intrinsic breakdown of silica (~10^7 V/cm) it is possible to justify the values of $\chi^{(2)} \leq .54$ pm/V via $\chi^{(3)}$ of silica. However about two times higher values have been measured experimentally. This discrepancy may have different explanations: by uncertainty in the thickness and distribution of the nonlinear layer, by a higher $\chi^{(3)}$ value in the poled layer, or by orientation of dipole defects (taking into account the number of defects available in silica glass for the latter to be true the hyperpolarizability of each defect must be unrealistically high).

New ideas and experiments are necessary to justify $\chi^{(2)}$ values ~ 1pm/V and higher. A better understanding of the mechanisms of glass poling, which are still not fully understood, may help to improve the value of second-order nonlinearity in poled glasses, perhaps to values competitive with the best ferroelectric crystals.

References

1. U. Österberg and W. Margulis, Opt. Lett. **11**, 516 (1986).
2. R.H. Stolen and H.W.K. Tom, Opt. Lett. **12**, 585 (1987).
3. N.B. Baranova and B.Ya. Zeldovich, JETP Lett. **45**, 716 (1987).
4. M.C. Farries, P.St.J. Russell, M.E. Fermann and D.N. Payne, Electron. Lett. **23**, 322 (1987).
5. V. Mizrahi, U. Osterberg, C. Krautchik, G.E. Stegeman, J.E. Sipe and T.P. Morse, Appl. Phys. Lett. **53**, 557 (1988).
6. E.M. Dianov, P.G. Kazansky and D.Yu. Stepanov, Sov. J. Quantum. Electron. **19**, 575 (1989); Sov. Lightwave Commun. **1**, 247 (1991); E.M. Dianov, P.G. Kazansky, C. Krautschik and D.Yu. Stepanov, Sov. Lightwave Commun. **1**, 381 (1991); E.M. Dianov, P.G. Kazansky, D.S. Starodubov and D. Yu. Stepanov, Sov. Lightwave Commun. **3**, 83 (1992).

7. F. Ouellette, K. Hill and D.C. Johnson, Appl. Phys. Lett. **54**, 1086 (1989).
8. R. Kashyap, J. Opt. Soc. Am. **B 6**, 313 (1989).
9. V. Mizrahi, Y. Hibino and G. Stegeman, Opt. Commun. **78**, 283 (1990).
10. A. Kamal, D.A. Weinberger and W.H. Weber, Opt. Lett. **15**, 613 (1990).
11. M.D. Selker and N.M. Lawandy, Opt. Commun. **77**, 339 (1991).
12. D. Anderson, V. Mizrahi and J.E. Sipe, Opt. Lett. **16**, 796 (1991).
13. F. Charra, F. Devaux, J.M. Nunzi and P. Raimond, Phys. Rev. Lett. **68**, 2440 (1992).
14. V. Dominic and J. Feinberg, Opt. Lett. **17**, 1761 (1992).
15. D.M. Krol, D.J. DiGiovanni, W. Pleibel and R.H. Stolen, Opt. Lett. **18**, 1220 (1993).
16. W. Margulis, F. Laurell, B. Lesche, Nature **378**, 699 (1995).
17. S. Harris, Physics Today **50**, 36 (1997).
18. Y.Y. Yin, C. Chen, D.S. Elliot, and A.V. Smith, Phys. Rev. Lett. **64**, 2353 (1992).
19. N.B. Baranova, A.N. Chudinov, A.A. Shulginov, and B.Ya. Zel'dovich, Opt. Lett. **16**, 1346 (1991).
20. E. Dupont, P. B. Corkum, H. C. Liu, M. Buchanan, and Z. R. Wasilevski, Phys. Rev. Lett. **74**, 3596 (1995).
21. R. J. Glauber, "Coherence and quantum detection," in *Quantum Optics* edited by R. J. Glauber, Proceedings of the E. Fermi International School in Physics, Vol. 62 (New York - London: Acad. Press, 1969).
22. J. C. Miller, R. N. Compton, M. G. Payne, and W. R. Garrett, Phys. Rev. Lett. **45**, 114 (1980).
23. S. M. Park, S. P. Lu, and R. J. Gordon, J. Chem. Phys. **94**, 8622 (1991).
24. C. Chen, Y. Y. Yin, and D. S. Elliot, Phys. Rev. Lett. **64**, 507 (1990).
25. P.G. Kazansky and V. Pruneri, Phys. Rev. Lett. **14**, 2956 (1997).
26. R.A. Myers, N. Mukherjee and S.R.J. Brueck, Opt. Lett. **16**, 1732 (1991).
27. A. Okada, K. Ishii, K. Mito and K. Sasaki, Appl.Phys.Lett. **60**, 2853 (1992).
28. P.G. Kazansky, A. Kamal and P.St.J. Russell, Opt. Lett. **18**, 693 (1993).
29. L.J. Henry, B.V. McGrath, T.G. Alley and J.J. Kester, J. Opt. Soc. Am. B **13**, 827 (1996).
30. T. Fujiwara, D. Wong, Y. Zhao, S. Fleming, S. Poole and M. Sceats, Electron. Lett. **31**, 573 (1995).
31. P.G. Kazansky, A. Kamal and P.St.J. Russell, Opt. Lett. **18**, 1141 (1993).
32. A.C. Liu, M.J.F. Digonnet and G.S. Kino, Opt. Lett. **20**, 1141 (1994).
33. N. Mukherjee, R.A. Myers, and S.R.J. Brueck, J.Opt. Soc. Am. **B 11**, 665 (1994).
34. X.-C. Long, R.A. Myers and S.R.J. Brueck, Opt. Lett. **19**, 1819 (1994).
35. P.G. Kazansky, L. Dong and P.St.J. Russell, Opt.Lett. **19**, 701 (1994).
36. P.G. Kazansky, L. Dong and P.St.J. Russell, Electron. Lett. **30**, 1345 (1994).
37. P.G. Kazansky and P.St.J. Russell, Opt. Comm. **110**, 611 (1994).
38. R. Kashyap, G.J. Veldhuis, D.C. Rogers and P.F. McKee, Appl. Phys. Lett. **64**, 1332 (1994).
39. H. Nasu, H. Okamoto, K. Kurachi, J. Matsuoka, K. Kamiya, A. Mito and H. Hosono, J. Opt. Soc. Am. B **12**, 644 (1995).
40. K. Tanaka, K. Kashima, K. Hirao, N. Soga, S. Yamagata, A. Mito and H. Nasu, Jpn. J. Appl. Phys. **34**, 75 (1995).
41. P.G. Kazansky, V. Pruneri and P.St.J. Russell, Opt. Lett. **20**, 843 (1995).
42. X.-C. Long, R.A. Myers and S.R.J. Brueck, IEEE Photon. Tech. Lett. **8**, 227 (1996).
43. O. Sugihara, T. Hirama, h. Fujimura and N. Okamoto, Optical Review **3**, 111 (1996).
44. H. Takebe, P.G. Kazansky, P.St.J. Russell and K. Morinaga, Opt. Lett. **21**, 468 (1996).
45. P.G. Kazansky, R.A. Smith, P.St.J. Russell, G.M. Yang and G.M. Sessler, Appl. Phys. Lett. **68**, 269 (1996).
46. W. Margulis and F. Laurell, Opt. Lett. **21**, 1786 (1996).
47. V. Pruneri and P.G. Kazansky, IEEE Photon. Tech. Lett. **9**, 185 (1997).
48. V. Pruneri and P.G. Kazansky, Electron. Lett. **33**, 318 (1997).
49. T.G. Alley and S.R.J. Brueck, March meeting of the APS (Kansas City, 1997), paper A22-6.
50. P.G. Kazansky and V. Pruneri, J. Opt. Soc. Am. B **11**, N11 (1997).

Bragg Gratings, Photosensitivity, and Poling in Glass Fibers and Waveguides: Applications and Fundamentals

Poling II

Tuesday, October 28, 1997

Raman Kashyap, BT Laboratories, U.K.
Presider

BTuD
3:45pm–5:15pm
Room 18

Creating a second order nonlinearity and a waveguide in soft glasses by poling

W. Margulis, F. C. Garcia, E. N. Hering, I. C. S. Carvalho
Departamento de Física, Pontifícia Universidade Católica do Rio de Janeiro,
Rio de Janeiro, 22453, Brazil;
Phone: (+55 21) 529 9517; FAX: (+55 21) 512 3222; e-mail: walter@fis.puc-rio.br
B. Lesche
Instituto de Física, Universidade Federal do Rio de Janeiro,
Rio de Janeiro, 21945, Brazil;
and
F. Laurell
Physics Department, Royal Institute of Technology,
Stockholm 10044, Sweden

Soft glasses, such as soda lime are the often used in waveguide fabrication by ion exchange. They are also cheap, readily available, and are potentially a base material for active components in fiber-to-the-home systems. Therefore, waveguide modulators based on poled soda lime glass are of great interest. In this work we demonstrate that it is possible to induce a large second-order optical nonlinearity in soda lime and borosilicate glass with the electro-thermal poling procedure described by Myers et al[1]. We also demonstrate a scheme based on poling to record single-mode waveguides in soda lime.

The poling current in silica usually does not exceed a few nanoamperes because of the low (few ppm) alkaly ion content. In contrast, typical poling currents in soda lime and borosilicate samples were in the milliampere range. For such high currents Joule dissipation starts to play a role, and we found that for 3 mm thick samples, temperatures above ~250 °C and bias voltages above ~1 kV thermal runaway occurred, were the current led to local heat, and the local increase in temperature led to even more current, and so on, until eventually the power supply (< 5 mA) would trip. Two approaches stopped thermal runaway: lower poling temperatures, and/or a gradual increase in poling voltage. Poling at 230 °C gave a monotonic decrease in current. When using higher temperatures, the voltage was raised in steps of ~0.5-1 kV, keeping the current always under 1 mA. As ionic migration led to the creation of a high resistivity layer under the anode, the voltage could be increased exploiting the fact that the current was limited by the depletion region. The poling times we used were typically several hours, and the total charge collected was a few (2-7) coulombs. SHG could be easily detected after a few minutes. The initial SHG signal measured with soda lime samples was always similar to that measured in silica samples poled to the same voltage at the same temperature.

The total charge circulating in the circuit has been related to the thickness of the depletion region formed by poling, assuming total removal of cations from the depletion region. For a 1 cm^2 anode area, a 13 % concentration of Na_2O, and a total charge of 1 C (6×10^{18} e), one infers a 11 μm deep depletion region. The charge due to the drift of K and Ca is of the same order to that of Na, and from the total charge colected the expected thickness in the present experiments with soda lime is ~10-20 μm. Similar calculations for silica give a depletion region thickness ~5 μm, in close agreement to previous measurements[1].

Several soda lime samples were poled at 2.5 kV at various temperatures, and although the current behaviour indicated that a depletion region was formed at relatively low temperatures, it was not possible to detect SHG for samples poled at 150 °C and 190 °C. The conversion efficiency was similar for poling at 230, 265 and 280 °C, and at 320 and 350 °C thermal runaway prevented poling of the 3 mm thick samples tested.

A scanning electron microscope (SEM) used in conjunction with a energy dispersion X-Ray spectrometer (EDS) analysed the content of calcium under the anode of a poled soda lime sample, and showed a depletion region that measured ~18 μm. Since the activation energy of Ca is higher than that of Na and of K, it is expected that this region is depleted of all three elements. The amount of calcium measured under the anode for depths > 20 μm into the glass sample is constant and equal to the bulk value of the unpoled region.

Since the high electric fields (10^8-10^9 V/m) recorded in poled soda lime are confined over a region only a few microns deep under the anode, a waveguide configuration is required that allows propagating guided light along the high field region. Ion exchange (including field assisted ion exchange) is the natural way to fabricate waveguides in soda lime, but this technique is difficult to conciliate with poling due to the heating stage required in both processes. Therefore, we exploited the reduction in refractive index that follows from poling as a means to fabricate waveguides in soda lime, which are then located at the depth where the nonlinearity exists. The waveguides were formed in a depressed cladding arrangement. The anode electrode was made with a number of longitudinal channels (gaps). A waveguide can be created provided the refractive index is lowered not only on either side of each channel, but also under the channel itself. This happens partly because of fringing fields, but also due to the fact that the field line distribution (i.e., the current flow) evolves during the poling process to deplete of cations the region under the channel as well, as the resistivity of the depletion region becomes much higher than that of the original glass.

Tests were made with square pieces of commercial grade soda lime glass (3 mm thick, 5 cm long) were coated with a ~0.3 μm thick Al film, used as anode. Channels of width 2 μm, 3 μm, 6 μm and 12 μm, as well as a number of 150 μm wide stripes were opened by photolithography on the otherwise continuous Al film. The waveguides were formed under the channels opened on the film. The soda lime samples were poled at 280 °C, and the dc bias was raised in steps of ~700 V to a maximum voltage of 3 kV. The anode side of a high voltage power supply was connected to the edges of the patterned Al film. The spatial resolution achieved by poling soda lime glass in the present set-up was found to be of the order of a micron.

After poling, the samples were cut in 1 cm long pieces and end face polished, and the waveguides characterized. A conventional near field measurement set-up was used with a HeNe laser. It was found that the waveguides with 2, 3 and 6 μm width were single mode. Even the 150 μm wide gaps led to waveguide formation. Another set-up was used, where a HeNe (0.6328 μm) laser beam was focused onto the samples and the reflected and the transmitted signals were measured. Spatial filtering was used to identify in the transmitted signal the contributions from guided and unguided light. Light was coupled into the channel waveguides, and the samples were scanned vertically and horizontally. Fig. 1 illustrates one set of results for a waveguide made under a 6 μm wide channel. The sample was poled to a maximum 2.5 kV bias at 280 °C and the total charge collected was 5.8 C. The convolved guided light data indicated by squares in both traces show that the waveguide here is ~7 μm wide (Fig. 1a) and ~7 μm deep (Fig. 1b) at FWHM. Deeper waveguides (19 μm) were also measured on the same substrate. The reflected light (circles in Fig. 1b) shows that the spot size in the measurements was ~3 μm, and that the waveguide is burried 1.5 μm under the top surface of the substrate, located at a height 39.5 μm. The

reflected signal was used with Fresnel equations to estimate that the refractive index change due to poling was -0.023, i.e., a percent change of -1.5%. The depth of the cladding was measured by monitoring the transmitted unguided light under the electrode at various depths, and found to be similar to the depth of the waveguide itself. This strongly suggests that the mechanism for waveguide formation is indeed the creation of a low refractive index cladding region (the depletion region) due to poling. This optical probing technique is a simple way to measure the depletion region in poled soda lime.

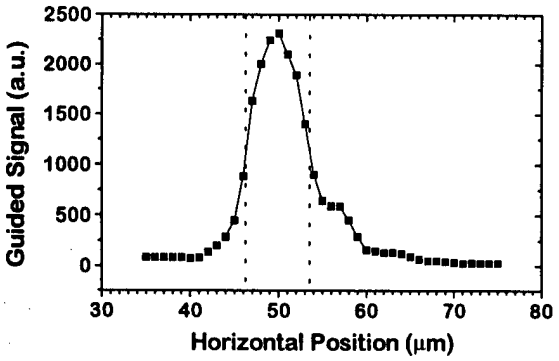

Fig. 1a- Guided optical signal measured scanning the probe beam horizontally across the substrate

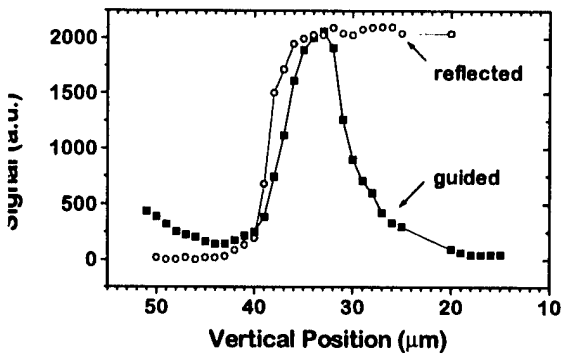

Fig. 1b- Optical signal measured scanning the probe beam vertically across the substrate

No changes in the waveguides described here were observed over several months evn without a protective film covering the glass substrate. We found, however, that the SHG efficiency induced decayed both spontaneously and also by a photostimulated process (optical erasure). In soda lime, whithin times as short as 1 hour the SHG efficiency could drop by an order of magnitude, if probed continuosly by a Q-switched and mode-locked Nd:YAG laser beam (average power ~0.5 W focused to ~20 μm spot size). However, if the sample was unexposed the SH signal could be measured several months after poling with a residual conversion efficiency ~10%. In order to render soda lime useful for long term applications this decay must be studied in more detail and prevented, possibly by a protective coating. Such studies will be described in the present talk.

References

1- R. A. Myers, N. Mukherjee, S. R. J. Brueck, Opt. Lett. 16, 1732 (1991).

Electro-thermal poling of microfibers

I. C. S. Carvalho, C.M.B. Cordeiro, L. C. Guedes Valente, E. N. Hering, W. Margulis
Departamento de Física, Pontifícia Universidade Católica do Rio de Janeiro,
Rio de Janeiro, 22453, Brazil;
Phone: (+55 21) 529 9517; FAX: (+55 21) 512 3222; e-mail: isabel@fis.puc-rio.br

F. Laurell[1] and R. Stubbe[2]
[1]Physics Department, [2]Institute of Optical Research,
Royal Institute of Technology, Stockholm 10044, Sweden

In-fiber modulators are extremely attractive for telecommunication applications, and electro-thermal polin can be used to induce the necessary second-order nonlinearity in the glass fiber [1]. Long et al. have recently reported a way of mounting and poling D-fibers that is extensible to volume manufacturing and a relatively low voltage modulator has been demonstrated [2]. D-fibers are rugged, particularly if inbeded i a resin such as polyimide, but restrict the choice of available fibers, are not easily spliced, and a part of the voltage applied externally is wasted in biasing the cladding, unless further polishing/etching is used to remove the cladding and leave only the core region of the fiber. In the present work, we describe an alternative approach to making a fiber modulator, where pieces of conventional fiber are used, the central part of which is etched to the core and subsequently poled. After etching, the fibers have a diameter of ~10 μm and therefore are referred to as microfibers. Microfibers are surprisingly strong for their diameter and have some unique advantages. They can be fabricated with any fiber, the two ends that are not etched are truly easily spliceable, and the applied voltage during poling and in later use of the modulator develops mainly in the core, ensuring a large overlap integral.

Standard telecom fibers were used in most experiments. Up to 20 pieces of fiber ~ 1m long were etched at a time, over the central ~ 5 cm region. The acid used was concentrated HF (40%). A DFB semiconductor laser at 1.55 μm coupled via a 3 dB coupler to one of the fibers etched was used as a source of light for an on-line monitoring of the etching process. The 4% reflection from the cleaved end face of the fiber was detected on the return port of the coupler. When the reflected signal (two passes through the etched region) dropped by 80%, etching was stopped, having in mind that the field at 1.55 μm extends much further than that at 1.06 μm or 0.63 μm. Alternatively, a control fiber was immersed in the acid 15 minutes before the fibers to be used for poling. The transmitted radiation of a 1.3 μm laser diode passing through the control fiber gave the etching rate, indicating when the core was reached and when the fiber was totally etched away. The fibers to be poled were etched until the cladding was 3.5 μm thick, a point at which the transmission losses were still negligible.

Poling was carried out on a hot plate, or alternatively in an oven. The temperature used in all experiments here was 250 °C. A 0.5 mm thick ~5 cm long silicon slice was used as anode, the edges of which were rounded by polishing to prevent mechanically breaking the microfiber. The silicon electrode was glued to a 15 cm diameter 3 mm thick circular soda lime glass plate, used as base. Two etched fibers were affixed parallel to each other on the base, so that the microfiber region was stretched on and in contact with the anode. A thin layer of two element clear silicone rubber (Rhodorsil RTV) was spread on the microfibers, silicon anode and the soda lime base, and helped both with the mechanical stability of the system and with the electrical insulation during and after poling. A distributed charging resistor rested upon the microfibers, and the cathode was again a piece of silicon, positioned against the other face of the charging resistor.

A crucial parameter in obtaining a large second order nonlinearity is the applied voltage. The SHG efficiency scales with the square of the poling voltage [3]. Therefore, it is imperative that the reduced fiber thickness that follows from etching is not accompanied by a reduction in the maximum possible applied voltage before electrical breakdown takes place. In order to circumvent the breakdown problem a distributed charging resistor was used, that allowed us to apply over 5 kV across a 10 μm fiber. The charging resistor rested on the microfibers, and consisted of a 3 mm thick piece of soda lime glass. Although the thickness of the soda lime piece was ~300 times that of the microfibers, its resistance at 250 °C was ~10^2-10^3 times lower than that of the microfibers. The distributed charging resistor effectively prevented sparks from developing across the poled fibers, and enabled us to apply voltages that are many times above the breakdown limit. The same procedure had been successfully used previously with bulk samples. Although the charging resistor was useful during poling, it was possible to remove it from the electrical circuit once the microfibers were poled and ready to be biased at lower voltages in modulation experiments at room temperature.

It is relatively easy to guarantee that in the vicinity of the microfibers the charging resistor does not come in contact with the Si anode, particularly if a number of microfibers are used as spacers near and parallel to each other. As a consequence, the microfibers are placed between equipotentials at the bias voltage and ground. It should be pointed out, however, that poling in our set-up should take place even if there is contact between the charging resistor and the silicon anode far away from the microfibers. In other words, it is not imperative that the relatively large surfaces of the anode and the charging resistor that are in principle separated by only ~10 μm should not be allowed to touch each other. Such a short circuit would only reduce marginally the effective poling voltage and increase the current drawn from the power supply (generally to a few μA). In fact, we succeeded in poling microfibers without any additional isolators such as silicone rubber between the anode and the charging resistor, but this was found not to be so conveninent from a mechanical point of view.

A Nd:YAG laser was used in a frequency doubling measurement in order to examine if the microfibers had been poled. The laser was operated Q-switched and mode-locked. Average optical powers as high as 220 mW have been measured after the microfibers, far above the necessary levels for seeded optical preparation. In the present measurement the average output power was limited to 50 mW, and no seeding was used. No SH signal has been measured in fibers that had not been poled. Fig. 1 shows a result of the SH signal generated by a microfiber poled at 4 kV and 250 °C against the input IR power (optical powers measured at the fiber output). Note that in this case the SH is not phase matched. The expected quadratic power dependence was observed.

In order to examine the behaviour of a poled microfiber as an electro-optical modulator, a Mach-Zehnder fiber interferometer was constructed. Poling was carried out at 5 kV, but the length of microfiber between the electrodes was only 1.5 cm. The available couplers were single-mode at 1.06 μm, but tests were carried out with a HeNe laser because of its short wavelength (low switching voltages) and long coherence length. A spliced piece of standard telecom fiber provided one path and the fiber etched in its central region provided the other path between the two 3 dB couplers at 1.06 μm. Equalization of the lengths of the two arms of the interferometer was atemped above all for stabilizing the interferometer for temperature fluctuations. Nevertheless, the detected optical signal at the output varied slowly (on a time scale of several seconds). The modulating bias signal was produced by an AC power supply delivering up to 2 kV after a half wave rectifying diode. With a bias frequency ~400 Hz it was possible to detect a corresponding modulation of the optical output relatively easily, that could be measured for amplitudes

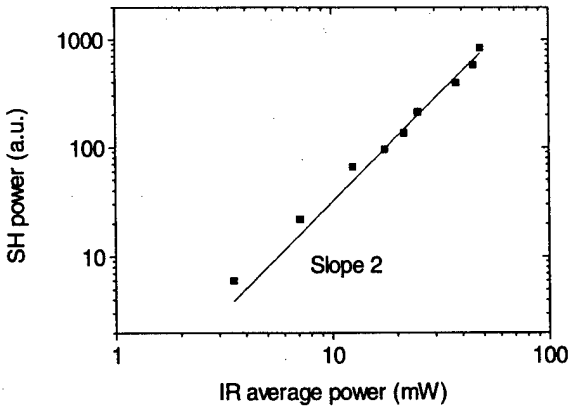

Fig. 1. SH generated in a microfiber poled to 4 kV at 250 °C

as low as 60 V. A Pockel's cell driver was then tested, capable of delivering 2.3 kV square pulses of duration 7 μs and of risetime 10 ns, and running at a repetition frequency 10 kHz. Since the electrode structure on the microfiber was not impedance matched, a large amount of electrical noise was generated, and a photomultiplier was used as detector for being relatively immune to noise. No modulation could be detected on a μs time scale even when the distributed charging resistor was removed from the set-up. It was concluded from our measurements that the slow modulation that we observed was likely to arise from the electrostatic attraction between the electrodes and not from the electro-optical effect. Attempts to make use of longer regions of poled microfibers and to demonstrate true electro-opical modulation in poled microfibers are presently under way and will be discussed.

References

[1] R. A. Myers et al, Opt. Lett. 16, 1732 (1991); T. Fujiwara et al, Elec. Lett. 31, 573 (1995); P.G. Kazansky et al, Elec. Lett. 31, 62 (1995).

[2] X.-C. Long et al, IEEE Phot. Tech. Lett. 8, 227 (1996); Proc. CLEO 97, p. 261, paper CWF58.

[3] S.R.J.Brueck, BGPP meeting, Portland 1995; H. Takebe et al, Opt. Lett. 21, 468 (1996).

Electric-Field Poling of Polymers

Reimund Gerhard-Multhaupt
Applied Condensed-Matter Physics, Institute of Physics, University of Potsdam
Am Neuen Palais 10, D-14469 Potsdam, Federal Republic of Germany
(Fax: +49 331 977 1577, E-mail: rgm@rz.uni-potsdam.de)

Amorphous polymers with strong second-order optical nonlinearities [1, 2] that are potentially useful for electro-optical or all-optical device applications [4] contain molecular chromophore dipoles [3] as guest molecules, as side groups, or as main-chain segments. In order to break the inherent centro-symmetry of the initially isotropic dipole orientation in these materials and to render them nonlinear optically active (and also piezo- and pyroelectric), preferential dipole alignment by means of poling is required [5]. Poled nonlinear optical (NLO) polymers are molecular dipole electrets [6, 7] so that the full range of techniques for the preparation and investigation of polar electrets may be utilized on them. In particular, the poling of polar polymers such as polyethylene terephthalate (PETP, Mylar) or polymethyl methacrylate (PMMA, Plexiglass) is not at all different from the poling of NLO polymers. Strongly pyro- and piezoelectric polymer electrets such as polyvinylidene fluoride (PVDF) and its copolymers or the odd polyamides (PA or Nylon 5, 7, 9, and 11), on the other hand, are ferroelectric and do therefore not require heating during poling and subsequent cooling under the electric field; however, their ferroelectric polarization switches only at field strengths higher than the respective coercive field.

Consequently, well-known electret-poling techniques have been used on NLO polymers as well; in addition, new and modified techniques were developed especially for this novel class of polymers [8]. Of particular interest are poling techniques that allow for the preparation of dipole-orientation patterns in the plane or across the thickness of a polymer film so that e.g. quasi phase matching with gratings or phase matching with mode conversion, respectively, permit rather high nonlinear optical efficiencies in poled-polymer waveguides. Since the dipole polarization is a vector quantity, not only its magnitude, but also its direction can be of importance: Waveguide polarization converters with continuously varying dipole orientation produced by means of four specially patterned poling electrodes were recently described and demonstrated [9].

Several techniques as listed in Table 1 are available for orienting the polar dye molecules within the polymer matrix which usually has to be softened by heating to temperatures above its glass-transition temperature T_G. These methods are described in more detail in the References given below and particularly in the original publications cited therein. The standard poling technique for NLO polymers is thermal poling with evaporated electrodes. Another technique often used on samples of new materials with a large number of defects or for achieving very high poling fields is corona poling with constant voltage or current.

Selective poling across the thickness of a NLO polymer electret or of a waveguiding film sandwich may be achieved with monoenergetic electron beams of limited range or by exploiting the light-induced *trans-cis* isomerization of azo and other dyes for enhancing their rotational mobility during photo-induced poling with absorption-limited light penetration. Since light can be easily focussed into a μm-sized spot and scanned across a polymer film, this technique as well as photothermal and all-optical poling are also suitable for patterned poling in the film plane. Orientation of the recently introduced octupolar molecules with large second-order hyperpolarizabilities and optical nonlinearities appears to be possible only with the all-optical technique [10] because these molecules do not exhibit permanent dipole moments which could be oriented with an electric field.

Poling Method	Orientation of Dipoles by	Mobility of Dipole Molecules from	Special Features and Possible Advantages
Thermal/ Electrode	Electric Field between Electrodes	Heating to $T > T_G$ (Glass Transition)	Poling with Device Electrodes Poling in Arbitrary Directions
Corona Discharge	Electric Field from Surface Charges	External or Local Heating to $T > T_G$	Poling in Spite of Defects Poling with Very High Fields
Electron Beam	Electric Field from Volume Charges	External or Local Heating to $T > T_G$	Well-Defined Selective Poling across the Film Thickness
Photo-thermal	Electric Field from the Above Sources	Local Heating with Light to $T > T_G$	Optically Defined Patterns in Plane and across Thickness
Gas-Assisted	Electric Field from the Above Sources	Lower T_G Induced by Pressurized Gas	Global Poling without Any Heating (Not Often Used)
Photo-Induced	Electric Field from Various Sources	*trans-cis* Isomerization of the Dye	(Selective) Poling at Room or Slightly Elevated Temperature
All-Optical	Optic Field (Orientation Bleaching)	*trans-cis* Isomerization of the Dye	(Selective) Poling at Room Temperature w/o Electrodes

Table 1: Essential characteristics and typical features of NLO-polymer poling techniques.

It was also proposed to use a gas with small molecules at high pressure to reduce the glass-transition temperature T_G of the polymer matrix below room temperature [11] so that the chromophore dipoles may be easily oriented with an electric field; this technique was apparently not explored any further, but it may be attractive for fundamental studies of the interactions between guest molecules and a polymer matrix.

It is not sufficient to orient the molecular dipoles in a NLO polymer as desired. The achieved dipolar order which can never be perfect in a glassy material at non-zero temperatures must be analyzed in detail. Since poled NLO polymers are molecular dipole electrets, the full range of electrical techniques for electret measurements may be employed. Also, because of their linear and nonlinear optical properties, the more or less well oriented chromophore dipoles can be easily investigated with optical techniques. Here, only the electrical and optical techniques that are suitable for microsopic inspection as listed in Table 2 will be mentioned; further details are again found in the review chapters and articles given below and particularly in the original publications cited therein.

The pyroelectrical methods which include the so-called thermal- or heat-pulse technique are very attractive because of their rather low cost, their ease of operation, and their versatility; in slightly different variants, they may be also utilized for isothermal and thermally stimulated relaxation measurements as well as for in-plane scanning microscopy and depth profiling of the dipole orientation. In principle, the direct piezoelectric effect gives a similar range of possibilities for global and microsopical studies as the pyroelectric effect, but on nonlinear optical polymers, only stability studies and laser-induced pressure-pulse measurements of the polarization distribution across the thickness of electron-beam poled nonlinear optical polymer films were reported so far.

Scanning Electro-Optical (EO) microscopy and interferometric EO imaging of dipole-orientation patterns were demonstrated in addition to EO stability investigations. Second-Harmonic Generation (SHG) has been employed already in early studies of poled NLO polymers. Being a purely optical technique, SHG does not require any electrodes and may therefore be used *in situ* e.g. during any poling experiment, but its implementation and operation are rather complicated and expensive. It has also been employed for scanning as well as imaging microscopy on samples with in-plane dipole-orientation patterns.

Scanning or Probing Technique	Underlying Physical Mechanism(s)	Parameter for Scanning	Employed for Studying
Scanning Pyroelectrical Microscopy	Thermally Induced Polarization Change	Sample Position on X-Y Plane	2D Pattern of Polarization
Pyroelectrical Depth Profiling	Thermally Induced Polarization Change	Frequency of Periodic Heating	Depth Profile of Polarization
Thermal Pulse (a.k.a. Heat Pulse)	Thermally Induced Polarization Change	Diffusion of Heat with Time	Depth Profile of Polarization
Pressure Pulse or Pressure Step	Mechanically Induced Polarization Change	Propagation of Pressure with Time	Depth Profile of Polarization
Scanning Electro-Optical Microscopy	Electrically Induced Refractive-Index Change	Sample Position on X-Y-Plane	2D Pattern of Polarization
Phase-Shift Interference Microscopy	Electrically Induced Refractive-Index Change	Parallel Imaging with Microscope	2D Pattern of Polarization
Scanning SHG Microscopy	Nonlinear Optical Frequency Doubling	Sample Position on X-Y Plane	2D Pattern of Polarization
Imaging SHG Microscopy	Nonlinear Optical Frequency Doubling	Parallel Imaging with Microscope	2D Pattern of Polarization

Table 2: Electrical and optical techniques suitable for the analysis of dipole-orientation patterns and profiles in nonlinear optical polymers with microscopic spatial resolution.

References

[1] J. Zyss (Ed.), *Molecular Nonlinear Optics* (Academic Press, San Diego 1994).

[2] G. A. Lindsay and K. D. Singer (Eds.), *Polymers for Second-Order Nonlinear Optics*, ACS Symp. Ser. **601** (American Chemical Society, Washington 1995).

[3] S. R. Marder and J. W. Perry, "Molecular Materials for Second-Order Nonlinear Optical Applications," Adv. Mater. **5**, 804–814 (1993).

[4] L. R. Dalton, A. W. Harper, Bo Wu, Rima Ghosn, J. Laquindanum, Ziyong Liang, A. Hubbel, and Chengzeng Xu, "Polymeric Electro-Optic Modulators: Materials Synthesis and Processing," Adv. Mater. **7**, 519–540 (1995).

[5] D. M. Burland, R. D. Miller, and C. A. Walsh, "Second-Order Nonlinearity in Poled-Polymer Systems," Chem. Rev. **94**, 31–75 (1994).

[6] G. M. Sessler (Ed.), *Electrets*, Top. Appl. Phys. **33**, 2nd Enlarged Ed. (Springer, Berlin, Heidelberg, New York 1987).

[7] R. Gerhard-Multhaupt and A. S. DeReggi (Eds.), *Electrets: Charged or Poled Dielectrics and Their Applications* (*CEIDP Digest of Literature on Dielectrics*), IEEE Trans. Diel. Electr. Insul. **3**, 603–734 (1996).

[8] S. Bauer-Gogonea and R. Gerhard-Multhaupt, "Nonlinear Optical Polymer Electrets," IEEE Trans. Diel. Electr. Insul. **3**, 677–705 (1996).

[9] M.-C. Oh, S.-S. Lee, & S.-Y. Shin, "Simulation of polarization converter formed by poling-induced polymer waveguides", IEEE J. Quantum Electron. **31**, 1698–1704 (1995); M.-C. Oh, S.-Y. Shin, W.-Y. Hwang, & J.-J. Kim, "Poling-induced waveguide polarizers in electrooptic polymers", IEEE Photon. Technol. Lett. **8**, 375–377 (1996).

[10] J.-M. Nunzi, F. Charra, C. Fiorini, and J. Zyss, "Transient Optically Induced Non-Centrosymmetry in a Solution of Octupolar Molecules," Chem. Phys. Lett. **219**, 349–354 (1994).

[11] S. E. Barry and D. S. Soane, "Poling of Polymeric Thin Films at Ambient Temperatures for Second-Harmonic Generation," Appl. Phys. Lett. **58**, 1134–1136 (1991).

Seeding and all-optical patterning of polymers

J.-M. Nunzi*, C. Fiorini*, A.-C. Etilé*, P. Raimond*, F. Charra**
*DEIN - SPE **DRECAM - SRSIM
CEA / Saclay, 91191 GIF-SUR-YVETTE Cedex, FRANCE
Tel. : (33) 1 6908 6812, Fax : (33) 1 6908 7679, e-mail : nunzi@cea.fr

1. Introduction

A key issue in the field of nonlinear optical polymers for second-order process is the achievement of a non-centrosymetric order. One challenging prospect is to achieve it by optical means in order to take full advantage of its rich processing capabilities. Indeed, the all-optical poling of polymers offers an interesting alternative to the realization of non-centrosymmetric structures. Of particular interest is the possibility **to control extensively the spatial and tensorial properties of polymers using optical beams.**[1]

At the microscopic level (figure 1), the all-optical poling mechanism involves a selective polar excitation of the molecules depending on the polarity of the seeding beam combination $E(t) = E_{\omega}(t) + E_{2\omega}(t)$. The orientation redistribution following each excitation-relaxation cycle leads to a quasi-permanent orientation of the dye molecules.[2] Orientation diffusion then tends to restore the initial isotropic equilibrium.

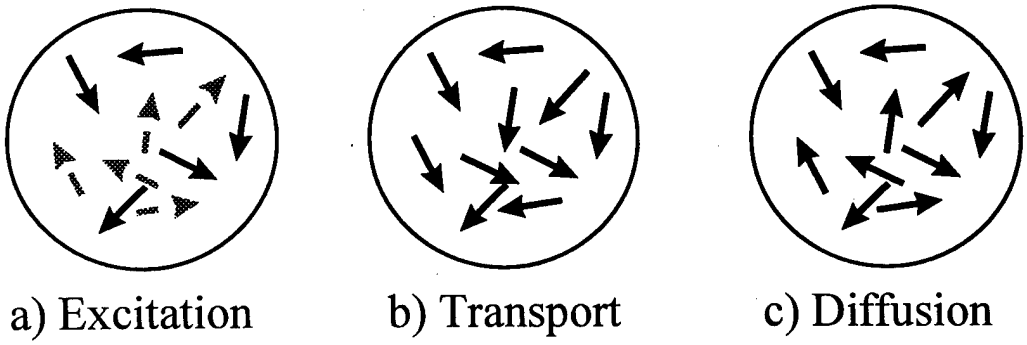

Figure 1 : effect of the all-optical poling on the evolution of the orientation distribution $N(\Omega)$. Molecules are initially excited with the polar field (a), non-radiative relaxation induces a reorientation which freezes the polar orientation (b), spontaneaus diffusion tends to restore the original equilibrium.

The process in molecules is driven by the same optical field[3] $\langle E^3(t) \rangle_t \neq 0$ as in the original seeding experiments performed in optical fibers.[4] From a fundamental point of view, study of photoinduced effects in polymer glasses is interesting because it can be used as a model for photoinduced effects in all other kinds of glasses. From a practical point of view, polymers present all the possibilities offered by molecular engineering for the tailoring of their properties in a broad sense. Using spin-coated films of dyed polymers and copolymers, we have demonstrated for the first time the possibility of achieving an efficient and quasi-permanent all-optical poling of the molecules.[5,6] Optimizing the preparation conditions, the same orientation efficiency as using the more standard corona poling method was achieved.[6] The influence of such "seeding" parameters as the relative phase and relative intensities between the writing beams at ω and 2ω frequencies were clarified. The tensor properties of the induced $\chi^{(2)}$-susceptibility were also analyzed and the mechanisms responsible for the permanent orientation of the molecules were identified. In this paper, we propose a simplified model which, based on 3 significant parameters, accounts for the essential physics relevant to the all-optical poling process and permits optimization of its efficiency. Predictions of the model are compared with the experiment. Finally, we give an insight into the all-optical tailoring of the 3-dimensional spatio-tensorial micro-optical properties of polymers.

2. All-optical poling dynamics : model

The macroscopic polarizability of an assembly of non-interacting molecules is theoretically obtained from the corresponding microscopic one after averaging over all possible orientations. We get $\chi^{(2)}_{\Delta\Delta\Delta} = \int N(\Omega)\beta_{\Delta\Delta\Delta}(\Omega)d\Omega$ where $N(\Omega)$ is the density of molecules oriented in a direction Ω. In order to describe $\chi^{(2)}$-growth and decay, we need a physical description of $N(\Omega)$. In every all-optical poling scheme,

$N(\Omega)$-dynamics is governed by : the rate of optical excitation which creates polar orientation ; the rate of non-radiative relaxation induced transport which freezes the orientation ; the rate of free diffusion which tends to restore the original equilibrium. Restricting ourselves to the simplest axial symmetry case, the optically driven rate equation for $N(\Omega)$ can be written :[6]

$$\frac{dN}{dt} = -\left(A\cos^2\theta + B\cos^4\theta + C\cos^3\theta\right)N + \int\left(A\cos^2\theta + B\cos^4\theta + C\cos^3\theta\right)Nd\Omega_i / 4\pi + D\nabla^2 N$$

In a two-level system description, excitation factors are : $A \propto \mu_{01}^2 \left\| E_{2\omega}^2 \right\|$, $B \propto \frac{\mu_{01}^2 \Delta\mu^2}{(2\hbar\omega)^2} \left\| E_{2\omega}^2 \right\|$, $C \propto 2\sqrt{AB}\cos(\Delta\Phi + \Delta k.z)$ in which $\cos(\Delta\Phi+\Delta k.z)$ is the self quasi-phase matching term. The writing process preserves symmetry around the polarization direction axis, so that $N(\Omega)$ depends only on the polar angle θ. In a weak orientation regime, we may write $N(\theta) = N_0 + N_1\cos(\theta)$. Under optimized seeding conditions, we have $A = B$ and $\cos(\Delta\Phi+\Delta k.z) = 1$. We get : $\chi^{(2)} \approx \frac{-N_0\beta/5\varepsilon_0}{1+D/A}\left[1 - e^{-(2D+A)t}\right]$. After orientation, it decays as e^{-2Dt}. Three parameters only describe the all-optical poling effect : the susceptibility $N_0\beta$, the excitation rate A and the decay rate D. Under resonant absorption conditions, the excitation rate is simply $A = \Phi\sigma I_{2\omega}\rho/2\hbar\omega$, in which Φ is the quantum yield for efficient reorientation after excitation, σ is the absorption cross-section at 2ω, $I_{2\omega}$ is the laser intensity at 2ω and ρ is its duty cycle. A competes with D for an optimal poling efficiency. Phenomenologically, the model may be applied to any other seeding situation, as long as we can ignore the microscopic nature of the 3 parameters involved. Its knowledge permits to develop an optimization strategy.

3. All-optical poling dynamics : experiment

Typical $\chi^{(2)}$ rise and decay dynamics obtained in polymers fit with our model. We checked the dependence of the experimental stationary regime $\chi^{(2)}$ on seeding intensity and temperature. Figure 2 shows the comparison between the experimental and theoretical dependences derived from the model. Excellence of the agreement is a proof for the self consistency of our description.

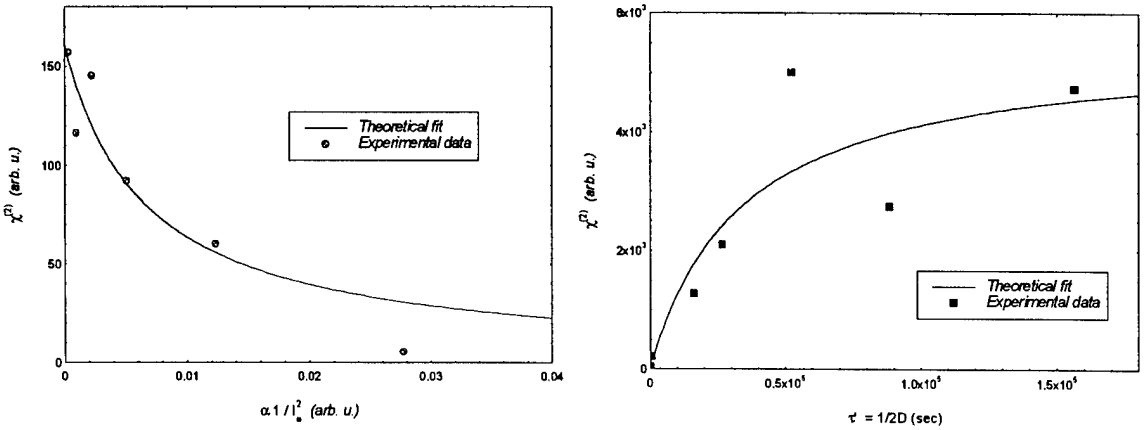

Figure 2 : influence of the fundamental beam energy (**left**) and seeding temperature (**right**). Samples were spin-coated thin films (0.3 µm) of a PMMA-DR1 copolymer. In each case, experimental data correspond to optimized relative intensities and phase for the seeding beams at ω and 2ω frequencies. The diffusion coefficient D is derived from the experimental $\chi^{(2)}$-decay.

4. All-optical tailoring of the 3-dimensional spatio-tensorial properties

We hereby present experiments aimed at a generalization of polarization holography techniques to the case of dual frequency fields.[7] The experiment consists in a seeding type process using a Nd-YAG laser with 25 ps-1064 nm-pulses at 10 Hz-repetition rate as a source, together with a KDP crystal. Polymer material was a Disperse-red-PMMA copolymer with 35% nonlinear moieties. It was spin-coated as 0.1 µm films with 0.3 optical density at 532 nm. Polarization properties of the photoinduced $\chi^{(2)}$ were investigated using two different sets of writing beam polarizations : (**a**) co-helical and (**b**) counter-helical polarizations. Circular polarizations were established using appropriate combinations of bichromatic half and quarter-wave plates. Phase between ω and 2ω writing beams was adjusted by tilting the angle of a BK 7-glass plate. Photoinduced $\chi^{(2)}$ tensor was

analyzed using SH-generation of a linear polarization beam inside the prepared sample which was mounted on an in-plane circular rotation stage.

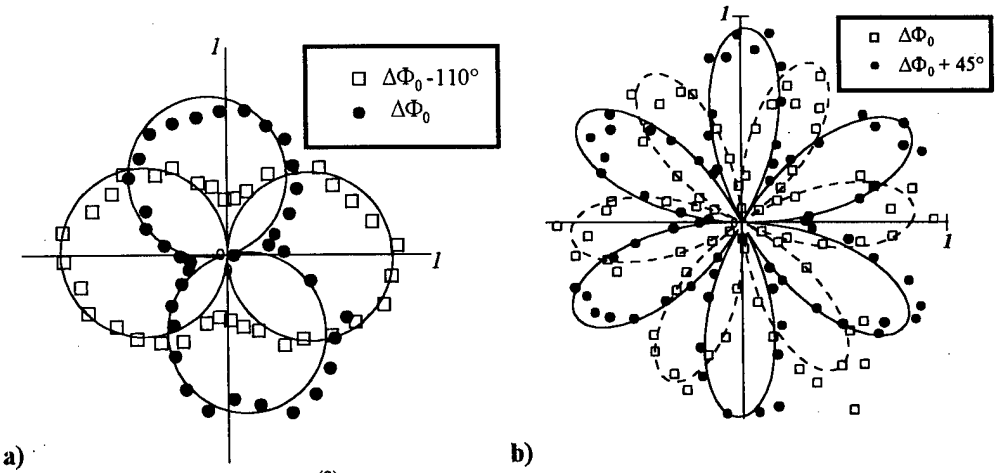

Figure 3 : In-plane map of $\chi^{(2)}$ obtained with a linear reading polarization along an axis Δ (angle δ) when writing beam polarizations were : **(a)** co-helical and **(b)** counter-helical.

Results of the $\chi^{(2)}$ tensor polarization analysis are given in figures 3 for the two different writing polarization sets. Calculation of the tensorial components of $\chi^{(2)}$ corresponding to the in-plane map of $\chi^{(2)}$ pictured in figure 3 yields :

$$\chi^{(2)}_{\Delta\Delta\Delta} \propto \cos(\Delta k.z + \Delta\Phi + \delta) \qquad \textbf{(case a)}$$

$$\chi^{(2)}_{\Delta\Delta\Delta} \propto \cos(\Delta k.z + \Delta\Phi + 3\delta) \qquad \textbf{(case b)}$$

In case **(a)**, the photoinduced $\chi^{(2)}$-pattern exhibits nearly perfect dipolar $\mathbf{C_1}$-symmetry with a magnitude independent of the relative phase ΔΦ between writing beams. In case **(b)**, the photoinduced $\chi^{(2)}$-pattern exhibits nearly perfect octupolar $\mathbf{C_3}$-symmetry with a magnitude independent of the relative phase ΔΦ between writing beams. In both cases, variation of ΔΦ yields in-plane rotation of the polarization pattern, as predicted theoretically.

5. Conclusion

From a fundamental point of view, study of photoinduced effects in polymer glasses is interesting because it can be used as a model for photoinduced effects in all other kinds of glasses. In this respect, we have developed and resolved a simple model which clarifies the role of the different physical parameters on the all-optical poling dynamics. The model has been successfully checked using the intensity and temperature dependence of the $\chi^{(2)}$ induced in a PMMA-DR1 film under resonant excitation.

From a practical point of view, polymers present all the possibilities offered by molecular engineering for the tailoring of their properties in a broad sense. In this respect, using appropriate combinations of circular polarizations, we have achieved perfect dipolar and perfect octupolar orders in a polymer consisting of mostly dipolar, linear molecules. This opens a new route to the tailoring of $\chi^{(2)}$-tensorial properties. Worth noting is that writing-beams phase retardation ΔΦ is then coded into a $\chi^{(2)}$-pattern rotation by the same angle. This permits the optical induction of chiral microstructures in achiral materials. Interestingly, the phase matched pattern is polarization insensitive to the frequency doubling of a linear polarization.

6. References

1. C. Fiorini, J.-M. Nunzi, F. Charra, P. Raimond, *Optics and Photonic news : Optics in 1996,* 7 (1996) 12.
2. Z. Sekkat, M. Dumont, *Appl. Phys. B* **54** (1992) 486.
3. R.H. Stolen, H.W.K. Tom, *Opt. Lett.* **12** (1987) 585.
4. N.B. Baranova, B.Ya. Zeldovich, *JETP Lett.* **45** (1987) 717.
5. F. Charra, F. Kajzar, J.-M. Nunzi, P. Raimond, E. Idiart, *Opt. Lett.* **18** (1993) 941.
6. C. Fiorini, F. Charra, J.-M. Nunzi, P. Raimond, *J. Opt. Soc. Am. B* **108** (1997) 1984.
7. A.-C. Etilé, C. Fiorini, F. Charra, J.-M. Nunzi, *Phys. Rev A* (Oct. 1997) in print.

1997
Technical
Digest
Series,
Volume 17

Bragg Gratings, Photosensitivity, and Poling in Glass Fibers and Waveguides:

Applications and Fundamentals

Postdeadline Papers

October 26–28, 1997
Williamsburg, Virginia

Contents

Fiber Bragg Gratings With Reflectivity > 97% Fabricated Through Polymer Jacket Using Near-UV Light

D. S. Starodubov*, V. Grubsky, and J. Feinberg
Department of Physics
University of Southern California
Los Angeles, CA 90089-0484

E. M. Dianov, S. L. Semjonov
Fiber Optics Research Center at General Physics Institute,
Russian Academy of Sciences, Moscow, Russia
and
A. N. Guryanov, N. N. Vechkanov
Institute of Chemistry of High-Purity Substances
Russian Academy of Sciences, N. Novgorod, Russia

* Permanent address: Fiber Optics Research Center, General Physics Institute, Russian Academy of Sciences, Moscow, Russia.

Fiber Bragg Gratings With Reflectivity > 97% Fabricated Through Polymer Jacket Using Near-UV Light

D. S. Starodubov, V. Grubsky, J. Feinberg,
E. M. Dianov, S. L. Semjonov, A. N. Guryanov, N. N. Vechkanov

Fiber Bragg gratings are important components for a variety of applications including WDM communications, fiber lasers and fiber sensors. An expensive and time consuming step for Bragg grating fabrication is the removal of the protective polymer coating of the fiber in order to expose the photosensitive fiber core [1]. Removing the fiber's polymer jacket and exposing the glass cladding surface to the atmosphere and UV light also substantially decreases the strength of the fiber [2,3].

One way to avoid fiber stripping and recoating is to fabricate Bragg gratings directly through the polymer coating. Unfortunately, standard polymer coatings are not sufficiently transparent at the usual mid-UV writing wavelength of 240 nm. Specially designed mid-UV transparent coatings have been developed recently [4]. However photodarkening of these coatings with mid-UV light makes it impossible to fabricate Bragg gratings with reasonable reflectivity even in hydrogen-loaded fibers. Undesirable side bands also appear (~0.3 dB for ~1.5 dB grating with 40 μm coating).

An alternative approach uses near-UV light around 330 nm [5]. Light in this wavelength region is much less destructive to polymers than 240 nm light. Moreover most of the standard polymer coatings are transparent to near-UV light, making it possible to write Bragg gratings through the standard polymer jacket [6].

In this paper we report the fabrication of strong Bragg gratings with reflectivity >15 dB through a common polymer (used to coat Russian fibers) in hydrogen-loaded fibers using near-UV light.

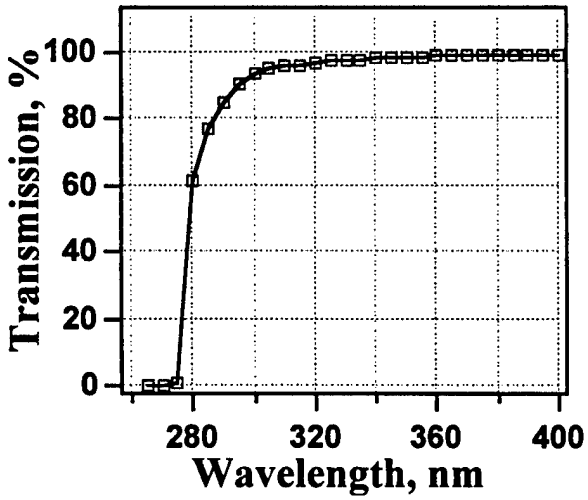

Fig. 1. Transmission spectrum of 150 μm thick film of silicone resin used for fiber coating.

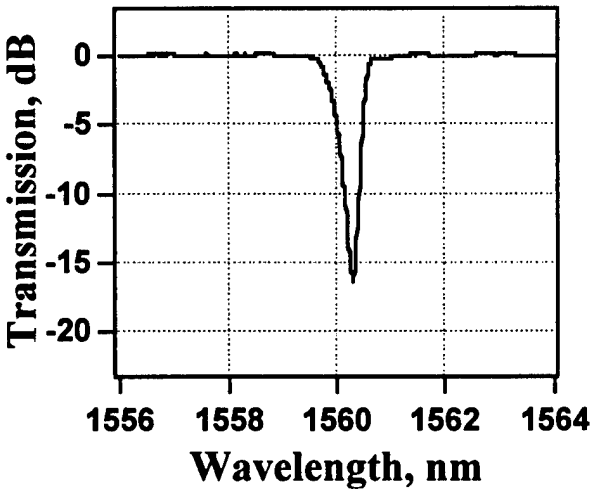

Fig. 2. Transmission spectrum of a Bragg grating written ***through*** a ~40 μm thick polymer fiber coating using near-UV light.

The fiber was provided by the Fiber Optic Research Center in Moscow. The thickness of the polymer coating was ~40 μm. The concentration of Ge in the core was ~20 mol. %. The transmission spectrum of 150 μm silicone resin film, which was used for the coating, is shown in Fig. 1. One can see that above 300 nm the absorption in this coating is negligible, making it ideal for fabricating

gratings through the jacket using near-UV light. The fibers were loaded with ~2.5 mol. % of hydrogen before near-UV exposure.

Fig. 2 shows the spectrum of a 7 mm-long grating fabricated using ~200 mW of near-UV light from an Ar laser at 302 nm after exposing for 4 minutes through a phase mask. Sidebands are absent. We could intentionally produce sidebands by damaging the polymer coating (Fig. 3). These experiments imply that the main reason for the distortion of the grating spectrum seen previously [4] is photoinduced degradation of the coating polymer (which is hard to avoid with mid-UV exposure) rather than imperfections in the polymer layer. We also observed that pre-exposure of the fiber coating with a uniform light beam can also decrease sidebands.

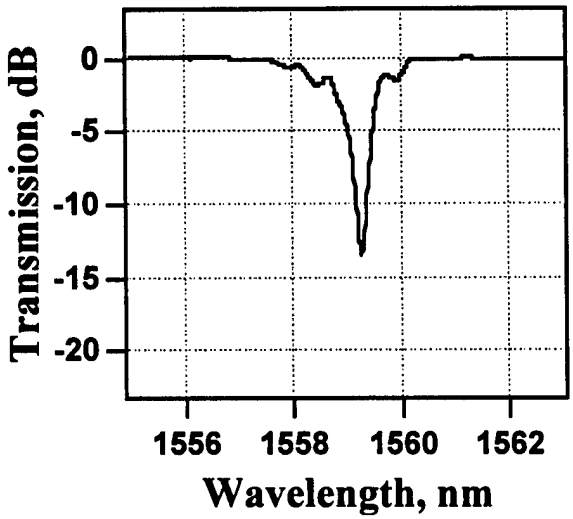

Fig. 3. Bragg grating transmission spectrum fabricated with intentional damage to the polymer coating. Note the sidebands.

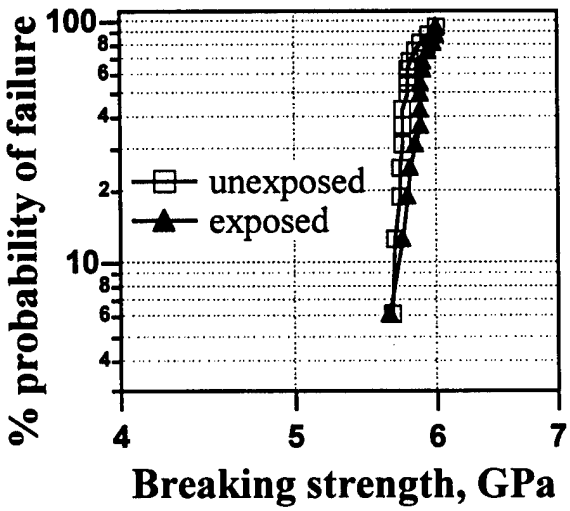

Fig. 4. Weibull plots of fiber breaking strengths with (▲) and without (□) Bragg grating. Note that the ***exposed fiber suffers no loss of strength.***

We observed no mechanical degradation or visible changes in the polymer layer after near-UV exposure. Our fiber gratings were strong enough to survive multiple winding on a metal rod of ~ 3 mm outer diameter. Results of more detailed measurements of the fiber strength using a bending technique (see Fig. 4) demonstrate no strength degradation (and even slight strength improvement) in fibers having gratings as compared to unexposed fibers.

In conclusion, we have demonstrated for the first time to our knowledge the fabrication of strong (>15 dB) Bragg gratings with no spectral sidebands through the polymer fiber coating in hydrogen-loaded germanosilicate fibers using near-UV light of an Ar laser. The gratings suffer no degradation in the fiber strength as compared to unexposed fiber.

References

1. W. Morey and G. Ball, Proc. LEOS'96, TuCC4, PP. 378-379, 1996.
2. R. Feced, M. P. Roe-Edwards, S. E. Kanellopoulos, N. H. Taylor, V. A. Handeric, Electron. Lett. 33(2), 157-159, 1997.
3. C. G. Askins, M. A. Putnam, H. J. Patric, E. J. Friebele, Electron. Lett. 33(15), 1333-1334, 1997.
4. R. P. Espindola, R. M. Atkins, D. A. Simoff, K. T. Nelson, M. A. Paczkowski, OFC'97 Postdeadline paper PD4, 1997.
5. E. M. Dianov, D. S. Starodubov, S. A. Vasiliev, A. A. Frolov, O. I. Medvedkov, Opt. Lett. 22(4), 221-223, 1997.
6. D. S. Starodubov, V. Grubsky, J. Feinberg, Electron. Lett. 33(15), 1331-1333, 1997.

40 dB Fiber Bragg Grating Written Through The Fiber Coating at 257 nm

R. P. Espindola, R. M. Atkins, N. P. Wang, D. A. Simoff, M. A. Paczkowski, R. S. Windeler, D. L. Brownlow, D. S. Shenk, P. A. Glodis, T. A. Strasser, J. J. DeMarco and P. J. Chandonnet
Bell Labs, Lucent Technologies
700 Mountain Avenue, Murray Hill, NJ 07974 USA

Summary

The writing of fiber Bragg gratings through the coating has important implications for the mass production of these devices. For instance, the time-consuming steps of stripping and recoating of the grating (potentially leading to fiber strength degradation), can be completely eliminated resulting in a simpler, more efficient and lower cost fabrication process. In the first demonstration of writing Bragg gratings through the coating, up to ~3 dB Bragg gratings were written through a UV-transparent acrylate-based 25 μm thick coating at 257 nm [1]. Subsequently, other researchers demonstrated a ~1 dB fiber Bragg grating written through a standard coating using 334 nm light [2]. Because the absorption band at 334 nm is much weaker than at 244 nm, these gratings required a very high germanium concentration (~20 mol%) and the addition of boron as a codopant to increase the photosensitivity of the fiber. The high level of germanium makes it difficult to achieve low-loss splices to standard communications grade fiber. Here we report for the first time highly reflective (99.99% Reflectivity, -40 dB transmission) Bragg gratings written through a novel polymer coating using a photosensitive germanium-doped fiber with 5 mole% germania.

The novel fiber coating used in this experiment is an improvement over the previous coating utilized in Ref. 1. This coating has substantially improved UV transmission at 257 nm, is photocurable allowing the coating to be applied in a conventional fiber draw tower, and has higher tolerance to photodarkening upon exposure to 257 nm continuous-wave (CW) light (at

intensities required for grating writing). The coating was ~55 μm thick and has mechanical properties similar to current production coatings.

We used a photosensitive fiber [3] doped with about 5 mole% GeO_2. Note that the fiber's germanium level and mode field diameter are compatible with communication grade fiber making low-loss splices possible. The grating writing setup is shown in Fig.1 and consisted of a CW frequency-doubled Ar^+ laser operating at 257 nm, a 10x telescope to increase the beam size, a 25 cm focal length cylindrical lens, a moving mirror and a phase mask. The fiber was deuterium-loaded with about 2.0 % D_2 [4].

Figure 2 shows the transmission spectrum of a ~40 dB fiber Bragg grating written through the coating. The spectrum is relatively clean, the small amount of fine structure seen at short wavelengths may be due to the fact that the grating was not apodized. The overall spectral shape indicates minimal distortion by the coating of the diffracted UV interference pattern. The grating was written using 45 mW of 257 nm light focused to a ~3 mm line and scanned uniformly over a 30 mm length in 1200 seconds. The calculated index change assuming a uniform exposure is > $1x10^{-4}$. We also wrote a second Bragg grating under similar conditions except that the scan time was reduced to 500 seconds and the power increased to 50 mW. This grating measured 36 dB in transmission. Mechanical strength measurements indicate that the fiber is comparable in strength to standard communications fibers and that the grating writing process does not degrade the strength. In addition, visual inspection of the coating and the phase mask after UV exposure showed no observable damage.

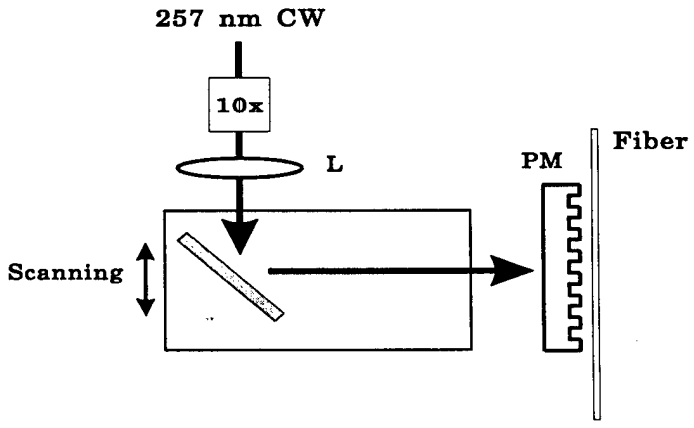

Figure 1. Experimental setup for writing Bragg gratings.

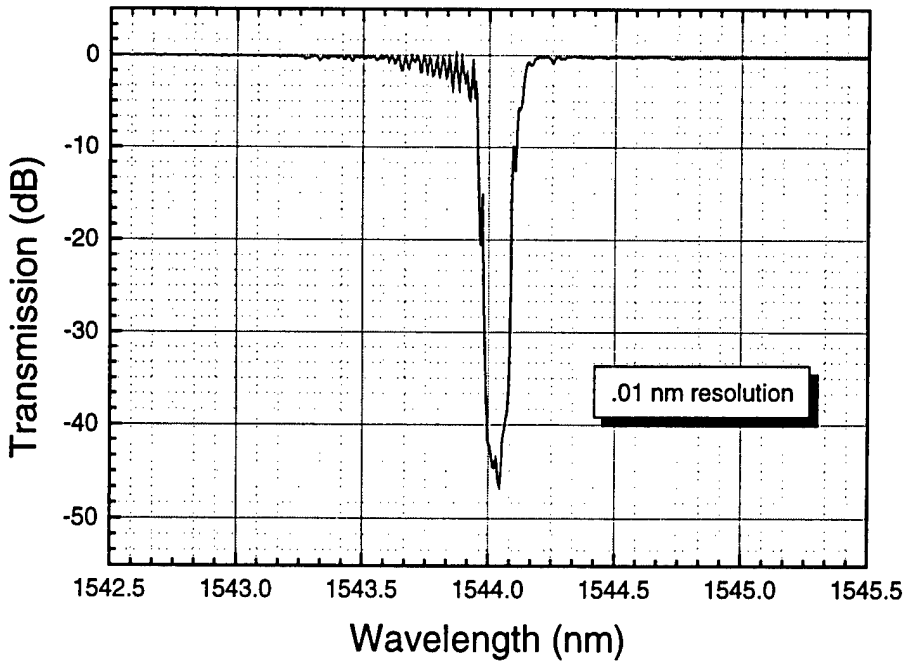

Figure 2. Transmission spectrum of a 30 mm long fiber Bragg grating written through a ~55 μm thick novel polymer coating using 45 mW of 257 nm light. The measurement was performed using a extended cavity laser.

In summary, we report for the first time highly reflective photoinduced fiber Bragg gratings were written through a ~55 μm thick novel UV transparent fiber coating. Bragg gratings with reflectivity in the order of 99.99% (~40 dB in transmission) for a 30 mm long grating were written in a coated deuterium-loaded photosensitive fiber. These results show that it is possible to develop an optically homogeneous polymer coating which is not only sufficiently transparent to 257 nm light to allow writing of gratings, but also does not distort the diffracted interference pattern, even when the grating is scanned over a 30 mm length.

Acknowledgments

We thank A. M. Vengsarkar, S. Cabot and P. J. Lemaire for their assistance in this work.

References

[1] R. P. Espindola, R. M. Atkins, D. A. Simoff, K. T. Nelson, and M. A. Paczkowski, "Fiber Bragg gratings written through a fiber coating," OFC'97 Tech. Dig. , 1997, paper PD-4.

[2] D. S. Starodubov, V. Grubsky and J. Feinberg, "Efficient Bragg grating fabrication in a fibre through its polymer jacket using near-UV light," *Electron. Lett.*, 1997, **33**, pp. 1331.

[3] R. M. Atkins, K. T. Nelson, and K. L. Walker, "Photorefractive Optical Fiber," US Patent 5157747.

[4] P. J. Lemaire, R. M Atkins, V. Mizrahi,, and W. A. Reed, "High Pressure H_2 as a technique for achieving ultrahigh UV photosensitivity in GeO_2 doped optical fibers," *Electron. Lett.*, 1993, **29**, pp. 1191.

Recoated temperature-insensitive long-period gratings

Anatoli A. Abramov, Arturo Hale and Ashish M. Vengsarkar
Bell Laboratories, Lucent Technologies
700 Mountain Avenue, Murray Hill, NJ 07974

Introduction

Long-period gratings are now being used as gain equalizers in broadband amplifiers [1] and as band-rejection filters in a variety of applications.[2] While these devices provide elegant in-fiber solutions to many problems in fiber communications, they can exhibit high temperature sensitivities if sufficient care is not taken in their design. When written in conventional communication-grade fibers, their spectra can shift by 4 - 10 nm per 100°C change in temperature. Two solutions to this problem have been successfully demonstrated using specially designed fibers, one based on tailoring the fiber refractive index profile [3] and the other based on the use of appropriate dopant materials in the core.[4] In this paper, we present long-period gratings written in conventional communication-grade fibers that use the properties of a specially-designed polymer recoat to provide the temperature-independent performance.

Principle of operation

Gratings operate on the principle that the induced periodic index changes match the phase difference between two spatial modes in a fiber. This coupling takes place at a peak wavelength λ_p, given by the phase matching condition, $\lambda_p = (n_{01} - n_{lm})\,\Lambda$, where Λ is the period of the grating and n_{01} and n_{lm} are the effective indices of the fundamental mode and the LP_{lm} modes, respectively. By differentiating the above equation, one can write,[5]

$$\frac{d\lambda_p}{dT} = \Lambda \cdot \frac{(\Delta n)^2}{\Delta n_g} \cdot \left(\frac{1}{(\Delta n)} \cdot \frac{d(\Delta n)}{dT} + \alpha \right), \qquad (1)$$

where α is the thermal expansion coefficient of the glass, Δn is the difference in effective indices ($\Delta n = n_{01} - n_{lm}$), and Δn_g is the difference in the group indices of the modes ($\Delta n_g = \Delta n - \lambda\, d(\Delta n)/d\lambda$). The effective index of a mode is determined by the refractive indices of the central core and all adjacent cladding layers. In our analysis, the polymer coating that surrounds the fiber is modeled as one of the cladding layers. The region surrounding the cladding contains some of the power of the LP_{lm} mode and both n_{lm} and dn_{lm}/dT ($= \partial n_{lm}/\partial n_p \times \partial n_p/\partial T$) are predominantly controlled by the material properties of this region, namely, by n_p and $\partial n_p/\partial T$,where n_p is the refractive index of the polymer material. We now have three design variables: *i)* the choice of the cladding mode (which can lead to different values of $\partial n_{lm}/\partial n_p$), *ii)* the absolute value of the refractive index of the polymer n_p (which dictates the spread of the cladding mode into the coating and hence affects $\partial n_{lm}/\partial n_p$), and *iii)* the temperature dependence of the refractive index of the polymer, $\partial n_p/\partial T$. Our design rule is to choose the right combination of the above three variables to satisfy the condition, $d(\Delta n)/dT = -(\Delta n)\alpha$, thus making $d\lambda_p/dT \rightarrow 0$ in Eq. (1). The design procedure comprises two steps. First, the mode is chosen using standard waveguide equations. Having evaluated the modal spread into the coating, we then choose the coating material using the relation,[6]

$$\partial n_p/\partial T = -[(n_p^2 + 2)(n_p^2 - 1)/6n_p]\,\alpha', \qquad (2)$$

where α' is the volumetric thermal expansion coefficient of the polymer. We have used amorphous polymers in the $\partial n_p/\partial T$ range of -2 to -4×10^{-4} /°C, with a glass transition temperature below the device-use temperature and with a refractive index lower than that of the glass cladding.

Results

Long-period gratings ($\Lambda = 260\ \mu m$) were written in a commercially available dispersion-shifted fiber. At room temperature, the peak wavelengths of coupling between the

fundamental LP_{01} mode and two cladding modes were measured to be 1573 nm and 1434 nm. With no coating, the temperature dependence of the peak wavelengths for the two modes was measured to be 6 and 4.8 nm/100°C, respectively. This grating was recoated, using a uv-curable acrylate-based polymer with a refractive index of 1.31 and a $\partial n_p/\partial T$ of $\approx -2 \times 10^{-4}$ /°C. The recoated grating was then temperature cycled between 20 and 60°C, giving temperature sensitivities for the two modes of −1.2 and + 0.4 nm/100°C. This behavior is depicted in Fig. 1. Figure 2 shows the spectra for one mode with and without the coating. The reduction of the temperature dependence by a factor of ten and the reversal of polarity indicate that the polymer can be designed to completely eliminate the temperature dependence of a grating written in a conventional communication grade fiber

Conclusion

We have shown that the proper choice of a polymer coating eliminates the temperature sensitivity of long period-gratings written in conventional dispersion shifted fibers. We have demonstrated an order of magnitude decrease of temperature sensitivity in recoated long-period gratings.

References

1. A. M. Vengsarkar *et al.*, Opt. Lett. vol. 21, p. 336, 1996.
2. A. M. Vengsarkar *et al.*, J. of Lightwave Technology, vol. 14, p. 58, 1996.
3. J. B. Judkins *et al.*, OFC '96, Postdeadline Papers, PD1-1, 1996.
4. K. Shima, *et al.*, Proc. OFC '97, Paper FB2, p. 347, Dallas, Texas, February 1997.
5. A. M. Vengsarkar, "Long period fiber gratings", *this issue*, Paper BSuB1.
6. L. Bohn, in "Polymer Handbook," J. Brandrup and E .H. Immergut, Eds., Second Edition, Wiley, p. III-241, 1975.

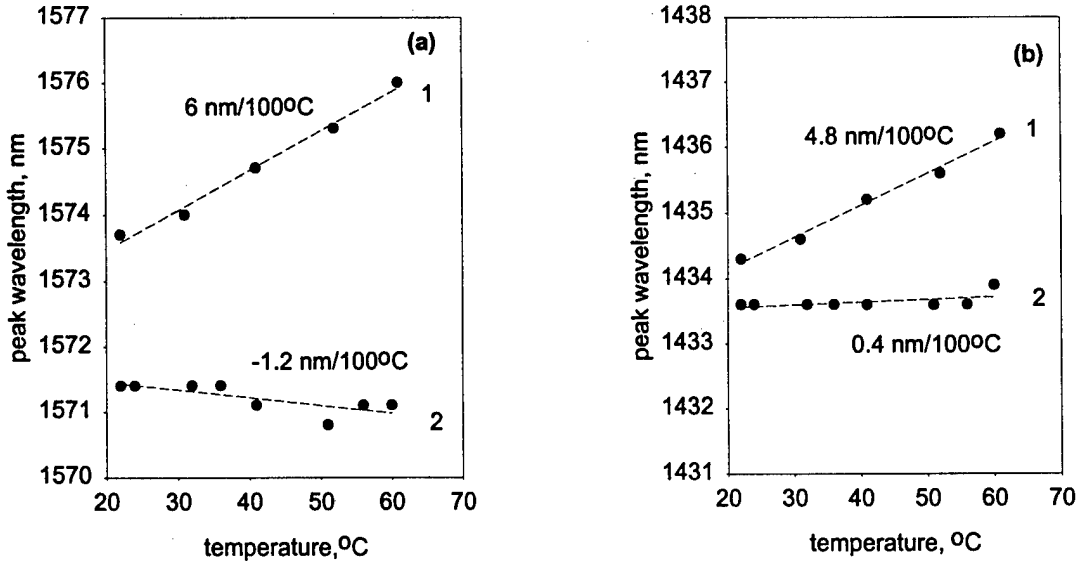

Fig.1. Temperature shifts of peak wavelengths in bare (1) and recoated (2) gratings for two different modes (a,b).

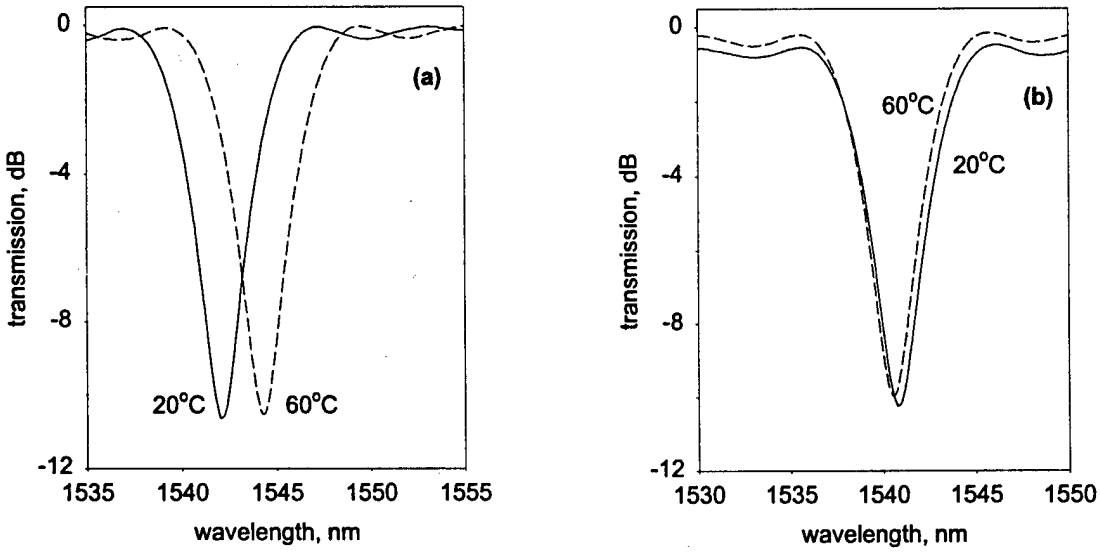

Fig.2. Temperature variation of the transmission spectra for bare (a) and recoated (b) gratings.

Improved Efficiency Narrow-Band Acoustooptic Tunable Reflector using Fibre Bragg Grating

W.F. Liu, L. Dong, L. Reekie, D.O. Culverhouse
Optoelectronics Research Centre, University of Southampton, Southampton SO17 1BJ, UK

P.St.J. Russell
Optoelectronics Group, Department of Physics, University of Bath, Claverton Down, Bath BA2 7EB, UK

All-fibre versions of bulk devices are very attractive in fibre systems where low insertion loss is always desirable. We have greatly improved the performance of a recently reported [1] Bragg-grating-based acousto-optic superlattice modulator (AOSLM) by reducing the fibre diameter by HF etching. This improves the overlap of acoustic and optical power, resulting in modulator efficiencies as high as 90%. The modulator produces narrow-band amplitude-adjustable reflections that can be tuned over several nm, which is attractive for WDM and laser applications. In the device, an extensional acoustic wave is launched along a fibre Bragg grating. The ensuing superlattice modulation causes additional bands of reflection to appear on both sides of the Bragg condition. The device works by coupling together the forward and backward propagating Bloch modes in the grating (a principle first proposed in 1986 [2,3]) and operates in *reflection mode*. This differentiates the AOSLM from all previously reported acousto-optic fibre devices, which all rely on intermodal coupling, examples being LP_{01} to LP_{11} coupling in dual-mode [4] and twin-core [5] fibres, four-port null-couplers [6], polarisation mode couplers in Hi-Bi fibre [7] and guided-to-cladding mode coupling in standard telecom fibre [8]. In all these devices the intermodal beat length $L_B = \lambda/(n_1 - n_2)$ at optical wavelength λ between two modes with phase indices n_1 and n_2 is matched by the acoustic wavelength v_s/f_s where v_s and f_s are the acoustic phase velocity and frequency.

When an acoustic wave is launched along a fibre Bragg grating, narrow-band frequency-shifted reflections appear on either side of the Bragg condition. These can be regarded as the consequence of side-bands in spatial frequency ("ghost" gratings) which form in a periodically phase-modulated Bragg grating:

$$\varepsilon = n_0^2\left(1 + M\cos\left[Kz + \frac{Ks_o}{k_s}\sin(k_s z)\right]\right)$$

where $K = 2\pi/\Lambda$ is the Bragg grating vector (Λ being its pitch), k_s is the acoustic wavevector and $s_o = \sqrt{2P_s/(EAv_{gs})}$ is the peak strain induced by an acoustic wave of power P_s in a fibre of cross sectional area *A*, Young's modulus *E* and acoustic group velocity v_{gs}. The mean phase index of the optical guided modes is n_o.

Provided they are not too strong, these "ghost" gratings will have an effective bandwidth which equals that of a weak grating of the same physical length *L* as the

---

Present address: Corning Inc., Corning, N.Y. 14831, USA

Bragg grating, i.e., $\Delta\lambda_{opt} = 1.39\lambda^2/(\pi L n_o)$. The distance of their reflection maxima from the main Bragg peak is given approximately by:

$$\frac{c\Delta\lambda}{\lambda^2} \approx \Delta\nu = \frac{mcf_s}{2n_o v_s}$$

where m is the side-band order. This expression neglects the dispersion of the Bloch waves, which is very strong near the stop-band edges.

A guided mode, incident on a Bragg grating carrying a counter-propagating acoustic wave, is reflected into a counter-propagating mode with a frequency shift $\pm f_s$, which is *positive* on the short wavelength side ($\lambda < \lambda_B$) and *negative* when $\lambda > \lambda_B$. Thus the Doppler shift is sometimes reversed. As reported in [8], the superlattice reflection efficiency in the first side-band takes the approximate form:

$$\eta = \tanh^2\left[\kappa L \, J_1\left(\frac{Ks_o}{k_s}\right)\right] = \tanh^2\left[\kappa L \, J_1\left(\frac{\lambda_s}{\Lambda}\sqrt{\frac{2P_s}{EAv_{gs}}}\right)\right]$$

where κ is the coupling constant of the Bragg grating. For given drive power, the efficiency can be improved by minimising the fibre cross-sectional area A. This has the effect of increasing the acousto-optic overlap. We have achieved this by HF etching away the cladding glass and thus reducing its overall diameter. A substantially improved the device performance results.

The experimental set-up of the device is shown in figure 1. A planar piezoelectric transducer is bonded to the base of a fused silica horn, the point of the horn being fusion-spliced to the fibre. Electrical drive powers of up to a few hundred mW were applied. The single side-band purity of the frequency-shifted signal was tested by splitting the light from a tunable single frequency diode laser into two paths. One was frequency shifted by an 80 MHz Bragg cell, and the other was directed at the superlattice modulator. The signal reflected from the superlattice modulator was then mixed at a square-law detector with the 80 MHz shifted signal. As reported in [8], excellent single-side-band purity was obtained in all cases.

The reflection spectrum of the AOSLM with and without acoustic power was measured (Figure 2) using a broad band LED as source. Notice that, in addition to the two strong side-bands, two additional weak reflection bands are apparent. These are caused by higher order "ghost" gratings and are further confirmation of the strength of the superlattice effect. First side-band AOSLM reflectivities as high as ~90% have been obtained in a fibre etched to a final diameter of ~30 μm, the acoustic frequency being ~10 MHz. The grating had an index modulation of 10^{-3} (yielding $\kappa = 4\ \text{mm}^{-1}$) and its length L = 3 mm. The tuning of side-band position with acoustic frequency (in a 10% device) is shown in figure 3, together with the theoretical prediction. Tuning over 2 nm is achieved for acoustic frequencies between 4 MHz and 15 MHz.

In conclusion, we report a highly efficient AOSLM using a fibre Bragg grating with an etched-away cladding. This device can function as an efficient frequency shifter in reflection mode with adjustable reflectivity. The optical bandwidth for the current device is in the region of ~0.2 nm. The turn-on and turn-off time of such device is limited by the propagation time of the acoustic wave in the device, which is of order 500 nsec for the current 3 mm long device. This suggests applications to Q-switching of fibre lasers at rates of up to a few MHz. The device can also act as a

tunable filter, a switch and an amplitude modulator.

References

1. W. F. Liu, P.St.J. Russell and L. Dong, Opt. Lett. **22** 1515 (1997)
2. P.St.J. Russell, J. Appl. Phys. **59** 596 (1986).
3. P.St.J. Russell, J. Mod. Opt **38** 1599 (1991).
4. B.Y. Kim, J.N. Blake, H.E. Engan and H.J. Shaw, Opt. Lett. **11** 389 (1986)
5. H. Sabert, L. Dong and P.St.J. Russell, Int.J. Optoeiectronics **7** 189 (1992).
6. Reviewed in: T.A. Birks, D.O. Culverhouse and P.St.J. Russell, J. Lightwave Techn. **14** 2519 1996
7. M. Berwick, C.N. Pannell, P.St.J. Russell and D.A. Jackson, Elect. Lett. **27** 713 (1991).
8. H.S. Kim, S.H. Yun, I.K. Hwang, B.Y. Kim, Optical Communications Conference, PD7 (1997).

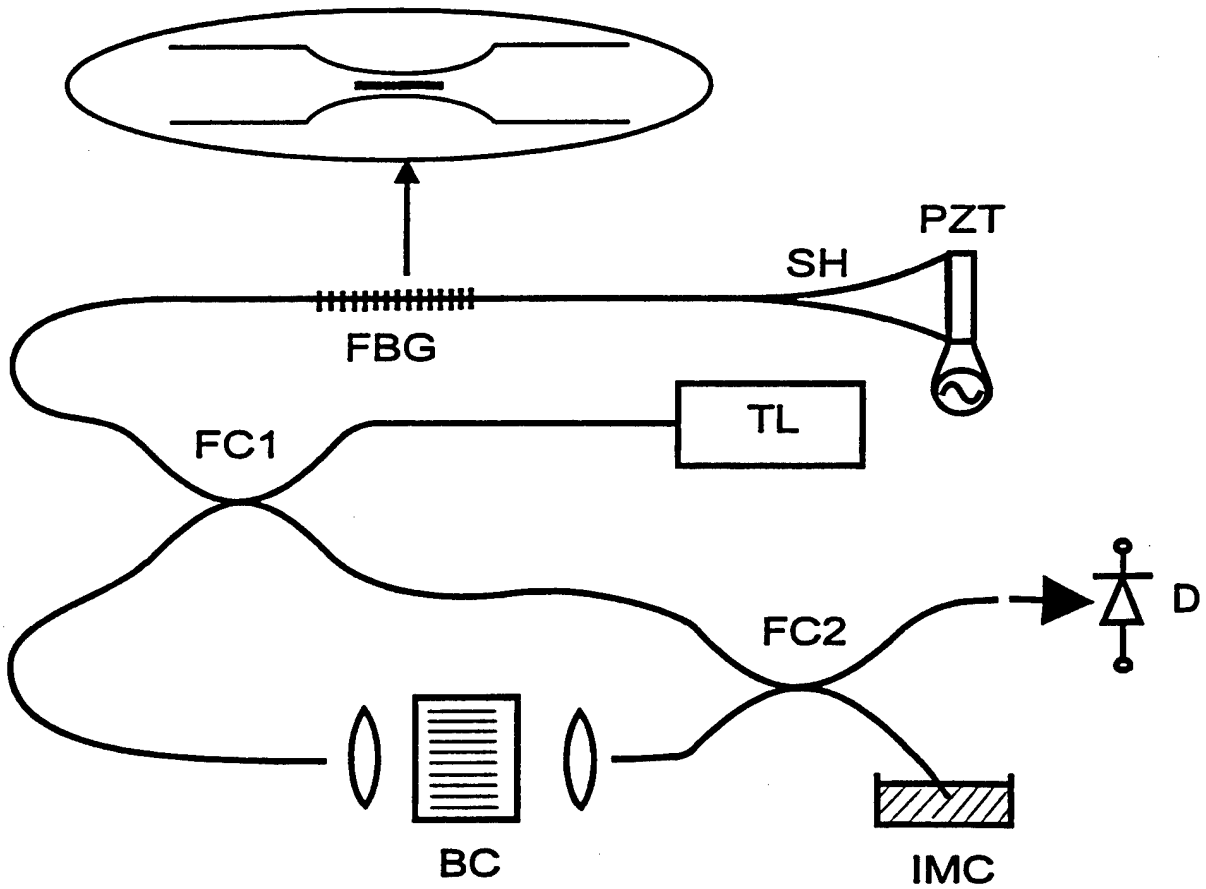

Figure 1 Experimental set-up. TL: tunable single frequency diode laser. D: square-law detector. SH: silica horn. FBG: fibre Bragg grating. FC: 3 dB fused coupler. BC: Bragg cell. IMC: Index matching fluid.

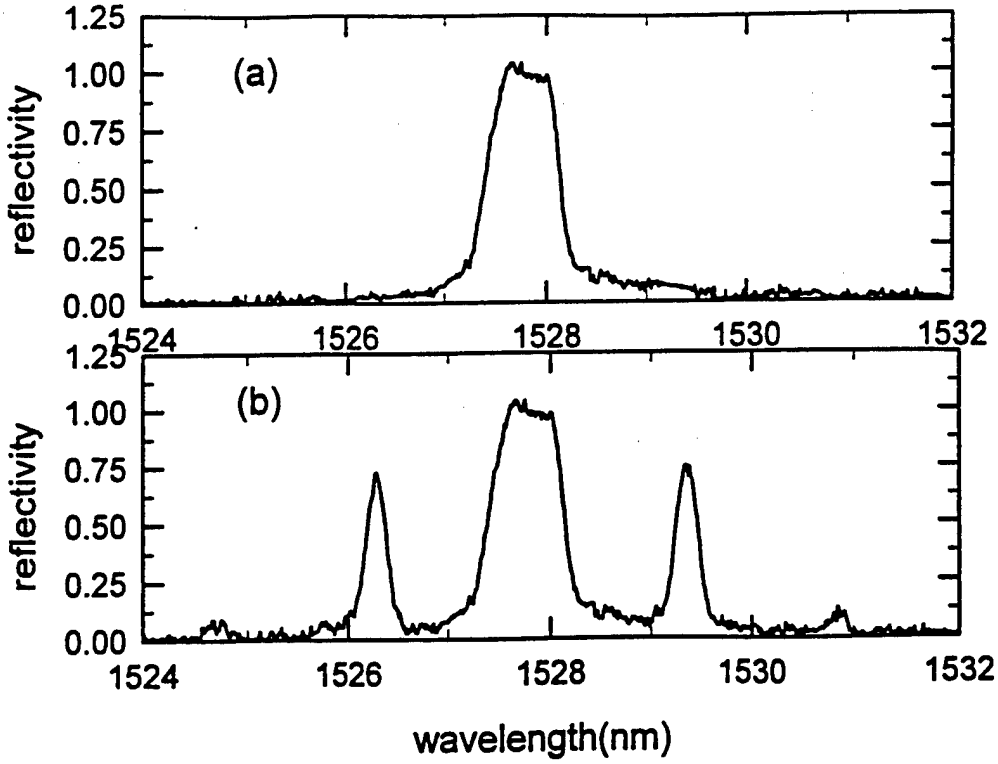

Figure 2 The reflection spectrum of the original grating (top) and that of the grating with acoustic wave applied (bottom).

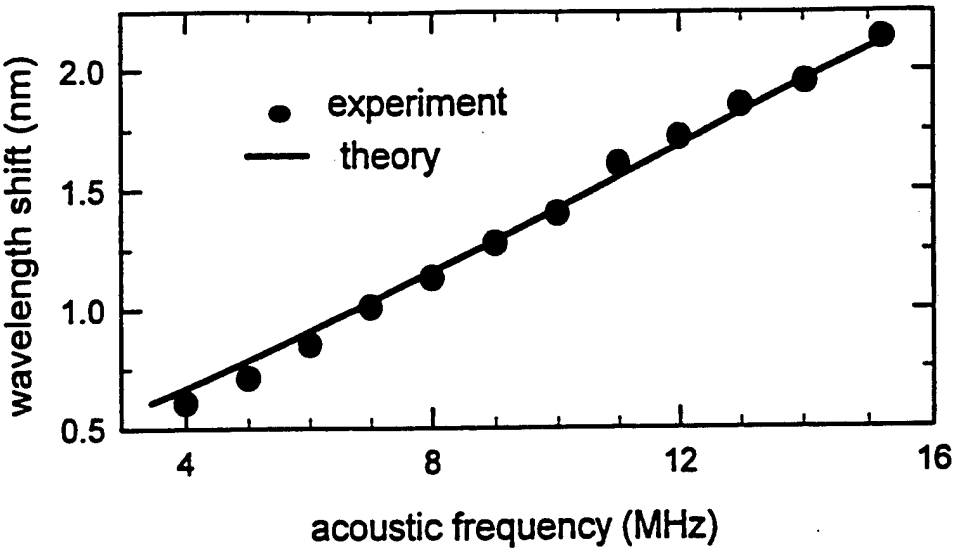

Figure 3 Position of the first order side-lobe as a function of acoustic frequency. The line is the theoretical prediction.

Experimental and theoretical study of the origin of the second-order nonlinearities induced in thermally poled glasses.

A. Le Calvez, E. Freysz, A. Ducasse.

Centre de Physique Moléculaire Optique et Hertzienne
Université de Bordeaux I
351, cours de la libération, 33405 Talence
Tel: (33) 5 56 84 83 13 Fax: (33) 5 56 84 69 70
Email: lecalvez@frbdx11.cribx1.u-bordeaux.fr

To model the poling process, the glass is assimilated to a neutral "solid electrolyte". During the poling process, an electric voltage V_0 is applied between the cathode and the anode respectively located at x=0 and x=L. The evolution of the ion concentrations is then described by a system of coupled equations containing the equations of diffusion for the different ionic species and Laplace's equation. Since in fused silica, at about 300°C, it is mainly sodium ions, which are mobile, the anions are assumed to be immobile[1]. According to these approximations and under usual poling conditions (T≈300°C, V_0≈3kV), we computed the expression of the potential across the sample during the poling. On Figure 1, we have plotted the potential V(x), the charge distribution $\rho(x)$ and the associated electric field E(x) for a typical silica sample. Since the screening distances d_1 and d_2 at the cathode and the anode are much smaller than the sample thickness, the electric field $E(x)\sim V_0/d_2\sim 10^8$ V/m at the glass interfaces is very high. The asymmetry between the anodic and cathodic sides results from the assumed immobility of the anions. We have noticed that the temperature T disappeared from the expressions of V(x), of d_1 and d_2, so T does not seem to play any role in the steady-state regime. However, by applying the Von Hippel et al. Method[2], we obtained the time necessary to reach the steady state: $\tau(T) \propto \exp\left[E_a^{Na+}/kT\right]$ where k is the Boltzman constant and E_a^{Na+} (~1.12 eV) is the activation energy for Na^+ in fused silica. This time is strongly dependent on the temperature: for example, τ(25°C)~15000 years while τ(300°C)~1 minute when V_0~3kV. Therefore, temperature may be seen up to now as being only a kinetic

parameter of the poling problem but with no influence on the amplitude of the electric field created.

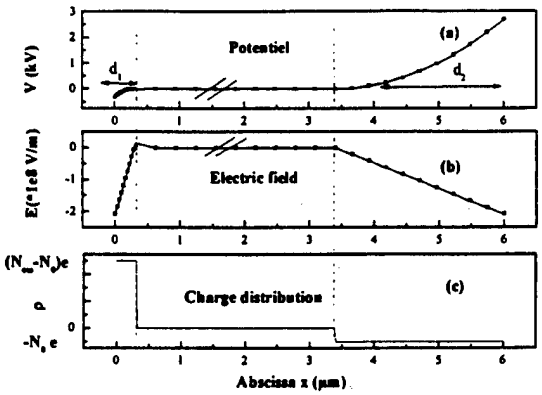

Fig. 1: Profiles of the potential V(x) (**a**), the electric field E(x) (**b**) and of the charge distribution ρ(x) (**c**) in the sample at high temperature (T=300°C) and under high voltage (V_0=3kV). The glass is assumed to contain N_0=3 ppm of Na^+ ions and a number of available sites $N_{cm}=10N_0$. The continuous line stand for the analytical and numerical results respectively

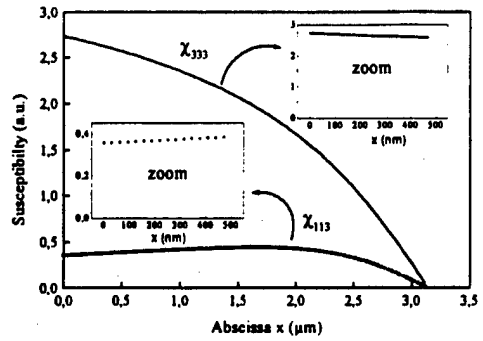

Fig. 2: Second-order susceptibility $\chi^{(2)}_{333}$ and $\chi^{(2)}_{311}$ resulting from the reorientational mechanism, as a function of depth in the sample on the anodic side. The glass is assumed to have N_0=2 ppm of sodium impurities with $N_{cm}=10N_{c0}$. The poling conditions are T=300°C, V_0=3kV. The reoriented dipoles are assumed to have a permanent dipole moment μ=10 Debyes.

Since during poling the electric field E(x) is non-null only close to the interfaces, any reorientation by this field of the dipoles of eventual hyperpolarizable entities could occur only in these regions. Therefore, the existence of the mechanism $\chi^{(2)}_d$ should be characterized by a location of the SH signal at the sample interfaces. On Figure 2, we have plotted the evolution of the induced nonlinearity when one considers the reorientation mechanism alone. Knowing, the charge distribution ρ(x) frozen in the sample, the induced permanent electrostatic field $E_0(x)$ can be determined by using the Gauss theorem. However, the induced electrostatic distribution ρ(x) is unstable in ambient air and may be screened by charges present in the air. According to the screening rate, the amplitude of $E_0(x)$ is shifted. In any respect, the electric field induced is again high ($E_0 \sim V_0/d_2 \sim 10^8$V/m). Then, the location in the sample of the induced effective second-order susceptibility $\chi^{(2)}_{eff}(x) = \chi^{(3)} E_0(x)$ depends on the screening rate: in the absence of screening, this nonlinearity is induced in the bulk of the glass, while for a total screening, only the interfaces over distances d_1 and d_2 contribute to $\chi^{(2)}_{eff}(x)$. The poling symmetry implies that only two elements of the tensor $\chi^{(2)}$ ($\chi^{(2)}_d$ or $\chi^{(2)}_{eff}$) are non-null

and independent: $\chi^{(2)}_{333}$ and $\chi^{(2)}_{311}$ (where axis 3 is parallel to the poling direction). An important difference between the two mechanisms comes from the value of $R_\chi = \chi^{(2)}_{333}/\chi^{(2)}_{311}$ since, for a frozen-in electric field mechanism, this ratio is equal to 3 in an isotropic medium[3] while for oriented dipoles, it depends on the parameter $a(x) = \mu E(x)/kT$ with μ the dipole moment of the hyperpolarizable entities present in the glass (Fig. 2).

Poling was carried out with brass contacting electrodes. The 1.2 mm and 5 mm thick samples of commercial fused silica (Vitreosil, Herasil which are known to contain a few ppm of Na^+ impurities) where poled in ambient air at 300°C and 2.7 kV at least 30 mn in order to reach the steady-state regime. The nonlinearity induced in these poled glasses were studied by an original Second harmonic generation (SHG) set-up using a continuous mode-locked Ti:sapphire oscillator. This set-up which has a great linearity of the harmonic signal (from 10 up to 30.10^6 photons/s) allows to achieve spectral Maker fringes experiment which is the equivalent of the spatial Maker fringes experiments and which can be performed in a single shot experiment by measuring the spectrum of the generated femtosecond harmonic pulses. The SHG experiments where carried out in transmission and in reflection to study both the bulk and the surface of the samples. To verify the symmetry of the induced second-order susceptibility, we detected the harmonic intensities for different angles or polarization configurations. The experimental results confirmed the expected symmetry. To probe the location of the induced non linearity, we have performed several bulk SHG experiments (in transmission with variable angle of incidence, perpendicularly to the poling direction,...). All these experiments conclude in favor of a nonlinearity induced over a distance shorter than the length of coherence on the anodic side of the samples. However according to our model, the nonlinearity should have been created on both sides of the sample on distance d_1 at the cathode and d_2 on the anode. Yet it is important to note that since the predicted distance d_1<500 nm is much smaller than the distance d_2 ~3μm, the SH signal generated by the cathodic region (S_{cat}) must be much smaller than the signal generated by the anodic region $S_{ano}/S_{cat} \sim (d_2/d_1)^2$. Therefore to detect an eventual nonlinearity induced on the cathodic side, we used an SHG experiment in reflection. In such a surface-specific technique, the depth probed in the sample is about the surface length of coherence (l_c^s=500nm for silica) whatever the interface (cathodic or anodic) studied. Since for this configuration the SH signal in reflection was too weak, we used more energetic pulses from a Ti:sapphire regenerative amplifier working at 1 kHz. The experiment revealed harmonic signals of comparable

amplitudes on both the anodic and cathodic interfaces. This signal disappeared after depoling of the glass. The ratio between the reflected [pp] and [sp], where the first (resp. the second) index denotes the s-or p-polarization of the fundamental (resp. the harmonic) wave, signals was n_R~1. The intensity recorded was calibrated against the SH reflected [ss] signal generated by a quartz crystal. The surface nonlinearities revealed by this experiment agree with our model and are consistent with either the reorientational mechanism or the frozen-in electric field with external charge screening. To get further information, we studied the ratio R_χ between the non-null independent elements. By considering a spatial homogeneous nonlinearity over the surface length of coherence (~500nm) in the glass samples it was possible to estimate the surface induced nonlinearity: $\chi^{(2)}_{333} \approx 0.93$ pm / V and $\chi^{(2)}_{113} \approx 0.13$ pm / V . The experimental ratio R_χ ~7 is in agreement with the theoretical ratio for a 2 ppm sodium sample concentration and considering non linearity results from reoriented entities with a dipole moment μ~10 Debyes (Fig. 2). On the other hand, to confirm that this contribution is predominant, an estimation of the frozen in electric field contribution is necessary. The third-order susceptibility $\chi^{(3)}_{3333} \approx 1.8\ 10^{-22}$ m^2V^{-2} of our samples was measured by an optical Kerr effect experiment and calibrated against a glass of SF59. Then by assuming against a sodium concentration of about 2 ppm and under our poling conditions, we estimated the static electric field $E_0(x)$ ($E_0(x=0)$~2.10^8 V/m). $E_0(x)$ decreases linearly from this value to 0 over d_1 and d_2. This led to an average $\chi^{(2)}_{eff}$ ~ 0.07 pm/V on the anodic side. This comparison between $\chi^{(2)}_{eff}$ and $\chi^{(2)}_{d}$ shows that the nonlinearity associated with the dc-Kerr effects is negligible in fused silica.

In summary, we have proposed a model for the occurrence of the second-order nonlinearities induced in thermally poled glasses. It is confirmed by our SHG experiments. SHG in reflection revealed the existence of the nonlinearity on both anodic and cathodic side of the sample, demonstrate the reorientational mechanism and make it possible to evaluate the dipole moment μ (~10 Debyes) of the reorientable moieties.

REFERENCES:

1. N. Mukherjee, R. A. Myers, S. R. J. Brueck, J. Opt. Soc. Am. B, **11**, 665 (1994).

2. A. Von Hippel, E. P. Gross, J. P. Jelatis, M. Geller, Phys. Rev., **91**, 568 (1953).

3. S. Kielich, IEEE J. Quantum Electron. QE-5, 562 (1969).

Strong Bragg Gratings Induced with 248 nm Light in Buried Silicon Oxynitride Waveguides

Jörg Hübner, Dorothea Wiesmann#, Roland Germann*, Bert J. Offrein*, and Martin Kristensen
Mikroelektronik Centret, Technical University of Denmark, DK-2800 Lyngby, Denmark
Electronics Laboratory, ETH Zürich, CH-8092 Zürich, Switzerland
* IBM Research Division, Zürich Research Laboratory, CH-8803 Rüschlikon, Switzerland

Abstract: Highly temperature-stable, 33-dB Bragg gratings have been induced in germanium-free silicon oxynitride waveguides. A fringeless pre-exposure is necessary to photosensitize the deuterium-loaded samples.

Introduction: The importance of phase gratings written by ultraviolet light [1] into buried waveguides and fibers is ever increasing because of their wide range of applications as wavelength selective filters, for gain flattening, and as sensors. To decrease the size of integrated optical devices, planar waveguides with a nitrogen-doped silica core are advantageous because doping with nitrogen allows the refractive index of SiO_2 to be raised to considerably higher values than doping with germanium. High-contrast planar waveguides allow excess-loss-free bending radii that are at least 10 times smaller than those of germanium-doped silica optical waveguides [2]. Compact, integrated optical devices and high component densities on the wafer can be achieved this way. In this paper we present for the first time to our knowledge substantial photosensitivity of germanium-free SiON planar waveguides towards 248-nm excimer laser light. We are able to induce refractive index changes as high as 1.4×10^{-3} and index modulations one order of magnitude larger than that in germanium-free SiON fibers induced by a comparable wavelength of 244 nm [3]. A large number of possible applications of almost arbitrarily shaped UV-written gratings can now be exploited in SiON waveguides. This introduces the possibility of combining the compactness of SiON waveguide structures with short Bragg gratings as wavelength-selective elements to make wavelength-division-multiplexing (WDM) network devices.

Experimental: The SiON waveguides were produced using plasma-enhanced chemical vapor deposition (PECVD) and reactive ion etching (RIE). The ridge waveguide core has a refractive index of 1.50 at 1550 nm and its dimensions are about 3 μm x 2 μm. To remove the residual hydrogen in the glass, the waveguides were annealed at 1145 °C in a nitrogen atmosphere and were subsequently covered by a 5-μm SiO_2 cladding [2]. To enhance photosensitivity analogous to the behavior of germanosilicate waveguides [4], the samples were loaded with deuterium at room temperature under a pressure of 130 bar for seven days prior to UV exposure. Photosensitisation with deuterium alone was found to be insufficient for writing strong Bragg gratings in these waveguides. A maximum transmission dip of about 2.5 dB was achieved using standard deuterium loading and high UV fluences at 248 nm, which were very close to the damage threshold of the waveguide material. To increase photosensitivity, a fringeless pre-exposure step was introduced, in which the samples were exposed to low fluence of 248-nm light upon removal from the deuterium chamber. After the pre-exposure step, the samples stayed photosensitive for at least a couple of days at room temperature, indicating that the deuterium was incorporated into the glass matrix. For the Bragg grating exposures we used a zero-order nulled phase mask placed directly on the sample. No visible fluorescence was detected during either of the two exposures. The Bragg gratings were measured in transmission and reflection using an erbium broadband source and an optical spectrum analyzer (OSA). For characterization with polarized light, a polariser and a polarization controller were inserted into the light path. The extinction ratio between the two polarisations was found to be around 35 dB.

Figure 1 shows transmission spectra taken with TM-polarized light for four simultaneously exposed waveguides of the same width separated by 125 μm. We used 20000 pulses with an average fluence of 600 mJ/cm^2 per pulse, which resulted in a transmission dip of greater than 30 dB for the strongest grating. The gratings are only 8 mm long.

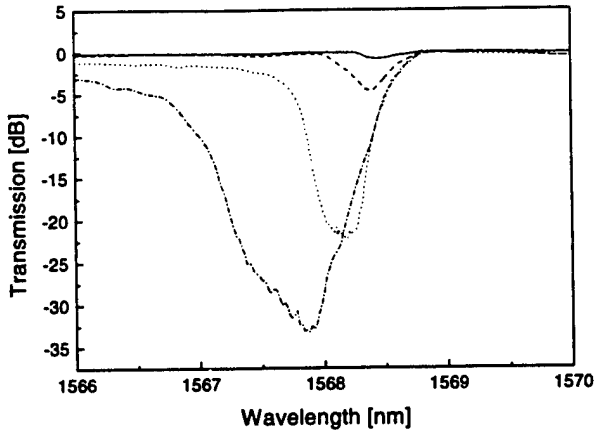

Figure 1 8-mm-long gratings in SiON waveguides simultaneously written with different UV intensities but same pulse numbers. The maximum transmission dip is greater than 30 dB.

The Bragg wavelength shifts to the left for increasing grating strength, indicating a negative index change.

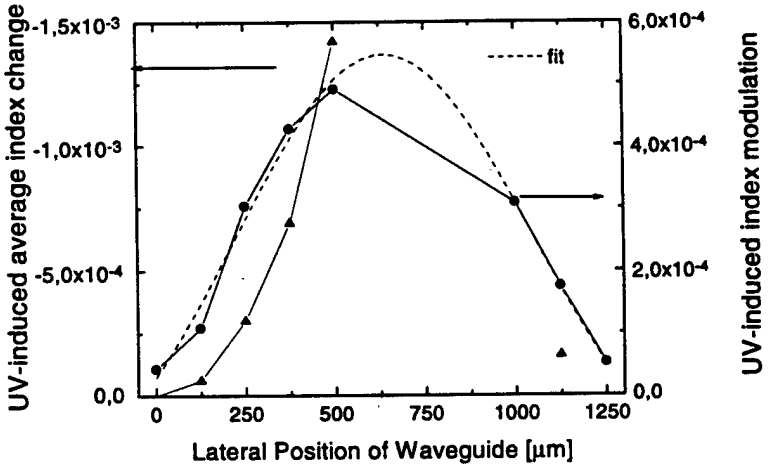

Figure 2 UV-induced average index change (up to $1.4x10^{-3}$) and UV-induced index modulation (up to $5x10^{-4}$) for a set of simultaneously exposed waveguides.

Figure 2 shows the refractive-index modulation of the resulting Bragg gratings (dots) for a set of eight waveguides. The exposure of several waveguides simultaneously allows us to correlate the modulation of the Bragg grating and the average UV-induced index change with the intensity of the excimer light. For the induced uniform Bragg gratings the index modulation can be calculated from the transmission dip, whereas the average index change can be deduced from the shift in center wavelength [5,6]. We assume a negligible shift in center wavelength for a grating with approximately 1 dB transmission dip and therefore use this grating to calculate the effective refractive index of the waveguides. Owing to the Gaussian-like intensity profile of the excimer laser beam transverse to the waveguides, the intensity varies with the waveguide position. The transmission spectra in Figure 1 correspond to the waveguides at the lateral positions of 125, 250, 375 and 500 µm, respectively. We fitted the refractive-index modulation to a Gaussian curve (dashed line) and found good agreement. A monotonic growth of the grating strength with the intensity can therefore be assumed. The maximum induced refractive-index modulation is as high as $5x10^{-4}$. The triangles in Figure 2 show the average UV-induced, refractive-index change for the same set of waveguides. The values for waveguide no. 6 (lateral position 1000 µm) and no. 8 (lateral position 1250 µm) were not included into the plot because the width of these waveguides was not the same,

resulting in different effective refractive indexes. The average effective index change is negative for all exposures, and the observed maximum change is -1.4×10^{-3}.
For applications in WDM networks, UV-induced Bragg gratings require long-term stability. To check the temperature dependence of the gratings we have performed isochronal annealing experiments in which the sample was annealed for 2 h between the measurements. The results are shown in Figure 3 for three initial grating strengths measured with nonpolarised light.

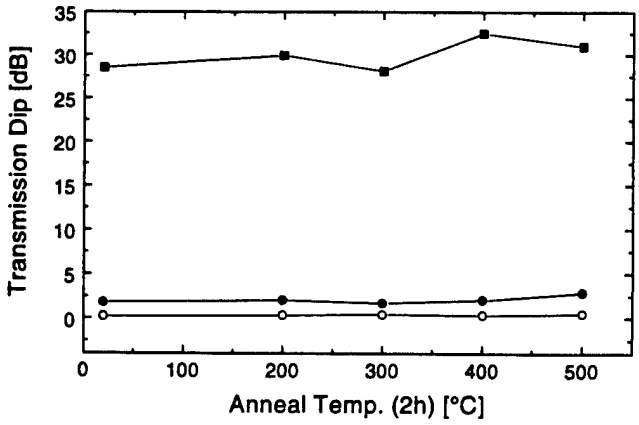

Figure 3 Isochronal anneal of three Bragg gratings. No decrease in grating strength is observed for annealing up to 500 °C.

We find that the grating strength of the weakest grating does not change within experimental accuracy up to a temperature of 500 °C. The grating with an initial transmission dip of 28 dB shows some fluctuations of the grating strength. These fluctuations are due to variations in the overlap of the TE and TM polarization gratings, which results in a stronger transmission dip for nonpolarised light. This also explains the slightly increased grating strength of the 3 dB grating represented by the solid dots in Figure 3. The 0.7 dB gratings are too narrow to be influenced by this effect.
To demonstrate that the gratings might be useful for WDM applications, we wrote an apodised grating using the Gaussian beam profile of the excimer laser, see Figure 4. The grating was measured in transmission and reflection, the latter by using an optical circulator.

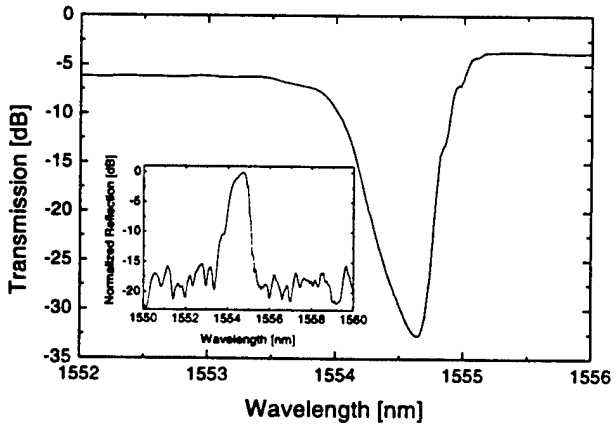

Figure 4 Transmission spectrum of an apodised grating. The inset shows the reflection spectrum.

The background rejection in reflection was measured to be 16 dB. This low value is partly due to the fact that the reflection spectrum was recorded by butt-coupling a standard single-mode fiber to the waveguide facet. The considerable index difference between waveguide and fiber

leads to reflections at the interface. These reflections together with the substantial mode mismatch impede precise background rejection measurements.

Discussion: The initial photosensitivity of SiON material is very low and not sufficient to induce gratings with 248-nm excimer light. Deuterium loading of the sample merely leads to an increase of photosensitivity when the sample is uniformly pre-exposed with 248-nm excimer light immediately after the loading step. A uniform pre-exposure without deuterium loading does not increase the sample's photosensitivity. We therefore assume that the deuterium is incorporated in the glass matrix by a chemical reaction, which requires a dissociation of the D_2 molecule by UV light that is enhanced by the glass matrix. The fact that the pre-exposure is effective only when the sample is exposed to a relatively low fluence (a fraction of the fluence we use to induce the gratings) suggests that the chemical reaction may be reversed by warming up the sample with too high fluences. On the other hand we noticed that the incorporation of deuterium is stable at room temperature for at least a couple of days, a period, during which most of the non-bound deuterium would have diffused out of the sample. This can be explained by a reaction of the deuterium with the glass under low fluences before out-diffusion through the only 5-μm-thick cladding layer can occur. We explain the increased photosensitivity after the pre-exposure step by an increased absorption of 248 nm light owing to the incorporated deuterium. When exposed through a phase mask the increased absorption will cause high temperatures at the locations of the interference maximum, which might result in local structural changes of the core glass or at the core-cladding border. This hypothesis is supported both by the fact that the fluence used for the second exposure is close to the damage threshold of the material and by the high temperature stability even of the very weak gratings. An explanation for the formation of these Bragg gratings based on color centers would not predict such high temperature stability. The fact that the index changes are negative also suggests that there might be a local annealing of the glass, causing NH groups to leave the glass matrix at the locations of the interference maxima.

Conclusion: Strong Bragg gratings with refractive-index modulations up to $5x10^{-4}$ have been induced in SiON waveguides, which initially showed very little photosensitivity towards 248-nm light. A novel method of photosensitizing these materials using a fringeless pre-exposure after deuterium loading has been demonstrated. The advantages of SiON waveguides, especially for making very compact devices can now be combined with the advantages of UV-induced index changes such as Bragg-grating inscription or UV-trimming of interferometric components. The mechanisms of the UV-induced index change in these materials are not yet understood. But there is evidence that an explanation based on structural changes or local annealing of the glass is more likely than one based on color centers.

Acknowledgment: We would like to thank I. Massarek, G.L. Bona, H.W.M. Salemink, and H. Jäckel for helpful discussions. The financial support by the Swiss government (KTI-project) is gratefully acknowledged.

References:

[1] G. Meltz, W. W. Moray, W.H. Glenn and D. J. Fritz: "UV-induced Bragg gratings in optical fibers and thin-film waveguides", SPIE, 1993, vol. 2044, pp. 236-245.

[2] B.J. Offrein, G.L. Bona, R. Germann, F. Krommendijk, I. Massarek, H.W.M. Salemink:"High contrast and low loss SiON optical waveguides by PECVD", Proceedings 1996 IEEE/LEOS Symposium Benelux Chapter, 28. Nov. 1996, Enschede (NL), pp. 290-293

[3] E.M. Dianov, K.M. Golant, R.R. Khrapko, A.S. Kurkov, B. Leconte, M. Douay, P. Bernage, and P. Niay: "Strong Bragg gratings formation in germanium-free nitrogen-doped silica fibers", *OFC '97*, paper PD 5-1.

[4] P.J. Lemaire, A.M. Vengsarkar, W.A. Reed, V. Mizrahi, and K.S. Kranz: "Refractive-index changes in optical fibers sensitized with molecular hydrogen", *OFC '94*, paper TuL1.

[5] C.V. Poulsen, J. Hübner, T. Rasmussen, L.-U.A. Andersen, and M. Kristensen: "Characterization of dispersion properties in planar waveguides using UV-induced Bragg gratings", Electron. Lett., 1995, Vol. 31, (17), pp. 1437-1438.

[6] J. Hübner, M. Svalgaard, L. G. Nielsen, and M. Kristensen: "Phenomenological Model of UV-induced Bragg Grating Growth in Germanosilicate Fibers", SPIE, 1997, vol. 2998, pp, 11-21

Bragg Gratings, Photosensitivity, and Poling in Glass Fibers and Waveguides: Applications and Fundamentals Technical Program Committee

Joe Friebele, *U.S. Naval Research Laboratory, General Chair*

Philip Russell, *University of Bath, U.K., General Chair*

Paul Lemaire, *Lucent Technologies, Specialty Fiber Devices, Program Chair*

Applications

Chair: **Gary Ball,** *Uniphase Telecom Products*

Jean Luc Archambault, *Ciena Corporation*

Vincent Handerek, *King's College, U.K.*

Ken Hill, *Communications Research Center, Canada*

Alan Kersey, *CiDRA Corporation, LIAISON to OFS*

Robert Lieberman, *Physical Optics Corporation*

Graeme Maxwell, *BT Labs, U.K.*

Lawrence Reekie, *University of Southampton, U.K.*

Rene Paul Salathe, *Swiss Federal Institute of Technology, Switzerland*

Ashish Vengsarkar, *Bell Labs, Lucent Technologies*

Gratings

Chair: **François Ouellette,** *Kromafibre Corporation, Canada*

Charles Askins, *U.S. Naval Research Laboratory*

Ian Bennion, *Aston University, U.K.*

Kevin Byron, *Bell-Northern Research, U.K.*

Marc Douay, *University Science and Technology Lille, France*

Turan Erdogan, *University of Rochester*

Gerry Meltz, *OFT Associates*

Pierre Sansonetti, *Alcatel, France*

Fundamentals

Co-chair: **David Griscom,** *U.S. Naval Research Laboratory*

Co-chair: **Susan Houde-Walter,** *University of Rochester*

Jacques Albert, *Communications Research Center, Canada*

Hideo Hosono, *Tokyo Institute of Technology, Japan*

Hiroaki Imai, *Keio University, Japan*

Ulf Osterberg, *Dartmouth University*

Bertrand Poumellec, *U. de Paris-Sud, France*

Krishnan Raghavachari, *Bell Labs, Lucent Technologies*

Alexey Rybaltovsky, *Moscow State University, Russia*

Anatoly Trukhin, *University of Latvia, Latvia*

Poling/SHG

Chair: **R. Stolen,** *AT&T Laboratories*

Steven Brueck, *University of New Mexico*

Simon Fleming, *University of Sydney, Australia*

Raman Kashyap, *BT Labs, U.K.*

Denise Krol, *Stanford University*

Walter Margulis, *PCU-Rio, Brazil*

Jean Michel Nunzi, *Centre d'etudes Nucleaires de Saclay, France*

Hiromichi Takebe, *Kyushu University, Japan*